MINERALOGICAL DISTRIBUTIONS OF RADIONUCLIDES IN COPPER-URANIUM ORES, OLYMPIC DAM, SOUTH AUSTRALIA

Danielle Sierra Schmandt

This thesis is submitted for the degree of Doctor of Philosophy

in the

School of Chemical Engineering,

Faculty of Engineering, Computer and Mathematical Sciences

at

The University of Adelaide



THE UNIVERSITY of ADELAIDE

December 2018

TABLE OF CONTENTS

Abstract ix

Declaration xi

Acknowledgements xii

Preface xiii

CHAPTER 1: INTRODUCTION 1

1. Introduction 3
2. Geology and mineralogy 5
   - 2.1. IOCG deposits 5
   - 2.2. South Australia regional geology: Olympic Dam Cu-Au region 6
   - 2.3. The Olympic Dam deposit: geology 8
   - 2.4. The Olympic Dam deposit: mineralogy 11
3. Extractive metallurgy 16
   - 3.1. The role of mineralogy: geometallurgy 17
4. Uranium, decay, and radionuclides 18
   - 4.1. ^{210}Pb and ^{210}Po 21
5. Research objectives and thesis structure 24

References 25

CHAPTER 2: RARE EARTH ELEMENT FLUOROCARBONATE MINERALS FROM THE OLYMPIC DAM CU-U-AU-AG DEPOSIT, SOUTH AUSTRALIA 35

Abstract 39

1. Introduction 40

2. Background 40

2.1. REE-fluorocarbonate minerals 40

2.2. Olympic Dam mineralogy 41

3. Sampling and analytical methods 41

3.1. Sampling 41

3.2. Analytical methods 42

4. Petrography 45

4.1. Bastnäsite 45

4.1.1. Matrix bastnäsite 47

4.1.2. Irregular bastnäsite associated with sulfides 48

4.1.3. Bastnäsite replacing breccia clasts 48

4.2. Synchysite 48

4.3. Other REE-minerals 49

5. Compositional data 49

5.1. Bastnäsite -(Ce) 50

5.2. Synchysite-(Ce) 50

5.3. Trace element concentrations 52

5.4. Compositional trends and chondrite-normalized fractionation patterns 54

6. Discussion 55

6.1. Data trends 55

6.2. Comparison with published compositional data 56

6.3. Formation conditions 58

6.4. Implications 59

7. Conclusions 59

References 60

CHAPTER 3: RARE EARTH ELEMENT PHOSPHATES FROM THE OLYMPIC DAM CU-U-AU-AG DEPOSIT, SOUTH AUSTRALIA: RECOGNIZING TEMPORAL-SPATIAL CONTROLS ON REE MINERALOGY IN AN EVOLVED IOCG SYSTEM 65

Abstract 69

1. Introduction 69

2. Background 70

2.1. REE mineralogy of the Olympic Dam deposit 70

2.2. REE-aluminum phosphate mineralogy 71

3. Sampling and methodology 71

3.1. Electron Probe Microanalysis 72

3.2. Laser Ablation Inductively Coupled Plasma Mass Spectrometry 73

4. Results 73

4.1. Mineral Liberation Analysis data 73

4.2. Petrography 73

4.2.1. Florencite 73

4.2.2. Xenotime 74

4.2.3. Monazite 74

4.3. Compositional data 75

4.3.1. Florencite-(La, Ce) 75

4.3.2. Xenotime-(Y) 75

4.4. Chondrite-normalized fractionation patterns 75

5. Discussion....75
5.1. Comparison with published compositional data for florencite....79
5.2. REE mineral speciation at Olympic Dam....81
5.3. Olympic Dam REE mineralization and fractionation....81
5.4. Implications for deposit evolution....86
6. Conclusions....87
References....87

CHAPTER 4: UPTAKE OF TRACE ELEMENTS BY BARYTE DURING COPPER ORE PROCESSING: A CASE STUDY FROM OLYMPIC DAM, SOUTH AUSTRALIA 93

Abstract....97
1. Introduction....97
2. Background....98
2.1. Baryte mineralogy....98
2.2. Baryte at Olympic Dam....98
2.3. Ore processing....98
3. Material and Methodology....98
3.1. Sampled material....98
3.1.1. Processing samples....99
3.1.2. Rock samples....99
3.2. Methodology....99
3.2.1. Mineral Liberation Analysis....100
3.2.2. Laser Ablation Inductively Coupled Mass Spectrometry....100
4. Results....100
4.1. Baryte appearance, morphology, and association....100
4.1.1. Processing materials....100

4.1.2. Vein baryte 101

4.2. Baryte chemistry 101

5. Discussion 102

6. Conclusions and implications 106

References 107

CHAPTER 5: MINERALOGY AND GEOCHEMISTRY OF FLUORITE IN THE OLYMPIC DAM CU-U-AU-AG DEPOSIT, SOUTH AUSTRALIA 111

Abstract 115

1. Introduction 115

2. Background 116

2.1. Fluorite at Olympic Dam 117

3. Sampling 118

3.1. Breccia-hosted fluorite 118

3.2. Vein fluorite 119

4. Methodology 119

5. Results 120

5.1. Petrography 120

5.1.1. Breccia-hosted fluorite 120

5.1.2. Vein fluorite 123

5.2. Fluorite geochemistry 123

5.2.1. REE distribution patterns 123

5.2.2. Other trace elements 127

6. Discussion 129

6.1. REE fractionation trends: implications for ore genesis 129

6.2. Other REE ratios 131

7. Conclusions 133

References 134

CHAPTER 6: LEAD CHALCOGENIDES AND PB-ISOTOPE SIGNATURE IN ORES AND CONCENTRATES FROM OLYMPIC DAM DEPOSIT, SOUTH AUSTRALIA 139

Abstract 143

1. Introduction 144

2. Background 145

3. Sampling 147

4. Analytical methodology 148

5. Results 149

    5.1. Sample descriptions and petrography 149

    5.2. Pb-isotope results 153

6. Discussion 154

7. Implications 159

References 160

CHAPTER 7: SUMMARY, RECOMMENDATIONS, AND CONCLUDING REMARKS 171

1. Summary 173

    1.1. Rare earth element-minerals 174

    1.2. Baryte, fluorite, and Pb-chalcogenides 175

        1.2.1. Baryte 175

        1.2.2. Fluorite 176

        1.2.3. Pb-chalcogenides 176

2. Recommendations 177

    2.1. Rare earth element-minerals 177

2.2. Fluorite 179

2.3. Pb-isotopes 180

2.4. Radionuclide distributions and minerals processing 180

3. Concluding remarks 182

References 183

CHAPTER 8: SUPPLEMENTARY AND ADDITIONAL MATERIAL 189

SUPPLEMENTARY MATERIAL A: FOR CHAPTER 2 191

SUPPLEMENTARY MATERIAL B: FOR CHAPTER 3 233

SUPPLEMENTARY MATERIAL C: FOR CHAPTER 4 243

SUPPLEMENTARY MATERIAL D: FOR CHAPTER 5 245

SUPPLEMENTARY MATERIAL E: FOR CHAPTER 6 275

ADDITIONAL MATERIAL F: Co-authored paper 281

ADDITIONAL MATERIAL G: Co-authored extended abstract 311

ADDITIONAL MATERIAL H: Conference abstract 315

ADDITIONAL MATERIAL I: Conference abstract 319

ADDITIONAL MATERIAL J: Conference abstract 321

ADDITIONAL MATERIAL K: Conference abstract 323

ADDITIONAL MATERIAL L: Conference abstract & poster 325

CHAPTER 9: REFERENCES 329

ABSTRACT

Deposits of iron-oxide-copper-gold (IOCG) type are the most important copper resource in South Australia. These deposits also contain uranium and other minor non-target elements which need to be removed for the successful generation of clean concentrates. This necessitates a sound understanding of the physical location and chemical speciation of non-target elements in ore and throughout processing. This information is only achievable through detailed mineralogy and understating of changes to mineral chemistry during processing.

The research composing this thesis is a contribution to a larger interdisciplinary research effort to ascertain the fundamental mineralogy of the Olympic Dam ore and processing materials in order to identify the hosts for non-target elements. The study used a complimentary suite of analytical methods, from assays on bulk material to comprehensive mineralogical characterization at the micron-scale. Characterization was focused on specific, hitherto sparsely documented mineral groups.

One of these mineral groups are the rare earth element (REE)-minerals, of which Olympic Dam is enriched, although not exploited at present. The dominant REE mineralization is composed of the REE-fluorocarbonate bastnäsite and appears generally coeval with sulfide mineralization. An early, spatially limited Ca-rich REE-fluorocarbonate (synchysite-parisite) assemblage is also noted, as is a later assemblage composed of florencite and other aluminum-phosphate minerals that overprint Cu-minerals, hematite, and pre-existing REE-minerals. The REE-minerals are determined not to be major hosts for non-target metals.

Barite is another major gangue mineral present throughout the deposit which is a notable contaminant during processing. Using chemical analysis on grains from ore feed through the leach product of the Cu-processing stream, barite has been identified not to be substantially or uniformly enriched in trace elements within the ore. However, barite shows a distinct enrichment in Pb during processing, mostly after the leaching stage. This has implications for similar incorporation of other elements, including Ra, which can be integrated into the barite structure.

Lead minerals and fluorite, two additional mineral groups considered deleterious for metallurgy, were also investigated using similar methodologies to address the distributions and variations of key trace elements within the deposit and through the processing cycle. Lead

chalcogenides are dominated by galena with minor altaite and clausthalite and are found to contain radiogenic to non-radiogenic Pb isotopes. Fluorite is also present throughout the orebody and within colorful late-stage veins that are both geologically and chemically distinct. Fluorite is determined not to be a major carrier of non-target metals.

Combined, the components of this thesis contribute to a deeper understanding of the complex mineralogy and chemistry of the Olympic Dam deposit and the chemical budget contributed by gangue minerals. The results carry implications for deposits of IOCG type within the Olympic Cu-Au province of South Australia and analogous deposits globally. Detailed mineralogical studies are essential to decipher the genesis of complex orebodies and facilitate their optimal exploitation. The new knowledge on element budgets, deportments, and chemical changes that occur during mineral processing impacts on the optimization of extractive metallurgy. Further studies linking fundamental geology, process mineralogy and metallurgy will enhance development of efficient processing procedures.

DECLARATION

I certify that this work contains no material which has been accepted for the award of any other degree or diploma in my name, in any university or other tertiary institution and, to the best of my knowledge and belief, contains no material previously published or written by another person, except where due reference has been made in the text. In addition, I certify that no part of this work will, in the future, be used in a submission in my name, for any other degree or diploma in any university or other tertiary institution without the prior approval of the University of Adelaide and where applicable, any partner institution responsible for the joint-award of this degree.

I acknowledge that copyright of published works contained within this thesis resides with the copyright holder(s) of those works.

I also give permission for the digital version of my thesis to be made available on the web, via the University's digital research repository, the Library Search and also through web search engines, unless permission has been granted by the University to restrict access for a period of time.

Signe Date __12/12/2018_____

ACKNOWLEDGEMENTS

I would like to deeply thank my primary academic supervisor, Prof. Nigel Cook, for sustained help, support, and encouragement, as well as tirelessly answering my many questions throughout my years of candidature. I also deeply thank my co-academic supervisor, Dr. Cristiana Ciobanu, for her continuous support and assistance with my research. I also owe many thanks to my external supervisor, Dr. Kathy Ehrig, for making this whole research project possible through providing sample material, funding, continued care and inspiration throughout the project's duration, and not least, the 'real world' context for my work.

I also have great appreciation for the extraordinary analytical support team at Adelaide Microscopy, Mr. Angus Netting, Dr. Animesh Basak, Mr. Ken Neubauer, Dr. Benjamin Wade, Dr. Sarah Gilbert, and Dr David Kelsey, for always finding time for assistance, explaining instrumental details, and for sharing their specialized expertise.

I am also deeply grateful for a scholarship from the ARC Research Hub for Australian Copper Uranium, and for the peer support of everyone in the 'Hub' over the past three years. Being able to work and learn with such an extraordinarily diverse group of researchers with expertise across so many disciplines was truly special. While there are too many to name, I would like to personally thank those in 'Hub Central', Dr. Ruth Shaw and Prof. Stephen Grano, for encouragement and the opportunity to share results and insights on a weekly basis. The 6-monthly sponsors review meetings, with all 30+ researchers across the Hub, offered a tremendous opportunity to exchange and compare results, and so ensure that the results in this thesis are pertinent to the overall objectives of the 'Hub'.

Extensive thank yous are deserved by my co-colleagues at the University of Adelaide, Adelaide: Nick, Liam, Max V-I, Maria, Jing, Wei Li, Mark, Zhiyong, Will, Urs, Wenyuan Gao, Wenyuan Liu, Max Frenzel. and the 'honorary geos', Frances and Nau, who were there for support and good times.

A final thanks to my states-side family and friends for not forgetting about me down-under.

PREFACE

This thesis comprises a portfolio of manuscripts which have been published in international peer-reviewed journals, as well as supplementary research not yet included in submitted publications. This thesis is submitted as part of the outputs of the ARC Research Hub for Australian Copper–Uranium, a large multi-disciplinary group with the shared goal of identifying methods to identify and remove non-target metals from copper concentrates in South Australia. This thesis reflects the broad nature of the research objectives by assessing the fundamental mineralogy of ores from the Olympic Dam deposit as well as materials from the processing plant.

The first two papers (Chapter 2 and Chapter 3, both published) present results of an in-depth mineralogical study of the REE-minerals from the Olympic Dam deposit, a mineral group that has largely been undocumented in previous published accounts of the deposit. The third paper (Chapter 4, published) details the chemistry of the mineral baryte in the ore body and through progressive stages of mineral processing (flotation and leaching). This study shows distinct element distribution patterns during sequential stages of processing which carry implications for the deportment of radionuclides. The fourth paper (Chapter 5) details the chemistry of the mineral fluorite, a common gangue mineral at Olympic Dam, from ore breccia and crosscutting veins of different color. The fifth paper (Chapter 6) details Pb-mineralogy and their Pb-isotopes from Olympic Dam. Recommendations for further work are included at the end of this thesis (Chapter 7) based on the results of these studies.

The five papers which form the basis of this thesis are:

1. Schmandt, D.S., Cook, N.J., Ciobanu, C.L., Ehrig, K., Wade, B.P., Gilbert, S. & Kamenetsky, V.S. (2017) Rare earth element fluorocarbonate minerals from the Olympic Dam Cu-U-Au-Ag deposit, South Australia. Minerals, 7. doi: 10.3390/min7100202.

2. Schmandt, D.S., Cook, N.J., Ciobanu, C.L., Ehrig, K., Wade, B.P., Gilbert, S. & Kamenetsky, V.S. (2019) Rare earth element phosphates from the Olympic Dam Cu-U-Au-Ag deposit, South Australia: Recognizing temporal-spatial controls on REE mineralogy in an evolved IOCG systems. The Canadian Mineralogist, 57, 1-22. doi: 10.3749/canmin.1800043.

3. Schmandt, D.S., Cook, N.J., Ehrig, K., Gilbert, S., Wade, B.P., Rollog, M., Ciobanu, C.L. & Kamenetsky, V.S. (2019) Uptake of trace elements by baryte during copper ore processing: a case study from Olympic Dam, South Australia. Minerals Engineering, 135, 83-94. doi: 10.1016/j.mineng. 2019.02.034.
4. Schmandt, D.S., Cook, N.J., Ehrig, K., Ciobanu, C.L., Gilbert, S., Wade, B.P., Verdugo-Ihl, M.R. & Keyser, W. Mineralogy and geochemistry of fluorite in the Olympic Dam Cu-U-Au-Ag depoist, South Australia.
5. Schmandt, D.S., Cook, N.J., Ehrig, K., Ciobanu, C.L., Owen, N.D., Verdugo-Ihl, M.R. & Wade, B.P. Lead chalcogenides and Pb-isotope signature in ores and concentrates from Olympic Dam deposit, South Australia.

The key finding and implications of this work is included in Chapter 7 along with the recommendations for future work.

Chapter 8 contains all supplementary material for the papers listed above, as well as co-authored publications and conference abstracts.

These materials include:

A. Supplementary material for Chapter 2 (Paper 1)
B. Supplementary material for Chapter 3 (Paper 2)
C. Supplementary material for Chapter 4 (Paper 3)
D. Supplementary material for Chapter 5 (Paper 4)
E. Supplementary material for Chapter 6 (Paper 5)

<u>Co-authored full-length papers</u>

F. Cook, N.J., Ehrig, K.J., Rollog, M., Ciobanu, C.L., Lane, D.J., Schmandt, D.S., Owen, N.D., Hamilton, T. & Grano, S. (2018) ^{210}Pb and ^{210}Po in geological and related anthropogenic materials: implications for their mineralogical distribution in base metal ores. Minerals. 8, 211. doi: 10.3390/min8050211.

<u>Co-authored peer-reviewed extended abstracts</u>

G. Cook, N.J., Ehrig, K.J., Ciobanu, C.L., Courtney-Davies, L., Verdugo-Ihl, M.R., Rollog, M., Schmandt, D.S., Owen, N.D., Macmillan, E., Kontonikas-Charos, A.,

Krneta, S. & Dmitrijeva, M. (2018) Why detailed mineralogy is important: Understanding evolution of the giant Olympic Dam iron-oxide copper-gold system, South Australia. 15th Quadrennial IAGOD Symposium, Salta, Argentina, 28-31 August 2018. Symposium Proceedings Volume, SegemAR, 371-372.

Peer-reviewed conference abstracts

H. Schmandt, D.S., Cook, N.J., Rollog, M., Ehrig, K.J., Triffett, B. & Ciobanu, C.L. (2016) Mineral hosts and deportment of radionuclides in uranium-bearing copper ores and concentrates. The AusIMM International Uranium Conference 2016 abstracts volume, June 7-8, Adelaide, South Australia. ISBN: 9781925100471.

I. Schmandt, D.S., Cook, N.J., Rollog, M., Ehrig, K.J., Triffett, B. & Ciobanu, C.L. (2016) Identifying hosts for non-target uranium and associated radionuclides in copper ores and concentrates. Goldschmidt 2016, June 26- July 1, Yokahama, Japan. Goldschmidt Conference Abstracts, 2771.

J. Schmandt, D.S., Cook, N.J., Ehrig, K.J., Wade, B.P. & Ciobanu, C.L. (2017) Rare earth element minerals in the Olympic Dam deposit, South Australia: petrography and compositional variation. SEG 2017: Ore Deposits of Asia: China and Beyond, September 17-20, Beijing, China

K. Schmandt, D.S., Cook, N.J., Ehrig, K.J., Wade, B.P. & Ciobanu, C.L. (2018) Rare earth element minerals and their compositional variation in the Olympic Dam deposit, South Australia. at SEG 2018: Minerals, Metals, and Society, September 22-25, Keystone, CO, USA.

L. Schmandt, D.S., Cook, N.J., Ciobanu, C.L Ehrig, K.J., Owen, N.D., Wade, B.P. & Gilbert, S.E. (2018) Rare Earth Element mineralogy at Olympic Dam, South Australia. Gordon Research Seminar and Conference, Geochemistry of Mineral Deposits: Mineralizing Processes Across All Scales, August 5-10, 2018, Waterville Valley, NH, USA.

The final chapter (Chapter 9) contains a complete reference list of all of the publications cited within the entire thesis including publications, chapters, and supplementary materials.

CHAPTER 1

INTRODUCTION

1 INTRODUCTION

Australia has the second largest copper resource in the world and copper mining sustains a multibillion-dollar industry across the country (Britt *et al*. 2016). A significant part of this industry exploits resources in South Australia which make up 68% of the national total (Britt *et al*. 2016). The dominant part of the South Australian resources identified to date are of iron-oxide copper-gold (IOCG) type deposits.

IOCG deposits are a geologically diverse group of mineral deposits identified around the world, most notably in Brazil, Chile, and Australia (Hitzman *et al.* 1992, Williams *et al.* 2005, Groves *et al.* 2010, Barton 2014). While the exact definition of IOCG systems continues to be intensely debated, a distinguishing feature of all known deposits is the presence of large volumes of iron-oxides and enrichment in a diverse set of elements in addition to the common commodities Cu and Au. Element enrichments relative to crustal values include, but are not limited to, variable amounts of F, P, Co, Ni, As, Mo, Ba, and notably rare earth elements (REE) and U (Hitzman *et al.* 1992, Williams *et al.* 2005). Globally, the relative enrichment in these elements is not uniform and displays significant regional variation. The archetypal IOCG systems of the Olympic Cu-Au Province on the eastern margin of the Gawler Craton in South Australia are unique globally, in part, due to the elevated concentrations of both REE and U (Skirrow *et al.* 2002, Hitzman & Valenta 2005).

Where the concentration of uranium is high enough, the additional processing associated with extraction of U, along with Cu and Au, becomes economically viable, as is the case for the Olympic Dam deposit, by far the largest IOCG system in the Olympic Cu-Au Province. Olympic Dam currently produces Cu, U, Ag, and Au and is the largest uranium resource under exploitation in the world, as well as the fifth-largest single copper resource and third-largest gold resource. Total resources are 10,400 Mt at grades of 0.77% Cu, 250 ppm U_3O_8, 0.32 ppm Au, and 1 ppm Ag (BHP 2017).

Even at such economic concentrations, however, uranium remains, in essence, a contaminant within the copper sulfide concentrates produced from IOCG ores. The presence of U introduces radiation through natural decay producing short half-life daughter radionuclides (RN). While almost all U can be recovered during processing, certain high-activity daughter RN

of ^{238}U decay, notably ^{226}Ra, ^{210}Pb, and ^{210}Po, become slightly enriched during concentration of copper sulfide minerals. This enrichment leads to the necessity for copper sulfide concentrates to be smelted on-site rather than being sold on the global concentrate market (BHP Billiton 2009).

All final products (copper cathode, uranium oxide concentrate, and gold and silver bullion) are produced on-site (Ehrig *et al.* 2012). The Olympic Dam mine and processing plant take all possible precautions to mitigate the activities of RN throughout all stages of mining, flotation, hydrometallurgical processing, solvent extraction, smelting, electrorefining, and electrowinning circuits.

Available information on the distribution and transportation of authigenic RN in solid media (*e.g.* rocks and minerals) is, except for U, relatively sparse (Cook *et al.* 2018). Much of the published data discussing RN deportment in the environment refers to introduction of natural (*e.g.* through volcanic activity), or anthropogenic (*e.g.* via nuclear accidents or mining activity) RN, and their distribution in air, soils, waters (groundwater, rivers, lakes *etc*.), and in recent sediments (Cook *et al.* 2018 and references therein). Understanding the physical location and chemical speciation of RN in minerals and ores is, however, critical for sustainable mining and processing of ore deposits world-wide that contain U and other radioactive isotopes.

These processing implications coupled with a number of outstanding geological questions concerning the formation and subsequent evolution of IOCG-type mineralization make Olympic Dam an excellent resource on which to study RN distributions and address these knowledge gaps. Olympic Dam continues to be the focus of much interest within the geological community because of its uniqueness; it is one of the largest deposits in the world, possesses a multi-commodity endowment, contains large amounts of U and REE, displays great textural complexity and diversity, and not least, a unique and variable mineralogy and mineral chemistry expressed at all scales.

The complex mineralogy and sheer size combine to make Olympic Dam an extraordinarily interesting, yet challenging deposit to study, with implications on a global scale. Results of an extensive mineralogical research program on Olympic Dam ores have been published in recent years (notably including characterization of the four most important U-bearing minerals: uraninite, coffinite, brannerite, and hematite; Ciobanu *et al.* 2013, Macmillan *et al.* 2016a, 2017, Verdugo-Ihl *et al.* 2017), providing an excellent foundation on which to build

and address outstanding research gaps. The latter, including the mineralogical-geochemical research contained in this thesis, carry both geological and metallurgical implications.

The remainder of Chapter 1 will summarize the geology and mineralogy of the Olympic Dam deposit, as well as the principles of U-radioactive decay and its implications for processing Cu ore from a U-bearing deposit. These topics are all fundamental concepts critical to the research areas focused on within this thesis and the published papers and manuscripts contained within it.

2 GEOLOGY AND MINERALOGY

2.1 IOCG DEPOSITS

The IOCG deposit class was first introduced in 1992 to group a number of iron oxide-rich occurrences from across the globe which share distinct chemical and geologic characteristics (Hitzman *et al.* 1992). At the time, this deposit classification was focused on a relatively limited group of deposits in very different geological settings, *e.g.* Olympic Dam, Kiruna (Sweden), the Great Bear belt (N.W.T., Canada). Despite their considerable differences, they shared the following characteristics: 1) age (early to mid-Proterozoic); 2) tectonic setting (major structural zones of cratonic or oceanic margin environments); 3) mineralogy (dominated by iron oxides and elevated REE); and 4) alteration (intense alteration from sodic, to potassic, to sericitic and silicification, as deep to shallow to very shallow expressions, respectively) (Hitzman *et al.* 1992). Some, notably Kiruna, are iron ore deposits without any economic copper and gold.

In the past 25 years, there has been increasing interest in IOCG systems, resulting in discovery of many other deposits or classification/re-classification as IOCG type, as well as continued research and major contributions committed to further understanding and refining the classification (Porter 2000, 2002, 2010, Hitzman & Valenta 2005, Williams *et al.* 2005, Corriveau 2007, Groves *et al.* 2010, Barton 2014,). Generally, the IOCG definition has grown more inclusive, leading to the introduction of subgroups or subtypes, as well as identifying deposit-system continua between IOCGs and what appear to be closely related deposit types, notably iron-oxide apatite (IOA) deposits, and even genetic links with skarns and porphyry systems (Corriveau 2007, Groves *et al.* 2010, Barton 2014). Even if the literature on individual systems is growing rapidly, the definition of an IOCG deposit *sensu stricto* remains the subject

of intense debate. This is exacerbated by the persistence of significant knowledge gaps in terms of ore genesis and associated hydrothermal alteration, including ore-forming processes and the source and character of ore-forming fluids. Currently, most researchers would accept that the IOCG-type deposit group contains systems that vary in age from the Archean (*e.g.* Salobo, Brazil) to the Mesozoic (*e.g.* Mantos Blancos, Chile), formation depth, and styles (*e.g.* breccia, veins, stratabound), however they are generally recognizable by a marked association with large and deep crustal scale structures, regional-scale sodic-potassic alteration haloes, large volumes of low-Ti iron oxides (magnetite or hematite), and the extent and type of polymetallic and elemental enrichment (Hitzman *et al.* 1992, Hitzman & Valenta 2005, Corriveau 2007, Groves *et al.* 2010, Barton 2014).

Within almost all publications that have attempted to review or classify IOCG deposits, Olympic Dam is considered as an end-member variety (Hitzman *et al.* 1992, Hitzman & Valenta 2005, Corriveau 2007, Groves *et al.* 2010, Barton 2014). This is due to its uniquely rich and highly variable mineral endowment, the predominance of hematite over magnetite, and, not least, the extreme size.

2.2 South Australia regional geology: Olympic Dam Cu-Au region

The Olympic Cu-Au province is an early Mesoproterozoic metallogenic belt extending over a distance of 500 km, roughly N-S, along the eastern margin of the Gawler Craton of South Australia (Figure 1a; Skirrow *et al.* 2002, 2007, 2018). The province has been divided into three districts defined by tectonics and alteration and which correlate with domains of IOCG alteration and mineralization (Skirrow *et al.* 2002, 2007, Hayward & Skirrow 2010). These domains, from north to south include, the Mount Woods Inlier (containing the Prominent Hill deposit, Freeman & Tomkinson 2010, Schlegel *et al.* 2015), the Olympic Dam district (containing the Olympic Dam and Carrapateena deposits, as well as many additional sub-economic prospects and others still being explored), and the Moonta-Wallaroo district (containing the Hillside deposit, various historical mines, and numerous prospects (Conor *et al.* 2010, Ismail *et al.* 2014) (Figure 1a). Exploration activity across the province in recent decades has identified many sub-economic occurrences, mostly within the basement, but also several within the overlying sedimentary rock sequence.

The primary commodities in this region are Cu, Au, and Ag, and although uranium is present in each of the noted IOCG deposits, U is only recovered at Olympic Dam. REE-minerals are also widespread across the IOCG systems of the Olympic Province (*e.g.* Davidson *et al.* 2007, Freeman & Tomkinson 2010).

The basement of the Olympic Cu-Au Province is comprised of the eastern Gawler Craton granulite-facies Archean core surrounded by Paleo- to Mesoproterozoic metasedimentary and metavolcanics rocks of the Hutchison Group (*e.g.* Ferris *et al.* 2002). These were intruded by the Donington granitoid suite, emplaced during the Cornian Orogeny at ~1850 Ma, followed by basin sedimentation and volcanism forming the Wallaroo Group (~1770-1740 Ma), which was subsequently terminated and metamorphosed by the Kimban Orogeny (~1730-1690 Ma) (*e.g.* Daly *et al.* 1998, Hand *et al.* 2007, Reid *et al.* 2008, Reid & Hand 2012). The impact of the Kimban Orogeny was widespread across the craton and created crustal-scale structures, magmatism, and metamorphism (Daly *et al.* 1998, Hand *et al.* 2007, Reid & Hand 2012).

Emplacement of the Gawler silicic large igneous province (SLIP) covering 25,000 km^2 of the central Gawler Craton took place at ~1600-1590 Ma (Allen *et al.* 2008, Wade *et al.* 2012). This event comprises intrusion of Hiltaba Suite I- and A-type granitoids, including the Roxby Downs Granite (RDG), which belongs to the Burgoyne Batholith (Creaser, 1989), and eruption of associated, bimodal volcanic rocks on a regional-scale (Gawler Range Volcanics). The latter cover large regions of the eastern Gawler Craton. Hiltaba Suite granitoids and Gawler Range Volcanics are considered broadly contemporaneous. A relatively poorly-defined metamorphic and intrusive event (the Kararan Orogeny) followed at ~1580–1540 Ma (Daly *et al.* 1998, Reid & Hand 2012). The impact of this event is only locally observable, notably in the Mount Woods Inlier and deposits therein (*e.g.* Bowden *et al.* 2017).

All deposits in the Olympic Cu-Au Province display strong structural control. Dating of the magmatic minerals from intrusive rocks belonging to the Hiltaba Suite and hydrothermal minerals within Cu-Au mineralization across the Province prove these to be broadly contemporaneous and associated with the ~1.6 Ga tectonothermal event (*e.g*. Creaser & Cooper 1993, Johnson & Cross 1995, Jagodzinski 2005, Skirrow *et al.* 2007, Ciobanu *et al.* 2013, Courtney-Davies *et al.* 2016, Apukhtina *et al.* 2017, Cherry *et al*. 2018). The IOCG deposits in this region all lie under at least several hundreds of meters of cover sediments of Neoproterozoic age and younger.

2.3 The Olympic Dam deposit: geology

The Olympic Dam deposit (Figure 1b) is located 520 km NNW of Adelaide, South Australia, on the eastern Gawler Craton. Olympic Dam was discovered by Western Mining Corporation (WMC) in 1975 during an exploration campaign targeting sediment-hosted copper deposits. Mining began in 1988.

The resource is located within the Olympic Dam Breccia Complex (ODBC) which formed entirely within, is largely derived from, and broadly coincident with, the ~1590 Ma RDG (Reeve *et al.* 1990, Creaser & Cooper 1993, Johnson & Cross 1995, Skirrow *et al.* 2002, 2007, Jagodzinski 2005, Ehrig *et al.* 2012, 2017, Ciobanu *et al.* 2013, Cherry *et al.* 2018, Courtney-Davies *et al.* 2019).

RDG and other granitoids within the Burgoyne batholith display weak to intense alteration, recognized as a regional-scale albitization superimposed by potassic alteration, which increases towards the orebody (Mauger *et al.* 2016, Kontonikas-Charos *et al.* 2017). Fe-metasomatism is the most intense expression of alteration and is associated with increased brecciation, both of which are strongest in the center of the deposit with waning intensity towards the peripheries and at depth (Ehrig *et al.* 2012, 2017). Brecciation zones are elongate, steeply-dipping, and up to two km in depth (the ore zone is still open at depth). The breccias can be thought of as a continuum, both texturally and chemically, ranging from granite- to hematite-rich, with clasts that may be angular to rounded and microscopic to meters in diameter, breccias range from clast supported to matrix supported and can be weakly to intensely altered (up to >90% hematite) (Ehrig *et al.* 2012). Breccia clasts are dominantly RDG protoliths but also include felsic to ultramafic volcanic rocks, successions of layered sedimentary units, mafic-ultramafic dykes, and vein fragments (Ehrig *et al.* 2012, Huang *et al.* 2015, 2017, McPhie *et al.* 2016).

Basaltic to doleritic dykes of the Gairdner Dyke Swarm (U-Pb apatite dated at 825±18 Ma; Huang *et al.* 2015, Apuhktina *et al.* 2016) are observed within the Olympic Dam resource and cross-cut the ODBC. The roof of the orebody and enclosing ODBC are cut by a major unconformity with overlying post-brecciation and -mineralization Neoproterozoic to Cambrian sedimentary rocks representing a gap of at least 800 Ma (Ehrig *et al.* 2012, Apukhtina 2016).

Although models for ore formation require additional investigation and refinement, the brecciation event was likely initiated not long after RDG emplacement and uplift, and was

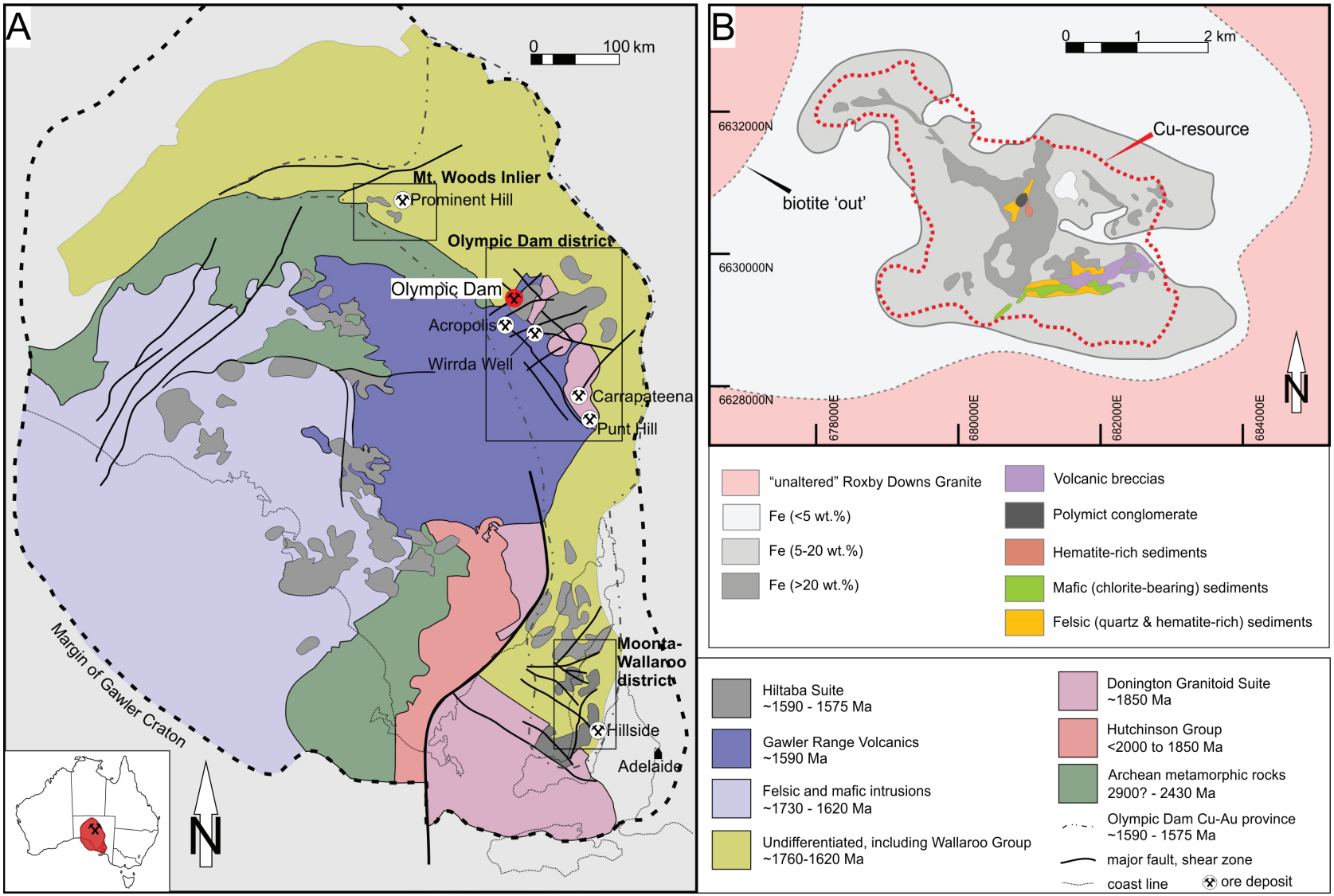


Figure 1. Geologic map A) Simplified regional pre-Neoproterozoic basement geology map of the Gawler craton, South Australia (after Direen & Lyons 2007 and Skirrow *et al.* 2007). B) Simplified Olympic Dam deposit map at -350 RL, showing lithologies, iron content, and resource outline. The entire resource is positioned within the RDG-hosted ODBC (after Ehrig *et al.* 2012).

facilitated by a relatively long-lived system of faulting and hydrothermal activity enhanced by emplacement of roughly coeval mafic/felsic plutons and mafic and dolerite dykes that exploited pre-existing structures and amplified brecciation (*e.g*. Reeve *et al.* 1990).

Recent studies have confirmed the impact of multiple regional tectonic events on the deposit after ore formation, including the Kararan Orogeny, a more recently defined event relating to the Musgravian Orogeny at ~1250-1150 Ma, emplacement of Gairdner dyke swarms at ~820 Ma, and the ~490-514 Ma Delamerian Orogeny. Despite these events, the overall geometry and mineral zoning in the deposit are broadly maintained.

Evidence for replacement, remobilization, and recrystallization has been presented for multiple mineral groups, including iron-oxides, Cu-(Fe)-sulfides, apatite, and U-minerals (Krneta *et al.* 2016, Macmillan *et al.* 2016a, 2017, Ciobanu *et al.* 2017a, Verdugo-Ihl *et al.* 2017). Structures at Olympic Dam are very complex and remain the focus of research attention with many and variable structures identified, from arrays of cutting brittle faults, local- and regional-scale structures, and multiple major, steeply-dipping pre- and/or syn- to post-mineralization fault sets (Ehrig *et al.* 2012, 2017, Clark *et al.* 2018).

These, and possibly other hitherto unrecognised events, superimposed onto primary assemblages have contributed to the challenge of unequivocally defining a genetic model for the deposit that accounts for all observations, or for identification of the source(s) of metals and fluids. Many authors have chosen to ascribe ore genesis to redox-controlled reaction of deeper hot, reducing, magma-derived hydrothermal fluids interacting with meteoritic, cool, oxidizing fluids (Reeve *et al.* 1990, Oreskes & Einaudi 1992, Haynes *et al.* 1995, Skirrow *et al.* 2006, Macmillan *et al.* 2016a). Even if most researchers currently agree that most, if not all, of the contained metals in the deposit were introduced during the main geologic event at ~1590 Ma (*e.g.* Johnson & Cross 1995), many will now also agree that the deposit evolved over at least 1,000 Ma and was modified by major regional-scale tectonic events.

Uranium isotope ratios strongly suggest that U was sourced from crustal rocks, specifically the host RDG, and likely at relatively high temperatures. The role of the RDG is clearly pivotal and is recorded by the strongly ‘granitophile’ (U, Pb, W, Mo, Sn) signature recognised in iron-oxides and other minerals (Ciobanu *et al.* 2013, Verdugo-Ihl *et al.* 2017). Uranium is, however, readily remobilized, even at low temperatures and the distribution of U in the deposit has clearly evolved over repeated cycles of remobilization and reprecipitation over an

extended period of time (Kirchenbaur *et al.* 2016, Macmillan *et al.* 2016a, 2017). This paragenetic evolution of U-bearing mineral assemblages coupled with the fact that this has occurred heterogeneously across the deposit due to widely varying permeability and fluid regimes, underscores the importance of careful mineralogical observation to understand the deportment of U and daughter RN.

2.4 The Olympic Dam deposit: mineralogy

The Olympic Dam deposit contains a wide array of minerals, in part because of its expansive element enrichment (over crustal levels) beyond the exploited metals. Anomalous elements include F, S, C, As, Ba, Bi, Cd, Co, Cr, Fe, In, Mo, Nb, Ni, P, Pb, Sb, Se, Sn, Te, V, W, Y, Zn, and REE. Over 95 identified minerals are reported from the deposit (Ehrig *et al.* 2012) and a further 20-30 have been identified since then. However, despite the mineralogical variety and complex fine-grained heterogeneous textures of the ODBC, there is a significant mineralogical and geochemical zonation at the deposit-scale (Ehrig *et al.* 2012, 2017, Dmitrijeva *et al.* 2019) that can be readily correlated with variations in mineralogy.

Alongside minerals originating from precursor granite, notably feldspars and quartz, deposit mineralogy is dominated by characteristic assemblages of alteration minerals. The major alteration minerals include iron-oxides (hematite and subordinate magnetite), sericite (sericite is used as an encompassing term throughout the thesis for fine-grained mica and clays including fine-grained muscovite (1M and 1M1 types, Ehrig *et al*. 2017), illite, phengite, and paragonite; consistent with previous usage at Olympic Dam, *e.g*., Apukhtina 2016), and quartz with lesser chlorite, fluorite, and barite (Ehrig *et al.* 2012, 2017). There is an overarching zonation pattern defined by increased iron and decreased silica towards the center of the deposit correlating with progressively increasing intensity of alteration and brecciation (Ehrig *et al.* 2012).

The sulfide mineralization is similarly largely zoned from distal to center with the pattern sphalerite → galena → pyrite→ chalcopyrite → bornite → chalcocite → non-sulfide, similar to the classic Zn-Pb-Cu sulfide zonation pattern (Ehrig *et al.* 2012). The principal Cu-bearing minerals are chalcopyrite, bornite, and chalcocite (including djurleite, digenite and other $Cu_{2-x}S$ sulfides; Ciobanu *et al.* 2017a), along with minor native copper, covellite, and tenorite/cuprite (Ehrig *et al.* 2012).

Alteration assemblages are also zoned from distal to center, with the margins of mineralization laterally and at depth having a reduced Fe-oxide zone of magnetite + apatite + siderite + chlorite + quartz which grades towards the center to an oxidized Fe-oxide alteration zone with an assemblage of hematite + sericite + fluorite (Ehrig *et al.* 2012). This grades to the center core zone of hematite + quartz + barite assemblage, which is notably devoid of aluminosilicates or sulfides (Ehrig *et al.* 2012).

Barite [$BaSO_4$] is an important gangue mineral at Olympic Dam, making up ~1.2 wt. % (Table 1) of the ore body and occurs in clasts and matrix as well as narrow veins (Ehrig *et al.* 2012). Barite grades outwards to fluorite [CaF_2], another prominent gangue mineral also comprising ~1.2 wt. % of the ore body in the clasts and veins (Table 1; Ehrig *et al.* 2012). Barite is most prevalent in the barren deposit core while fluorite is more commonly associated with the copper-(iron)-sulfide minerals peripheral to the core. Barite and fluorite are present together in late stage veins that cross-cut the deposit (~1000 Ma after mineralization; Maas *et al.* 2011). The occurrence of both gangue minerals has important consequences for mineral processing as well as geological significance (Schmandt *et al.* 2019b, Chapter 5)

Minerals containing essential REE are another mineral group of interest which occur within the deposit. REE are generally ubiquitous across the deposit, with the light rare earth elements (LREE) hosted primarily in bastnäsite [$(REE)CO_3F$] (Ehrig *et al.* 2012, Schmandt *et al.* 2017), although there are other less abundant REE-minerals, such as the Ca-bearing REE-fluorocarbonates, synchysite [$Ca(REE)(CO_3)_2F$] and parisite (Ciobanu *et al.* 2017b). The REE-fluorocarbonate minerals are considered broadly coeval with Cu-(Fe)-sulfides and an appreciation of their formation conditions can be valuable for understanding constraints on deposit genesis (Ehrig *et al.* 2012, Schmandt *et al.* 2017). There is also an overprinting event at Olympic Dam that included formation of the REE aluminium-phosphate mineral florencite, [$REEAL_3(PO_4)_2(OH)_6$], and other aluminium-phosphate-sulfate (APS) group minerals, forming an assemblage considered similar to advanced argillic alteration (Ehrig *et al.* 2012, Schmandt *et al.* 2019a, Owen *et al.* in review). REE-phosphates are represented by monazite [$(REE)PO_4$], and xenotime, [$(Y,HREE)PO_4$], both of which are minor constituents. Many other minerals may also host REE, such as apatite (Krneta *et al.* 2017), U-minerals (Macmillan *et al.* 2016a, 2017) and others. The LREE grade generally correlates positively with Cu grade, increasing towards the

Table 1: Short list of Olympic Dam minerals with generic formula and abundance (wt. %) based on Modal Mineralogy of the 10,000-Sample MLA Data Set (Ehrig *et al.* 2012)

Mineral	Generic formula	wt. %	Mineral	Generic formula	wt. %
Assorted Sulfides			***Cu Sulfides***		
Pyrite	FeS_2	0.4614	Chalcopyrite	$CuFeS_2$	0.9261
Sphalerite	ZnS	0.0115	Bornite	Cu_5FeS_4	0.3346
Pyrrhotite	FeS	0.0090	Chalcocite	Cu_2S	0.1388
Molybdenite	MoS_2	0.0015	Tennantite	$Cu_{12}As_4S_{13}$	0.0072
Cobaltite	CoAsS	0.0012	Covellite	CuS	0.0068
Bismuthinite	Bi_2S_3	0.0003	Carrollite	$CuCo_2S_4$	0.0004
	total	*0.4849*		*total*	*1.4139*
Pb Minerals			***Assorted metal minerals***		
Galena	PbS	0.0012	Safflorite	$(Co, Fe)As_2$	0.0001
Clausthalite	PbSe	0.0002	Löllingite	$FeAs_2$	0.0003
Altaite	PbTe	0.0000	Domeykite	Cu_3As	0.0001
	total	*0.0014*		*total*	*0.0005*
REE and REE-bearing minerals			***U and Th minerals***		
Bastnäsite	$REE(CO_3)F$	0.0833	Coffinite	$U(SiO_4)\cdot nH_2O$	0.0159
Florencite	$REEAl_3(PO_4)_2(OH)_6$	0.0660	Brannerite	UTi_2O_6	0.0119
Monazite	$REEPO_4$	0.0184	Uraninite	UO_2	0.0049
Synchysite	$CaREE(CO_3)_2F$	0.0124			
Xenotime	YPO_4	0.0045	Uranothorite	$(Th,U)SiO_4$	0.0028
	total	*0.1846*	Thorite	$ThSiO_4$	0.0023
APS minerals	varied, $AB_3(XO_4)_2(OH)_6$	0.1097		*total*	*0.0378*
Apatite	$Ca_5(PO_4)_3(F,Cl,OH)$	0.1029			
	total	*0.213*			
Rock-forming minerals			***Assorted minor minerals***		
Quartz	SiO_2	30.840	Albite	$NaAlSi_3O_8$	0.6371
Fe oxide (hematite and magnetite)	Fe_2O_3 and Fe_3O_4	30.534	Rutile	TiO_2	0.2411
Sericite	$KAl[AlSi_3O_{10}](OH)_2$	18.193	Ankerite	$Ca(Fe,Mg)(CO_3)_2$	0.1849
Orthoclase	$KAlSi_3O_8$	9.842	Dolomite	$CaMg(CO_3)_2$	0.1327
Siderite (+/- Mn)	$FeCO_3$	2.901	Zircon	$ZrSiO_4$	0.0549
Chlorite group	$(Mg,Fe)_3(Si,Al)_4O_{10}(OH)_2 \cdot (Mg,Fe)_3(OH)_6$	1.324	Schorl	$NaFe_3Al_6(Si_6O_{18})(BO_3)_3(OH)_3(OH)$	0.0521
Barite	$BaSO_4$	1.225	Ilmenite	$FeTiO_3$	0.0447
Fluorite	CaF_2	1.180	Anhydrite	$Ca(SO_4)$	0.0108
	total	*96.03*	Kaolinite	$Al_2Si_2O_5(OH)_4$	0.0060
			Zunyite	$Al_{13}Si_5O_{20}(OH,F)_{18}Cl$	0.0042
			Sellaite	MgF_2	0.0002
			Corundum	Al_2O_3	0.0001
			Diaspore	AlO(OH)	0.0001
			Ilmenorutile	$(Ti,Nb,Fe)O_2$	0.0001
				total	*1.37*

mineral formulas are simplified
does not account for all minerals within the entire deposit
REE-rare earth elements

center and absent in the barren core (Ehrig *et al.* 2012). REE are not currently exploited at Olympic Dam although the deposit represents a global scale REE anomaly (Weng *et al.* 2015).

Uranium is mainly present (>90%) as uraninite/pitchblende, coffinite, and brannerite; and based on current data there is no identified deposit zonation of U-minerals or correlation with specific sulfide phases (Ehrig *et al.* 2017). Uranium-minerals occur as massive aggregates and disseminations, and less frequently as microveinlets, and are associated with all sulfides and gangue minerals (Ehrig *et al.* 2012, Macmillan *et al.* 2016a, b, c, 2017). The U-minerals do show a paragenetic progression from uraninite to brannerite to coffinite, with brannerite and coffinite formed at the expense of uraninite (Ehrig *et al.* 2012, Macmillan *et al.* 2016a, 2017). The abundances and relative proportions of these minerals vary across the deposit but, in general, higher-grade uranium zones (U > ~500 ppm) are dominated by uraninite, whereas, in lower grade U zones (U < ~500 ppm) the main U-minerals are brannerite and coffinite (Ehrig *et al.* 2015). Recent work has shown numerous uraninite crystallization events, as well as multiple stages of U dissolution and reprecipitation within the Olympic Dam deposit (Kirchenbaur *et al.* 2016, Macmillan *et al.* 2016a, 2017).

Uranium is also present in other minerals, such as thorite-uranothorite and thorianite, as well as in trace concentrations within many other minerals including REE-minerals, apatite, and zircon. U-minerals also occur as nanoscale inclusions in a wide variety of minerals, including hematite (*e.g.* Figure 8 in Cook *et al.* 2017) and all sulfides (pyrite, chalcopyrite, bornite, and chalcocite) (Ehrig *et al.* 2012). Moreover, widespread U-rich (up to several wt. % U within individual grains) hematite has been identified at Olympic Dam (Oreskes 1990, Ciobanu *et al.* 2013), resulting in gangue hematite being the 4th most significant uranium carrier mineral in the deposit. The contemporaneous precipitation of Fe and U is likely because of the fine disseminations of micro- to nanoscale U-minerals in hematite and lattice-bound uranium zoned in hematite (Ciobanu *et al.* 2013, Cook *et al.* 2017). Identification of this element-mineral relationship has proven useful as a geochronological tool for Olympic Dam and other mineralization in the Olympic Cu-Au Province (Ciobanu *et al.* 2013, Courtney-Davies *et al.* 2016, 2019), hematite-bearing ores of IOCG-type elsewhere (*e.g.* Brazil, Courtney-Davies *et al.* 2016), and in iron ores in South Australia formed by hydrothermal upgrading of banded iron formations (Keyser *et al.* 2019).

Acknowledging the prevalence of U-bearing minerals across the deposit, the presence of uranium in both ore and gangue minerals, and the complex cycles of replacement, remobilization, and crystallization associated with the multi-stage evolution of Olympic Dam, is important when aiming at appreciating the deportment of U-decay products within ore and during mineral processing.

The most common and stable product of ^{238}U decay is ^{206}Pb. Lead occurs across the deposit, both as common Pb, introduced during deposit formation, and as Pb produced over time from natural U-decay. Lead occurs principally as chalcogenide minerals, galena (PbS), altaite (PbTe), and clausthalite (PbSe). Although these minerals are only minor components of the deposit, composing just ~0.0014 wt. % of the entire deposit (Table 1, Ehrig *et al.* 2012), careful study of these phases contributes to an understanding of the evolution and distribution of Pb and intermediate RN in the ^{238}U decay series. All four main U- and U-bearing minerals contain some amount of radiogenic lead (Ciobanu *et al.* 2013, Macmillan *et al.* 2016a, 2017), including preserved early U-minerals (up to 12 wt. % in uraninite, Macmillan *et al.* 2016) and hematite (Ciobanu *et al.* 2013, Courtney-Davies *et al.* 2016, Verdugo-Ihl *et al.* 2017). Lead is also present in trace amounts within several other minerals such as zircon, apatite (Krneta *et al.* 2017), and carbonates (Apukhtina 2016).

The presence of radiogenic Pb in secular equilibrium with U within a range of refractory minerals has proven valuable for dating purposes, and has assisted with reconstruction of the prolonged history of the deposit (Johnson & Cross 1995, Jagodzinski 2005, Ciobanu *et al.* 2013, Apukhtina *et al.* 2017, Courtney-Davies *et al.* 2016, 2019, Cherry *et al.* 2018). Lead isotopes have also been identified within Cu-Fe- and Fe-sulfides (Meffre *et al.* 2010), although they likely represent minute inclusions of Pb-bearing minerals rather than lattice-hosted Pb (as demonstrated in Owen *et al*. 2018). Few previous studies have, however, focused on the occurrence and isotope systematics of the Pb-chalcogenides (Chapter 6).

Overall the Olympic Dam deposit hosts an extraordinarily wide range of minerals, only a selection of which are detailed here. Importantly, almost all can display significant compositional variability. The composition of species containing U and Pb carries implications for both mineral genesis and for the location of RN and its impact on behaviour during processing.

3 EXTRACTIVE METALLURGY

A major component of developing an ore deposit is the economic extraction of the ore minerals from the rock. The target ore mineral occurrence is unique to each deposit and can be extremely variable. Because of these natural inconsistencies, extensive testing and planning is required to optimise economic recovery. Olympic Dam is a complex multi-commodity ore body, and, thus, ore processing is highly intricate. This section provides a simplified and basic overview of metallurgical processes employed at Olympic Dam, highlighting the Cu-processing procedure which produces the product material studied as part of this thesis.

Extractive metallurgy includes all processes and methods used to separate the desired economic minerals from gangue. Common methods are grinding/milling, physical separation (*e.g*. gravity circuits), froth flotation, hydrometallurgy, and electrometallurgy, all of which are used at Olympic Dam, and shown in the flow diagram illustrated in Figure 2.

The first step toward Cu concentration takes advantage of the physical characteristics of the different minerals to promote separation of the economic minerals from the gangue minerals. In most hard rock sulfide deposits, this usually includes crushing and grinding (comminution) where the material is crushed to below than a specific particle size (based on ore mineral size and other factors) and represents the *flotation feed* or *ore feed*. After crushing/grinding, the material goes through froth flotation. Froth flotation uses the differences of particle mineral surface chemistry to separate gangue from sulfide minerals. After floatation, two materials are produced: *flotation concentrate* containing sulfides and other hydrophobic minerals, and *flotation tailings* containing non-sulfide gangue minerals and most of the U-minerals. Although flotation tailings represent waste in many concentration circuits, at Olympic Dam they are further processed via sulfuric acid leach for extraction of U before being placed in the tailings storage facilities.

The flotation concentrate contains Cu-(Fe)-sulfides together with modest amounts of gangue minerals. Sulfuric acid is used to dissolve unwanted minerals, notably fluorite, and also any remaining U-bearing minerals in concentrate leach. Selective dissolution takes place within large agitated tanks to increase grain exposure to solution and enhancing dissolution. Uranium is then recovered from solution, as is any dissolved Cu. *Concentrate leach discharge* (*e.g.* residue remaining at concentrate leach) is then smelted, generating copper anode, after which electrometallurgy is used to refine the copper further, producing copper cathodes and anode slimes. The slimes are further refined to recover precious metals.

3.1 THE ROLE OF MINERALOGY: GEOMETALLURGY

Each ore deposit has distinct mineral characteristics including, but not limited to, differences in texture, grain size, and mineral associations. These properties directly affect how the bulk material responds during processing. Design and optimization of processing flowsheets is thus highly dependent upon a detailed knowledge of mineralogy and its variability throughout

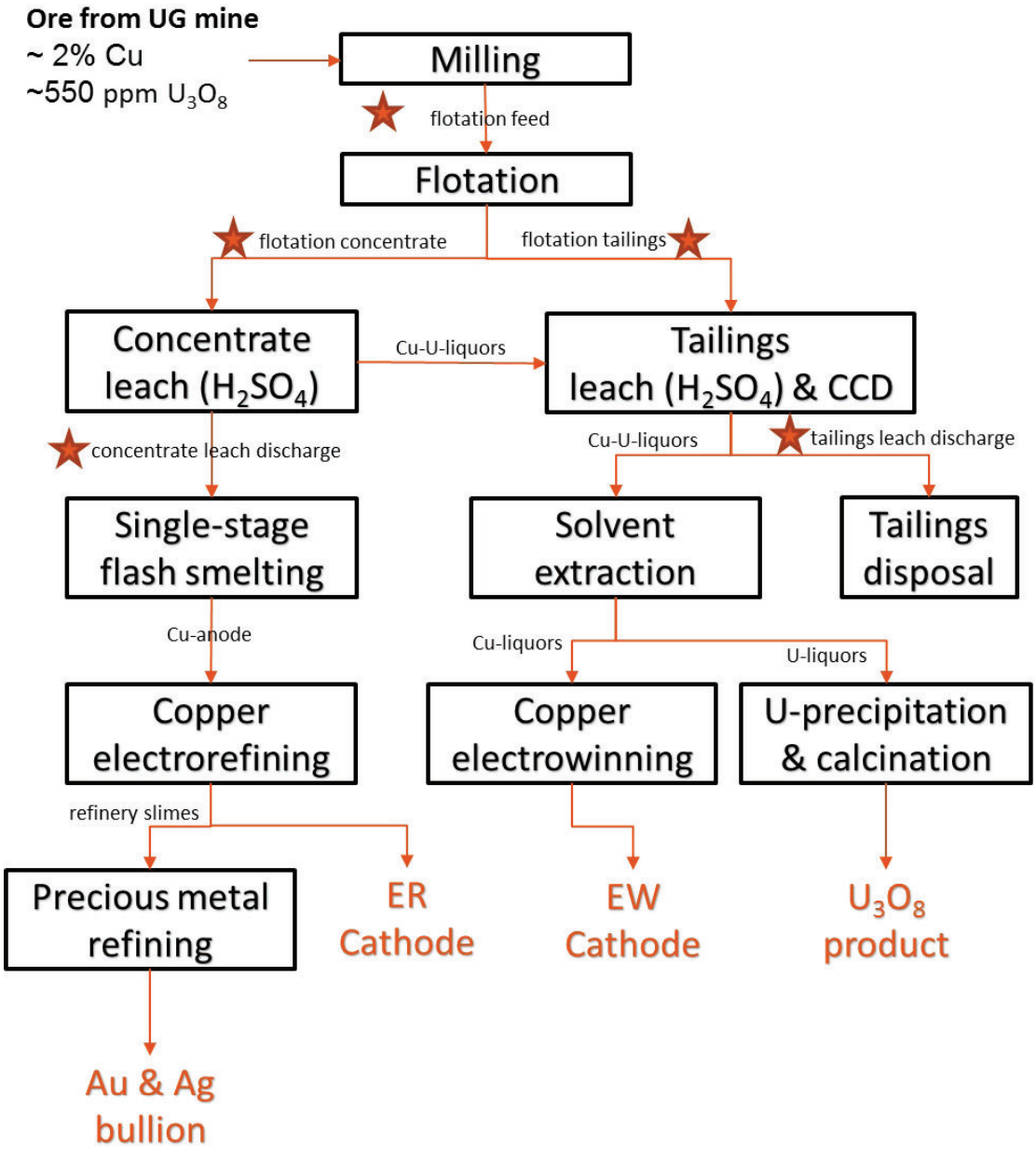


Figure 2. Olympic Dam processing plant simplified flowsheet. Stars indicate location of materials sampled.

the deposit. At Olympic Dam, process optimization is achievable through extraordinarily careful mineralogical control and via input of predicted geometallurgical variables into the resource model (Ehrig 2013).

Minerals have characteristic responses to different processing procedures which are exploited to separate the mineral phases. Each processing stage is reliant on the efficiency of the previous stage, for example, efficient flotation can only be achieved with the initial successful physical separation of the gangue minerals from the sulfides, and successful comminution is dependent on accurate identification of mineralogy as well as mineral texture and size (*e.g.* Tungpalan *et al.* 2015a, b).

With regards to U-minerals, uraninite, coffinite, and brannerite as well as uranium-bearing hematite, all are soluble during leaching but at different rates, thus the leaching intensity is greatly dependent on the minerals in the feed (Ehrig *et al.* 2015). Therefore, at Olympic Dam a sound understanding of the spatial variation of U-minerals as well as Cu-mineral speciation throughout the deposit is essential to correctly conduct economic extraction.

4 URANIUM, DECAY, AND RADIONUCLIDES

Uranium is found in all rocks and soils at a range of concentrations, making-up approximately 0.0004% of the Earth's crust (crustal abundance of ~2.7 ppm; Gupta 2003), which is nearly 1,000 times more abundant than gold (Morrell & Jackson 2013). The three major naturally-occurring uranium isotopes have masses of 238, 234, and 235. Uranium-238 is by far the most common isotope, comprising 99.28% of all the uranium in the Earth's crust and is the parent isotope of the Uranium Series, found in equilibrium or near equilibrium with Uranium-234, one of its decay products, which only makes up 0.006% of uranium (Eisenbud & Gesell 1997). Uranium-235 accounts for 0.71% of the earth's uranium content and is the parent isotope of the Actinium Series (Eisenbud & Gesell 1997); uranium-235 is the only uranium isotope that can sustain a fission chain reaction and is thus used for nuclear reactors. ^{238}U and ^{235}U are primordial isotopes, meaning they formed at the birth of the universe and, because of their long half-lives, are still present (Lehto & Hou 2011).

Uranium-minerals in the Olympic Dam ore body are almost completely composed of ^{238}U. The uranium-238 decay chain contains 14 decay steps, eight of which involve alpha decay (Figure 3). Radioactive isotopes, or *radionuclides*, undergo decay because they are unstable and

need to physically change to become more stable, either by shedding mass, causing *alpha decay*, or, to balance the neutron-to-proton ratio by losing a neutron and gaining a proton, causing *beta decay* (beta decay can also occur by losing a proton and gaining a neutron). Decay is a natural and spontaneous process and *radioactivity* is produced from the energy emitted, *i.e*. *radiation*, during each decay.

Radioactivity is quantified in terms of the *Becquerel (Bq)*, the International System of Units (SI) unit of intrinsic radioactivity in a material. One Bq indicates one disintegration per second, leading to the *activity* of a material, which is expressed as the Bq per unit weight or volume (*i.e.*, activity is measured as one disintegration/second/unit weight or volume). Activity is the unit used for reporting radioactivity in copper concentrates globally and reflects the number of Becquerels produced per second from 1 kg of material.

The rate at which a particular radioisotope decays, or its *half-life*, is specific to each isotope. The half-life is the amount of time it takes for half of the atoms of an element isotope to decay to the next isotope. The observed concentration of any radionuclide is thus a function of formation rate vs. decay rate (Airey *et al.* 2012).

Thirteen different radionuclides are generated during ^{238}U decay, which ends with creation of stable, non-radioactive ^{206}Pb (Figure 3). Each RN along the decay chain has a distinct physical and geochemical behaviour such that daughter isotopes retain no features of the parent, including color, melting point, charge, solubility, physical state (*e.g.* radon gas), *etc*. These, often major differences in physical properties among the RN and Pb can cause fractionation when exposed to external conditions (temperature, pressure, oxidation state, *etc*.) both geologic or simulated, *i.e.* during materials processing, namely the extreme chemical environments of acid leaching. Understanding the complexing and evolving behaviour of RN from the ^{238}U decay chain is critical for appreciating likely host minerals and the potential for decoupling and disequilibria (*e.g.,* Ivanovich & Harmon 1992, Weiss *et al.* 1997, Bourdon *et al*. 2003).

A large amount of energy is emitted during alpha decay, as well as an alpha particle, which can both cause considerable damage on the mineral bonds and crystal lattice of a mineral *i.e.* metamictization, as well as generate nanopathways for fluid flow at the grain scale. Minerals,

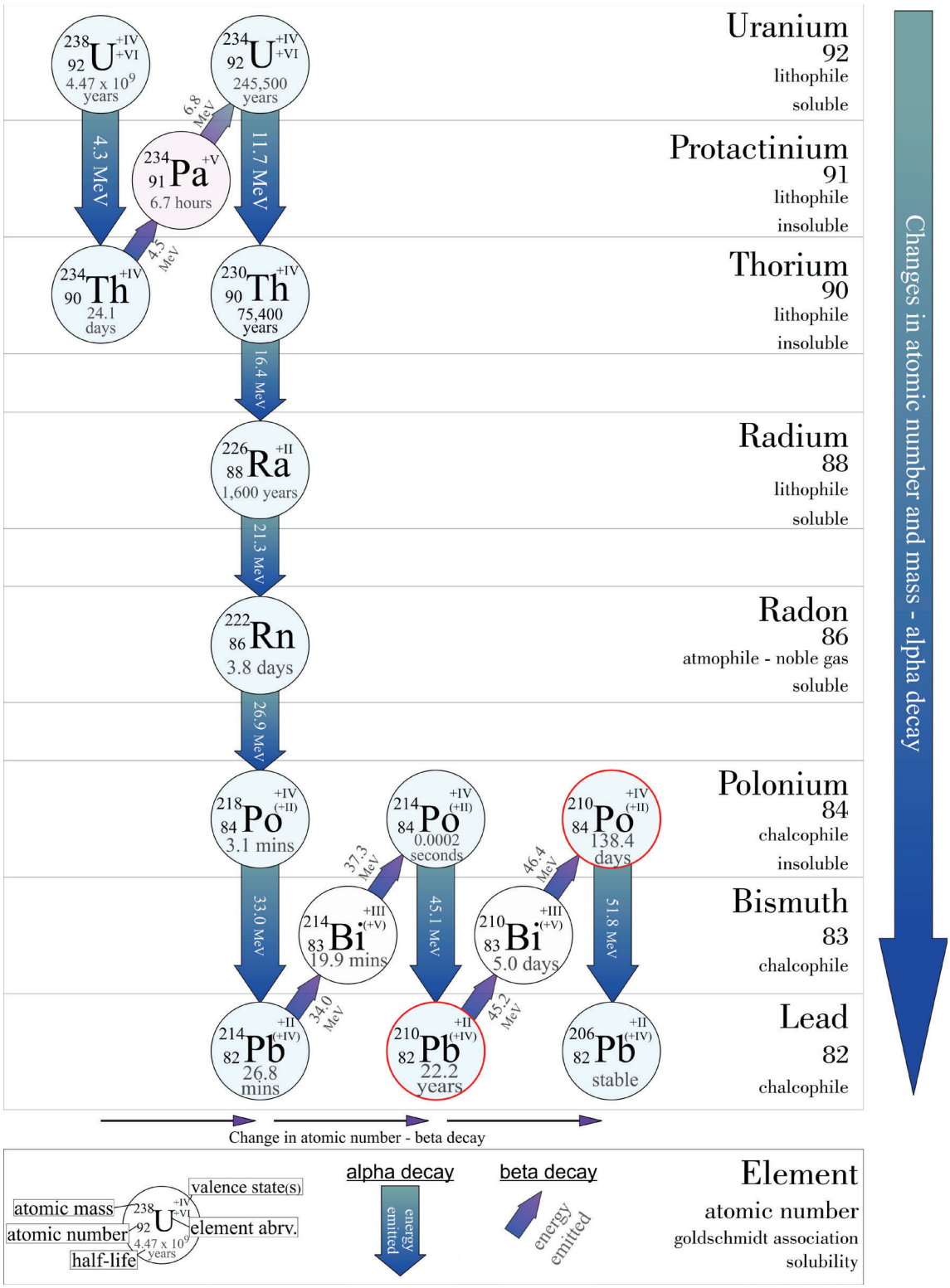


Figure 3. Cartoon of the Uranium - 238 decay chain showing the progression of element isotopes from 238-Uranium through to stable 206-Lead. Each alpha decay results in a decrease in atomic mass by four and atomic number by two; each beta decay results in an increase in atomic mass by one. Created with information from www.radioactivity.eu.com.

such as zircon, which experience this internal atomic damage and weakening are more susceptible to later chemical and physical influences that may change their internal chemistry, and also release RN and/or Pb (Ivanovich & Harmon 1992). With this concept, it is also recognised that the longer the time subsequent daughters remain with their parents, the more fragile the crystal lattice can become. This is, however, not the case for some minerals, notably uraninite, which can 'self-heal' over geologically short time scales. In these types of minerals, the crystal structure may become more amorphous (and thus less well defined) but that structure will have greater capacity to retain newly-produced isotopes (*e.g*. Hazen *et al.* 2009). Since U can be present in almost every mineral at Olympic Dam, in concentrations of ppm to wt. %, as either part of the crystal lattice or as inclusions, or both, (*e.g*, Ciobanu *et al.* 2013, Courtney-Davies *et al.* 2016, Krneta *et al.* 2016, Kontonikas-Charos *et al.* 2017, Verdugo-Ihl *et al.* 2017), this implies that RN are being produced in almost every mineral as well, so understanding the variability of mineral responses to decay energy is important.

Numerous factors impact on RN mobility including, but not limited to, geochemical behaviour, solubility, half-life, and mineralogical association. An adequate understanding of all of these components is essential for a predictive understanding of which minerals are major hosts for which RN in the orebody and subsequently during processing.

4.1 ^{210}Pb and ^{210}Po

Of principal interest to this research project are the radionuclides ^{226}Ra, ^{210}Pb, and ^{210}Po. While the total ^{238}U-to-^{206}Pb decay chain takes billions of years, ^{226}Ra, ^{210}Pb, and ^{210}Po have relatively short half-lives (1,600 years, 22.3 years, and 138.4 days, respectively) and it is known that these specific isotopes can become preferentially enriched during copper processing (Weiss *et al.* 1997, BHP Billiton 2009). At Olympic Dam, the relative concentration of ^{210}Po in concentrates is closely monitored because, although most of the RN are removed to smelter slags via smelting on-site (BHP Billiton 2009), the more volatile ^{210}Po readily evaporates and becomes accumulated as dust in the smelter gas cleaning circuit. Although often unacknowledged, U enrichment in copper ores is a global issue in metals processing and thus understanding these systems is critical for future successful removal of RN from concentrates, and will therefore increase their marketability.

Table 2 shows the activities of specific RN in material from three stages of copper concentration, starting with the ore feed, then after flotation, and then after sulfuric acid leaching of flotation concentrates and flotation tailings (Figure 2). Activities of ^{238}U, ^{230}Th, ^{226}Ra, ^{210}Pb, and ^{210}Po remain broadly in equilibrium from ore and during flotation but show a marked departure from equilibrium after leaching. This change demonstrates that during acid leaching ^{226}Ra, ^{210}Po, and ^{210}Pb are not removed along with U. This suggests that these RN are either not entirely originally co-hosted with U, or are readily decoupled during processing via dissolution and possibly subsequent reincorporation with other minerals, and thus do not report with U.

Table 2. Radionuclide activities from copper processing stream at Olympic Dam (Bq/g) based on ore grade 600 – 700 ppm U. After BHP Billiton (2011), Figure 26.6.

	Flotation Feed	Flotation Concentrate	Flotation Tailings	Concentrate Leach Discharge	Tailings Leach Discharge
^{238}U	7.4	26	6.6	1.8	12
^{230}Th	7.5	30	7.5	2.5	7.9
^{226}Ra	7.2	24	6.8	27.5	0.009
^{210}Pb	6.6	30	7.2	26	0.78
^{210}Po	7.6	30	6.3	58	0.10

In the ore and Cu concentrates, the actual concentrations of ^{210}Po and ^{210}Pb (^{210}RN) are so low (fractions of one part-per-trillion) that their presence in individual minerals cannot be measured directly by conventional microanalytical methods. In order to identify their distribution, we strive to recognize indirect information, drawn from assays, radionuclide measurements on bulk material, comprehensive mineralogical classification at micron scales, and determination of concentrations of proxy elements and isotopes within specific minerals, to predict RN mineralogical locations (Table 3). One of the goals of the project was to determine if the use of routine instrumentation to identify the location of end-product ^{206}Pb isotope, which is more abundant and thus easier to measure, could represent a proxy for identifying the host for these short half-life isotopes. This hypothesis is expanded upon in Chapters 4 (Schmandt *et al.* 2019b), 5, and 6.

Table 3: Short list of Olympic Dam minerals and possible methods of U and RN association

Group	Mineral	Possible RN association
Cu Sulfides	Chalcopyrite	Inclusions of U-minerals
	Bornite	
	Chalcocite	
	Tennantite	
	Covellite	
	Carrollite	
Assorted Sulfides	Pyrite	Inclusions of U-minerals
	Sphalerite	
	Pyrrhotite	
	Molybdenite	
	Cobaltite	
	Bismuthinite	Atomic incorporation of radiogenic Bi
U and Th minerals	Coffinite	Radiogenic U, atomic incorporation of daughter RN and Pb
	Brannerite	
	Uraninite	
	Uranothorite	
	Thorite	
Rock forming minerals	Quartz	Inclusions of U-minerals
	Fe oxide (hematite and magnatite)	Inclusions of U-minerals; atomic incorporation of RN
	Sericite	Absorption/adsorption
	Orthoclase	Inclusions of U-minerals
	Siderite (+/- Mn)	Inclusions of U-minerals
	Chlorite group	Absorption/adsorption
	Baryte	Solid solution with radiobaryte and Pb- sulfate; atomic incorporation of daughter RN and Pb; inclusions of U-minerals
	Fluorite	Inclusions of U-minerals; atomic incorporation of RN and Pb; lattice substitution of Pb for Ca
REE and REE-bearing minerals	Bastnäsite	Radiogenic Th; substitution of U, Th, and Pb for REE
	Florencite	
	Monazite	
	Synchysite	
	Xenotime	
	APS minerals	Absorption/adsorption
	Apatite	Lattice-hosted U, Th; Pb substitution for Ca; atomic incorporation of RN and Pb
Pb Minerals	Galena	Radiogenic Pb; atomic incorporation of RN Pb; absorption/adsorption RN Pb
	Clausthalite	
	Altaite	

does not account for all minerals within the entire deposit
RN - radionuclide, REE - rare earth elements

It is likely that there is RN release from the dissolution of U-minerals during processing (overwhelmingly during the leach stage). RN released to solution could dissolve to ions and re-locate, via absorption or adsorption, onto and into other minerals. Preliminary data presented in this thesis and elsewhere (Rollog *et al.* 2018, 2019) indicates that barite grains can scavenge RN from solution due to the similarities in geochemical behavior between Ba and Ra, and also Ba

and Pb. Ca-Sr-(REE)-Al-phosphate-sulfates of the Alunite Supergroup display similar behavior (Owen *et al.* in review). Also, the research of Rollog *et al*. (2019) has highlighted that an unknown, possibly major, proportion of the RN are present not within specific host minerals but rather within microfractures, at grain boundaries, and within pores within Cu-(Fe)-sulfides, hematite, and other minerals. These observations are suggestive of enhanced radionuclide mobility, both within the ore body, possibly at the scale of nanometers to meters, and also during processing.

5 RESEARCH OBJECTIVES AND THESIS STRUCTURE

Understanding the mineral hosts for ^{226}Ra and ^{210}RN and the deportment of these elements is a fundamental pre-requisite for successful implementation of the South Australian State Government's plan to triple copper production by 2030 (www.energymining.sa.gov.au/minerals). The fundamental mineralogical knowledge gained through this study also contributes to the further understanding of Olympic Dam, how it formed, and its relationship to other U- and REE-bearing IOCG deposits globally.

Samples used for this project included a combination of (i) rock samples, taken from drill core and *in-situ* from mine workings, and (ii) mineral processing samples, drawn from ore feed, flotation stages, and leach stages of the Cu-processing stream. Following preparation, samples were analyzed using a range of complimentary qualitative and quantitative microanalytical techniques capable of characterization at different scales of observation, including microscopy (optical, scanning electron), automated mineralogy (mineral liberation analysis (MLA)), and chemical analysis (electron probe microanalysis, and laser-ablation inductively coupled plasma mass spectrometry). Proprietary datasets from BHP Olympic Dam, such as whole rock assays, were made available and also used.

Each chapter of this thesis is written as an independent published or to-be-published manuscript, and therefore further details on methodology and sampling are included within each chapter.

One of the fundamental knowledge gaps explored in this thesis is the REE mineralogy of the Olympic Dam deposit. **Chapter 2** (Schmandt *et al.* 2017) documents the petrography and chemistry of the two most common REE-fluorocarbonates, bastnäsite and synchysite, and **Chapter 3** (Schmandt *et al.* 2019a) addresses the petrography and chemistry of the REE-

phosphate minerals in the deposit. The results of these studies permit insights into the geochemical behavior of REE within the deposit, the evolution of REE-bearing mineral assemblages, and the potential source of these elements. Both chapters include an assessment of the potential roles of these minerals as RN carriers within the deposit.

Chapter 4 (Schmandt *et al.* 2019b) looks further into mineral chemistry variability in ore and through processing via the mineral barite. The study identifies the diverse chemistry of barite when associated with different geologic events (*i.e*. main ore or late, cross-cutting veins) and from different processing materials. This chapter emphasizes processing implications, linking mineralogy with metallurgy, and effects from processing on element deportment and mineral chemistry.

Similarly, **Chapter 5** investigates the mineral chemistry of different occurrences of fluorite associated with Olympic Dam ore and differently colored fluorite from late stage veins. The elemental variations in the ore and different colored fluorite carry implications for genesis as well as elemental controls on fluorite color.

Chapter 6 delves into the occurrence, mineralogy, chemistry, and Pb-isotope systematics of the main Pb-chalcogenides at Olympic Dam (PbS, PbSe, and PbTe). Lead distributions are of inherent interest because of the abundant U and thus production of radiogenic Pb over geological time, as well as Pb introduced at the time of initial formation.

Chapter 7 provides a summary of key findings and implications of this research, as well as identifying a number of areas for future investigation. Supplemental and appendix material for each chapter are all included within **Chapter 8**, as well as additional materials of co-authored publications and conference contributions.

REFERENCES

Airey, P., Hinton, T. & Twining, J. (2012) The Scientific Basis. In J. R. Twining (ed.) Radioactivity in the Environment Vol 18, Chapter 1, Elsevier Ltd. doi: 10.1016/B978-0-08-045016-2.00001-1.

Allen, S.R., McPhie, J., Ferris, G. & Simpson, C. (2008) Evolution and architecture of a large felsic Igneous Province in western Laurentia: The 1.6 Ga Gawler Range Volcanics, South Australia. Journal of Volcanology and Geothermal Research, 172, 132–147. doi: 10.1016/j.jvolgeores.2005.09.027.

Apukhtina, O.B. (2016) Distribution, petrology, geochemistry and geochronology of carbonate assemblages at the Olympic Dam deposit. Unpublished Ph.D. thesis, University of Tasmania, Hobart. https://eprints.utas.edu.au/23013/.

Apukhtina, O.B., Kamenetsky, V.S., Ehrig, K., Kamenetsky, M.B., McPhie, J., Maas, R., Meffre, S., Goemann, K., Rodemann, T., Cook, N.J. & Ciobanu, C.L. (2016) Postmagmatic magnetite–apatite assemblage in mafic intrusions: a case study of dolerite at Olympic Dam, South Australia. Contributions to Mineralogy and Petrology, 171, 1–15. doi: 10.1007/s00410-015-1215-7.

Apukhtina, O.B., Kamenetsky, V.S., Ehrig, K., Kamenetsky, M.B., Maas, R., Thompson, J., McPhie, J., Ciobanu, C.L. & Cook, N.J. (2017) Early, deep magnetite-fluorapatite mineralization at the Olympic Dam Cu-U-Au-Ag deposit, South Australia. Economic Geology, 112, 1531–1542. doi: 10.5382/econgeo.2017.4520.

Barton, M.D. (2014) Iron Oxide (-Cu-Au-REE-P-Ag-U-Co) Systems. Treatise on Geochemistry: Second Edition, Vol. 13. Elsevier Ltd. doi: 10.1016/B978-0-08-095975-7.01123-2.

BHP Annual Report (2017) Copper Mineral Resources, 256–257. www.bhp.com.

BHP Billiton (2009) Olympic Dam Expansion. Draft Environmental Impact Statement. Appendix S, 30. www.bhp.com. ISBN: 978-0-9806218-4-6.

BHP Billiton (2011) Olympic Dam Expansion Supplementary Environmental Impact Statement, Chapter 26, 689–758. www.bhp.com. ISBN: 978-0-9806218-5-3, 978-0-9806218-6-0.

Bourdon, B., Henderson, G.M., Lundstrom, C.C. & Turner, S.P. (eds.) (2003) Uranium-Series Geochemistry, Volume 52, Reviews in Mineralogy & Geochemistry. Washington: Mineralogical Society of America, Geochemical Society. ISSN 1529-6466.

Bowden, B., Fraser, G., Davidson, G.J., Meffre, S., Skirrow, R., Bull, S. & Thompson, J. (2017) Age constraints on the hydrothermal history of the Prominent Hill iron oxide copper-gold deposit, South Australia. Mineralium Deposita 52, 863–881.

Britt, A., Summerfield, D., Senior, A., Roberts, D., Kay, P., Hitchman, A., Champion, D., Huston, D., Simpson, R., Smith, M., Sexton, M. & Schofield, A. (2016) Australia's Identified Mineral Resources 2016. Canberra: Geoscience Australia. doi: 10.11636/1327-1466.2016.

Cherry, A.R., Ehrig, K., Kamenetsky, V.S., Ehrig, K., McPhie, J., Croley, J.L. & Kamenetsky, M.B. (2018) Precise geochronological constraints on the origin, setting and incorporation of ca. 1.59 Ga surficial facies into the Olympic Dam Breccia Complex, South Australia. Precambrian Research 315, 162–178.

Ciobanu, C.L., Cook, N.J. & Ehrig, K. (2017a) Ore minerals down to the nanoscale: Cu- (Fe) - sulphides from the iron oxide copper gold deposit at Olympic Dam, South Australia. Ore Geology Reviews, 81, 1218–1235.

Ciobanu, C.L., Kontonikas-Charos, A., Slattery, A., Cook, N.J., Ehrig, K. & Wade, B.P. (2017) Short-Range Stacking Disorder in Mixed-Layer Compounds: A HAADF STEM Study of Bastnäsite-Parisite Intergrowths. Minerals, 7, 227. doi: 10.3390/min7110227.

Ciobanu, C.L., Wade, B.P., Cook, N.J., Schmidt Mumm, A. & Giles, D. (2013) Uranium-bearing hematite from the Olympic Dam Cu-U-Au deposit, South Australia: A geochemical tracer and reconnaissance Pb-Pb geochronometer. Precambrian Research, 238, 129–147. doi: 10.1016/j.precamres.2013.10.007.

Clark, J.M., Poznik, N., Ehrig, K., Cherry, A., McPhie, J. & Kamenetsky, V.S. (2018) Syn- to Postmineralization Structural Dismemberment of the Olympic Dam Fe-Cu-U-Au-Ag Deposit, Gawler Craton in SEG 2018 Conference Proceeding, Keystone 22-15, eds. Enders, M.S. & Broughton, D.W.

Conor, C., Raymond, O.L., Baker, T., Teale, G., Say, P. & Lowe, G. (2010) Alteration and mineralisation in the Moonta-Wallaroo Copper-Gold Mining Field Region, Olympic Domain, South Australia; in Porter, T.M. (ed.) Hydrothermal Iron Oxide Copper-Gold & Related Deposits: A Global Perspective vol. 3-4, 1–24. Adelaide: PGC Publishing.

Cook, N.J., Ciobanu, C.L., Ehrig, K., Slattery, A., Verdugo-Ihl, M.R., Courtney-Davies, L. & Gao, W. (2017) Advances and opportunities in ore mineralogy. Minerals 7, 233. doi: 10.3390/min7120233.

Cook, N.J., Ehrig, K., Rollog, M., Ciobanu, C.L., Lane, D.J., Schmandt, D.S., Owen, N.D., Hamilton, T. & Grano, S.R. (2018) ^{210}Pb and ^{210}Po in geological and related anthropogenic materials: Implications for their mineralogical distribution in base metal ores. Minerals, 8. doi: 10.3390/min8050211.

Corriveau, L. (2007) Iron Oxide Copper-Gold (±Ag ±Nb ±P ±Ree ±U) Deposits: a Canadian Perspective; in W. D. Goodfellow (ed.) Mineral Deposits of Canada: A Synthesis of Major Deposit-Types, District Metallogeny, the Evolution of Geological Provinces, and Exploration Methods. Special Publication, Geological Association of Canada, Mineral Deposits Division, 307–328.

Courtney-Davies, L., Tapster, S.R., Ciobanu, C.L., Cook, N.J., Verdugo-Ihl, M.R., Ehrig, K., Kennedy, A., Gilbert, S., Condon, D.J. & Wade, B.P. (2019) A multi-technique evaluation of hydrothermal hematite U-Pb isotope systematics: Implications for ore deposit geochronology. Chemical Geology, 513, 54-72. doi: 10.1016/j.chemgeo.2019.03.005.

Courtney-Davies, L., Zhu, Z., Ciobanu, C.L., Wade, B.P., Cook, N.J., Ehrig, K., Cabral, A.R. & Kennedy, A. (2016) Matrix-Matched Iron-Oxide Laser Ablation ICP-MS U–Pb Geochronology Using Mixed Solution Standards. Minerals, 6, 85. doi: 10.3390/min6030085.

Creaser, R.A. & Cooper, J.A. (1993) U-Pb Geochronology of Middle Proterozoic felsic magmatism surrounding the Olympic Dam Cu-U-Au-Ag and Moonta Cu-Au-Ag deposits, South Australia. Geology, 88, 186–197.

Creaser, R.A. (1989). The geology and petrology of Middle Proterozoic felsic magmatism of the

Stuart Shelf, South Australia. Unpublished Ph.D. thesis, La Trobe University, Melbourne.

Daly, S.J., Fanning, C.M. & Fairclough, M.C. (1998) Tectonic evolution and exploration potential for the Gawler Craton, South Australia. AGSO Journal of Australian Geology and Geophysics, 17, 145–168.

Davidson, G.J., Paterson, H., Meffre, S. & Berry, R.F. (2007) Characteristics and Origin of the Oak Dam East Breccia-Hosted, Iron Oxide Cu-U-(Au) Deposit: Olympic Dam Region, Gawler Craton, South Australia. Economic Geology, 102, 1471–1498.

Direen, N.G. & Lyons, P. (2007) Regional Crustal Setting of Iron Oxide Cu-Au Mineral Systems of the Olympic Dam Region, South Australia: Insights from Potential-Field Modeling. Economic Geology, 102, 1397-1414.

Dmitrijeva, M., Ehrig, K., Ciobanu, C.L., Cook, N.J., Verdugo-Ihl, M.R. & Metcalfe, AV. (2019) Defining IOCG signatures through compositional data analysis: a case study of lithogeochemical zoning at Olympic Dam, South Australia. Ore Geology Reviews, 105, 86-101. doi: 10.1016/j.oregeorev.2018.12.013.

Ehrig, K. (2013) Geometallurgy-What do you really need to know from exploration through to production?: In Proceedings MetPlant 2013, 28–33. The Australasian Institute of Mining and Metallurgy: Melbourne.

Ehrig, K., Kamenetsky, V.S., McPhie, J., Cook, N.J. & Ciobanu, C.L. (2017) Olympic Dam iron oxide Cu-U-Au-Ag deposit; in Phillips, G.N. (ed.), Australian Ore Deposits, 601–610. Melbourne: The Australasian Institute of Mining and Metallurgy.

Ehrig, K., Liebezeit, V., Macmillan, E., Lower, C., Kamenetsky, V.S., Cook, N.J. & Ciobanu, C.L. (2015) Uranium mineralogy versus the recovery of uranium at Olympic Dam. The AusIMM International Uranium Conference 2015.

Ehrig, K., McPhie, J. & Kamenetsky, V.S. (2012) Geology and Mineralogical Zonation of the Olympic Dam Iron Oxide Cu-U-Au-Ag Deposit, South Australia. In J. W. Hedenquist, M. Harris & F. Camus (eds.) Geology and Genesis of Major Copper Deposits and Districts of the World, a Tribute to Richard Sillitoe, Society of Economic Geology Special Publication, Vol. 16, 237–267. Littleton, CO, USA: SEG.

Eisenbud, M. & Gesell, T. (1997) Environmental Radioactivity from Natural, Industrial & Military Sources. Oxford, UK: Academic Press.

Ferris, G.M., Schwarz, M.P. & Heithersay, P. (2002) The geologic framework, distribution, and controls of Fe-oxide Cu-Au mineralisation in the Gawler Craton, South Australia: Part I: Geological and tectonic framework; in Porter, T.M. (ed.) Hydrothermal Iron Oxide Copper–Gold and Related Deposits: A Global Perspective, vol. 2, 9-31. Adelaide: PGC Publishing.

Freeman, H. & Tomkinson, M. (2010) Geological setting of iron oxide related mineralisation in the Southern Mount Woods Domain, South Australia; in Porter, T.M. (ed.) Hydrothermal Iron Oxide Copper-Gold & Related Deposits: A Global Perspective, v.3 - Advances in the

Understanding of IOCG Deposits, 1-20. Adelaide: PGC Publishing.

Government of South Australia Department for Energy and Mining (2016, Feb) South Australia's Copper Strategy. http://www.energymining.sa.gov.au/minerals.

Groves, D.I., Bierlein, F.P., Meinert, L.D. & Hitzman, M.W. (2010) Iron Oxide Copper-Gold (IOCG) Deposits through Earth History: Implications for Origin, Lithospheric Setting, and Distinction from Other Epigenetic Iron Oxide Deposits. Economic Geology, 105, 641–654.

Gupta, C. K. (2003) Chemical Metallurgy. Principles and Practice. Weinheim, Germany: Wiley-VCH. doi: 10.1016/B978-0-408-00567-8.50011-0.

Hand, M., Reid, A. & Jagodzinski, L. (2007) Tectonic Framework and Evolution of the Gawler Craton, Southern Australia. Economic Geology, 102, 1377–1395.

Haynes, D.W., Cross, K. C., Bills, R.T. & Reed, M. H. (1995) Olympic Dam Ore Genesis: A Fluid-Mixing Model. Economic Geology, 90, 281–307. doi: 10.2113/gsecongeo.90.2.281.

Hayward, N. & Skirrow. R.G. (2010) Geodynamic Setting and Controls on Iron Oxide Cu-Au-(+-U) Ore in the Gawler Craton, South Australia; in Porter, T.M. (ed.) Hydrothermal Iron Oxide Copper-Gold & Related Deposits: A Global Perspective, v. 3 - Advances in Understanding of IOCG deposits, PGC Publishing, Adelaide, 1-28.

Hazen, R.M., Ewing, R.C. & Sverjensky, D.A. (2009) Evolution of uranium and thorium minerals. American Mineralogist, 94, 1293–1311. doi: 10.2138/am.2009.3208.

Hitzman, M.W. & Valenta, R.K. (2005) Uranium in iron oxide-copper-gold (IOCG) systems. Economic Geology, 100, 1657–1661. doi: 10.2113/gsecongeo.100.8.1657.

Hitzman, M.W., Oreskes, N. & Einaudi, M.T. (1992) Geological characteristics and tectonic setting of Proterozoic iron oxide (Cu-U-Au-REE) deposits. Precambrian Research, 58, 241–287.

Huang, Q., Kamenetsky, V.S., Ehrig, K., McPhie, J., Kamenetsky, M., Apukhtina, O. & Chambefort, I. (2017) Effects of hydrothermal alteration on mafic lithologies at the Olympic Dam Cu-U-Au-Ag deposit. Precambrian Research, 292, 305-322. doi: 10.1016/j.precamres.2017.02.013.

Huang, Q., Kamenetsky, V.S., McPhie, J., Ehrig, K., Meffre, S., Maas, R., Thompson, J., Kamenetsky, M., Chambefort, I., Apukhtina, O. & Hu, Y. (2015) Neoproterozoic (ca. 820-830Ma) mafic dykes at Olympic Dam, South Australia: Links with the Gairdner Large Igneous Province. Precambrian Research, 271, 160–172. doi: 10.1016/j.precamres.2015.10.001.

Institute of Nuclear Physics and Particle Physics & EDP-Sciences (2018, Dec) Radioactive Series, http://www.radioactivity.eu.com.

Ismail, R., Ciobanu, C.L., Cook, N.J., Teale, G.S., Giles, D., Schmidt Mumm, A. & Wade, B. (2014) Rare Earths and other trace elements in minerals from skarn assemblages, Hillside iron oxide-copper-gold deposit, Yorke Peninsula, South Australia. Lithos, 184–187,456-

477. doi: 10.1016/j.lithos.2013.07.023.

Ivanovich, M. & Harmon, R.S. (eds.) (1992) Uranium-series Disequilibrium: Applications to Earth, marine, and Environmental Sciences. 2nd ed, 910. Oxford, UK: Clarendon Press. ISBN 0 19 854278 X.

Jagodzinski, E.A. (2005) Compilation of SHRIMP U-Pb geochronological data, Olympic domain, Gawler craton, South Australia, 2001-2003.

Johnson, J.P. & Cross, K.C. (1995) U-Pb Geochronological Constraints on the Genesis of the Olympic Dam Cu-U-Au-Ag Deposit, South Australia. Economic Geology, 90, 1046–1063.

Keyser, W.M., Ciobanu, C.L., Cook, N.J., Dmitrijeva, M., Courtney-Davies, L., Feltus, H., Gilbert, S., Johnson, G. & Ehrig, K. (2019) Iron-oxides constrain BIF evolution in terranes with protracted geological histories: the Iron Count prospect, Middleback Ranges, South Australia. Lithos, 324–325, 20–38.

Kirchenbaur, M., Maas, R., Ehrig, K., Kamenetsky, V.S., Strub, E., Ballhaus, C. & Münker, C. (2016) Uranium and Sm isotope studies of the supergiant Olympic Dam Cu–Au–U–Ag deposit, South Australia. Geochimica et Cosmochimica Acta, 180, 15–32. doi: 10.1016/j.gca.2016.01.035.

Kontonikas-Charos, A., Ciobanu, C.L., Cook, N.J., Ehrig, K., Krneta, S. & Kamenetsky, V.S. (2017) Feldspar evolution in the Roxby Downs Granite, host to Fe-oxide Cu-Au-(U) mineralisation at Olympic Dam, South Australia. Ore Geology Reviews, 80, 838–859. doi: 10.1016/j.oregeorev.2016.08.019.

Krneta, S., Ciobanu, C.L., Cook, N.J., Ehrig, K. & Kontonikas-Charos, A. (2016) Apatite at Olympic Dam, South Australia: a petrogenetic tool. Lithos, 53, 1689–1699. doi: 10.1017/CBO9781107415324.004.

Krneta, S., Ciobanu, C.L., Cook, N.J., Ehrig, K. & Kontonikas-Charos, A. (2017) Rare earth element behaviour in apatite from the Olympic Dam Cu-U-Au-Ag deposit, South Australia. Minerals, 7, 1-26. doi: 10.3390/min7080135.

Lane, D.J., Cook, N.J., Grano, S.R. & Ehrig, K. (2016) Selective leaching of penalty elements from copper concentrates: A review. Minerals Engineering, 98, 110–121.

Lehto, J. & Hou, X. (2011) Chemistry and Analysis of Radionuclides, Laboratory Techniques and Methodology, 426. Weinheim, Germany: Wiley-VCH. ISBN 978-3-527-63302-9.

Maas, R., Kamenetsky, V.S., Ehrig, K., Meffre, S., McPhie, J. & Diemar, G. (2011) Olympic Dam U-Cu-Au deposit, Australia: New age constraints. Mineralogical Magazine, 75, 1375.

Macmillan, E., Ciobanu, C.L., Ehrig, K., Cook, N.J. & Pring, A. (2016b) Chemical zoning and lattice distortion in uraninite from Olympic Dam, South Australia. American Mineralogist, 101, 2351-2354.

Macmillan, E., Ciobanu, C.L., Ehrig, K., Cook, N.J. & Pring, A. (2016c) Replacement of uraninite by bornite via coupled dissolution-reprecipitation: Evidence from texture and

microstructure. The Canadian Mineralogist, 54, 1369-1383.

Macmillan, E., Cook, N.J., Ehrig, K. & Pring, A. (2017) Chemical and textural interpretation of late-stage coffinite and brannerite from the Olympic Dam IOCG-Ag-U deposit. Mineralogical Magazine, 81, 1323–1366. doi: 10.1180/minmag.2017.081.006.

Macmillan, E., Cook, N.J., Ehrig, K., Ciobanu, C.L. & Pring, A. (2016a) Uraninite from the Olympic Dam IOCG-U-Ag deposit: Linking textural and compositional variation to temporal evolution. American Mineralogist, 101, 1295–1320. doi: 10.2138/am-2016-5411.

Mauger, A.J., Ehrig, K., Kontonikas-Charos, A., Ciobanu, C.L., Cook, N.J. & Kamenetsky, V.S. (2016) Alteration at the Olympic Dam IOCG–U deposit: insights into distal to proximal feldspar and phyllosilicate chemistry from infrared reflectance spectroscopy. Australian Journal of Earth Sciences, 63, 959-972.

McPhie, J., Orth, K., Kamenetsky, V., Kamenetsky, M. & Ehrig, K. (2016) Characteristics, origin and significance of Mesoproterozoic bedded clastic facies at the Olympic Dam Cu–U–Au–Ag deposit, South Australia. Precambrian Research, 276, 85-100. doi: 10.1016/j.precamres.2016.01.029.

Meffre, S., Kamenetsky, V., McPhie, J., Maas, R., Ehrig, K. & Chambefort, I. (2010) Pb isotopes at Olympic Dam: constraining sulphide growth. 13th Quadrennial IAGOD Symposium; Giant Ore Deposits Down-Under, Adelaide. Abstract volume, p. 78–79.

Morrell, J.S. & Jackson, M.J. (eds.) (2013) Uranium Processing and Properties. New York: Springer.

Oreskes, N. & Einaudi, M.T. (1992) Origin of hydrothermal fluids at Olympic Dam: preliminary results from fluid inclusions and stable isotopes. Economic Geology, 87, 64–90. doi: 10.2113/gsecongeo.87.1.64.

Oreskes, N. (1990) Uranium content of Olympic Dam hematite: Implications for fluid chemistry and ore depositional mechanisms. Abstracts, A137, Eighth International Association on the Genesis of Ore Deposits: Ottawa.

Owen, N., Ciobanu, C., Cook, N., Slattery, A. & Basak, A. (2018) Nanoscale Study of Clausthalite-Bearing Symplectites in Cu-Au-(U) Ores: Implications for Ore Genesis. Minerals, 8, 1-28. doi: 10.3390/min8020067.

Owen, N.D., Cook, N.J., Rollog, M., Ehrig, K., Schmandt, D.S., Ram, R., Brugger, J., Ciobanu, C.L., Wade, B.P. & Guagliardo, P. (in review) REE-, Sr-Ca-aluminum phosphate-sulphate minerals of the woodhouseite series and role as hosts for radionuclides. American Mineralogist.

Porter, T.M. (ed.) (2000) In: Hydrothermal Iron Oxide Copper–Gold and Related Deposits: A Global Perspective, vol. 1, 349. Adelaide: PGC Publishing.

Porter, T.M. (ed.) (2002) In: Hydrothermal Iron Oxide Copper–Gold and Related Deposits: A Global Perspective, vol. 2, 378. Adelaide: PGC Publishing.

Porter, T.M. (ed.) (2010) In: Hydrothermal Iron Oxide Copper–Gold and Related Deposits: A Global Perspective – Advances in the Understanding of IOCG Deposits, vols 3 and 4, 600. Adelaide: PGC Publishing.

Reeve, J.S., Cross, K. C., Smith, R.N. & Oreskes, N. (1990) Olympic Dam Cu-U-Au-Ag deposit; in Hughes, F.E. (ed.) Geology of the Mineral Deposits of Australia and Papua New Guinea. Victoria, Australia, 1828. Australasian Institute of Mining and Metallurgy. ISBN 0949106534, 9780949106537.

Reid, A.J. & Hand, M. (2012) Mesoarchean to Mesoproterozoic evolution of the southern Gawler Craton, South Australia. Episodes, 35, 216–225.

Reid, A.J., Hand, M., Jagodzinski, E., Kelsey, D. & Pearson, N. (2008) Paleoproterozoic orogenesis in the southeastern Gawler Craton, South Australia Paleoproterozoic orogenesis in the southeastern Gawler. Australian Earth Sciences Convention, 55, 449–471. doi: 10.1080/08120090801888594.

Rollog, M., Cook, N.J., Gugliardo, P., Ciobanu, C.L., Ehrig. K. & Kilburn, M. (2018) Mobility of radionuclides in the Olympic Dam Cu-U-Au-Ag deposit, South Australia. Extended abstract, International Association on the Genesis of Ore Deposits Quadrennial Symposium, Salta Argentina, August 2018.

Rollog, M., Cook, N.J., Gugliardo, P., Ehrig. K. & Kilburn, M. (2019) In situ spatial distribution mapping of radionuclides in minerals by nanoSIMS. Geochemistry: Exploration. Environment, Analysis. doi: 10.1144/geochem2018-038.

Schmandt, D.S., Cook, N.J., Ciobanu, C.L., Ehrig, K., Wade, B.P., Gilbert, S. & Kamenetsky, V.S. (2017) Rare earth element fluorocarbonate minerals from the Olympic Dam Cu-U-Au-Ag deposit, South Australia. Minerals, 7. doi: 10.3390/min7100202.

Schmandt, D.S., Cook, N.J., Ciobanu, C.L., Ehrig, K., Wade, B.P., Gilbert, S. & Kametetsky, V.S. (2019a) Rare earth element phosphates from the Olympic Dam Cu-U-Au-Ag deposit, South Australia: Recognizing temporal-spatial controls on REE mineralogy in an evolved IOCG system. The Canadian Mineralogist, 57, 1-22. doi: 10.3749/canmin.1800043.

Schmandt, D.S., Cook, N.J., Ehrig, K., Gilbert, S., Wade, B.P., Ciobanu, C.L. & Kamenetsky, V.S. (2019b) Uptake of trace elements during copper ore processing: a case study from Olympic Dam, South Australia. Minerals Engineering, 135, 83-94. doi: 10.1016/j.mineng.2019.02.034.

Skirrow, R.G., Bastrakov, E., Davidson, G., Raymond, O.L. & Heithersay, P. (2002) The Geological Framework, Distribution and Controls of Fe-Oxide Cu-Au Mineralization in the Gawler Craton, South Australia. Part II - Alteration and Mineralisation; in Porter, T.M. (ed.) Hydrothermal Iron Oxide Copper–Gold and Related Deposits: A Global Perspective, vol. 2. Adelaide: PGC Publishing.

Skirrow, R.G., Bastrakov, E.N. & Barovich, K. (2006) Metals and fluids in IOCG systems of the Gawler Craton: Constraints from Nd, O, H and S isotopes. Goldschmidt Conference Abstracts, A595. doi: 10.1016/j.gca.2006.06.1105.

Skirrow, R.G., Bastrakov, E.N., Barovich, K., Fraser, G.L., Creaser, R.A., Fanning, C.M., Raymond, O.L. & Davidson, G.J. (2007) Timing of Iron Oxide Copper-Gold Hydrothermal Activity and Nd Isotope Constraints on Metal Sources in the Gawler Craton, South Australia. Economic Geology, 102, 1441–1470. doi: 10.2113/gsecongeo.102.8.1441.

Skirrow, R.G., van der Wielen, S.E., Champion, D.C., Czamota, K. & Thiel, S. (2018) Lithospheric Architecture and Mantle Metasomatism Linked to Iron Oxide Cu-Au Ore Formation: Multidisciplinary Evidence from the Olympic Dam Region, South Australia. Geochemistry, Geophysics, Geosystems, 19, 2673–2705. doi 10.1029/2018GC007561.

Tungpalan, K., Manlapig, E., Andrusiewicz, M., Keeney, L., Wightman, E. & Edraki, M. (2015a) An integrated approach of predicting metallurgical performance relating to variability in deposit characteristics. Minerals Engineering, 71, 49–54. doi: 10.1016/j.mineng.2014.10.004.

Tungpalan, K., Wightman, E. & Manlapig, E. (2015b) Relating mineralogical and textural characteristics to flotation behaviour. Minerals Engineering, 82, 136–140. doi: 10.1016/j.mineng.2015.02.005.

Verdugo-Ihl, M.R., Ciobanu, C.L., Cook, N.J., Ehrig, K., Courtney-Davies, L. & Gilbert, S. (2017) Textures and U-W-Sn-Mo signatures in hematite from the Olympic Dam Cu-U-Au-Ag deposit, South Australia: Defining the archetype for IOCG deposits. Ore Geology Reviews, 91, 173–195. doi: 10.1016/j.oregeorev.2017.10.007.

Wade, C.E., Reid, A.J., Wingate, M.T.D., Jagodzinski, E.A. & Barovich, K. (2012) Geochemistry and geochronology of the c. 1585Ma Benagerie Volcanic Suite, southern Australia: Relationship to the Gawler Range Volcanics and implications for the petrogenesis of a Mesoproterozoic silicic large igneous province. Precambrian Research, 206–207, 17–35. doi: 10.1016/j.precamres.2012.02.020.

Weng, Z., Jowitt, S.M., Mudd, G.M. & Haque, N. (2015) A Detailed Assessment of Global Rare Earth Element Resources: Opportunities and Challenges. Economic Geology, 110, 1925–1952.

Williams, P.J., Barton, M.D., Johnson, D.A., Fontbote, L., de Haller, A., Mark, G., Oliver, N.H.S. & Marschik, R. (2005) Iron Oxide Copper-Gold Deposits: Geology, Space-Time Distribution, and Possible Modes of Origin. Economic Geology 100th Anniversary Volume, 371–405.

CHAPTER 2

RARE EARTH ELEMENT FLUOROCARBONATE MINERALS FROM THE OLYMPIC DAM CU-U-AU-AG DEPOSIT, SOUTH AUSTRALIA

Danielle S. Schmandt[1], Nigel J. Cook[1] Cristiana L. Ciobanu[1], Kathy J. Ehrig[2], Benjamin P. Wade[3], Sarah Gilbert[3], Vadim S. Kamenetsky[4]

[1] School of Chemical Engineering, The University of Adelaide, Adelaide, S.A. 5005, Australia

[2] BHP Olympic Dam, Adelaide 5000, S.A., Australia

[3] Adelaide Microscopy, The University of Adelaide, Adelaide, S.A. 5005, Australia

[4]School of Physical Sciences, University of Tasmania, Hobart, TAS 7001, Australia

Minerals. volume 7, 2017

doi: 10.3390/min7100202

Statement of Authorship

Title of Paper	Rare Earth Element Fluorocarbonate Minerals from the Olympic Dam Cu-U-Au-Ag Deposit, South Australia
Publication Status	☑ Published ☐ Accepted for Publication ☐ Submitted for Publication ☐ Unpublished and Unsubmitted work written in manuscript style
Publication Details	Published in Minerals 2017, Volume 7, Issue 10, as part of the Special Issue 'Rare-Earth Carbonates'. doi: /10.3390/min7100202

Principal Author

Name of Principal Author (Candidate)	Danielle S. Schmandt
Contribution to the Paper	Performed analytical work, carried out data processing and interpretation, oversaw development of work, and wrote manuscript
Overall percentage (%)	65
Certification:	This paper reports on original research I conducted during the period of my Higher Degree by Research candidature and is not subject to any obligations or contractual agreements with a third party that would constrain its inclusion in this thesis. I am the primary author of this paper.

Signature		Date	Dec 3rd, 2018

Co-Author Contributions

By signing the Statement of Authorship, each author certifies that:

i. the candidate's stated contribution to the publication is accurate (as detailed above);
ii. permission is granted for the candidate in include the publication in the thesis; and
iii. the sum of all co-author contributions is equal to 100% less the candidate's stated contribution.

Name of Co-Author	Nigel J. Cook		
Contribution to the Paper	10%; Helped define direction of research, supervised development of work, assisted with data interpretation, and contributed to manuscript preparation.		
Signature		Date	5/12/2018

Name of Co-Author	Cristiana L. Ciobanu		
Contribution to the Paper	5%; Helped define direction of research, supervised development of work, assisted with data interpretation, and contributed to manuscript preparation.		
Signature		Date	5/12/2018

Name of Co-Author	Kathy Ehrig		
Contribution to the Paper	5%; Provided sample material and helped to evaluate and edit manuscript.		
Signature		Date	10/12/2018

Name of Co-Author	Ben P. Wade		
Contribution to the Paper	5%; Assisted in operating analytical instrumentation and data processing.		
Signature		Date	11/12/2018

Name of Co-Author	Sarah Gilbert		
Contribution to the Paper	5%; Assisted in operating analytical instrumentation and data processing.		
Signature		Date	6/12/2018

Name of Co-Author	Vadim S. Kamenetsky		
Contribution to the Paper	5%; Helped to evaluate and edit manuscript.		
Signature		Date	09/12/2018

minerals

MDPI

Article

Rare Earth Element Fluorocarbonate Minerals from the Olympic Dam Cu-U-Au-Ag Deposit, South Australia

Danielle S. Schmandt [1,*], Nigel J. Cook [1], Cristiana L. Ciobanu [1], Kathy Ehrig [2], Benjamin P. Wade [3], Sarah Gilbert [3] and Vadim S. Kamenetsky [4]

1 School of Chemical Engineering, The University of Adelaide, Adelaide, SA 5005, Australia; nigel.cook@adelaide.edu.au (N.J.C.); cristiana.ciobanu@adelaide.edu.au (C.L.C.)
2 BHP Olympic Dam, Adelaide, SA 5000, Australia; kathy.ehrig@bhpbilliton.com
3 Adelaide Microscopy, The University of Adelaide, Adelaide, SA 5005, Australia; benjamin.wade@adelaide.edu.au (B.P.W.); sarah.gilbert@adelaide.edu.au (S.G.)
4 School of Physical Sciences, University of Tasmania, Hobart, TAS 7001, Australia; dima.kamenetsky@utas.edu.au
* Correspondence: danielle.schmandt@adelaide.edu.au; Tel.: +61-472-665-835

Received: 31 August 2017; Accepted: 17 October 2017; Published: 23 October 2017

Abstract: Olympic Dam is a world-class breccia-hosted iron-oxide copper-gold-uranium ore deposit located in the Gawler Craton, South Australia. It contains elevated concentrations of rare earth elements (REE) which occur as the REE minerals bastnäsite, synchysite, florencite, monazite, and xenotime. This is the first study to focus on the mineralogy and composition of the most abundant REE mineral at Olympic Dam, bastnäsite, and subordinate synchysite. The sample suite extends across the deposit and represents different sulfide mineralization styles (chalcopyrite-bornite and bornite-chalcocite) and breccias of various types, ranging from those dominated by clasts of granite, dykes, and hematite. The REE-fluorocarbonates (bastnäsite and synchysite) typically occur as fine-grained (<50 μm) disseminations in Cu-Fe-sulfides and gangue minerals, and also within breccia matrix. They are also locally concentrated within macroscopic REE-mineral-rich pockets at various locations across the deposit. Such coarse-grained samples formed the primary target of this study. Three general textural groups of bastnäsite are recognized: matrix (further divided into disseminated, fine-grained, and stubby types), irregular (sulfide-associated), and clast replacement. Textures are largely driven by the specific location and prevailing mineral assemblage, with morphology and grain size often controlled by the associated minerals (hematite, sulfides). Major element concentration data reveal limited compositional variation among the REE-fluorocarbonates; all are Ce-dominant. Subtle compositional differences among REE-fluorocarbonates define a spectrum from relatively La-enriched to (Ce + Nd)-enriched phases. Granite-derived hydrothermal fluids were the likely source of F in the REE-fluorocarbonates, as well as some of the CO_2, which may also have been contributed by associated mafic-ultramafic magmatism. However, transport of REE by Cl-ligands is the most likely scenario. Stubby bastnäsite and synchysite may have formed earlier, coincident with hydrothermal alteration of granite releasing Ca from feldspars. Other categories of bastnäsite, notably those co-existing with sulfides, and reaching the top of the IOCG mineralization at Olympic Dam (chalcocite + bornite zone) are relatively younger. Such an interpretation is concordant with subtle changes in the REE patterns for the different categories. The common association of bastnäsite and fluorite throughout the deposit is typical of the hematite breccias and can be deposited from neutral, slightly acidic fluids (sericite stability) at T ≈ 300 °C.

Keywords: Olympic Dam; bastnäsite; synchysite; mineral compositions

1. Introduction

The >10,000 million ton Olympic Dam Cu-U-Au-Ag deposit [1] is the largest iron oxide copper gold (IOCG)-type deposit in the world, and by far the largest of several deposits and smaller prospects within the Gawler Craton. Rare earth elements (REE) are prominent components of many IOCG systems (e.g., [2,3]). Approximate concentrations of the light REE (LREE) and heavy REE plus yttrium (HREE + Y) within the Olympic Dam total resource are 3053 ppm and 110 ppm, respectively. The deposit thus represents a global-scale anomaly with respect to REE. Despite this considerable endowment, no REE are currently recovered at Olympic Dam, or elsewhere in the Olympic Cu Province. This is primarily due to relatively low REE grades, small grain size of host minerals, their dissemination throughout the deposit, and the dominance of LREE over the more economically attractive HREE. Nevertheless, the distribution and mineralogy of REE in the deposit are of major interest and potentially significant for reconstructing ore genesis and regional-scale exploration with respect to potential future exploitation.

The fluorocarbonate bastnäsite [$REE(CO_3)F$] and florencite [$REEAl_3(PO_4)_2(OH)_6$] form the two most prominent REE-minerals at Olympic Dam. They were first identified and described by Roberts and Hudson [4], who noted the good correlation between concentrations of REE and Fe, Cu, Au, U, and F. Oreskes and Einaudi [5] highlighted REE enrichment at Olympic Dam and included brief descriptions of four major REE-minerals (bastnäsite, florencite, monazite, and xenotime), on which Lottermoser [6] provided additional description. The most recent review of the Olympic Dam deposit [7] refers to an additional REE-fluorocarbonate, synchysite [$CaREE(CO_3)_2F$], as well as REE-Al-bearing phosphate-sulphates of the beudantite group. There has, however, been no prior systematic study of REE-minerals from Olympic Dam, with respect to either petrography, relationships with other minerals, or with respect to chemical composition and variation. This is despite much recent work providing detailed description of other REE-carriers at Olympic Dam, including the U-minerals (uraninite, brannerite, and coffinite) [8,9], apatite [10,11], and feldspars [12,13]. These contributions have helped understand REE distributions at the deposit-scale, and allowed insights into deposit formation.

In this contribution, we address the petrography and chemical composition of the REE-fluorocarbonates, bastnäsite and synchysite, from the Olympic Dam orebody. Bastnäsite is by far the most abundant discrete REE-mineral, and is found throughout the orebody. We have aimed at describing the occurrence of bastnäsite and subordinate synchysite, including samples containing anomalously high REE concentrations and/or macroscopic REE-minerals. Petrographic description is followed by analysis of their compositions, in terms of both major oxides and trace elements. The results permit an evaluation of the occurrence of the dominant REE-minerals at Olympic Dam, as well as insights into the geochemical behavior of REE and the potential source(s) of these elements.

2. Background

2.1. REE-Fluorocarbonate Minerals

Rare earth element fluorocarbonates of the bastnäsite-synchysite group (BSG) are defined as mixed-layer compounds with hexagonal and rhombohedral symmetry in which REE- and Ca-bearing layers with various stacking arrangements can adapt to any intermediate composition between the end-members bastnäsite [$REE(CO_3)F$; *B*-slab] and synchysite [$CaREE(CO_3)_2F$; *S*-slab] [14–16]. However, there are only two other named minerals within the group: parisite (*BS*); and röntgenite (BS_2), as well as a handful of B_nS_m polytypes (*n*, *m*-number of *B* and *S* slabs, respectively) defined only as long-range stacking sequences (observed over hundreds of nm), e.g., B_2S, based on TEM investigations, e.g., [15,17,18]. Monoclinic symmetry is considered for parisite and synchysite based upon refinement of single crystal studies [19,20]. The stability of such mixed-layer compounds is useful for tracking the thermodynamic conditions of ore deposition [21,22].

The recognition of the low-temperature hydroxyl-bastnäsite group indicates that bastnäsite can accommodate some OH in place of F, before altering structurally [23]. The completeness of

solid solution and the stability of bastnäsite with intermediate OH–F composition are, however, questionable [24,25]. A further group is the REE-oxyfluorides (e.g., haleniusite [REEOF]) that may form at high-temperature as a breakdown product of bastnäsite [22,26].

The REE-fluorocarbonates are typically LREE-enriched and the dominant minerals making up global LREE reserves, e.g., [22].

2.2. Olympic Dam Mineralogy

The Olympic Dam deposit is located 520 km NNW of Adelaide, South Australia, on the Western Gawler Craton. The Olympic Dam deposit is contained completely within the Olympic Dam Breccia Complex (ODBC; Figure 1), hosted in the Roxby Downs Granite (RDG) within the greater Gawler silicic large igneous province (SLIP; [27]). The main mineralizing event is interpreted to have taken place at ~1590 Ma [28–31], coincident with RDG emplacement.

The geological setting and mineralogy of the Olympic Dam deposit have been described in detail elsewhere, e.g., [7]. The dominant minerals in the ODBC are hematite, quartz, sericite, feldspars, barite, fluorite, siderite, chlorite, pyrite, chalcopyrite, bornite, and chalcocite. The REE-minerals make up a total of ~0.18 wt % of the deposit: bastnäsite (~0.0833%), florencite (~0.066%), monazite (~0.0184%), synchysite (~0.0124%), and xenotime (~0.0045%) from modal mineralogy based on a 10,000 sample Mineral Liberation Analysis (MLA) dataset [7]. Along with the discrete REE-minerals, REEs are also present in solid solution within various abundant common minerals, including apatite, brannerite, coffinite, uraninite, thorite, *uranothorite*, and zircon [7,8,10].

The concentration of many elements, including REE, correlates with total whole-rock Fe concentration across the deposit [7]. The abundance of REE is broadly coincident with copper sulfide mineralization, and correlates positively with Fe wt %, increasing towards the center, although depleted in the Fe-dominant, sulfide-poor deposit core. REE-minerals and Cu-(Fe)-sulfides are often associated with one another on the scale of individual polished sections [5,7].

The two primary REE-fluorocarbonates at Olympic Dam are bastnäsite and synchysite. Bastnäsite accounts for 2.5% of all carbonates, while synchysite represents 0.4%. The other carbonates are siderite, ankerite, and dolomite-calcite, in order of decreasing abundance [7,32]. Two other REE-fluorocarbonates, parisite and an unnamed compound *B2S* (these have Ca content lying intermediate between bastnäsite and synchysite), have been identified distal to the deposit within the RDG [13,33].

3. Sampling and Analytical Methods

3.1. Sampling

The sample suite analyzed here includes 20 specimens collected from diamond drill core located across the orebody (Table 1, Figure 1) and were originally collected as part of an earlier project [34] to characterize the REE minerals. Samples were identified, and subsequently sampled, by querying the BHP Olympic Dam drill core assay database for anomalously high REE drill core intersections (see [7]). While anomalous, they are invaluable for this study of REE mineralogy as the majority of REE-minerals are typically fine-grained and disseminated throughout the deposit and often intergrown with other minerals making microanalysis difficult. X-ray diffraction (XRD) was carried out by CSIRO (in Adelaide) on each of the high-REE drill core intervals to determine the major mineral composition (Supplementary Table S1). Each sample was mounted in epoxy as a one-inch diameter polished block.

The samples were taken from lithologies logged as: (1) breccias containing dyke clasts; (2) granite-rich breccias; (3) hematite-rich breccia; and (4) sericitized dyke (Table 1). The "breccias containing dyke clasts" are zones of breccias with associated undifferentiated mafic dyke clasts; these breccias have a recognizable mafic component which has survived alteration. Such breccias occur across the deposit, with the sample suite including representative examples from the NW arm, central, and eastern edge of the deposit. The "granite-rich breccias" are breccia zones dominated by granite breccia clasts which occur across the deposit; samples include examples from the NW arm, central, and eastern edge

of the deposit. The "hematite-rich breccias" contain abundant hematite as both clasts and matrix. The samples of this lithology are derived from the center and eastern edge of the deposit. Sericitized dykes are recognized as paragenetically early within the deposit and are highly altered; the dyke sampled in this study is located towards the far NW edge of the resource.

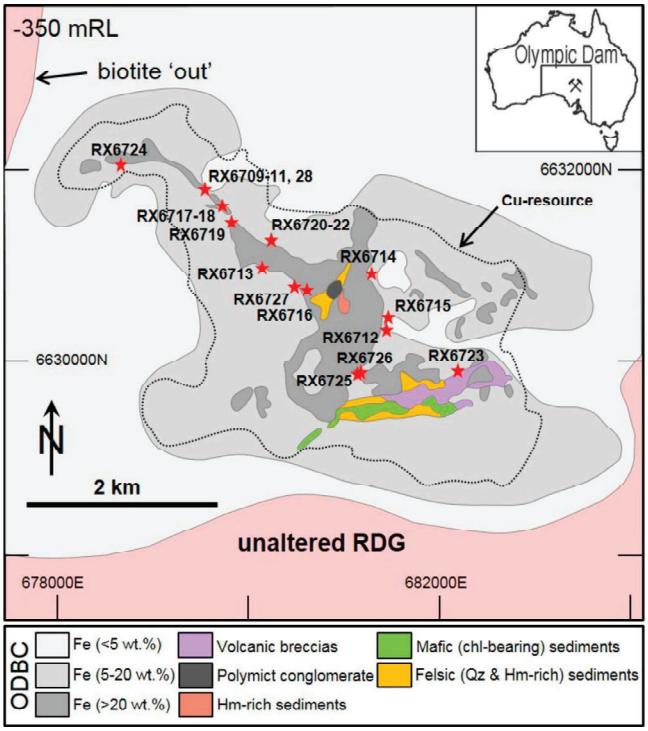


Figure 1. Sketch map of Olympic Dam orebody (−350 mRL) showing sample locations.

3.2. Analytical Methods

All microanalytical work was undertaken at Adelaide Microscopy, The University of Adelaide. Each polished block was examined and imaged using a reflected light optical microscope and using a FEI Quanta 450 Field Emission Gun (FEG) scanning electron microscope (SEM) (FEI, Eindhoven, The Netherlands) equipped with a silicon-drift detector energy-dispersive X-ray (EDAX) spectrometer. Quantitative compositional element data were acquired using a Cameca SX-Five electron probe microanalyzer (EPMA) (Cameca, Paris, France), supplemented with trace element determinations by laser ablation inductively coupled plasma mass spectrometry (LA-ICP-MS) (RESOlution-LR ArF excimer laser ablation system, Australian Scientific Instruments, Canberra, Australia, coupled to an Agilent 7700x Quadrupole ICP mass spectrometer; Agilent Technologies, Santa Clara, CA, USA). The latter method proved valuable to obtain quantitative concentration data for elements present in low abundance, including heavy REE, U, Th, and Pb. Full details on the two analytical methods can be found in Supplementary Material 1, Tables S2 and S3 (EPMA), and Supplementary Material 2 and Table S4 (LA-ICP-MS).

Table 1. Summary description and mineralogy of samples discussed in this study.

Lithology	Sample Location				Brief Sample Description [1]	REE Fluorocarbonate Occurances					
						Bastnasite					Synch-Ysite
						Matrix			Irregular Sulfide Associated	Clast Replace-Ment	
	Area	Drill Hole	Sample No.	Core Depth (m)		Stubby	Cement	Dissem-Inated			
Breccias containing dyke clasts	NW arm	RU34-3829	RX6709	72.8–73.0	Strong Bst matrix zone with clasts of Ser and Chl. Around Bst zones are Hm dominate zones with Hm as matrix and clasts with Ser-Chl. Rt and Zr present.	X					
			RX6710	73.6–73.7	Hm is the major mineral, present in clasts and with strong lineaments in matrix. Distinct zones with abundant angular-rounded clasts of Ser-Chl. Zr present.	X					
			RX6711	74.7–74.8	Strong foliation across the sample. More fine-grained sample of mostly Ser with Chl, few and small clasts, mostly composed of Hm. Flo occurs along "pressure shadows" around mineral grains. Rt and Zr present.			X			
		RU41-2571	RX6728	174.8–174.9	Mostly Hm with "crackle" Bar veinlets with Bst around clasts and Hm. Some clasts of Hm, Qz, and Ser.	X					
	East edge	RU33-159	RX6714	66.3–66.4	Sample dominated by Hm as clasts and matrix with Ser. Hm makes rounded thick rims around cores of Ser and Bar. Bst concentrated in light-colored zone on edge.			x		X	X
		RU37-7354	RX6723	4.3–4.4	Bst occurs as blades in the matrix, both disseminated and abundant in distinct zones, and in relict clasts. Abundant clasts of mostly Qz in sample, rounded-angular, all sizes. Orange areas on hand sample are mostly Qz + Hm.			x		X	
	Central	RU34-454	RX6716	82.9–83.0	Very abundant Bst throughout sample, concentrated in more fine-grained conduit, as matrix and clast replacement. Around Bst zone is mostly Hm as clasts and matrix.		X			x	
		RU45-2661	RX6727	51.8–51.9	Chaotic sample with blocky zones of fine grained Ser and Hm matrix. Other areas of breccia conduits with abundant clasts of Qz, Hm, sulfides, and Bar.		X			x	
Granite-rich breccias	East edge	RU3-558	RX6712	23.7–23.8	Clasts are mostly Qz with some Bar and Hm, rounded to angular. Ser matrix. Rt and Zr present.			x			
		RU4-105	RX6715	12.2–12.3	Abundant clasts, rounded to angular, matrix supported heterolithic breccia but clasts mostly of Qz and Hm, matrix is microbreccia and Ser.			x			
	Central	RU3-954	RX6713	70.1–70.2	Hm abundant as matrix and clasts. Other clats of sulfide, Qz, and Ser. Bn vein. Lacking pervasive disseminated bast in the matrix, Flo is present instead. Rt present.					X	

Table 1. *Cont.*

Lithology	Sample Location				Brief Sample Description [1]	REE Fluorocarbonate Occurances					
						Bastnasite					Synch-Ysite
						Matrix			Irregular Sulfide Associated	Clast Replace-Ment	
	Area	Drill Hole	Sample No.	Core Depth (m)		Stubby	Cement	Dissem-Inated			
Granite-rich breccias	NW arm	RU31-751	RX6717	90.3–90.4	Large cross cutting vein of Fl Abundant Qz clasts of ranging size, rounded to angular. Bst in matrix concentrated in localized zones, otherwise Ser and Hm. Rt and Zr present.		X	x			
			RX6718	90.8–91.0	Similar to above. Bst mostly occurs as fine-grained blades concentrated in zones as the matrix. More abundant irregular Bst "clumps". Zr and Rt present.		X	x			
		RU31-767	RX6719	5.3–5.4	Zone of Qz clasts with strong veinlet features. Other zone dominated by Hm with less defined directional features. Fine grained blade Bst as matrix around fine-grained rounded Qz clasts.		X	x			
Hematite-rich breccia	Central	RU40-1407	RX6720	19.0–19.2	Primarily composed of coarse-grained Hm with a range of textures. Cluster of clasts of rounded to angular Fl and minor Qz and Cp/Bn. Bst matrix in distinct veinlet zone with Cp and Bn.				X		
			RX6721	19.4–19.5	Strong linear zones from veins of Hm and Ser with Cp-Bn between bands of Fl clasts with matrix of Ser, Hm, Bst, and Cp-Bn.				X		
			RX6722	19.7–19.8	Matrix supported; abundant clasts, rounded to angular, composed primarily of either Fl, Qz, and Cu-(Fe) sulfides in matrix of blade Hm. Rare irregular Bst. Fl clasts are the largest.				X		
	East edge	RU38-2994	RX6725	92.8–92.9	Heterolithic clasts and clasts of mostly Qz and Hm in microbreccia of mostly Ser with also fine-grained bladed Hm and Bst.		x	X			
		RU38-2685	RX6726	77.1–77.3	Clasts of mostly Qz, Ser, Hm, and Bst. Microbreccia matrix of fine-grained Hm blades and Ser with veinlets and lineation around clasts. Rt and Zr are present.			x		X	X
Sericitized dyke	NW arm	RU41-5181	RX6724	183.7–183.8	Bst in distinct zones in darker red areas. Fine grained Bst in matrix to massive clumps. Clumps are dirty with possible faint zoning from inclusions of Hm and Ser but mostly irregular. Some distinct zones of Flo with distinct hexagonal textures with Ser in shape. Fine grained irregular Bst in Ser around Flo.		X	x			

[1] Mineral abbreviations: Hm—hematite; Qz—quartz; Chl—chlorite; Fl—fluorite; Bar—barite; Flo—florencite; Bst—bastnäsite; Ser—sericite; Cp—chalcopyrite; Bn—bornite; Cc—chalcocite; Rt—rutile; Zr—zircon. XRD analysis of major minerals of sample areas are included in Supplementary Table S1. X—major, x—minor.

Minerals **2017**, *7*, 202

4. Petrography

The occurrence of discrete REE-minerals at Olympic Dam is extremely varied but they can be generally typified as fine-grained (<50 μm), and occurring as disseminations with sulfide and gangue minerals throughout all ore zones in the deposit. They can, however, also be locally concentrated to macroscopic REE-mineral rich pockets which are described in detail here.

The various lithologies represented in this study display mineralogical and textural differences across the sample set (Table 1, Supplementary Figure S1). "Breccias containing dyke clasts" are generally hematite–sericite dominant with variable to high abundance of quartz or bastnäsite, and can also contain florencite. The sulfide assemblage in these samples mostly comprises bornite and chalcocite. "Granite-rich breccias" can be recognized from their color and bulk composition and typically contain trace amounts of Cu-(Fe)-sulfides (chiefly bornite and chalcocite). Florencite is a minor but persistent component of these samples. The "hematite-rich breccia" is represented by two domain types, one dominated by hematite and fluorite; the second domain contains no fluorite but more abundant quartz and sericite with hematite. Fluorite occurs either as clasts, agglomerated or evenly distributed, or as veinlets (Supplementary Figure S1) within the hematite-sericite matrix. Bastnäsite and sulfides (chalcopyrite-bornite) are present in variable amounts within both domains. The sericitized dyke sample is aptly named as it comprises ~78% sericite with abundant bastnäsite and some hematite, minor florencite, but no Cu-(Fe)-sulfides. All samples contain minor amounts of uranium minerals (uraninite and subordinate brannerite and coffinite) and a variety of other accessories, including cobaltite (CoAsS), altaite (PbTe), hessite (Ag_2Te), löllingite ($FeAs_2$), native copper, and gold (electrum).

4.1. Bastnäsite

In these samples bastnäsite occurs in three main forms: within the matrix, as irregular grains associated with sulfides, and replacing breccia clasts (Figures 2–5).

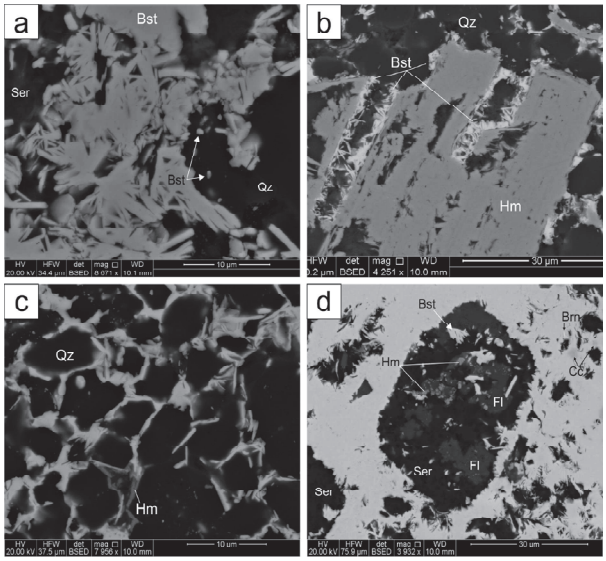


Figure 2. Backscatter electron (BSE) images showing textural aspects of fine-grained matrix bastnäsite: (**a**) Fine-grained bladed matrix bastnäsite (Bst) concentrated along boundaries of other gangue minerals (quartz-Qz, sericite-Ser) in the breccia matrix (sample RX6717); (**b**) Platy bastnäsite on hematite (Hm) and interstitial between quartz (sample RX6719); (**c**) Detail of (**b**) showing fine-grained bladed bastnäsite (white) interstitial to quartz with hematite; (**d**) Aggregated fine-grained matrix bastnäsite as a cement for other minerals (fluorite-Fl, hematite, sericite) within the breccia. Minor brannerite (Brn) and chalcocite (Cc) are enclosed by bastnäsite cement (sample RX6719).

Minerals **2017**, *7*, 202

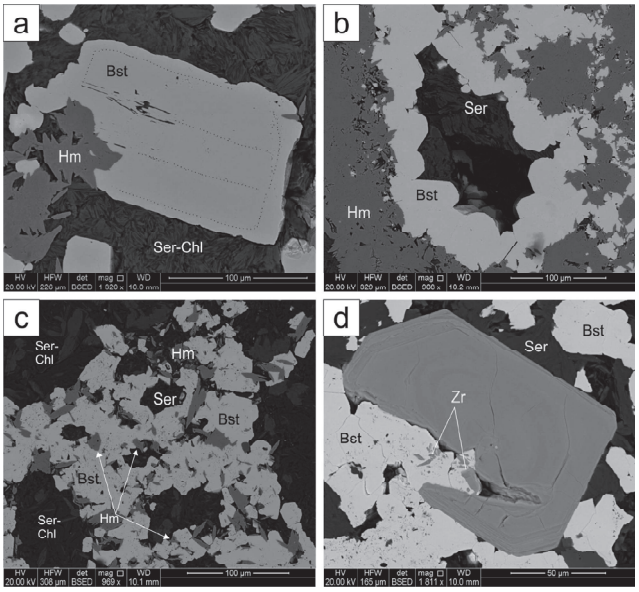


Figure 3. BSE images showing textural aspects of stubby matrix bastnäsite: (**a**) Individual stubby bastnäsite (Bst). Black line outlines pattern of hematite (Hm) and sericite (Ser) inclusions (sample RX6728). Chl-chlorite; (**b**) Stubby bastnäsite along margins of cavity with open space filled by sericite (sample RX6728); (**c**) Stubby bastnäsite forming a cement to other matrix minerals (sample RX6710); (**d**) Zircon (Zr) enclosed and partially replaced by bastnäsite cement (sample RX6709).

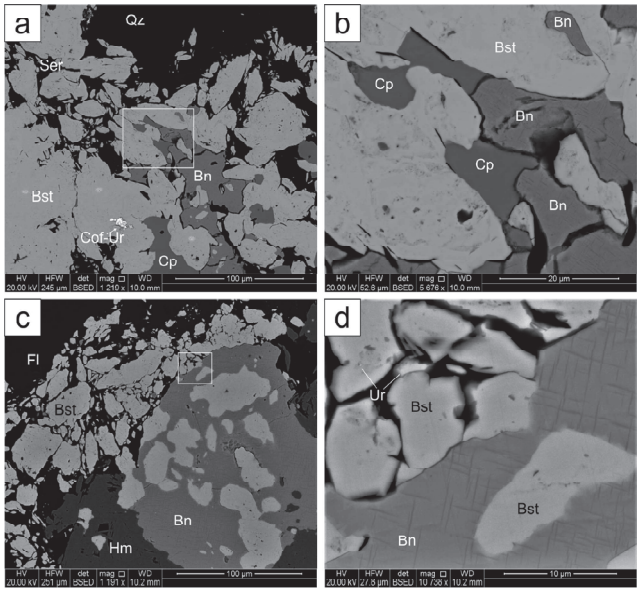


Figure 4. BSE images showing textural aspects of sulfide-associated bastnäsite: (**a**) Bastnäsite (Bst) with interstitial chalcopyrite (Cp) and bornite (Bn). Note scalloped boundaries between sulfides and bastnäsite (sample RX6720). Cof-Ur: uraninite with rim of coffinite, Qz-quartz, Ser-sericite; (**b**) Detail of domain shown by white box on (**a**). Discolorations in bastnäsite are fine inclusions of hematite and sericite; (**c**) Patchy, subhedral bastnäsite in matrix and within bornite (Sample RX6721). Fl-fluorite, Hm-hematite; (**d**) Detail of domain shown by white box on (**c**). Bornite displays lamellar exsolution of chalcopyrite. Uraninite is included in, and interstitial to bastnäsite.

Minerals **2017**, *7*, 202

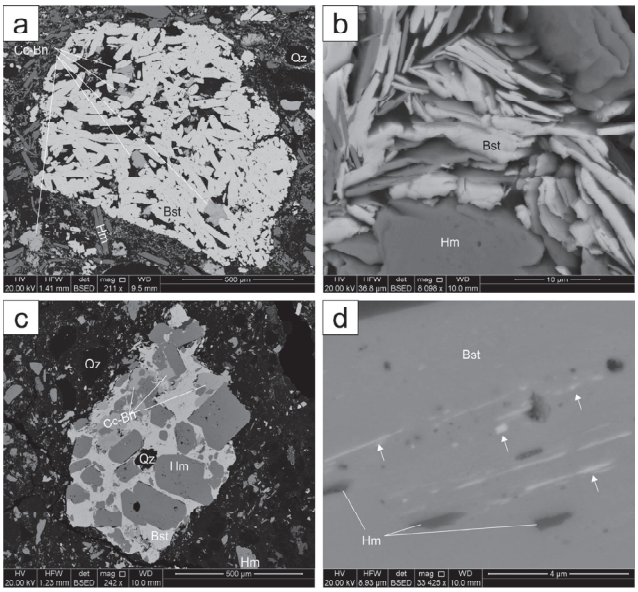


Figure 5. BSE images showing petrographic aspects of clast replacement bastnäsite: (**a**) Bladed aggregates of bastnäsite psuedomorphing the outline of a replaced clast (sample RX6726). Qz-quartz, Cc-chalcocite, Bn-bornite, Hm-hematite; (**b**) Feather-like bastnäsite with hematite (sample RX6713); (**c**) Bastnäsite forming a cement around hematite within breccia clast (sample RX6723); (**d**) Coarse-grained bastnäsite with hematite inclusions; arrows indicate brighter bands, which may be richer in HREE or contain more F and less CO_3 (sample RX6714).

4.1.1. Matrix Bastnäsite

Bastnäsite in the matrix is the most varied of the bastnäsite occurrences in terms of grain size, abundance, and morphology. Breccias with matrix bastnäsite can be either clast- or matrix-supported. The appearance of both types and bastnäsite growth patterns are suggestive of high transient porosity, which is preserved in some domains. The most common and pervasive form of bastnäsite across the entire deposit is fine-grained (1–50 μm-sized) disseminations with morphologies ranging from blades to laths and irregular grains. Although pervasively distributed throughout the breccia matrix, bastnäsite may reach high abundance in the matrix within restricted breccia domains. For example, aggregates of bladed bastnäsite are locally concentrated along the boundaries between other gangue minerals in the breccia matrix (Figure 2a). Thin, acicular, or platy bastnäsite outgrow coarser aggregates of hematite, or form an interstitial network between quartz grains (Figure 2b,c). Exceptionally, as matrix bastnäsite becomes most abundant, it can appear as a fine-grained, aggregated cement for other minerals and/or clasts within the breccia (Figure 2d). In such cases, the clasts can contain a variety of other minerals including fluorite, hematite, U-minerals, and Cu-(Fe)-sulfides.

The fine-grained matrix bastnäsite is most pervasive in samples from the NW arm and central parts of the deposit consisting of breccias with granite or mafic clasts. In these samples, the bastnäsite matrix is concentrated within distinct, mm-scale, relatively porous zones that may represent pathways with enhanced permeability allowing greater fluid interaction (Supplementary Figure S1).

A second category of matrix bastnäsite occurs as stubby, coarser (tens to hundreds of μm in size) grains with euhedral tendency (Figure 3). Marked variations in grain size can co-exist whereby single, coarser grains feature minute inclusions and replacement by other gangue minerals (sericite, hematite), with which the smaller bastnäsite is intimately associated (Figure 3a). Such textural relationships suggest different generations of stubby bastnäsite formed during cycles of mineral growth/fluid percolation throughout the breccia matrix and around cavities (Figure 3b). Stubby bastnäsite is also

seen as more massive accumulations, forming a type of composite cement together with minor gangue minerals as part of the breccia matrix (Figure 3c,d). In such cases, the bastnäsite contains abundant, minute inclusions of a wide range of minerals, including sericite ± chlorite, hematite, as well as florencite, and occasional U-minerals (Figure 3c). Such inclusions can define grain-scale zonation, or growth stages within the stubby bastnäsite. These inclusions can result from replacement of pre-existing minerals during episodes of brecciation and milling such as seen in the case of magmatic zircon (Figure 3d). Stubby bastnäsite is best developed in samples from the NW arm (RX6709, RX6710, and RX6728). These samples are from breccias containing mafic clasts in which there is a marked lineation, again suggestive of enhanced fluid permeability (Supplementary Figure S1).

4.1.2. Irregular Bastnäsite Associated with Sulfides

Bastnäsite associated with Cu-Fe-sulfides (chalcopyrite and bornite) is highly irregular with respect to size and morphology (Figure 4). The sulfides can occur interstitial to bastnäsite aggregates, whereby scalloped boundaries are observed between the two minerals (Figure 4a,b). As in stubby bastnäsite, minute inclusions of other minerals can be locally abundant, including U-minerals, Cu-Fe-sulfides, and gangue minerals. In other cases, bastnäsite is present as sub-euhedral grains to patchy areas within sulfides (Figure 4c,d). In both cases the sulfide assemblage is from the intermediate zone of the orebody and consists of bornite with exsolutions of chalcopyrite, and adjacent chalcopyrite. Irregular bastnäsite is most pronounced in samples (samples RX6720-6722) from one drill core intersecting hematite-rich breccias from the center of the deposit towards the northern edge. These samples contain fluorite and quartz clasts, abundant coarse-grained hematite, and Cu-Fe-sulfides. Bastnäsite is concentrated within veinlets and pockets with sulfides.

4.1.3. Bastnäsite Replacing Breccia Clasts

Clast replacement bastnäsite (Figure 5) is observed in many samples, some of which also contain other forms of bastnäsite. When replacing clasts, bastnäsite displays textures that depend upon the mineralogy of the replaced clast. Outstanding examples show bastnäsite as bladed aggregates that pseudomorph the outline of the clast in hematite-rich breccias from the SE part of the deposit (sample RX6726; Figure 5a).

The clast is vuggy and includes sulfides (bornite + chalcocite). When occurring together with hematite, bastnäsite may adopt a feather-like intergrowth texture (Figure 5b). In breccias containing dyke clasts (sample 6723), bastnäsite occurs as an interstitial cement to euhedral grains of hematite (Figure 5c). Such clasts also include bornite + chalcocite intergrown with bastnäsite and minor quartz. Interestingly, wherever the bastnäsite is coarser and more euhedral, REE-rich lamellae or spots can be recognized within the grain core as brighter areas on the BSE images (Figure 5d). These are too small (<1 μm) to be analyzed by the present techniques but we can speculate they may represent a REE-oxyfluoride phase (haleniusite?) resulting from decarbonation. A variety of mineral assemblages can be found interstitial to the bastnäsite within the clasts and these include sericite, chlorite, quartz, Cu-(Fe)-sulfides, and hematite, as well as rarer rutile and synchysite.

4.2. Synchysite

Synchysite is a minor phase and is only observed in two samples, one from breccia containing dyke clasts (RX6714), and the second from hematite-rich breccia (RX6726). Both samples are located around the middle part of the deposit. Unlike bastnäsite, discrete grains of synchysite can be rarely observed as 10–50 μm-sized crystals within porous sericite or hematite. Importantly, the two BSG end-member species are present in both samples (Figure 6a,b). Synchysite occurs as patchy, interstitial filling between aggregates of bladed bastnäsite suggesting it is replaced by the latter (Figure 6a). However, in detail, the synchysite which is intergrown with chalcocite and sericite, locally replaces the adjacent bastnäsite lamellae (Figure 6b). It is interesting to note that minute inclusions of bornite and chalcocite are also present within the coarser bastnäsite.

High-magnification imaging at the direct contact between the two REE-fluorocarbonates shows even more complex textures (Figure 6c,d). Such textures include diffuse boundaries characterized by sets of sub-μm size, darker (Ca-bearing BSG species) lamellae within bastnäsite (Figure 6c). These boundaries are overgrown, in turn, by well-shaped bastnäsite grains. Another texture indicative of more complexity in terms of BSG speciation, are the μm-sized lamella edges on the margin of coarse bastnäsite showing compositional "polysynthetic twinning" between the dark and bright phases (Figure 6d). Such edges protrude into the immediately adjacent bornite. These sub-μm scale features are beyond the scope of the present study and will be addressed in future research.

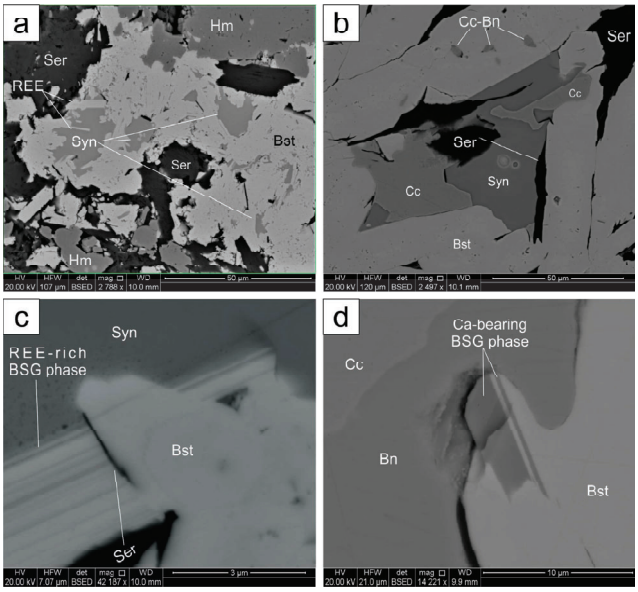


Figure 6. BSE images showing petrographic aspects of synchysite: (**a**) Synchysite (Syn) as patchy, interstitial filling between aggregates of bladed bastnäsite (Bst) (Sample RX6714). Hm-hematite, Ser-sericite; (**b**) Synchysite intergrown with chalcocite (Cc) and sericite locally replacing bastnäsite (sample RX6726). Bn-bornite; (**c**) Synchysite with intergrowths of a second REE-bearing phase (REE-rich BSG phase) along long axis. Sericite and bastnäsite crosscut both synchysite and REE intergrowths (sample RX6714); (**d**) Polysynthetic twinning between bright and dark phases. (Sample RX6726).

4.3. Other REE-Minerals

Although less abundant than bastnäsite, florencite is common throughout the sample suite. Florencite is usually anhedral and mostly occurs as fine-grained aggregates positioned between the coarser minerals. Florencite can occasionally be seen to overprint bastnäsite and synchysite but more often there are no clear relationships among the LREE-dominant minerals. Heavy REE-dominant minerals such as xenotime are relatively rare in these samples; xenotime is best preserved as overgrowths on zircon but can also be found together with coffinite, or included within bastnäsite. No monazite was observed in any of the samples investigated. Petrographic and compositional data for these minerals will be presented in a companion paper.

5. Compositional Data

The data presented here is strongly biased towards coarser REE-fluorocarbonates from samples that are particularly rich in REE-minerals. None of the small-scale intergrowths between bastnäsite and synchysite, or the REE-rich zones in bastnäsite have been analyzed as they are beyond the scope of the present study.

Minerals **2017**, *7*, 202

5.1. Bastnäsite-(Ce)

EPMA data for bastnäsite shows that all analyzed grains correspond to bastnäsite-(Ce) (Table 2). The complete analytical dataset for bastnäsite is given in Supplementary Table S5. In three single spot analyses, however, La slightly exceeds Ce, which is attributed to interference from the brighter REE-bearing phase exsolved in bastnäsite (Figure 5d). All analyzed grains are LREE-dominant with La/Ce ratio averaging ~0.61 (range 0.3–0.96). LREE abundances generally follow the order Ce > La > Nd > Pr > Sm > Eu. On average, (HREE + Y) makes up ~2.5% atoms per formula unit (a.p.f.u.) of total REE + Y.

Both Ca and Sr can be present at measurable concentrations in bastnäsite (up to 1.2 and 0.3 wt %, respectively). Time-resolved LA-ICP-MS depth profiles reveal that measured Fe, Si, and Al, which are other elements present at concentrations above EPMA mdl, relate to mineral inclusions and are hence not included in the calculated formulae. Bastnäsite formulae are calculated assuming full occupancy of one full position by REE, with CO_2 calculated on the basis of charge balance. An expanded representative formula for Olympic Dam bastnäsite-(Ce) is: $(Ca_{0.013}Sr_{0.001}La_{0.313}Ce_{0.488}Nd_{0.120}Pr_{0.043}Y_{0.012}Sm_{0.010}Gd_{0.005}Eu_{0.005}Dy_{0.002}Tb_{0.001}Er_{0.001})_{1.000}(F_{0.743}Cl_{0.002})_{0.745}(CO_3)$. Concentrations of F, as measured by EPMA, are consistently lower than the stoichiometric ideal and Cl contents are very low. One explanation may be diffusion away from the beam when using 20 s count times. Different F standards were tried to no avail, as was our attempt using different F standards against each other (i.e., using apatite as the F standard to calculate F for the EuF_3 standard), for which correct numbers were obtained. A second possibility is that full occupancy in the halogen site is met by (OH). This has, however, not been included in our calculation since the maximum limits of (OH) substitution in bastnäsite remain unknown [23–25].

5.2. Synchysite-(Ce)

EPMA data for the Ca-bearing REE-fluorocarbonates show they correspond to synchysite-(Ce) (Table 2, Supplementary Table S5). All analyzed grains are LREE-dominant, with mean La/Ce ratio of ~0.42 (range: 0.33–0.48), and LREE in order of abundances as Ce > La > Nd > Pr > Sm > Eu. (HREE + Y) makes up ~5% a.p.f.u. on average of the total REE + Y in synchysite. Measurable but minor Sr is present. Time-resolved LA-ICP-MS depth profiles show that the measured Fe relates to inclusions and this element is thus ignored in the calculated formulae. As with bastnäsite, concentrations of F are consistently lower than stoichiometric ideal (mean ~3.6 wt % F compared to ~6 wt % F in ideal end-member synchysite-(Ce)). Very minor concentrations of Cl, up to 0.03 wt %, were detected.

The structural formula for synchysite is calculated on the basis of and one divalent (Ca, Sr) and one trivalent (REE) cation with CO_2 calculated on the basis of charge balance. The mean empirical expanded formula for synchysite-(Ce) from Olympic Dam is thus: $(Ca_{0.998}Sr_{0.002})_{1.000}(La_{0.196}Ce_{0.471}Nd_{0.183}Pr_{0.055}Y_{0.029}Sm_{0.026}Gd_{0.017}Eu_{0.013}Dy_{0.006}Tb_{0.002})_{1.000}(F_{0.551}Cl_{0.001})_{0.552}(CO_3)_2$.

Of the two samples which contained abundant synchysite, RX6714 has generally higher La/Ce ratios and higher La, Ce, and HREE + Y values, while RX6726 had comparatively elevated contents of Nd, Sm, and Eu.

Table 2. Summary of EPMA compositional data for bastnäsite and synchysite. Average and standard deviations of major mineral groupings in weight percent (wt %) and atoms per formula unit (a.p.f.u.).

Mineral/Type	Bastnäsite										Synchysite	
	Matrix						Clast Replacement		Irregular			
	Stubby		Fine-Grained Cement		Disseminated							
	(n = 46)		(n = 93)		(n = 22)		(n = 66)		(n = 79)		(n = 20)	
	RX: 6709, 6710, 6728		RX: 6714, 6716, 6717, 6718, 6719, 6723, 6724, 6727		RX: 6711, 6712, 6715, 6723, 6725		RX: 6713, 6714, 6716, 6726		RX: 6720, 6721, 6722		RX: 6714, 6726	
(wt %)	Mean	St.dev.	Mean	St.dev.	Mean	St.dev.	Mean	St.dev.	Mean	St.dev.	Mean	St.dev.
Ca	0.04	0.02	0.35	0.21	0.29	0.33	0.23	0.14	0.32	0.19	12.30	0.58
Sr	0.03	0.03	0.07	0.04	0.08	0.06	0.05	0.02	0.05	0.02	0.05	0.01
La	17.03	1.65	21.97	3.63	15.38	2.27	19.93	2.38	22.49	1.86	9.88	1.23
Ce	33.77	2.00	33.13	2.80	33.49	1.63	34.34	2.06	32.00	1.22	23.76	1.20
Pr	3.61	0.18	2.74	0.44	3.56	0.49	3.14	0.36	2.67	0.19	2.67	0.15
Nd	10.91	1.18	7.29	1.97	11.06	2.11	8.91	1.67	7.39	0.74	8.91	0.79
Sm	0.95	0.31	0.57	0.33	1.16	0.38	0.84	0.34	0.55	0.15	1.18	0.18
Eu	0.44	0.14	0.28	0.12	0.48	0.10	0.43	0.16	0.25	0.08	0.56	0.10
Gd	0.36	0.21	0.33	0.21	0.60	0.29	0.43	0.24	0.30	0.11	0.77	0.13
Tb	0.07	0.02	0.07	0.02	0.09	0.03	0.08	0.03	0.07	0.02	0.09	0.02
Dy	0.18	0.09	0.15	0.09	0.27	0.14	0.19	0.08	0.14	0.05	0.34	0.08
Y	0.38	0.30	0.60	0.29	0.67	0.35	0.64	0.29	0.59	0.13	0.93	0.32
Ho	b.d.l.	b.d.l.	b.d.l.	b.d.l.	b.d.l.	b.d.l.	b.d.l.	b.d.l.	0.14	0.00	0.13	0.00
Er	0.084	0.02	0.08	0.02	0.09	0.03	0.08	0.03	0.08	0.02	0.09	0.02
Tm	b.d.l.	b.d.l.	0.07	0.01	b.d.l.	b.d.l.	0.05	0.00	0.064	0.01	b.d.l.	b.d.l.
Yb	0.07	0.00	0.07	0.02	b.d.l.	b.d.l.	0.49	0.43	0.08	0.01	b.d.l.	b.d.l.
F	7.35	0.14	7.19	0.30	7.24	0.34	7.25	0.23	7.15	0.17	3.62	0.46
Cl	0.02	0.01	0.04	0.02	0.03	0.02	0.03	0.01	0.03	0.02	0.02	0.01
Na	b.d.l.	b.d.l.	0.10	0.11	0.11	0.05	b.d.l.	b.d.l.	0.03	0.00	b.d.l.	b.d.l.
Al	0.18	0.23	0.20	0.26	0.10	0.09	0.34	0.62	0.67	1.80	0.30	0.36
K	0.01	0.00	0.05	0.09	0.06	0.04	0.03	0.05	0.06	0.24	0.07	0.08
Fe^{3+}	0.25	0.21	0.33	0.41	0.57	0.37	0.30	0.32	0.47	0.74	0.11	0.06
S	0.04	0.02	0.03	0.02	0.05	0.03	0.07	0.21	0.02	0.02	0.01	0.00
U	b.d.l.	b.d.l.	0.33	1.11	0.06	0.03	0.06	0.03	0.17	0.09	0.03	0.00
Th	0.08	0.07	0.11	0.09	0.43	0.32	0.16	0.12	0.07	0.04	0.05	0.00
Pb	b.d.l.	b.d.l.	0.03	0.01	0.04	0.01	b.d.l.	b.d.l.	0.05	0.02	b.d.l.	b.d.l.
Measured Total	75.30	2.12	75.30	3.28	75.41	3.66	76.98	2.64	74.66	2.76	65.32	2.04
∑REE + Y	67.62	2.15	67.18	3.75	66.79	3.61	69.06	2.82	66.48	2.50	48.20	1.95
La/Ce	0.51	0.06	0.67	0.15	0.46	0.06	0.58	0.09	0.70	0.05	0.42	0.05
CO_2 wt %	21.20	0.68	21.16	1.17	20.96	1.13	21.71	0.88	20.94	0.78	28.98	0.99
Calc. Total	96.24	2.81	95.98	4.78	95.38	4.84	98.32	3.76	94.96	3.30	94.09	2.92
(a.p.f.u.)												
Ca	0.002	0.001	0.018	0.010	0.014	0.016	0.011	0.007	0.016	0.009	0.998	0.001
Sr	0.001	0.001	0.002	0.001	0.002	0.001	0.001	0.001	0.001	0.000	0.002	0.001
Total 2+	0.002	0.001	0.020	0.011	0.016	0.017	0.012	0.008	0.017	0.010	1.000	0.000
La	0.254	0.023	0.329	0.050	0.233	0.034	0.291	0.032	0.340	0.022	0.202	0.021
Ce	0.500	0.026	0.492	0.031	0.502	0.018	0.497	0.024	0.480	0.006	0.483	0.011
Pr	0.053	0.003	0.040	0.006	0.053	0.006	0.045	0.005	0.040	0.003	0.054	0.003
Nd	0.157	0.016	0.105	0.027	0.161	0.027	0.125	0.022	0.108	0.011	0.176	0.017
Sm	0.013	0.004	0.008	0.004	0.016	0.005	0.011	0.004	0.008	0.002	0.022	0.004
Eu	0.006	0.002	0.004	0.002	0.007	0.001	0.006	0.002	0.003	0.001	0.011	0.002
Gd	0.005	0.003	0.004	0.003	0.008	0.004	0.005	0.003	0.004	0.001	0.014	0.002
Tb	0.001	0.000	0.001	0.000	0.001	0.000	0.001	0.000	0.001	0.000	0.002	0.000
Dy	0.002	0.001	0.002	0.001	0.003	0.002	0.002	0.001	0.002	0.001	0.006	0.001
Y	0.009	0.007	0.014	0.007	0.016	0.008	0.014	0.007	0.014	0.003	0.030	0.010
Ho	b.d.l.	b.d.l.	b.d.l.	b.d.l.	b.d.l.	b.d.l.	b.d.l.	b.d.l.	0.002	0.000	0.000	0.000
Er	0.001	0.000	0.001	0.000	0.001	0.000	0.001	0.000	0.001	0.000	0.001	0.001
Tm	b.d.l.	b.d.l.	0.001	0.000	b.d.l.	b.d.l.	0.001	0.000	0.001	0.000	0.000	0.000
Yb	0.001	0.000	0.001	0.000	b.d.l.	b.d.l.	0.006	0.005	0.001	0.000	0.000	0.000
Total 3+	0.998	0.001	0.980	0.011	0.984	0.017	0.988	0.008	0.983	0.010	1.000	0.000
F	0.802	0.030	0.774	0.055	0.790	0.060	0.765	0.031	0.777	0.031	0.545	0.079
Cl	0.001	0.000	0.002	0.001	0.002	0.001	0.002	0.001	0.002	0.001	0.001	0.001
F+Cl	0.803	0.030	0.776	0.055	0.791	0.059	0.767	0.031	0.779	0.031	0.546	0.079

* b.d.l.—below detection limit. Si, As, P, Zr were all b.d.l.

Minerals **2017**, *7*, 202

5.3. Trace Element Concentrations

Concentrations of trace elements in bastnäsite and synchysite are minor and display significant variance both within and between samples. Nevertheless, distinctions between the mineral classes can be recognized (Table 3). The full LA-ICP-MS dataset is given as Supplementary Table S6.

Stubby matrix bastnäsite, occurring together with barite, contains less Ca as well as elevated Sr (mean 531 ppm), thus a greater Sr/Ca ratio on average compared to the other bastnäsites (Table 3, Figure 7a). Stubby matrix bastnäsite is also distinguished by elevated Th (mean 213 ppm) compared to U (mean 28 ppm), which is the lowest amount of U of all the bastnäsite. Fine-grained matrix cement bastnäsite has significantly more Th to U (533 and 388 ppm, respectively), which is also the highest Th of all bastnäsite types. The clast replacement bastnäsite has almost equal mean Th and U (272 and 266 ppm, respectively) while irregular bastnäsite has vastly more U than Th (mean 1840 and 78 ppm, respectively) and both the lowest Th and highest U means of all bastnäsite. Compared to the bastnäsite values, synchysite is low in both U and Th, but with more than three times as much U than Th (mean 62 and 20 ppm, respectively) (Figure 7b). Time-resolved downhole laser profiles show that U and Th can occur both within sub-microscopic mineral inclusions and within the lattice of the bastnäsite (Supplementary Figure S2). The profiles suggest that in the coarser-grained bastnäsite, stubby matrix and clast replacement, much of the U and Th is inclusion-hosted, while lattice-hosted U and Th dominates in fine-grained matrix cement or irregular bastnäsite. The sericitized dyke, included in the fine-grained cement bastnäsite group, has bastnäsite that most consistently includes measurable proportions of ^{204}Pb as well as ^{206}Pb, ^{207}Pb, and ^{208}Pb. On average, sodium is higher in the fine-grained cement bastnäsite; of the bastnäsites, P and Zr are higher in matrix stubby and fine-grained bastnäsite but Zr is highest in synchysite. All other trace elements analyzed were extremely low (e.g., Nb), consistently < mdl (e.g., Sc), or entirely present in the form of mineral inclusions (e.g., Fe, Al, and Si).

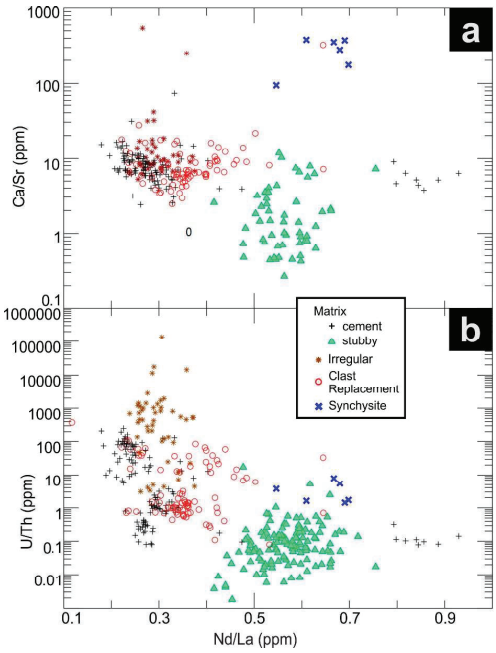


Figure 7. Trace element ratios in bastnäsite and synchysite: (**a**) Ca/Sr vs. Nd/La. Note most stubby matrix bastnäsite is richer in Sr compared to Ca; (**b**) U/Th vs. Nd/La. Note that relative proportions of U to Th separate the textural groupings with the irregular, sulfide-associated group containing more U compared to Th. The stubby matrix group, and to a lesser extent, the clast replacement sub-type, contains more Th than U.

Table 3. Summary of LA-ICP-MS trace element data for bastnäsite and synchysite. Mean, minimum (min), and maximum (max) values for major mineral groupings (in ppm).

Mineral/Type	Bastnäsite														
	Matrix						Clast Replacement			Irregular			Synchysite		
	Stubby			Fine-Grained Cement											
	(n = 137)			(n = 123)			(n = 84)			(n = 49)			(n = 6)		
	RX: 6709, 6710, 6728			RX: 6714, 6716, 6717, 6718, 6719, 6723, 6724, 6727			RX: 6713, 6714, 6716, 6726			RX: 6720, 6721, 6722			RX: 6714		
	Mean	Min.	Max.	Mean	Min.	Max.	Mean	min.	Max.	Mean	Min.	Max.	Mean	Min.	Max.
La	180,000	139,700	237,000	233,000	102,800	320,000	235,000	159,000	395,000	241,000	213,100	271,000	117,900	114,200	123,000
Pr	35,300	29,380	40,600	26,900	11,800	37,960	30,700	21,800	58,100	26,600	24,000	29,400	25,000	21,700	26,140
Nd	101,400	78,000	124,000	67,600	29,140	129,000	81,200	43,200	163,000	71,200	64,400	86,900	76,500	62,400	83,500
Sm	9170	5520	13,200	5760	2860	16,600	7500	1860	16,800	6230	4670	8520	9140	6550	10,500
Eu	2790	1460	4820	1710	435	4820	2510	347	7200	1700	870	2690	3160	2110	3680
Gd	3290	1470	5720	2870	1190	8420	3480	627	9820	3220	2270	4700	5660	3680	6550
Tb	289	93.2	561	302	95.4	819	343	41.4	830	320	218	455	684	376	835
Dy	1180	278	2340	1430	335	3510	1480	153	3290	1440	1020	1890	3230	1630	3890
Y	2990	664	6450	5170	1030	10,600	4230	378	11,600	5320	3860	7370	9050	3430	11,500
Ho	161	29.0	324	216	39.1	456	210	19.2	460	225	156	309	420	189	545
Er	313	44.4	682	466	55.9	920	430	36.7	935	512	309	757	695	297	1003
Tm	28.2	3.0	66.0	44.9	3.8	106	42.0	2.7	108	53.6	25.6	91.9	49.9	21.5	74.0
Yb	129	13.0	322	219	12.6	620	211	11.4	617	284	105	623	178	75.0	290
Lu	13.3	1.0	34.9	23.5	1.2	72.3	21.7	1.1	60.8	33.6	12.5	90.0	13.3	5.9	26.2
Ca	897	158	3100	3980	820	9950	2290	790	6100	3920	1440	9800	111,000	20,200	155,000
Sr	531	27.1	6500	591	26.9	2940	294	24.1	752	377	217	872	427	214	890
Th	213	0.14	4960	533	0.23	3760	272	0.08	5290	78.3	0.88	619	20.2	8.3	29.5
U	28.1	0.07	1510	388	7.4	7200	266	1.5	1040	1840	781	10,100	62.3	29.0	114
Pb	36.2	1.8	606	352	5.2	1370	196	1.0	2840	751	422	2150	23.7	3.0	69.5
Ba	108	0.67	7000	266	0.53	2320	82.7	0.5	1560	47.4	5.0	205	182	22.9	690
Mn	10.8	0.50	126	21.4	3.9	142	19.5	2.7	450	19.2	3.5	147	48.6	18.6	78.5
Na	229	8.5	2910	710	71.0	3250	449	69.0	3740	260	83	1100	59.0	59.0	59.0
Nb	17.0	0.1	250	6.1	0.09	150	19.0	0.07	560	2.4	0.22	10.2	3.6	0.66	7.4
P	1730	52.0	31,400	1450	69.0	9700	260	260	260	275	75.0	1100	b.d.l.	b.d.l.	b.d.l.
Zr	20.7	0.09	1220	5.0	0.11	110	5.1	0.10	155	0.42	0.10	0.84	258	4.5	690

b.d.l.—below detection limit. Si, As, P, Zr were all b.d.l.

Minerals **2017**, *7*, 202

5.4. Compositional Trends and Chondrite-Normalized Fractionation Patterns

Subtle compositional variation is present between the different textural forms of bastnäsite. There is a progressive change in the dominant REE (La, Ce, and Nd) from types containing more La towards those relatively enriched in Ce and Nd (Figure 8a). Fine-grained matrix cement (Figure 2) and irregular bastnäsite (Figure 4) are the richest in La, with Ce and Nd increasing through clast replacement bastnäsite (Figure 5), disseminated matrix and stubby bastnäsite (Figure 3), to synchysite (Figure 6), which contains the most Nd. Synchysite consistently contains more Nd and less La compared to most bastnäsite (Figure 8a). Fine-grained disseminated and stubby matrix bastnäsite show considerable overlap in La-Ce-Nd composition, as do irregular and fine-grained cementing matrix bastnäsite, with clast replacement bastnäsite positioned between those two groups. While maintaining similar La/Ce values, the irregular and fine-grained cement matrix bastnäsite are separated by their slight differences in Nd values, with irregular bastnäsite being slightly more elevated in that element (Figure 8b). Stubby matrix bastnäsite shows a deviation from other fluorocarbonates on Figure 8c, plotting below the curve, with lower La relative to other LREE if compared to the other bastnäsite types.

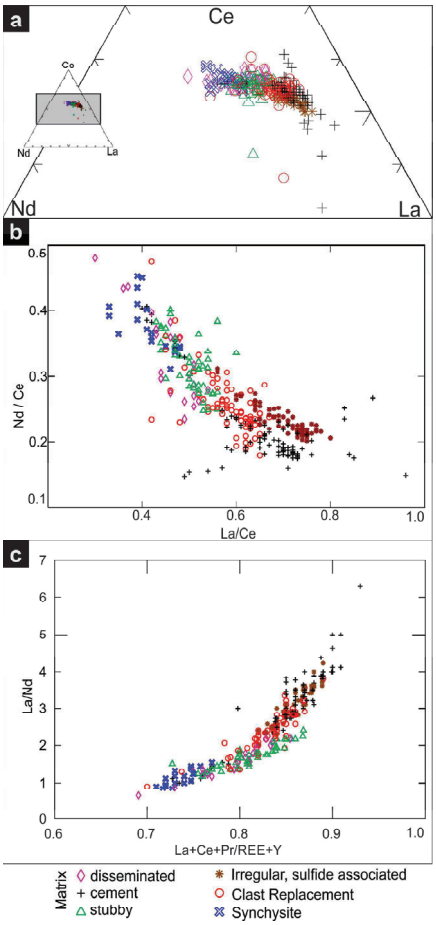


Figure 8. REE compositions of bastnäsite and synchysite (EMPA data, a.p.f.u.): (**a**) Ternary Nd-Ce-La plot showing progression of bastnäsite sub-groups from Ce- and Nd- to La-enriched; (**b**) La/Ce vs. Nd/Ce showing clustering of bastnäsite textural groups and separation of irregular and fine-grained cement bastnäsite; (**c**) Relative LREE ratios (after [35]) showing a continuous curve through synchysite, clast replacement, irregular, and fine-grained matrix bastnäsite, and stubby bastnäsite plotting astray from the curve.

When comparing the full spectrum of REE (using concentrations measured by LA-ICP-MS for those at lowest concentrations), the fine-grained matrix cement and irregular bastnäsite show elevated (HREE + Y) relative to MREE, and also greater La enrichment compared to clast replacement bastnäsite and stubby matrix bastnäsite (Figure 9a). Synchysite plots closer to stubby matrix bastnäsite albeit with slightly elevated (HREE + Y). Within the stubby matrix bastnäsite there are some compositional differences between bastnäsite formed in cavities and those within the matrix; cavity bastnäsite shows relatively elevated La and Ce and depletion in the other REE.

Chondrite-normalized fractionation trends show subtle variations in the different bastnäsite groups and synchysite (Figure 9b). The more LREE-enriched stubby bastnäsite can be distinguished from the slightly more HREE-enriched fine-grained matrix cement and irregular bastnäsite. Synchysite is shown to be enriched in only certain HREE (Dy, Y, and Ho) and is depleted in LREE and Tm, Yb, and Lu relative to bastnäsite. Synchysite and stubby bastnäsite show similar chondrite-normalized patterns although synchysite is richer in MREE and stubby bastnäsite is richer in LREE (Figure 9b). Chondrite-normalized fractionation patterns of the fine-grained matrix cement and irregular bastnäsite are similar, with slight separation among the heaviest HREE. Clast replacement bastnäsite shows similarity to the stubby bastnäsite group in the LREE segment but becomes more HREE-enriched. Stubby bastnäsite and synchysite have similar Y/Ho ratios, and more pronounced negative Y-anomaly than the irregular and fine-grained matrix cement, which shows flatter patterns and smaller Y-anomalies.

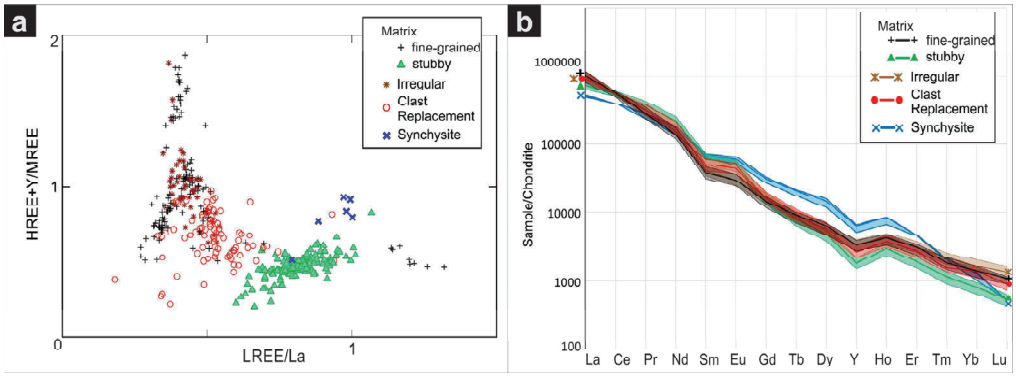


Figure 9. Compositional variation (LA-ICP-MS data) for REE in bastnäsite and synchysite; (**a**) (HREE + Y)/MREE vs. LREE/La, where HREE = (Tm + Yb + Lu + Y), MREE = (Gd + Tb + Dy + Ho + Er), and LREE = (Pr + Nd + Sm). LREE/La separates out those grains relatively enriched in La (irregular, fine-grained cement and clast replacement bastnäsite) from those with a more diverse LREE signature (stubby matrix bastnäsite and synchysite). The plot also exposes the relative enrichment in (HREE + Y) in irregular and fine-grained cement bastnäsite (those with highest HREY/MREY are fine-grained cements from sample RX6724) and relative MREE enrichment in stubby matrix bastnäsite and synchysite. Fine-grained cement bastnäsite with high (Pr + Nd + Sm) plots at the extreme right (sample RX6723); (**b**) Chondrite-normalized REY fractionation trends for the different groups of REE-fluorocarbonates (LA-ICP-MS data). Chondrite values after [36]. See also text for additional explanation.

6. Discussion

6.1. Data Trends

REE-fluorocarbonates from Olympic Dam are Ce-dominant but there is nevertheless a subtle yet measurable variation in the relative abundances of the different REE + Y within these minerals from different samples. Bastnäsite and synchysite compositions show consistent compositional differences and clustering on the plots which can be correlated with textures. Synchysite, disseminated matrix

bastnäsite, and stubby bastnäsite cluster together forming one field, while irregular, sulfide-associated and fine-grained matrix cement bastnäsite cluster within a second field. Compositions of clast replacement bastnäsite typically fall between the two groups, or tend to spread across both. The clustering of the mineral groups is consistent on all plots (Figures 7–9), and although this may yet be better exposed by a more extensive sample set, we believe these patterns carry genetic significance. Stubby bastnäsite and synchysite are clearly separated from the other bastnäsite categories. Texturally, these two groups are probably earlier—possibly linked to hydrothermal alteration of granites, with Ca for synchysite being sourced from the replacement of plagioclase feldspar. The other categories of bastnäsite are thus later and are associated with subsequent stages of IOCG deposit evolution, including the late deposition of chalcocite-bornite assemblages at shallow levels.

Smith et al. [35] report variation in REE-fluorocarbonate composition from Bayan Obo. Decrease in La/Nd is inferred to reflect changes in fluid composition from CO_2-rich hydrothermal fluids to aqueous solutions, and a decrease in temperature. Compositions are controlled by changes in REE speciation in the hydrothermal fluid, and the relative solubilities of those species and precipitated REE minerals. Smith et al. [35] model La/Nd fractionation and believe that it should be recognized in other REE-rich hydrothermal systems. We believe that our work goes some way to recognizing similar trends at Olympic Dam. The unequivocal positioning of distinct REE-fluorocarbonate compositions within the temporal-spatial development of the deposit is, however, hampered by the superimposed cycles of replacement and recrystallization recognized in many component minerals at Olympic Dam.

Apart from Ca, Sr, Th, and U, the REE-fluorocarbonates generally contain negligible trace elements at measurable concentrations. Elements that might have been expected within these REE minerals, notably Sc, As, and Nb, would appear to have partitioned into other co-existing minerals. Thorium and U is always present, although often at concentrations of only a few ppm.

Synchysite is restricted in its occurrence at Olympic Dam compared to the ubiquitous bastnäsite. When present, the relationship between the two minerals is often ambiguous, although synchysite may appear crosscut by larger grains of bastnäsite. The temporal relationship between the two minerals requires further work to be properly assessed.

Pseudomorphic replacement of feldspars by micron- to lattice-scale intergrowths among BSG species in the compositional range between parisite and bastnäsite is documented from a distal satellite (mineralized red-stained granite interval) at Olympic Dam [13,33]. These assemblages, which are associated with sericite, molybdenite, and hematite, prove the point that during the early stages of granite alteration, in which plagioclase feldspars are replaced but K-feldspars are still present, the REE-fluorocarbonates are Ca-bearing.

Synchysite from the OD orebody is distinctly poorer in La and richer in Nd and Ce than bastnäsite where they co-exist spatially, mostly as clast replacement (Figures 5a and 6b,d). Ca^{2+} is required for precipitation of synchysite, and needs to be unavailable to allow bastnäsite to form. Variation in aCa^{2+}, together with aCO_3 and aF, thus defines the stability fields for minerals across the BSG group [22]. Bastnäsite occurs in samples with abundant fluorite which could explain why no Ca-bearing REE-fluorocarbonates are present if the two minerals are precipitated simultaneously. Such an assumption implies high F activity e.g., $\log aF > -3$ at 300 °C; in a fluorocarbonate–CO_2–fluid buffered system at a pH of ~4.5 to 5.2 concordant with sericite stability [22]. The limited occurrence of synchysite in this sample set may suggest that formation is constrained by the local assemblage and limited availability of Ca, such as during the early albitization event leading to replacement of plagioclase feldspar [12].

6.2. Comparison with Published Compositional Data

The volume of published compositional data for bastnäsite and synchysite is rather limited but nonetheless instructive, as it demonstrates both the variability in natural REE-fluorocarbonates and the dependence of composition on the formational environment and conditions. The La/Nd ratio in REE-fluorocarbonates is used to identify and define variable hydrothermal systems and REE

fractionation within, or between deposits. Fleischer [37] reports compositional variability among REE-fluorocarbonates from different rocks using La/Nd as a "useful indicator of paragenetic type of occurrence". Others (e.g., [35,38]) have shown that changes in this ratio represent a useful indicator of evolving conditions, and can also be used to interpret fluid compositions and temperature. Figure 10 compares the La/Nd and La/Ce ratios of Olympic Dam synchysite and bastnäsite from this study with published datasets for the two minerals.

Most published work on synchysite has proposed that REE are leached from the host rock and precipitated as independent REE-minerals. Carbonatites are typified by greater enrichment in La compared to other deposit types. The "hydrothermal" group displays the least enrichment in La. "Hydrothermal" synchysite, in which REE is sourced from fluids associated with igneous host rocks (syenite, granite) has average ratios La/Nd of 1.157 and La/Ce ratios of 0.470 [39–41]. In contrast, carbonatite-hosted synchysite has average La/Nd and La/Ce ratios of 2.471 and 0.617, respectively [42,43]. Pegmatite-hosted synchysite [44] has average La/Nd and La/Ce ratios of 1.692 of 0.524; synchysite precipitated in basalts has average ratios of La/Nd = 1.459 and La/Ce = 0.543 [45]. Lastly, synchysite from hydrothermal fluorite veins, where REE are thought not to have been sourced not from the host rocks but rather from the basement, has average La/Nd as 1.238 and La/Ce 0.525 [46]. Average La/Nd and La/Ce ratios in Olympic Dam synchysite are 1.147 and 0.419, respectively, within the field of published data for occurrences associated with felsic intrusive rocks (Figure 10).

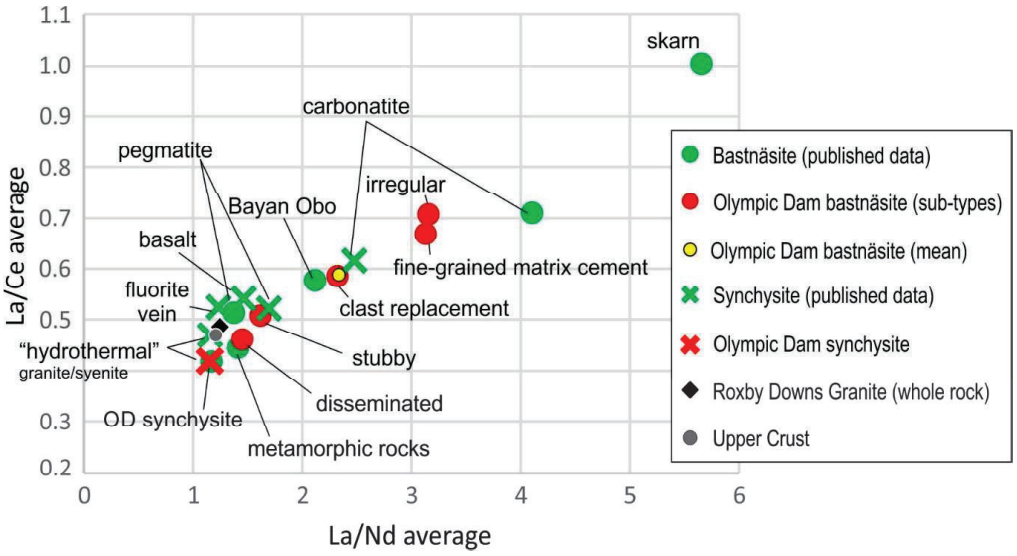


Figure 10. Plot showing mean La/Ce and La/Nd ratios in bastnäsite and synchysite from published data [35,38–48] compared to measured ratios from Olympic Dam (this study). See text for details.

Published compositional data for bastnäsite tend to be more varied than for synchysite, but overall, data for carbonatite-hosted bastnäsite [42], skarn bastnäsite [38], and from Bayan Obo [35] have higher La/Nd (4.103, 5.653, and 2.117, respectively) than bastnäsite associated with felsic intrusions: pegmatites [47]; alkaline igneous rocks [40]; or metamorphic rocks [48], which have lower La/Nd (1.372, 1.162, and 1.424, respectively). The distinction in terms of La/Ce ratios is less marked but ratios for intrusion-associated bastnäsite are nevertheless lower than for carbonatite- and skarn-hosted types. Figure 10 shows that different textural types of Olympic Dam bastnäsite plot apart on the diagram, within the fields of both carbonatite and hydrothermal bastnäsite. Despite the clear discrimination suggested by using average values on the plot, variability in bastnäsite compositions across a broad range of values appears characteristic of many other occurrences and may be attributed to changes in fluid composition, temperature, or pH.

Figure 10 shows a continuum of these ratios from more La-rich to La-poor/Nd- and Ce-enriched in different deposit types. Generally, carbonatite-hosted REE-fluorocarbonates display La-enrichment, even if published data suggests that skarn bastnäsite is even more elevated in La. Synchysite is concentrated towards the lower La/Nd and La/Ce corner, with Olympic Dam synchysite having the lowest values of both ratios. Whole-rock La/Nd and La/Ce ratios of the Roxby Downs Granite (RDG), which hosts the ODBC and thus the orebody, are also plotted on Figure 10. The RDG has ratios close to that of the average upper crust RDG La/Nd = 1.248, La/Ce = 0.487, avg. upper crust La/Nd = 1.2, La/Ce = 0.47 [38] and plots within that part of the diagram with the greatest concentration of data points, also close to the average for Olympic Dam synchysite. The average composition of Olympic Dam bastnäsite is also close to the average for the giant REE deposit of Bayan Obo [35]. This observation is particularly interesting in light of the hypothesis [49] that there should be a communality of fluid compositions associated with IOCG deposits *sensu stricto* and carbonatite-hosted ore systems such as Bayan Obo and Phalaborwa, South Africa.

The mean Y/Ho ratio of Olympic Dam REE-fluorocarbonates (20.8, std. dev. 3.4) is lower than the CHArge-and-RAdius-Controlled (CHARAC; [50]) trace element behavior field ($24 < Y/Ho < 34$) and "bulk earth" (Y/Ho = 28) [50,51]. Olympic Dam REE-fluorocarbonates thus fall within the field of hydrothermal carbonates [50]; magmatic and marine sedimentary carbonates Y/Ho values are within and above the CHARAC field, respectfully [50,51].

6.3. Formation Conditions

The deviation of bastnäsite from the whole-rock ratio of host RDG demonstrates a fractionation across the deposit which could have several causes: an evolution of bastnäsite crystallization in space and/or time, control by local conditions, or partitioning with co-existing phases. Despite the deposit showing an overall enrichment in LREE relative to HREE, REE fractionation is reported for other minerals from Olympic Dam. Distinct LREE depletion and relative MREE-enrichment are documented from hydrothermal apatite associated with hematite-sericite alteration and high-grade ore [11]. This was taken to support LREE transport as soluble chloride complexes, with which LREE are most compatible and remain in solution at high temperatures [43,52,53]. McPhie [54] extrapolate data for melt inclusions containing fluorite to claim that hydrothermal fluids at Olympic Dam were strongly acidic and very rich in F. Although this is yet to be unequivocally proven for the hydrothermal stages at OD, the presence of abundant fluorite throughout parts of the ODBC, including within the samples studied here, allows for an interpretation in which F-rich hydrothermal fluids were present at least during some stages of breccia formation and ore deposition. Under such conditions, it likely that the REE were mobilized and bastnäsite-Ce deposited by the reaction: $REECl_2^+ + HF + HCO_3^- = REECO_3F + 2H^+ + Cl^-$ [53]. REE-chloride complexes dominate under acidic conditions [55] and precipitation of REE minerals could be initiated via an increase in pH or $(CO_2)^-$ activity or a decrease in Cl-activity, with fluoride acting as a binding ligand to promote mineralization [53].

The dominance of REE-fluorocarbonates over other REE-minerals also suggests high aCO_2. While Olympic Dam contains abundant carbonates [7,32], the deposit lacks (carbonatite) carbonate, as at Bayan Obo [35], or limestone in the Bastnäs Fe-Cu-REE skarn deposit [38] to supply HCO_3. We can therefore presume that CO_2 was supplied by the hydrothermal fluids.

Changes in fluid redox or pH conditions should be exposed through marked Ce- or Eu-anomalies on the chondrite-normalized fractionation patterns. Such anomalies are, however, not observed for REE-fluorocarbonates from Olympic Dam, suggesting that these conditions are unlikely to have driven REE-fluorocarbonate deposition. This is indirectly corroborated by the interpretation that albitization is controlled by pH and not by a change in redox conditions [12]. Similarly, the influence of high pH, rather than redox, on CO_2-buffered fluids is proposed to have caused fractionation of MREE-rich apatite in high-grade bornite ores [11].

The source of REE concentrated within the Olympic Dam deposit is granite-related, either directly from hydrothermal fluids, or via hydrothermal alteration and breakdown of granite-forming minerals,

notably feldspars [12]. Bastnäsite is not a secondary mineral formed via alteration or replacement of a pre-existing REE mineral, but rather a primary LREE phase. Such a scenario does not discount the possibility of a precursor LREE mineral phase, such as monazite, that has since been altered or dissolved, with LREE "recycled" into synchysite (e.g., [56]) or bastnäsite. There is, however, no direct evidence of synchysite or bastnäsite replacing monazite or any other LREE-bearing mineral, apart from bastnäsite replacing synchysite. Broadly similar hydrothermal fluids and physicochemical conditions coincided with the stability field of bastnäsite, leading to its dominance over other REE-minerals across the deposit. The high-grade REE zones studied here may be attributed to enhanced permeability/porosity, and potentially to localized conditions promoting REE deposition.

6.4. Implications

The reproducible compositional differences among textural groups of REE-fluorocarbonates from Olympic Dam carry several implications for fluid evolution. Some texturally and compositionally distinct bastnäsite groupings are restricted to narrow intersections, only a few cm across, in just one or two drill holes (stubby and irregular, sulfide-associated), indicating a degree of spatial control. Other compositionally distinct textural types (matrix fine-grained disseminated and cement and clast replacement) are more widespread across the deposit. Because of the limited and highly targeted sample set, it is difficult to say if these are true clusters or only points on a continuous spectrum. Bastnäsite textures are highly dependent on co-existing mineral assemblages; fine-grained bladed bastnäsite develops within fine-grained sericite-dominant matrices and coarser crystals also occur, suggesting that relative REE and trace element concentrations may be dependent on co-existing minerals.

The absence of monazite in the studied samples is conspicuous and will be examined, together with the petrography of florencite, xenotime and other phosphates, which commonly replace the REE-fluorocarbonates, in a subsequent companion publication.

7. Conclusions

1. Bastnäsite-(Ce) is the most abundant REE-fluorocarbonate across the Olympic Dam deposit; synchysite-(Ce) is subordinate. Representative formulae for Olympic Dam bastnäsite-(Ce) and synchysite-(Ce) are: $((Ca,Sr_{0.01})La_{0.31}Ce_{0.49}Nd_{0.12}RE^*_{0.08})_{1.00}(F,Cl)_{0.75}(CO_3)$ and $(Ca,Sr)_{1.00}(La_{0.20}Ce_{0.47}Nd_{0.18}RE^*_{0.15})_{1.00}(F,Cl)_{0.55}(CO_3)_2$, respectively [RE* = REE other than La, Ce, and Nd]. Both show significant deficiencies in the halogen site, which may possibly be due to F migration under the beam, or met by hydroxl ions.
2. Bastnäsite occurs in a range of different textural forms, defined here as matrix, including fine-grained disseminated matrix, fine-grained cement matrix, and stubby matrix, as well as irregular bastnäsite associated with sulfides, and clast replacement bastnäsite. Textures and occurrences of bastnäsite at Olympic Dam are largely driven by the specific location and prevailing mineral assemblage, with morphology and grain size often controlled by the associated minerals (hematite, sulfides). High REE-grade zones formed due to enhanced permeability/porosity and localized conditions that promoted REE deposition.
3. Compositionally, REE-fluorocarbonates define a spectrum from relatively La-enriched to (Ce + Nd)-enriched minerals, although Ce is the dominant element in all grains analyzed. The fractionation of REE in bastnäsite and synchysite may reflect two distinct episodes of precipitation during the IOCG-forming event. The earlier, represented by stubby bastnäsite and synchysite may be associated with hydrothermal alteration of granite and Ca release from plagioclase, whereas the latter (bastnäsite only) is contemporaneous with the onset of sulfide deposition.

Supplementary Materials: The following are available online at www.mdpi.com/2075-163X/7/10/202/s1, Supplementary Material 1: Analytical Methods, Electron Probe Microanalysis, Supplementary Material 2: Analytical Methods, Laser Ablation Inductively Coupled Mass Spectrometry; Table S1: Sample XRD data,

Table S2: Full details of analytical set-up for EPMA analysis, Table S3: Full EPMA standard list, Table S4: Full details of analytical set-up for LA-ICP-MS analysis, Table S5: Complete EPMA dataset for REE-fluorocarbonates, Table S6: Full LA-ICP-MS dataset for REE-fluorocarbonates; Figure S1: Detailed images of the sample set, Figure S2: Examples of LA-ICP-MS downhole laser profiles.

Acknowledgments: This research is a contribution to the ARC Research Hub for Australian Copper–Uranium, co-supported by BHP Olympic Dam and the South Australian Mining and Petroleum Services Centre of Excellence. We thank two anonymous Minerals reviewers for their helpful comments which helped us improve this manuscript.

Author Contributions: Danielle S. Schmandt performed all analytical work and data processing under the guidance of Benjamin P. Wade and Sarah Gilbert. Nigel J. Cook and Kathy Ehrig devised the project; Kathy Ehrig and Vadim S. Kamenetsky contributed samples and deposit information; Danielle S. Schmandt, Nigel J. Cook and Cristiana L. Ciobanu wrote the paper, assisted by all other authors. This research forms part of the Ph.D. project of Danielle S. Schmandt.

Conflicts of Interest: The authors declare no conflict of interest. The project sponsors approve publication of the manuscript.

References

1. BHP Annual Reporting Suite 2016. Available online: http://www.bhp.com/investor-centre/annual-reporting-2016 (accessed on 27 September 2017).
2. Williams, P.J.; Barton, M.D.; Johnson, D.A.; Fontbote, L.; de Haller, A.; Mark, G.; Oliver, N.H.S.; Marschik, R. Iron Oxide Copper-Gold Deposits: Geology, Space-Time Distribution, and Possible Modes of Origin. *Econ. Geol.* **2005**, *Anniversary*, 371–405.
3. Groves, D.I.; Bierlein, F.P.; Meinert, L.D.; Hitzman, M.W. Iron Oxide Copper-Gold (IOCG) Deposits through Earth History: Implications for Origin, Lithospheric Setting, and Distinction from Other Epigenetic Iron Oxide Deposits. *Econ. Geol.* **2010**, *105*, 641–654. [CrossRef]
4. Roberts, D.E.; Hudson, G.R.T. The Olympic Dam Copper-Uranium-Gold Deposit, Roxby Downs, South Australia. *Econ. Geol.* **1983**, *78*, 799–822. [CrossRef]
5. Oreskes, N.; Einaudi, M.T. Origin of Rare Earth Element-Enriched Hematite Breccias at the Olympic Dan Cu-U-Au-Ag Deposit, Roxby Downs, South Australia. *Econ. Geol.* **1990**, *85*, 1–18. [CrossRef]
6. Lottermoser, B.G. Rare Earth Element Mineralogy of the Olympic Dam Cu-U-Au-Ag Deposit, Roxby Downs, South Australia: Implications for Ore Genesis. *Neues Jahrb. Mineral. Monatshefte* **1995**, *8*, 371–384.
7. Ehrig, K.; McPhie, J.; Kamenetsky, V.S. Geology and mineralogical zonation of the Olympic Dam iron oxide Cu-U-Au-Ag deposit, South Australia. In *Geology and Genesis of Major Copper Deposits and Districts of the World, a Tribute to Richard Sillitoe*; Society of Economic Geologists Special Publication; Hedenquist, J.W., Harris, M., Camus, F., Eds.; SEG: Littleton, CO, USA, 2012; Volume 16, pp. 237–268.
8. Macmillan, E.; Cook, N.J.; Ehrig, K.; Ciobanu, C.L.; Pring, A. Uraninite from the Olympic Dam IOCG-U-Ag deposit: Linking textural and compositional variation to temporal evolution. *Am. Mineral.* **2016**, *101*, 1295–1320. [CrossRef]
9. Macmillan, E.; Cook, N.J.; Ehrig, K.; Pring, A. Chemical and textural interpretation of late stage coffinite and brannerite from the Olympic Dam IOCG-Ag-U deposit. *Mineral. Mag.* **2017**. [CrossRef]
10. Krneta, S.; Ciobanu, C.L.; Cook, N.J.; Ehrig, K.; Kontonikas-Charos, A. Apatite at Olympic Dam, South Australia: A petrogenetic tool. *Lithos* **2016**, *262*, 470–485. [CrossRef]
11. Krneta, S.; Ciobanu, C.L.; Cook, N.J.; Ehrig, K.; Kontonikas-Charos, A. Rare earth element behaviour in apatite from the Olympic Dam Cu-U-Au-Ag deposit, South Australia. *Minerals* **2017**, *7*, 135. [CrossRef]
12. Kontonikas-Charos, A.; Ciobanu, C.L.; Cook, N.J.; Ehrig, K.; Krneta, S.; Kamenetsky, V.S. Feldspar Evolution in the Roxby Downs Granite, Host to Fe-Oxide Cu-Au-(U) Mineralisation at Olympic Dam, South Australia. *Ore Geol. Rev.* **2017**, *80*, 838–859. [CrossRef]
13. Kontonikas-Charos, A.; Ciobanu, C.L.; Cook, N.J.; Ehrig, K.; Ismail, R.; Krneta, S.; Basak, A. Feldspar mineralogy and rare earth element (re)mobilization in iron-oxide copper gold systems from South Australia: A nanoscale study. *Mineral. Mag.* **2017**. [CrossRef]
14. Donnay, G.; Donnay, J.D.H. The crystallography of bastnaesite, parisite, roentgenite and synchysite. *Am. Mineral.* **1953**, *38*, 932–963.
15. Van Landuyt, J.; Amelinckx, S. Multiple Beam Direct Lattice Imaging of New Mixed-Layer Compounds of the Bastnaesite-Synchisite Series. *Am. Mineral.* **1975**, *60*, 351–358.

16. Ni, Y.; Hughes, J.M.; Mariano, A.N. The Atomic Arrangement of Bastnäsite-(Ce), $Ce(CO_3)F$, and Structural Elements of Synchysite-(Ce), Rontgenite-(Ce), and Parisite-(Ce). *Am. Mineral.* **1993**, *78*, 415–418.
17. Wu, X.; Dawei, M.; Zhaolu, P.; Guangming, Y. Transmission Electron Microscopic Study of New, Regular, Mixed-Layer Structures in Calcium-Rare-Earth Fluorocarbonate Minerals. *Mineral. Mag.* **1998**, *62*, 55–64.
18. Meng, D.; Wu, X.; Han, Y.; Meng, X. Polytypism and microstructures of the mixed-layer member B_2S, $CaCe_3(CO_3)_4F_3$ in the bastnaesite-(Ce)-synchysite-(Ce) series. *Earth Planet. Sci. Lett.* **2002**, *203*, 817–828. [CrossRef]
19. Wang, L.; Ni, Y.; Hughes, J.M.; Bayliss, P.; Drexler, J.W. The atomic arrangement of synchysite-(Ce), $CeCaF(CO_3)_2$. *Can. Mineral.* **1994**, *32*, 865–871.
20. Ni, Y.; Post, J.E.; Hughes, J.M. The Crystal Structure of Parisite-(Ce), $Ce_2CaF_2(CO_3)_3$. *Am. Mineral.* **2000**, *85*, 251–258. [CrossRef]
21. Williams-Jones, A.E.; Wood, S.A. A preliminary petrogenetic grid for REE fluorocarbonates and associated minerals. *Geochim. Cosmochim. Acta* **1992**, *56*, 725–738. [CrossRef]
22. Gysi, A.P.; Williams-Jones, A.E. The Thermodynamic Properties of Bastnäsite-(Ce) and Parisite-(Ce). *Chem. Geol.* **2015**, *392*, 87–101. [CrossRef]
23. Yang, H.; Dembowski, R.F.; Conrad, P.G.; Downs, R.T. Crystal Structure and Raman Spectrum of Hydroxyl-Bästnasite-(Ce), $CeCO_3(OH)$. *Am. Mineral.* **2008**, *93*, 698–701. [CrossRef]
24. Hsu, L.C. Synthesis and Stability of Bastnaesites in a Part of the System (Ce,La)-F-H-C-O. *Mineral. Petrol.* **1992**, *47*, 87–101. [CrossRef]
25. Shivaramaiah, R.; Anderko, A.; Riman, R.E.; Navrotsky, A. Thermodynamics of Bastnaesite: A Major Rare Earth Ore Mineral. *Am. Mineral.* **2016**, *101*, 1129–1134. [CrossRef]
26. Holtstam, D.; Grins, J.; Nysten, P. Haleniusite-(La) from the Bastnäs deposit, Västmanland, Sweden: A new REE Oxyfluoride mineral species. *Can. Mineral.* **2004**, *42*, 1097–1103. [CrossRef]
27. Allen, S.R.; McPhie, J.; Ferris, G.; Simpson, C. Evolution and Architecture of a Large Felsic Igneous Province in Western Laurentia: The 1.6 Ga Gawler Range Volcanics, South Australia. *J. Volcanol. Geotherm. Res.* **2008**, *172*, 132–147. [CrossRef]
28. Johnson, J.P.; Cross, K.C. U-Pb geochronological constraints on the genesis of the Olympic Dam Cu-U-Au-Ag deposit, South Australia. *Econ. Geol.* **1995**, *90*, 1046–1063. [CrossRef]
29. Creaser, R.A.; Cooper, J.A. U-Pb Geochronology of Middle Proterozoic Felsic Magmatism Surrounding the Olympic Dam Cu-U-Au-Ag and Moonta Cu-Au-Ag Deposits, South Australia. *Geology* **1993**, *88*, 186–197. [CrossRef]
30. Ciobanu, C.L.; Wade, B.; Cook, N.J.; Schmidt Mumm, A.; Giles, D. Uranium-bearing hematite from the Olympic Dam Cu-U-Au deposit, South Australia; a geochemical tracer and reconnaissance Pb-Pb geochronometer. *Precambrian Res.* **2013**, *238*, 129–147. [CrossRef]
31. Courtney-Davies, L.; Zhu, Z.; Ciobanu, C.L.; Wade, B.P.; Cook, N.J.; Ehrig, K.; Cabral, A.R.; Kennedy, A. Matrix-matched iron-oxide laser ablation ICP-MS U-Pb geochronology using mixed solutions standards. *Minerals* **2016**, *6*, 85. [CrossRef]
32. Apukhtina, O.B. Distribution, Petrology, Geochemistry and Geochronology of Carbonate Assemblages at the Olympic Dam Deposit. Ph.D. Thesis, University of Tasmania, Hobart, Australia, 2016.
33. Ciobanu, C.L.; Kontonikas-Charos, A.; Slattery, A.; Cook, N.J.; Ehrig, K.; Wade, B.P. Short-range stacking disorder inmixed layer compounds A HAADF STEM study of bastnäsite-parisite intergrowths. *Minerals* **2017**. under review.
34. Diemar, G.A. The Petrology of Hydrothermal Rare Earth Element Bearing Minerals in the Olympic Dam IOCG Deposit Support a 1.3 Ga formation. MSc Thesis, University of Tasmania, Hobart, Australia, 2014.
35. Smith, M.P.; Henderson, P.; Campbell, L.S. Fractionation of the REE during Hydrothermal Processes: Constraints from the Bayan Obo Fe-REE-Nb Deposit, Inner Mongolia, China. *Geochim. Cosmochim. Acta* **2000**, *64*, 3141–3160. [CrossRef]
36. McDonough, W.F.; Sun, S.-S. Composition of the Earth. *Chem. Geol.* **1995**, *120*, 223–253. [CrossRef]
37. Fleischer, M. Relative proportions of the lanthanides in minerals of the bastnaesite group. *Can. Mineral.* **1978**, *16*, 361–363.
38. Holtstam, D.; Andersson, U.B. The REE minerals of the Bastnäs-type deposits, South-Central Sweden. *Can. Mineral.* **2007**, *45*, 1073–1114. [CrossRef]

39. Forster, H.J. Cerite-(Ce) and thorian synchysite-(Ce) from the Niederbobritzsch Granite, Erzgebirge, Germany: Implications for the differential mobility of the LREE and Th during alteration. *Can. Mineral.* **2000**, *38*, 67–79. [CrossRef]
40. Grammatikopoulos, T.; Mercer, W.; Gunning, C.; Prout, S. Quantitative characterization of the REE minerals by QEMSCAN from the Nechalacho Heavy Rare Earth Deposit, Thor Lake Project, NWT, Canada. *SGS Miner. Serv. Tech. Pap.* **2011**, *7*, 1–11.
41. Papoutsa, A.; Pe-Piper, G. Variation of REE-Hydrothermal Circulation in Complex Shear Zones: The Cobequid Highlands, Nova Scotia. *Can. Mineral.* **2014**, *52*, 943–968. [CrossRef]
42. Zaitsev, A.N.; Wall, F.; Le Bas, M.J. REE-Sr-Ba minerals from the Khibina Carbonatites, Kola Peninsula, Russia: Their mineralogy, paragenesis and evolution. *Mineral. Mag.* **1998**, *62*, 225–250. [CrossRef]
43. Broom-Fendley, S.; Brady, A.E.; Wall, F.; Gunn, G.; Dawes, W. REE Minerals at the Songwe Hill Carbonatite, Malawi: HREE-Enrichment in Late-Stage Apatite. *Ore Geol. Rev.* **2017**, *81*, 23–41. [CrossRef]
44. Guastoni, A.; Nestola, F.; Giaretta, A. Mineral Chemistry and Alteration of Rare Earth Element (REE) Carbonates from Alkaline Pegmatites of Mount Malosa, Malawi. *Am. Mineral.* **2009**, *94*, 1216–1222. [CrossRef]
45. Augé, T.; Bailly, L.; Wille, G. An Unusual Occurrence of Synchysite-(Ce) in Amygdules from the Esterel Volcanic Rocks, France: Implications for Rare-Earth Element Mobility. *Can. Mineral.* **2014**, *52*, 1–19. [CrossRef]
46. Mondillo, N.; Boni, M.; Balassone, G.; Spoleto, S.; Stellato, F.; Marino, A.; Santoro, L.; Spratt, J. Rare Earth Elements (REE)—Minerals in the Silius Fluorite Vein System (Sardinia, Italy). *Ore Geol. Rev.* **2016**, *74*, 211–224. [CrossRef]
47. Vasyukova, O.; Williams-Jones, A.E. The Evolution of Immiscible Silicate and Fluoride Melts: Implications for REE Ore-Genesis. *Geochim. Cosmochim. Acta* **2016**, *172*, 205–224. [CrossRef]
48. Savko, K.A.; Bazikov, N.S. Phase Equilibria of Bastnaesite, Allanite, and Monazite: Bastnaesite-out Isograde in Metapelites of the Vorontsovskaya Group, Voronezh Crystalline Massif. *Petrology* **2011**, *19*, 445–469. [CrossRef]
49. Groves, D.I.; Vielreicher, N.M. The Phalabowra (Palabora) carbonatite-hosted magnetite-copper sulfide deposit, South Africa: An end-member of the iron-oxide copper-gold-rare earth element deposit group? *Miner. Depos.* **2001**, *36*, 189–194. [CrossRef]
50. Bau, M. Controls on the Fractionation of Isovalent Trace Elements in Magmatic and Aqueous Systems: Evidence from Y/Ho, Zr/Hf, and lanthanide tetrad effect. *Contrib. Mineral. Petrol.* **1996**, *123*, 323–333. [CrossRef]
51. Tanaka, K.; Takahashi, Y.; Shimizu, H. Local structure of Y and Ho in calcite and its relevance to Y fractionation from Ho in partitioning between calcite and aqueous solution. *Chem. Geol.* **2008**, *248*, 104–113. [CrossRef]
52. Brugger, J.; Liu, W.; Etschmann, B.; Mei, Y.; Sherman, D.M.; Testemale, D. A Review of the Coordination Chemistry of Hydrothermal Systems, or Do Coordination Changes Make Ore Deposits? *Chem. Geol.* **2016**, *447*, 219–253. [CrossRef]
53. Williams-Jones, A.E.; Migdisov, A.A.; Samson, I.M. Hydrothermal Mobilisation of the Rare Earth Elements—A Tale of 'Ceria' and 'Yttria'. *Elements* **2012**, *8*, 355–360. [CrossRef]
54. McPhie, J.; Kamenetsky, V.; Allen, S.; Ehrig, K.; Agangi, A.; Bath, A. The fluorine link between a supergiant ore deposit and silicic large igneous province. *Geology* **2011**, *39*, 1003–1006. [CrossRef]
55. Haas, J.R.; Shock, E.L.; Sassani, D.C. Rare Earth Elements in Hydrothermal Systems: Estimates of Standard Partial Molal Thermodynamic Properties of Aqueous Complexes of the Rare Earth Elements at High Pressures and Temperatures. *Geochem. Explor. Environ. Anal.* **1995**, *59*, 4329–4350. [CrossRef]
56. Didier, A.; Bosse, V.; Boulvais, P.; Bouloton, J.; Paquette, J.-L.; Montel, J.-M.; Devidal, J.-L. Disturbance versus preservation of U-Th-Pb ages in monazite during fluid-rock interaction: Textural, chemical and isotopic in situ study in microgranites (Velay Dome, France). *Contrib. Mineral. Petrol.* **2013**, *165*, 1051–1072. [CrossRef]



© 2017 by the authors. Licensee MDPI, Basel, Switzerland. This article is an open access article distributed under the terms and conditions of the Creative Commons Attribution (CC BY) license (http://creativecommons.org/licenses/by/4.0/).

CHAPTER 3

RARE EARTH ELEMENT PHOSPHATES FROM THE OLYMPIC DAM CU-U-AU-AG DEPOSIT, SOUTH AUSTRALIA: RECOGNIZING TEMPORAL-SPATIAL CONTROLS ON REE MINERALOGY IN AN EVOLVED IOCG SYSTEM

Danielle S. Schmandt[1], Nigel J. Cook[1] Cristiana L. Ciobanu[1], Kathy J. Ehrig[2], Benjamin P. Wade[3], Sarah Gilbert[3], Vadim S. Kamenetsky[4]

[1] School of Chemical Engineering, The University of Adelaide, Adelaide, S.A. 5005, Australia

[2] BHP Olympic Dam, Adelaide 5000, S.A., Australia

[3] Adelaide Microscopy, The University of Adelaide, Adelaide, S.A. 5005, Australia

[4]School of Physical Sciences, University of Tasmania, Hobart, TAS 7001, Australia

The Canadian Mineralogist. volume 57, 2019

doi: 10.3749/canmin.1800043

Statement of Authorship

Title of Paper	RARE EARTH ELEMENT PHOSPHATES FROM THE OLYMPIC DAM Cu-U-Au-Ag DEPOSIT, SOUTH AUSTRALIA: RECOGNIZING TEMPORAL-SPATIAL CONTROLS ON REE MINERALOGY IN AN EVOLVED IOCG SYSTEM
Publication Status	☑ Published ☐ Accepted for Publication ☐ Submitted for Publication ☐ Unpublished and Unsubmitted work written in manuscript style
Publication Details	Published with The Canadian Mineralogist, v. 57, 2019. doi: 10.3749/canmin.1800043

Principal Author

Name of Principal Author (Candidate)	Danielle S. Schmandt		
Contribution to the Paper	Performed analytical work, carried out data processing and interpretation, oversaw development of work, and wrote manuscript		
Overall percentage (%)	65		
Certification:	This paper reports on original research I conducted during the period of my Higher Degree by Research candidature and is not subject to any obligations or contractual agreements with a third party that would constrain its inclusion in this thesis. I am the primary author of this paper.		
Signature		Date	Dec 3rd, 2018

Co-Author Contributions

By signing the Statement of Authorship, each author certifies that:

i. the candidate's stated contribution to the publication is accurate (as detailed above);

ii. permission is granted for the candidate in include the publication in the thesis; and

iii. the sum of all co-author contributions is equal to 100% less the candidate's stated contribution.

Name of Co-Author	Nigel J. Cook		
Contribution to the Paper	10%; Helped define direction of research, supervised development of work, assisted with data interpretation, and contributed to manuscript preparation.		
Signature		Date	5/12/2018

Cristiana L. Ciobanu	Cristiana L. Ciobanu		
Contribution to the Paper	5%; Helped define direction of research, supervised development of work, assisted with data interpretation, and contributed to manuscript preparation.		
Signature		Date	5/12/2018

Name of Co-Author	Kathy Ehrig		
Contribution to the Paper	5%; Provided sample material and helped to evaluate and edit manuscript.		
Signature		Date	10/12/2018

Name of Co-Author	Benjamin P. Wade		
Contribution to the Paper	5%; Assisted in operating analytical instrumentation and data processing.		
Signature		Date	11/12/2018

Name of Co-Author	Sarah Gilbert		
Contribution to the Paper	5%; Assisted in operating analytical instrumentation and data processing.		
Signature		Date	6/12/2018

Name of Co-Author	Vadim S. Kamenetsky		
Contribution to the Paper	5%; Helped to evaluate and edit manuscript.		
Signature		Date	09/12/2018

The Canadian Mineralogist
Vol. 57, pp. 1-22 (2019)
DOI: 10.3749/canmin.1800043

RARE EARTH ELEMENT PHOSPHATE MINERALS FROM THE OLYMPIC DAM Cu-U-Au-Ag DEPOSIT, SOUTH AUSTRALIA: RECOGNIZING TEMPORAL-SPATIAL CONTROLS ON REE MINERALOGY IN AN EVOLVED IOCG SYSTEM

DANIELLE S. SCHMANDT[§], NIGEL J. COOK, AND CRISTIANA L. CIOBANU

School of Chemical Engineering, The University of Adelaide, Adelaide, South Australia 5005, Australia

KATHY EHRIG

BHP Olympic Dam, Adelaide, South Australia 5000, Australia

BENJAMIN P. WADE AND SARAH GILBERT

Adelaide Microscopy, The University of Adelaide, Adelaide, South Australia 5005, Australia

VADIM S. KAMENETSKY

School of Physical Sciences, University of Tasmania, Hobart, Tasmania 7001, Australia

ABSTRACT

Florencite, $[REEAl_3(PO_4)_2(OH)_6]$, is the most abundant REE-phosphate mineral in the giant Olympic Dam Cu-U-Au-Ag deposit, South Australia. Florencite typically occurs as fine-grained crystals and occasional aggregates in the matrix of the granite-dominant breccia that hosts the majority of the copper mineralization. Olympic Dam florencite, with the compositional range and extended formula $(Ca_{0.01–0.24}Sr_{0.03–0.40}La_{0.14–0.49}Ce_{0.20–0.47}Pr_{0.00–0.03}Nd_{0.00–0.05})_{\Sigma 0.43–0.96}Al_{2.89–3.33}(P_{1.42–1.96}S_{0.05–0.34}As_{0.0–0.20})_{\Sigma 1.77–2.21}O_4(OH)_6]$, is LREE-enriched, typically La-dominant, while HREEs are minor. There is also compositional variability with respect to Sr, Ca, SO_4, and AsO_4 components. Chondrite-normalized fractionation trends are steeply downwards-sloping with a relatively low and flat HREE segment. Such a fractionation trend is markedly different from that seen for REE-fluorocarbonates, the dominant REE host at Olympic Dam, which contain relatively higher MREE and HREE components. Xenotime is relatively rare at Olympic Dam and is most commonly seen as overgrowths on zircon. Compositional data for xenotime show HREE concentrations in which Y > Yb > Er > Dy > Ho. Thorium, U, and Pb are minor components in both xenotime and florencite. Monazite is a minor phase and co-existing monazite and florencite are never observed. Texturally, florencite appears to belong to a later stage of LREE mineralization at Olympic Dam, following and less prominent than the main REE-fluorocarbonate stage. Olympic Dam florencite is more La-rich and Ca-poor than it is in most of the localities worldwide for which compositional data have been published. The REE mineralization trends of florencite are compared with published REE trends for other mineral groups from Olympic Dam. Uraninite, brannerite, coffinite, and apatite show patterns of progressive LREE depletion from generation to generation, suggesting enhanced solubility of LREE over geological time. All LREE minerals (fluorocarbonates and phosphates), on the other hand, display progressive LREE enrichment correlating with a paragenetic sequence from REE-fluorocarbonates with essential Ca, through bastnäsite, to florencite. The late-stage florencite reported here is the most La-rich of all REE-bearing phases and is interpreted to record either the end of a continuous fluid evolution, or a later separate event at changed physicochemical conditions under which REE-aluminum phosphate minerals are stable.

Keywords: Olympic Dam, REE-phosphates, florencite, xenotime, mineral compositions.

INTRODUCTION

As awareness of potential rare earth element (REE) resources continues to increase across the minerals industry due to their many applications in advanced technologies (*e.g.*, Lucas *et al*. 2015, Grandell *et al*. 2016), it is critical to characterize and document these minerals in existing deposits in which they are known

[§] *Corresponding author e-mail address*: danielle.schmandt@adelaide.edu.au

to be concentrated in order to aid development of models that can assist with future exploration. Studying rare earth element and yttrium mineral deposition and evolution in an economic ore deposit can also constrain processes of deposit formation (*e.g.*, Lottermoser 1992, Williams-Jones *et al*. 2012), which can be particularly helpful for large and complex deposits, such as Olympic Dam.

The REE minerals at Olympic Dam can be useful tools because they are persistent accessory phases throughout the deposit (Oreskes & Einaudi 1990, Ehrig *et al*. 2012). Although La and Ce are routinely assayed, the disseminated and fine-grained morphology of the host REE minerals are generally not readily identifiable in hand sample, necessitating microscopic study to understand their speciation and paragenesis.

The Olympic Dam Cu-U-Au-Ag deposit, South Australia (Ehrig *et al*. 2012, 2017) represents a major global anomaly with respect to REE. In a prior publication (Schmandt *et al*. 2017), we described the petrography, composition, and significance for ore genesis of the main light rare earth element (LREE: La, Ce, Pr, Nd)-bearing mineral in the deposit, bastnäsite-(Ce) [$REE(CO_3)F$], and minor synchysite-(Ce) [$CaREE(CO_3)_2F$] (hereafter referred to as 'bastnäsite' and 'synchysite').

In the present contribution, we address the mineralogy of the second most abundant group of REE minerals in the deposit, the REE-aluminum phosphates, notably minerals of the florencite group, [$REEAl_3(PO_4)_2(OH)_6$], as well as other REE-phosphates, including xenotime-(Y) [$(Y,REE)PO_4$] and monazite-(Ce) [$(Ce,La,Nd)PO_4$]. Florencite occurs in both Ce- and La-dominant forms [*e.g.*, florencite-(Ce) and florencite-(La)] at Olympic Dam, and for clarity we mean both of these when referring to 'florencite', unless otherwise indicated. All xenotime analyzed is xenotime-(Y) and will be referred to as 'xenotime'.

The petrography and chemical compositions of these minerals are described based on 15 representative samples from across the deposit and evidence for the paragenetic relationships among REE-bearing minerals. The relative stabilities of REE-phosphate minerals are compared to REE-fluorocarbonates and other REE-hosting phases during initial deposition and subsequent deposit evolution.

Florencite occurs in a wide range of geological settings from sedimentary, igneous, and metamorphic environments, as hypogene, supergene, and diagenetic products, and interestingly as a fissiogenic product (Janeczek & Ewing 1996) and is thus found in many different deposit types. Occurrences of florencite and other aluminum phosphate-sulfate (APS) minerals are extensively covered by Dill (2001). Despite this widespread distribution, there are remarkably few studies that have addressed the petrography, compositional variation (including trace elements), and substitution mechanisms in any significant detail. This may be because the crystals are often very small, indistinct, and only present in low concentrations, making it difficult to find and analyze with common microanalytical techniques. The present contribution is the first to specifically address florencite in an iron oxide-copper-gold (IOCG) system.

Monazite and xenotime are relatively scarce at Olympic Dam and are not the main focus of the present contribution. Ample background information on these minerals can be found elsewhere (*e.g.*, Ni *et al*. 1995, Hetherington *et al*. 2008, Montel *et al*. 2018).

Background

REE mineralogy of the Olympic Dam deposit

The geological setting and ore and alteration mineralogy of the Olympic Dam IOCG-type deposit have been described in detail elsewhere (*e.g.*, Ehrig *et al*. 2012, 2017). The dominant gangue alteration minerals within the deposit area are hematite (~30 wt.%), quartz (~30 wt.%), and sericite (~18 wt.%); there is also significant orthoclase (~10 wt.%) inherited from the host granite. Cu-(Fe)-sulfides (chalcopyrite, bornite, and chalcocite) make up ~1.5 wt.% of the deposit (Ehrig *et al*. 2012).

IOCG-type deposits are known to be enriched in REE (*e.g.*, Hitzman *et al*. 1992, Williams *et al*. 2005, Groves *et al*. 2010, Barton 2013). Concentrations of REEs at Olympic Dam correlate positively with copper sulfide minerals and display spatial zoning in which they increase in abundance towards the center of the deposit before reaching the barren core in which they are generally absent (Ehrig *et al*. 2012). Olympic Dam is relatively enriched in light rare earth elements (LREE), with an average LREE grade of approximately 3050 ppm, compared to middle and heavy rare earth elements (MREE: Sm, Eu, Gd, Tb, Dy; HREE: Ho, Er, Tm, Yb, Lu, Y) (110 ppm). By far the most abundant REE mineral in the deposit is the REE-fluorocarbonate bastnäsite (Ehrig *et al*. 2012, Schmandt *et al*. 2017). The second-most abundant REE-mineral group at Olympic Dam are the REE-phosphates, of which florencite dominates (~0.0660 wt.%), followed by monazite (~0.0184 wt.%) and xenotime (~0.0045 wt.%; Ehrig *et al*. 2012).

Florencite-group minerals were first mentioned by Roberts & Hudson (1983) as a principal mineral of the LREE mineralization of Olympic Dam, who noted it occurs within the matrix of the granite breccia that hosts most of the Cu-(Fe)-sulfides. Other early descriptions of the deposit (Oreskes & Einaudi 1990, Lottermoser 1995) also note the presence of florencite

and comment on the fine-grained and pervasive, yet inconsistent, abundance of the LREE minerals. Florencite is also reported from high-grade bornite ores (Ciobanu *et al*. 2013, Krneta *et al*. 2017a) as nanometer- to micron-sized inclusions in fine-grained hematite-rich clasts (Cook *et al*. 2016). Florencite can also replace magmatic apatite in altered granites at the immediate contact with the orebody in the SE part of the deposit (Krneta *et al*. 2016), as well as in sedimentary units (Apukhtina 2016, McPhie *et al*. 2016) and in mafic lithologies (Huang *et al*. 2017) that make up lesser proportions of the Olympic Dam deposit.

Aside from the primary REE minerals, REEs are present in a wide range of minerals within the deposit, including but not limited to apatite (Krneta *et al*. 2016, 2017a), U-minerals (uraninite, brannerite, and coffinite; Lottermoser 1995, Macmillan *et al*. 2016a, b, 2017), hematite (Ciobanu *et al*. 2013, Cook *et al*. 2016, Verdugo-Ihl *et al*. 2017), and magnetite (Ciobanu *et al*. 2015). Florencite is also mentioned as a component of other IOCG systems in the Olympic Cu-U province, including Oak Dam, Prominent Hill, and Wirrda Well (Davidson *et al*. 2007, Freeman & Tomkinson 2010, Krneta *et al*. 2017b).

REE-aluminum phosphate mineralogy

The REE-aluminum phosphate mineral florencite is a member of the plumbogummite group of the alunite supergroup, which is a large mineral family of 52 named phosphates, sulfates, and arsenates, almost exclusively with trigonal symmetry [$DG_3(TX_4)_2X_6$; Bayliss *et al*. 2010]. Minerals from the supergroup are commonly referred to as APS minerals, a generalized term used in deposit characterizations encompassing any solid solution of minerals within the supergroup, although commonly restricted to a selection of minerals present within the described deposit.

Florencite is a REE-dominant mineral of the alunite supergroup. It has the ideal formula $REEAl_3(PO_4)_2(OH)_6$, with four (-Ce, -La, -Nd, and -Sm) dominant endmembers. Almost all natural florencite contains varied proportions of these four endmembers, as well as including all other REEs in generally minor or below measurable concentrations. Common substitutions in florencite at the *D*-cation site normally occupied by $REE^{2+,3+}$ include Ca^{2+} and Sr^{2+}, which can extend florencite into broader compositional fields and solid solutions, most notably with minerals of the crandallite group, including crandallite [$CaAl_3(PO_4)(PO_3OH)(OH)_6$)] and goyazite [$SrAl_3(PO_4)PO_3OH)(OH)_6$)]. Other common substituted cations include Ba^{2+} and Pb^{2+} for $REE^{2+,3+}$ and Fe^{3+} for Al^{3+}. The main anionic substitutions are SO_4 or AsO_4 for PO_4, extending compositions into the kemmlitzite [$(Sr,Ce)Al_3(AsO_4)(SO_4)(OH)_6$] – woodhouseite [$CaAl_3(PO_4)(SO_4)(OH)_6$] – svanbergite [$SrAl_3(PO_4)(SO_4)(OH)_6$] mineral series (*e.g*., Stoffregen & Alpers 1987).

The florencite subgroup also includes arsenoflorencite-(Ce) (Nickel & Temperly 1987) and arsenoflorencite-(La) (Mills *et al*. 2010), with the formula [$REEAl_3(AsO_4)_2(OH)_6$]. A further REE-rich mineral of the alunite supergroup (beudantite subgroup) is graulichite-(Ce), which resembles an Fe-rich arsenoflorencite-(Ce) with ideal chemistry $CeFe_3(AsO_4)_2(OH)_6$ (Hatert *et al*. 2003). These minerals are uncommon and have not been identified at Olympic Dam.

Sampling and Methodology

Although REE minerals occur throughout the Olympic Dam deposit, they are generally sparse, disseminated, fine-grained, and almost always intergrown with other minerals, making quantitative microanalysis difficult. The data presented here are from a suite of 15 samples selected based on routine BHP Olympic Dam core assays indicating anomalously high La and Ce values. The same sample suite was also used by Diemar (2014) and Schmandt *et al*. (2017). These samples are representative of high-REE-concentration intervals throughout the deposit and come from various breccia lithologies (logged as breccias containing dike clasts, granite-rich breccias, and hematite-rich breccias), and one sample from a sericitized dike (RX6724; Fig. 1). Each of the anomalous drill core intervals was assayed in greater detail for a 72-element suite and X-ray diffraction (XRD) was carried out to determine the major minerals. These values and sample descriptions can be found in Appendices 1 and 2, respectively[1].

All microanalytical work was undertaken at Adelaide Microscopy, University of Adelaide, following routines outlined by Schmandt *et al*. (2017). Each polished block was examined using a reflected light optical microscope and an FEI Quanta 450 Field Emission Gun scanning electron microscope (SEM) equipped with an energy-dispersive X-ray spectrometer with a silicon-drifted detector.

The petrographic description presented here is focused on samples from particularly REE-rich

[1] Appendices are available from the Depository of Unpublished Data on the MAC website (http://mineralogicalassociation.ca/), document "Olympic Dam REEs. CM56, 18-00043".

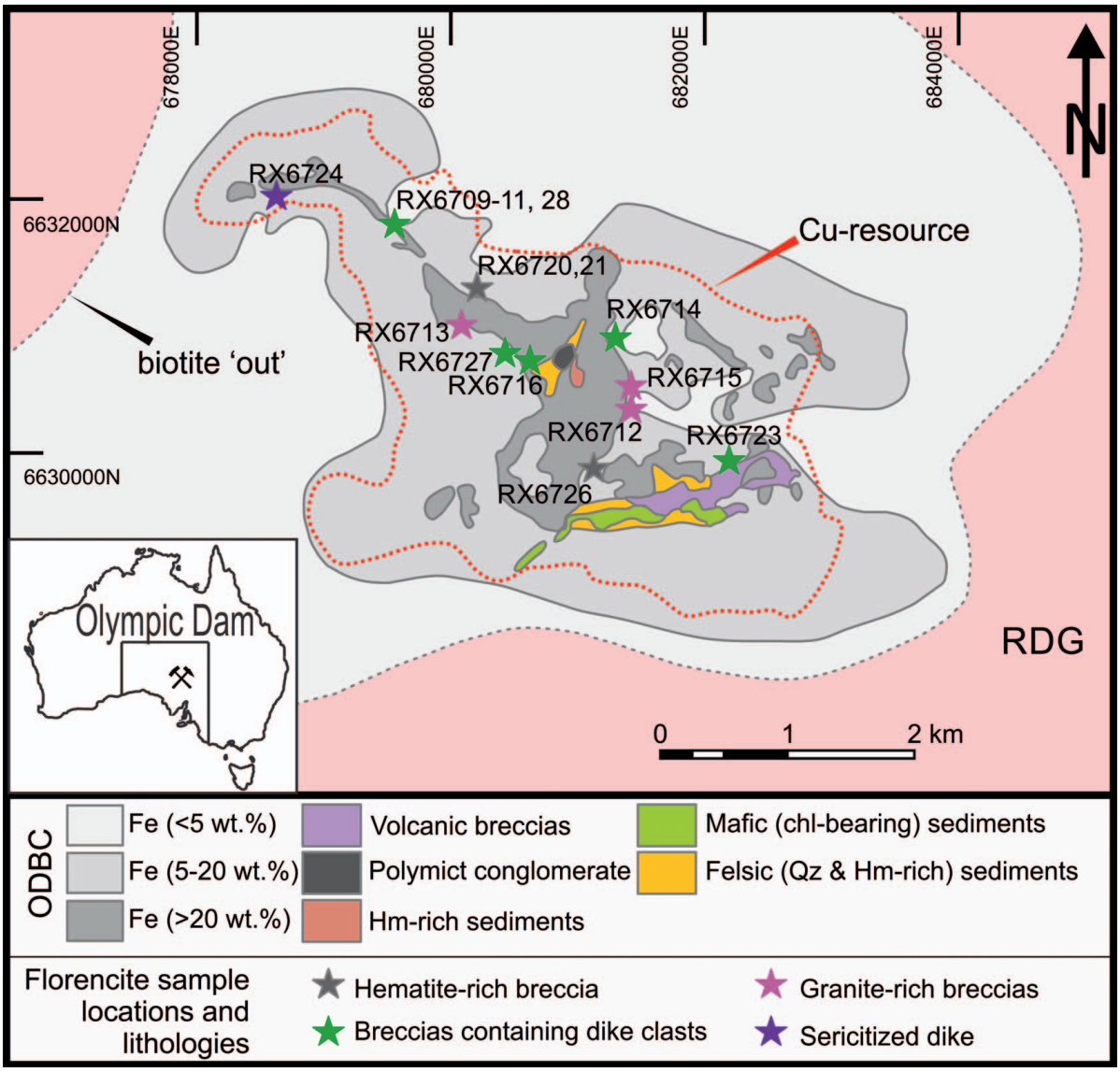


FIG. 1. Simplified Olympic Dam deposit map at –350 m RL. Stars indicate locations of samples containing florencite and are color-coded with logged lithology. RDG: Roxby Downs Granite.

pockets. This is complemented by Mineral Liberation Analyzer (MLA; Gu 2003) data that describe the overall abundance and associations of these minerals across the deposit. The MLA generates quantitative mineralogy and mineral relationship frequency data and is thus well suited to characterization of disseminated minerals like florencite and minerals such as monazite and xenotime that are sparse in the REE-rich pockets. We acknowledge, however, that the small size of the florencite crystals and xenotime overgrowths may be problematic in that they are, in some cases, below the resolution of the MLA. The MLA data set used for this analysis consists of 607 15 m-long composites drill core samples from the southeastern lobe of the deposit.

Electron probe microanalysis

Quantitative compositions of REE minerals were determined using a Cameca SX-Five electron probe microanalyzer (EPMA) equipped with five tunable wavelength-dispersive spectrometers. The microprobe uses PeakSite software for microscope operation and Probe for EPMA software (distributed by Probe Software Inc.) for data acquisition and processing. Measured elements, spectra, reference

standards, count times, and other parameters are included in Appendix 3.

Laser ablation inductively coupled plasma mass spectrometry

Trace element and isotopic analyses were performed by laser ablation inductively coupled plasma mass spectrometry (LA-ICP-MS) using a RESOlution-LR ArF excimer laser ablation system (Australian Scientific Instruments) equipped with a large format S155 sample chamber (Laurin Technic Inc.) and coupled to an Agilent 7900x ICP-MS. Data reduction was performed using the software Iolite v3.4 (Paton *et al*. 2011) and processed using the "Trace_Elements_IS" data reduction scheme with the internal standard Al values obtained from EPMA. Analytical parameters are described in detail in Schmandt *et al*. (2017).

Results

Mineral liberation analysis data

Identifying trends in the overall occurrence of the REE-phosphates with respect to other minerals can help recognize zonation and mineral-alteration assemblages. In order to organize the large numerical MLA data set into a geological context, the data were divided into percentiles based on the assayed wt.% Fe. The variability of the Fe content has been shown to be an indication of alteration intensity (Ehrig *et al*. 2012). All samples in this data set are from within the Cu-resource, meaning that all of the samples are altered to some extent. The low Fe wt.% (Q1) represents the least altered and Q4 represents the most altered, highest-Fe samples. Detailed description of the deposit alteration and mineral assemblages are given by Ehrig *et al*. (2012).

Florencite is the most abundant REE-phosphate mineral throughout all percentiles. All REE-phosphates are most often in grain contact with the most abundant minerals in the samples (hematite, sericite, and quartz; Fig. 2 A1, A2). Among the REE-phosphate minerals, xenotime is most commonly in grain contact with hematite, whereas florencite is most commonly in grain contact with sericite and quartz (Fig. 2 A2). The association of all REE-phosphates with quartz increases with greater Fe despite the total quartz wt.% decreasing with greater Fe wt.% (Fig. 2 A1, A2). Florencite shows a similar relationship with sericite; the association between florencite and sericite becomes more significant through Q3 despite a decrease in total sericite abundance.

All of the REE-phosphate minerals, including florencite, increase in abundance with increased wt.% Fe (Fig. 2 B1). In contrast, bastnäsite, the dominant REE mineral, shows an overall decreasing abundance as wt.% Fe increases (Fig. 2 B1). Both monazite and xenotime are in contact with florencite more than with each other, and florencite displays more common grain boundaries with monazite than xenotime (Fig. 2 B2), although this relationship is never observed in the sample blocks. Among the REE minerals, xenotime has the strongest association with zircon, which it commonly overgrows. Florencite is predictably most associated with APS minerals of the alunite group, which, in part, display a series of REE-depleted solid solutions with florencite (Owen *et al*. 2018). Of the accessory minerals, monazite is most commonly associated with bastnäsite.

Petrography

Florencite. Florencite is ubiquitous across the deposit and occurs mostly as disseminations within the sericite–chlorite breccia matrix, primarily as fine-grained (seldom >20 μm) disseminations. Local concentrations of florencite occur in pockets and as aggregates. In these samples florencite is subordinate to bastnäsite, the dominant LREE mineral, whereas the other REE-phosphates, monazite and xenotime, are rare. Generally, florencite appears to be secondary relative to the other minerals in the associations or represents a later phase of LREE mineralization that post-dates other minerals.

Florencite occurs as grains of variable morphology from euhedral to irregular, or as aggregates of different sizes within a matrix comprising mostly sericite and/or sericite–chlorite (Fig. 3). The aggregates also vary in shape from irregular to angular. Florencite aggregates in the matrix may be composed of more euhedral grains (Fig. 3a), while very fine-grained florencite aggregates may either fill or outline angular shapes, suggesting selective replacement of a pre-existing mineral or clast (Fig. 3b, c). In some of these cases florencite crystals of variable size form a halo surrounding a core of silicate minerals (Fig. 3c, d). Coarser grains of bastnäsite in the vicinity of the 'halo' show tiny inclusions of florencite (Fig. 3d). In both cases, aggregates appear vuggy.

Distinct florencite crystals also overprint bastnäsite and synchysite (Fig. 3d, e) and form aggregates around relicts of partially replaced bastnäsite (Fig. 3f). Where florencite grains form larger aggregates (up to ~40 um in size) there are usually fine-grained inclusions of other phases, most often hematite, U-minerals, Cu-(Fe)-sulfides, and sericite. Florencite can be found in Cu-rich intervals (samples RX6720 and RX6713) forming aggregates conspicuously enclosing bornite and other Cu-(Fe)-sulfides (Fig. 4a). Fine-grained florencite occurs as tiny inclusions within and along fractures in Cu-(Fe)-sulfides (Fig. 4b). In one sample (RX6720), a

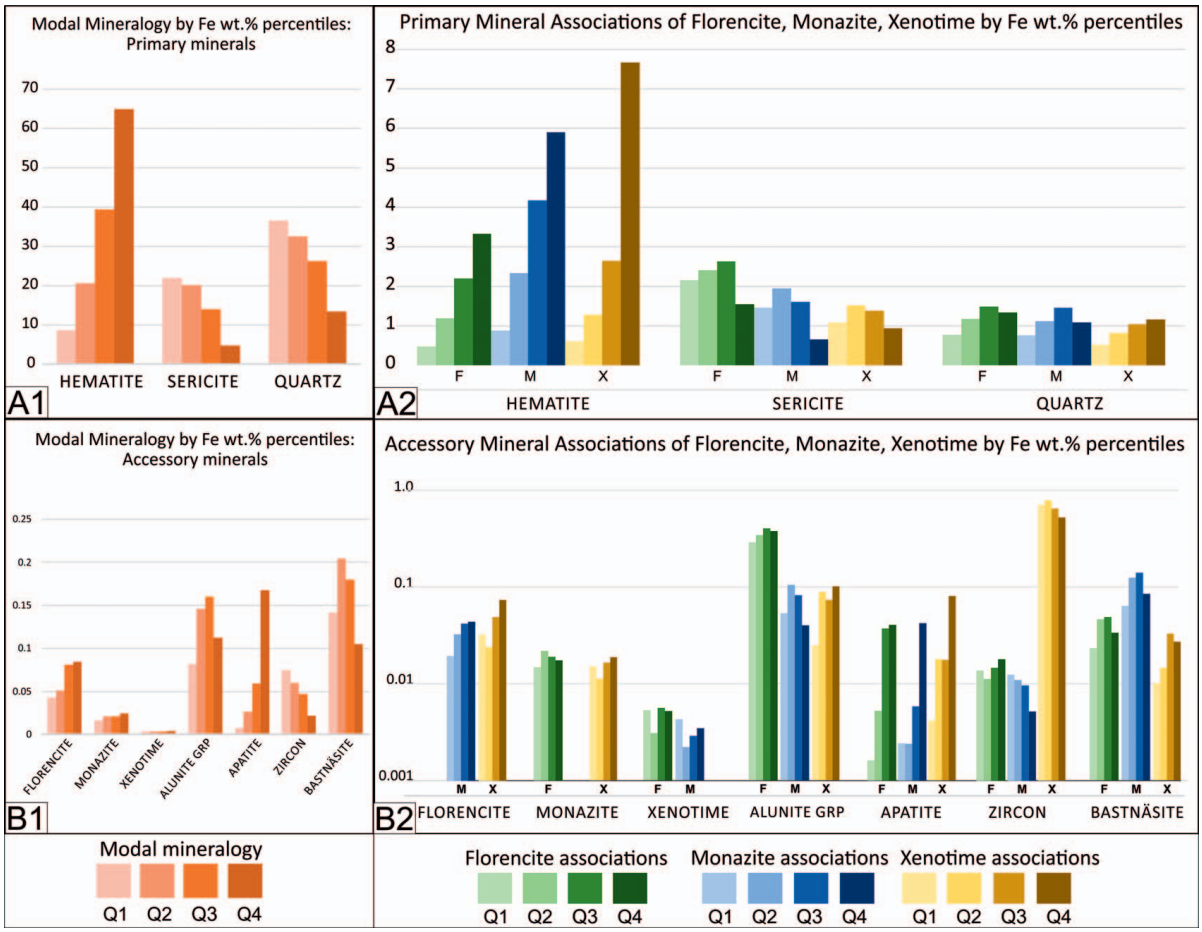


FIG. 2. Average modal mineralogy (MLA data, wt.%) and % frequency of mineral associations (Y-axis) by mineral in each Fe wt.% percentile, Q1 through Q4 (X-axis). Data bars get progressively darker with greater Fe wt.%. (A1) Clustered column chart showing modal mineralogy (wt.%) for the three most abundant minerals by Fe wt.% percentiles. The diagram shows the change in mineral abundances as hematite becomes more abundant. The other major minerals are sericite and quartz; these are less abundant as hematite alteration increases. (A2) Clustered column chart comparing the degree of association with the major minerals shown by florencite (F, green), monazite (M, blue), and xenotime (X, yellow/brown). Xenotime shows a greater association with hematite than the others, and florencite shows a greater association with sericite and quartz than the other two REE-phosphates. (B1) Clustered column chart showing modal wt.% abundance for the accessory minerals most associated with REE-phosphates by Fe wt.% percentiles. Chart shows the change in abundance of minerals as hematite becomes more abundant. (B2) Clustered column chart comparing the degree of association (logarithmic-scale) with other accessory minerals shown by florencite (F, green), monazite (M, blue), and xenotime (X, yellow/brown). Xenotime is most often associated with zircon, florencite is most often associated with alunite group minerals, and monazite is most often associated with bastnäsite. All REE-phosphate minerals show increased association with apatite with greater Fe wt.%, correlating with increased abundance of apatite.

clearly late florencite is the main component of veinlets that crosscut hematite (Fig. 4c). Florencite also occurs as μm-sized, skeletal grains with hexagonal habit (Fig. 4d) in the sericite dike sample (RX6724). This morphology appears unique to this host lithology and is suggestive of replacement of a pre-existing mineral in mafic rocks, such as perhaps rutile.

Xenotime. Xenotime is rare at Olympic Dam. It is observed most commonly as overgrowths on zircon (Fig. 5a). When xenotime occurs as isolated grains, they are often very small and coexist with coffinite and/or brannerite. In hematite-rich breccias (sample RX6721) more abundant xenotime is observed within a relict clast which is associated with bornite, hematite, rutile, and U-minerals within a larger bastnäsite-rich zone (Fig. 5b).

Monazite. Monazite is an accessory phase and was only noted in a single sample, where it occurs as

irregular, very fine-grained inclusions in a hematite clast. Monazite is more abundant towards the edges of the deposit and can be found together with florencite replacing magmatic apatite (Krneta *et al*. 2017a).

Compositional data

Florencite–(La,Ce). Summary EPMA and LA-ICP-MS data for florencite are reported in Tables 1 and 2, respectively; the full EPMA data set is given in Appendix 4.

Florencite in samples RX6714, RX6720, and RX6711 displays La/Ce ratios close to 1 but is mostly La-dominant; those in samples RX6710, RX6712, and RX6724 are entirely La-dominant, whereas florencite from sample RX6713 is Ce-dominant (Fig. 6). Florencite in sample RX6713 also contains relatively elevated concentrations of Pr and Nd, while florencite in sample RX6724, from the sericitized dike, has overall the least amount of these elements and the highest amounts of La. MREE and HREE are generally below detection limit in most florencite analyzed by EPMA.

Florencite contains minor amounts of both Sr and Ca, which substitute for REE at the *D* site. Strontium concentrations are generally the higher of the two elements (Fig. 7). Florencite also contains SO_4 and a minor yet measurable AsO_4 component, with both anions substituting for PO_4. Florencite in sample RX6714 has elevated As, and in RX6712 has more As than S (Table 1). Both (Ca+Sr) and S display predictable negative correlations with ΣREE (Fig. 8a, b). Substitution of SO_4^{2-} for PO_4^{3-} creates a charge imbalance that may be met by greater substitution of divalent cations for REE, contributing to the negative trend between S and ΣREE (Fig. 8b). Note that samples RX6710 and RX6711 are the only two samples from the same drill core and are only a few centimeters apart. The major differences in these samples is in bulk mineralogy: RX6710 has ∼36 wt.% bastnäsite while RX6711 has <1 wt.% bastnäsite; RX6710 has ∼15 wt.% sericite and RX6711 has ∼65 wt.% sericite. The only sample with more sericite is the seriticized dike RX6724, with ∼78 wt.% sericite.

The preference for Sr and S substitutions in these minerals pushes florencite towards a solid solution with svanbergite [$SrAl_3(PO_4)(SO_4)(OH)_6$]. The extended formula for florencite from Olympic Dam can be expressed as $(Ca_{0.01–0.24}Sr_{0.03–0.40}La_{0.14–0.49}Ce_{0.20–0.47}Pr_{0.00–0.03}Nd_{0.00–0.05})_{\Sigma 0.43–0.96}Al_{2.89–3.33}(P_{1.42–1.96}S_{0.05–0.34}As_{0.0–0.20})_{\Sigma 1.77–2.21}O_4(OH)_6$.

The LA-ICP-MS analysis of florencite shows that the phase contains very low concentrations of trace elements. Elevated concentrations of Fe and Si are assumed to be due to contamination from fine-grained intergrown hematite and sericite included within the ablated volume. Concentrations of U, Th, and Pb are mostly low, with values up to 44.2 ppm U, up to 124 ppm Th, and up to 216 ppm Pb (Table 2). Reliable LA-ICP-MS data could not be obtained for florencite in sample RX6724 due to the abundance of fine-grained included sericite. The EPMA data for florencite in this sample did, however, give concentrations of U and Pb that were significantly higher than in other samples (up to 1000 and 1300 ppm, respectively), while Th was below limits of detection.

Xenotime-(Y). The EPMA data for xenotime (Table 3) are limited to the coarse-grained occurrence of this phase in sample RX6721 (Fig. 5). These data show concentrations in which Y > Yb > Er > Dy > Ho. Thorium, U, and Pb are minor components: ∼0.4 wt.% UO_2, ∼0.05 wt.% PbO, and ∼0.03 wt.% ThO_2 on average.

Xenotime displays an extensive range of solid solutions towards isostructural minerals, including coffinite ($USiO_4$), zircon ($ZrSiO_4$), and thorite ($ThSiO_4$) (*e.g*., Förster 2006). The xenotime grains analyzed here are endmember in composition; intermediate members of the coffinite–xenotime solid solution series are reported from Olympic Dam (Macmillan *et al*. 2017). The extended formula for xenotime can be expressed as $Y_{0.73–0.82}REE_{0.20–0.22}(P_{0.97–1.03}Si_{0–0.02})O_4$.

Chondrite-normalized fractionation patterns

Chondrite-normalized REE fractionation trends for florencite and xenotime are shown in Figure 9a, overlain with the REE fractionation trends for Olympic Dam fluorocarbonates, bastnäsite, and synchysite (Schmandt *et al*. 2017) for comparison. The dominance of LREE in florencite is apparent from these plots, with a steep drop through the LREE and a relative flattening out in the HREE segment. Such a trend is markedly different from the REE-fluorocarbonates, which display a much more consistent and gradual slope through the LREE to HREE. Xenotime displays a smooth increase across the trend with a high, flat HREE segment. Neither florencite nor xenotime display Eu- or Y-anomalies.

Discussion

The florencite at Olympic Dam is compositionally variable and shows little consistent correlation with bulk mineralogy or whole rock assays of the samples, although there are a number of interesting relationships. For example, sample RX6713 is the only sample in which florencite is Ce-dominant and contains the greatest abundance of Cu- and U-minerals; florencite

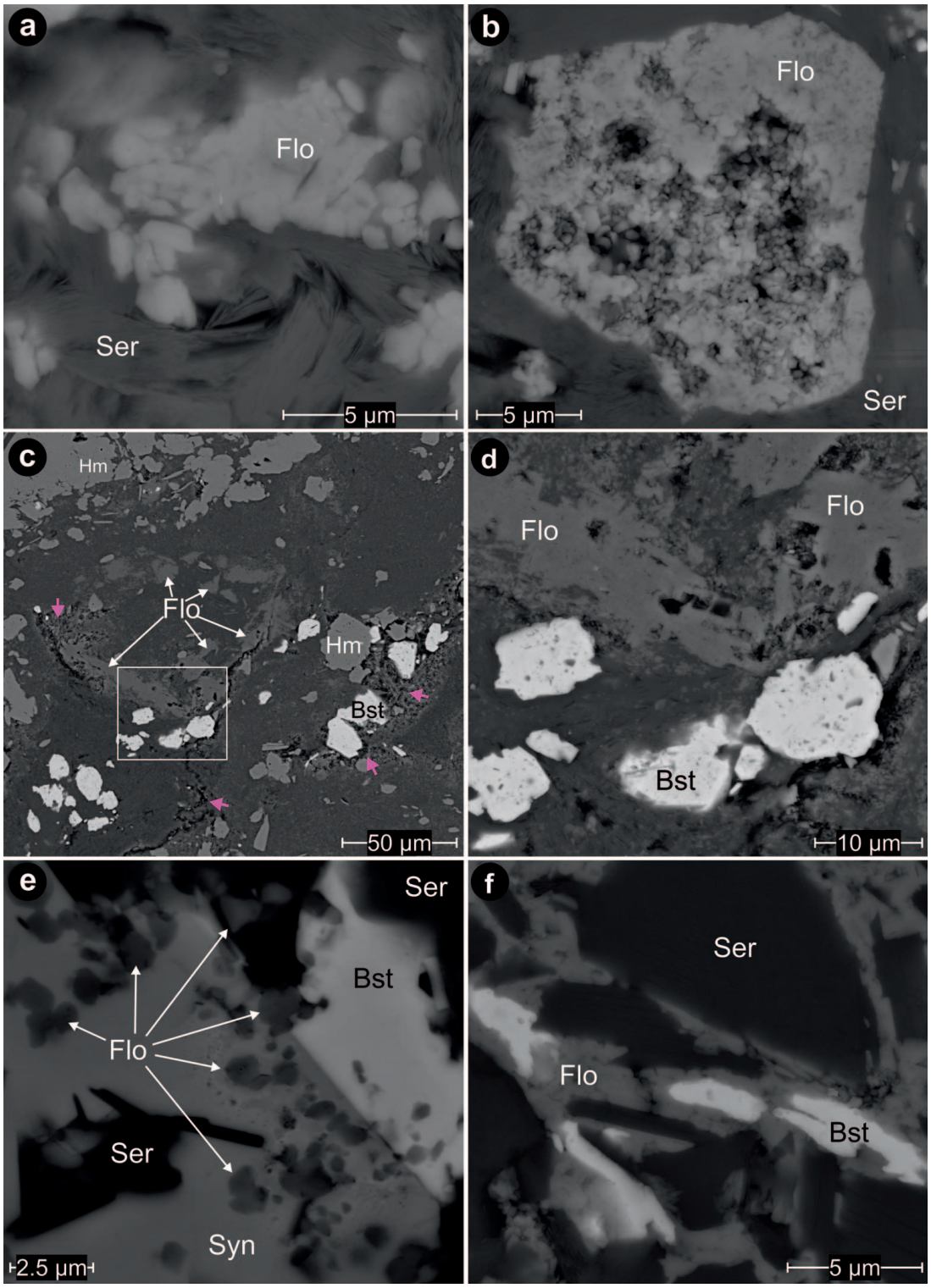


FIG. 3. BSE images showing representative textures and mineral assemblages comprising florencite (Flo). (a) Fine-grained, euhedral grains of florencite in sericite (Ser) (sample RX6713). (b) Vuggy aggregate of florencite with distinct angular shape suggestive of preferential mineral/clast replacement (sample RX6714). (c) Relict clast/mineral replaced by silicates with marginal halo formed by florencite grains. The fine-grained matrix is also florencite-rich with a variable proportion between florencite and sericite ± chlorite (lighter zones > florencite, darker zones > silicates). Note high-porosity (pink arrows) and

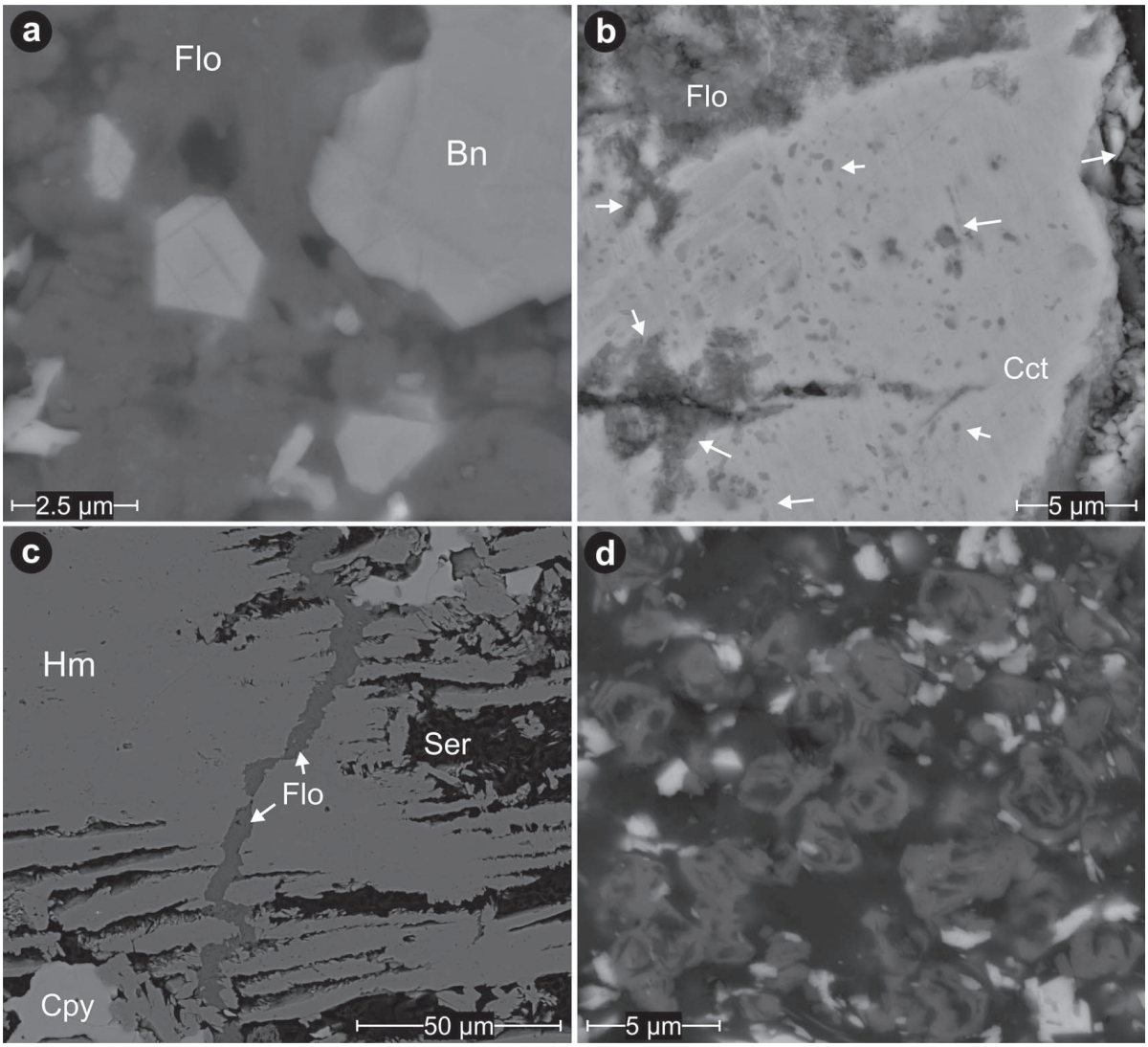


FIG. 4. BSE images showing the occurrence of florencite (Flo) in sulfide-bearing samples (a–c) and from the sericitized dike (d; sample RX6724). (a) Florencite aggregate with sericite (black) surrounding angular bornite (Bn) fragments showing basket-weave texture with chalcopyrite (sample RX6713). (b) Florencite (white arrows) crystals are inclusions in a chalcocite (Cct) grain. Florencite is concentrated along fractures within chalcocite and along grain boundaries (sample RX6710). (c) Florencite veinlet crosscutting hematite (Hm). Sericite (Ser) and chalcopyrite (Cpy) around hematite (sample RX6720). (d) Skeletal florencite with hexagonal shape. Sericite (black) is both matrix and filling the skeletal florencite. Note small bastnäsite grains (bright). This sample is from one of the intensively sericitized dikes (sample is ~78% sericite) considered to represent an altered ultramafic rock. Florencite occurs in distinct pockets that appear oriented, while the micron-sized florencite crystals themselves have textures indicative of rapid growth during sericitization of the dike.

←
coarser clasts and/or grains of hematite (Hm) and bastnäsite (Bst) within the same area. White box shows the area of (d). (d) Detail showing that bastnäsite also contains minute florencite inclusions (grey). Note also pores and fine specks of florencite in the matrix (sample RX6710). (e) Swarms of fine-grained florencite across synchysite (Syn) and bastnäsite. The latter are in close association with sericite (sample RX6714). (f) Florencite replacing bastnäsite. Note again the porosity (sample RX6714).

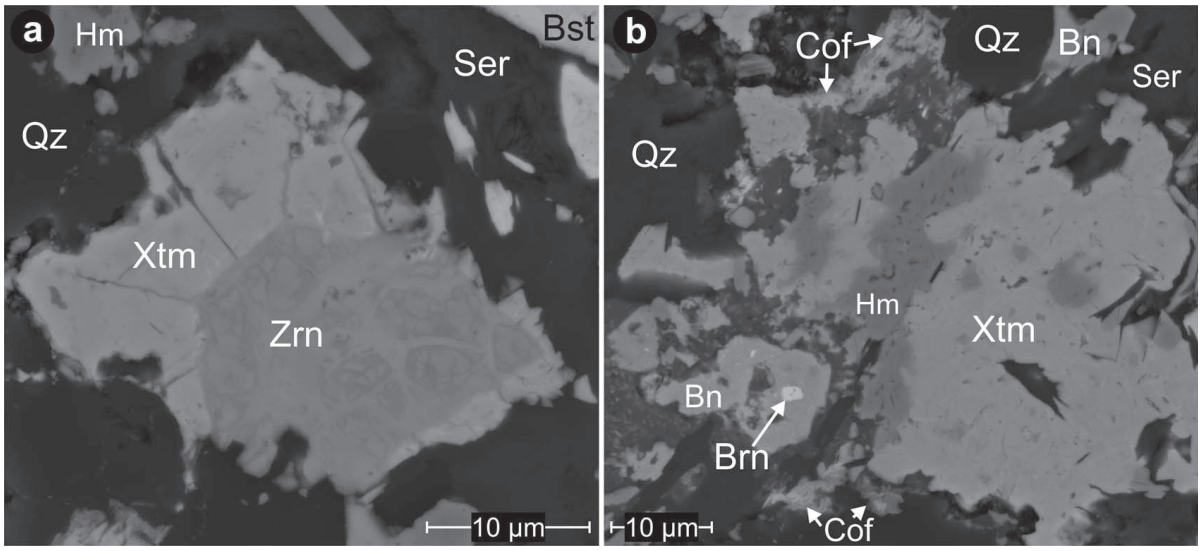


FIG. 5. BSE images of xenotime (Xtm) from sample RX6721. (a) Xenotime overgrowth on zircon (Zrn) in quartz (Qz) and sericite (Ser). Quartz shows irregular and concave textures into the edges of the xenotime and zircon. Note also hematite (Hm) and bastnäsite (Bst) in the assemblage. (b) Occurrence of coarse xenotime with inclusions of hematite and sericite blades (black). Dark inclusions in hematite are rutile or ilmenite. Brighter zones at the xenotime margins are coffinite (Cof) intergrown with the xenotime. Bornite contains inclusions of brannerite (Brn). The host is a mixture of quartz and sericite.

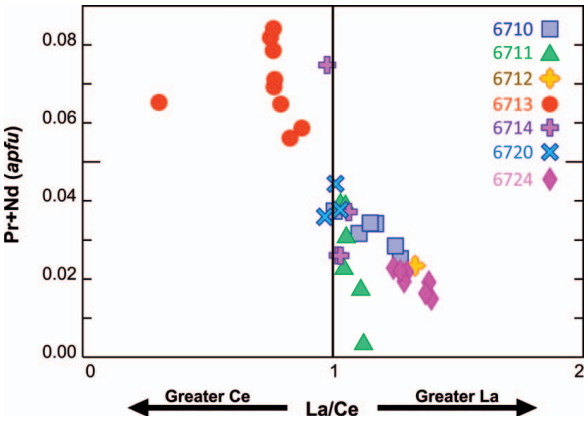


FIG. 6. LREE (*apfu*) composition of analyzed florencite expressed as La/Ce *versus* Pr+Nd. Greater concentrations of Ce correlate with increased Pr and Nd and lesser concentrations of La, while greater amounts of La correlate with lesser concentrations of the other LREE. RX6713 is the only sample that contains persistently Ce-dominant florencite. RX6713 also has the highest Cu and U grade and the lowest ΣREE grade of the analyzed samples.

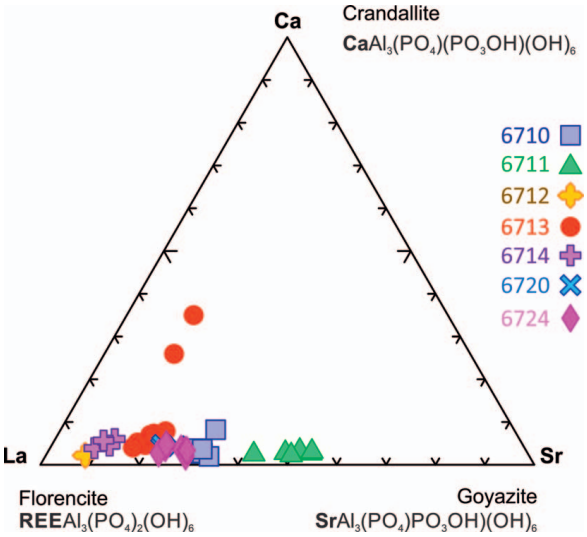


FIG. 7. Ternary La–Ca–Sr plot showing EPMA data for florencite divided by sample block in terms of *apfu* to represent APS endmembers florencite–crandallite–goyazite based on D-site occupancy. Most data cluster near florencite and towards goyazite. Only two samples from RX6713 trend towards crandallite.

in the sericitized dike (RX6724) is the most La-rich (and the sample farthest from the deposit center); and samples RX6712 and RX6714 have elevated As in the florencite, as well as in the whole rock assays. Compositional variability is also very localized. In one example, samples taken only a few centimeters apart (RX6710 and RX6711) contain compositionally distinct florencite in terms of both LREE ratios and the substituted elements Ca, Sr, and S. This variability suggests that highly localized variations in element

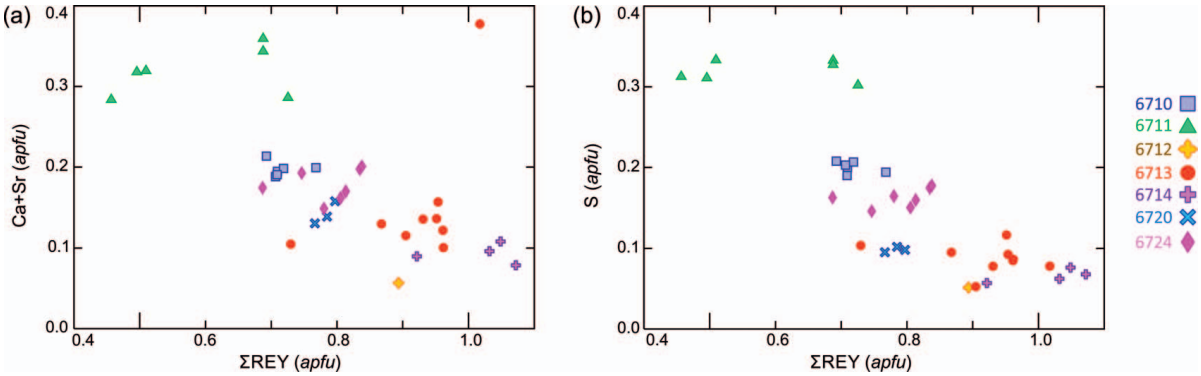


FIG. 8. EPMA data for florencite in terms of *apfu* data. (a) Ca+Sr *versus* ΣREY showing a negative correlation due to variable abundances sharing the *D* site. (b) S *versus* ΣREY showing a negative correlation due to charge balancing of SO_4^{2-} substitution for PO_4^{3-}. RX6711 florencite displays the greatest substitutions of Ca, Sr, and S, while RX6714 has the least. RX6711 has the highest abundance of florencite relative to coexisting bastnäsite, the most baryte, and overall low totals of REY in the whole rock assay. REY = REE + Y.

availability during florencite crystallization impacted compositions. Florencite occurs across the deposit, texturally appearing as replacive and paragenetically late-stage relative to REE-fluorocarbonates, Cu-(Fe)-sulfides, and hematite.

Comparison with published compositional data for florencite

Florencite can form in a wide range of geological settings, ranging from diagenetic florencite (*e.g.*, Rasmussen 1996, Pe-Piper & Dolansky 2015) to high *P-T* metamorphic terranes (~500 °C, ~6 kbar; Nagy *et al*. 2002, Chakraborty *et al*. 2014).

Figure 10 compares compositional data for Olympic Dam florencite with published data from a wide range of settings. From the reported florencite occurrences, the relative distributions of LREE (La-, Ce-, and Nd-oxide components, Fig. 10a) show a systematic compositional trend across the different deposits. Olympic Dam florencite is one of the most La-rich [Lefebvre & Gasparrini (1987) report a slightly more La-rich florencite], followed by florencite from a carbonatite setting, through metamorphic, unconformity, paleosol, and epithermal florencite (which overlap significantly), and then the rhythmically zoned crystal of Repina *et al*. (2014) being the most varied and Nd-rich (Fig. 10a).

Figure 10b shows the relative concentrations of CaO, SrO, and La_2O_3 in florencite from different mineralization settings. Florencite from Olympic Dam and metamorphic environments have the least Ca and Sr; the metamorphic florencite have greater Ca than Sr, different from the rest of the florencite data, which show higher SrO compared to CaO. Florencite from Olympic Dam and carbonatite settings have less Ca, compared to other low temperature and vein florencite.

Where florencite is reported occurring within hydrothermal ores, it is usually minor and grouped together with other APS minerals, which can also show zonation with respect to REE (*e.g.*, Arribas *et al*. 1995, Bajnoczi *et al*. 2004, Khashgerel *et al*. 2008). Such details can be helpful in determining changes in fluid chemistry in long-lived hydrothermal regimes (*e.g.*, Fulignati *et al*. 1999, Williams-Jones *et al*. 2012). In these systems, florencite and other APS group minerals are often interpreted to be generated during the retrograde or prograde stage in the evolution and are included as part of the advanced argillic alteration assemblage. The presence of these minerals may thus be indicative of lower pH and/or temperature. Examples include porphyry-epithermal environments (*e.g.*, Aoki *et al*. 1993, Arribas *et al*. 1995, Bajnoczi *et al*. 2004, Khashgerel *et al*. 2008, Hikov *et al*. 2010, Georgieva & Velinova 2014, Hikov *et al*. 2017) and a wide range of other deposit settings (*e.g.*, Lefebvre & Gasparrini 1987, Davidson *et al*. 2007, Gaboreau *et al*. 2007, Doroshkevich *et al*. 2009, Rasmussen & Muhling 2009, Repina *et al*. 2014). In some of these settings, florencite is interpreted to form *via* replacement of pre-existing monazite and/or apatite, or in response to their dissolution (as in the magmatic apatite in granites at Olympic Dam; Krneta *et al*. 2016). Other physiochemical parameters that have been interpreted to correspond with assemblages including florencite are high REE and P availability/activity in fluid, low pH, higher fO_2, high water/rock ratios, and often also higher fS_2 (due to the common association with APS minerals). The pressure-temperature stability range reported for florencite varies

TABLE 1. FLORENCITE EPMA COMPOSITONAL DATA, MEAN PER SAMPLE

	RX6710		RX6711		RX6712	RX6713		RX6714		RX6720		RX6724	
	(*n* = 6)		(*n* = 7)		(*n* = 1)	(*n* = 9)		(*n* = 4)		(*n* = 3)		(*n* = 7)	
wt.%	mean	2σ	mean	2σ	mean	mean	2σ	mean	2σ	mean	2σ	mean	2σ
La_2O_3	11.23	1.3	7.85	4.5	14.38	10.33	4.6	13.91	1.6	11.23	0.1	13.34	1.5
Ce_2O_3	9.79	1.0	7.55	4.1	10.91	14.13	1.4	13.71	1.3	11.29	0.5	10.22	1.8
Pr_2O_3	0.42	0.1	0.34	0.1	0.39	0.77	0.2	0.44	0.3	0.48	0.1	0.28	0.1
Nd_2O_3	0.58	0.2	0.52	0.5	0.31	1.30	0.4	0.74	0.9	0.74	0.1	0.34	0.1
Sm_2O_3	-	-	0.07	0.10	-	0.10	-	-	-	-	-	-	-
Eu_2O_3	0.05	-	-	-	-	0.07	0.08	-	-	0.04	0.0	0.04	-
Gd_2O_3	-	-	-	-	-	-	-	-	-	-	-	-	-
Tb_2O_3	0.04	0.01	0.06	0.06	-	0.05	0.00	-	-	-	-	-	-
Dy_2O_3	-	-	0.10	-	-	0.06	-	-	-	-	-	-	-
Ho_2O_3	0.09	-	0.14	0.1	-	0.09	-	-	-	-	-	-	-
Er_2O_3	-	-	-	-	-	-	-	-	-	0.05	-	-	-
Yb_2O_3	0.05	0.00	0.06	0.1	0.05	0.16	0.2	0.22	0.0	-	-	0.05	-
Y_2O_3	-	-	0.03	-	-	0.02	0.0	0.03	0.0	0.03	0.0	0.07	0.1
ΣREY_2O_3	22.1	1.7	16.4	8.7	26.0	26.7	6.0	28.9	2.7	23.8	0.3	24.2	3.4
CaO	0.22	0.2	0.17	0.0	0.12	0.60	1.5	0.28	0.1	0.23	0.0	0.23	0.1
SrO	3.44	0.3	4.99	3.3	0.82	1.70	0.8	1.15	0.2	2.32	0.4	3.06	0.8
PbO	-	-	0.02	0.0	-	0.02	-	0.02	0.0	0.02	0.01	0.05	0.1
ThO_2	0.02	0.01	0.05	0.1	-	-	-	-	-	0.02	-	-	-
UO_2	0.03	0.01	0.18	0.32	-	0.16	0.4	0.13	0.2	-	-	0.06	0.1
Na_2O	0.05	0.02	-	-	-	0.05	0.1	0.07	0.1	0.02	-	0.02	0.0
K_2O	0.12	0.15	0.06	0.0	0.03	0.34	0.7	0.17	0.2	0.02	0.0	0.30	0.3
Al_2O_3	29.8	1.4	31.0	3.3	30.3	30.8	3.2	30.2	1.7	28.1	2.1	30.7	2.6
FeO	1.05	0.9	1.17	0.5	0.19	2.65	2.7	1.80	2.8	1.72	0.5	1.21	2.1
P_2O_5	24.2	1.3	19.9	1.5	21.0	19.0	3.4	18.8	1.6	25.7	0.1	22.5	2.6
SO_4	3.62	0.2	5.45	0.6	0.88	1.48	0.6	1.09	0.2	1.76	0.1	2.94	0.4
As_2O_3	0.07	0.04	0.16	0.1	3.50	0.03	0.02	0.60	0.3	0.04	0.0	0.08	0.0
Nb_2O_5	0.12	0.21	0.03	0.0	0.02	0.02	0.00	0.02	-	-	-	0.03	-
SiO_2	0.04	-	-	-	-	1.49	2.69	0.50	-	-	-	0.92	1.6
F	0.12	0.1	0.18	0.2	0.11	0.25	0.4	0.24	0.2	0.18	0.0	0.23	0.2
Cl	0.07	0.1	0.03	0.0	0.06	0.04	0.0	0.06	0.04	0.03	0.0	0.04	0.1
Total	84.9	2.95	79.7	12.4	83.1	84.0	10.5	83.6	3.1	83.9	1.6	86.4	3.7
						apfu							
La	0.37	0.04	0.27	0.14	0.49	0.36	0.15	0.49	0.06	0.37	0.01	0.43	0.04
Ce	0.32	0.03	0.26	0.12	0.37	0.49	0.04	0.48	0.06	0.37	0.02	0.33	0.05
Pr	0.01	0.00	0.01	0.00	0.01	0.03	0.01	0.02	0.01	0.02	0.00	0.01	0.00
Nd	0.02	0.01	0.02	0.02	0.01	0.04	0.01	0.03	0.03	0.02	0.00	0.01	0.00
Sm	-	-	0.00	0.00	-	0.00	-	-	-	-	-	-	-
Eu	0.00	-	-	-	-	0.00	0.00	-	-	0.00	0.00	0.00	-
Gd	-	-	-	-	-	-	-	-	-	-	-	-	-
Tb	0.00	0.00	0.00	0.00	-	0.00	0.00	-	-	-	-	-	-
Dy	-	-	0.00	-	-	0.00	-	-	-	-	-	-	-
Ho	0.00	-	0.00	0.00	-	0.00	-	-	-	-	-	-	-
Er	-	-	-	-	-	-	-	-	-	0.00	-	-	-
Yb	0.00	0.00	0.00	0.00	0.00	0.00	0.00	0.01	0.00	-	-	0.00	-
Y	-	-	0.00	-	-	0.00	0.00	0.00	0.00	0.00	0.00	0.00	0.00
ΣREY	0.72	0.05	0.56	0.26	0.89	0.92	0.16	1.02	0.12	0.78	0.02	0.78	0.10
Ca	0.02	0.02	0.02	0.01	0.01	0.06	0.15	0.03	0.01	0.02	0.00	0.02	0.01
Sr	0.18	0.02	0.27	0.17	0.04	0.09	0.04	0.06	0.01	0.12	0.02	0.16	0.04
Pb	-	-	0.00	0.00	-	0.00	-	0.00	0.00	0.00	0.00	0.00	0.00
Th	0.00	0.00	0.00	0.00	-	-	-	-	-	0.00	-	0.00	-
U	0.00	0.00	0.00	0.01	-	0.00	0.01	0.00	0.00	-	-	0.00	0.00

TABLE 1. CONTINUED.

	RX6710		RX6711		RX6712	RX6713		RX6714		RX6720		RX6724	
	($n = 6$)		($n = 7$)		($n = 1$)	($n = 9$)		($n = 4$)		($n = 3$)		($n = 7$)	
wt.%	mean	2σ	mean	2σ	mean	mean	2σ	mean	2σ	mean	2σ	mean	2σ
Na	0.01	0.00	-	-	-	0.01	0.01	0.01	0.01	0.00	-	0.00	0.00
K	0.01	0.02	0.01	0.00	0.00	0.04	0.08	0.02	0.02	0.00	0.00	0.03	0.03
Total (D)	0.93	0.07	0.85	0.39	0.95	1.12	0.28	1.15	0.12	0.93	0.05	1.00	0.09
Al	3.11	0.10	3.41	0.20	3.33	3.41	0.13	3.41	0.18	2.96	0.14	3.19	0.31
Fe	0.08	0.07	0.09	0.04	0.01	0.21	0.20	0.14	0.22	0.13	0.04	0.09	0.15
Total (G)	3.18	0.13	3.50	0.23	3.35	3.62	0.28	3.55	0.20	3.09	0.11	3.28	0.26
P	1.81	0.09	1.58	0.21	1.66	1.52	0.30	1.52	0.10	1.94	0.05	1.68	0.16
S	0.20	0.01	0.32	0.02	0.05	0.09	0.03	0.07	0.01	0.10	0.01	0.16	0.02
As	0.00	0.00	0.01	0.01	0.20	0.00	0.00	0.04	0.02	0.00	0.00	0.00	0.00
Nb	0.01	0.01	0.00	0.00	0.00	0.00	0.00	0.00	-	-	-	0.00	-
Si	0.00	-	-	-	-	0.13	0.24	0.05	-	-	-	0.08	0.14
Total (T)	2.02	0.10	1.91	0.21	1.91	1.64	0.19	1.64	0.11	2.04	0.05	1.92	0.19
O	8.00	-	8.00	-	8.00	8.11	0.63	8.00	-	8.00	-	8.57	2.80
F	0.04	0.03	0.05	0.05	0.03	0.08	0.13	0.07	0.05	0.05	0.01	0.06	0.06
OH	5.96	0.03	5.95	0.05	5.97	5.93	0.13	5.93	0.05	5.95	0.01	5.94	0.06
% Flor-La	51.0	4.3	47.7	7.3	55.3	38.3	12.5	48.3	2.9	47.3	1.0	55.2	2.4
% Flor-Ce	44.1	3.2	45.8	1.1	41.7	53.4	11.4	47.2	1.0	47.2	1.6	41.9	1.8
% Flor-Nd	2.6	0.8	3.2	4.2	1.1	4.8	1.3	2.5	2.9	3.0	0.6	1.4	0.3
cation sum	6.1	0.1	6.3	0.2	6.2	6.4	0.3	6.3	0.1	6.1	0.0	6.2	0.1

Note: (-) indicates below detection limit. Flor = florencite; REY = REE + Y; *apfu* F as oxygen equivalent. Average detection limits and statistics for each sample are included in Appendix 3.

depending on the system documented (*e.g.*, diagenetic to metamorphic).

REE mineral speciation at Olympic Dam

While REE-phosphate minerals were present at an early stage during the evolution of the Olympic Dam deposit (*i.e.*, during the magmatic-to-hydrothermal transition) and demonstrate zonation or alteration halos in the form of apatite and monazite (Krneta *et al*. 2016, 2017a, Macmillan *et al*. 2016a), the main stage of REE-mineral crystallization was dominated by fluorocarbonates, likely coeval with the main hematite-sulfide-forming event at ~1590 Ma (Schmandt *et al*. 2017). This is suggestive of high activities of CO_2 and F during formation and physicochemical conditions at which other REE minerals, notably monazite, would not have been stable. Florencite overprints hematite, Cu-Fe-sulfides, and REE-fluorocarbonates and is widespread across the deposit, albeit volumetrically limited. This suggests a shift in fluid chemistry and/or conditions from REE-fluorocarbonate to REE-aluminum-phosphate stability.

These later fluids would be characterized by high aAl and $a$$PO_4$ to facilitate formation of florencite. The fluid would also need to have been LREE-enriched, potentially from preferential LREE leaching of pre-existing REE-bearing minerals (such as apatite, monazite, and synchysite/bastnäsite), or to have maintained enhanced LREE mobility, or potentially both.

The distinct lack of monazite suggests a lack of available phosphate, unfavorable physicochemical conditions for monazite formation, and/or the dominance of REE-carbonate complexes during the main stage of REE mineralization. The subsequent shift to aluminum-phosphate stability implies that conditions remained unfavorable for monazite formation, despite the availability of PO_4 (likely from the breakdown of pre-existing minerals such as apatite). Aluminum would also need to have become available for the formation of florencite and other APS minerals and would likely be sourced locally from sericite.

Olympic Dam REE mineralization and fractionation

Olympic Dam is a large and complex deposit with a prolonged geological history (*e.g.*, Oreskes & Einaudi 1990, Ehrig *et al*. 2012, 2017). Documentation of REE-bearing minerals and investigation of REE fractionation trends within different mineral groups presented here and in previous work (Krneta *et al*. 2016, 2017a, Macmillan *et al*. 2016a, b, 2017, Schmandt *et al*. 2017,

TABLE 2. LA-ICP-MS COMPOSITIONAL DATA FOR REPRESENTATIVE FLORENCITE GRAINS

	RX6710				RX6711			RX6713	RX6714					
(ppm)	1	2	3	4	1	2	3	1	1	Mean	Median	Min	Max	σ
Major and Minor Elements														
P	176000	169000	170000	145000	148600	146200	132800	128000	110000	147289	146200	110000	176000	20527
Sr	33200	32880	30100	29700	46900	55000	40400	16200	7490	32430	32880	7490	55000	13668
Ca	10900	10600	11000	8800	17200	19600	18300	28000	-	15550	14100	8800	28000	6063
As	1311	1200	1180	853	2280	927	545	457	3530	1365	1180	457	3530	915
Pb	94.6	119	86.8	66.1	164	216	95.2	206	172	136	119	66.1	216	52.0
Th	1.94	7.10	8.80	4.27	69.5	124	65.0	42.9	-	40.4	25.9	1.94	124	40.8
U	4.05	6.79	1.93	0.84	26.3	44.2	5.90	22.3	12.2	13.8	6.79	0.84	44.2	13.6
Rare Earth Elements														
Y	79.9	110	80.1	68.8	151	128	155	173	93.0	115	110	68.8	173	35.8
La	103100	104700	91200	80200	77000	65200	83600	66800	62000	81533	80200	62000	104700	14860
Ce	94700	100100	82800	76000	79500	71200	69000	85300	61400	80000	79500	61400	100100	11627
Pr	4450	4800	3990	3320	4160	4140	3440	4880	2130	3923	4140	2130	4880	808
Nd	5970	6650	5300	4560	6230	7100	5320	7530	3100	5751	5970	3100	7530	1287
Sm	112	199	104	88.1	153	271	142	220	118	156	142	88.1	271	57.8
Eu	19.2	38.9	14.8	12.3	32.9	63.0	32.1	57.8	27.0	33.1	32.1	12.3	63.0	16.8
Gd	32.8	54.0	31.9	29.4	47.9	95.0	47.4	73.0	52.0	51.5	47.9	29.4	95.0	20.0
Tb	1.97	4.10	1.68	1.84	3.20	5.90	3.90	6.90	5.00	3.83	3.90	1.68	6.90	1.75
Dy	8.50	21.6	10.2	7.30	20.3	32.6	21.4	31.0	33.0	20.7	21.4	7.3	33.0	9.66
Ho	2.39	4.10	2.44	1.83	4.15	5.70	3.86	5.60	3.90	3.77	3.90	1.83	5.70	1.28
Er	8.90	13.4	10.4	9.00	17.9	19.0	12.3	15.6	10.4	13.0	12.3	8.90	19.0	3.56
Tm	1.55	2.25	1.49	1.44	2.91	1.48	1.66	1.56	1.09	1.71	1.55	1.09	2.91	0.51
Yb	10.3	10.9	11.2	7.40	21.1	10.2	13.8	13.1	6.60	11.6	10.9	6.60	21.1	4.00
Lu	1.12	0.89	1.02	0.78	2.88	1.16	1.48	1.57	0.39	1.25	1.12	0.39	2.88	0.66
ΣREY (wt.%)	20.8	21.7	18.4	16.4	16.7	14.8	16.2	16.5	12.9	17.2	16.5	12.9	21.7	2.6
Other Trace Elements														
Na	533	562	225	<152	497	680	1210	1300	2150	895	621	225	2150	585
Si	7900	8300	23100	40300	20300	20300	24500	96000	137900	42067	23100	7900	137900	42189
Sc	2.70	-	-	3.00	<2.40	<2.50	2.60	7.70	8.40	4.88	3.00	2.60	8.40	2.60
Mn	<6.26	7.70	114	158	48.6	40.0	24.2	147	76.0	76.9	62.3	7.7	158	53.1
Fe	2040	1500	69000	97000	26500	33400	16200	40700	44000	36704	33400	1500	97000	29296
Cu	3880	3620	2700	1870	1880	692	1380	810	382	1913	1870	382	3880	1190
Zr	-	-	0.95	-	104	0.79	0.65	0.69	3.80	18.5	0.87	0.65	104	38.3
Nb	0.89	0.92	10.2	1.97	44.0	15.0	7.30	3.40	21.0	11.63	7.30	0.89	44.0	13.2
Ba	539	513	521	496	1010	819	1860	1910	1450	1013	819	496	1910	551
W	0.49	0.67	1.95	1.18	13.5	11.9	9.10	1.44	35.0	8.36	1.95	0.49	35.0	10.6

Note: (-) indicates value excluded due to high analytical uncertainty and (<) indicates value below reported detection limit.
Fe, Cu, and Si are considered present as coexisting inclusions of common minerals such as hematite, Cu-Fe-sulfides, and sericite.
REY = REE + Y

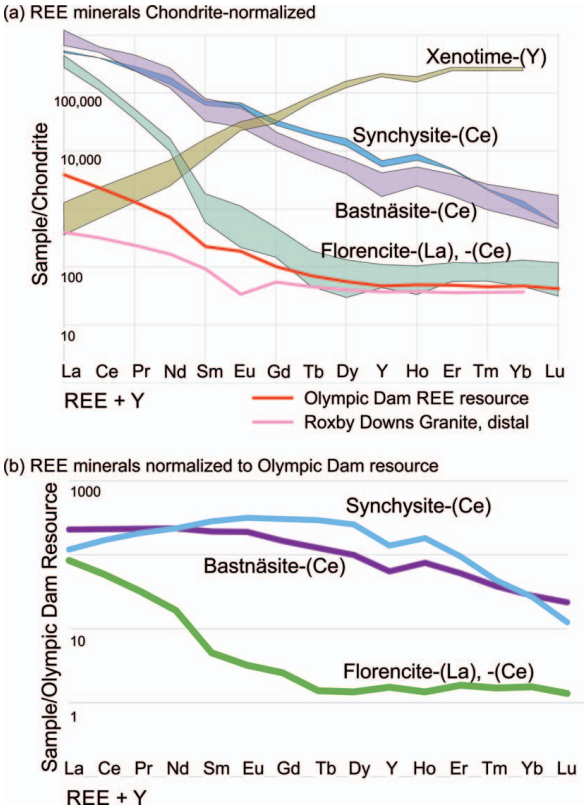


FIG. 9. (a) Chondrite-normalized REE fractionation trends for the primary REE minerals analyzed in this study and previously (bastnäsite and synchysite; Schmandt *et al*. 2017). The dominant mineral in these samples is bastnäsite, followed by florencite, synchysite, and xenotime. The plot also includes whole-rock REE values for the Olympic Dam resource and for the host RDG. These further emphasize the LREE-rich character of florencite, the relative LREE enrichment of the deposit, and because of the similarity between the fractionation trends for bastnäsite and the Olympic Dam resource, the dominance of bastnäsite as the dominant REE carrier for the deposit. Chondrite values from McDonough & Sun (1995). (b) Average value for major REE minerals at Olympic Dam normalized to the total Olympic Dam resource. Data from Schmandt *et al*. (2017) and this paper. The REE minerals show a pattern of relative LREE enrichment with sequence of mineralization. Synchysite is more MREE enriched than bastnäsite, nearly flat in the LREE segment, and then the final REE mineralization stage (florencite) is relatively enriched in LREE.

Ciobanu *et al*. 2017a) nonetheless enables discernment of a number of systematic trends.

Uranium is a major economic byproduct at Olympic Dam and U-minerals also display evolving REE fractionation trends. Macmillan *et al*. (2016a, 2017) showed multiple stages of U-mineralization, represented by different minerals and their textures. The REE+Y content decreases from early to later uraninite as well as to later brannerite and then coffinite; however, with an overall greater proportion of M,HREE, correlating with progressively younger U-mineral ages. This interpretation of multiple mineralization stages of uraninite, and the recognition that coffinite and brannerite form largely at the expense of uraninite alteration and breakdown (Macmillan *et al*. 2016a, b, 2017, Ehrig *et al*. 2017), implies that REE fractionation occurs throughout the evolution of the U-minerals, resulting in relative loss of LREE and comparative enrichment in M,HREE. This is in agreement with LREE being more easily mobilized (Migdisov *et al*. 2016), as well as their likely preferential partitioning into discrete LREE minerals, either bastnäsite or later florencite. Fractionation induced by crystal structure is also likely important, as the coffinite structure can more easily accept M,HREE, causing further enrichment of M,HREE relative to LREE in coffinite.

Apatite history is preserved in the REE fractionation trends from magmatic to early hydrothermal to late hydrothermal apatite, showing sustained relative LREE depletion and MREE enrichment (Krneta *et al*. 2017a, 2018). The greatest MREE enrichment, and strongest positive Eu anomaly, is in the late hydrothermal apatite observed in high-grade bornite ores. The pattern of greater LREE depletion and MREE enrichment in apatite is similar to the pattern observed in U-minerals and again indicates REE fractionation during mineral evolution. The REEs are considered to be mobilized as Cl complexes, then destabilized with F- and/or CO_3- and/or P-complexation causing REE mineralization, resulting in progressive enrichment of MREE in apatite and the general LREE enrichment of the deposit (Krneta *et al*. 2017a, 2018). Krneta *et al*. (2018) attribute the REE fractionation trends in apatite to be controlled by pH variation during the transition from early to late hydrothermal conditions from neutral to mildly acidic (K-feldspar to sericite transition) to alkaline (CO_2-buffered fluids in high-grade bornite ore).

The discrete LREE minerals also demonstrate REE fractionation with progressive stages of mineralization; however, the trends are inverse to those displayed by U-minerals or apatite. There is a marked trend of relative LREE ratios from synchysite to bastnäsite and florencite, suggesting that the REE minerals are showing progressive relative enrichment in LREE and corresponding depletion in M,HREE (Fig. 9). The data show the formation of LREE minerals at Olympic Dam can mainly be considered in terms of a sequence of events, evolving from synchysite to bastnäsite and then florencite, but is also dependent on the buffering effect of pre-existing lithologies, particularly felsic

TABLE 3. XENOTIME EPMA COMPOSITIONAL DATA, SAMPLE RX6721

wt.%	1	2	3	4	5	Mean	Median	Min	Max	2σ	AvgDL
Y_2O_3	39.6	40.9	39.7	41.2	40.6	40.4	40.6	39.6	41.2	1.3	0.02
La_2O_3	0.03	0.03	-	0.04	-	0.03	0.03	0.03	0.04	0.0	0.02
Ce_2O_3	0.17	0.05	0.08	0.18	0.15	0.13	0.15	0.05	0.18	0.1	0.02
Pr_2O_3	-	-	-	-	-	-	-	-	-	-	0.08
Nd_2O_3	0.37	0.19	0.16	0.13	0.29	0.23	0.19	0.13	0.37	0.2	0.07
Sm_2O_3	0.28	0.13	0.17	0.17	0.25	0.20	0.17	0.13	0.28	0.1	0.08
Eu_2O_3	0.21	0.14	0.18	0.15	0.19	0.17	0.18	0.14	0.21	0.0	0.04
Gd_2O_3	0.71	0.82	1.01	0.96	1.05	0.91	0.96	0.71	1.05	0.3	0.09
Tb_2O_3	0.33	0.31	0.36	0.29	0.31	0.32	0.31	0.29	0.36	0.05	0.06
Dy_2O_3	3.61	3.94	4.53	3.81	3.92	3.96	3.92	3.61	4.53	0.6	0.05
Ho_2O_3	1.14	1.05	1.22	1.02	1.01	1.09	1.05	1.01	1.22	0.2	0.11
Er_2O_3	4.68	4.64	5.35	4.75	4.77	4.84	4.75	4.64	5.35	0.5	0.06
Yb_2O_3	6.24	5.22	5.81	5.66	5.70	5.73	5.70	5.22	6.24	0.7	0.06
ΣREY_2O_3	57.3	57.4	58.6	58.4	58.2	52.3	52.3	50.3	54.8	1.0	
P_2O_5	35.2	35.4	34.9	32.0	30.4	33.6	34.9	30.4	35.4	4.1	0.03
CaO	0.05	0.15	0.11	0.23	0.07	0.12	0.11	0.05	0.23	0.1	0.01
PbO	0.05	0.04	0.04	0.06	0.07	0.05	0.05	0.04	0.07	0.02	0.03
ThO_2	0.03	-	-	0.04	0.02	0.03	0.03	0.02	0.04	0.02	0.02
UO_2	0.71	0.24	0.36	0.46	0.45	0.44	0.45	0.24	0.71	0.3	0.03
Na_2O	0.03	0.03	0.03	0.04	0.03	0.03	0.03	0.03	0.04	0.01	0.02
K_2O	0.01	0.01	-	-	-	0.01	0.01	0.01	0.01	0.00	0.01
Al_2O_3	-	-	-	-	-	-	-	-	-	-	0.02
SiO_2	-	-	0.19	0.48	-	0.34	0.34	-	0.48	0.3	0.02
ZrO_2	0.10	-	-	-	-	0.10	0.10	-	0.10	0.0	0.04
SO_2	-	0.03	0.04	0.12	-	0.06	0.04	-	0.12	0.1	0.03
As_2O_3	-	-	0.62	0.16	0.07	0.28	0.16	-	0.62	0.5	0.02
Fe_2O_3	0.81	3.07	2.02	6.46	15.4	5.55	3.07	0.81	15.40	10.5	0.05
SrO	-	-	-	-	-	-	-	-	-	-	0.02
Nb_2O_5	0.06	0.06	0.08	0.05	0.08	0.06	0.06	0.05	0.08	0.0	0.03
F	0.03	0.18	0.08	0.21	0.08	0.12	0.08	0.03	0.21	0.1	0.02
Cl	-	0.01	0.06	-	0.02	0.03	0.02	-	0.06	0.0	0.01
Total	94.5	96.6	97.1	98.7	105	98.3	97.1	94.5	105	7.1	
					apfu						
Y	0.73	0.75	0.73	0.79	0.82	0.76	0.75	0.73	0.82	0.07	
La	0.00	0.00	-	0.00	-	0.00	0.00	-	0.00	0.00	
Ce	0.00	0.00	0.00	0.00	0.00	0.00	0.00	0.00	0.00	0.00	
Pr	-	-	-	-	-	-	-	-	-	-	
Nd	0.00	0.00	0.00	0.00	0.00	0.00	0.00	0.00	0.00	0.00	
Sm	0.00	0.00	0.00	0.00	0.00	0.00	0.00	0.00	0.00	0.00	
Eu	0.00	0.00	0.00	0.00	0.00	0.00	0.00	0.00	0.00	0.00	
Gd	0.01	0.01	0.01	0.01	0.01	0.01	0.01	0.01	0.01	0.00	
Tb	0.00	0.00	0.00	0.00	0.00	0.00	0.00	0.00	0.00	0.00	
Dy	0.04	0.04	0.05	0.04	0.05	0.05	0.04	0.04	0.05	0.01	
Ho	0.01	0.01	0.01	0.01	0.01	0.01	0.01	0.01	0.01	0.00	
Er	0.05	0.05	0.06	0.05	0.06	0.05	0.05	0.05	0.06	0.01	
Yb	0.07	0.06	0.06	0.06	0.07	0.06	0.06	0.06	0.07	0.01	
ΣREY	0.93	0.93	0.93	0.98	1.03	0.96	0.93	0.93	1.03	0.08	
Ca	0.00	0.01	0.00	0.01	0.00	0.00	0.00	0.00	0.01	0.00	
Pb	0.00	0.00	0.00	0.00	0.00	0.00	0.00	0.00	0.00	0.00	
Th	0.00	-	-	0.00	0.00	0.00	0.00	-	0.00	0.00	
U	0.01	0.00	0.00	0.00	0.00	0.00	0.00	0.00	0.01	0.00	
Na	0.00	0.00	0.00	0.00	0.00	0.00	0.00	0.00	0.00	0.00	
K	0.00	0.00	-	-	-	0.00	0.00	-	0.00	0.00	
Total (A)	0.94	0.94	0.94	1.00	1.04	0.97	0.94	0.94	1.04	0.08	

TABLE 3. CONTINUED.

	1	2	3	4	5	Mean	Median	Min	Max	2σ	AvgDL
P	1.03	1.03	1.02	0.97	0.97	1.00	1.02	0.97	1.03	0.06	
Si	-	-	0.01	0.02	-	0.01	0.01	-	0.02	0.01	
Al	-	-	-	-	-	-	-	-	-	-	
Zr	0.00	-	-	-	-	0.00	0.00	-	0.00	0.00	
S	-	0.00	0.00	0.00	-	0.00	0.00	-	0.00	0.00	
As	-	-	0.01	0.00	0.00	0.01	0.00	-	0.01	0.01	
Nb	0.00	0.00	0.00	0.00	0.00	0.00	0.00	0.00	0.00	0.00	
Total (X)	1.04	1.03	1.04	1.00	0.97	1.02	1.03	0.97	1.04	0.05	
O = 3											
F	0.00	0.02	0.01	0.02	0.01	0.01	0.01	0.00	0.02	0.01	
% Xeno-Y	78.8	80.5	77.9	80.1	79.4	79.3	79.4	77.9	80.5	1.87	
% Xeno-Yb	7.3	6.0	6.7	6.4	6.5	6.6	6.5	6.0	7.3	0.81	
% Xeno-Dy	4.4	4.7	5.4	4.5	4.6	4.7	4.6	4.4	5.4	0.71	
% Xeno-Gd	0.9	1.0	1.2	1.2	1.3	1.1	1.2	0.9	1.3	0.30	

Note: (-) indicates below detection limit. Fe is considered present as coexisting hematite and has not been included for the purpose of formula calculation. Xeno = xenotime; REY = REE + Y; *apfu* F as oxygen equivalent.

(*e.g.*, granite and volcanics) *versus* mafic/ultramafic lithologies.

In this context, the LREE-fluorocarbonates that formed early include Ca-bearing species such as parisite, an unnamed polytype B_2S (Ciobanu *et al.* 2017a, Kontonikas-Charos *et al.* 2017, 2018a), and synchysite (Schmandt *et al.* 2017), and could relate to either alkali + Fe metasomatism and granite alteration (areas of weak alteration, magmatic K-feldspar still present) or mafic protoliths which would be richer in Ca and CO_2, respectively. The presence of synchysite in the early stages of alkali metasomatism is a prominent feature within Hiltaba-affiliated granitoids and has also been reported in the Moonta area (Yorke Peninsula; Kontonikas-Charos *et al.* 2014) and in the Samphire pluton on the Eyre Peninsula (Domnick *et al.* 2018). In the Olympic Dam orebody synchysite is found in direct associ-

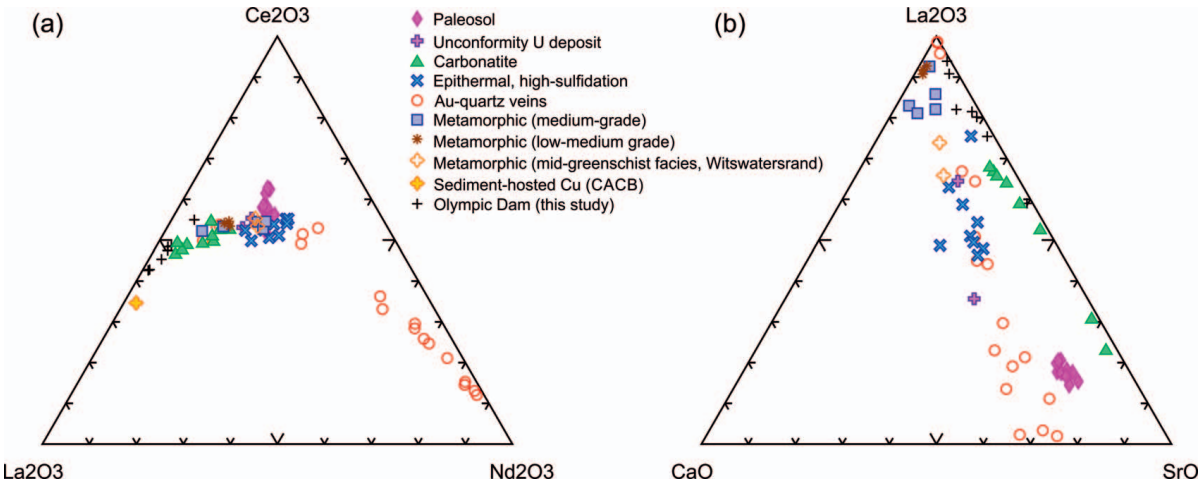


FIG. 10. Compositional variability in florencite from Olympic Dam compared with literature data for different deposit types. (a) Ternary plot of the major LREE (Ce-, La-, and Nd-oxide components, in wt.%). (b) Ternary plot of reported CaO, SrO, and La_2O_3 (wt.%). SrO is not reported for sediment-hosted Cu (CACB) and thus not included in this plot. Literature sources: Paleosol – Vircava *et al.* (2015); Unconformity U deposit – Gaboreau *et al.* (2007); Carbonatite – Doroshkevich *et al.* (2009); Epithermal, high-sulfidation – Georgieva & Velinova (2014); Au-quartz veins – Repina *et al.* (2014); Metamorphic florencite (medium-grade) – Nagy *et al.* (2002); Metamorphic florencite (low-medium grade) – Chakraborty *et al.* (2014); Metamorphic florencite (mid-greenschist facies) – Rasmussen & Muhling (2009); Sediment-hosted Cu [Central African Copper Belt (CACB)] – Lefebvre & Gasparrini (1987).

ation with bastnäsite, in some cases in sulfide-rich ores (Schmandt *et al*. 2017). Synchysite is a minor REE mineral but when present in the same samples shows a distinct MREE enrichment compared to bastnäsite (Fig. 9). The lack of intermediate Ca-fluorocarbonates in such assemblages, at least at the micron-scale of observation, could be attributed to either a sharp variation in the Ca activity of the fluids if the two species are co-crystallizing, or alternatively it could be attributed to a different generation of REE-fluorocarbonates.

Importantly, florencite appears to be later than either of the two fluorocarbonates and has a notably different REE trend with greater LREE compared to MREE and HREE (Fig. 9).

One way such patterns (*i.e*., increasing LREE enrichment from synchysite to bastnäsite to florencite) could be interpreted is in terms of fractionation, caused by the greater solubility of the lightest REE and stability of REE-Cl complexes in fluid, resulting in their retention in fluid and deferred precipitation within a long-duration hydrothermal event. Another possibility could be that florencite preferentially scavenges LREE from other pre-existing REE-bearing minerals, notably REE-fluorocarbonates and apatite, which in some instances it directly replaces. Conversely, crystal-structural controls that may induce fractionation between the two REE-fluorocarbonates and between REE-fluorocarbonate and REE-aluminum phosphate minerals are poorly documented but could be influential.

Broom-Fendley *et al*. (2017) described the REE mineralogy of the Songwe Hill carbonatite, Malawi, which displays comparable REE fractionation trends from apatite and fluorocarbonates as those observed at Olympic Dam. Broom-Fendley *et al*. (2017) interpreted the trends in terms of LREE remaining in solution with M,HREE partitioning into apatite and LREE deposited as fluorocarbonates. These authors proposed a dominance of REE-carbonate complexes in the fluid and HREE–LREE fractionation caused by CO_2 degassing. They also observed florencite-(Ce) occurring in feldspar-rich samples with Fe-oxides and as replacement or alteration of apatite. The Songwe Hill carbonatite is a further example of a system in which REE-fluorocarbonates (and apatite) are stable over other REE minerals, notably monazite, also emphasizing the parallels between IOCG and carbonatite systems hinted at by Groves & Vielreicher (2001).

Implications for deposit evolution

The REE-fluorocarbonates, primary uraninite, and hydrothermal apatite all display intimate associations with hematite and Cu-(Fe)-sulfides and likely formed together at relatively high temperatures (up to 425 °C; Ciobanu *et al*. 2017b). Florencite and paragenetically late U-minerals are evidence for an evolution towards later, lower-temperature conditions. Uranium minerals and apatite both show similar patterns of M,HREE enrichment and LREE depletion as mineralization progresses; the discrete REE minerals, on the other hand, show progressive LREE enrichment and MREE depletion. These REE trends of apatite, U-minerals, and REE-minerals are evidence of enhanced LREE transport during deposit evolution, resulting in REE fractionation and dominance of LREE across the entire deposit, as well as LREE leaching (in the case of apatite; Krneta *et al*. 2017a).

Based on data accumulated so far, the formation of LREE minerals at Olympic Dam can be approached in terms of a sequence of events. Minerals that formed early include Ca-bearing REE-fluorocarbonates, comprised of species such as parisite (K-feldspar stable; Ciobanu *et al*. 2017a, Kontonikas-Charos *et al*. 2018a) or synchysite (Schmandt *et al*. 2017). These were followed by the REE-fluorocarbonate bastnäsite, which is the phase formed during the major stage of mineralization and is closely associated with hematite and Cu-(Fe)-sulfide formation. Paragenetically late, and possibly representing a different stage or evolved formation conditions, is florencite, which overprints the REE-fluorocarbonates, hematite, and Cu-(Fe)-sulfides and replaces the magmatic and early hydrothermal apatite (Krneta *et al*. 2017a). Minerals of the woodhousite–svanbergite series are also typically late and replace all earlier-formed REE-minerals, Fe-oxides, and Cu-(Fe)-sulfides. This sequence is an excellent example of mineral evolution within a single ore deposit.

From geological data and modeling of REE-bearing systems (Gysi & Williams-Jones 2015, Migdisov *et al*. 2016), it seems most likely that LREE preferentially formed REE-fluorocarbonate minerals, effectively removing LREE from solution. This left the MREE and HREE to become concentrated in minerals, such as late U-minerals, hydrothermal apatite, and xenotime, that can more readily incorporate HREE, and these HREE-rich minerals probably formed during or after the REE-fluorocarbonates. Mixing of hydrothermal and carbonate-rich fluids or REE-carbonate complexes precipitating from magma degassing are both viable options for the promotion of fluorocarbonate-dominant minerals.

Leaching of LREE from pre-existing minerals, including but not restricted to early U-minerals, magmatic apatite, monazite, and feldspars (Kontonikas-Charos *et al*. 2017, 2018a, b), likely contributed to the LREE-dominant mineralogy of the deposit. Florencite appears late and likely represents the result of a LREE-

dominant remobilization event that took place after REE-fluorocarbonate and sulfide formation.

The predominance of REE-fluorocarbonate minerals during initial mineralization suggests a lack of available PO_4, perhaps already partitioned into apatite; possibly an overabundance of CO_2; or physiochemical conditions that favored fluorocarbonate formation. Phosphate would need to become available to form florencite in the later REE event. This could be achieved *via* release of phosphate from the breakdown of apatite (Krneta *et al*. 2017a). Florencite is often associated with other APS minerals in advanced argillic alteration, which is defined by low pH and relatively low temperature, and likely formed under such conditions.

Conclusions

Florencite is ubiquitous across the Olympic Dam deposit, is almost always fine-grained, and occurs primarily as disseminated irregular to euhedral crystals within the sericite–chlorite breccia matrix. Occasionally, florencite-rich pockets and aggregates are found with some textures suggestive of selective replacement of pre-existing minerals. The other REE-phosphate minerals, xenotime and monazite, are rare. Xenotime forms most commonly as rims on zircon grains, and monazite is absent in most samples investigated.

The MLA analysis shows that, on the deposit-scale, florencite appears to be more closely associated with alteration minerals, including hematite, sericite, and quartz, than with other REE-phosphates. Florencite is positively correlated with the alunite group minerals, xenotime is strongly associated with zircon, and monazite shows a slightly greater preferential association with bastnäsite in comparison with other REE-phosphates.

The extended formula for Olympic Dam florencite is $(Ca_{0.01–0.24}Sr_{0.03–0.40}La_{0.14–0.49}Ce_{0.20–0.47}Pr_{0.00–0.03}Nd_{0.00–0.05})_{\Sigma 0.43–0.96}Al_{2.89–3.33}(P_{1.42–1.96}S_{0.05–0.34}As_{0.0–0.20})_{\Sigma 1.77–2.21}O_4(OH)_6$ and the mean formula for xenotime is $Y_{0.73–0.82}REE_{0.20–0.22}(P_{0.97–1.03}Si_{0–0.02})O_4$. Compared to florencite from other deposits and settings, Olympic Dam florencite is generally mostly La-rich with less Ca substitution and is compositionally most similar to florencite from a carbonatite setting.

Texturally, florencite appears to belong to a later stage of LREE mineralization at Olympic Dam, following, and generally weaker than, the main REE-fluorocarbonate-dominant stage associated with the main hematite-Cu-Fe-S hydrothermal event. Florencite also appears late relative to other phosphate minerals, such as apatite.

Chondrite-normalized fractionation trends for florencite are distinct from other REE minerals because they are extremely LREE-enriched. Uranium minerals and apatite both show similar patterns of M,HREE enrichment and LREE depletion with progressive mineralization while the discrete REE minerals show progressive LREE enrichment and MREE depletion.

Florencite likely formed at low pH and relatively lower temperature during a later phase of deposit evolution. The LREE were likely sourced from breakdown of preexisting REE-minerals, including REE-fluorocarbonates and apatite.

Acknowledgments

This research is a contribution to the ARC Research Hub for Australian Copper–Uranium, co-supported by BHP Olympic Dam and the South Australian Mining and Petroleum Services Centre of Excellence. We acknowledge Adelaide Microscopy as part of the Australian Microscopy and Microanalysis Research Facility (AMMRF). Insightful comments from Henrik Friis, an anonymous reviewer, Associate Editor Leo Millonig, and Editor Lee Groat are highly appreciated.

References

Aoki, M., Comsti, E.C., Lazo, F.B., & Matsuhisa, Y. (1993) Advanced argillic alteration and geochemistry of alunite in an evolving hydrothermal system at Baguio, Northern Luzon, Philippines. *Resource Geology* **43**, 155–164.

Apukhtina, O.B. (2016) *Distribution, petrology, geochemistry and geochronology of carbonate assemblages at the Olympic Dam deposit*. Unpublished Ph.D. Thesis, University of Tasmania, available from https://eprints.utas.edu.au/23013/

Arribas, A., Jr., Cunningham, C.G., Rytuba, J.J., Rye, R.O., Kelly, W.C., Podwysocki, M.H., & Tosdal, R.M. (1995) Geology, geochemistry, fluid inclusion, and isotope geochemistry of the Rodalquilar gold-alunite deposit, Spain. *Economic Geology* **90**, 795–822.

Bajnoczi, B., Seres-Hartai, E., & Nagy, G. (2004) Phosphate-bearing minerals in the advanced argillic alteration zones of high-sulphidation type ore deposits in the Carpatho-Pannonian region. *Acta Mineralogica-Petrographica (Szeged)* **45**, 81–92.

Barton, M.D. (2013) Iron Oxide(-Cu-Au-REE-P-Ag-U-Co) Systems. *In* Treatise on Geochemistry: 2nd Edition (K. Turekian & H. Holland, eds.). Volume 13, Elsevier Inc. (515–541).

Bayliss, P., Kolitsch, U., Nickel, E.H., & Pring, A. (2010) Alunite supergroup: recommended nomenclature. *Mineralogical Magazine* **74**, 919–927.

Broom-Fendley, S., Brady, A.E., Wall, F., Gunn, G., & Dawes, W. (2017) REE minerals at the Songwe Hill carbonatite, Malawi: HREE-enrichment in late-stage apatite. *Ore Geology Reviews* **81**, 23–41.

Chakraborty, M., Biswas, S., Sengupta, N., & Sengupta, P. (2014) First Report of Florencite from the Singhbhum Shear Zone of the East Indian Craton. *International Journal of Mineralogy*, 1–9.

Ciobanu, C.L., Wade, B.P., Cook, N.J., Schmidt Mumm, A., & Giles, D. (2013) Uranium bearing hematite from the Olympic Dam Cu-U-Au deposit, South Australia: A geochemical tracer and reconnaissance Pb–Pb geochronometer. *Precambrian Research* **238**, 129–147.

Ciobanu, C.L., Cook, N.J., Ehrig, K., Wade, B.P., & Kamenetsky, V.S. (2015) Trace element signatures in iron oxides from the Olympic Dam IOCG deposit, South Australia. 13th SGA Biennial Meeting 2015, *Mineral Resources for a Sustainable World* **3**, 1071–1074.

Ciobanu, C.L., Kontonikas-Charos, A., Slattery, A., Cook, N.J., Ehrig, K., & Wade, B.P. (2017a) Short-range stacking disorder in mixed-layer compounds: A HAADF STEM study of bastnäsite-parisite intergrowths. *Minerals* **7**, 227.

Ciobanu, C.L., Cook, N.J., & Ehrig, K. (2017b) Ore minerals down to the nanoscale: Cu-(Fe)-sulphides from the iron oxide copper gold deposit at Olympic Dam, South Australia. *Ore Geology Reviews* **81**, 1218–1235.

Cook, N.J., Ciobanu, C.L., George, L., & Ehrig, K. (2016) Trace element analysis of minerals in magmatic-hydrothermal ores by laser ablation inductively-coupled plasma mass spectrometry: Approaches and opportunities. *Minerals* **6**, 111.

Davidson, G.J., Paterson, H., Meffre, S., & Berry, R.F. (2007) Characteristics and origin of the Oak Dam East Breccia-Iron-Oxide Cu-U-(Au) Deposit: Olympic Dam Region, Gawler Craton. *Economic Geology* **102**, 1471–1498.

Diemar, G.A. (2014) *The petrology of hydrothermal rare earth element bearing minerals in the Olympic Dam IOCG deposit support a 1.3 Ga formation*. M.Sc. Thesis, University of Tasmania, Hobart, Australia.

Dill, H.G. (2001) The geology of aluminium phosphates and sulphates of the alunite group minerals: a review. *Earth-Science Reviews* **53**, 35–93.

Domnick, U., Cook, N.J., Bluck, R., Brown, C., & Ciobanu, C.L. (2018) Petrography and geochemistry of granitoids from the Samphire Pluton, South Australia: Implications for uranium mineralisation in overlying sediments. *Lithos* **300–301**, 1–19.

Doroshkevich, A.G., Viladkar, S.G., Ripp, G.S., & Burtseva, M.V. (2009) Hydrothermal REE mineralization in the Amba Dongar carbonatite complex, Gujarat, India. *Canadian Mineralogist* **47**, 1105–1116.

Ehrig, K., McPhie, J., & Kamenetsky, V.S. (2012) Geology and mineralogical zonation of the Olympic Dam iron oxide Cu-U-Au-Ag Deposit, South Australia. *In* Geology and Genesis of Major Copper Deposits and Districts of the World, a Tribute to Richard Sillitoe (J.W. Hedenquist, M. Harris, & F. Camus, eds.). Society of Economic Geologists, Inc., Special Publication **16**, Littleton, Colorado (237–267).

Ehrig, K., Kamenetsky, V.S., Mcphie, J., Cook, N.J., & Ciobanu, C.L. (2017) Olympic Dam iron oxide Cu-U-Au-Ag deposit. *In* Australian Ore Deposits (N. Phillips, ed.). AusIMM, Australia (601–610).

Förster, H.J. (2006) Composition and origin of intermediate solid solutions in the system thorite-xenotime-zircon-coffinite. *Lithos* **88**, 35–55.

Freeman, H. & Tomkinson, M. (2010) Geological setting of iron oxide related mineralisation in the southern Mount Woods Domain, South Australia. *In* Hydrothermal Iron Oxide Copper-Gold & Related Depoits: A Global Perspective, Volume 3: Advances in the Understanding of IOCG Deposits (T.M. Porter, ed.). PGC Publishing, Adelaide, Australia (1–19).

Fulignati, P., Gioncada, A., & Sbrana, A. (1999) Rare-earth element (REE) behaviour in the alteration facies of the active magmatic-hydrothermal system of Vulcano (Aeolian Islands, Italy). *Journal of Volcanology and Geothermal Research* **88**, 325–342.

Gaboreau, S., Cuney, M., Quirt, D., Beaufort, D., Patrier, P., & Mathieu, R. (2007) Significance of aluminum phosphate-sulfate minerals associated with U unconformity-type deposits: The Athabasca basin, Canada. *American Mineralogist* **92**, 267–280.

Georgieva, S. & Velinova, N. (2014) Florencite-(Ce, La, Nd) and crandallite from the advanced argillic alteration in the Chelopech high-sulphidation epithermal Cu-Au deposit, Bulgaria. *Comptes rendus de l'Académie bulgare des sciences: sciences mathématiques et naturelles* **67**, 1669–1678.

Grandell, L., Lehtilä, A., Kivinen, M., Koljonen, T., Kihlman, S., & Lauri, L.S. (2016) Role of critical metals in the future markets of clean energy technologies. *Renewable Energy* **95**, 53–62.

Groves, D.I. & Vielreicher, N.M. (2001) The Phalabowra (Palabora) carbonatite-hosted magnetite-copper sulfide deposit, South Africa: An end-member of the iron-oxide copper-gold-rare earth element deposit group? *Mineralium Deposita* **36**, 189–194.

Groves, D.I., Bierlein, F.P., Meinert, L.D., & Hitzman, M.W. (2010) Iron oxide copper-gold (IOCG) deposits through earth history: Implications for origin, lithospheric setting, and distinction from other epigenetic iron oxide deposits. *Economic Geology* **105**, 641–654.

Gu, Y. (2003) Automated scanning electron microscope based mineral liberation analysis. *Journal of Minerals & Materials Characterization & Engineering* **2**, 33–41.

Gysi, A.P. & Williams-Jones, A.E. (2015) The thermodynamic properties of bastnasite-(Ce) and parisite-(Ce). *Chemical Geology* **392**, 87–101.

Hatert, F., Lefevre, P., Pasero, M., & Fransolet, A. (2003) Graulichite-(Ce), a new arsenate mineral from the Stavelot Massif, Belgium. *European Journal of Mineralogy* **15**, 733–739.

Hetherington, C.J., Jercinovic, M.J., Williams, M.L., & Mahan, K. (2008) Understanding geologic processes with xenotime: Composition, chronology, and a protocol for electron probe microanalysis. *Chemical Geology* **254**, 133–147.

Hikov, A., Lerouge, C., & Velinova, N. (2010) Geochemistry of alunite group minerals in advanced argillic altered rocks from the Asarel porphyry copper deposit, Central Srednogorie. *Review of the Bulgarian Geology Society* **71**, 133–148.

Hikov, A., Velinova, N., Lerouge, C., & Kunov, A. (2017) Geochemistry of advanced argillic altered rocks in the area of Breznik, Western Srednogorie Unit (Bulgaria). *Geological Balcanica* **1**, 93–108.

Hitzman, M.W., Oreskes, N., & Einaudi, M.T. (1992) Geological characteristics and tectonic setting of Proterozoic iron oxide (Cu-U-Au-REE) deposits. *Precambrian Research* **58**, 241–287.

Huang, Q., Kamenetsky, V.S., Ehrig, K., Mcphie, J., Kamenetsky, M., Apukhtina, O., & Chambefort, I. (2017) Effects of hydrothermal alteration on mafic lithologies at the Olympic Dam Cu-U-Au-Ag deposit. *Precambrian Research* **292**, 305–322.

Janeczek, J. & Ewing, R.C. (1996) Florencite-(La) with fissiogenic REEs from a natural fission reactor at Bangombe, Gabon. *American Mineralogist* **81**, 1263–1269.

Khashgerel, B., Kavalieris, I., & Hayashi, K. (2008) Mineralogy, textures, and whole-rock geochemistry of advanced argillic alteration: Hugo Dummett porphyry Cu-Au deposit, Oyu Tolgoi mineral district, Mongolia. *Mineralium Deposita* **43**, 913–932.

Kontonikas-Charos, A., Ciobanu, C.L., & Cook, N.J. (2014) Albitization and redistribution of REE and Y in IOCG systems: Insights from Moonta-Wallaroo, Yorke Peninsula, South Australia. *Lithos* **208**, 178–201.

Kontonikas-Charos, A., Ciobanu, C.L., Cook, N.J., Ehrig, K., Krneta, S., & Kamenetsky, V.S. (2017) Feldspar evolution in the Roxby Downs Granite, host to Fe-oxide Cu-Au-(U) mineralisation at Olympic Dam, South Australia. *Ore Geology Reviews* **80**, 838–859.

Kontonikas-Charos, A., Ciobanu, C.L., Cook, N.J., Ehrig, K., Ismail, R., Krneta, S., & Basak, A. (2018a) Feldspar mineralogy and rare earth element (re)mobilization in iron-oxide copper gold systems from South Australia: a nanoscale study. *Mineralogical Magazine* **82(S1)**, S173–S197.

Kontonikas-Charos, A., Ciobanu, C.L., Cook, N.J., Ehrig, K., Krneta, S., & Kamenetsky, V.S. (2018b) Rare earth element geochemistry of feldspars: examples from Fe-oxide Cu-Au systems in the Olympic Cu-Au Province, South Australia. *Mineralogy and Petrology* **112**, 145–172.

Krneta, S., Ciobanu, C.L., Cook, N.J., Ehrig, K., & Kontonikas-Charos, A. (2016) Apatite at Olympic Dam, South Australia: A petrogenetic tool. *Lithos* **262**, 470–485.

Krneta, S., Ciobanu, C.L., Cook, N.J., Ehrig, K., & Kontonikas-Charos, A. (2017a) Rare earth element behaviour in apatite from the Olympic Dam Cu-U-Au-Ag deposit, South Australia. *Minerals* **7**, 1–26.

Krneta, S., Cook, N.J., Ciobanu, C.L., Ehrig, K., & Kontonikas-Charos, A. (2017b) The Wirrda Well and Acropolis prospects, Gawler Craton, South Australia: Insights into evolving fluid conditions through apatite chemistry. *Journal of Geochemical Exploration* **181**, 276–291.

Krneta, S., Ciobanu, C.L., Cook, N.J., & Ehrig, K. (2018) Numerical Modeling of REE Fractionation Patterns in Fluorapatite from the Olympic Dam Deposit (South Australia). *Minerals* **8**, 342.

Lefebvre, J. & Gasparrini, C. (1987) Florencite, an occurrence in the Zairian Copperbelt. *Canadian Mineralogist* **18**, 301–311.

Lottermoser, B.G. (1992) Rare earth elements and hydrothermal ore formation processes. *Ore Geology Reviews* **7**, 25–41.

Lottermoser, B.G. (1995) Rare earth element mineralogy of the Olympic Dam Cu-U-Au-Ag deposit, Roxby Downs, South Australia: Implications for ore genesis. *Neues Jahrbuch für Mineralogie Monatshefte* **8**, 371–384.

Lucas, J., Lucas, P., Le Mercier, T., Rollat, A., & Davenport, W. (2015) *Rare Earths: Science, Technology, Production, and Use*. Elsevier, Amsterdam, Netherlands.

Macmillan, E., Cook, N.J., Ehrig, K., Ciobanu, C.L., & Pring, A. (2016a) Uraninite from the Olympic Dam IOCG-U-Ag deposit: Linking textural and compositional variation to temporal evolution. *American Mineralogist* **101**, 1295–1320.

Macmillan, E., Ciobanu, C.L., Ehrig, K., Cook, N.J., & Pring, A. (2016b) Replacement of uraninite by bornite via coupled dissolution-reprecipitation: Evidence from texture and microstructure. *Canadian Mineralogist* **54**, 1369–1383.

Macmillan, E., Cook, N.J., Ehrig, K., & Pring, A. (2017) Chemical and textural interpretation of late-stage coffinite and brannerite from the Olympic Dam IOCG-Ag-U deposit. *Mineralogical Magazine* **81**, 1323–1366.

McDonough, W.F. & Sun, S.S. (1995) Composition of the Earth. *Chemical Geology* **120**, 223–253.

McPhie, J., Orth, K., Kamenetsky, V., Kamenetsky, M., & Ehrig, K. (2016) Characteristics, origin and significance of Mesoproterozoic bedded clastic facies at the Olympic Dam Cu–U–Au–Ag deposit, South Australia. *Precambrian Research* **276**, 85–100.

Migdisov, A., Williams-Jones, A.E., Brugger, J., & Caporuscio, F.A. (2016) Hydrothermal transport, deposition, and fractionation of the REE: Experimental data and thermodynamic calculations. *Chemical Geology* **439**, 13–42.

Mills, S.J., Kartashov, P.M., Kampf, A.R., & Raudsepp (2010) Arsenoflorencite-(La), a new mineral from the Kommi Republic, Russian Rederation: description and crystal sturcutre. *European Journal of Mineralogy* **22**, 613–621.

Montel, J.M., Kato, T., Enami, M., Cocherie, A., Finger, F., Williams, M., & Jercinovic, M. (2018) Electron-microprobe dating of monazite: The story. *Chemical Geology* **484**, 4–15.

Nagy, G., Draganits, E., Demeny, A., Panto, G., & Arkai, P. (2002) Genesis and transformations of monazite, florencite and rhabdophane during medium grade metamorphism: examples from the Sopron Hills, Eastern Alps. *Chemical Geology* **191**, 25–46.

Ni, Y., Hughes, J.M., & Mariano, A.N. (1995) Crystal chemistry of the monazite and xenotime structures. *American Mineralogist* **80**, 21–26.

Nickel, E.H. & Temperly, J.E. (1987) Aresenoflorencite-(Ce): a new arsenate mineral from Australia. *Mineralogical Magazine* **51**, 605–609.

Oreskes, N. & Einaudi, M.T. (1990) Origin of Rare Earth Element-Enriched Hematite Breccias at the Olympic Dam Cu-U-Au-Ag Deposit, Roxby Downs, South Australia. *Economic Geology* **85**, 1–28.

Owen, N.D., Cook, N.J., Rollog, M., Ehrig, K.J., Schmandt, D.S., & Ciobanu, C.L. (2018) REE-, Sr-Ca-arsenate-phosphate-sulphate minerals of the woodhouseite series and their role as hosts for radionuclides. Extended abstract, 15th Quadrennial IAGOD Symposium, Salta, Argentina (187–188).

Paton, C., Hellstrom, J., Paul, B., Woodhead, J., & Hergt, J. (2011) Iolite: Freeware for the visualisation and processing of mass spectrometric data. *Journal Analytical Atomic Spectrometry* **26**, 2508–2518.

Pe-Piper, G. & Dolansky, L.M. (2015) Early diagenetic origin of Al phosphate-sulfate minerals (woodhouseite and crandallite series) in terrestrial sandstones, Nova Scotia, Canada. *American Mineralogist* **90**, 1434–1441.

Rasmussen, B. (1996) Early diagenetic REE-phosphate minerals (florencite, gorceixite, crandallite, and xenotime) in marine sandstones: A major sink for oceanic phosphorus. *American Journal of Science* **296**, 601–632.

Rasmussen, B. & Muhling, J.R. (2009) Reactions destroying detrital monazite in greenschist-facies sandstones from the Witwatersrand basin, South Africa. *Chemical Geology* **264**, 311–327.

Repina, S.A., Khiller, V.V., & Makagonov, E.P. (2014) Microheterogeneity of crystal growth zones as a result of REE fractionation. *Geochemistry International* **52**, 1057–1071.

Roberts, D.E. & Hudson, G.R.T. (1983) The Olympic Dam copper-uranium-gold deposit, Roxby Downs, South Australia. *Economic Geology* **78**, 799–822.

Schmandt, D.S., Cook, N.J., Ciobanu, C.L., Ehrig, K., Wade, B.P., Gilbert, S., & Kamenetsky, V.S. (2017) Rare Earth Element Fluorocarbonate Minerals from the Olympic Dam Cu-U-Au-Ag Deposit, South Australia. *Minerals* **7**, 202.

Stoffregen, R.E. & Alpers, C.N. (1987) Woodhouseite and svanbergite in hydrothermal ore deposits: products of apatite destruction during advanced argillic alteration. *Canadian Mineralogist* **25**, 201–211.

Verdugo-Ihl, M.R., Ciobanu, C.L., Cook, N.J., Ehrig, K.J., Courtney-Davies, L., & Gilbert, S. (2017) Textures and U-W-Sn-Mo signatures in hematite from the Olympic Dam Cu-U-Au-Ag deposit, South Australia: Defining the archetype for IOCG deposits. *Ore Geology Reviews* **91**, 173–195.

Vircava, I., Somelar, P., Liivamägi, S., Kirs, J., & Kirsimäe, K. (2015) Origin and paleoenvironmental interpretation of aluminum phosphate – sulfate minerals in a Neoproterozoic Baltic paleosol. *Sedimentary Geology* **319**,114–123.

Williams, P.J., Barton, M.D., Johnson, D.A., Fontbote, L., De Haller, A., Mark, G., Oliver, N.H.S., & Marschik, R. (2005) Iron oxide copper-gold deposits: Geology, space-time distribution, and possible modes of origin. *Economic Geology 100th Anniversary Volume*, 371–405.

Williams-Jones, A.E., Migdisov, A.A., & Samson, I.M. (2012) Hydrothermal mobilisation of the rare earth elements – a tale of "Ceria" and "Yttria". *Elements* **8**, 355–360.

Received June 20, 2018. Revised manuscript accepted November 14, 2018.

CHAPTER 4

UPTAKE OF TRACE ELEMENTS BY BARYTE DURING COPPER ORE PROCESSING: A CASE STUDY FROM OLYMPIC DAM, SOUTH AUSTRALIA

Danielle S. Schmandt [1], Nigel J. Cook [1], Kathy Ehrig [2], Sarah Gilbert [3], Benjamin P. Wade [3], Mark Rollog[1], Cristiana L. Ciobanu [2], Vadim S. Kamenetsky [4]

[1]School of Chemical Engineering, The University of Adelaide, Adelaide, SA 5005, Australia

[2] BHP Olympic Dam, Adelaide, SA, 5000, Australia

[3] Adelaide Microscopy, The University of Adelaide, Adelaide, SA 5005, Australia

[4] School of Physical Sciences, University of Tasmania, Hobart, TAS 7001, Australia

Minerals Engineering. volume 135, 2019

doi: 10.1016/j.mineng.2019.02.034

Statement of Authorship

Title of Paper	Uptake of trace elements by baryte during copper ore processing: a case study from Olympic Dam, South Australia
Publication Status	☑ Published ☐ Accepted for Publication ☐ Submitted for Publication ☐ Unpublished and Unsubmitted work written in manuscript style
Publication Details	Published in Minerals Engineering, v. 135, p. 83-94, 2019. doi: 10.1016/j.mineng.2019.02.034.

Principal Author

Name of Principal Author (Candidate)	Danielle S. Schmandt		
Contribution to the Paper	Performed analytical work, carried out data processing and interpretation, oversaw development of work, and wrote manuscript.		
Overall percentage (%)	60		
Certification:	This paper reports on original research I conducted during the period of my Higher Degree by Research candidature and is not subject to any obligations or contractual agreements with a third party that would constrain its inclusion in this thesis. I am the primary author of this paper.		
Signature		Date	Dec 3rd, 2018

Co-Author Contributions

By signing the Statement of Authorship, each author certifies that:

i. the candidate's stated contribution to the publication is accurate (as detailed above);

ii. permission is granted for the candidate in include the publication in the thesis; and

iii. the sum of all co-author contributions is equal to 100% less the candidate's stated contribution.

Name of Co-Author	Nigel J. Cook		
Contribution to the Paper	10%; Helped define direction of research, supervised development of work, assisted with data interpretation, and contributed to manuscript preparation.		
Signature		Date	5/12/2018

Name of Co-Author	Kathy Ehrig		
Contribution to the Paper	5%; Provided sample material, helped define direction of research, assisted with data interpretation, contributed to manuscript preparation, and helped to evaluate and edit manuscript.		
Signature		Date	10/12/2018

Name of Co-Author	Sarah Gilbert		
Contribution to the Paper	5%; Assisted in operating analytical instrumentation and data processing.		
Signature		Date	6/12/18

Name of Co-Author	Benjamin P. Wade		
Contribution to the Paper	5%; Assisted in operating analytical instrumentation and data processing.		
Signature		Date	11/12/2018

Name of Co-Author	Mark Rollog		
Contribution to the Paper	5%; Contributed to manuscript preparation and helped to evaluate and edit manuscript.		
Signature		Date	10/12/2018

Name of Co-Author	Cristiana L. Ciobanu		
Contribution to the Paper	5%; Contributed to manuscript preparation and helped to evaluate and edit manuscript.		
Signature		Date	5/12/2018

Name of Co-Author	Vadim S. Kamenetsky		
Contribution to the Paper	5%; Helped to evaluate and edit manuscript.		
Signature		Date	9/12/18

Minerals Engineering 135 (2019) 83–94

Contents lists available at ScienceDirect

Minerals Engineering

journal homepage: www.elsevier.com/locate/mineng

Uptake of trace elements by baryte during copper ore processing: A case study from Olympic Dam, South Australia

Danielle S. Schmandt[a,*], Nigel J. Cook[a], Kathy Ehrig[b], Sarah Gilbert[c], Benjamin P. Wade[c], Mark Rollog[a], Cristiana L. Ciobanu[a], Vadim S. Kamenetsky[d]

[a] School of Chemical Engineering, The University of Adelaide, Adelaide, SA 5005, Australia
[b] BHP Olympic Dam, Adelaide, SA 5000, Australia
[c] Adelaide Microscopy, The University of Adelaide, Adelaide, SA 5005, Australia
[d] School of Physical Sciences, University of Tasmania, Hobart, TAS 7001, Australia

ARTICLE INFO

Keywords:
Baryte
Mineral processing
LA-ICP-MS
Olympic Dam
Radionuclides

ABSTRACT

Baryte is a common gangue mineral in many ore systems. Here, we report on a study of baryte chemistry in samples of ore and processing materials (flotation feed, flotation concentrate, flotation tailings, concentrate leach discharge, and tailings leach discharge) from the Olympic Dam Cu-U-Au-Ag deposit, South Australia. Elements that commonly substitute for Ba in the baryte lattice, including Sr and Ca, are measured in variable concentrations reflecting grain-scale zonation and heterogeneity at the scale of the deposit but appear unaffected during processing. Variation in the concentration of some other elements, notably Cu, reflect both the heterogeneous nature of flotation feed and the intimately intergrown character of the sulfide-sulfate assemblage. Measured Pb concentrations in baryte progressively increase during processing from flotation feed to flotation concentrate, and particularly in concentrate leach discharge. Such data suggest that, during sulfuric acid leaching, baryte contained within the concentrate is able to incorporate quantities of Pb that have been mobilized during break-down of Pb-bearing minerals (notably U-minerals containing radiogenic lead). This takes place via surface adsorption followed by rapid coupled dissolution-replacement driven incorporation throughout the grain. Results suggest that baryte may scavenge non-target elements during processing and contribute to an understanding of mobility, mineralogical location, and evolution in the deportment of radionuclides through the processing cycle.

1. Introduction

Mineralogy, grain size, grain shape, and intergrowth relationships between minerals are the fundamental controllers of sulfide liberation and sulfide concentrate quality in processing plants. Although recovery is optimized for the economic metals, the presence and distribution of non-payable (often process deleterious) elements within an ore (e.g., Lane et al., 2016) needs to be taken into consideration. Identifying and quantifying the physical location and chemical speciation of non-target elements in an ore at the mineral grain scale can be challenging, especially when that ore is heterogeneous, fine-grained, texturally complex, and mineralogically diverse.

Models of element deportment and distributions can be calculated from a combination of assays and measurements of mineral abundances via automated mineralogical data collection. For this method to be entirely accurate, a comprehensive understanding of mineral chemistry is needed. Targeted detailed geochemical analysis of mineral grains, including quantification of the concentrations of trace elements in common minerals, can underpin the chemical budget for elements of interest and facilitate in-depth understanding of the relative contributions made by each mineral. A knowledge of mineral chemistry in ore or flotation feed is important, as is understanding how distributions of a given element or isotope might change during processing.

The processing facilities at Olympic Dam, South Australia (Ehrig et al., 2012), produces copper cathode, uranium oxide concentrate, and gold and silver bullion from a complex, fine-grained ore that contains anomalous concentrations of several non-target elements, including the products of natural U decay. In this study we targeted the mineral baryte because it is a relatively abundant gangue phase in the deposit and is known to incorporate non-target elements such as Pb (e.g., Takano and Watanuki, 1974) as well as actively scavenge elements, including radium (Ra), Pb, and other products of U decay (e.g., Courtin-

* Corresponding author.
E-mail address: danielle.schmandt@adelaide.edu.au (D.S. Schmandt).

https://doi.org/10.1016/j.mineng.2019.02.034
Received 21 August 2018; Received in revised form 10 December 2018; Accepted 18 February 2019
0892-6875/ © 2019 Elsevier Ltd. All rights reserved.

Nomade et al., 2008; Curti et al., 2010). Using laser ablation inductively coupled plasma mass spectrometry (LA-ICP-MS), we have obtained comprehensive compositional data for baryte within ores and at several stages of the Olympic Dam processing circuit to assess the natural variability and sulfuric acid leach modification of baryte chemistry from ore through sulfide flotation to concentrate and tailings leach discharge.

2. Background

2.1. Baryte mineralogy

Baryte [$BaSO_4$] is common mineral that forms in a variety of geologic settings. Although its primary use is as an industrial mineral in oil and gas drilling mud (Johnson et al., 2017), it is a frequent gangue mineral in many hydrothermal ore deposits and can often be an important indicator mineral in ore deposit exploration. Baryte is relatively soft, has a high density, and is essentially insoluble in oxidizing environments.

The Ba^{2+} ion is relatively large (1.35 Å) and ions of similar size, notably Pb^{2+} (1.19 Å) and Sr^{2+} (1.18 Å), commonly substitute for Ba^{2+} in the baryte structure. Baryte forms complete solid solutions with the Pb- and Sr-bearing end-members, anglesite [$PbSO_4$] and celestine [$SrSO_4$]. The slightly smaller Ca^{2+} (1.00 Å) can also substitute for Ba^{2+} in baryte (Johnson et al., 2017).

The chemical similarity of Ra^{2+} (1.48 Å) and Ba^{2+} also facilitates the substitution of Ra into baryte, which forms a solid solution to *radiobaryte* [(Ba,Ra)SO_4]. Baryte has been shown to retain *in-situ* Ra decay products, which results in stable Pb, providing a useful dating tool in geologic environments (Uchida et al., 2015; Ditchburn and de Ronde, 2017). This relationship, and the low reactivity of baryte, makes it a valuable implement in environmental remediation and thus many studies have explored mechanisms of Ra uptake and retention into baryte (e.g., Wang et al., 1993; Curti et al., 2010; Rosenberg et al., 2011a,b, 2013, 2014, 2018; Vinograd et al., 2013; Klinkenberg et al., 2014; Brandt et al., 2015; Weber et al., 2016, 2017; Curti et al., 2019; Heberling et al., 2018; Vinograd et al., 2018a,b). Heberling et al. (2018) provided an overview of experimental research, starting in 1925, which has addressed *radiobaryte*. Many of these studies focused on long-term (multiple years) experiments on the recrystallization of baryte grains in the presence of ^{226}Ra in solution which resulted in Ra-enriched baryte.

Factors impacting Ra incorporation into baryte includes effective surface area (grain-size and particle morphology) and mineral porosity (Klinkenberg et al., 2014; Brandt et al., 2015; Weber et al., 2016, 2017; Heberling et al., 2018). These experiments have shown that the recrystallization rates of baryte increase with decreasing pH (Rosenberg et al., 2014; Torapava et al., 2014; Ruiz-Agudo et al., 2015; Heberling et al., 2018), thus also increase the incorporation of available Ra, and likely radiogenic Pb, under acidic conditions. Although there are fewer studies on the direct uptake of Pb in baryte, similar processes likely control the incorporation of Pb into baryte (Takano and Watanuki, 1974; Rashed, 2001; Courtin-Nomade et al., 2008). Higher amounts of Ra within the baryte would also result in elevated Pb, produced *in-situ*. In an ore body or processing slurry, important factors enabling baryte to gain Pb or Ra include availably of elements, permeability, and accessibility of those elements to the baryte surface.

Although the direct presence of Ra in baryte is difficult to measure with traditional techniques, it has been demonstrated from synthetic experiments (Weber et al., 2017) and, now, the *in-situ* visualization of ^{226}Ra and its Pb decay product, ^{210}Pb, in baryte has only recently been achieved (Rollog et al., 2018, 2019). The direct characterization of radionuclides (RN) in natural materials has great implications for understanding the distribution and mobility of RN between ^{226}Ra and ^{206}Pb in the ^{238}U decay chain from different geologic settings, as well as during mineral processing. Importantly, these studies have shown the potentially significant role played by baryte as a RN scavenger whenever this mineral is present. Understanding the physical/chemical distributions and mobility pathways of these RN is critical for efforts to reduce or eliminate them during processing (Cook et al., 2018).

2.2. Baryte at Olympic Dam

Baryte is an abundant gangue mineral throughout the Olympic Dam Cu-U-Au-Ag deposit, occurring within the breccia matrix and clasts within the breccia. Baryte is intimately intergrown with sulfides, hematite and other minor gangue minerals including fluorapatite, fluorite, and carbonates. Together with siderite and fluorite, baryte distribution defines a deposit-scale zonation in which baryte is most prominent in the shallower and central parts of the deposit and siderite is more abundant at depth and at the periphery of the deposit; fluorite reaches greatest abundance between the two (Ehrig et al., 2012). The average abundance of baryte in Olympic Dam ore is ~1.2 wt%, based on a 10,000 MLA sample dataset (Ehrig et al., 2012) and range from fine-grained (< 20 μm) to several mm in size.

Post-ore fluorite-baryte-(carbonate) veins containing coarse-grained (mm- to cm- sized) euhedral baryte cross-cut the mineralized breccia. Although these veins mostly comprise an assemblage of baryte + fluorite, they may be carbonate-dominant and can also contain Cu-(Fe)-sulfides and U-minerals (Apukhtina, 2016). Such veins have been dated as ~500 Ma (Sm-Nd on fluorite and accompanying carbonate; Maas et al., 2011), and hence emplaced ~1000 Ma years after the main deposit formation. Baryte from these late veins makes up an extremely minor proportion of total deposit volume.

2.3. Ore processing

The BHP Olympic Dam processing facility consists of several circuits because of the complex multi-commodity mineralogy of the deposit; i.e. grinding/milling, sulfide flotation concentrator, sulfuric acid leaching, solvent extraction (SX), smelter, electro-refining (ER) and electro-winning (EW), and a precious metals refinery, all of which are fully integrated (Fig. 1). Final-products are ER and EW copper cathode, uranium ore concentrate, and gold and silver bullion. The sulfide concentrator separates copper sulfides from the gangue minerals (e.g. hematite, quartz, sericite, fluorite, baryte, siderite, U-minerals, etc.) creating a chalcocite, bornite, chalcopyrite, pyrite, Au-Ag concentrate, and U-bearing tailings. The Cu-concentrate is leached with sulfuric acid to further reduce the fluorine and uranium content as well as slightly upgrade % Cu via the partial leaching of hematite.

Concentrate leach discharge containing ~41% chalcopyrite, ~27% bornite, ~8% covellite, and ~4% chalcocite (roughly 80% copper minerals) is then smelted to produce a Cu-anode, which is then refined in the ER circuit to produce ER Cu-cathode. ER refinery slimes are processed in the precious metals refinery yielding Au and Ag bullion. The U-bearing flotation tailings are processed via a sulfuric acid tailings leach circuit to extract U and recover any remaining Cu. Copper and U in the tailings leach liquors are separated via solvent extraction. Cu is then recovered via the EW circuit, and U via calcination.

Uranium mineralogy at Olympic Dam is complex (Macmillan et al., 2016, 2017). The three primary U-minerals, uraninite, coffinite, and brannerite, have different leaching responses; uraninite readily dissolves in acidic environments, coffinite dissolves slower than uraninite, and brannerite is the most resistant (Lottering et al., 2008; Bowell et al., 2011; Pownceby and Johnson, 2014).

3. Material and methodology

3.1. Sampled material

Studying minerals from processing material is beneficial since each grain mount contains thousands of particles representative of multiple areas of the orebody being mined at a particular period of time, thus

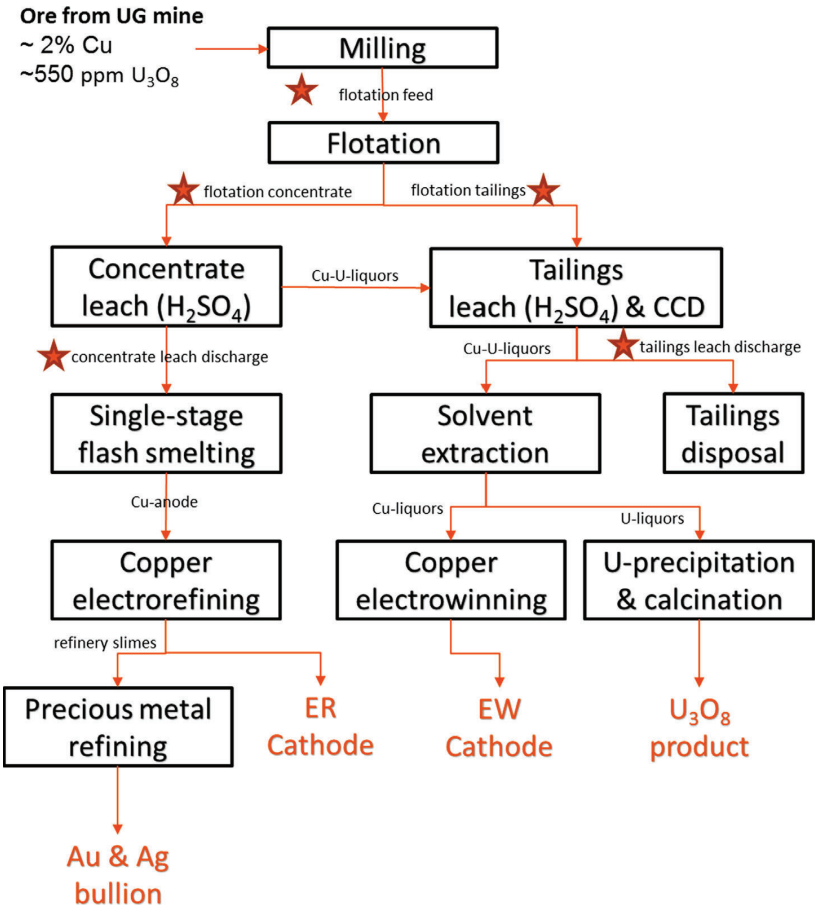


Fig. 1. Olympic Dam processing plant simplified flowsheet. Stars indicate the location of materials sampled in this study.

eliminating any geological bias introduced by analysis of individual drill core or grab samples. Use of samples that are as representative as possible of the whole orebody is particularly valuable at Olympic Dam which is heterogeneous at the scale of hand specimens upwards, and where baryte can be relatively sparse, fine-grained, and disseminated in some parts of the resource. Sample representativity is important for not only a greater understanding of the orebody, but also for evaluation of baryte chemistry throughout the processing cycle.

For comparison to the breccia-hosted baryte sampled as flotation feed, geologically distinct samples from structurally late, cross-cutting baryte-bearing veins were included in the study. The objective was to identify whether these are compositionally distinct.

3.1.1. Processing samples

Samples used for this study are from plant monthly composite samples (from a single month) of flotation feed and the resultant flotation concentrate, flotation tailings, concentrate leach discharge, and tailings leach discharge materials. Representative examples of baryte grains from these materials are shown in Fig. 2. In the processing stream studied, baryte comprises ~1.2 wt% of the flotation feed. The majority of this baryte is only ~7–20 μm in size which is too small for analysis; baryte grains analyzed were mostly 20–60 μm in size. Of these larger baryte grains, ~30% were liberated grains in the flotation feed.

The primary grind and concentrate regrind sizes are 80% passing −75 μm and −30 μm, respectively. Each processing material sample is sized using two methods. The larger size fractions (> 75 μm and 53–75 μm) are wet screened, which separates on size and, to an extent, shape. The sub-53 μm fractions are separated using elutriation with a cyclosizer, which separates on size, shape, and density. Because baryte is mostly of a small grain size as well as dense, baryte is typically most abundant in the first split from the cyclosizer (grain sizes 26–53 μm, baryte concentrated here namely due to its density) and the smallest size fractions (grain sizes < 9 μm). The different size fractions from each material were mounted into 25-mm grain blocks to determine the modal mineralogy, mineral associations, liberation, and trace element composition of baryte. However, because accurate trace element analysis of minerals by laser ablation inductively coupled mass spectrometry is dependent upon ablation of a relatively large sample volume, only the largest baryte grains, in the > 75 μm, 53–75 μm, and 26–53 μm size fractions, could be analyzed.

3.1.2. Rock samples

Nine samples prepared as polished blocks were analyzed for this study. One sample (BAR 2) is from a drillcore in a ~1 cm-wide vein cross-cutting hematite-quartz-breccia. The other eight samples are from veins and vugs with coarse baryte from grab samples collected at underground mining faces.

3.2. Methodology

All microanalytical work was undertaken at Adelaide Microscopy, The University of Adelaide. Polished blocks were initially examined and

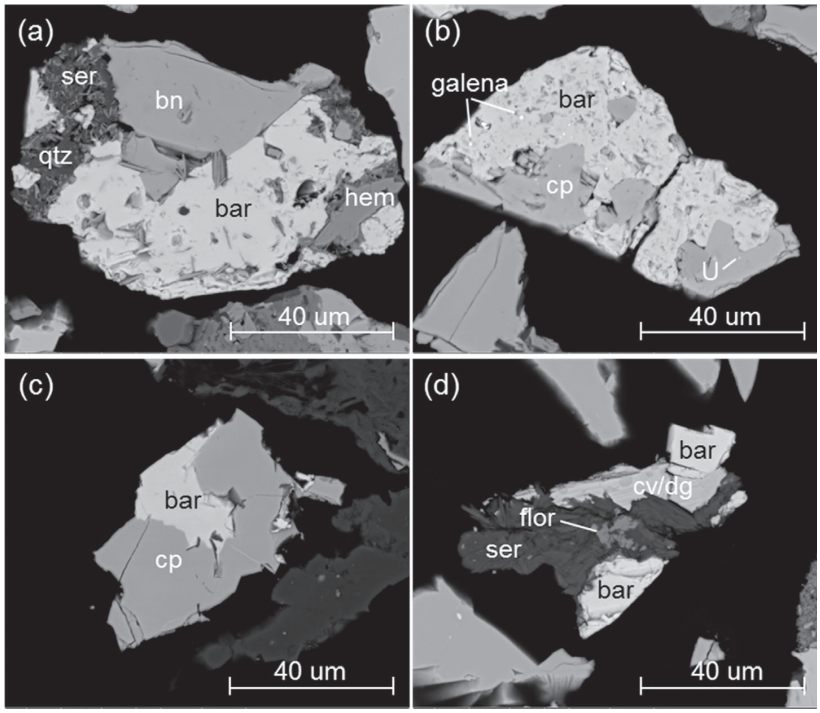


Fig. 2. BSE images of grains, size fraction 53–75 μm, showing baryte and associated minerals. (a) Composite particle of primarily bornite (bn), baryte (bar), hematite (hem), sericite (ser) and quartz (qtz) (flotation concentrate) (b) Composite particle of baryte and chalcopyrite (cp) (flotation concentrate). Coarse- and fine-grained inclusions of both U-minerals and galena are observed; galena is mostly in baryte but U-minerals exclusively in chalcopyrite in this example. (c) Chalcopyrite associated with 'clean' baryte (concentrate leach discharge). (d) Composite particle with baryte, chalcopyrite, sericite, florencite (flor) and covellite/digenite (cv/dg) (concentrate leach discharge).

imaged using a reflected light optical microscope and using a FEI Quanta 450 Field Emission Gun (FEG) scanning electron microscope (SEM) equipped with a silicon-drift detector, back-scatter electron (BSE) detector, and energy-dispersive X-ray (EDAX) spectrometer.

3.2.1. Mineral liberation analysis

Mineral Liberation Analyser (MLA; Gu, 2003) data was used to describe the overall abundance and association of baryte and associated minerals within each sample. MLA generates quantitative mineralogy and mineral relationship frequency data and is thus well suited to characterization of heterogenous mineral particles. Full MLA analysis was carried out on identical sample material by ALS Brisbane. The MLA dataset used for this analysis consists of a single grain mount for each size fraction from each of the five processing steps, making a total of 35 mounted samples.

3.2.2. Laser ablation inductively coupled mass spectrometry

Trace element and isotopic analyses were performed by Laser Ablation Inductively Coupled Mass Spectrometry (LA-ICP-MS) using an ASI RESOlution-LR ArF excimer laser ablation system equipped with a large format S155 sample chamber (Laurin Technic Inc.) and coupled to an Agilent 7900x ICP-MS. Operating conditions were set at a repetition rate of 5 Hz and a fluence of 3.5 J/cm^2 for baryte and the reference standards GSD-1G and NIST-610 glasses.

Analysis of baryte included 28 s of gas background measurement following 5 pulses of pre-ablation cleaning. Ablation time was 30 s followed by a 2 s delay giving a total of 60 s acquisition time. Isotopes measured were ^{23}Na, ^{27}Al, ^{29}Si, ^{31}P, ^{43}Ca, ^{57}Fe, ^{65}Cu, ^{85}Rb, ^{88}Sr, ^{89}Y, ^{133}Cs, ^{137}Ba, ^{139}La, ^{140}Ce, ^{141}Pr, ^{143}Nd, ^{146}Nd, ^{147}Sm, ^{151}Eu, ^{153}Eu, ^{157}Gd, ^{159}Tb, ^{163}Dy, ^{165}Ho, ^{166}Er, ^{169}Tm, ^{172}Yb, ^{175}Lu, ^{182}W, ^{202}Hg, ^{204}Pb, ^{206}Pb, ^{207}Pb, ^{208}Pb, ^{209}Bi, ^{226}Ra, ^{232}Th, and ^{238}U. Dwell times were 0.005 s for ^{23}Na, ^{27}Al, ^{29}Si, and ^{31}P, 0.02 s for ^{206}Pb, ^{207}Pb, and ^{238}U, 0.03 s for ^{232}Th, ^{209}Bi, and ^{226}Ra, and 0.01 s for all others, giving a total sweep time of 0.517 s. Quantification used Ba as the internal standard element assuming stoichiometric values. Data reduction was performed using the software Iolite v3.4 (Paton et al., 2011) and processed using the "Trace_Elements" data reduction scheme. Analytical parameters are described in Appendix A.

Spot size varied depending on the material available and size of the target zone; spot sizes on grains were generally small (9–29 μm) whereas spot size for coarser baryte in rock samples were as large as 43 μm. Data variability due to spot size was tested with different spot sizes on a large baryte grain from a vein baryte sample. Major elements of interest (e.g., Sr, Ca, and La), appeared unaffected while elements with low concentration were, as expected, more frequently below minimum detection limits at smaller spot sizes. Mass interference on concentrations of REE from Ba-bearing and other molecular species is documented (Deconinck et al., 2006; Oostingh, 2011) and thus quantification based on measured masses where interference is likely should be treated with caution. Interfering species (e.g., ^{137}Ba^{16}O = ^{153}Eu) were readily identified and other elements with very low concentrations displayed a limit of quantification that could be applied to the dataset, e.g., doubly-charged ^{130}Ba^{++} caused interference with low levels of Cu (Cu analysis uses ^{65}Cu), but concentrations above 60 ppm were considered reliable. Many elements are consistently less than detection limit irrespective of spot size.

4. Results

4.1. Baryte appearance, morphology, and association

4.1.1. Processing materials

Baryte contained within composite particles from the processing materials display a wide range of textural types (Fig. 2). Baryte can occur as fully liberated grains, or is hosted in complex composite particles with one or more other minerals, often showing intimately intergrown textures (Fig. 2). Baryte may be 'clean' (i.e., without visible inclusions), but commonly contains abundant inclusions of many different minerals including hematite, sericite, galena, U-minerals, and Cu-(Fe)-sulfides. Grains with abundant inclusions were not analyzed for

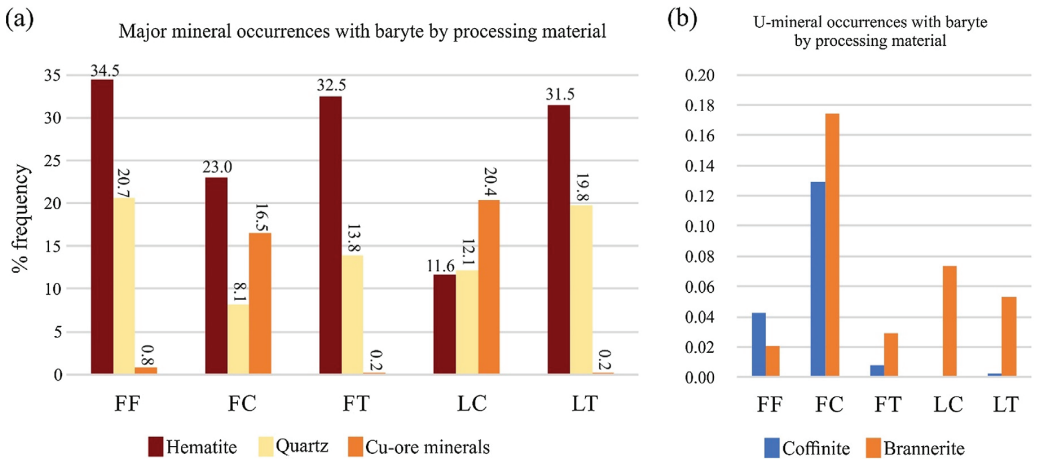


Fig. 3. Clustered column charts of MLA data to display the frequency of baryte occurrences with other minerals in particles from the different processing samples (flotation feed – FF, flotation concentrate – FC, flotation tailings – FT, concentrate leach discharge – LC and tailings leach discharge – LT). (a) Main minerals occurring with baryte across the different processing materials. Apart from sulfides, baryte is mostly associated with other common gangue minerals in concentrates. (b) Frequency of the occurrence of U-minerals with baryte across the different processing materials. Uraninite is effectively unassociated with baryte (very small and infrequent occurrences). The baryte-brannerite association is most consistent through concentration and leaching.

trace elements in this study to avoid interference from such phases. In the concentrate leach discharge samples investigated here, textures displayed by baryte suggest that it is primary and not newly-formed during sulfate leaching. SEM imaging down to the micron-scale indicates that baryte in concentrate leach discharge shows no observable effects of leaching at grain boundaries or otherwise.

In flotation feed, flotation tailings and tailings leach discharge, baryte is associated with gangue minerals, chiefly hematite (~30–35% frequency) or quartz (~15–20% frequency) and only rarely with Cu-(Fe)-sulfides (< 1% frequency, Fig. 3a). In flotation concentrate and concentrate leach discharge, the association of baryte with Cu-(Fe)-sulfides greatly increases because of the increased sulfide concentration (Fig. 3). The occurrence of baryte with Cu-(Fe)-sulfides increases from ~17% to 20% frequency from the concentrate to concentrate leach discharge (Fig. 3a). The occurrence of baryte with U-minerals is greatest in the concentrate, and in the leach products the U-minerals are almost exclusively brannerite as the other U-minerals have dissolved (Fig. 3b). We note that baryte occurs much more often with brannerite than with coffinite, and only very rarely with uraninite in any of the streams (Fig. 3b).

4.1.2. Vein baryte

The late-stage veins and vugs are almost completely comprised of baryte or baryte with fluorite, with very minor carbonate or other minerals present. Baryte in these veins range in color from colorless to white to red, co-existing fluorite can be white, purple, or green. Scarce inclusions in both baryte and fluorite are mostly hematite and carbonate, and less commonly Cu-(Fe)-sulfides: chalcopyrite, bornite, and chalcocite. Where baryte and fluorite occur together in the vein samples, the veins appear multi-stage with baryte preceding the fluorite. Baryte occurs as massive or as well-formed prisms, suggestive of open space growth, with fluorite filling in around the elongated crystals that often have corroded edges into the baryte (Fig. 4).

Baryte sometimes shows elemental zoning that can be oscillatory or irregular/patchy. There is also occasionally a 'leached' edge that follows the grain boundaries and/or fractures into the baryte overprinting the zoned crystals (Fig. 4b).

4.2. Baryte chemistry

Minor and trace element data for baryte is reported in Table 1 and shown graphically in Fig. 5.

Flotation feed baryte is characterized by concentrations of Sr that vary over three orders of magnitude from some tens of ppm up to > 2 wt%, with a mean of 3750 ppm. Calcium (mean 1835 ppm) and Fe (mean 760 ppm) are the other two most abundant minor components. Concentrations of REE are also quite variable but on average are generally low (mean ΣREE ~4 ppm) with essentially no HREE in any sample. Although U concentrations as high as 172 ppm were measured in individual spots, these likely relate to inclusions (Fig. 5a); mean U is 1.0 ppm. Lead concentrations range from below minimum detection limits to 138 ppm (mean 6.2 ppm). The only other elements present at concentrations of more than a couple of ppm are Na, Al, Si, and Cu. The latter is almost certainly present as inclusions of Cu-(Fe)-sulfides, given outliers as high as 8100 ppm, but with a mean of only ~100 ppm (Fig. 5b).

Baryte from flotation concentrates and tailings have concentrations of most minor and trace elements (e.g., Sr, Ca, REE) broadly within the same ranges as those in flotation feed, as would be expected. Flotation concentrate baryte does, however, display slightly elevated Pb values (mean 36 ppm, range from less than the minimum limit of detection, LOD, to 2991 ppm) compared to flotation feed and flotation tailings (Fig. 5c, e). Flotation concentrate baryte also contains greater Cu (mean 819 ppm) compared to the flotation tailings and flotation feed, possibly consistent with a greater proportion of intergrown sulfide-sulfate particles (Fig. 5d, f).

Further modification of some trace element distributions is observable by comparison of post-leached products compared to pre-leached products (Fig. 5c–f). The most noticeable variation is with respect to Pb. In concentrate leach discharge, Pb concentrations in baryte are, on average, two orders of magnitude higher (242 ppm, with individual points up to almost 9000 ppm). Interestingly, baryte in tailings leach discharge contains more Pb (mean 14 ppm) than in flotation feed (mean 6 ppm), and the flotation tailings (mean 7 ppm) (Fig. 5e). Mean U concentrations in concentrate leach discharge are only 4.5 ppm, albeit still higher than in leach tailings (0.7 ppm). Concentrations of Cu and Fe plot also display an overall increase from flotation concentrate to concentrate leach discharge (Fig. 5d) and a marked difference between concentrate leach and tailings leach discharge (Fig. 5d, f). Other elements are mostly within similar ranges as in flotation feed and flotation concentrate, although there is a slight increase in ΣREE (mean ΣREE ~74 ppm) in concentrate leach discharge. Radium was measured but

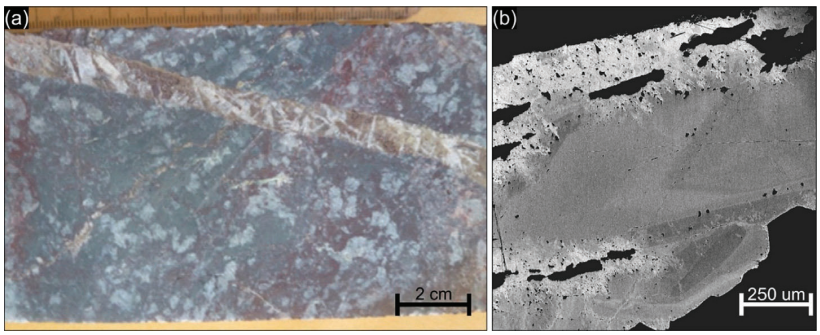


Fig. 4. Examples of late-stage vein baryte. (a) Photograph of a drill core sample showing ~1 cm-wide baryte vein (white prismatic grains) cross-cutting Cu-barren hematite-quartz breccia. (b) BSE image of baryte (grey-white) laths in late-stage vein. Fluorite enclosed baryte and also occurs as inclusions (black). Prismatic baryte displays darker and brighter oscillatory zones that are compositionally controlled by amount of Sr and Ca (zones with greater Sr and Ca are darker). The lightest areas along the edges of the crystals contain more abundant inclusions, cross-cut the oscillatory zoning, and likely formed from elemental leaching during subsequent mineralization within the vein (i.e., fluorite). Fluorite (black) surrounds the baryte and also occurs as inclusions.

no counts were recorded.

In comparison, vein barytes are depleted in most trace elements compared to ore baryte in the flotation feed (Table 1; Fig. 5a, b). They do, however, display both higher average concentrations and greater variation with respect to Sr and Ca, consistent with the grain-scale zoning illustrated above (Fig. 4b). The only other trace elements above (at most) a couple of ppm are Na, Si, and Al. Concentrations of Pb and ΣREE are both ~1 ppm.

The vein baryte shows clear stages of growth zonation as shown by variations in mineral chemistry across the grain. This zonation is mostly expressed by Sr and Ca, however, some other elements also appear to be heterogeneously distributed. Among these, Pb is generally elevated in the darkest zones and progressively more depleted in the brighter zones, whereas LREE are elevated in the brighter zones (Table 2). The majority of baryte identified in the veins do not display such strong zonation as shown in Fig. 4b, although usually with some compositional variations indicated.

5. Discussion

The wide chemical variability in flotation feed baryte reflects the characteristic heterogeneity of the Olympic Dam orebody (Ehrig et al., 2012), a feature documented for many other constituent minerals, e.g., Cu-(Fe)-sulfides (Ciobanu et al., 2017), or hematite (Verdugo-Ihl et al., 2017). Moreover, flotation feed baryte can contain a range of sub-micron- to micron-scale mineral inclusions, including Cu-(Fe)-sulfides, Fe-oxides, and U-minerals, that likely precipitated together with baryte. Late vein baryte is, in contrast, appreciably compositionally purer and contains fewer and lower concentrations of Cu, Fe, U, and Pb.

Lead concentrations in baryte from different stages of processing are distinct (Fig. 5) and display a notable "upgrading" beyond the compositional range of flotation feed baryte. This implies that primary baryte grains are preferentially scavenging Pb that has been liberated via dissolution of Pb- and/or Pb-bearing minerals (e.g., uraninite) during processing. This may be happening throughout processing but is particularly accentuated during sulfate leaching.

Concentrations of Ra could not be determined by the LA-ICP-MS method due to the extremely low concentrations and lack of a suitable standard. However, the geochemical similarities between Ra and Pb strongly suggest that they, and intermediate RN, are also spatially co-located. This is corroborated by the nanoSIMS isotope maps in Fig. 6, which show overlapping concentrations of RN within a baryte grain from concentrate leach discharge.

Sorption (Wang et al., 1993; Jones et al., 2011) or surface kinetics (Watson, 2004; DePaolo, 2011; Brandt et al., 2015) may play a role in the initial association of liberated ions (such as Pb^{2+} and Ra^{2+}) with exposed baryte surfaces in the processing slurries. Lead (and also Ra) is, however, likely retained within the baryte crystals via *in-situ* re-crystallization achieved by coupled dissolution-reprecipitation reaction (CDRR; e.g., Putnis and Ruiz-Agudo, 2013; Ruiz-Agudo et al., 2014), a process that results in incorporation of elements into the crystal, or their redistribution at the grain-scale (Curti, 1997; Grandia et al., 2008; Bosbach et al., 2010; Curti et al., 2010; Rosenberg et al., 2011a,b; Prieto et al., 2013; Weber et al., 2017). CDRR is an extraordinarily efficient mechanism, in which complete mineral replacement can occur within only a few hours (e.g., Putnis et al., 2005), no longer than the time-frame of a mineral passing through processing.

Significant solid-state diffusion (typically a water-free and slow reaction) is not expected to occur for baryte under relatively low temperature plant leach conditions of ~60–70 °C (Bosbach et al., 2010; Heberling et al., 2018).

Substantial incorporation of Ra into baryte crystals has been modeled to take tens to hundreds of days, and multiple years to reach equilibrium under ambient conditions (Bosbach et al., 2010; Vinograd et al., 2013; Brandt et al., 2015; Heberling et al., 2018). Since the processing conditions, especially leaching, are not ambient, it is reasonable to assume that this process of element incorporation into baryte could be accelerated within the 8–12-h leach time in the plant. Also, Ra, and presumably Pb, incorporation rate into baryte is shown to increase with decreasing pH (Rosenberg et al., 2014; Torapava et al., 2014; Ruiz-Agudo et al., 2015; Heberling et al., 2018), consistent with plant leaching at a pH of ~1–1.5.

Some limitations of the present study include the issue of grain size. It would be expected that smaller grains, with larger effective surface areas, react faster, and thus may experience greater chemical alteration, during processing. These could not, however, be directly analyzed by LA-ICP-MS. Data from Brandt et al. (2015), who tested Ra uptake efficiency between two different baryte grain sizes over ~3 years, show that smaller grains are more efficient at incorporating Ra initially than larger grains, especially with lower concentrations of Ra in solution. The larger grains are, however, able to include more Ra with extended time as the grain approached equilibrium with the Ra in solution. Since resident time of grains in processing slurries are short and with low concentration of Ra in solution, the initial trends of Brandt et al. (2015) study are most applicable to conditions during acidic leaching at Olympic Dam, and therefore the smaller grains could be predicted to contain more Ra and Pb. The study of Klinkenberg et al. (2014) also showed greater changes in their measured Ra concentration in small baryte grains compared to large baryte grains after prolonged exposure to Ra in solution.

Furthermore, the LA-ICP-MS analyses reported here were generally made in the center of each baryte grain to avoid interference from associated minerals, and thus may not have captured the chemistry of any thin alteration rims. Many of the studies on Ra incorporation into baryte argue against the mechanism being a "surface feature", however these studies are generally at ambient conditions, aimed at achieving crystal equilibrium, and do not consider Pb and other RN (e.g., Klinkenberg et al., 2014; Heberling et al., 2018), thus they do not allow for direct comparison with mineral processing conditions.

Research by Weber et al. (2016, 2017) showed that nano- and

Table 1
Mean, minimum, and maximum trace element concentrations in baryte from processing samples and late baryte veins from LA-ICP-MS analysis (ppm).

	Flotation feed (n = 58)			Flotation concentrate (n = 34)			Flotation tailings (n = 149)			Concentrate leach discharge (n = 38)			Tailings leach discharge (n = 77)			Vein (n = 344)		
	AVG	MIN	MAX	AVG	MIN	MAX	AVG	MIN	MAX	AVG	MIN	MAX	AVG	MIN	MAX	AVG	MIN	MAX
Sr	3752	58	20,360	7419	550	36,500	3419	25	20,860	4958	29	22,260	3216	155	22,060	12,514	78.8	58,900
Ca	1835	< LOD	8700	3310	< LOD	12,200	1799	< LOD	8900	1977	< LOD	8680	1551	< LOD	9570	6054	90.0	27,900
Fe	760	< LOD	9800	1925	< LOD	6500	572	< LOD	9900	2929	< LOD	9900	680	< LOD	8700	269	< LOD	9800
Pb	6.2	< LOD	138	36	< LOD	2991	7.3	< LOD	159	242	7.8	8889	14	< LOD	270	1.14	< LOD	607
U	1.0	< LOD	172	3.1	< LOD	1290	1.2	< LOD	300	4.5	< LOD	300	0.7	< LOD	176	0.01	< LOD	6.6
Th	0.03	< LOD	24	0.2	< LOD	4.0	0.03	< LOD	54	0.3	< LOD	5.0	0.12	< LOD	4.2	0.004	< LOD	2.1
La	1.6	< LOD	750	6.5	< LOD	400	1.6	< LOD	2340	33	0.40	2270	4.5	< LOD	700	0.6	0.3	90
Ce	1.4	< LOD	910	7.6	< LOD	500	1.5	< LOD	2750	33	< LOD	3910	5.2	< LOD	950	0.05	< LOD	116
Pr	0.1	< LOD	71	0.4	< LOD	27	0.1	< LOD	180	2.3	< LOD	329	0.4	< LOD	93	0.003	< LOD	10
Nd	0.4	< LOD	187	1.7	< LOD	46	0.3	< LOD	377	5.0	< LOD	930	0.9	< LOD	300	0.02	< LOD	28
Sm	0.1	< LOD	19	0.2	< LOD	5.6	0.1	< LOD	19	0.5	< LOD	133	0.2	< LOD	33	0.2	< LOD	3.4
Gd	0.2	< LOD	11	0.2	< LOD	2.9	0.3	< LOD	7.6	0.5	< LOD	40	0.2	< LOD	20	0.34	< LOD	1.6
ΣREE	3.9	< LOD	1948	16.5	< LOD	981	3.8	< LOD	5673	73.7	0.4	7612	11.4	< LOD	2095	1.2	0.3	249
Na	24	< LOD	322	35	< LOD	125	35	< LOD	940	33	< LOD	186	23	< LOD	370	91	< LOD	8300
Al	80	< LOD	4530	241	< LOD	2600	80	< LOD	5800	344	< LOD	4710	123	< LOD	9000	6.8	< LOD	2780
Si	456	< LOD	4800	822	< LOD	4900	753	< LOD	9900	1485	< LOD	8500	740	< LOD	9800	142	< LOD	4500
Cu	99	< LOD	8100	819	< LOD	7700	88	< LOD	1430	2596	< LOD	9900	78	< LOD	1720	< LOD	< LOD	84
Rb	0.3	< LOD	4.8	0.8	< LOD	8.7	0.5	< LOD	11	0.9	< LOD	8.9	0.5	< LOD	13.7	< LOD	< LOD	7.4
W	0.2	< LOD	17	0.9	< LOD	53	0.2	< LOD	15	1.4	< LOD	17	0.5	< LOD	20.7	0.3	< LOD	17
Bi	0.03	< LOD	2.5	2.7	< LOD	147	0.1	< LOD	1.3	4.1	< LOD	42	0.1	< LOD	14.0	0.01	< LOD	5.5

< LOD: less than the limit of detection.
Average value is filtered mean with 20% deviation from the mean excluded and calculated with LOD/2 when value reported was < LOD due to pervasive < LOD counts.
Elements P, Cs, Tb, Dy, Ho, Er, Tm, Yb, and Lu excluded from table due to pervasive < LOD counts.
Y and Eu excluded due to interferences.
ΣREE includes only measured values for La, Ce, Pr, Nd, Sm and Gd, without values < LOD.

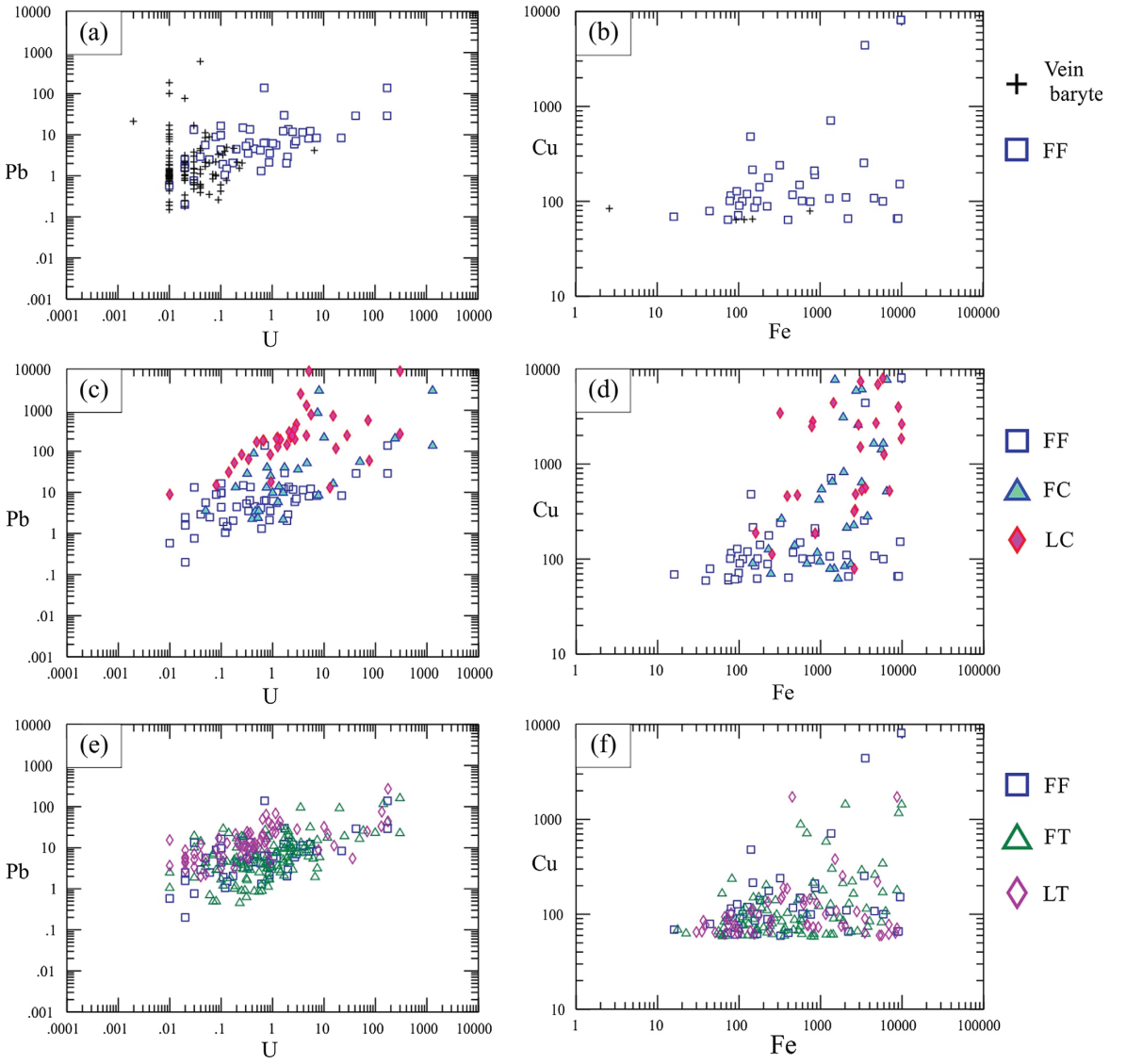


Fig. 5. Plots comparing trace element concentrations in different types of baryte (LA-ICP-MS data, concentrations in ppm). (a) Pb vs. U and (b) Cu vs. Fe comparing flotation feed (FF) and late-stage baryte veins, (c) Pb vs. U and (d) Cu vs. Fe comparing flotation feed and concentrated products (FC and LC), (e) Pb vs. U and (f) Cu vs. Fe comparing flotation feed and tailings products (FT and LT). Plots of Pb vs. U show progressive enrichment in Pb through processing and in concentrated material. The Cu vs. Fe plots show distinct separation in the concentrate and tailings fractions. LC and LT display a clear relative elevation in Pb compared to FC and FT, respectively.

micro-porosity in baryte provides larger surface areas for Ra incorporation than just at the outer grain surface, and is a critical factor in the ability of a baryte grain to incorporate trace elements. Weber et al. (2017) also showed that at the stage of Ra 'entering' the baryte, there is an initial concentration of Ra in the baryte around the pore edges, suggesting that the degree of porosity in a grain is integral to the amount of element-uptake possible. Permeability, permitted via interconnected pores or fractures would also be important, especially in the relatively rapid environment of minerals processing. Similarly, the dissolution-reprecipitation process has been shown to generate porosity within the host mineral thereby enhancing its rate of alteration (e.g., Putnis et al., 2005; Ruiz-Agudo et al., 2014).

Fig. 6 demonstrates the incorporation of RN within a baryte grain during acid leaching. In the grain imaged, the internal fractures provide permeability within the grain. There are also "hot spots" of RN which likely indicate the presence of pores. The grain boundaries also appear elevated in RN which would have had direct exposure to the leach solution. Unfortunately, the visualized degree of enrichment is not quantifiable and may be exacerbated due to an effect from the irregular surfaces at these regions, as evidenced in the ^{138}Ba image. Regardless, the RN are clearly incorporating into baryte along exposed surfaces at outer edges, permeable internal fractures, and likely internal pores. In contrast, U shows no association with baryte.

Given the particularly marked increase of Pb in baryte in leached concentrates, we suggest that the RN and Pb are gained by baryte during processing and do not reflect a geological feature. The source of RN and Pb is likely from the dissolution of U-minerals, such as uraninite, coffinite, and (to a limited extent) also brannerite. Uraninite in

Table 2
LA-ICP-MS data (mean, minimum, and maximum values, in ppm) for zoned baryte in late vein samples (Fig. 4b).

	Crystalline, dark osc. zones (n = 74)			Crystalline, light osc. zones (n = 70)			Leached, lightest edges (n = 76)		
	AVG	MIN	MAX	AVG	MIN	MAX	AVG	MIN	MAX
Sr	46,649	41,000	65,220	33,525	21,100	40,930	7145	3140	12,600
Ca	22,309	19,250	30,970	15,954	10,260	20,900	3504	1670	6170
Fe	12.6	< LOD	9100	45.7	< LOD	28,600	746	21.2	5400
Pb	1.35	0.40	6.69	0.93	0.48	7.55	0.40	0.15	0.73
U	0.002	< LOD	0.12	0.002	< LOD	0.07	0.02	< LOD	0.10
Th	0.002	< LOD	0.04	0.002	< LOD	0.04	0.002	< LOD	0.01
La	0.66	0.39	3.1	0.56	0.38	1.65	1.91	0.98	2.97
Ce	0.09	0.01	2.9	0.05	< LOD	0.89	0.97	0.25	2.22
Pr	0.003	< LOD	0.15	0.002	< LOD	0.12	0.03	< LOD	0.09
Nd	0.01	< LOD	0.44	0.01	< LOD	0.30	0.03	< LOD	0.05
Sm	0.18	0.09	0.29	0.17	0.10	0.26	0.15	0.09	0.20
Gd	0.31	0.20	0.39	0.33	0.19	0.59	0.30	0.23	0.36
ΣREE	1.25	0.86	7.53	1.13	0.76	4.00	3.39	1.73	5.44
Na	175	< LOD	810	145	< LOD	2780	1174	85.0	3150
Al	0.69	< LOD	90.0	4.04	< LOD	690	523	< LOD	2480
Si	123	78.0	262	134	87.0	1300	944	91.0	3890
P	28.4	23.5	38.5	28.0	19.2	34.9	28.1	25.9	30.1
W	0.02	< LOD	16.6	0.07	< LOD	48.0	0.83	0.07	5.60
Bi	0.01	< LOD	0.04	0.004	< LOD	0.03	0.004	< LOD	0.01

< LOD: less than the limit of detection, osc. = oscillatory.
Average value is filtered mean with 20% deviation from the mean excluded and calculated with LOD/2 when value reported was < LOD due to pervasive < LOD counts.
Elements Rb, Cs, Tb, Dy, Ho, Er, Tm, Yb, Lu, and Cu are excluded from this table due to pervasive < LOD counts.
Y and Eu excluded due to interferences.
ΣREE includes only present LREE measured values, not < LOD.

Olympic Dam can contain as much as ~18 wt% PbO_2 (Macmillan et al., 2016), and break-down would result in the liberation of this Pb as well as other U-decay products, including ^{226}Ra. Additional Pb may derive from other Pb-, or Pb-bearing-minerals, such as Pb-chalcogenides included in Cu-(Fe)-sulfides (Owen et al., 2018).

Liberated Pb from these two sources, break-down of U-(Pb)-minerals vs. break-down of Pb-minerals, such as sulfides, would result in different Pb forms, either dissolved Pb in cationic form in solution or as extremely fine-grained (< 1 μm) Pb-mineral nano- or micro-particles. These two different forms of Pb would associate with baryte in different ways, either incorporating into the baryte (in the case of the cations, via CDRR), or alternatively, by physical attachment by surface kinetics onto baryte surfaces (as may be the case for the Pb-mineral nano- and micro-particles). The retention ability of baryte with Pb shown by this study as well as the RN location evidenced in Fig. 6, suggests that Pb is likely sourced from the break-down of Pb- and RN-bearing minerals, such as uraninite, releasing liberated Pb ions as well as RN that are naturally chemically attracted to baryte, and that any surface adsorption along grain edges, fractures, and pores is followed by CDRR-driven incorporation into the grain.

Baryte is a known efficient scavenger of Ra in environmental settings (e.g., Curti et al., 2010), and nanoSIMS imaging shows that baryte scavenges Ra as well as other decay-chain products such as ^{210}Pb during metals processing (Fig. 6). Moreover, because baryte is retained (i.e.,

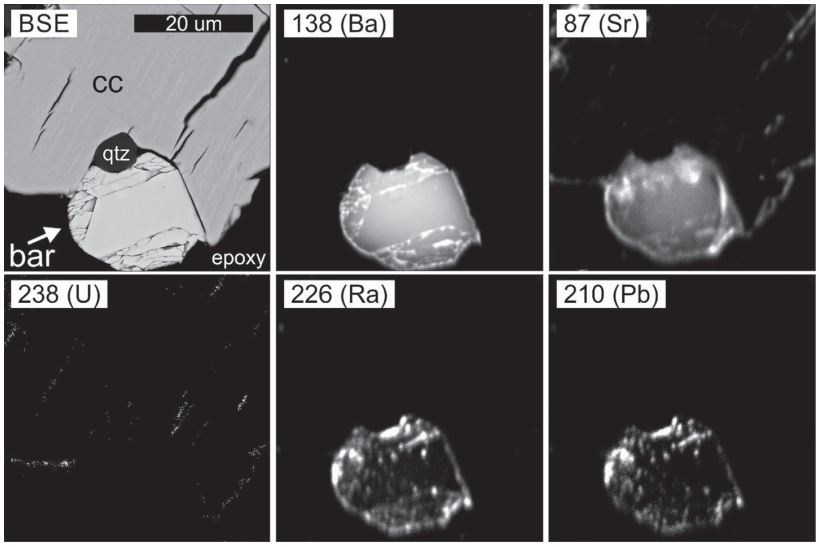


Fig. 6. BSE image and corresponding nanoSIMS isotope maps of composite particle of chalcocite (cc), baryte (bar), and minor quartz (qtz) from concentrate leach discharge. Fractures are present in both minerals. Note elevated counts for ^{226}Ra and ^{210}Pb in baryte, particularly along fine fractures. Baryte does not show ^{238}U counts, which are only present at the margin of the sulfide. The reader is referred to Rollog et al. (2019) for details of nanoSIMS methodology.

not dissolved) during leaching it represents a highly efficient sink for these RN, by not only being able to incorporate these elements within the crystal structure but also naturally retain them through all processing stages.

Variability in the concentrations of specific (but not all elements) in baryte from different processing material provides insights into the reactions undergone by minerals during processing. The many studies on the efficient Ra uptake by baryte (referred to in this section), the visualization of ^{226}Ra and ^{210}Pb in baryte (Fig. 6; Rollog et al., 2018, 2019), and the proven uptake of Pb in baryte during processing from this study are all strongly suggestive that baryte represents a viable sink for liberated RN and Pb and can retain them within the time scale of hydrometallurgical processing. This raises the possibility of using the natural geochemical characteristics of baryte as the basis for methods that could reduce or eliminate RN concentrations during processing. This study may also catalyze investigation of other minerals that display similar geochemistry.

6. Conclusions and implications

(1) Common substituting elements in the baryte lattice, Sr and Ca, are present in variable concentrations. These concentrations are unaffected during processing.
(2) Variation in the concentration of other elements, notably Cu, reflect both the heterogeneous nature of the flotation feed and the intimately intergrown character of the sulfide-sulfate assemblage.
(3) Lead concentrations in baryte significantly increase during sulfuric acid leaching, as compared to pre-leached plant samples (i.e. flotation concentrates and flotation tailings). This is strongly suggestive of Pb being liberated and mobilized from the break-down of Pb-bearing minerals, such as U-minerals or released from grain boundaries, and subsequently incorporated into baryte grains during leaching.
(4) The observed uptake of Pb into baryte is concordant with published experimental studies of element incorporation into baryte crystals and that alongside stable ^{206}Pb (and ^{207}Pb, ^{208}Pb), that liberated ^{226}Ra and ^{210}Pb is also concentrated into baryte.
(5) Results carry critical implications for understanding the mobility, the mineralogical location, and evolution in the deportment of radionuclides through the processing cycle.

Acknowledgements

This research is a contribution of the ARC Research Hub for Australian Copper-Uranium (Grant IH130200033), co-supported by BHP Olympic Dam and the South Australian Mining and Petroleum Services Centre of Excellence. We greatly appreciate the insightful comments from two anonymous reviewers, Assistant Editor Grant R. Ballantyne, and Editor-in-Chief, Barry A. Wills.

Appendix A

Analytical set-up for LA-ICP-MS analysis of baryte

Baryte operating conditions

Unknowns	Spot size (um)	Hz	Fluence (J/cm^2)
Standards (GSD-1G, NIST-610)	9–43 51	5	3.5

Baryte analysis details

Mass	Element	Dwell time (s)	Avg limit of detection (ppm)	
			Grains	Veins
23	Na	0.005	68.7	6.46
27	Al	0.005	6.57	0.55
29	Si	0.005	1325	98.8
31	P	0.005	204	10.5
43	Ca	0.01	1024	59.9
57	Fe	0.01	66.8	7.49
65	Cu	0.01	5.09	0.34
85	Rb	0.01	0.80	0.12
88	Sr	0.01	0.18	1.71
89	Y	0.01	0.04	0.01
133	Cs	0.01	0.32	0.05
137	Ba	0.01	–	–
139	La	0.01	0.04	0.01
140	Ce	0.01	0.03	0.01
141	Pr	0.01	0.11	0.00
143	Nd	0.01	0.17	0.04
146	Nd	0.01	0.16	0.03
147	Sm	0.01	0.21	0.04
151	Eu	0.01	0.22	0.06
153	Eu	0.01	0.26	0.08
157	Gd	0.01	0.57	0.12
159	Tb	0.01	0.02	0.00
163	Dy	0.01	0.11	0.02
165	Ho	0.01	0.02	0.00
166	Er	0.01	0.07	0.01
169	Tm	0.01	0.03	0.01
172	Yb	0.01	0.17	0.02
175	Lu	0.01	0.04	0.01
182	W	0.01	0.14	0.02
202	Hg	0.01	–	–
204	Pb	0.01	17.9	1.44

206	Pb	0.02	0.52	0.05
207	Pb	0.02	0.47	0.04
208	Pb	0.01	0.41	0.03
209	Bi	0.03	0.10	0.01
226	Ra	0.03	0.00	0.00
232	Th	0.03	0.03	0.004
238	U	0.02	0.10	0.005

References

Apukhtina, O.B., 2016. Distribution, petrology, geochemistry and geochronology of carbonate assemblages at the Olympic Dam deposit. Ph.D. Thesis (unpublished). University of Tasmania.

Bosbach, D., Böttle, M., Metz, V., 2010. Experimental study on Ra2+ uptake by barite (BaSO4). Svensk Kärnbranslehantering AB. Technical report TR-10-43, 111 p.

Bowell, R.J., Grogan, J., Hutton-Ashkenny, M., Brough, C., Penman, K., Sapsford, D.J., 2011. Geometallurgy of uranium deposits. Miner. Eng. 24, 1305–1313. https://doi.org/10.1016/j.mineng.2011.05.005.

Brandt, F., Curti, E., Klinkenberg, M., Rozov, K., Bosbach, D., 2015. Replacement of barite by a (Ba, Ra)S_O4 solid solution at close-to-equilibrium conditions: A combined experimental and theoretical study. Geochim. Cosmochim. Acta 155, 1–15.

Ciobanu, C.L., Cook, N.J., Ehrig, K., 2017. Ore minerals down to the nanoscale: Cu-(Fe)-sulphides from the iron oxide copper gold deposit at Olympic Dam, South Australia. Ore Geol. Rev. 81, 1218–1235.

Cook, N.J., Ehrig, K., Rollog, M., Ciobanu, C.L., Lane, D., Schmandt, D.S., Owen, N.D., Hamilton, T., Grano, S., 2018. ^{210}Pb and ^{210}Po in geological and related anthropogenic materials: implications for their mineralogical distribution in base metal ores. Minerals 8 (5), 211. http://www.mdpi.com/2075-163X/8/5/211https://doi.org/10.3390/min8050211.

Courtin-Nomade, A., Soubrand-Colin, M., Marcus, M.A., Fakra, S.C., 2008. Evidence for the incorporation of lead into barite from waste rock pile materials. Environ. Sci. Technol. 42, 2867–2872.

Curti, E., 1997. Coprecipitation of radionuclides: basic concepts, literature review and first applications. Report 97-10, Paul Scherrer Institut, Villigen, Switzerland, pp. 1–116.

Curti, E., Fujiwara, K., Iijima, K., Tits, J., Cuesta, C., Kitamura, A., Glaus, M.A., Muller, W., 2010. Radium uptake during barite recrystallization at 23 ± 2 °C as a function of solution composition: an experimental ^{133}Ba and ^{226}Ra tracer study. Geochim. Cosmochim. Acta 74, 3553–3570.

Curti, E., Xto, J., Borca, C.N., Henzler, K., Huthwelker, T., Prasianakis, N.I., 2019. Modelling Ra-bearing baryte nucleation/precipitation kinetics at the pore scale: application to radioactive waste disposal. Eur. J. Mineral. 1–16. https://doi.org/10.1127/ejm/2019/0031-2818. (in press).

Deconinck, I., Latkoczy, C., Cunther, D., Govaert, F., Vanhaecke, F., 2006. Capabilities of laser ablation—inductively coupled plasma mass spectrometry for (trace) element analysis of car paints for forensic purposes. J. Anal. Atom. Spectrom. 21, 279–287. https://doi.org/10.1039/b514007b.

DePaolo, D.J., 2011. Surface kinetic model for isotopic and trace element fractionation during precipitation of calcite from aqueous solutions. Geochim. Cosmochim. Acta 75, 1039–1056. https://doi.org/10.1016/j.gca.2010.11.020.

Ditchburn, R.G., de Ronde, C.E.J., 2017. Evidence for remobilization of barite affecting radiometric dating using ^{228}Ra, ^{228}Th, and ^{226}Ra/Ba values: implications for the evolution of sea-floor volcanogenic massive sulfides. Econ. Geol. 112, 1231–1245.

Ehrig, K., McPhie, J., Kamenetsky, V.S., 2012. Geology and mineralogical zonation of the Olympic Dam iron oxide Cu-U-Au-Ag deposit, South Australia. In: Hedenquist, J.W., Harris, M., Camus, F. (Eds.), Geology and Genesis of Major Copper Deposits and Districts of the World, a Tribute to Richard Sillitoe. Society of Economic Geologists Special Publication 16, Littleton, USA, pp. 237–267.

Grandia, F., Merino, J., Bruno, J., 2008. Assessment of the radium-barium co-precipitation and its potential influence on the solubility of Ra in the near-field. Svensk Kärnbranslehantering AB. Technical Report TR-08-07, 52 p.

Gu, Y., 2003. Automated scanning electron microscope based mineral liberation analysis: an introduction to JKMRC/FEI Mineral Liberation Analyzer. J. Min. Mater. Charact. Eng. 2, 33–41.

Heberling, F., Metz, V., Böttle, M., Curti, E., Geckeis, H., 2018. Barite recrystallization in the presence of ^{226}Ra and ^{133}Ba. Geochim. Cosmochim. Acta 232, 124–139. https://doi.org/10.1016/j.gca.2018.04.007.

Johnson, C.A., Piatak, N.M., Miller, M.M., 2017. Chapter D, Barite (Barium). In: Schulz, K. J., DeYoung, J.H., Jr., Seal, R.R., II, Bradley, D.C. (Eds.), Critical Mineral Resources of the United States—Economic and Environmental Geology and Prospects for Future Supply: U.S. Geological Survey Professional Paper 1802. D1–D18. https://doi.org/10.3133/ pp1802D.

Jones, M.J., Butchins, L.J., Charnock, J.M., Pattrick, R.A.D., Small, J.S., Vaughan, D.J., Wincott, P.L., Livens, F.R., 2011. Reactions of radium and barium with the surfaces of carbonate minerals. Appl. Geochem. 26, 1231–1238.

Klinkenberg, M., Brandt, F., Breuer, U., Bosbach, D., 2014. Uptake of Ra during the recrystallization of barite: a microscopic and time of flight-secondary ion mass spectrometry study. Environm. Sci. Tech. 48, 6620–6627. https://doi.org/10.1021/es405502e.

Lane, D.J., Cook, N.J., Grano, S.R., Ehrig, K., 2016. Selective leaching of penalty elements from copper concentrates: a review. Miner. Eng. 98, 110–121.

Lottering, M.J., Lorenzen, L., Phala, N.S., Smit, J.T., Schalkwyk, G.A.C., 2008. Mineralogy and uranium leaching response of low grade South African ores. Miner. Eng. 21, 16–22. https://doi.org/10.1016/j.mineng.2007.06.006.

Maas, R., Kamenetsky, V.S., Ehrig, K., Meffre, S., McPhie, J., Diemar, G., 2011. Olympic Dam U-Cu-Au Deposit, Australia: new age constraints. Min. Mag. 75, 1375.

Macmillan, E., Cook, N.J., Ehrig, K., Ciobanu, C.L., Pring, A., 2016. Uraninite from the Olympic Dam IOCG-U-Ag deposit: linking textural and compositional variation to temporal evolution. Am. Mineral. 101, 1295–1320. https://doi.org/10.2138/am-2016-5411.

Macmillan, E., Cook, N.J., Ehrig, K., Pring, A., 2017. Chemical and textural interpretation of late-stage coffinite and brannerite from the Olympic Dam IOCG-Ag-U deposit. Min. Mag. 81, 1323–1366. https://doi.org/10.1180/minmag.2017.081.006.

Oostingh, K., 2011. Analysis of Rare Earth Element concentrations in barite ($BaSO_4$). Determination of the environment of formation of Archean barites by Rare Earth Element fractionation measurements. MSc. Thesis. Utrecht University.

Owen, N.D., Ciobanu, C.L., Cook, N.J., Slattery, A., Basak, A., 2018. Nanoscale Study of Clausthalite-Bearing Symplectites in Cu-Au-(U) Ores: implications for Ore Genesis. Minerals. 8, 67. https://doi.org/10.3390/min8020067.

Paton, C., Hellstrom, J., Paul, B., Woodhead, J., Hergt, J., 2011. Iolite: Freeware for the visualisation and processing of mass spectrometric data. J. Anal. Atom. Spectrom. 26, 2508.

Pownceby, M.I., Johnson, C., 2014. Geometallurgy of Australian uranium deposits. Ore Geol. Rev. 56, 25–44. https://doi.org/10.1016/j.oregeorev.2013.07.001.

Prieto, M., Astilleros, J.M., Fernández-Díaz, L., 2013. Environmental remediation by crystallization of solid solutions. Elements. 9, 195–201. https://doi.org/10.2113/gselements.9.3.195.

Putnis, C.V., Ruiz-Agudo, E., 2013. The mineral–water interface. Elements 9, 177–182. https://doi.org/10.2113/gselements.9.3.177.

Putnis, C.V., Tsukamoto, K., Nishimura, Y., 2005. Direct observations of pseudomorphism: compositional and textural evolution at a fluid–solid interface. Am. Mineral. 90, 1909–1912. https://doi.org/10.2138/am.2005.1990.

Rashed, M.N., 2001. Lead removal from contaminated water using mineral adsorbents. Environmentalist 21, 187–195.

Rollog, M., Cook, N.J., Gugliardo, P., Ciobanu, C.L., Ehrig. K., Kilburn, M., 2018. Mobility of radionuclides in the Olympic Dam Cu-U-Au-Ag deposit, South Australia. Extended abstract, International Association on the Genesis of Ore Deposits Quadrennial Symposium, Salta Argentina, August 2018.

Rollog, M., Cook, N.J., Gugliardo, P., Ehrig, K., Kilburn, M., 2019. In situ spatial distribution mapping of radionuclides in minerals by nanoSIMS. Geochem.: Explor. Environ., Anal. https://doi.org/10.1144/geochem2018-038.

Rosenberg, Y.O., Metz, V., Ganor, J., 2011a. Co-precipitation of radium in high ionic strength systems: 1. Thermodynamic properties of the Na-Ra-Cl-SO_4-H_2O system – estimating Pitzer parameters for $RaCl_2$. Geochim. Cosmochim. Acta 75, 5489–15402.

Rosenberg, Y.O., Metz, V., Oren, Y., Volkman, Y., Ganor, J., 2011b. Co-precipitation of radium in high ionic strength systems: 2. Kinetic and ionic strength effects. Geochim. Cosmochim. Acta 75, 5403–5422.

Rosenberg, Y.O., Metz, V., Ganor, J., 2013. Radium removal in a large scale evaporitic system. Geochim. Cosmochim. Acta 103, 121–137.

Rosenberg, Y.O., Sadeh, Y., Metz, V., Pina, C.M., Ganor, J., 2014. Nucleation and growth kinetics of $Ra_xBa_{1-x}SO_4$ solid solution in NaCl aqueous solutions. Geochim. Cosmochim. Acta 125, 290–307.

Rosenberg, Y.O., Sade, Z., Ganor, J., 2018. The precipitation of gypsum, celestine, and barite and coprecipitation of radium during seawater evaporation. Geochim. Cosmochim. Acta 233, 50–65. https://doi.org/10.1016/j.gca.2018.04.019.

Ruiz-Agudo, E., Putnis, C.V., Putnis, A., 2014. Coupled dissolution and precipitation at mineral–fluid interfaces. Chem. Geol. 282, 132–146. https://doi.org/10.1016/j.chemgeo.2014.06.007.

Ruiz-Agudo, C., Putnis, C.V., Ruiz-Agudo, E., Putnis, A., 2015. The influence of pH on barite nucleation and growth. Chem. Geol. 391, 7–18. https://doi.org/10.1016/j.chemgeo.2014.10.023.

Takano, B., Watanuki, K., 1974. Geochemical implications of the lead content of barite from various origins. Geochem. J. 8, 87–95.

Torapava, N., Ramebäck, H., Curti, E., Lagerkvist, P., Ekberg, C., 2014. Recrystallization of 223Ra with barium sulfate. J. Radioanal. Nucl. Chem. 301, 545–553. https://doi.org/10.1007/s10967-014-3170-6.

Uchida, A., Toyoda, S., Ishibashi, J., Nakai, S., 2015. ^{226}Ra-^{210}Pb and ^{228}Ra-^{228}Th dating of barite in submarine hydrothermal sulfide deposits collected at the okinawa trough and the southern Mariana trough. In: Ishibashi, J., Okino, K., Sunamura, M. (Eds.), Subseafloor Biosphere Linked to Hydrothermal Systems. Springer, Tokyo, pp. 607–615.

Verdugo-Ihl, M.R., Ciobanu, C.L., Cook, N.J., Ehrig, K., Courtney-Davies, L., Gilbert, S., 2017. Textures and U-W-Sn-Mo signatures in hematite from the Cu-U-Au-Ag orebody at Olympic Dam, South Australia: defining the archetype for IOCG deposits. Ore Geol. Rev. 91, 173–195.

Vinograd, V.L., Brandt, F., Rozov, K., Klinkenberg, M., Refson, K., Winkler, B., Bosbach, D., 2013. Solid-aqueous equilibrium in the $BaSO_4$-$RaSO_4$-H_2O system: first-principles calculations and a thermodynamic assessment. Geochim. Cosmochim. Acta 122, 398–417.

Vinograd, V.L., Kulik, D.A., Brandt, F., Klinkenberg, M., Weber, J., Winkler, B., Bosbach, D., 2018a. Thermodynamics of the solid solution-Aqueous solution system (Ba, Sr, Ra)$_S$O4 + H2O: I. The effect of strontium content on radium uptake by barite. Appl. Geochem. 89, 59–74. https://doi.org/10.1016/j.apgeochem.2017.11.009.

Vinograd, V.L., Kulik, D.A., Brandt, F., Klinkenberg, M., Weber, J., Winkler, B., Bosbach, D., 2018b. Thermodynamics of the solid solution-Aqueous solution system (Ba, Sr, Ra)$_S$O4 + H2O: II. Radium retention in barite-type minerals at elevated temperatures. Appl. Geochem. 93, 190–208. https://doi.org/10.1016/j.apgeochem.2017.10.019.

Wang, R.S., Chau, A.S.Y., Liu, F., Cheng, H., Nar, P., Chen, X.M., Wu, Q.Y., 1993. Studies on the adsorption and migration of radium in the natural minerals. J. Radioanal. Nucl. Chem. Art. 171, 347–364.

Watson, E.B., 2004. A conceptual model for near-surface kinetic controls on the trace-element and stable isotope composition of abiogenic calcite crystals. Geochim. Cosmochim. Acta 68, 1473–1488. https://doi.org/10.1016/j.gca.2003.10.003.

Weber, J., Barthel, J., Brandt, F., Klinkenberg, M., Breuer, U., Kruth, M., Bosbach, D., 2016. Nano-structural features of barite crystals observed by electron microscopy and atom probe tomography. Chem. Geol. 424, 51–59.

Weber, J., Barthel, J., Klinkenberg, M., Bosbach, D., Kruth, M., Brandt, F., 2017. Retention of ^{226}Ra by barite: the role of internal porosity. Chem. Geol. 466, 722–732.

CHAPTER 5

MINERALOGY AND GEOCHEMISTRY OF FLUORITE IN THE OLYMPIC DAM CU-U-AU-AG DEPOSIT, SOUTH AUSTRALIA

Danielle S. Schmandt[1], Nigel J. Cook[1], Kathy J. Ehrig[2], Cristiana L. Ciobanu[1], Sarah Gilbert[3], Benjamin P. Wade[3], Max R. Verdugo-Ihl[1], William Keyser[1]

[1] *School of Chemical Engineering, The University of Adelaide, Adelaide, S.A. 5005, Australia*

[2] *BHP Olympic Dam, Adelaide 5000, S.A., Australia*

[3] *Adelaide Microscopy, The University of Adelaide, Adelaide, S.A. 5005, Australia*

Statement of Authorship

Title of Paper	Mineralogy and geochemistry of fluorite in the Olympic Dam Cu-U-Au-Ag deposit, South Australia
Publication Status	☐ Published ☐ Accepted for Publication ☐ Submitted for Publication ☑ Unpublished and Unsubmitted work written in manuscript style
Publication Details	

Principal Author

Name of Principal Author (Candidate)	Danielle S. Schmandt		
Contribution to the Paper	Performed majority of analytical work, carried out data processing and interpretation, oversaw development of work, and wrote manuscript.		
Overall percentage (%)	60%		
Certification:	This paper reports on original research I conducted during the period of my Higher Degree by Research candidature and is not subject to any obligations or contractual agreements with a third party that would constrain its inclusion in this thesis. I am the primary author of this paper.		
Signature		Date	Dec 3rd, 2018

Co-Author Contributions

By signing the Statement of Authorship, each author certifies that:

i. the candidate's stated contribution to the publication is accurate (as detailed above);
ii. permission is granted for the candidate in include the publication in the thesis; and
iii. the sum of all co-author contributions is equal to 100% less the candidate's stated contribution.

Name of Co-Author	Nigel J. Cook		
Contribution to the Paper	10%; Helped define direction of research, supervised development of work, assisted with data interpretation, and contributed to manuscript preparation.		
Signature		Date	5/12/2018

Name of Co-Author	Kathy Ehrig		
Contribution to the Paper	5%; Provided sample material, performed analytical work, and helped to evaluate and edit manuscript.		
Signature		Date	10/12/18

Name of Co-Author	Cristiana L. Ciobanu		
Contribution to the Paper	5%; Oversaw analytical work, contributed to manuscript preparation, and helped to evaluate and edit manuscript.		
Signature		Date	5/12/2018

Name of Co-Author	Sarah Gilbert		
Contribution to the Paper	5%; Assisted in operating analytical instrumentation and data processing.		
Signature		Date	6/12/2018

Name of Co-Author	Benjamin P. Wade		
Contribution to the Paper	5%; Assisted in operating analytical instrumentation and data processing.		
Signature		Date	11/12/18

Name of Co-Author	Max R. Verdugo-Ihl		
Contribution to the Paper	5%; Performed analytical work.		
Signature		Date	6/12/2018

Name of Co-Author	William Keyser		
Contribution to the Paper	5%; Performed analytical work.		
Signature		Date	6/12/2018

Mineralogy and geochemistry of fluorite in the Olympic Dam Cu-U-Au-Ag deposit, South Australia

Danielle S. Schmandt[1,*], Nigel J. Cook[1], Kathy J. Ehrig[2], Cristiana L. Ciobanu[1], Sarah Gilbert[3], Benjamin P. Wade[3], Max R. Verdugo-Ihl[1], William Keyser[1]

[1] *School of Chemical Engineering, The University of Adelaide, Adelaide, S.A. 5005, Australia*
[2] *BHP Olympic Dam, Adelaide 5000, S.A., Australia*
[3] *Adelaide Microscopy, The University of Adelaide, Adelaide, S.A. 5005, Australia*

Abstract

Fluorite is an accessory gangue mineral in the Olympic Dam iron-oxide copper gold deposit, South Australia, making up more than 1% of the total >10 billion-tonne resource. This fluorite is present in the deposit-host breccia, both in matrix and clasts, where it is closely associated with Cu-(Fe)-sulfides. Rare, late-stage fluorite-bearing veins are also present at Olympic Dam, where they cross-cut the breccia ore and are interpreted to have been emplaced nearly 1000 Ma after the onset of brecciation. Fluorite from these late-stage veins displays macroscopic variations in color, including purple, white, and green. The mineralogy and geochemistry of fluorite in breccia ore (based on representative grains in flotation feed) and from late-veins has been investigated. Breccia-hosted fluorite is enriched in LREE and displays variable chemistry, consistent with observed heterogeneity in other hydrothermal minerals. Fluorite from late-stage veins has a markedly different chemical signature. Macro-scale color variations in vein fluorite reflect differences in major and trace element geochemistry. Paragenetically, purple fluorite precedes white fluorite, and the white fluorite is depleted in most trace and minor elements. Green fluorite is most enriched in REY.

Keywords: Olympic Dam; IOCG deposits; fluorite; trace elements; rare earth elements; chondrite-normalized fractionation patterns

1. Introduction

Fluorite [CaF_2] is a relatively abundant accessory mineral in Cu-U-Au-Ag ores from the >10 billion-tonne Olympic Dam iron-oxide copper gold deposit, South Australia, making up more

* Corresponding author. E-mail address: danielle.schmandt@adelaide.edu.au

than 1% of the total resource [1]. Fluorite occurs throughout the deposit within the matrix of hematite-dominant breccias hosting sulfide ores formed at ~1590 Ma. Fluorine is one of more than 20 elements that occur in the deposit at concentrations well above crustal averages. Fluorite is the main carrier of F in the deposit; other F-bearing minerals include fluorapatite [2], rare earth element-fluorocarbonates (bastnäsite and synchysite; [3]), sericite, and chlorite. Fluorite is a contaminant in copper concentrates and is effectively removed prior to smelting by sulfuric acid leaching [1].

The deposit also contains a series of structurally late fluorite-bearing veins that cross-cut hematite breccias. Although these veins are volumetrically negligible on the scale of the deposit, they are conspicuous in that they contain distinct white, purple, and green varieties of fluorite.

In this contribution, we compare the physical appearance, petrography, and geochemistry of breccia-hosted and vein fluorite from the deposit and assess whether ore-related fluorite and late vein-hosted fluorite have unique chemical signatures with respect to rare earth elements (REE), yttrium, and other trace elements, and whether fluorite is a significant carrier of other minor elements, including non-target metals, in the ores. We also aim to establish whether the differently colored vein fluorites are also chemically distinct.

2. Background

Fluorite is a common mineral found in many types of ore deposits and can be used as an indicator mineral for mineralization in base metal exploration (e.g., [4–6]). Fluorite can also display extremely variable morphology and colors and has thus been the focus of many studies. Explanations for the wide color spectrum are varied and can range by locality; some explanations include crystal structure disturbance by various trace elements, including substitutions of REE+Y (REY) within the structure, radioactive inclusions or emanations, inclusion of carbonaceous material, hydrocarbons, oxygen, or other types of inclusions/nano-inclusions of element complexes (e.g., [7–10]).

Fluorite crystallizes in the cubic system with a simple close-packed structure in which each Ca^{2+} (1.00 Å) cation is surrounded by eight F^- ions. Reported substituents include Sr^{2+} (1.26 Å), Y^{3+} (1.019 Å), REE (0.985–1.109 Å) and a wide range of other trace elements (e.g., [8]). Fluorite is isomorphous with strontiofluorite [SrF_2] and fluorocronite [PbF_2]. Other related species include the Mg- and Ba-fluoride end-members sellaite [MgF_2] and frankdicksonite [BaF_2], respectively, and REE-fluorides including fluorcerite-(Ce) and –(La) [$(Ce,La)F_3$ and $(La,Ce)F_3$], and tveitite-(Y) [$Ca_{0.7}Y_{0.3}F_{2.3}$; [11]]. *Yttrocerite* ([$CaY_{0.75}Ce_{0.25}F_5$] is a non-IMA-approved name describing Y- and REE-enriched fluorite; [12]).

2.1 Fluorite at Olympic Dam

Hydrothermal fluorite is found throughout the Olympic Dam deposit and is considered as a primary hydrothermal mineral making-up ~1.2% of the total resource (based on a 10,000 sample MLA data set; [1]). It is a characteristic accessory mineral of the hematite-sericite-fluorite alteration assemblage that is strongly associated with chalcopyrite-bornite-chalcocite sulfide mineralization [1,13,14]. In ores, fluorite generally occurs disseminated within the matrix of hematite breccias, as clasts, or as clast rims. The mineral co-exists with Cu-(Fe)-sulfides, hematite, quartz, fluorapatite, and feldspars [2,15,16], as well as REE-phosphates and REE-fluorocarbonates, and is also intimately intergrown with U-minerals [17,18].

Although most fluorite at Olympic Dam is considered hydrothermal, trace fluorite is present within the host Roxby Downs Granite (RDG) and in basaltic dykes cross-cutting the deposit [1,16]. Krneta et al. [2] described fluorite inclusions co-crystallized with magmatic apatite and suggest that these inclusions formed from felsic melts. Fluorine enrichment is considered as a notable feature of hydrothermal fluids produced by magmas associated with the Gawler Siliceous Large Igneous Province [19].

As part of the hydrothermal alteration halo enveloping the Olympic Dam deposit, fluorite displays spatial zonation relative to siderite and baryte [1]. Siderite is most abundant at depth and on the deposit edges, baryte is concentrated in the deposit center and at shallow depths, and fluorite is most abundant between the two. Fluorite can occur with both siderite and baryte, however, siderite and baryte generally do not occur together [1]. Fluorite is more strongly associated with hematite and sulfide alteration but decreases in abundance in the most hematite-rich parts of the deposit [1].

Swarms of structurally-late hydrothermal veins containing coarse, mm- to cm-sized euhedral fluorite and baryte cross-cut mineralized breccias across the deposit [1,20–22]. Locally, these veins extend into the overlying undeformed and non-mineralized cover sequence of Neoproterozoic to Cambrian sedimentary units [23,24]. The veins can range in thickness from a few mm up to as much as ~1 m, generally strike NE-SW or E-W, typically conjugate with fault zones, and can have vertical extensions of up to ~800 m. The distribution of these veins displays no spatial correlation with the aforementioned deposit-scale zonation. The veins can also contain other minerals, including notably pink- to white-colored Ca-Mg-Fe-Mn-carbonates, as well as minor REE-fluorocarbonates, a diverse suite of minor sulfides and ore minerals, and uranium minerals. In some cases, the dominant mineral can be carbonate or (colloform) uraninite [20,21].

These cross-cutting veins have been dated as ~500 Ma based on Sm-Nd geochronology on fluorite and carbonates [25], coincident with emplacement during the Delamerian Orogeny and

the final stages of Rodinia break-up and the beginning of the Gondwana amalgamation in southern Australia. They are thus ~1.1 Ga younger than the initial ore-forming event at Olympic Dam at ~1595 Ma (e.g., [26,27]). Carbonates within these veins have been documented in some detail with respect to composition, stable isotopes, and Sm-Nd dating [21,22]. Schmandt et al. [28] give compositional data for co-existing baryte, noting that the latter is compositionally zoned with respect to Sr, and is geochemically distinct from breccia-hosted baryte.

Apukhtina et al. [21] have suggested, as there is no evidence for local magmatic activity after ~0.82 Ga, that these veins may have precipitated from meteoric or metamorphic waters migrating along faults from the nearby Adelaide Geosyncline. The Delamerian Orogeny generated extensive deformation across the region and associated veining (e.g., [29–32]). Swarms of fluorite veins are recognized in several Hiltaba-aged granites, for example in ~1590 Ma granite bedrock subjacent to the Samphire uranium deposit, northern Eyre Peninsula [33], even if the veins themselves are not yet dated.

Oreskes and Einaudi [14] conducted a fluid inclusion study at Olympic Dam and included samples from purple fluorite veins outside the deposit cutting the RDG and also late green fluorite veins that cut hematite breccia near the center of the deposit. Results gave low temperature ranges: primary inclusions at 130-230 ℃ and secondary inclusions at 120-150 ℃ for purple fluorite; and 90-160 ℃ for green fluorite with a salinity of 6.6-22.8 wt.% NaCl equivalent. The same authors [14] interpreted the purple fluorite to have a similar timing to the hematite breccias but regarded the green fluorite as the product of a possible late low-temperature event. No compositional data for fluorite was, however, available before the present study.

3. Sampling

Breccia-hosted fluorite was sampled from the deposit via crushed flotation feed, whereas vein fluorite was sampled *in-situ* from specific colored fluorite veins in drillcore and from underground mine workings.

3.1 Breccia-hosted fluorite

Macroscopic fluorite is rarely observed in breccia-hosted ores impeding direct sampling from drillcore. Thus, samples of flotation feed comprising crushed grains were used to represent breccia-hosted fluorite. Such samples are representative of all ores mined at the time of sampling, sourced from different parts of the deposit. Trace element analysis of fluorite by laser ablation inductively coupled plasma mass spectrometry (LA-ICP-MS) requires grains of

appropriate size (preferably at least 30-40 μm in diameter), so only the largest grains were analyzed.

3.2 Vein fluorite

Five polished blocks were prepared from three separate grab samples from veins and vugs collected underground from mining faces without the location being recorded. Two additional samples were taken from drillcore, samples RX11077 and RX11078 (hereafter '77' and '78'), are from a ~5 cm-wide vein cutting hematite breccia. These veins are volumetrically extremely minor in the deposit. The sampled veins are unique and limited in occurrence and should not be considered representative of the deposit.

4. Methodology

All microanalytical work was undertaken at Adelaide Microscopy, The University of Adelaide. Polished blocks were examined and imaged using a reflected light optical microscope and using a FEI Quanta 450 Field Emission Gun (FEG) scanning electron microscope (SEM) equipped with a silicon-drift detector energy-dispersive X-ray (EDAX) spectrometer.

Trace element and isotopic analyses were performed by LA-ICP-MS using an ASI RESOlution-LR ArF excimer laser ablation system equipped with a large format S155 sample chamber (Laurin Technic Inc.) and coupled to an Agilent 7900x ICP-MS. Operating conditions were set at 5 Hz and a fluence of 10 J/cm^2. Reference standards used were GSD-1G and NIST-610 glasses analyzed at 5 Hz and 3.5 J/cm^2 fluence.

Fluorite analysis included 20 s delay followed 5 pulses of pre-ablation cleaning and then 30 s gas background collection. There was 40 s ablation time followed by a 2 s delay giving a total of 72 s acquisition time. Isotopes measured included ^{9}Be, ^{23}Na, ^{24}Mg, ^{27}Al, ^{29}Si, ^{31}P, ^{39}K, ^{45}Sc, ^{49}Ti, ^{51}V, ^{52}Cr, ^{55}Mn, ^{57}Fe, ^{65}Cu, ^{66}Zn, ^{85}Rb, ^{88}Sr, ^{89}Y, ^{90}Zr, ^{93}Nb, ^{107}Ag, ^{137}Ba, ^{139}La, ^{140}Ce, ^{141}Pr, ^{146}Nd, ^{147}Sm, ^{153}Eu, ^{157}Gd, ^{159}Tb, ^{163}Dy, ^{165}Ho, ^{166}Er, ^{169}Tm, ^{172}Yb, ^{175}Lu, ^{201}Hg, ^{202}Hg, ^{203}Tl, ^{204}Pb, ^{206}Pb, ^{205}Tl, ^{207}Pb, ^{208}Pb, ^{209}Bi, ^{226}Ra, ^{232}Th, ^{235}U, and ^{238}U. Dwell times for ^{23}Na, ^{27}Al, ^{29}Si, ^{31}P, and ^{39}K were 0.005 s, ^{206}Pb and ^{207}Pb were 0.02 s, and all others' were 0.01 s for a sweep time of 0.558 s. Analytical parameters are described in detail in Appendix A.

Fluorite is known to behave badly during ablation due to its poor absorptivity and strong cleavage creating "catastrophic" ablation pits [34,35]. This was also observed during this study (Figure 1), although the shatter phenomena could be somewhat mitigated using higher fluence (10 J/cm^2 was used in this study compared to normal fluences of ~3.5 J/cm^2).

Data reduction was performed using the software Iolite v3.4 [36] and processed using the "Trace_Elements" data reduction scheme using Ca as the internal standard element. Statistical

summaries of the LA-ICP-MS data for fluorite are in Table 1. Filtered mean LA-ICP-MS values (excluding values that deviate from the mean by than 20%) are reported in the tables and used for calculation of chondrite-normalized REE fractionation patterns. The full dataset is given as Appendix B.

A Cameca SX-Five electron probe microanalyzer (EPMA) equipped with 5 tunable wavelength-dispersive spectrometers were used to confirm the LA-ICP-MS data for minor elements, including REE, in two samples (RX11077 and RX11078). The instrument uses PeakSite v6.2 software for microscope operation, and Probe for EPMA software (distributed by Probe Software Inc.) for data acquisition and processing. Measured elements, spectra, reference standards, count times and other parameters are described in detail in Appendix C. Elements present at concentrations above minimum detection limits are presented in Table 2. The full dataset of all EPMA analysis data is given as Appendix D.

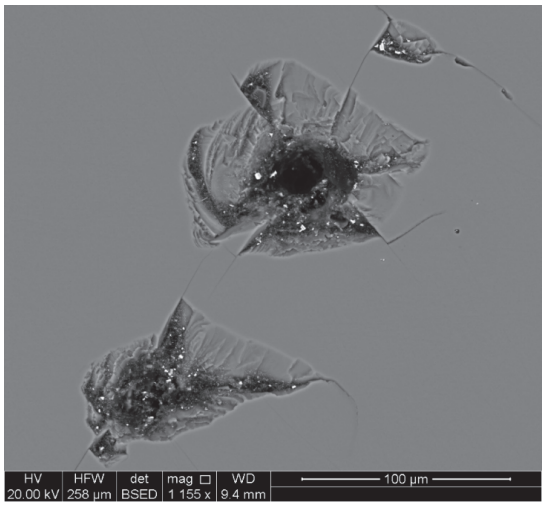


Figure 1. Catastrophic laser ablation pits in fluorite vein. Note shatter fractures extending from the pits and the sharp straight lines likely following cleavage.

5. Results

5.1 Petrography

5.1.1 Breccia-hosted fluorite

Mesoproterozoic fluorite within the breccia ore occurs in a wide range of textures and assemblages and is found across the deposit and associated with all major minerals. Fluorite often appears as blocky grains (Figure 2a) and can contain a range of submicron to micron scale inclusions, commonly hematite and U-minerals (Figure 2a-d). Fluorite also occurs included within Cu-(Fe)-sulfides (Figure 2b), hematite, and other gangue minerals. In the studied ore samples, fluorite is often observed as part of composite grains containing several minerals (Figure 2e), more rarely in a simpler assemblage (Figure 2a, f), and in some cases, completely liberated.

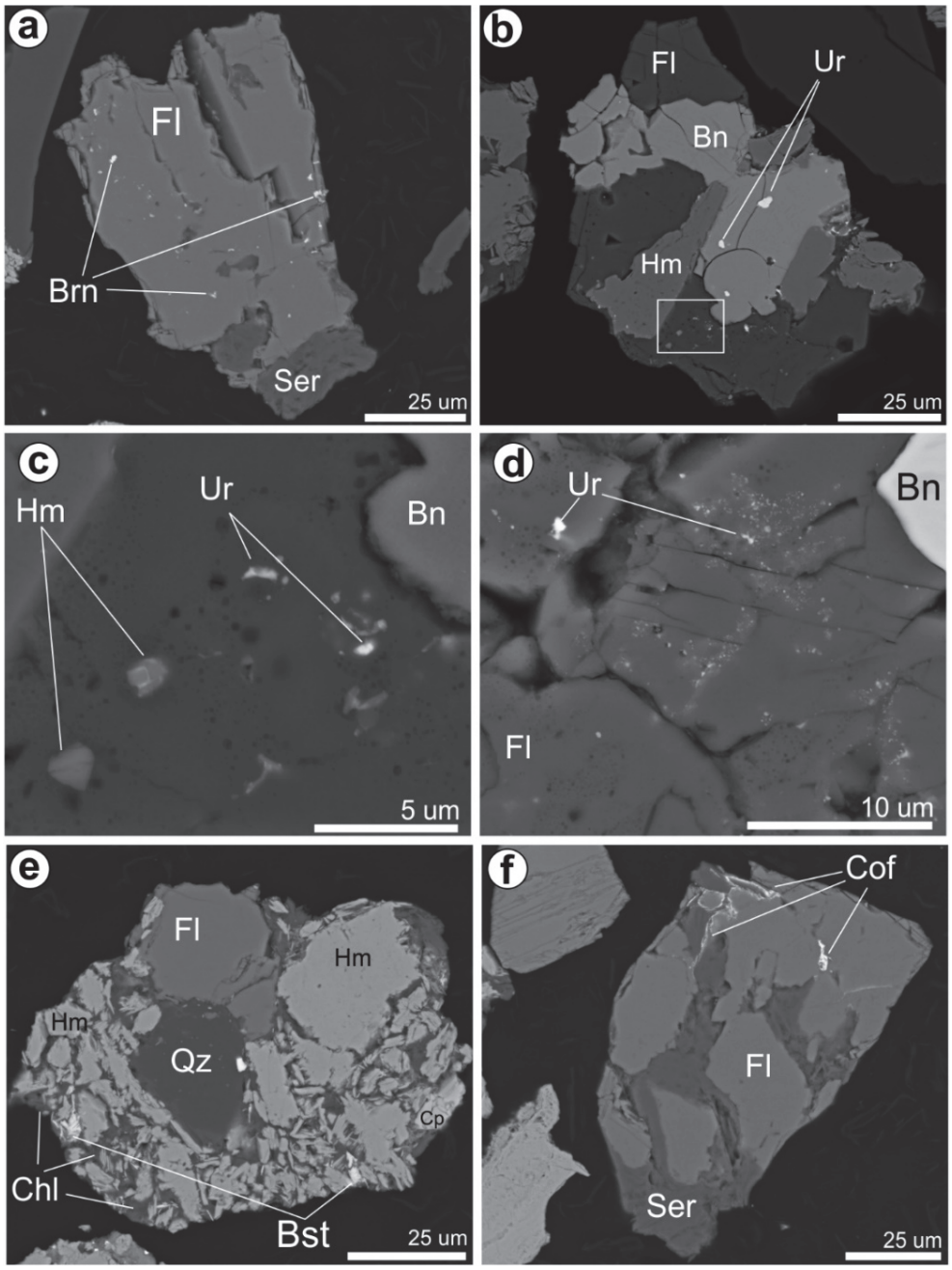


Figure 2. Backscatter electron (BSE) images illustrating examples of breccia-hosted fluorite in ore feed sample. **a)** Relatively coarse subhedral fluorite with small inclusions of brannerite and minor accompanying sericite. **b)** Particle dominantly composed of bornite, fluorite, and hematite. Note micron-scale inclusions of hematite in fluorite, and of uraninite in fluorite, bornite, and hematite. **c)** Enlargement of white box in (b) showing fine inclusions of blocky and irregular hematite and uraninite in fluorite. Note that fluorite displays a porous texture. **d)** Fine-grained uraninite inclusions in fluorite adjacent to bornite. Fluorite displays a similar porous texture as in c). **e)** Complex particle containing two textural sub-types of hematite: bladed with interstitial chlorite and bastnäsite; and a second, coarser-grained subhedral type, similar in size and shape to accompanying grains of quartz and fluorite. **f)** Euhedral fluorite in sericite with marginal rims of coffinite-xenotime solid solution. Abbreviations: Bn - bornite; Brn - brannerite; Bst - bastnäsite; Chl – chlorite; Cof - coffinite; Fl - fluorite; Hm - hematite; Qz – quartz; Ser - sericite; Ur - uraninite.

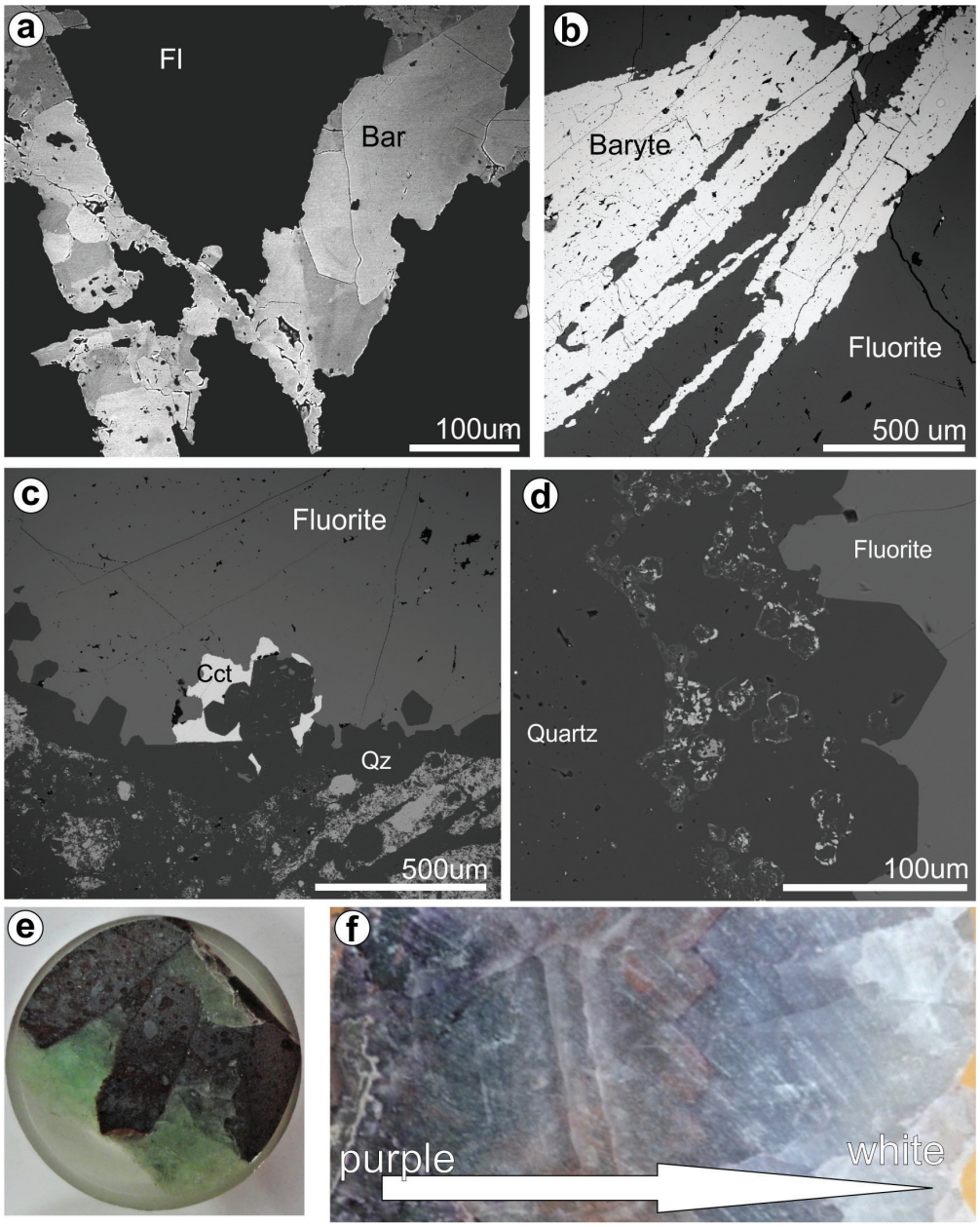


Figure 3. Characteristics of fluorite in late veins. **a)** BSE image of purple fluorite comprised of corroded baryte laths in fluorite (black). Note that baryte displays strong but patchy compositional zoning with respect to Sr and that crystal growth appears truncated by fluorite. **b)** BSE image of purple fluorite showing elongate, mm-scale baryte laths in fluorite. Baryte crystals display ragged, irregular margins with fluorite and abundant inclusions of fluorite (dark). **c)** BSE image of green fluorite showing contact boundary with hematite-quartz breccia (bottom of image). Euhedral quartz occurs between the breccia and crystalline fluorite; crystals protrude into the fluorite. Chalcocite surrounds one quartz crystal. Quartz also features inclusions of fluorite. **d)** Boundary between green fluorite and quartz, similar to (c), with defined zone of "ghost" crystals made-up of very fine-grained hematite and xenotime. **e)** Image of mounted sample of green fluorite shown in c and d, breccia clasts are "suspended" in bright green fluorite vein. **f)** Representative example of macroscopic color variation, showing unidirectional growth from purple to white fluorite. Red discoloration is attributed to inclusions of fine-grained hematite and iron-hydroxides. Abbreviations: Bar - baryte; Cct - chalcocite; Fl - fluorite; Qz - quartz.

5.1.2 Vein fluorite

There are two main groupings of fluorite veins in the sample set, the first group is purple and white fluorite with minor baryte, and the second group is green fluorite with minor quartz. All polished blocks prepared for this study are almost completely composed of fluorite, but also contain minor baryte or quartz, and with very minor carbonate or other minerals. Inclusions are scarce, and where present, are mostly hematite, carbonate, or Cu-(Fe)-sulfides.

Where baryte and fluorite co-exist in the veins, the veins clearly show sequential precipitation in which baryte is closer to the vein margin, thus preceding fluorite. Well-formed, prismatic crystals of baryte show corroded edges when observed in contact with fluorite, which often shows an "infill" texture (Figure 3a, b). In one location the purple and white fluorite show uni-directional and zoned growth from purple to white within an open space cavity (Figure 3f).

The green fluorite samples have a rim of irregular to euhedral quartz crystals between the breccia and infill fluorite (Figure 3c, d); quartz rather than baryte precedes fluorite in these samples. Minor Cu-(Fe)-sulfides occur in this vein (Figure 3c). Relict, partially replaced, skeletal crystals of xenotime reveal multiple stages of growth in the quartz rim, prior to fluorite deposition (Figure 3d). The green fluorite appears as coarse-grained aggregates and supports fragments of hematite-rich breccia (Figure 3e).

5.2 Fluorite geochemistry

Trace element datasets for the different fluorite groups (Table 1) reveal marked differences between breccia-hosted and vein fluorite, and also consistent compositional differences between vein fluorites of different colors. EPMA data for green fluorite (Table 2) fully corroborates the LA-ICP-MS results and confirms the proposed substitution mechanisms (Figure 4).

5.2.1 REE distribution patterns

Total REY concentrations within fluorite are distinct for each sub-type (ore fluorite and vein fluorite of different color). In REY fractionation trends normalized to chondrite values (Figure 5), all sub-types of fluorite display a generally flat MREE (Sm, Eu, Gd, Tb, and Dy) segment with a marked positive Y-anomaly. The breccia-hosted (ore) fluorite is the only fluorite type that shows a downwards-sloping LREE (La, Ce, Pr, Nd) segment and a slightly upwards-sloping

Table 1. Mean, minimum, and maximum trace element concentrations (ppm; LA-ICP-MS) in fluorite from ore material and in veins grouped by hand sample color

	Ore fluorite (n=28)			White (n=39)			Purple (n=190)			Green (n=177)		
	AVG	MIN	MAX	AVG	MIN	MAX	AVG	MIN	MAX	AVG	MIN	MAX
Y	480	38	3910	231	127	406	183	43	419	851	64	1354
La	94	0.7	2020	0.2	0.0	11	6.7	0.8	79	23	3.9	56
Ce	182	3.0	2710	1.1	0.4	28	15	2.2	132	107	15	154
Pr	19	0.3	216	0.3	0.1	4.5	2.4	0.4	20	20	2.9	29
Nd	72	0.5	600	2.1	1.3	23	12	2.3	102	101	13	152
Sm	13	0.2	62	1.9	0.9	7.5	4.2	1.2	31	20	2.2	27
Eu	4.3	<LOD	45	1.6	0.8	3.0	1.6	0.4	8.4	9.5	1.2	13
Gd	13	0.3	114	6.0	3.5	16	7.3	1.9	35	26	2.6	37
Tb	3.4	<LOD	26	1.4	0.8	2.4	1.2	0.2	5.8	4.9	0.6	7.2
Dy	18	1.4	272	10	6.6	20	7.7	0.9	33	33	4.8	49
Ho	5.1	0.3	78	2.3	1.3	4.6	1.6	0.2	5.8	7.4	1.1	12
Er	17	0.4	271	6.4	4.1	12	4.7	0.7	15	18	2.7	30
Tm	3.3	<LOD	39.4	0.7	0.5	1.7	0.6	0.1	1.9	2.0	0.3	3.2
Yb	18	0.1	299	3.4	2.4	8.5	3.4	0.5	11	12	1.5	20
Lu	3.4	<LOD	39.3	0.4	0.3	1.1	0.4	0.1	1.4	1.3	0.2	2.1
∑REE	523	17	5689	38	29	127	71	27	427	387	55	506
Pb	4.4	0.1	56.2	0.5	<LOD	2.6	0.9	<LOD	43	3.5	<LOD	89
U	13	0.5	163	0.01	<LOD	0.02	0.03	<LOD	3.6	0.1	<LOD	1.3
Th	2.7	<LOD	87	0.1	0.032	0.2	0.1	<LOD	1.0	1.2	0.0	4.2
Fe	1286	<LOD	6500	146	113	2610	165	<LOD	9740	72	46	151
Sr	157	21	1590	21	<LOD	60	76	<LOD	820	49	8.9	1040
Ba	18	<LOD	1110	2.4	<LOD	32	13	<LOD	3600	4.0	<LOD	246
Na	460	<LOD	640	268	<LOD	2260	637	<LOD	9100	195	<LOD	33000
Al	1196	<LOD	6880	1.0	<LOD	1340	3.4	<LOD	3870	1.2	<LOD	2.4
Si	6120	<LOD	9500	202	<LOD	1720	191	<LOD	4850	281	<LOD	419
P	2495	<LOD	3880	24	<LOD	73	29	<LOD	1870	15	<LOD	30
Cu	40	<LOD	598	0.4	<LOD	0.6	0.8	<LOD	9.4	1.9	<LOD	163

Average value is filtered mean with 20% deviation from the mean excluded; calculated with LOD/2 when value reported was <LOD due to consistent <LOD counts. <LOD = less than limit of detection

K, Sc, Ti, V, Cr, Mn, Ni, Zn, Nb, Ag, Bi, Mg, and Rb are excluded (consistently <LOD across the dataset)

∑REE includes only measured values not <LOD

HREE (Ho, Er, Tm, Yb, Lu) segment. All vein fluorites show a slight downwards-sloping HREE segment. The purple fluorite is flat across the LREE whereas white fluorite shows a marked upward-sloping pattern and becomes slightly more elevated in Dy-Er than the purple fluorite. The LREE fractionation trend for green fluorite is uniquely concave down. Of the vein fluorite, the green fluorite has the most elevated concentrations of all REY.

Chondrite-normalized REY whole-rock data for both the RDG and Olympic Dam REY resource show flat HREE trends without any recognizable Y-anomaly (Figure 5). The LREE fractionation trend for ore fluorite is similar to the whole-rock RDG trend but is conspicuous by a slightly more elevated HREE segment and a distinctive positive Y-anomaly that is lacking in the whole-rock patterns. The REY fractionation trends for vein fluorite are, in general, dissimilar from the whole-rock trends.

Figure 6a shows the relative variation of the LREE, Sm, and Eu among the groups of fluorite analyzed. White fluorite is clearly relatively depleted in La, Ce, Pr, and Nd, green fluorite mostly clusters towards Pr and Nd, ore fluorite is strongly relatively enriched in La and Ce, and purple fluorite occupies a broad range between them. Figure 6b compares the components of trivalent LREE (La, Pr, and Nd) vs. Na, and shows a generally positive correlation in the white, purple, and ore fluorite supporting the involvement of Na^{+} to achieve charge balance when REE^{3+} substitutes for Ca^{2+}. The green fluorite does not show this trend but rather a linear LREE concentration with variable Na (over two orders of magnitude).

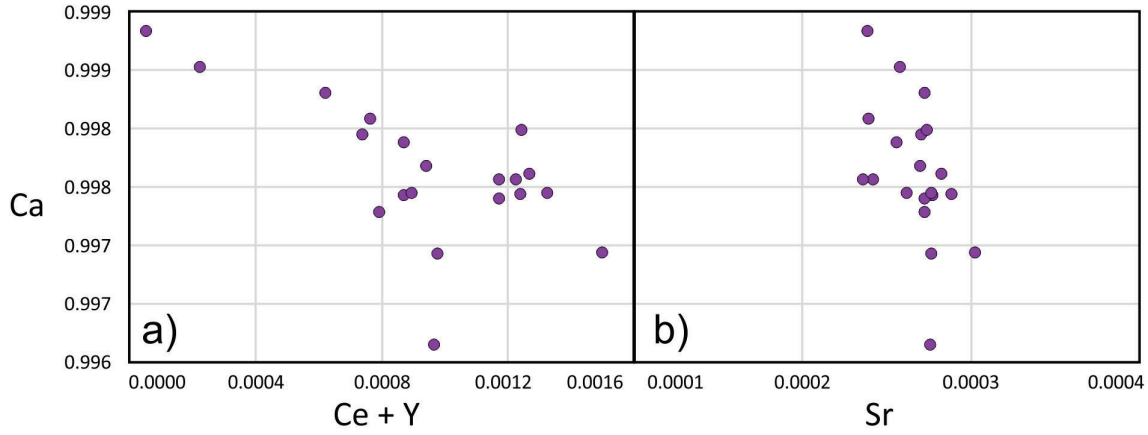


Figure 4. Compositional data for green fluorite (EPMA data). **a)** Ca vs. Ce + Y *apfu* (atoms per formula unit) values, the two major REY in green fluorite. These show a generally negative trend due to cation substitution. **b)** Ca vs. Sr (*apfu*), also showing the expected negative trend.

Table 2. EPMA wt. % and apfu values from green fluorite, samples RX11077 and RX11078.

Sample	RX11077									
wt. %	1	2	3	4	5	6	7	8	9	10
Ca	55.7	51.1	51.5	51.9	51.6	51.4	52.0	51.9	51.4	51.7
F	46.0	48.6	48.1	47.1	47.3	47.6	47.6	47.7	48.1	48.0
Ce	0.01	0.01	0.01	0.01	0.02	0.01	0.01	0.02	0.01	0.01
Y	0.09	0.10	0.08	0.06	0.09	0.10	0.08	0.09	0.10	0.11
Sr	0.03	0.03	0.03	0.03	0.03	0.03	0.03	0.03	0.03	0.03
Si	0.00	0.00	0.01	0.01	0.01	0.01	0.01	0.01	0.01	0.01
P	0.02	0.02	0.02	0.02	0.03	0.02	0.02	0.02	0.02	0.02
Sc	0.02	0.03	0.01	0.01	0.01	0.01	0.02	0.02	0.01	0.02
Ce + Y	0.10	0.11	0.09	0.08	0.11	0.10	0.09	0.11	0.11	0.12
Total	101.9	99.9	99.8	99.1	99.2	99.2	99.8	99.8	99.7	99.9
apfu	1	2	3	4	5	6	7	8	9	10
Ca	0.998	0.996	0.997	0.998	0.997	0.997	0.998	0.998	0.998	0.997
F	1.889	1.998	1.977	1.935	1.945	1.957	1.957	1.960	1.979	1.972
Ce	0.000	0.000	0.000	0.000	0.000	0.000	0.000	0.000	0.000	0.000
Y	0.001	0.001	0.001	0.001	0.001	0.001	0.001	0.001	0.001	0.001
Sr	0.000	0.000	0.000	0.000	0.000	0.000	0.000	0.000	0.000	0.000
Si	0.000	0.000	0.000	0.000	0.000	0.000	0.000	0.000	0.000	0.000
P	0.000	0.000	0.001	0.000	0.001	0.001	0.001	0.000	0.001	0.001
Sc	0.000	0.001	0.000	0.000	0.000	0.000	0.000	0.000	0.000	0.000
Ce + Y	0.001	0.001	0.001	0.001	0.001	0.001	0.001	0.001	0.001	0.001
Total	2.89	3.00	2.98	2.94	2.94	2.96	2.96	2.96	2.98	2.97
Sample	RX11078									
wt. %	1	2	3	4	5	6	7	8	9	10
Ca	52.3	51.5	52.7	52.5	52.6	51.5	51.3	51.6	51.2	51.6
F	48.1	49.2	47.0	46.8	47.2	48.2	48.0	48.3	47.7	47.8
Ce	0.01	0.01	0.01	0.01	<LOD	0.01	0.01	0.01	0.01	0.01
Y	0.14	0.17	0.13	<LOD	0.03	0.13	0.13	0.14	0.15	0.14
Sr	0.03	0.03	0.03	0.03	0.03	0.03	0.03	0.03	0.03	0.03
Si	<LOD	0.01	0.01	-	0.01	0.00	<LOD	0.00	0.00	0.00
P	0.02	0.02	0.02	0.02	0.02	0.02	0.02	0.02	0.02	0.02
Sc	<LOD	0.02	0.01	0.02	0.02	0.02	0.02	0.01	0.01	0.02
Ce + Y	0.15	0.17	0.14	0.01	0.03	0.14	0.14	0.15	0.15	0.15
Total	100.6	100.9	99.9	99.4	99.9	99.8	99.5	100.2	99.1	99.6
apfu	1	2	3	4	5	6	7	8	9	10
Ca	0.998	0.997	0.998	0.999	0.999	0.997	0.998	0.998	0.997	0.997
F	1.979	2.020	1.932	1.922	1.941	1.979	1.972	1.986	1.959	1.965
Ce	0.000	0.000	0.000	0.000		0.000	0.000	0.000	0.000	0.000
Y	0.001	0.001	0.001		0.000	0.001	0.001	0.001	0.001	0.001
Sr	0.000	0.000	0.000	0.000	0.000	0.000	0.000	0.000	0.000	0.000
Si		0.000	0.000		0.000	0.000		0.000	0.000	0.000
P	0.000	0.001	0.001	0.000	0.001	0.001	0.000	0.001	0.001	0.001
Sc		0.000	0.000	0.000	0.000	0.000	0.000	0.000	0.000	0.000
Ce + Y	0.001	0.001	0.001	0.000	0.000	0.001	0.001	0.001	0.001	0.001
Total	2.98	3.02	2.93	2.92	2.94	2.98	2.97	2.99	2.96	2.97

<LOD = less than limit of detection; - = unreliable value from exaggerated error; *apfu* = atoms per formula unit
Many elements analyzed are excluded from this table due to consistent <LOD counts.
Full dataset is in Appendix D.
Sums do not include <LOD values.

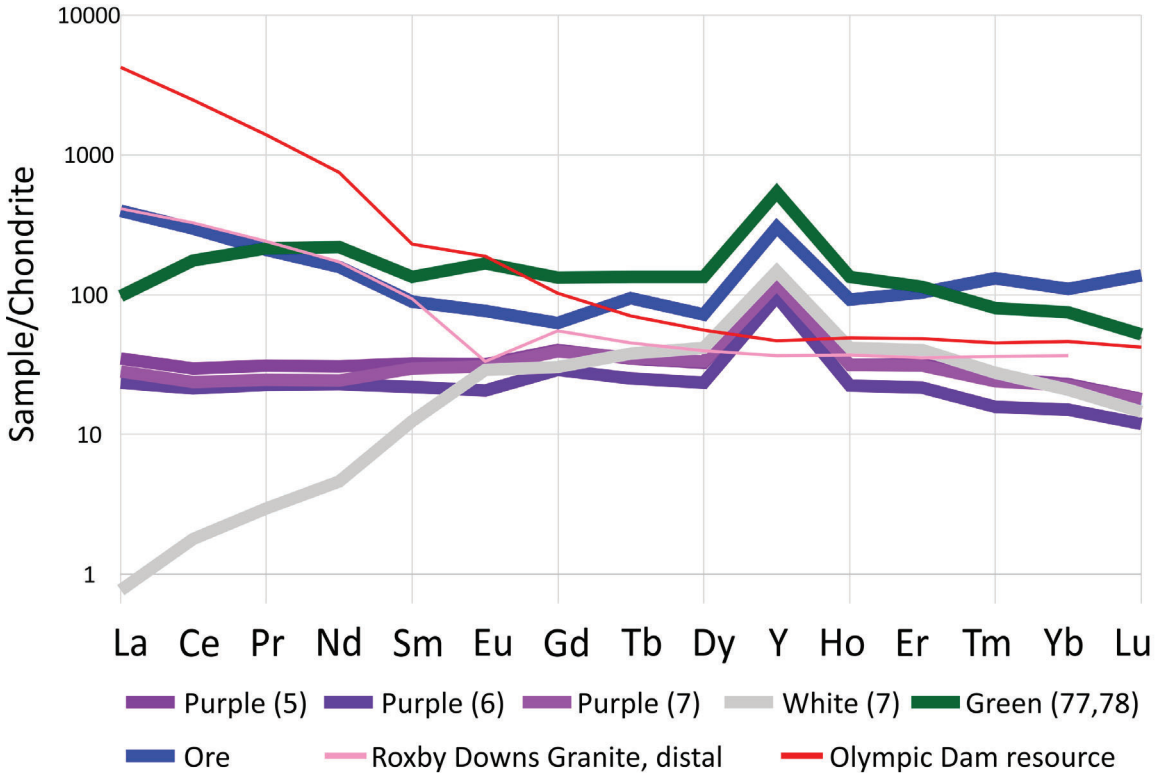


Figure 5. Chondrite-normalized REY fractionation trends (average with <20% deviation) for fluorite in breccia-hosted ores and in cross-cutting veins separated by crystal color and sample ID. Whole-rock REY data for the OD resource and host Roxby Downs Granite are shown for comparison. Chondrite values after [37].

5.2.2 Other trace elements

Differences in the trace element endowment are observed between ore fluorite and differently colored vein fluorites (Table 1; Figure 7). Generally, white fluorite is depleted in most trace elements relative to other vein fluorite types, whereas higher trace element concentrations are shown by purple fluorite, and green fluorite is variable between them. Ore fluorite consistently displays the most elevated and widest range of trace element concentrations. Figure 7 depicts some of these trends.

Ore fluorite contains the highest values for U (mean ~13 ppm), Pb (mean ~4 ppm), and Th (mean ~3 ppm) of all the fluorite, with U the most elevated (Figure 7a,b). Of the vein fluorite, green fluorite is the most elevated in these elements, with generally higher Th (mean ~ 1.2 ppm) and Pb (mean ~ 4 ppm) and lesser U (mean ~ 0.1 ppm) (Figure 7a,b). White fluorite has virtually none of these elements. Also interesting is that ore fluorite shows a positive trend between Pb and U while the vein fluorite shows no trend (Figure 7a).

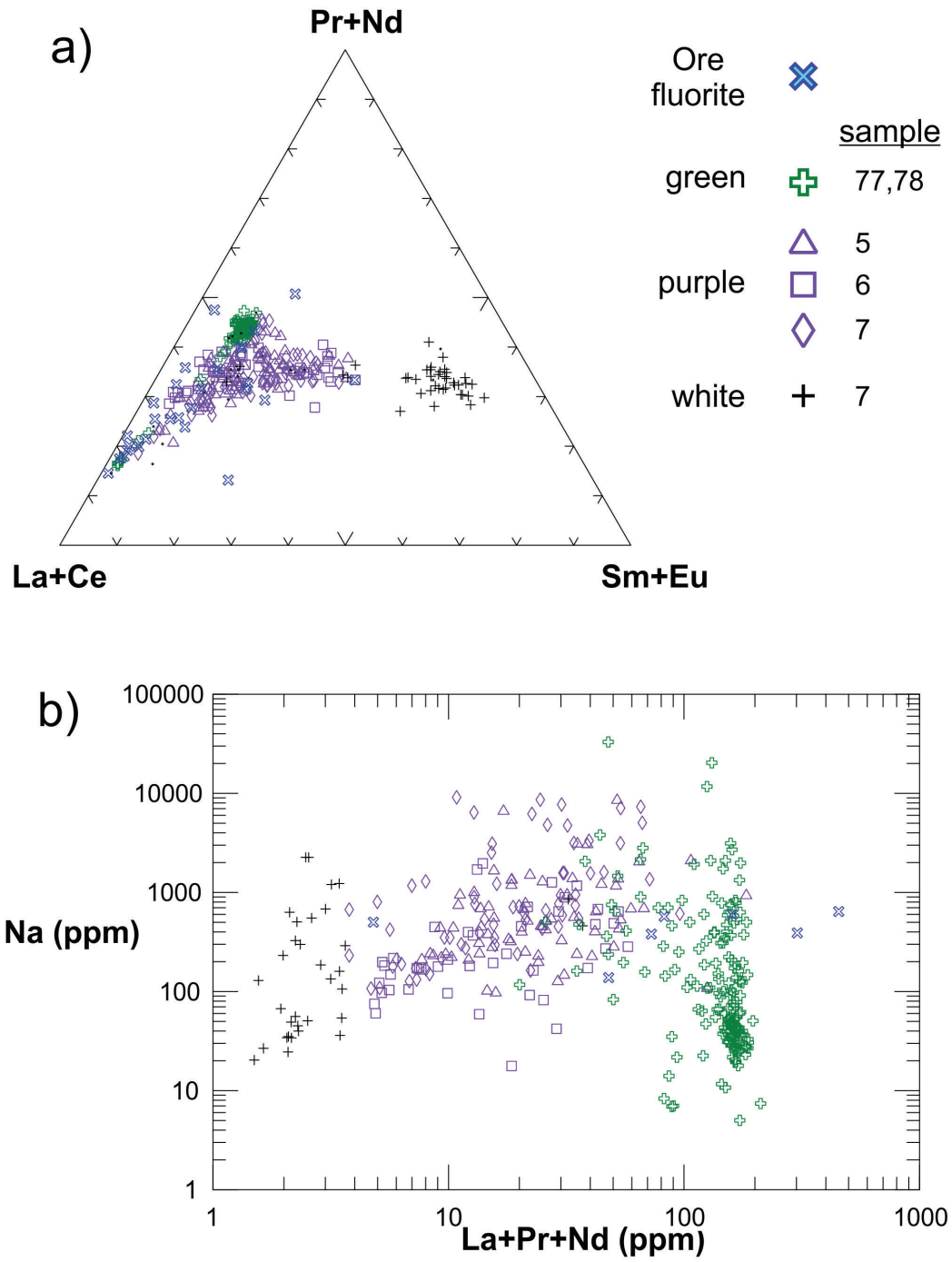


Figure 6: LA-ICP-MS data (ppm) comparing compositions of different fluorite types. **a)** Ternary plot comparing the relative values of (La+Ce), (Pr+Nd) and (Sm+Nd) in breccia- and vein-hosted fluorite. The fluorite from the ore grains are the most La and Ce-rich compared to the vein fluorite. Of the vein fluorite colors, purple shows a wide range of values, white is the most (Sm+Eu)-rich and depleted in the others (La, Ce, Pr, Nd) and green is generally slightly higher in Pr + Nd. **b)** Binary plot of log La+Pr+Nd, *i.e.*, trivalent LREE, vs. log Na. Green fluorite shows relative enrichment in LREE and Na does not have the general positive linear relationship seen in the ore, purple, and white fluorite.

There is a general positive trend for all vein fluorite in terms of Sr vs Ba (Figure 7c), both elements would substitute for Ca (Figure 4). Green and white fluorite show greater variation in Ba values while purple fluorite has a much broader range for both Ba and Sr; ore fluorite shows higher mean values for both Ba and Sr (mean ~18 and ~157 ppm, respectively) and a greater range in Sr concentrations than the vein fluorite, however there are fewer points and a trend is not strongly distinguished. In Figure 7d the purple and white fluorite show elevated Fe (mean ~165 and ~146 ppm) values compared to the green fluorite (mean ~72 ppm), while green shows on average higher Cu values (mean ~2 ppm). Ore fluorite has the most elevated Fe and Cu (mean ~1290 ppm and 40 ppm) values of all the analyzed fluorite. Anomalous high values of Fe in all fluorite are attributed to inclusions of hematite.

6. Discussion

The dataset shows distinct chemical differences between ore and vein fluorite, and between vein fluorites of different color, expressed both in ΣREY values and in chondrite-normalized fractionation trends. Among the other trace elements, the most distinguishing elements between the ore and vein fluorite are Pb and U. Vein fluorite may contain elevated Pb, and occasionally Th, and lesser U, without any identified consistency. Contrastingly, ore fluorite shows elevated values and a positive correlation between U and Pb. Variance in the dataset may, however, reflect the presence of micro- to nanoscale inclusions of U-minerals rather than lattice-bound U and Pb.

6.1 REE fractionation trends: implications for ore genesis

The majority of breccia-hosted (ore) fluorite likely formed during initial deposit formation from hydrothermal fluids during which time much of the available LREE would have been partitioned into REE-fluorocarbonates, chiefly bastnäsite [1,3]. The latter minerals preferentially incorporated LREE, and would thus lead to a relative HREE-enrichment in co-existing minerals, concordant with the fractionation trend for ore fluorite shown in Figure 5, which is enriched in HREE and Y compared to the deposit.

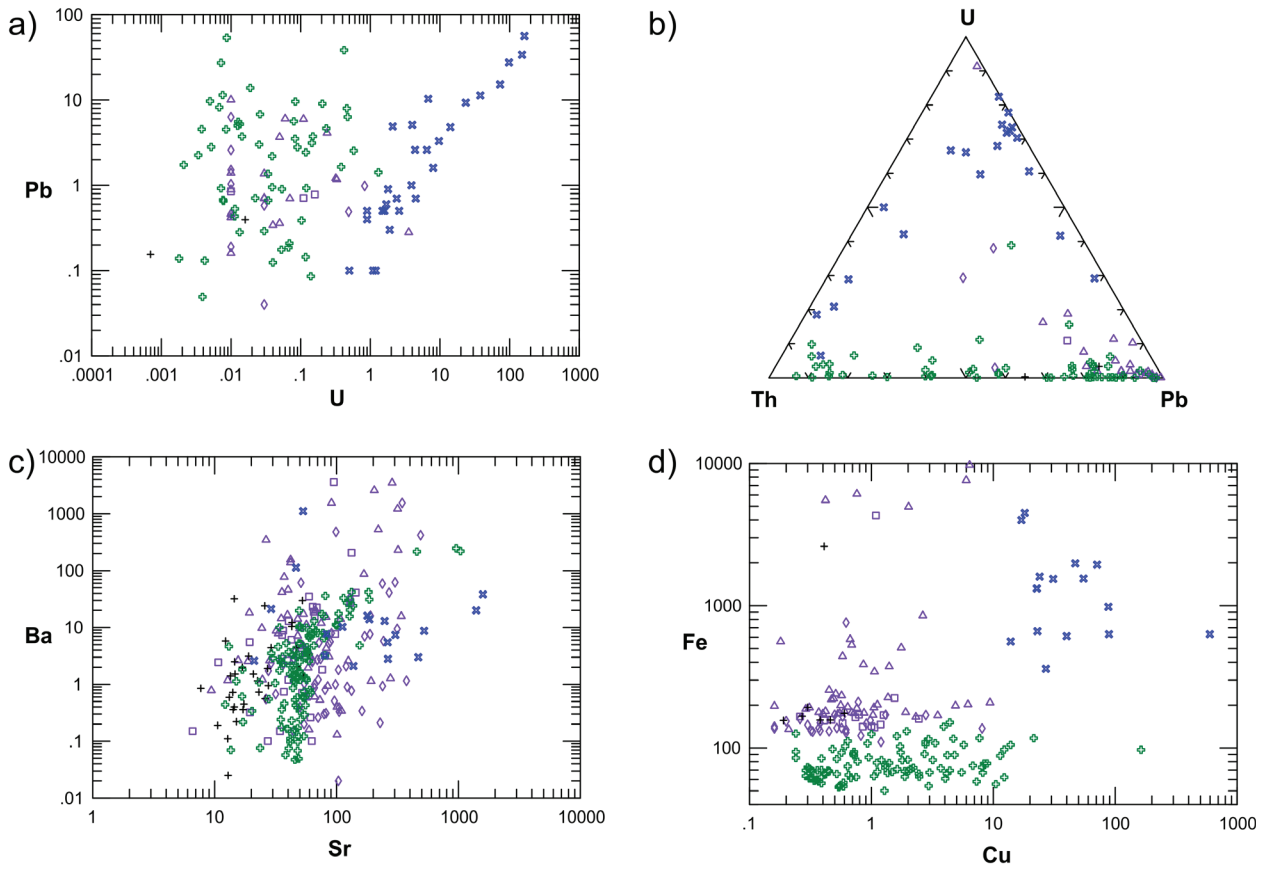


Figure 7: LA-ICP-MS trace element data for fluorite (in ppm). Symbols same as Figure 5. **a)** total Pb vs. U: most analysis were <LOD but those that are present show elevated U and Pb in ore fluorite compared to the vein fluorite, both breccia- and vein- fluorite show variable Pb but green vein fluorite is richest in Pb. White fluorite contains the least Pb and U. **b)** Tri-plot showing relative amounts of Th, U, and Pb in vein and ore fluorite. Ore fluorite is generally concentrated in U and Pb, purple vein fluorite in Pb, and green fluorite in Th and Pb. **c)** Ba vs. Sr plot showing generally positive correlation in the vein fluorites and weak to no correlation with ore fluorite. **d)** Fe vs. Cu showing clustering by fluorite type. White and purple fluorite have elevated Fe but lower Cu compared to the green fluorite. Ore fluorite is elevated in Fe and Cu compared to all vein fluorite.

The late, cross-cutting vein fluorite show distinct colors of purple, white, and green. Purple and white fluorite are most common, and, where they occur together, the purple and white fluorite exhibit a progressive sequence of crystallization from purple to white (Figure 3f). This color change is expressed chemically in terms of a relative depletion in LREE and other trace elements, while preserving consistent values for MREE and HREE and the Y anomaly, from purple fluorite on the vein edge to white fluorite in the vein center. The fractionation of LREE could be a result of differential REY solubility as fluoride complexes, which is greater for HREE and lower for LREE, causing LREE to precipitate first and maintain MREE and HREE concentration levels in the fluids as fluorite continues to crystallize [38]. The vein fluorites are

not enriched in LREE, despite being hosted in generally LREE-rich rocks, suggesting that the REY for the fluorite veins are not scavenged locally. The REY content of the veins could reflect fluid source and/or fractionation through transport of REY by SO_4- or Cl-ligands since these allow for greater MREE and HREE solubility over LREE [38].

The relative timing or relationship between the green fluorite and the purple/white fluorite veins is unknown, but color variations between the different vein fluorites appears to be dominantly controlled by mineral chemistry. Green fluorite contains relatively elevated concentrations of REY, Th, and Pb, possibly contributing to the color [39]. White fluorite is depleted in LREE and many trace elements, possibly explaining the lack of color; a similar conclusion was also reached by [40]. The purple fluorite has no particular chemical distinction, suggesting possibly, that an unmeasured element (Cl, or OH?), could be affecting color, or that there are other factors, such as defects in the crystal structure [39] or radiation damage. Purple fluorite is located adjacent to ore breccia which contains U, raising the possibility that natural irradiation may contribute to the purple color [41].

6.2 Other REE ratios

Ratios among the REE in fluorite can be indicative of the hydrothermal environment in which they formed (Figure 8). Patterns among LREE are the least consistent among the analyzed fluorite samples (Figure 8a), while the HREE *versus* Y show a distinct positive linear trend in all samples (Figure 8b). LREE can be more easily leached and (re)mobilized (as chloride complexes, [38]) and this may be reflected by the more chaotic LREE patterns observed compared to the MREE and HREE and Y trends.

The positive Y anomaly consistently observed across the sample suite is an example of crystallographic control in which the partition coefficient for Y in fluorite exceeds that of the adjacent REE, leading to preferential incorporation [44]. The positive Y anomaly is present neither in host granite (Figure 5) nor in other minerals such as apatite [2], or REE-fluorocarbonates [3]. Figure 8c shows that the Y anomaly is the lowest in the green fluorite and highest in the ore and purple fluorite. Bau and Dulski [42] suggested that a greater Y anomaly can be brought about by increased migration of fluids and interaction between rock/mineral and fluids. Schonenberger et al. [43] reported lower ΣREE and larger Y-anomalies in late-stage, lower temperature fluorite. If these interpretations are applicable here, then the green fluorite may have formed more proximal to its REY source, and possibly at higher temperatures, than the purple and white fluorite. The ore fluorite displays the greatest scatter, again, consistent with the heterogeneity of most minerals in the Olympic Dam deposit.

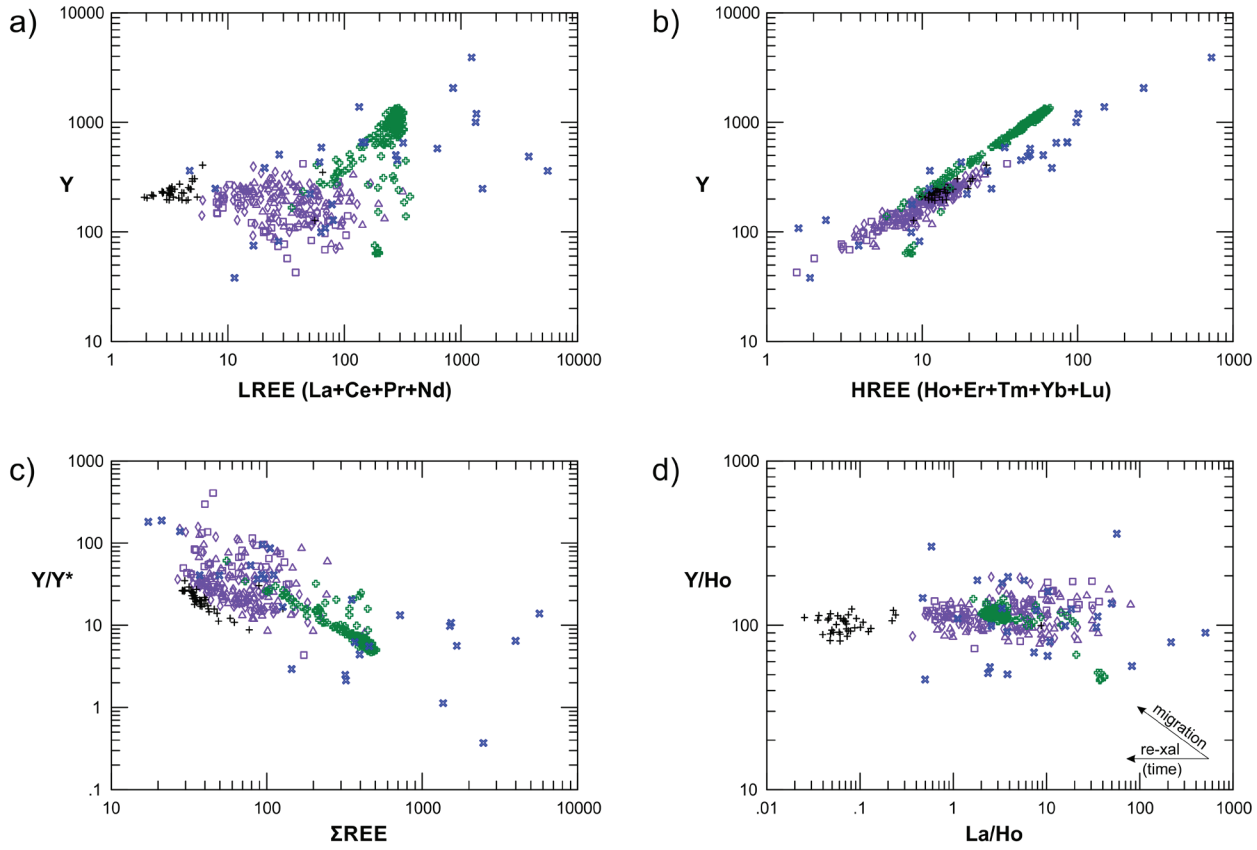


Figure 8: Plots of various REE ratios (from LA-ICP-MS ppm concentrations). Symbols are as in Figure 5. **a)** Y vs ∑LREE showing irregular clusters of differently colored vein fluorite and a wider spread of ore fluorite, generally only very weakly correlated. **b)** Y vs ∑HREE showing strong positive correlations in all samples. Green fluorite has a slightly different slope from the slope shared by the purple, white, and ore fluorite. **c)** Y anomaly (Y*=Y/((Dy*Ho)/2), from [43]) showing a negative trend of greater Y anomaly to ∑REE in all fluorite. The Y anomaly in the green fluorite with the most ∑REE while purple and white fluorite and, to an extent, the ore fluorite decreasing ∑REE with increasing Y anomaly. **d)** La/Ho vs Y/Ho from ppm concentrations modified from [42] and [45]. Green fluorite shows a negative trend suggested by [42] as representative of fluid migration while the purple to white fluorite shows a flat trend suggested to represent (re)crystallization (re-xal) of fluorite over time [42,45]. Ore fluorite shows no correlation.

Figure 8d compares the ratios Y/Ho *versus* La/Ho after Bau and Dulski [42] and Sizaret et al. [45]. Because of the similarity in atomic radii between Y and Ho, they are often expected not to fractionate greatly, which is consistent here with the order of magnitude lower variation of Y/Ho compared to the La/Ho ratio in all samples. The purple and white fluorite have a more limited range of Y/Ho than the green and ore fluorite; the wider range seen in the green and ore fluorite is suggestive of greater fractionation caused by fluid evolution or later remobilization [42,44]. The La/Ho ratio in ore fluorite is likely perturbed by precipitation of LREE-dominant minerals,

notably bastnäsite. Considering the complex, multi-stage, and highly heterogeneous nature of the Olympic Dam deposit, the wide range of both Y/Ho and La/Ho measured in breccia-hosted fluorite is not unexpected. Among the vein fluorites, white fluorite displays a limited range of La/Ho and Y/Ho, whereas the purple and green fluorite have extremely variable La/Ho ratios (Figure 8d). The wide range of La/Ho with minor Y/Ho variability, as seen in the purple fluorite, can also indicate post-crystallization processes resulting in partial loss of the more mobile REE and fractionation [42]. Sizaret et al. [45] interpreted a "movement" of data horizontally on the plot with lowering La/Ho ratios as relatable to time or progressive sequences of crystallization, comparable to the purple and white fluorite. The green fluorite shows a slight negative correlation between Y/Ho and La/Ho suggesting little alteration after crystallization, but may suggest greater migration, an interpretation at odds with the patterns implied from Figure 7c [42].

Regardless of the interpretations, the reproducibly distinct trends identified for the green compared to the purple/white fluorite, and between the vein and ore fluorite, is suggestive of different genetic histories for the two vein sets and the breccia-hosted fluorite. If these colored veins are similar to the vein sets identified by Oreskes and Einaudi [14], this study also supports different conditions for the colored veins. Overall, the breccia-hosted, green, and purple and white fluorite show variable chemical trends indicative of different mineralization histories; the lack of textural relationships between the green and purple/white vein fluorite limits interpretation, but the extreme chemical differences suggest different hydrothermal histories.

7. Conclusions

1) Hydrothermal fluorite is found within clasts and matrix throughout the Olympic Dam deposit. Coarse-grained colored fluorite is also a significant component of late hydrothermal veins, although volumetrically minor within the deposit.
2) Fluorite from late-stage veins has a different chemical signature compared to breccia-hosted fluorite. Color variations in vein fluorite identified on the macroscale likely reflect differences in REY and trace element chemistry.
3) Breccia-hosted fluorite is enriched in LREE and relatively depleted in HREE and displays variable chemistry, consistent with observed heterogeneity in other hydrothermal minerals. Ore fluorite also contains relatively elevated, although still low, values of Pb and U.
4) The purple to white vein fluorite paragenesis follows chemical patterns of progressive LREE and trace element depletion. Purple fluorite chemistry is remarkably consistent across different samples. Green fluorite contains elevated concentrations of REY, Th, and Pb relative to the white and purple fluorite.

5) Despite some similarities, the ore, purple/white, and green fluorite are chemically distinct from one another and likely do not share a common fluid source. Mineralizing conditions also likely differ.

Acknowledgements

This research is a contribution to the ARC Research Hub on Australian Copper-Uranium (project number: IH130200033), funded by the Australian Research Council, BHP Olympic Dam, and the South Australian Department of State Development.

Supplementary materials

Appendix A: LA-ICP-MS set up details

Appendix B: Complete LA-ICP-MS

Appendix C: EPMA methodology and set up details

Appendix D: Complete EPMA dataset

References

1. Ehrig, K.; McPhie, J.; Kamenetsky, V.S. Geology and Mineralogical Zonation of the Olympic Dam Iron Oxide Cu-U-Au-Ag Deposit, South Australia. In *Geology and Genesis of Major Copper Deposits and Districts of the World, a Tribute to Richard Sillitoe. Society of Economic Geology Special Publication*; Hedenquist, J.W.; Harris, M.; Camus, F. Eds.; SEG: Littleton, CO, USA, **2012**, *16*, 237–267, ISBN 1938-4548.
2. Krneta, S.; Ciobanu, C.L.; Cook, N.J.; Ehrig, K.; Kontonikas-Charos, A. Apatite at Olympic Dam, South Australia: a petrogenetic tool. *Lithos* **2016**, *53*, 1689–1699, doi:10.1017/CBO9781107415324.004.
3. Schmandt, D.S.; Cook, N.J.; Ciobanu, C.L.; Ehrig, K.; Wade, B.P.; Gilbert, S.; Kamenetsky, V.S. Rare earth element fluorocarbonate minerals from the Olympic Dam Cu-U-Au-Ag deposit, South Australia. *Minerals* **2017**, *7*, doi:10.3390/min7100202.
4. Eppinger, R.G.; Closs, L.G. Variation of Trace Elements and Rare Earth Elements in Fluorite: A Possible Tool for Exploration. *Econ. Geol.* **1990**, *85*, 1896–1907.
5. Gagnon, J.E.; Samson, I.M.; Fryer, B.J.; Williams-Jones, A.E. Compositional heterogeneity in fluorite and the genesis of fluorite deposits: Insights from LA-ICP-MS analysis. *Can. Mineral.* **2003**, *41*, 365–382.
6. Mao, M.; Simandl, G.J.; Spence, J.; Neetz, M.; Marshall, D. Trace element composition of fluorite and its potential use as an indicator in mineral exploration. In *Geological Fieldwork, 2015*; British Columbia Ministry of Energy and Mines, **2015**, 181–206.

7. Bill, H.; Calas, G. Color centers, associated rare-earth ions and the origin of coloration in natural fluorites. *Phys. Chem. Miner.* **1978**, *3*, 117–131, doi:10.1007/BF00308116.

8. Deer, W.A.; Howie, R.A.; Zussman, J. *An Introduction to the Rock-Forming Minerals*; 2nd ed.; Harlow, Essex, England : New York, NY: Longman Scientific & Technical, **1992**.

9. Calas, G.; Allard, T.; Balan, E.; Morin, G. Radiation-induced Defects in Nonradioactive Natural Minerals: Mineralogical and Environmental Significance. *Symp. R - Radiat. Eff. Ion Beam Process. Mater.* **2003**, *792*, R2.6, doi:10.1557/PROC-792-R2.6

10. Dill, H.G.; Weber, B. Variation of color , structure and morphology of fluorite and the origin of the hydrothermal F-Ba deposits at Nabburg- Wölsendorf, SE Germany. *N. Jahrb. Mineral. Abh.* **2010**, *187*, 113–132, doi:10.1127/0077-7757/2010/0169.

11. Bevan, D.J.M.; Strähle, J.; Greis, O. The crystal structure of tveitite, an ordered yttrofluorite mineral. *J. Solid State Chem.* **1982**, *44*, 75–81, doi:10.1016/0022-4596(82)90402-9.

12. Sverdrup, T.L. Contribution to the Mineralogy of Norway no. 37: Yttrofluorite-yttrocerite-cerfluorite in Norwegian Pegmatites. *Norsk geol. Tidsskr.* **1968**, *48*, 245–252.

13. Roberts, D.E.; Hudson, G.R.T. The Olympic Dam Copper-Uranium-Gold Deposit, Roxby Downs, South Australia. *Econ. Geol.* **1983**, *78*, 799–822.

14. Oreskes, N.; Einaudi, M.T. Origin of hydrothermal fluids at Olympic Dam: preliminary results from fluid inclusions and stable isotopes. *Econ. Geol.* **1992**, *87*, 64–90, doi:10.2113/gsecongeo.87.1.64.

15. Krneta, S.; Ciobanu, C.L.; Cook, N.J.; Ehrig, K.; Kontonikas-Charos, A. Rare earth element behaviour in apatite from the Olympic Dam Cu-U-Au-Ag deposit, South Australia. *Minerals* **2017**, *7*, 135, doi:10.3390/min7080135.

16. Kontonikas-Charos, A.; Ciobanu, C.L.; Cook, N.J.; Ehrig, K.; Krneta, S.; Kamenetsky, V.S. Feldspar evolution in the Roxby Downs Granite, host to Fe-oxide Cu-Au-(U) mineralisation at Olympic Dam, South Australia. *Ore Geol. Rev.* **2017**, *80*, 838–859, doi:10.1016/j.oregeorev.2016.08.019.

17. Macmillan, E.; Ciobanu, C.L.; Ehrig, K.; Cook, N.J.; Pring, A. Chemical zoning and lattice distortion in uraninite from Olympic Dam, South Australia. *Am. Mineral.* **2016**, *101*, 2351–2354, doi:10.2138/am-2016-5753.

18. Macmillan, E.; Cook, N.J.; Ehrig, K.; Pring, A. Chemical and textural interpretation of late-stage coffinite and brannerite from the Olympic Dam IOCG-Ag-U deposit. *Mineral. Mag.* **2017**, *81*, 1323–1366, doi:10.1180/minmag.2017.081.006.

19. McPhie, J.; Kamenetsky, V.; Allen, S.; Ehrig, K.; Agangi, A.; Bath, A. The fluorine link between a supergiant ore deposit and a silicic large igneous province. *Geology* **2011,** *39*, 1003–1006, doi:10.1130/G32205.1.

20. Apukhtina, O.B. Distribution, petrology, geochemistry and geochronology of carbonate assemblages at the Olympic Dam deposit. Unpublished Ph.D. thesis, University of Tasmania, Hobart, **2016**, https://eprints.utas.edu.au/23013/

21. Apukhtina, O.B.; Ehrig, K.J.; Kamenetsky, V.S.; Kamenetsky, M.B.; Geomann, K.; Maas, R.; McPhie, J.; Ciobanu, C.L.; Cook, N.J. Carbonates in the Olympic Dam Cu-U-Au-Ag deposit. Part I: Distribution, textures, associations and stable isotope (C, O) signatures. *Ore Geol. Rev. in preparation*.

22. Maas, R.; Apukhtina, O.B.; Kamenetsky, V.S.; Ehrig, K.J.; Sprung, P. Carbonates at the supergiant Olympic Dam deposit, South Australia. Part II: Radiogenic isotopes (Sr, Nd, Pb, Hf). *in*

preparation.

23. Preiss, W.V. The Adelaide Geosyncline: Late Proterozoic stratigraphy, sedimentation, palaeontology and tectonics. Geological Survey of South Australia Bulletin 53, *Dep. Mines Energy* **1987**.
24. Sugden, T.J.; Cross, K.C. Significance of overprinting fault systems in the Olympic Dam Breccia Complex. In *Structural Geology in Mining and Exploration*; Geology Department (Key Centre) & University Extension, The University of Western Australia, **1991**, 93–98.
25. Maas, R.; Kamenetsky, V.S.; Ehrig, K.J.; Apukhtina, O.B.; Kamenetsky, V.S.; Ehrig, K.; Meffre, S.; McPhie, J.; Diemar, G. Olympic Dam U-Cu-Au deposit, Australia: New age constraints. *Mineral. Mag.* **2011**, *75*, 1375.
26. Johnson, J.P. The Geochronology and Radiogenic Isotope Systematics of the Olympic Dam Copper-Uranium-Gold-Silver deposit, South Australia. Unpublished PhD thesis, Australian National University, **1993,** https://openresearch-repository.anu.edu.au/handle/1885/10918.
27. Ciobanu, C.L.; Wade, B.P.; Cook, N.J.; Schmidt Mumm, A.; Giles, D. Uranium-bearing hematite from the Olympic Dam Cu-U-Au deposit, South Australia: A geochemical tracer and reconnaissance Pb-Pb geochronometer. *Precambrian Res.* **2013**, *238*, 129–147, doi:10.1016/j.precamres.2013.10.007.
28. Schmandt, D.S.; Cook, N.J.; Ehrig, K.J.; Gilbert, S.; Wade, B.; Rollog, M.; Ciobanu, C.L.; Kamenetsky, V.S. Uptake of trace elements by baryte during copper ore processing: a case study from Olympic Dam, South Australia. *Miner. Eng.* **2019***,* 135, 83-94. doi: 10.1016/j.mineng.2019.02.034.
29. Bierlein, F.P.; Foster, D.A.; Plimer, I.R. Tectonotermal implications of laser $^{40}Ar/^{39}Ar$ ages of sulphide-bearing veins and their host rocks in in the Willyama Supergroup, South Australia. *Mineral. Petrol.* **1996**, *58*, 1–22.
30. Webster, A.E. The Structural Evolution of the Broken Hill Pb-Zn-Ag Deposit, New South Wales, Unpublished PhD Thesis, University of Tasmania **2004**, 430.
31. Brugger, J.; Ogierman, J.; Pring, A.; Waldron, H.; Kolitsch, U. Origin of the secondary REE - minerals at the Paratoo copper deposit near Yunta , South Australia. *Mineral. Mag.* **2006**, *70*, 609–627, doi:10.1180/0026461067060361.
32. Foden, J.; Elburg, M.A.; Dougherty-Page, J.; Burtt, A. The Timing and Duration of the Delamerian Orogeny: Correlation with the Ross Orogen and Implications for Gondwana Assembly. *J. Geol.* **2006**, *114*, 189–210, doi:10.1086/499570.
33. Domnick, U; Cook, N.J.; Bluck, R.; Brown, C.; Ciobanu, C.L. Petrography of granitoids from the Samphire Pluton, South Australia: implications for uranium mineralisation in overlying sediments. *Lithos* **2018**, *300*, 1–19.
34. Jackson, S.E.; Longerich, H.P.; Dunning, G.R.; Fryer, B.J. The application of laser-ablation microprobe - inductively coupled plasma- mass spectrometry (LAM-ICP-MS) to in situ trace-element determinations in minerals. *Can. Mineral.* **1992**, *30*, 1049–1064.
35. Sylvester, P. Laser Ablation–ICP–MS in the Earth Sciences Current Practices and Outstanding Issues. *Mineralogical Association of Canada Short Course* **2008**, *40*.
36. Paton, C.; Hellstrom, J.; Paul, B.; Woodhead, J.; Hergt, J. Iolite: Freeware for the visualisation and processing of mass spectrometric data. *J. Anal. At. Spectrom.* **2011**, *26*, 2508.
37. McDonough, W.F.; Sun, S.S. Composition of the Earth. *Chem. Geol.* **1995**, *120*, 223–253.

38. Migdisov, A.; Williams-Jones, A.E.; Brugger, J.; Caporuscio, F.A. Hydrothermal transport, deposition, and fractionation of the REE: Experimental data and thermodynamic calculations. *Chem. Geol.* **2016**, *439*, 13–42, doi:10.1016/j.chemgeo.2016.06.005.

39. Allen, R.D. Variations in Chemical and Physical Properties of Fluorite. *Am. Mineral.* **1952**, *37*, 910–930.

40. Eppinger, R.G. Trace element and rare earth element variation in fluorites collected from skarn and epithermal mineral deposits in the Sierra Cuchillo area, south-central New Mexico. *USGS*. **1988**, Open-File Report 88-566, 108.

41. Berman, R. Some Physical Properties of Naturally Irradiated Fluorite. *USGS Trace Elem. Investig.* **1956**, *Report 372*, 191–203, doi:10.3133/tei569.

42. Bau, M.; Dulski,P. Comparative study of yttrium and rare-earth element behaviours in fluorine-rich hydrothermal fluids. *Contrib Miner. Pet.* **1995**, *119*, 213–223.

43. Schönenberger, J.; Köhler, J.; Markl, G. REE systematics of fluorides, calcite and siderite in peralkaline plutonic rocks from the Gardar Province, South Greenland. *Chem. Geol.* **2008**, *247*, 16–35, doi:10.1016/j.chemgeo.2007.10.002.

44. Veksler, I.V.; Dorfman, A.M.; Kamenetsky, M.; Dulski, P.; Dingwell, D.B. Partitioning of lanthanides and Y between immiscible silicate and fluoride melts , fluorite and cryolite and the origin of the lanthanide tetrad effect in igneous rocks. *Geochim. Cosmochim. Acta.* **2005**, *69*, 2847–2860, doi:10.1016/j.gca.2004.08.007.

45. Sizaret, S.; Marcoux, E.; Jébrak, M.; Touray, J.C. The Rossignol Fluorite Vein, Chaillac, France: Multiphase hydrothermal activity and intravein sedimentation. *Econ. Geol.* **2004**, *99*, 1107–1122, doi:10.2113/gsecongeo.99.6.1107.

CHAPTER 6

LEAD CHALCOGENIDES AND PB-ISOTOPE SIGNATURE IN ORES AND CONCENTRATES FROM OLYMPIC DAM DEPOSIT, SOUTH AUSTRALIA

Danielle S. Schmandt [1], Nigel J. Cook [1], Kathy J. Ehrig [2], Cristiana L. Ciobanu [1], Nicholas D. Owen [1], Max R. Verdugo-Ihl [1], Benjamin P. Wade [3]

[1] School of Chemical Engineering, The University of Adelaide, Adelaide, SA 5005, Australia

[2]BHP Olympic Dam, Adelaide, SA, 5000, Australia

[3] Adelaide Microscopy, The University of Adelaide, Adelaide, SA 5005, Australia

Statement of Authorship

Title of Paper	Lead chalcogenides and Pb-isotope signature in ores and concentrates from Olympic Dam deposit, South Australia
Publication Status	☐ Published ☐ Accepted for Publication ☐ Submitted for Publication ☑ Unpublished and Unsubmitted work written in manuscript style
Publication Details	

Principal Author

Name of Principal Author (Candidate)	Danielle S. Schmandt		
Contribution to the Paper	Performed analytical work, carried out data processing and interpretation, oversaw development of work, and wrote manuscript.		
Overall percentage (%)	65		
Certification:	This paper reports on original research I conducted during the period of my Higher Degree by Research candidature and is not subject to any obligations or contractual agreements with a third party that would constrain its inclusion in this thesis. I am the primary author of this paper.		
Signature		Date	Dec 3rd, 2018

Co-Author Contributions

By signing the Statement of Authorship, each author certifies that:

i. the candidate's stated contribution to the publication is accurate (as detailed above);

ii. permission is granted for the candidate in include the publication in the thesis; and

iii. the sum of all co-author contributions is equal to 100% less the candidate's stated contribution.

Name of Co-Author	Nigel J. Cook		
Contribution to the Paper	10%; Helped define direction of research, supervised development of work, assisted with data interpretation, and contributed to manuscript preparation.		
Signature		Date	5/12/2018

Name of Co-Author	Kathy Ehrig		
Contribution to the Paper	5%; Provided sample material, helped define direction of research, assisted with data interpretation, and helped to evaluate and edit manuscript.		
Signature		Date	10/12/18

Name of Co-Author	Cristiana L. Ciobanu		
Contribution to the Paper	5%; Contributed to manuscript preparation and helped to evaluate and edit manuscript.		
Signature		Date	5/12/2018

Name of Co-Author	Nicholas D. Owen		
Contribution to the Paper	5%; Contributed to manuscript preparation and helped to evaluate and edit manuscript		
Signature		Date	06/12/2018

Name of Co-Author	Max R. Verdugo-Ihl		
Contribution to the Paper	5%; Contributed sample material and helped to evaluate and edit manuscript.		
Signature		Date	6/12/18

Name of Co-Author	Benjamin P. Wade		
Contribution to the Paper	5%; Assisted in operating analytical instrumentation and data processing.		
Signature		Date	11/12/18

Lead chalcogenides and Pb-isotope signature in ores and concentrates from Olympic Dam deposit, South Australia

Danielle S. Schmandt [1,*], Nigel J. Cook [1], Kathy Ehrig [2], Cristiana L. Ciobanu [1], Nicholas D. Owen [1], Max R. Verdugo-Ihl [1], Benjamin P. Wade [3]

[1] *School of Chemical Engineering, The University of Adelaide, Adelaide, SA 5005, Australia*

[2] *BHP Olympic Dam, Adelaide, SA, 5000, Australia*

[3] *Adelaide Microscopy, The University of Adelaide, Adelaide, SA 5005, Australia*

Abstract

Olympic Dam (OD) is one the largest copper-gold deposits on Earth and the World's largest known uranium resource. Radioactivity associated with the ^{238}U, ^{235}U, and ^{232}Th decay chains necessitates a mineralogical-geochemical understanding of radionuclide distributions in ore and throughout the processing cycle. Previous lead isotope studies at OD are based on whole rock assays or target specific minerals for U-Pb geochronology. None have addressed the Pb isotopic composition of Pb-chalcogenide species within the ore, or the variability of Pb-isotope ratios at the mineral- and deposit-scales. Elemental and isotopic data was obtained on Pb-minerals in flotation concentrates and selected ore samples from across the deposit using *in-situ* laser-ablation inductively coupled plasma mass spectrometry. Lead isotope ratios of galena, clausthalite, and altaite define a range of signatures. Most are strongly radiogenic, although non-radiogenic minerals are also identified, notably in samples from the deposit margins. Variability of Pb-isotope signatures, both spatially and with respect to relative contributions from ^{238}U, ^{235}U, and ^{232}Th decay, has broad scale implications for the evolution of the OD deposit. The range of isotopic signatures is suggestive of cyclicity of uranium and lead dissolution, remobilization, recrystallization, and mixing of signatures; an interpretation compounded by the observation of U-minerals included within non-radiogenic galena, and an absence of U-minerals associated with some of the most highly radiogenic grains. It is proposed that some non-radiogenic Pb was introduced at the time of initial ore formation. The dominant feature of the dataset is, however, the broad variation, which can be attributed to localized remobilization processes and isotopic mixing. Although the timing of these fluid-driven events cannot be directly constrained, we assume that they occurred multiple times throughout the evolutionary lifetime of the deposit. Lead-isotope ratios in Pb-chalcogenides also offer indirect insights into likely mineral hosts for deleterious short-half-life radionuclides resulting from ^{238}U decay. The results provide compelling evidence for U and Pb mobility as well as deposit and grain-scale decoupling of U and Th-decay isotopes.

Keywords: Olympic Dam; IOCG deposits; galena; Pb-isotopes; radionuclides

INTRODUCTION

^{204}Pb, ^{206}Pb, ^{207}Pb, and ^{208}Pb are the four most abundant stable Pb isotopes on Earth. ^{238}U, ^{235}U, and ^{232}Th introduced at that time have since decayed, gradually decreasing in abundance, whereas their respective stable end-of- chain products (^{206}Pb, ^{207}Pb, and ^{208}Pb, respectively) have increased. Among lead isotopes, ^{204}Pb is the only isotope present in the same abundance now as at the time of Earth's formation.

Lead isotopes and their ratios serve as useful exploration tracer tools for vectoring to uranium and lead/base metal deposits (Rosholt et al. 1973, Holk et al. 2003, Beyer et al. 2012), support fluid evolution models for both deposit- and regional-scale hydrothermal systems (Champion and Huston 2016, McFarlane et al. 2016), and provide the foundations for precision U-Pb geochronology (Mattinson 2013). *In-situ* analysis of Pb-isotopes in minerals via e.g., laser-ablation inductively-coupled plasma mass spectrometry (LA-ICP-MS; Woodhead et al. 2009, Darling et al. 2012, McFarlane et al. 2016), allows for acquisition of isotopic signatures with grain-scale resolution.

The Olympic Dam (OD) Cu-U-Au-Ag iron-oxide copper gold (IOCG) deposit, South Australia, is one of the largest ore deposits in the world and the single largest uranium resource (10,410 Mt @ 0.78% Cu, 250 ppm U_3O_8, 0.33 ppm Au, 1 ppm Ag; BHP 2018). The deposit is also significantly enriched in Th, REE, and many other trace elements relative to crustal values (Ehrig et al. 2012, 2017). One of these anomalous elements is Pb, although Pb-minerals reported so far, the chalcogenides galena (PbS), altaite (PbTe), and clausthalite (PbSe), are only very minor components, comprising just ~0.0014 wt. % of the entire deposit (based on 10,000 sample MLA dataset, Ehrig et al. 2012).

Published Pb-isotope data for OD and have largely focused on analysis of host rocks to establish potential crustal reservoirs (Chapman et al. 2016), or for fingerprinting of concentrates (Švedkauskaitė-LeGore et al. 2007, Varga et al. 2009). Data for OD "uranium

ore" given by Švedkauskaitė-LeGore et al. (2007) shows significant variation in the proportions of all four stable Pb isotopes from sample to sample. Meffre et al. (2010) provided Pb-isotope data for pyrite, chalcopyrite and galena in ore samples from different parts of the deposit. $^{207}Pb/^{206}Pb$ ratios were found to vary between 0.93 and 0.75. Strongly radiogenic sulfides were documented in late veins ($^{207}Pb/^{206}Pb$ between 0.12 and 0.13 with very low ^{204}Pb). These results suggest that distinct Pb-isotope ratios are preserved in individual sulfide grains, and that the deposit contains Pb from different sources with only partial homogenization at the grain scale. Courtney-Davies et al. (2019) also show Pb isotope heterogeneity within grains of zoned hematite grains from OD. The study demonstrates both the large variability of Pb isotope ratios possible within single crystals but also the preservation of isotopically homogeneous zones that can be successfully dated.

The present study provides a first glimpse into Pb-isotope compositions in Pb-chalcogenides from the OD system and demonstrates the variability of primordial *vs*. radiogenic Pb signatures within the deposit. Detailed mineralogical studies such as this continue to provide clues to further unravel the mineralization history of OD, one of the largest and most complex ore bodies in the world.

BACKGROUND

Ores at OD are complex, fine-grained, and contain more than 100 different minerals (Ehrig et al. 2012). The mine produces by-product uranium oxide concentrate (U_3O_8), with ~90% of U occurring as uraninite, brannerite, and coffinite (Macmillan et al. 2016, 2017), and the remainder substituted within hematite (Ciobanu et al. 2013) and other gangue minerals. Galena is a minor phase (0.0012 wt. %, based on a 10,000 sample MLA dataset, Ehrig et al. 2012) and occurs in a range of mineral assemblages. Fine-grained, often sub-microscopic galena is observed enclosed within, or immediately adjacent to uraninite or other U-bearing minerals

(e.g., abundant and characteristic galena inclusions in metamict zircon), as well as with other sulfides or gangue. Less common Pb-chalcogenides are clausthalite and altaite; 0.0002 and <0.0001 wt. %, respectively (Ehrig et al. 2012). Lead minerals are volumetrically minor but display deposit-scale zonation in which the highest Pb concentrations are observed on the deposit margins, mostly present as galena (Ehrig et al. 2012).

Other Pb-bearing minerals include uraninite (up to 12 wt. % Pb in preserved, early sub-types; Macmillan et al. 2016), brannerite and coffinite (up to ~4 wt. %; Macmillan et al. 2017), and hematite (thousands of ppm to several wt. % in U-rich hematite; Ciobanu et al. 2013, Verdugo-Ihl et al. 2017). Parts-per-million-level concentrations of Pb are also measured in fluorapatite (Krneta et al. 2017), REE-fluorocarbonates, -phosphates and phosphate-sulfates (Schmandt et al. 2017, 2019a, Owen et al. in review), baryte (Schmandt et al. 2019b), some carbonates (Apukhtina 2016), and other accessory minerals including zircon and thorite.

Several minerals from OD have been successfully dated using U-Pb geochronology, including igneous, hydrothermal, and sedimentary zircon (Creaser and Cooper 1993, Johnson 1993, Johnson and Cross 1995, Jagodzinski, 2005, 2014, McPhie et al. 2016, Cherry et al. 2017, 2018a), uraninite (Reed et al. 1987, Apukhtina et al. 2017) and hematite (Ciobanu et al. 2013, Courtney-Davies et al. 2016, 2019). These studies have identified a main formation event at ~1590 Ma during which hydrothermal fluids supplied Cu, U, Fe, and other ore components. There are, however, evidence of at least three superimposed tectonothermal events that have impacted on the deposit. Among these, dating of apatite and titanite from cross-cutting dolerite dykes gives an age of ~825 Ma associated with Rodinia break-up (Huang et al. 2015, Apukhtina et al. 2016), whereas other age data infer a significant ~500 Ma resetting during Delamerian tectonism (Kamenetsky et al. 2015). Other published U-Pb and Pb-Pb (Ciobanu et al. 2013, Courtney-Davies et al. 2016, 2019), Sm-Nd fluorite (Maas et al. 2011), Re-Os molybdenite (McInnes et al. 2008) and monazite Th–Pb and xenotime U–Pb ages (Cherry et al. 2018b)

represent further evidence for complex deposit evolution, including a yet ill-defined overprinting event at 1.4-1.2 Ga. These multiple ages are supported by textural evidence among different minerals for multiple cycles of replacement, remobilization and recrystallization of individual minerals (Macmillan et al. 2016, 2017, Verdugo-Ihl et al. 2017). Lastly, Kirchenbaur et al. (2016) provided high-precision $^{238}U/^{235}U$ evidence coincident with an origin of uranium from the host 1593 Ma granitoid, associated felsic volcanic rocks and similar igneous crustal sources but with a signature that doesn't preclude input of younger uranium.

SAMPLING

This study includes analysis of five samples from three spatially distinct zones of the deposit known to contain Pb-minerals (Fig. 1). These samples are: (1) two drill core samples, located a few cm apart, from underground drillhole RU27-7550 intersecting hematite breccia on the NW arm of the deposit near the resource edge; (2) two drill core samples, ~6 m apart, from hematite breccia in drillhole RD3554 from the SE edge of the deposit; and (3) a single grab sample from underground mining operations in the barren quartz-hematite breccia in the center of the deposit. Summary sample descriptions and Pb isotope data can be found in Appendix A. Lead minerals are uncommon at Olympic Dam, however Pb minerals can be found more frequently in the deposit margins, as sampled here.

These rock samples are supplemented by Pb-chalcogenides in a suite of Cu-sulfide flotation concentrate samples. Studying concentrate material has the advantage of providing minerals representative of multiple parts of the deposit, at least those under exploitation at that time. However, using concentrate material is particularly helpful in this study since the Pb-minerals at OD are sparse and fine-grained in the ore samples. From the concentrate material, seven size fractions (consecutively sized from >53 μm to <7 μm) mounted onto individual ~25 mm blocks were investigated. Each of these blocks contained ~40 to 80 grains of lead minerals larger than

3 μm in size.

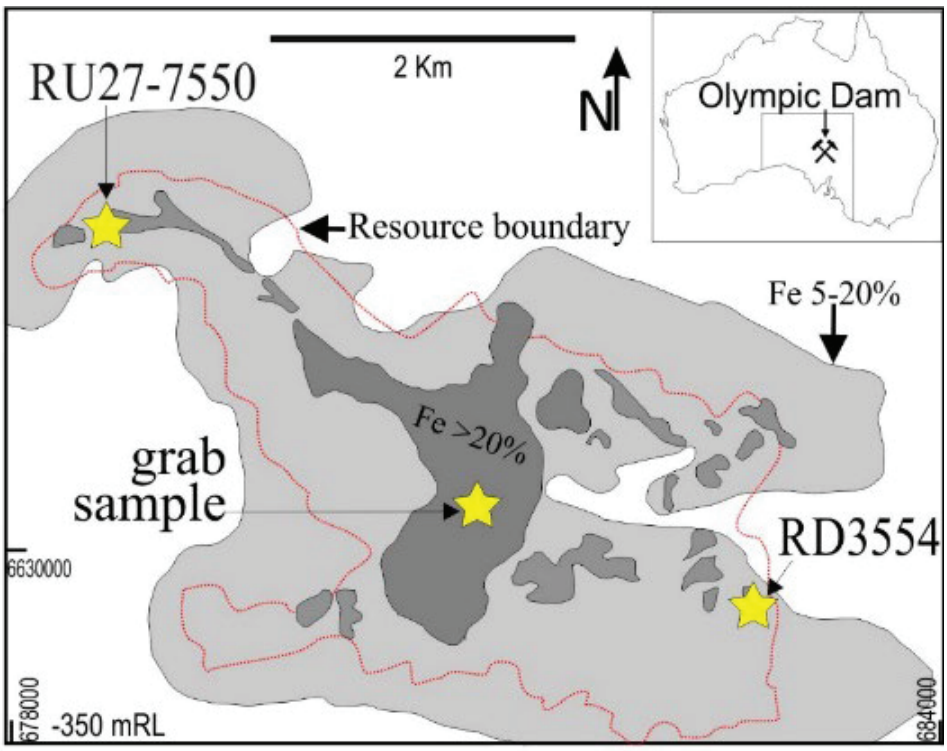


Figure 1: Simplified resource map of Olympic Dam (after Ehrig et al. 2012) with rock sample locations (stars). Inset map of Australia with location of OD marked.

ANALYTICAL METHODOLOGY

Samples were characterized using reflected light petrography and SEM analysis using a Quanta 450 Field Emission Gun (FEG) SEM with silicon-drift detector (Adelaide Microscopy (AM); University of Adelaide). Elemental assays from drill core composites taken every foot for samples in RD3554 were available from company data.

Mineral Liberation Analyser (MLA; Gu, 2003) data was used to describe the overall abundance and association of Pb minerals within ore concentrate samples. MLA generates quantitative mineralogy and mineral relationship frequency data and is thus well suited to characterization of heterogenous mineral particles. Full MLA analysis was carried-out on identical sample material by ALS Brisbane. Size fractions used for this study included grains

sized >53 μm and 26-53 μm due to analytical size constraints on in-situ grain analysis. Bulk assay values of these samples from company data were also made available.

Elemental and isotopic analysis was performed via LA-ICP-MS using an ASI M50 laser ablation system coupled to an Agilent 7700s ICP-MS mass spectrometer (AM). NIST610 glass and MASS-1 were used as standard reference material with non-radiogenic galena from Kabwe, Zambia (Kamona et al. 1999) and Broken Hill, Australia (Cumming and Richards, 1975) as internal standards. Ablation conditions followed McFarlane et al. (2016), modified to accommodate smaller grain sizes when necessary. Isotopes measured were ^{82}Se, ^{125}Te, ^{201}Hg, ^{202}Hg, ^{203}Tl, ^{204}Pb, ^{205}Tl, ^{206}Pb, ^{207}Pb, ^{208}Pb, ^{209}Bi, ^{232}Th, ^{235}U, and ^{238}U. Dwell times were 0.1 s for Pb isotopes, 0.05 s for Tl and Hg isotopes, 0.02 s for Th and U isotopes, and 0.01 for Bi, Te, and Se. Data reduction was performed using the software Iolite v3.4 (Paton et al. 2011). Data was processed using the "Pb Isotopes FarIC" (Paul et al. 2011) data reduction scheme. Data were not plotted if errors on the plotted axes exceeded 10%. Full dataset of measured Pb ratio values are available in Appendix B.

RESULTS

Sample descriptions and petrography

In the Cu-sulfide concentrate samples, the most common grain size for galena, clausthalite, and altaite is <5 μm, however much of the analysis reported here was conducted on coarser grains of these minerals due to analytical constraints. According to accumulated MLA data from Cu concentrate material, both altaite and clausthalite are chiefly associated (i.e., share common boundaries) with bornite, then chalcocite, and then chalcopyrite. In contrast, galena is associated with chalcopyrite, pyrite, and then chalcocite. When not associated with sulfides, all three minerals are most commonly associated with hematite. Clausthalite can be texturally

distinct, occurring as semi-regular, and commonly spherical inclusions locked within host Cu-(Fe)-sulfides (Fig. 2a). In the present samples, rare altaite displays comparable textures and shares the same host minerals as clausthalite.

In drill core samples from the NW arm (RU27-7550), galena is the only Pb-mineral identified within a complex sulfide (pyrite-chalcopyrite-bornite-sphalerite-carrollite-cobaltite) and non-sulfide (hematite-quartz-baryte-fluorite-bastnäsite-florencite) assemblage. Galena occurs in a variety of textures (Fig. 2b-f). Galena may be up to 100 μm in size and always contains inclusions of other minerals, including commonly sphalerite, Cu-(Fe)-sulfides, and hematite (Fig. 2b). Galena displays several, often conflicting, textural relationships with U-minerals in that galena can envelope uraninite (Fig. 2c), contain inclusions of U-minerals, and can even have a rim of uraninite (Fig. 2d). Galena displays a net-like texture when intergrown with Cu-(Fe)-sulfides (Fig. 2e) and sometimes displays scalloped edges when with gangue hematite and quartz (Fig. 2f).

Lead minerals identified in samples from the SE edge, RD3554, are mostly galena (Fig. 3a-c) and some altaite (Fig. 3d). The Pb minerals generally do not exceed 50 μm in size (mostly <20 μm), and are always intergrown with, or occur as inclusions within, other minerals. The two adjacent samples analyzed from this drill core, RX7319 and RX7316, are both from zones of fine-grained breccia, with disseminated and 'clots' of Cu sulfides, and minor Pb minerals. In sample RX7319, the Pb minerals are limited to a few small clusters of mostly fine-grained rounded inclusions in gangue minerals, often sphalerite (Fig. 3a) or quartz. Rarely galena occurs with copper sulfides and is then more angular and irregular in texture (Fig. 3b). In sample RX7316 the galena and altaite occur consistently with Cu-(Fe)-sulfides, mostly chalcocite (Fig. 3c, d) and some bornite. This sample, RX7319, contains a greater abundance of U- and REE-minerals than RX7316. Sample RX7316 contains more sphalerite and also tourmaline.

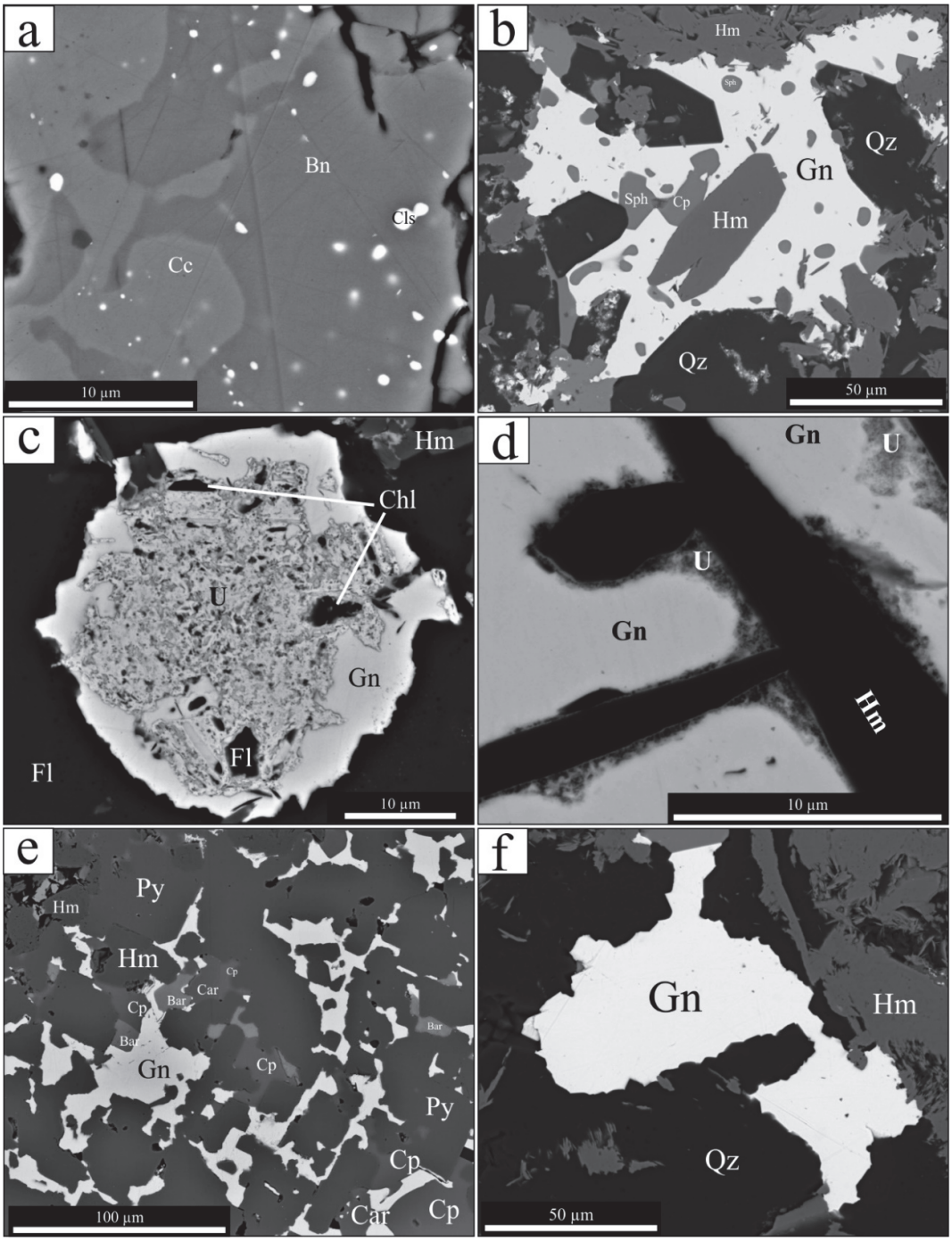


Figure 2: Backscatter electron (BSE) images of Pb-minerals in ore concentrate (a) and sample RU27-7550 (b-f). **(a)** Chalcocite (Cc) - bornite (Bn) particle from flotation concentrate (>53 µm fraction) with typical rounded inclusions of clausthalite (Cls, brightest phase). **(b)** Coarse galena (Gn) with rounded and elongate inclusions of sphalerite (Sph), chalcopyrite (Cp) and a large rounded hematite grain (Hm). Galena is located around subhedral quartz (Qz) partially replaced by hematite. **(c)** Galena surrounding uraninite (U) containing inclusions of fluorite (Fl) and chlorite (Chl), also enclosed by fluorite and minor hematite. **(d)** Galena rimmed by porous uraninite between coarse laths of hematite. **(e)** Net-textured galena within pyrite (Py) with minor chalcopyrite, carrollite (Car), and baryte (Bar) and hematite on the margins. **(f)** Coarse galena with hematite inclusions and scalloped margins against enveloping quartz indicative of replacement.

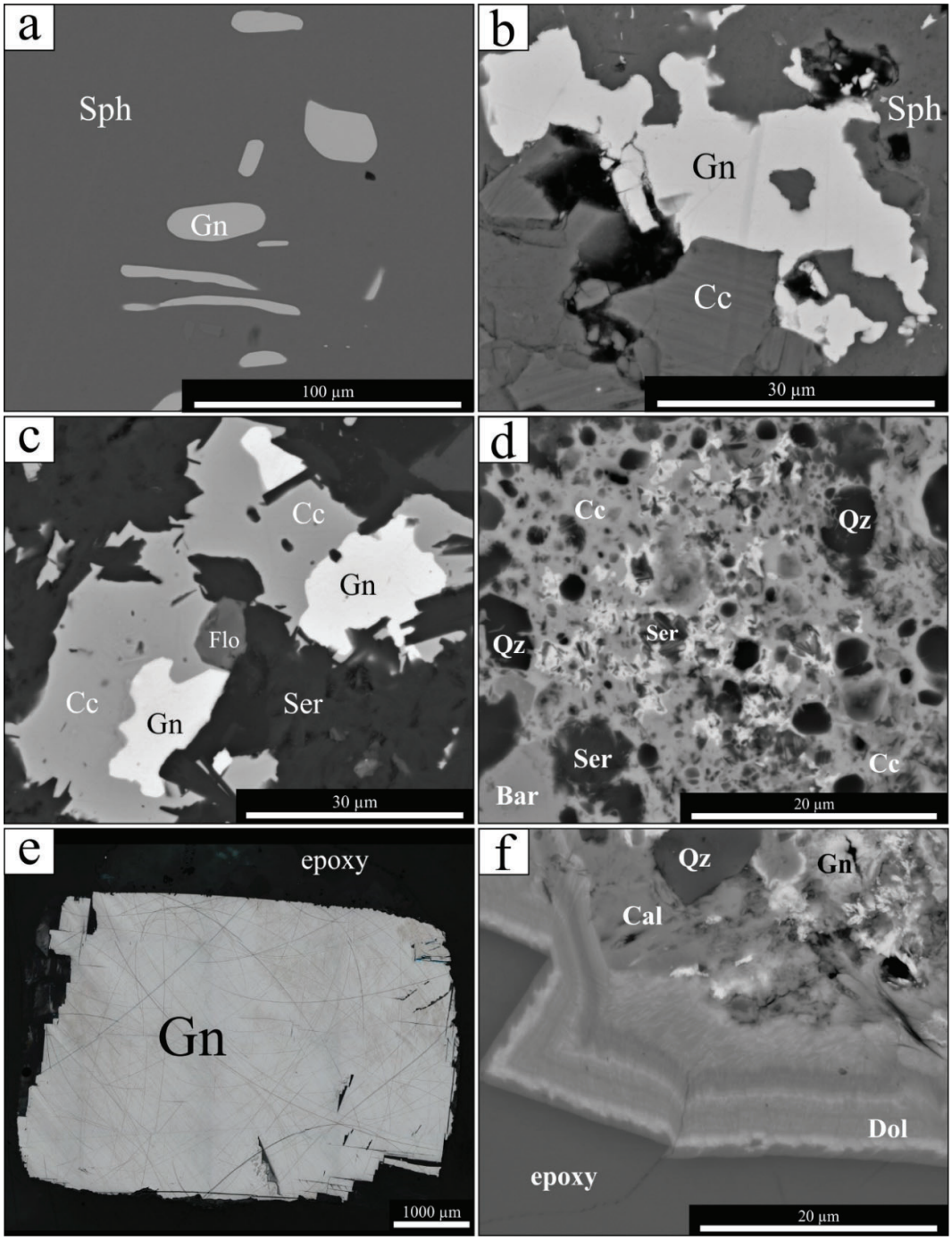


Figure 3: BSE images of Pb-minerals from drillhole RD3554 [samples RX7319 (a-b), RX7316 (c-d), and sample 1036 (e-f)]. **(a)** Rounded and elongate galena (Gn) inclusions in coarse sphalerite (Sph). **(b)** Angular and irregular galena with chalcocite (Cc) and sphalerite. **(c)** Sub-rounded galena with chalcocite in sericite (Ser) with crystal of florencite (Flo). **(d)** Moderately radiogenic altaite (brightest phase) within blotchy chalcocite also containing included quartz (Qz), sericite, and baryte (Bar). **(e)** Large clean galena cube from vug. Galena shows characteristic scratch marks and triangular pitting from polishing. This large well-formed crystal is very unique from other occurrences of galena in the sample set. **(f)** Oscillatory-zoned carbonate from outer Mn-dolomite (Dol) to inner calcite (Cal); bright zones in carbonate zones contain elevated Pb. Galena (brightest phase) is intergrown with the inner calcite surrounding quartz. This is from the vug edge containing the galena shown in (f).

Sample 1036 has the most distinct galena texture (Fig. 3e, f). This sample comes from a grab sample from underground exposure of the barren deposit core and contains a ~4 mm^3 euhedral galena crystal on the edge of a cm-scale vug (Fig. 3e). Trace ~5 μm-sized galena inclusions are also seen within oscillatory-zoned Ca-Mg-Mn-carbonate along the vug margins (Fig. 3f). Compositional zoning in the carbonate is expressed by varying Ca/(Ca+Mg+Mn) and by varying concentrations of Pb that result in the dark and bright bands within the carbonate, as seen on the BSE image (Fig. 3f). The only other sulfide identified is pyrite.

Pb-isotope results

Lead-isotope data is displayed as ratios of $^{206}Pb/^{204}Pb$ *vs.* $^{207}Pb/^{204}Pb$ (Fig. 4a, b), $^{206}Pb/^{204}Pb$ *vs.* $^{208}Pb/^{204}Pb$ (Fig. 4c, d), and $^{208}Pb/^{206}Pb$ *vs.* $^{207}Pb/^{206}Pb$ (Fig. 4e, f).

In each of these plots, the analyzed minerals from flotation concentrate samples are more varied and typically more radiogenic compared to their analogues in the rock samples which show distinct clustering by sample. Analyzed Pb-minerals in the concentrate samples are dominantly galena with lesser Pb-selenide and -telluride data (only a single data point for altaite) but values for clausthalite show a tendency to cluster towards the less radiogenic end of the field for ore galena, although a couple of datapoints are more radiogenic and plot closer to the altaite. Data for Pb-minerals in the ore concentrate define a continuous spectrum from very radiogenic to non-radiogenic and overlap the data points of the rock samples.

Among the drill core samples, samples from the NW arm (RU27-7550), consistently plot close to present-day ratios on all diagrams. The two samples from RD3554 (samples RX3716 and RX3719) on the SE edge, show two definitive clusters: one more radiogenic; and one non-radiogenic. In sample RX7316, all Pb-isotope ratios from Pb minerals plot in the more radiogenic cluster and are associated with ore sulfides. In the neighboring sample RX3719, the majority of the Pb-isotope ratios form the non-radiogenic cluster, except for two data points

that plot with the more radiogenic cluster. These two, more radiogenic data points are hosted with ore sulfides, while the rest of the non-radiogenic galena in that sample are hosted with gangue minerals, including sphalerite.

Galena in the sample from the deposit barren center (1036), is consistently more radiogenic than in the two drill core sample locations. Pb-isotope ratios of these galena grains also plot aside from the trend defined by the other rock samples and ore concentrate. This anomaly is best exhibited in Fig. 4c, on which the cluster of points for sample 1036 displays some of the highest $^{208/204}$Pb ratios, and Fig. 4e, f, where the low $^{207/206}$Pb ratio distinguishes the cluster from all other samples. Within this sample, the galena hosted in the carbonate is slightly less radiogenic than the large galena crystal. The large galena crystal shows no zoning with respect to Pb-isotopes.

DISCUSSION

The majority of the Pb-minerals analyzed from concentrate samples appear strongly radiogenic, albeit with considerable variation from point to point. A minority of data points from the concentrate show non-radiogenic signatures. The presence in the deposit of both non-radiogenic and radiogenic Pb-chalcogenides with varying signatures is supported by data for the drill core and rock samples.

Galena from RU27-7550 on the NW arm, shows consistently less-radiogenic signatures than other samples, regardless of associated mineralogy, including Cu- and U-minerals, or prevailing textural relationship. The presence of non- or only slightly-radiogenic Pb minerals coexisting with U-minerals may imply remobilization of U from elsewhere in the deposit and precipitation of new-formed U-minerals after crystallization of galena. Samples from RD3554 in the SE edge however, show variation of radiogenic ratios seemingly related to direct associated mineral assemblage. The sample from the barren deposit center, 1036, is

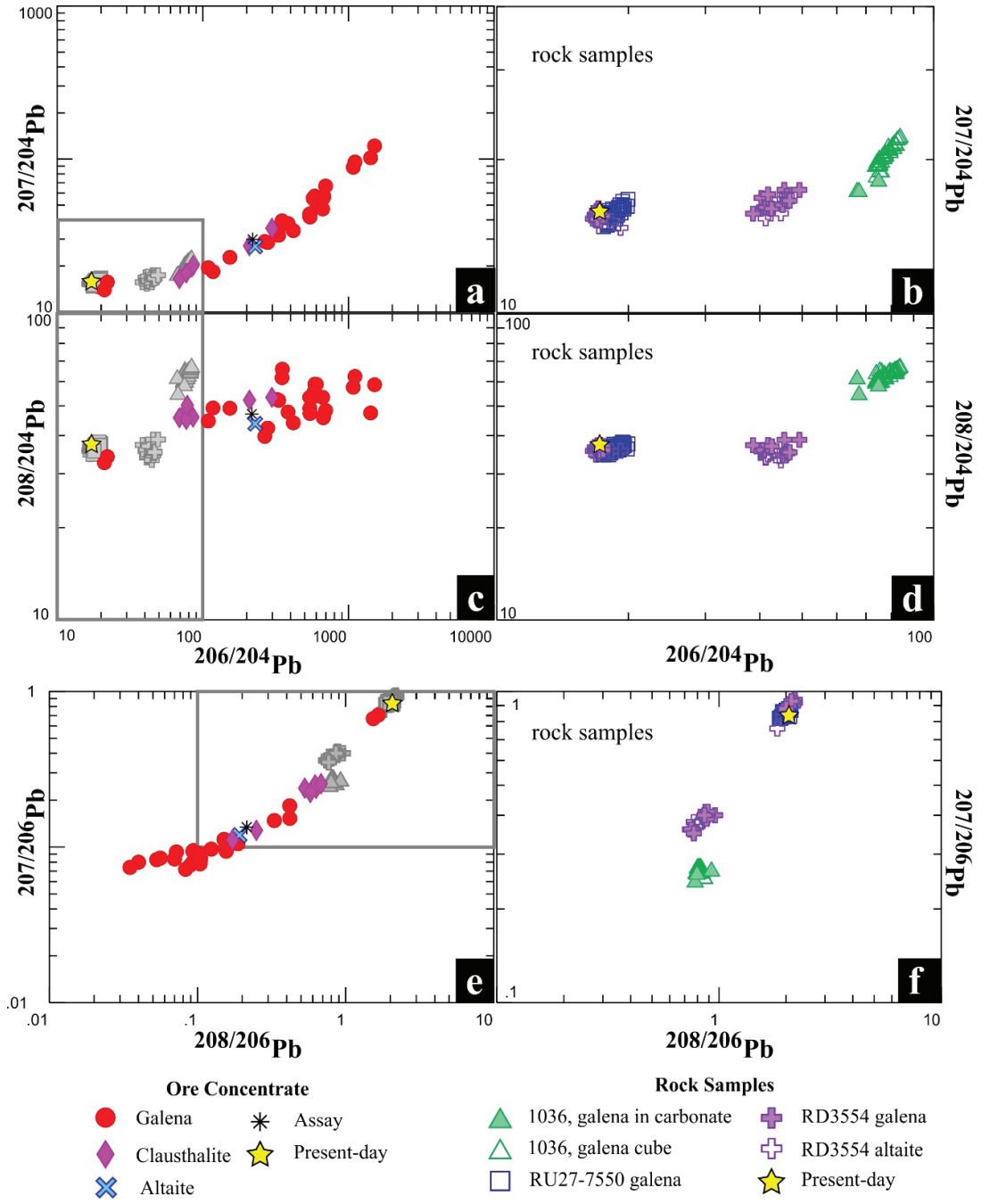


Figure 4: Pb-isotope ratio plots divided by sample and mineralogy: **(a-b)** $^{206}Pb/^{204}Pb$ *vs.* $^{207}Pb/^{204}Pb$; **(c-d)** $^{206}Pb/^{204}Pb$ *vs.* $^{208}Pb/^{204}Pb$; and **(e-f)** $^{208}Pb/^{206}Pb$ *vs.* $^{207}Pb/^{206}Pb$. Plots on the left show the full range of all data, focusing on compositions for the concentrate samples (colored) and the rock sample data is greyed out. The grey box shows the detailed area, displayed on the right with only the rock sample data shown and colored. Pb-isotope data for bulk assay of ore concentrate material is also included and generally plots in the middle of all the individual analysis. Present-day Pb-isotope values (Cumming and Richards 1975) are included as a proxy for least radiogenic end-members of the continuum.

mineralogically and isotopically distinct from all other samples. These galena data show elevated ^{208}Pb and ^{207}Pb relative to ^{206}Pb and ^{204}Pb, and data for this sample thus plot astray from the trend for the rest of the data. Because of the uniqueness of this sample, both spatially and in morphology, there could be many explanations for this, ranging from locally derived isotope signatures, to fluid evolution, to supply of Pb from a different fluid altogether.

The somewhat less radiogenic character of clausthalite compared to much of the observed galena might be explained in terms of distinct paragenesis. The characteristic occurrence of clausthalite as inclusions within Cu-(Fe)-sulfides, a textural environment distinct from much of the analyzed galena. Although we cannot unequivocally place constraints on the timing on clausthalite formation, we suggest it may relate to a partial or total recrystallization of Se-bearing Cu-(Fe)-sulfides that incorporated remobilized lead upon recrystallization, from which clausthalite was subsequently exsolved during cooling due to incompatibility of Pb in sulfides in the system Cu-Fe-S (Owen et al. 2018).

Lead minerals are most abundant on the deposit margins, a feature that may be attributed to the well-established Cu-Fe sulfide zonation from the deposit periphery toward the center, of sphalerite → galena → pyrite → chalcopyrite → bornite → chalcocite → native copper (Ehrig et al. 2012). The two locations, RD3554 and RU27-7550, are from opposite edges of the deposit, and share some similarities in their Pb-isotope signatures. All are nonetheless generally less radiogenic than the Pb-minerals analyzed from the sulfide concentrate, which were presumably sourced from higher Cu-grade ore from more central locations within the deposit.

The overall variability in Pb-isotope concentrations from grain to grain could be due to various and likely multiple reasons. These include the broadly positive correlation between the abundance of U-minerals and Cu grade, prolonged fluid evolution, and multiple episodes of remobilization (of Cu, U, and Pb). The diverse Pb-isotope signatures also point to the influence

of local environments and lithologies, breccia clast and matrix compositions, and not least, highly heterogeneous fluid pathways.

Using Pb-isotope ratios for feldspars in host Roxby Downs Granite (RDG) reported by Chapman et al. (2016), there is a clear linear trend from the host granite to the more- and less-radiogenic signatures identified in the deposit (Fig. 5). There is, however, also a noticeable gap in data points along the trend which may infer the presence of two distinct groups but may also be due to limited/selective sampling. Similarly, both the ore galena and clausthalite seem to show two distinctive clusters of Pb-isotope ratios which could indicate two stages or episodes of formation. More research would be required to identify the inferences for deposit evolution. The galena from the deposit center associated with carbonate is also noticeably astray from the trend on Fig. 5, suggesting a different Pb-isotope source, either locally influenced by ^{232}Th availability, or a marked change in fluid composition. We might alternatively speculate that this galena may be significantly younger than 1590 Ma and was precipitated from an as-yet unknown fluid introduced during an overprinting event.

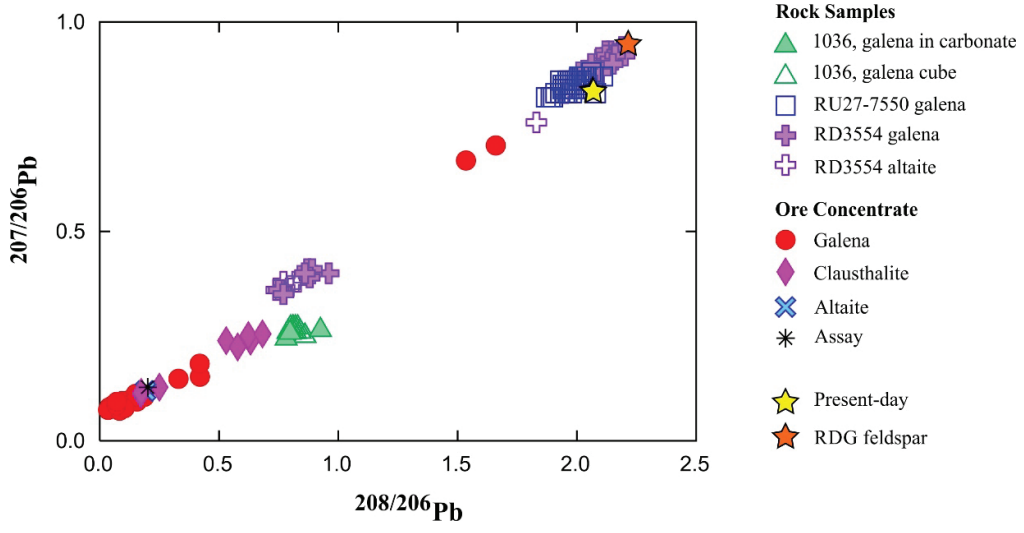


Figure 5: Plot of ^{208}Pb/^{206}Pb *vs.* ^{207}Pb/^{206}Pb for all analyzed Pb-mineral grains, as well as ratios reported for feldspar in host RDG (Chapman et al. 2016).

The presence of distinct non-radiogenic Pb in samples from distal parts of the deposit, and suggestion of deposit-scale Pb-isotope zonation resembling the distinctive Cu–Pb–Zn zonation pattern seen in many deposit types, prompts comment. We propose that some non-radiogenic Pb was introduced, alongside Cu, U, Fe, etc., at the time of initial magmatic-hydrothermal ore formation. ^{206}Pb-rich signatures can only be derived from the decay of U introduced early during deposit evolution. This is concordant with multiple lines of evidence favoring introduction of U (and Th) at the onset of mineralization together with Cu-sulfides (e.g., Johnson 1993, Creaser and Cooper 1993, Ciobanu et al. 2013, Macmillan et al. 2016, Courtney-Davies et al. 2019).

A conspicuous feature of the Pb-isotope dataset for the concentrate samples is the marked variation from spot to spot. This can be reconciled with the fact that whereas some U-bearing minerals can rapidly heal and behave as effectively closed isotopic systems, others appear inefficient at retaining the products of ^{238}U decay, or are readily replaced by other minerals (Macmillan et al. 2016, 2017, Verdugo-Ihl et al. 2017). Subsequent dissolution, remobilization, and recrystallization of U and daughters Ra and Pb into new minerals has been documented at the nano-scale (Rollog et al. 2019). Moreover, evidence for incorporation of mobilized radionuclides, including ^{226}Ra and subsequent decay-chain products, into both baryte (Schmandt et al. 2019b) and REE-Al-phosphate-sulphates (Owen et al. in review.), and for reaction between migrating radiogenic Pb and available Se (Owen et al. 2018), support a decoupling of Pb from U at scales from single mineral grains upwards. Remobilization processes likely occurred at multiple stages, over variable distances, and probably at different physicochemical conditions, during the evolution of the OD deposit. The degree, timing, and frequency of such events remains, however, poorly constrained. They may also have been heterogeneous at the deposit-scale, based upon the abundance of primary minerals and primary mineral assemblages that are well-preserved and retain primary zonation patterns (e.g.,

Ciobanu et al. 2013, Krneta et al. 2016, 2017, Macmillan et al. 2016, Verdugo-Ihl et al. 2017, Cook et al. 2018b, Courtney-Davies et al. 2019). The highly variable measured Pb-isotope signatures shown in Fig. 4 and 5 probably reflect mixing of non-radiogenic Pb (potentially of various ages and provenances) with heterogeneous radiogenic Pb over the lifetime of the deposit.

IMPLICATIONS

Data presented here have implications for deciphering zonation patterns and fluid evolution. The results highlight the importance of potentially highly variable and localized conditions in the OD deposit. Moreover, the results provide compelling evidence for extensive Pb mobility and grain-scale decoupling of radiogenic Pb from precursor minerals. Dissociation of U from Pb minerals and degrees of radiogenic origin raises many, as-yet incompletely answered questions about the mechanisms impacting on U-minerals in the deposit (post-decay healing, break-down and recrystallization), the pathways of Pb migration, the potential scales of U and Pb migration, and the formation of new Pb-minerals.

These data are also highly relevant to the need to constrain the physical location within individual mineral grains and chemical speciation of decay products of ^{238}U in ores and their concentrates. Concentrations of daughter radionuclides produced from decay of ^{238}U, notably ^{210}Pb, can be sufficiently high to warrant efforts to identify their hosts in ore and their relative behaviors during processing as a requisite step for developing processing solutions to reduce or eliminate radionuclide activity in concentrates (Cook et al. 2018a). Determination of Pb-isotope ratio variations at the mineral and deposit scales, coupled with microscale petrographic observation, can complement visualization of ^{210}Pb distributions in individual minerals from OD (Rollog et al. 2019). The latter study has also confirmed that ^{206}Pb and ^{210}Pb distributions are often fundamentally different due to the impact of extensive remobilization of Pb over

geological time and, to some degree, also during processing.

Acknowledgements

This research is a contribution to the Australian Research Council Research Hub for Australian Copper-Uranium, also supported by BHP Olympic Dam, and the South Australian Government Department of State Development.

Supplementary Materials

Appendix A: Summary sample descriptions with Pb-ratio summaries.

Appendix B: Full LA-ICP-MS dataset of Pb-ratios.

References

Apukhtina, O.B. (2016) Distribution, petrology, geochemistry and geochronology of carbonate assemblages at the Olympic Dam deposit. Unpublished Ph.D. thesis, University of Tasmania.

Apukhtina, O.B., Kamenetsky, V.S., Ehrig, K., Kamenetsky, M.B., McPhie, J., Maas, R., Meffre, S., Goemann, K., Rodemann, T., Cook, N.J., and Ciobanu, C.L. (2016) Postmagmatic magnetite–apatite assemblage in mafic intrusions: a case study of dolerite at Olympic Dam, South Australia. Contributions to Mineralogy and Petrology, 171. doi: 10.1007/s00410-015-1215-7.

Apukhtina, O.B., Kamenetsky, V.S., Ehrig, K., Kamenetsky, M.B., Maas, R., Thompson, J., McPhie, J., Ciobanu, C.L., and Cook, N.J. (2017) Early, deep magnetite-fluorapatite mineralization at the Olympic Dam Cu-U-Au-Ag deposit, South Australia. Economic Geology, 112, 1531-1542.

Beyer, S.R., Kyser, T.K., Hiatt, E.E., Polito, P.A., Alexandre, P., and Hoksbergen, K. (2012) Basin evolution and unconformity-related uranium mineralization: The Camie River U prospect, Paleoproterozoic Otish Basin, Quebec. Economic Geology, 107, 401–425.

BHP Annual Report (2018) https://www.bhp.com/-/media/documents/investors/annual-reports/2018/bhpannual report2018.pdf .

Champion, D.C., and Huston, D.L. (2016) Radiogenic isotopes, ore deposits and metallogenic terranes: Novel approaches based on regional isotopic maps and the mineral systems concept. Ore Geology Reviews, 76, 229–256.

Chapman, N.D., Meffre, S., Kamenetsky, V., Kathy, E., and Kontonikas-Charos, A. (2016) The Pb-isotopes of Olympic Dam and beyond – the uranium story of the Gawler Craton. Australian Earth Sciences Convention 2016, June 26-30, Adelaide, SA, Geological Society of Australia Abstract No 118. ISSN: 0729 011 X Abstracts book p. 72–73.

Cherry, A.R., Ehrig, K., Kamenetsky, V.S., McPhie, J., Crowley, J.L., and Kamenetsky, M.B. (2018a) Precise geochronological constraints on the origin, setting and incorporation of ca. 1.59 Ga surficial facies into the Olympic Dam Breccia Complex, South Australia. Precambrian Research, 315, 162-178. doi: 10.1016/j.precamres.2018.07.012.

Cherry, A.R., Kamenetsky, V.S., McPhie, J., Thompson, J.M., Ehrig, K., Meffre, S., Kamenetsky, M.B., and Krneta, S. (2018b) Tectonothermal events in the Olympic IOCG Province constrained by apatite and REE-phosphate geochronology. Australian Journal of Earth Sciences. doi: 10.1080/08120099.2018.1465473.

Cherry, A.R., McPhie, J., Kamenetsky, V.S., Ehrig, K., Keeling, J.L., Kamenetsky, M.B, Meffre, S., and Apukhtina, O.B. (2017) Linking Olympic Dam and the Cariewerloo Basin: Was a sedimentary basin involved in formation of the world's largest uranium deposit?.

Precambrian Research, 300, 168-180. doi: 10.1016/j.precamres.2017.08.002.

Ciobanu, C.L., Wade, B.P., Cook, N.J., Schmidt Mumm, A., and Giles, D. (2013) Uranium-bearing hematite from the Olympic Dam Cu–U–Au deposit, South Australia: A geochemical tracer and reconnaissance Pb–Pb geochronometer. Precambrian Research, 238, 129–147.

Cook, N.J., Ehrig, K.J., Ciobanu, C.L., Courtney-Davies, L., Verdugo-Ihl, M.R., Rollog, M., Schmandt, D.S., Owen, N.D., Macmillan, E., Kontonikas-Charos, A., Krneta, S., and Dmitrijeva, M. (2018b) Why detailed mineralogy is important: Understanding evolution of the giant Olympic Dam iron-oxide copper-gold system, South Australia. 15th Quadrennial IAGOD Symposium, Salta, Argentina, 28-31 August 2018. Symposium Proceedings Volume, SegemAR, 371–372.

Cook, N.J., Ehrig, K.J., Rollog, M., Ciobanu, C.L., Lane, D.J., Schmandt, D.S., Owen, N.D., Hamilton, T., and Grano, S. (2018a) ^{210}Pb and ^{210}Po in geological and related anthropogenic materials: implications for their mineralogical distribution in base metal ores. Minerals, 8, 211. doi: 10.3390/min8050211.

Courtney-Davies, L., Tapster, S.R., Ciobanu, C.L., Cook, N.J., Verdugo-Ihl, M.R., Ehrig, K., Kennedy, A., Gilbert, S., Condon, D.J., and Wade, B.P. (2019) A multi-technique evaluation of hydrothermal hematite U-Pb isotope systematics: Implications for ore deposit geochronology. Chemical Geology, 513, 54-72. doi: 10.1016/j.chemgeo.2019.03.005.

Courtney-Davies, L., Zhu, Z., Ciobanu, C.L., Wade, B.P., Cook, N.J., Ehrig, K., Cabral, A.R., and Kennedy, A. (2016) Matrix-matched iron-oxide laser ablation ICP-MS U–Pb geochronology using mixed solution standards. Minerals, 6, 85. doi: 10.3390/min6030085.

Creaser, R.A., and Cooper, J.A. (1993) U-Pb geochronology of middle Proterozoic felsic magmatism surrounding the Olympic Dam Cu-U-Au-Ag and Moonta Cu-Au-Ag deposits, South Australia. Economic Geology, 88, 186–197.

Cumming, G L., and Richards, J.R. (1975) Ore lead isotope ratios in a continously changing Earth. Earth and Planetary Science Letters, 28, 155–171.

Darling, J.R., Storey, C.D., Hawkesworth, C.J., and Lightfoot, P.C. (2012) In-Situ Pb isotope analysis of Fe-Ni-Cu sulphides by Laser Ablation Multi-Collector ICPMS: New insights into ore formation in the Sudbury Impact Melt Sheet. Geochimica et Cosmochimica Acta, 99, 1–17.

Ehrig, K., Kamenetsky, V., McPhie, J., Cook, N.J., and Ciobanu, C.L. (2017) Olympic Dam iron-oxide Cu-U-Au-Ag deposit. In: G.N. Phillips, ed., Australian Ore Deposits. AusIMM, Melbourne, p. 601–610.

Ehrig, K., McPhie, J., and Kamenetsky, V. (2012) Geology and mineralogical zonation of the Olympic Dam Iron Oxide Cu-U-Au-Ag deposit, South Australia. SEG Special Publication Number 16—Geology and Genesis of Major Copper Deposits, 237–267.

Gu, Y. (2003) Automated scanning electron microscope based mineral liberation analysis: an introduction to JKMRC/FEI Mineral Liberation Analyzer. Journal of Minerals and Materials Characterization and Engineering. 2, 33–41.

Holk, G.J., Kyser, T.K., Chipley, D., Hiatt, E.E., and Marlatt, J. (2003) Mobile Pb-isotopes in Proterozoic sedimentary basins as guides for exploration of uranium deposits. Journal of Geochemical Exploration, 80, 297–320.

Huang, Q., Kamenetsky, V.S., McPhie, J., Ehrig, K., Meffre, S., Maas, R., Thompson, J., Kamenetsky, M., Chambefort, I., Apukhtina, O., and Hu, Y. (2015) Neoproterozoic (Ca.

820-830 Ma) Mafic Dykes at Olympic Dam, South Australia: Links with the Gairdner Large Igneous Province. Precambrian Research, 271, 160–172.

Jagodzinski, E. (2005) Compilation of SHRIMP U-Pb geochronological data, Olympic Domain, Gawler Craton. South Australia, 2001-2003. Geoscience Australia Record 2005/020

Jagodzinski, E. (2014) The age of magmatic and hydrothermal zircon at Olympic Dam. Proceedings, Australian Earth Sciences Convention, Sustainable Australia, Newcastle, NSW: July 7-10, Abstract 110, 260.

Johnson, J.P. (1993) The geochronology and radiogenic isotope systematics of the Olympic Dam copper-uranium-gold-silver deposit, South Australia. Unpublished Ph.D. thesis, The Australian National University, Canberra.

Johnson, J.P., and Cross, K.C. (1995) U-Pb geochronological constraints on the genesis of the Olympic Dam Cu-U-Au-Ag deposit, South Australia. Economic Geology, 90, 1046–1063.

Kamenetsky, V.S., Ehrig, K., Maas, R., Meffre, A., Kamenetsky, M., McPhie, J., Apukhtina, O., Huang, Q., Thompson, J., Ciobanu, C.L., and Cook, N.J. The Supergiant Olympic Dam Cu-U-Au-Ag Ore Deposit: Toward a New Genetic Model. SEG 2015: World Class Ore Deposits: Discovery to Recovery. Hobart: Society of Economic Geologists.

Kamona, A.F., Lévêque, J., Friedrich, G., and Haack, U. (1999) Lead Isotopes of the carbonate-Hosted Kabwe, Tsumeb, and Kipushi Pb-Zn-Cu sulphide deposits in relation to Pan African orogenesis in the Damaran-Lufilian Fold Belt of Central Africa. Mineralium Deposita, 34, 273–283.

Kirchenbaur, M., Maas, R., Ehrig, K., Kamenetsky, V.S., Strub, E., Ballhaus, C., and Münker, C. (2016) Uranium and Sm isotope studies of the supergiant Olympic Dam Cu–Au–U–Ag

Deposit, South Australia. Geochimica et Cosmochimica Acta, 180, 15–32.

Krneta, S., Ciobanu, C.L., Cook, N.J., Ehrig, K., and Kontonikas-Charos, A. (2016) Apatite at Olympic Dam, South Australia: a petrogenetic tool. Lithos 262, 470–485.

Krneta, S., Ciobanu, C.L., Cook, N.J., Ehrig, K., and Kontonikas-Charos, A. (2017) Rare earth element behaviour in apatite from the Olympic Dam Cu-U-Au-Ag deposit, South Australia. Minerals, 7, 135. doi: 10.3390/min7080135.

Maas, R., Kamenetsky, V.S., Ehrig, K., Meffre, S., McPhie, J., and Diemar, G. (2011) Olympic Dam U-Cu-Au deposit, Australia: New age constraints. Mineralogical Magazine, 75, 1375.

Macmillan, E., Cook, N.J., Ehrig, K., and Pring, A. (2017) Chemical and textural interpretation of late-stage coffinite and brannerite from the Olympic Dam IOCG-Ag-U deposit. Mineralogical Magazine, 81, 1323–1366.

Macmillan, E., Cook, N.J., Ehrig, K., Ciobanu, C.L., and Pring, A. (2016) Uraninite from the Olympic Dam IOCG-U-Ag deposit: Linking textural and compositional variation to temporal evolution. American Mineralogist, 101, 1295–1320.

Mattinson, J.M. (2013) Revolution and evolution: 100 years of U-Pb geochronology. Elements, 9, 53–57.

McFarlane, C., Lentz, D., and Dehnavi, A. (2016) Pb-Isotopic study of galena by LA-Q-ICP-MS : Testing a new methodology with applications to base-metal sulphide deposits. Minerals, 6, 1–17. doi: 10.3390/min6030096.

McInnes, B.I.A., Keays, R.R., Lambert, D.D., Hellstrom, J., and Allwood, J.S. (2008) Re-Os geochronology and isotope systematics of the Tanami, Tennant Creek and Olympic Dam Cu-Au deposits. Australian Journal of Earth Sciences, 55, 967–981.

McPhie, J., Orth, K., Kamenetsky, V., Kamenetsky, M., and Ehrig, K. (2016) Characteristics, origin and significance of Mesoproterozoic bedded clastic facies at the Olympic Dam Cu–U–Au–Ag deposit, South Australia. Precambrian Research, 276, 85–100. doi: 10.1016/j.precamres.2016.01.029.

Meffre, S., Kamenetsky, V., McPhie, J., Maas, R., Ehrig, K., and Chambefort, I. (2010) Pb isotopes at Olympic Dam: constraining sulphide growth. 13th Quadrennial IAGOD Symposium; Giant Ore Deposits Down-Under, Adelaide. Abstract volume, 78–79.

Owen, N.D., Ciobanu, C.L., Cook, N.J., Slattery, A., and Basak, A. (2018) Nanoscale study of clausthalite-bearing symplectites in Cu-Au-(U) ores: Implications for ore genesis. Minerals, 8, 67. doi: 10.3390/min8020067.

Owen, N.D., Cook, N.J., Rollog, M., Ehrig, K., Schmandt, D.S., Ram., R., Brugger, J., Ciobanu, C.L., Wade, B.P., and Gugliardo, P. (in review) REE-, Sr- Ca-aluminium-phosphate-sulfate minerals of the woodhouseite series and their role as hosts for radionuclides. American Mineralogist.

Paton, C., Hellstrom, J., Paul, B., Woodhead, J., and Hergt, J. (2011) Iolite: Freeware for the visualisation and processing of mass spectrometric data. Journal of Analytical Atomic Spectrometry. 26, 2508–2518. doi: 10.1039/c1ja10172b.

Paul, B., Woodhead, J., Hergt, J., Danyushevsky, L., Kunihiro, T., and Nakamura, E. (2011) Melt inclusion Pb-isotope analysis by LA-MC-ICPMS: Assessment of analytical performance and application to OIB genesis. Chemical Geology, 289, 210–223.

Reed, S. J. B., Trueman, N. A., and Long, J. V. P. (1987) Ion microprobe U-Pb dating of pitchblende: In Benninghaven, A., Huber, A.W. & Werner, H.W. (eds) Secondary Ion Microscopy (SIMS VI). Wiley, 945-948.

Rollog, M., Cook, N.J., Gugliardo, P., Ehrig. K., and Kilburn, M. (2019) In situ spatial distribution mapping of radionuclides in minerals by nanoSIMS. Geochemistry – Exploration, Environment, Analysis, (in press). doi: 10.1144/geochem2018-038.

Rosholt, J.N., Zartman, R.E., and Nkomo, I.T. (1973) Lead isotope systematics and uranium depletion in the Granite Mountains, Wyoming. Bulletin of the Geological Society of America, 84, 989–1002.

Schmandt, D.S., Cook, N.J., Ciobanu, C.L., Ehrig, K., Wade, B.P., Gilbert, S., and Kametetsky, V.S. (2019a) Rare earth element phosphates from the Olympic Dam Cu-U-Au-Ag deposit, South Australia: Recognising temporal-spatial controls on REE mineralogy in an evolved IOCG system. The Canadian Mineralogist, 57, 1-22. doi: 10.3749/canmin.1800043.

Schmandt, D.S., Cook, N.J., Ehrig, K., Ciobanu, C.L., Wade, B.P., Gilbert, S., and Kamenetsky, V.S. (2017) Rare earth element fluorocarbonate minerals from the Olympic Dam Cu-U-Au-Ag deposit, South Australia. Minerals, 7, 202. doi: 10.3390/min7100202.

Schmandt, D.S., Cook, N.J., Ehrig, K., Gilbert, S., Wade, B.P., Rollog, M., Ciobanu, C.L., and Kamenetsky, V.S., (2019b) Uptake of trace elements by baryte during copper ore processing: a case study from Olympic Dam, South Australia. Minerals Engineering, 135, 83-94. doi: 10.1016/j.mineng.2019.02.034.

Švedkauskaitė-LeGore, J., Mayer, K., Millet, S., Nicholl, A., Rasmussen, G., and Baltrūnas, D. (2007) Investigation of the isotopic composition of lead and of trace elements concentrations in natural uranium materials as a signature in nuclear forensics. Radiochimica Acta, 95, 601–605.

Varga, Z., Wallenius, M., Mayer, K., Keegan, E., and Millet, S. (2009) Application of lead and strontium isotope ratio measurements for the origin assessment of uranium ore

concentrates. Analytical Chemistry, 81, 8327–8334.

Verdugo-Ihl, M.R., Ciobanu, C.L., Cook, N.J., Ehrig, K., Courtney-Davies, L., and Gilbert, S. (2017) Textures and U-W-Sn-Mo signatures in hematite from the Cu-U-Au-Ag orebody at Olympic Dam, South Australia: defining the archetype for IOCG deposits. Ore Geology Reviews, 91, 173–195.

Woodhead, J.A., Hergt, J., Meffre, S., Large, R.R., Danyushevsky, L., and Gilbert, S. (2009) In situ Pb-isotope analysis of pyrite by Laser Ablation (Multi-Collector and Quadrupole) ICPMS. Chemical Geology, 262, 380–390.

CHAPTER 7

SUMMARY, RECOMMENDATIONS, AND CONCLUDING REMARKS

1 SUMMARY

The petrography and geochemistry of four important minerals/mineral groups from the Olympic Dam ore deposit have been assessed: rare earth element (REE)-fluorocarbonates and -phosphates, baryte, fluorite, and Pb-chalcogenides. Although all are gangue minerals, each of these minerals or mineral groups carries significance, both geologically and metallurgically. The extraordinary mineralogical and compositional diversity expressed by these minerals, as with other mineral groups from Olympic Dam (Macmillan *et al.* 2016a, 2017, Ciobanu *et al.* 2017a, Krneta *et al.* 2017a, Verdugo-Ihl *et al.* 2017) demonstrates the need for a careful, systematic approach, and in many cases, for micron-scale observation to be supplemented by characterization at the atomic scale (Macmillan *et al.* 2016b, 2016c, Ciobanu *et al.* 2017a, 2017b, Kontonikas-Charos *et al.* 2018). The criticality of such an approach, as presented within this thesis, is necessary to not only unravel the mineralization history of complex deposits such as Olympic Dam, but also to identify the mineralogical deportment of specific elements (Cook *et al.* 2018). This research was conducted as a contribution to the development of the ARC Research Hub for Australian Copper-Uranium (https://www.adelaide.edu.au/copper-uranium-research/).

With respect to identification of mineralogical hosts for trace level radionuclides (RN), the research reported in this thesis, has enabled identification of potential RN-carriers, on which little previous data was available, and also allowed other mineral groups to be ruled-out as major contributors to the RN budget. Nonetheless, all minerals studied were shown to contain measurable concentrations of U and/or Pb. These are, however, minor and cannot be considered significant contributors to the total RN budget. A persistent feature was, however, that each mineral or mineral group displayed a wide range of trace element concentrations, further highlighting the heterogeneous nature of the deposit and underlining the need to analyze large, representative sample suites and to back-up geochemical data with petrographic observation at an appropriate scale.

Among the minerals studied, the impact on processing and understanding of RN distributions, was greatest for baryte. The observation and quantification of increased Pb content within baryte grains after each progressive processing stage implies that the sulphate is a scavenger of liberated Pb (and by inference Ra and possibly other RN as well), providing additional support

to the findings of Rollog *et al.* (2018, 2019). The results demonstrate not only that RN may be liberated and dissolved during processing but that these elements can be readily re-integrated into pre-existing minerals, and may also form new minerals. Such empirical evidence of RN mobility is critical for overarching models of RN behavior.

The new data for Pb-chalcogenide minerals is of equal overall importance in terms of the main objectives of the project. Pb-isotope ratios are shown to fall broadly into two groups, demonstrating both the presence of non-radiogenic lead within the deposit (probably introduced at the time of primary formation), and the substantial mixing of radiogenic lead that has migrated from parent phases to form new minerals over geological time (see also Owen *et al.* 2018). The latter observation, in particular, provides critical support for a holistic model for the evolution of RN distributions in the deposit, and with implications for other U-bearing copper ores with protracted geological histories.

1.1 Rare earth element-minerals

The new research on REE-minerals fills a substantial knowledge gap concerning their chemistry and geologic context within the Olympic Dam deposit. The deposit represents one of the largest potential REE resources on Earth, even though extraction is not currently economic, and there is a dominance of LREE over the currently more valuable HREE. Analogous to previous studies dealing with apatite (Krneta *et al.* 2016, 2017a, 2017b, 2018), understanding the multiple stages of REE-mineralization nevertheless helps to further constrain formation of the Olympic Dam deposit, ore-forming fluids, and the importance of superimposed cycles of replacement, remobilization and recrystallization.

The Ca-free REE-fluorocarbonate bastnäsite is found to be the dominant REE mineral in the deposit and appears to be coeval with early (~1593 Ma) Fe-metasomatism and Cu-U-Au mineralization. Data suggest that bastnäsite deposition followed a limited stage of Ca-REE-fluorocarbonate deposition, in which synchysite was formed. Observed patterns suggest a transition in the composition of hydrothermal fluid during the initial episode of mineralization, a finding consistent with other studies on other key minerals in the deposit (e.g., apatite; Krneta *et al.* 2017a, 2018). The new data for REE-fluorocarbonates also illustrates that careful petrographic and textural characterization is an essential prerequisite before microanalysis (see also section 7.2.1 below).

Identifying that the Al-being REE-phosphate florencite largely overprints pre-existing REE mineralization corroborates previous mineralogical studies that show a prolonged evolution of the deposit involving replacement, remobilization, and recrystallization (*e.g.* Macmillan *et al.* 2016a, 2017). This later event, and possibly the still later replacement of REE-minerals by complex Ca-Sr-REE-Al-phosphate-sulfates of the Alunite Supergroup (Owen *et al.* in review) is recognized across the deposit. Remarkably, despite the widespread evidence for remobilization among all but the most resistant minerals in the deposit, many of the primary features of the deposit, including Cu- sulfide zonation, are preserved.

The transition from relatively simple REE-compounds like bastnäsite, through florencite, to the complex solid solutions represented by the Alunite Supergroup minerals described by Owen *et al.* (in review) represents an illustrative example of an evolving mineralogical complexity at Olympic Dam. In this model, presented by Krivovichev *et al*. (2018), successive mineral phases display ever greater structural and chemical complexity.

1.2 Baryte, fluorite, and Pb-chalcogenides

The studies of baryte, fluorite and Pb-chalcogenides have a stronger focus on their chemical variability in the ore and thus on the potential influence on processing. Importantly, these took advantage of crushed ore material to provide a balanced representation of a mineral within the whole deposit, generating many data points with a minimization of geologic bias. Significantly, all three minerals displayed significant variation in chemistry, validating such an approach.

1.2.1 Baryte

Baryte is shown to be a scavenger of liberated Pb and RN during processing. However, baryte in Cu-ore feed samples are only slightly elevated in these elements. This may suggest that migration of lead (and radium?) and subsequent incorporation into baryte may occur over geological time but that this is not volumetrically significant. In contrast, the acid leach environment catalyzes rapid adsorption and incorporation. This is in agreement with the well-studied, and even quantified geochemistry of baryte and documented capability to host Ra and other RN. The observations represent valuable empirical evidence for the hitherto poorly constrained role of sulfates as RN hosts during processing, and provide a foundation for continuing studies by others within the ARC Research Hub for Australian Copper-Uranium.

1.2.2 Fluorite

Fluorite is an important mineral at Olympic Dam, the presence and abundance of which is carefully monitored. This is primarily because of its potential deleterious impact on processing if not removed before smelting. Geology and metallurgy teams at Olympic Dam put great effort into detailing the location and abundance of fluorite going into the ore stream in order to effectively remove the mineral. Understanding the compositional spectrum of the mineral thus represents valuable information, with implications for processing. Results show that despite the simple formula, CaF_2, the chemical variation expressed by fluorite is large. It is not a carrier of more than a few ppm U and/or Pb, although, like baryte, it does contain relatively abundant inclusions of U-minerals. These are, however, not sufficiently abundant to be a significant contributor of RN into the processing stream.

Breccia-hosted fluorite is LREE-enriched and with a broader compositional range in terms of other trace elements than the late colored fluorite veins. The most distinct and consistent difference between the breccia- and vein-hosted fluorites are the chondrite-normalized fractionation patterns, in which marked differences are seen, specifically for LREE. This elemental variability seems to be an influence on fluorite color.

1.2.3 Pb-chalcogenides

The Pb-isotope dataset emphasizes the long, complex and likely cyclic history of U and Pb in the deposit, from initial introduction of common lead, and continued production of radiogenic Pb from natural decay of U (and Th). The extraordinary wide range of Pb-isotopes in analyzed galena, clausthalite, and altaite in the orebody suggests heterogeneity and likely often localized U and Pb mobility and fluid-assisted mixing. All evidence points to formation of Pb-minerals at different times, and likely through a variety of different processes and reaction mechanisms, and mobility at scales from nanometers upwards. Important for the overarching objectives of the ARC Research Hub for Australian Copper-Uranium, the study showed: (1) the critical importance of lead mobility; (2) that ^{206}Pb or total lead are not suitable proxies for ^{210}Pb; and not least, (3) the often very small size of Pb-chalcogenide minerals that makes physical separation difficult or impossible (as was also shown in Owen *et al.* 2018).

2 RECOMMENDATIONS

The extraordinarily diverse, often enigmatic nature, and giant size of the Olympic Dam deposit inevitably means that no single study can fully address all outstanding issues. Several other minerals and mineral groups remain to be investigated in greater detail, and due to the highly heterogenous nature of the Olympic Dam ore body, future work on the minerals and mineral groups included here may result in slightly different interpretations and conclusions. Further holistic mineral studies are needed both to constrain deposit evolution, as well as more completely understand mineral chemistry that may impact on deportment models for elements of interest. Among the mineral groups addressed here, the research within this thesis has generated a range of new ideas that could not all be fully tested within the time available. The new data has, inevitably, also exposed other knowledge gaps that demand attention, on topics ranging from fundamental mineralogy to metallurgical processes. Some of these are explored in the following paragraphs.

2.1 RARE EARTH ELEMENT-MINERALS

Despite the solid advances reported by Schmandt *et al.* (2017, 2019a), there is still much to learn about the REE-minerals at Olympic Dam. One area of particular interest is the relationship between the REE- and Ca-REE-fluorocarbonates, with implications for understanding crystallization conditions and stabilities of the different phases and polytypes within the bastnäsite-synchysite group. These are modular minerals particularly well-suited for nanoscale study using high-angle annular dark-field scanning transmission electron microscopy (HAADF-STEM), a technique that enhances Z-contrast, enabling the arrangement of different layers to be visualized. The potential value of the technique for understanding the fundamental nature of the bastnäsite-synchysite group was demonstrated by Ciobanu *et al.* (2017a) and Kontonikas-Charos *et al.* (2018), based on samples from outside the Olympic Dam deposit.

The nanometer-scale inter-laminations of synchysite (S) and bastnäsite (B) identified in Schmandt *et al.* (2017) were considered an ideal first step for such nanoscale studies. Building on the work of both Ciobanu *et al*. (2017a) and Schmandt *et al.* (2017), preparation of thinned foils by focused ion beam – SEM and initial HAADF STEM imaging and nanoscale mapping was undertaken in late 2018 within the framework of a University of Adelaide honors project (Zainurin *et al.* 2018). Results revealed a remarkable, hitherto unrecognized complexity, including extensive

disordering at the nanoscale, explaining apparent non-stoichiometry measured on the micron-scale (Figure 1). Bastnäsite-(Ce) and synchysite-(Ce) are confirmed as stable phases and are overwhelmingly stoichiometric. Both minerals, however, display a degree of disordering whereby fine lamellae consist of lattice-scale intergrowths of synchysite in bastnäsite and bastnäsite in synchysite. These intergrowths may attain a degree of regularity, with the short-range presence (typically not more than 2-7 repeats) of parisite [BS], röntgenite [B2.S], and unnamed [B.S2] recognized. Bulk compositions measured from counting of sequences across disorder domains suggest they may have formed by decomposition of an unstable parent phase. Nanoscale re-equilibration among REE-fluorocarbonates was also recognized.

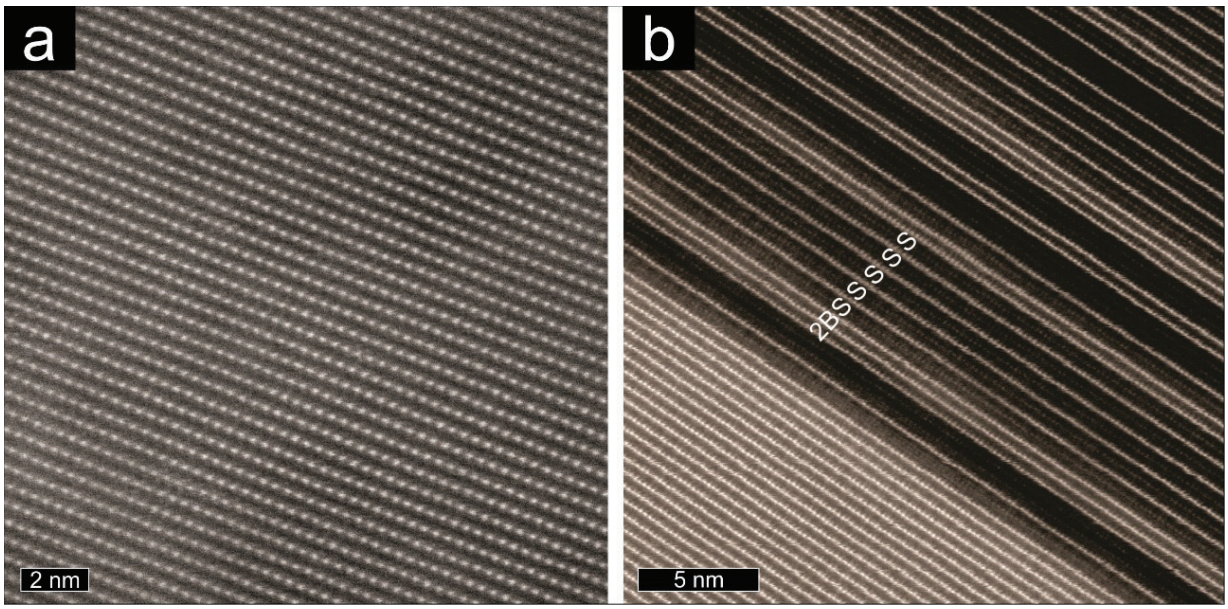


Figure 1: Atomic-scale HAADF STEM images showing (a) regular sequence of bastnäsite and (b) a REE-fluorocarbonate sequence containing layers of both bastnäsite ('B') and synchysite ('S'). The B and S stacking patterns can vary greatly across a mineral grain (note fine scale of (a) and (b)). Image from Zainurin *et al*. (2018).

A second area in which valuable new information should be sought concerning the mineralizing conditions of REE-minerals is experimental research (*e.g.* Migdisov *et al.* 2016) accompanied by thermodynamic modelling, as has been performed for apatite from Olympic Dam (Krneta *et al.* 2018). Provided that thermodynamic databases of adequate quality to address phase

relationships among complex REE-minerals could be obtained, constraints on the physiochemical conditions at which these minerals were formed would be insightful.

Further work on the distribution of florencite and its paragenetic relationship with APS minerals (Owen *et al.* in review) would also be beneficial. Specifically, this should target a greater understanding of the timing, conditions and mechanisms of the later overprinting event(s) recorded by these minerals. Greater emphasis might also be placed on achieving a deeper understanding of HREE distributions in the deposit. This would be appreciably more challenging that the LREE because of the lower concentrations.

Elevated concentrations of REE are an inherent feature of IOCG deposits (*e.g.* Hitzman *et al.* 1992, Barton, 2014). REE mineralogy has not, however, been documented in great detail in many IOCG deposits and the fundamental reasons for why IOCG deposits display enrichment in REE is not well understood. Defining the paragenesis and REE mineralogy within other analogous ore systems has the potential to contribute to the overall understanding of these systems globally. This is not insignificant given that they represent a potential future REE resource if economically viable extractive technologies can be found.

2.2 Fluorite

Although not formed at the same time as the iron-oxide-Cu-U-Au-Ag resource, the late, coarse-grained fluorite + barite veins detailed in Chapters 4 and 5 represent a geologic curiosity, underlined by their large crystals and bold colors. Preliminary imaging of vein fluorite using a cathodoluminescence (CL) detector shows far more varied textures than had been expected. These variably sharp and diffuse textures (Figure 2) thus reveal that the geologic history of these veins may be more complex than initially envisaged. A careful follow-up study on the veins, correlating appearance in CL and BSE images with mineral chemistry would be fruitful and may advance understanding of the impact of the Delamerian Orogeny at Olympic Dam and throughout the Olympic Cu-Au Province. Potentially, such a study might incorporate nanoscale studies on the colored fluorites to identify atomic-scale crystal defects resulting from the various minor/trace element substitutions and/or radiation damage that may controlling colors observed on the macroscopic scale.

A further research direction, might be an evaluation of fluorite chemistry in the Roxby Downs Granite distal to Olympic Dam and in intrusive rocks of Hiltaba age associated with other

IOCG-type deposits prospects, such as Acropolis or Wirrda Well. This may reveal differences in element concentrations and patterns in productive vs. barren intrusive rocks that could serve as an exploration vector tool in IOCG systems at the regional scale.

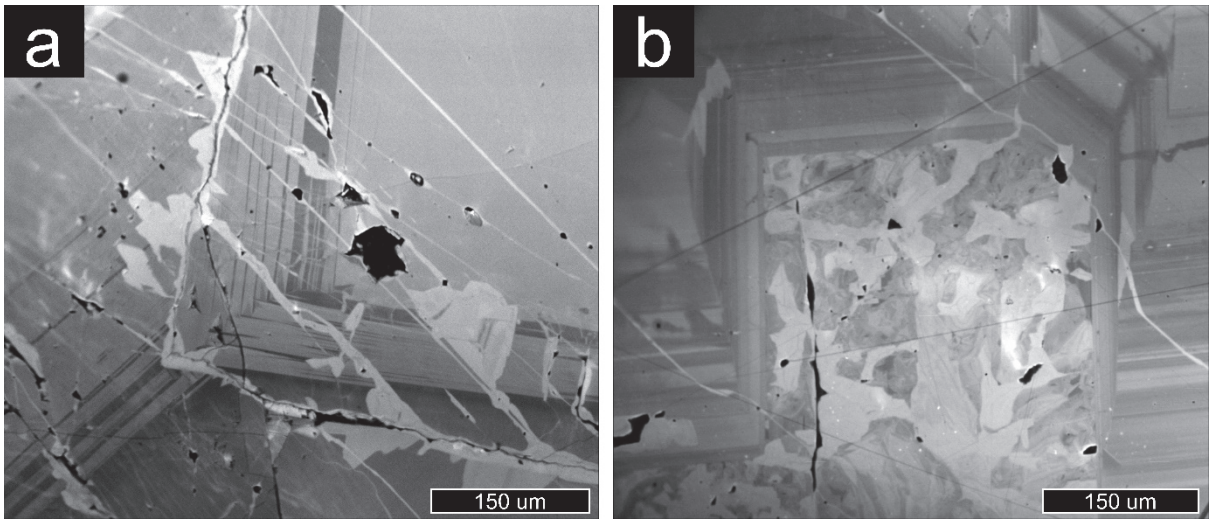


Figure 2. Cathodoluminescence images of fluorite from late veins. (a) Green fluorite with distinct cubic crystals with light and dark oscillatory zoning. There are also brighter, apparently overprinting and cross-cutting zones along grain boundaries, fractures, and veinlets. (b) Purple fluorite showing two distinct textural zones: an internal irregular and mottled texture surrounded by what appear to be oscillatory growth-zoned crystals.

2.3 Pb-isotopes

Unraveling Pb-isotope signatures in a U-bearing sulfide orebody is challenging but insightful. A detailed, very large study of Pb-isotope systematics in Pb-chalcogenide minerals measured *in-situ* in ore, including samples collected proximal to U-rich zones, and from surrounding alteration zones (*i.e.* with geological information) might help unravel and define the scale and relative timing of element mobility in time and space within Olympic Dam.

2.4 Radionuclide distributions and minerals processing

The work contained in this thesis supports the evolutionary model for Olympic Dam outlined in several recent publications (*e.g.* Krneta *et al.* 2016, Macmillan *et al.* 2016a, 2017, Ciobanu *et al.* 2017a, Verdugo-Ihl *et al.* 2017). Although primary mineralogical-geochemical zoning patterns in the deposit are preserved, evidence is widespread for cycles of replacement,

remobilization (on the scale of nanometers upwards) and recrystallization. Uranium minerals are among those which show the most persuasive evidence for these processes, in turn suggesting that the distribution of uranium, and implicitly, its daughter isotopes, has been modified over geological time.

In broad terms, minerals in the Olympic Dam ore can be divided into:

(i) minerals that retain uranium and the full ^{238}U decay chain, preserving primary isotope ratios: some early uraninite (Macmillan *et al*. 2016a), oscillatory-zoned hematite (Ciobanu *et al.* 2013, Verdugo-Ihl *et al.* 2017), and a sub-population of some accessory minerals, including fluorapatite (Krneta *et al.* 2016) and zircon (Courtney-Davies *et al.* in review). REE-fluorocarbonates (Schmandt *et al.* 2017) also fall into this category. Some of these minerals are sufficiently refractory to be valuable for U-Pb geochronology (Ciobanu *et al.* 2013, Courtney-Davies *et al.* 2016, 2019, Apukhtina *et al.* 2017, Cherry *et al*. 2018, and others);

(ii) minerals that have, due to crystal structural limitations, been unable to retain daughter radionuclides: U-minerals with characteristically low Pb contents, notably brannerite and coffinite (Macmillan *et al.* 2017);

(iii) uranium minerals of uncertain though generally young age without significant Pb-content, notably the fine-grained aphanitic uraninites that are clearly late relative to early euhedral uraninite (Macmillan *et al.* 2016a);

(iv) minerals which incorporate mobilized decay products: paragenetically early baryte (Schmandt *et al.* 2019b) and paragenetically late Sr-Ca-Al-sulphate-phosphates of the woodhouseite-svanbergite series (Owen *et al.* in review);

(v) younger (post-1.6 Ga) minerals with incorporated ^{206}Pb, the final stable product of ^{238}U decay, including Pb-chalcogenides, which are commonly although not always, spatially associated with U-minerals on the micron-scale (Chapter 6).

Characterization work, particularly nanoSIMS isotope mapping (Rollog *et al.* 2018, 2019), has demonstrated that ^{238}U and daughter RN also occur as nano- to submicron-sized particles at grain boundaries, within microfractures, and within pores and other voids throughout the ore. The contribution of these particles to the overall balance for U and Pb is difficult to estimate based on information available today. Irrespective of any quantitative estimate of proportional contribution,

the likely impact on behavior during processing must be considered of major significance given their location within features accessible to solutions, particularly during sulphate leaching.

The modification of baryte chemistry during processing documented in this thesis opens a large door to similar studies that could result in improved understanding of processing-induced alteration and associated changes in deportment of elements/isotopes of interest. While this may be well understood for ore minerals, notably copper sulfides, it is clear that the impact of other minerals and gangue phases present in a copper concentrate may actually be significantly greater than their relatively small modal proportions. Complete element budgets and deportment models during processing depend, at least ideally, on a level of understanding of all minerals present. This would require detailed chemistry of many minerals from different stages of processing materials.

In addition, a greater understanding of the mechanisms involved in the liberation and uptake of RN, notably by baryte, through experimentation of minerals in doped solutions (such as the environmental baryte studies of Curti *et al*. (2010) and Brandt *et al*. (2015)) at conditions analogous to that during leaching would be helpful for development of metallurgical methods. Such a study should acknowledge the importance of mineral textures and contained porosity in controlling mineral response during processing.

A further concept worthy of future exploration, and currently limited by instrument capabilities, is an assessment of the very finest mineral particles within the processing material. Not only do they differ in terms of trace/minor element concentrations but their greater surface area relative to mass may result in differential behavior during leaching. The fine-grained size (<7 μm) requires advanced instrumentation for detailed microscopy and chemical analysis and places limitations on the use of routine mineral identification methods such as mineral liberation analyser (MLA), which may not have the resolution to adequality identify or quantify the finest particles.

3 CONCLUDING REMARKS

The research contained within this thesis adds to the foundation of knowledge on the mineralogy and ore deposit formation of Olympic Dam. As one of the largest single deposits in the world, with resources allowing for production for more than 100 years at present rates, detailed mineral-by-mineral research is critical for understanding ore genesis and subsequent history of the deposit (Cook *et al.* 2018). New information in this thesis supplements recent data for other key

minerals in the deposit such as uranium-minerals *(e.g.* Macmillan *et al.* 2016, 2017), apatite (*e.g.* Krneta *et al.* 2016, 2017a), hematite (*e.g.* Ciobanu *et al.* 2013, Verdugo-Ihl *et al.* 2017) and copper sulfides (*e.g.* Ciobanu *et al.* 2017b). Collectively, these data contribute to a fuller picture of the world-class Olympic Dam deposit.

The wide range of trace element and isotope compositions displayed by all minerals investigated likely holds inferences to the fundamental origin of the deposit. Localized chemical variation within the broad context of a large expansive singular event can be readily linked to heterogeneous fluid regimes and permeabilities across the system. Although there is evidence for substantial post-formation modification of the ore, none seem to have greatly redefined or altered the initial chemical nature and zonation of the deposit.

The use of detailed mineral microscopy and chemical analysis to guide process metallurgy has become increasingly acknowledged as a necessary and often critical tool to maximize recovery and optimize production efficiency. The increasing demands on product quality and emphasis on health/safety in today's minerals industry have contributed to the need to identify not only those minerals containing economic, or potentially economic commodities, but also any minerals contributing deleterious (penalty) elements into the system (*e.g.* Lane *et al*. 2016). As demonstrated in this thesis and in other published research, mineralogy and mineral textures can be extraordinarily complicated at Olympic Dam, a reality that is compounded by the very fine-grained nature of the ore. A full understanding of each mineral and the chemistry that each contributes to the ore stream is thus essential to understand both where recovery might be lost, or where penalty elements are introduced. Research in this thesis has demonstrated that an interdisciplinary approach may be needed to recognize potential processing solutions based on the properties and behavior of minerals and their geological histories. This supports the need for the design of metallurgical processes that take advantage of geological information, as well as the development of potential "scrubbers" during processing. It also simply highlights that detailed element deportments in process streams represent significant knowledge gaps.

REFERENCES

Apukhtina, O.B., Kamenetsky, V.S., Ehrig, K., Kamenetsky, M.B., Maas, R., Thompson, J., McPhie, J., Ciobanu, C.L. & Cook, N.J. (2017) Early, deep magnetite-fluorapatite mineralization at the Olympic Dam Cu-U-Au-Ag deposit, South Australia. Economic

Geology, 112, 1531–1542. doi: 10.5382/econgeo.2017.4520.

Barton, M.D. (2014) Iron Oxide (-Cu-Au-REE-P-Ag-U-Co) Systems. In Turekian, K. & Holland, H. (eds.) Treatise on Geochemistry: 2nd Edition, Vol. 13, 515–541. Elsevier Ltd. doi: 10.1016/B978-0-08-095975-7.01123-2.

Brandt, F., Curti, E., Klinkenberg, M., Rozov, K. & Bosbach, D. (2015) Replacement of barite by a (Ba,Ra)SO_4 solid solution at close-to-equilibrium conditions: A combined experimental and theoretical study. Geochimica et Cosmochimica Acta, 155, 1–15.

Cherry, A.R., Ehrig, K., Kamenetsky, V.S., Ehrig, K., McPhie, J., Croley, J.L. & Kamenetsky, M.B. (2018) Precise geochronological constraints on the origin, setting and incorporation of ca. 1.59 Ga surficial facies into the Olympic Dam Breccia Complex, South Australia. Precambrian Research 315, 162–178. doi: 10.1016/j.precamres.2018.07.012.

Ciobanu, C.L., Cook, N.J. & Ehrig, K. (2017b) Ore minerals down to the nanoscale: Cu-(Fe)-sulphides from the iron oxide copper gold deposit at Olympic Dam, South Australia. Ore Geology Reviews, 81, 1218-1235.

Ciobanu, C.L., Kontonikas-Charos, A., Slattery, A., Cook, N.J., Ehrig, K. & Wade, B.P. (2017a) Short-Range Stacking Disorder in Mixed-Layer Compounds: A HAADF STEM Study of Bastnäsite-Parisite Intergrowths. Minerals 7, 227; doi: 10.3390/min7110227.

Ciobanu, C.L., Wade, B.P., Cook, N.J., Schmidt Mumm, A. & Giles, D. (2013) Uranium-bearing hematite from the Olympic Dam Cu–U–Au deposit, South Australia: A geochemical tracer and reconnaissance Pb–Pb geochronometer. Precambrian Research, 238, 129–147. doi: 10.1016/j.precamres.2013.10.007.

Cook, N.J., Ehrig, K.J., Ciobanu, C.L., Courtney-Davies, L., Verdugo-Ihl, M.R., Rollog, M., Schmandt, D.S., Owen, N.D., Macmillan, E., Kontonikas-Charos, A., Krneta, S. & Dmitrijeva, M. (2018) Why detailed mineralogy is important: Understanding evolution of the giant Olympic Dam iron-oxide copper-gold system, South Australia. 15th Quadrennial IAGOD Symposium, Salta, Argentina, 28-31 August 2018. Symposium Proceedings Volume, SegemAR, 371–372.

Courtney-Davies, L., Ciobanu, C.L., Verdugo-Ihl, M.R., Slattery, A., Cook, N.J., Dmitrijeva, M., Keyser, W., Wade, B.P., Domnick, U.I., Ehrig, K., Xu, J. & Kontonikas-Charos, A. (in review) Zircon down to the nanoscale: A record of metasomatic processes leading to large magmatic-hydrothermal ore systems. Earth and Planetary Science Letters.

Courtney-Davies, L., Tapster, S.R., Ciobanu, C.L., Cook, N.J., Verdugo-Ihl, M.R., Ehrig, K., Kennedy, A.K., Gilbert, S.E, Condon, D.J. & Wade, B.P. (2019) A multi-technique evaluation of hydrothermal hematite U-Pb isotope systematics: Implications for ore deposit geochronology. Chemical Geology, 513, 54-72. doi: 10.1016/j.chemgeo.2019.03.005.

Courtney-Davies, L., Zhu, Z., Ciobanu, C.L., Wade, B.P., Cook, N.J., Ehrig, K., Cabral, A.R. & Kennedy, A. (2016) Matrix-Matched Iron-Oxide Laser Ablation ICP-MS U–Pb

Geochronology Using Mixed Solution Standards. Minerals, 6, 85. doi:10.3390/min6030085.

Curti, E., Fujiwara, K., Iijima, K., Tits, J., Cuesta, C., Kitamura, A., Glaus, M.A. & Muller, W. (2010) Radium uptake during barite recrystallization at 23 ± 2 °C as a function of solution composition: An experimental ^{133}Ba and ^{226}Ra tracer study. Geochimica et Cosmochimica Acta, 74, 3553–3570.

Hitzman, M.W., Oreskes, N. & Einaudi, M.T. (1992) Geological characteristics and tectonic setting of Proterozoic iron oxide (Cu-U-Au-REE) deposits. Precambrian Research, 58, 241–287.

Kontonikas-Charos, A., Ciobanu, C.L., Cook, N.J., Ehrig, K., Ismail, R., Krneta, S. & Basak, A. (2018) Feldspar mineralogy and rare earth element (re)mobilization in iron-oxide copper gold systems from South Australia: a nanoscale study. Mineralogical Magazine, 82(S1), S173–S197. doi: 10.1180/minmag.2017.081.040.

Krivovichev, S.V., Krivovichev, V.G. & Hazen, R.M. (2018) Structural and chemical complexity of minerals: correlations and time evolution. European Journal of Mineralogy, 30, 231-236.

Krneta, S., Ciobanu, C.L., Cook, N.J. & Ehrig, K. (2018) Numerical Modeling of REE Fractionation Patterns in Fluorapatite from the Olympic Dam Deposit (South Australia). Minerals, 8, 342. doi: 10.3390/min8080342.

Krneta, S., Ciobanu, C.L., Cook, N.J., Ehrig, K. & Kontonikas-Charos, A. (2016) Apatite at Olympic Dam, South Australia: a petrogenetic tool. Lithos, 53, 1689–1699. doi: 10.1017/CBO9781107415324.004.

Krneta, S., Ciobanu, C.L., Cook, N.J., Ehrig, K. & Kontonikas-Charos, A. (2017a) Rare earth element behaviour in apatite from the Olympic Dam Cu-U-Au-Ag deposit, South Australia. Minerals, 7, 1-26. doi: 10.3390/min7080135.

Krneta, S., Cook, N.J., Ciobanu, C.L., Ehrig, K. & Kontonikas-Charos, A. (2017b) The Wirrda Well and Acropolis prospects, Gawler Craton, South Australia: Insights into evolving fluid conditions through apatite chemistry. Journal of Geochemical Exploration, 181, 276–291.

Lane, D.J., Cook, N.J., Grano, S.R. & Ehrig, K. (2016) Selective leaching of penalty elements from copper concentrates: A review. Minerals Engineering, 98, 110–121.

Macmillan, E., Ciobanu, C.L., Ehrig, K., Cook, N.J. & Pring, A. (2016b) Chemical zoning and lattice distortion in uraninite from Olympic Dam, South Australia. American Mineralogist, 101, 2351-2354.

Macmillan, E., Ciobanu, C.L., Ehrig, K., Cook, N.J. & Pring, A. (2016c) Replacement of uraninite by bornite via coupled dissolution-reprecipitation: Evidence from texture and microstructure. The Canadian Mineralogist, 54, 1369-1383.

Macmillan, E., Cook, N.J., Ehrig, K. & Pring, A. (2017) Chemical and textural interpretation of

late-stage coffinite and brannerite from the Olympic Dam IOCG-Ag-U deposit. Mineralogical Magazine, 81, 1323–1366. doi: 10.1180/minmag.2017.081.006.

Macmillan, E., Cook, N.J., Ehrig, K., Ciobanu, C.L. & Pring, A. (2016a) Uraninite from the Olympic Dam IOCG-U-Ag deposit: Linking textural and compositional variation to temporal evolution. American Mineralogist, 101, 1295–1320. doi: 10.2138/am-2016-5411.

Migdisov, A., Williams-Jones, A.E., Brugger, J. & Caporuscio, F.A. (2016) Hydrothermal transport, deposition, and fractionation of the REE: Experimental data and thermodynamic calculations. Chemical Geology, 439, 13–42. doi:1 0.1016/j.chemgeo.2016.06.005.

Owen, N.D., Ciobanu, C.L., Cook, N.J., Slattery, A. & Basak, A. (2018) Nanoscale study of clausthalite-bearing symplectites in Cu-Au-(U) ores: Implications for ore genesis. Minerals, 8, 67; doi: 10.3390/min8020067.

Owen, N.D., Cook, N.J., Rollog, M., Ehrig, K.J., Schmandt, D.S., Ram, R., Brugger, J., Ciobanu, C.L., Wade, B.P. & Guagliardo, P. (in review) REE-, Sr-Ca-aluminum phosphate-sulphate minerals of the woodhouseite series and role as hosts for radionuclides. American Mineralogist.

Rollog, M., Cook, N.J., Guagliardo, P., Ciobanu, C.L., Ehrig. K. & Kilburn, M. (2018) Mobility of radionuclides in the Olympic Dam Cu-U-Au-Ag deposit, South Australia. Extended abstract, International Association on the Genesis of Ore Deposits Quadrennial Symposium, Salta Argentina, August 2018.

Rollog, M., Cook, N.J., Guagliardo, P., Ehrig. K. & Kilburn, M. (2019) In situ spatial distribution mapping of radionuclides in minerals by nanoSIMS. Geochemistry: Exploration. Environment, Analysis. doi: 10.1144/geochem2018-038.

Schmandt, D.S., Cook, N.J., Ciobanu, C.L., Ehrig, K., Wade, B.P., Gilbert, S. & Kamenetsky, V.S. (2017) Rare Earth Element Fluorocarbonate Minerals from the Olympic Dam Cu-U-Au-Ag Deposit, South Australia. Minerals, 7, 202. doi: 10.3390/min7100202

Schmandt, D.S., Cook, N.J., Ciobanu, C.L., Ehrig, K., Wade, B.P., Gilbert, S. & Kametetsky, V.S. (2019a) Rare earth element phosphates from the Olympic Dam Cu-U-Au-Ag deposit, South Australia: Recognizing temporal-spatial controls on REE mineralogy in an evolved IOCG system. The Canadian Mineralogist, 57, 1-22. doi: 10.3749/canmin.1800043.

Schmandt, D.S., Cook, N.J., Ehrig, K., Gilbert, S., Wade, B.P., Rollog, M., Ciobanu, C.L. & Kamenetsky, V.S. (2019b) Uptake of trace elements by baryte during copper ore processing: a case study from Olympic Dam, South Australia. Minerals Engineering, 135, 83-94. doi: 10.1016/j.mineng.2019.02.034.

University of Adelaide Institute for Mineral and Energy Resources (Aug 2018) https://www.adelaide.edu.au/copper-uranium-research/

Verdugo-Ihl, M.R., Ciobanu, C.L., Cook, N.J., Ehrig, K. J., Courtney-Davies, L. & Gilbert, S.

(2017) Textures and U-W-Sn-Mo signatures in hematite from the Olympic Dam Cu-U-Au-Ag deposit, South Australia: Defining the archetype for IOCG deposits. Ore Geology Reviews, 91, 173–195. doi: 10.1016/j.oregeorev.2017.10.007.

Zainurin, A.H.M., Cook, N.J., Ciobanu, C.L., Slattery, A., Schmandt, D.S. & Liu, W. (2018) Compositional and Textural Characterization of Rare Earth Element Fluorocarbonate Minerals. University of Adelaide, B. Eng. (Hons.) poster, Ingenuity 2018.

CHAPTER 8

SUPPLEMENTARY AND ADDITIONAL MATERIAL

SUPPLEMENTARY MATERIAL A

SUPPLEMENTARY MATERIAL FOR CHAPTER 2

Rare earth element fluorocarbonate minerals from the Olympic Dam Cu-U-Au-Ag deposit, South Australia

INCLUDES:

SUPPLEMENTARY MATERIAL 1: ANALYTICAL METHODS, ELECTRON PROBE MICROANALYSIS

SUPPLEMENTARY MATERIAL 2: ANALYTICAL METHODS, LASER ABLATION INDUCTIVELY COUPLED MASS SPECTROMETRY

FIGURE S1: DETAILED IMAGES OF THE SAMPLE SET

FIGURE S2: EXAMPLES OF LA-ICP-MS DOWNHOLE LASER PROFILES

TABLE S1: SAMPLE XRD DATA

TABLE S2: FULL DETAILS OF ANALYTICAL SET-UP FOR EPMA ANALYSIS

TABLE S3: FULL EPMA STANDARD LIST

TABLE S4: FULL DETAILS OF ANALYTICAL SET-UP FOR LA-ICP-MS ANALYSIS

TABLE S5: COMPLETE EPMA DATASET FOR REE-FLUOROCARBONATES

TABLE S6: FULL LA-ICP-MS DATASET FOR REE-FLUOROCARBONATES

Supplementary Material 1: Analytical Methods, Electron Probe Microanalysis

Quantitative compositions of REE-fluorocarbonates were determined using a Cameca SX-Five electron probe microanalyzer (EPMA) equipped with 5 tunable wavelength-dispersive spectrometers. The microscope uses PeakSite software for microscope operation, and Probe for EPMA software (distributed by Probe Software Inc.) for data acquisition and processing. The REE-fluorocarbonate structure is able to substitute a diverse range of elements at highly variable concentrations. As such it was necessary to analyze for a large list of elements at variable operating conditions to minimize any dead time and beam damage effects. For major to minor elements operating conditions were 15 keV/20nA, with trace elements acquired at an increased beam current of 100 nA (see supplementary Table S2).

Initially, a set of 42 elements was measured F (Kα), Na (Kα), Mg (Kα), Al (Kα), Si (Kα), P (Kα), S (Kα), Cl (Kα), K (Kα), Ca (Kα), Sc (Kα), Ti (Kα), V (Kα), Mn (Kα), Fe (Kα), Cu (Kα), As (Lα), Sr (Lα), Y (Lα), Zr (Lα), Nb (Lα), Te (Lα), Ba (Lα), Ta (Lα), W (Lα), Pb (Mβ), Bi (Mα), La (Lα), Ce (Lα), Pr (Lβ), Nd (Lβ), Sm (Lβ), Eu (Lα), Gd (Lβ), Tb (Lα), Dy (Lα), Ho (Lβ), Er (Lα), Tm (Lα), Yb (Lα), Th (Mα), and U (Mβ). This list was subsequently shortened by elimination of Mg, Sc, Ti, V, Mn, Cu, Te, Ba, Ta, and W since concentrations of these elements were consistently below minimum limits of detection (mdl). Detailed wave-scans were acquired on standards and unknowns to best determine positions for background measurements of these elements. A combination of traditional 2-point linear, multipoint fits, and "shared" background fits were used across the list of elements. In simple background regions, a traditional 2-point linear fit was used. For more complex regions of the spectrum, more background points were required, in which multipoint or "shared" fits were used [1-3]. Calibration and data reduction were carried-out in Probe for EPMA, distributed by Probe Software Inc.

Mindful of the extended element list and beam damage effects, on-peak count times were 15-20 s for elements which are not the primary focus of this study (i.e. non-target elements) (Cu, Fe, Si, and others), 20-40 s for target elements (REE, Sr, and others), and 60-100 s for trace elements of interest (including Pb, U, and Th). Total acquisition time per analytical point was ~20 minutes. In addition, elements that are traditionally seen as "mobile" under the electron beam were analyzed first within the first 2 minutes of analysis, and include Na, F, Ca, K, P, and S.

The primary calibration and interference standards used in the analysis were of both synthetic and natural, and include the Smithsonian and Edinburgh REE, Astimex, P&H, and Taylor standard sets. Full detail of set up and standards can be found in supplementary Tables S2 and S3.

Supplementary Material 1 References

1. Goemann, K.; Donovan, J.J.; Feig, S.T.; Thompson, J. "Sharing" Background Measurements in Wavelength Dispersive Electron Probe Microanalysis. In: *Program Guide with Abstracts,* Microanalysis Society - Topical Conference on Electron-Probe Microanalysis, Madison, WI, USA, 16-19 May 2016; 28-29. ISBN 978-1-5323-0217-6.
2. Goemann, K.; Donovan, J.J.; Feig, S.T.; Thompson, J. Shared backgrounds in wavelength-dispersive electron probe microanalysis. In: *Book of Tutorials and Abstracts*, 15th European Workshop on Modern Developments and Applications in Microbeam Analysis, 7th Meeting of the International Union of Microbeam Analysis Societies, Konstanz, Germany, 7-11 May 2017; *European Microbeam Analysis Society eV*, 378-379. ISBN 978-90-8827-693-0.
3. Goemann, K.; Donovan, J.J. Electron probe microanalysis of complex natural sulphides using shared background measurements. In: *The Australian Microscopy & Micronalysis Society AMAS 2017*, 14th Biennial Australian Microbeam Analysis Symposium, Brisbane, Australia, 6-10 February 2017; 61-62. ISBN 978-0-9580408-6-0.

Supplementary Material 2: Analytical Methods, Laser Ablation Inductively Coupled Mass Spectrometry

Trace element and isotopic analysis was performed by Laser Ablation Inductively Coupled Mass Spectrometry (LA-ICP-MS) using a RESOlution-LR ArF excimer laser ablation system (Australian Scientific Instruments) equipped with a large format S155 sample chamber (Laurin Technic Inc.) and coupled to an Agilent 7900x ICP-MS. Reference standards used were GSD-1G and NIST-610 glasses. Operating conditions were set at 5 Hz and a fluence of 3.5 J/cm2. This dataset supplements the EPMA data by: providing quantitative data for (H)REE elements at low concentrations approaching the mdl by EPMA; and concentration data for other potential trace elements well below EPMA mdl values.

Spot-size was generally 9 μm, although occasionally up to 29 μm where the mineral grain in question was large enough. Following 5 pulses of pre-ablation cleaning, 30 s of gas background was collected, followed by a sample ablation of 40 s, giving 70 s of instrument analysis. Isotopes measured were ^{23}Na, ^{27}Al, ^{29}Si, ^{31}P, ^{43}Ca, ^{45}Sc, ^{55}Mn, ^{57}Fe, ^{65}Cu, ^{75}As, ^{88}Sr, ^{89}Y, ^{90}Zr, ^{93}Nb, ^{137}Ba, ^{139}La, ^{140}Ce, ^{141}Pr, ^{146}Nd, ^{147}Sm, ^{153}Eu, ^{157}Gd, ^{159}Tb, ^{163}Dy, ^{165}Ho, ^{166}Er, ^{169}Tm, ^{172}Yb, ^{175}Lu, ^{178}Hf, ^{181}Ta, ^{182}W, ^{202}Hg, ^{204}Pb, ^{206}Pb, ^{207}Pb, ^{208}Pb, ^{209}Bi, ^{232}Th, and ^{238}U. Dwell times for ^{23}Na, ^{27}Al, ^{29}Si, and ^{31}P were 0.005 s, ^{206}Pb and ^{207}Pb were 0.02 s, ^{232}Th, and ^{238}U were 0.03 s, and all others were 0.01 s giving a total sweep time of 0.513 seconds. ^{202}Hg was collected in order to correct for the interference of ^{204}Hg on ^{204}Pb. Calibration used Ce as the internal standard element based on the wt.% Ce measured from each location by EPMA. Supplementary Table S4 details the set up and mdl values.

Data reduction was performed using the software Iolite v3.4 [1] and processed using the "Trace_Elements_IS" data reduction scheme. LA-ICP-MS data presented in Table 3 of the manuscript shows mean and range data values for textural and mineral groupings. Filtered mean and range LA-ICP-MS values (excluding more than 20% deviation from the mean) was used for the chondrite-normalized REE fractionation patterns given as Figure 9b of the manuscript to aid in the visibility of the individual ranges. The full LA-ICP-MS dataset can be found in supplementary Table S6.

Supplementary Material 2 References

1. Paton, C.; Hellstrom, J.; Paul, B.; Woodhead, J.; Hergt, J. Iolite: Freeware for the visualisation and processing of mass spectrometric data. *J. Anal. Atom. Spectrom*. **2011**, *26*, 2508.

Figure S1: Detailed description of the sample set. Backscatter electron scans of sample blocks illustrating macroscopic textures and dominant mineralogy.

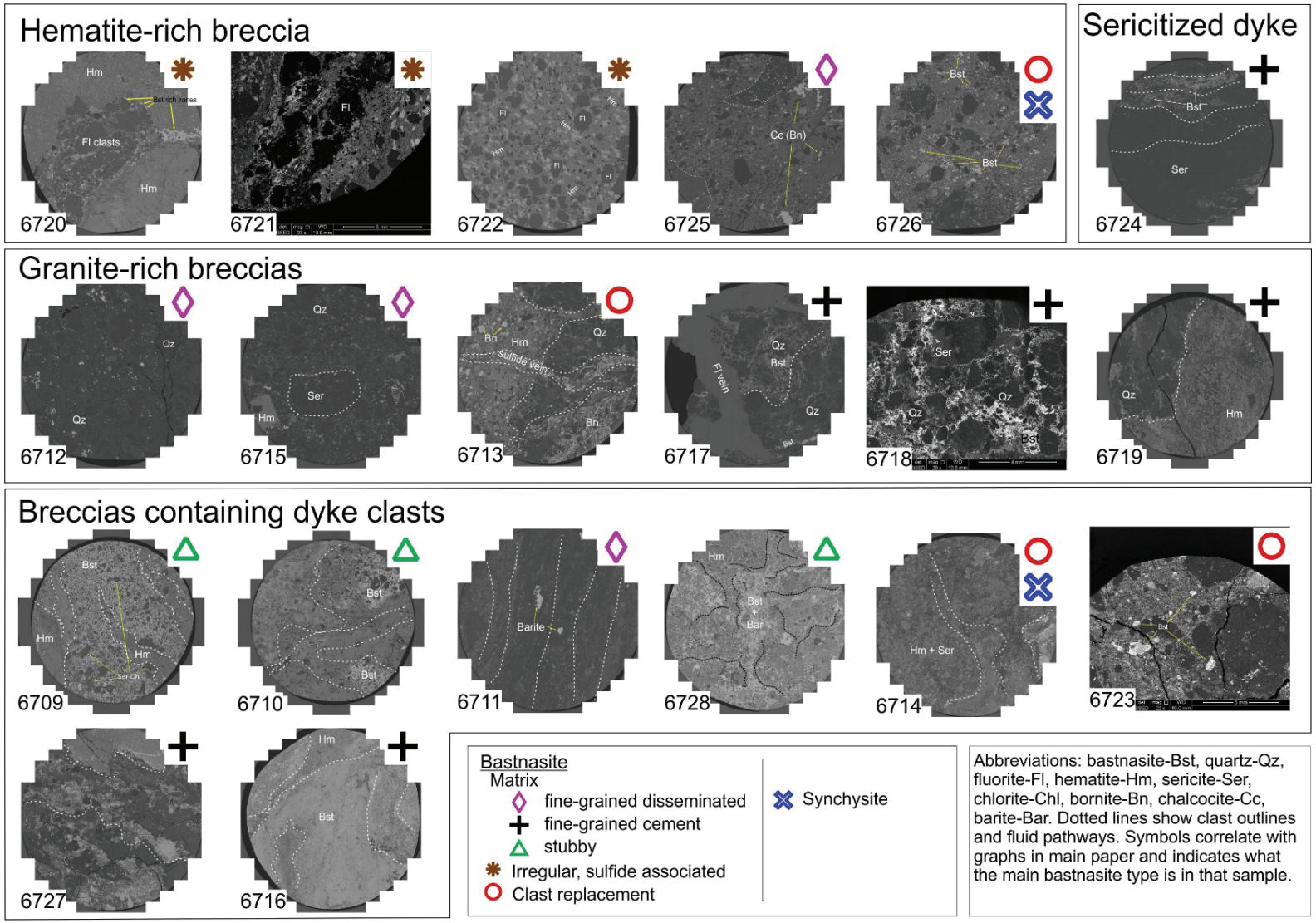


Figure S2: Downhole profiles from LA-ICP-MS analysis demonstrating variation in U and Th and other elements in bastnäsite. Figures A and B show counts-per-second (CPS) vs. time (seconds). Arrows to highlight signals caused by inclusions.

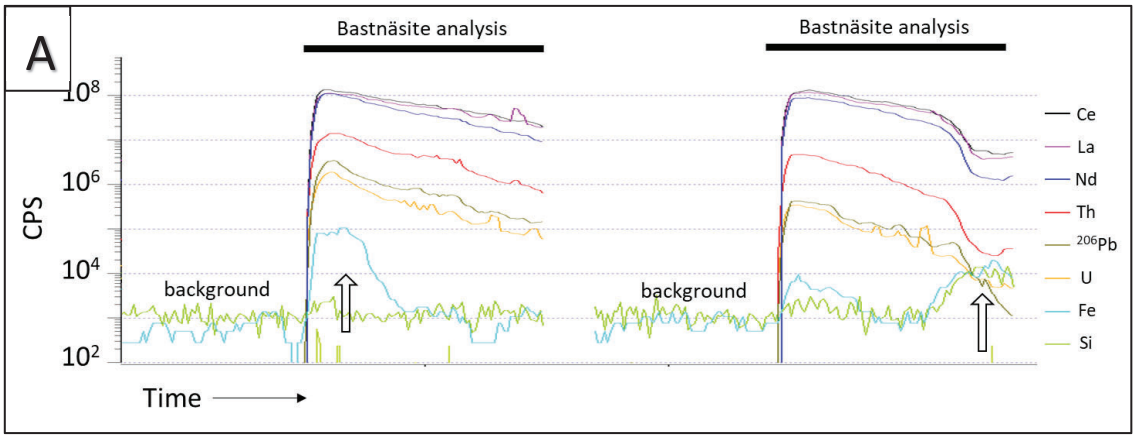


Figure A: Bastnäsite analysis with elevated Th, U, and ^{206}Pb with REE in bastnäsite, and with Fe and Si contained within inclusions. RX6726.

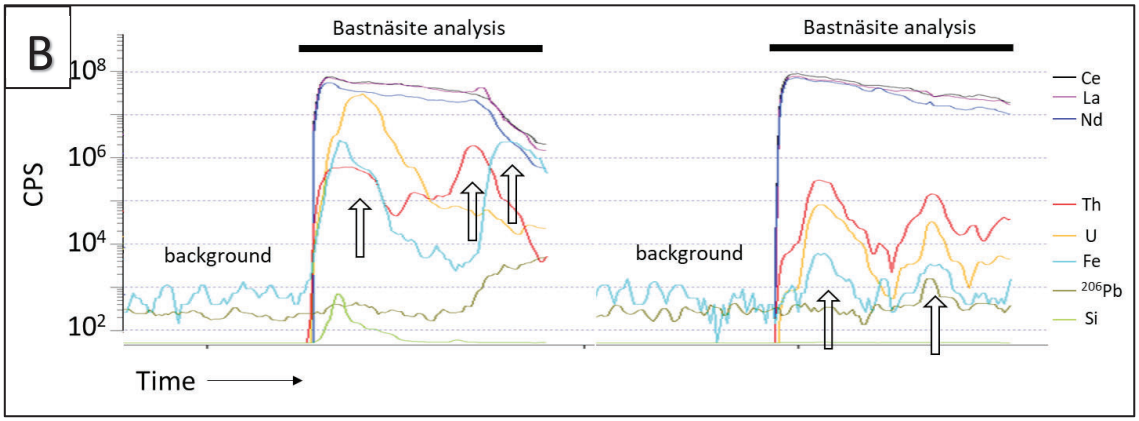


Figure B: Bastnäsite analysis with inclusions containing U, Th, and Fe. RX6709.

Table S1: XRD values from expanded sample material of sample block location for detailed analysis.

Lithology	Sample location				Mineral abundance wt% (XRD)*										
	Area	Drill hole	Sample no.	Core depth (m)	Hm	Qz	Chl	Fl	Bar	Flo	Bst	Ser	Cp	Bn	Cc
Breccias containing dyke clasts	NW arm	RU34-3829	RX6709	72.8-73.0	32	-	10	-	2	3	44	8	-	2	-
			RX6710	73.6-73.7	38	-	6	-	1	4	36	15	-	-	-
			RX6711	74.7-74.8	20	-	9	-	1	4	1	65	-	-	-
		RU41-2571	RX6728	174.8-174.9	72	-	6	-	7	1	9	4	-	-	-
	East edge	RU33-159	RX6714	66.3-66.4	47	-	-	-	0	4	11	38	-	-	-
		RU37-7354	RX6723	4.3-4.4	20	39	-	1	-	1	1	35	-	1	3
	Central	RU34-454	RX6716	82.9-83.0	46	2	-	-	-	1	37	14	-	-	-
		RU45-2661	RX6727	51.8-51.9	16	14	-	1	4	2	14	39	-	2	8
Granite-rich breccias	East edge	RU3-558	RX6712	23.7-23.8	11	39	-	-	1	1	4	45	-	-	-
		RU4-105	RX6715	12.2-12.3	33	30	1	-	19	0	5	12	-	-	-
	Central	RU3-954	RX6713	70.1-70.2	15	32	0	8	1	1	1	34	-	8	-
	NW arm	RU31-751	RX6717	90.3-90.4	7	36	4	2	-	-	6	45	-	-	-
			RX6718	90.8-91.0	8	43	1	2	-	-	5	42	-	-	-
		RU31-767	RX6719	5.3-5.4	21	47	-	1	-	-	8	18	-	3	3
Hematite-rich breccia	Central	RU40-1407	RX6720	19.0-19.2	60	3	-	21	-	0	1	9	5	1	-
			RX6721	19.4-19.5	32	3	-	33	-	-	15	7	3	6	-
			RX6722	19.7-19.8	62	2	-	19	-	-	1	-	0	16	-
	East edge	RU38-2994	RX6725	92.8-92.9	NO DATA										
		RU38-2685	RX6726	77.1-77.3	22	21	1	-	-	1	9	41	-	1	4
Sericitized dyke	NW arm	RU41-5181	RE6724	183.7-183.8	5	-	-	-	-	-	17	78	-	-	-

mineral abbreviations: Hm - hematite; Qz - quartz; Chl - chlorite; Fl - fluorite; Bar - barite; Flo - florencite; Bst - bastnasite; Ser - sericite; Cp - chalcopyrite; Bn - bornite; Cc - chalcocite.

*Sericite includes Muscovite-1M and -2M1 and chlorite includes chamosite.

Table S2: Full details of analytical set-up for EPMA analysis; elements analyzed, peak/background positions, count times, standards, elemental overlap corrections used in REE mineral package.

Element and Line	Diffracting Crystal (Sp#)	Background type/fit	kV/nA	Peak Count Time	Bkgd Count Times		# bkgd points acquired	Standards[1]				Overlaping element and order with their overlap correction standard											
					Lo	Hi		Primary standards	Secondary standards 1	Secondary standards 2	Interference standards	Interfering line	Int std	Interfering line	Int std	Interfering line	Int std	Interfering line	Int std	Interfering line	Int std	Interfering line	Int std
Cu Ka	LLIF (3)	Shared	15/20	20	10	10	1/3	556				Tm I	815	Tb I	814	Er I	805						
Ho Lb	LLIF (3)	Shared	15/100	40	10	10	4/8	1109	808			Y II	816	Yb I	817	Sm I	635	Eu I	806	Th II	629		
Yb La	LLIF (3)	Shared	15/100	40	10	10	4/12	1112	817			Y II	816	Ho I	808	Dy I	804	Tb I	814				
Tm La	LLIF (3)	Shared	15/100	40	10	10	7/12	1111	815			Dy I	804	Sm I	635								
Er La	LLIF (3)	Shared	15/100	40	10	10	5/8	1110	805			Tb I	814										
Gd Lb	LLIF (3)	Shared	15/100	40	10	10	7/8	634	1106			U II	631	Ho I	808								
Dy La	LLIF (3)	Shared	15/100	40	10	10	8/6	1108	804			Th II	629	Eu I	806	Pb II	627	Yb I	817				
Fe Ka	LLIF (3)	Shared	15/20	20	10	10	8/6	502				Th II	629										
Tb La	LLIF (3)	Shared	15/100	40	10	10	8/6	1107	814			Pb II	627	Pr I	637	Sm I	635						
Sm Lb	LLIF (3)	Shared	15/100	40	10	10	12/9	635	1104			Tb I	814	Nd I	636								
Mn Ka	LLIF (3)	Shared	15/20	20	10	10	12/6	557				As II	562										
Eu La	LLIF (3)	Shared	15/100	40	10	10	3/6	1105	806			Pr I	637	Nd I	636								
Nd Lb	LLIF (3)	Shared	15/100	40	10	10	4/3	636	1103			U II	631										
Pr Lb	LLIF (3)	Shared	15/100	40	10	10	4/1	637	1102			U III	631										
Ce La	PET (1)	Linear	15/100	20	40	40	1/1	633	1101			Y III	816	Yb II	817	Tm II	815						
La La	PET (1)	Linear	15/100	20	40	40	1/1	632	1100			Nd I	636	Tm II	815								
Ti Ka	PET (1)	Multipoint	15/20	30	20	20	2/2	559				U III	631										
Ba La	PET (1)	Multipoint	15/100	20	20	20	1/2	554			816	Ti I	559	U III	631	Pr I	637						
Te La	PET (1)	Multipoint	15/100	20	20	20	2/2	560				Sm II	635	U I	631								
Ca Ka	PET (1)	Multipoint	15/20	20	20	20	2/2	535				Y IV	816	Yb II	817	Th III	629	Dy II	804	Tb II	814		
U Mb	LPET (1)	Multipoint	15/100	60	20	20	2/2	631				K I	541	Th I	629	Ho II	808	Gd II	634				
K Ka	LPET (1)	Multipoint	15/20	20	20	20	2/2	541				U I	631										
Th Ma	LPET (5)	Linear	15/100	60	40	40	1/1	629				Gd II	634	Y V	816								
Cl Ka	LPET (5)	Linear	15/20	15	40	40	1/2	545				Ce II	633	Nd II	636	Er III	805	Ho III	808				
Pb Mb	LPET (5)	Multipoint	15/100	100	30	30	3/2	627	520			U I	631	S I	530	Ce II	633	Y VI	638				
S Ka	LPET (5)	Multipoint	15/20	20	20	20	1/2	530				Nd II	636	La II	632								
Nb La	LPET (5)	Multipoint	15/100	20	10	20	1/2	616				Mn III	557										
Zr La	LPET (5)	Multipoint	15/100	30	20	20	2/1	599				Nd III	636	P I	740	Tb IV	814						
P Ka	LPET (5)	Multipoint	15/20	15	20	20	2/2	504				Ca II	558	Cu IV	556	Tm IV	815	Gd III	1106	Ce III	1101		
Y La	LPET (5)	Multipoint	15/100	40	20	20	2/2	628	1115	638		La III	632	Ho IV	808								
F Ka	PC0 (2)	Multipoint	15/20	20	40	40	4/4	2001	2002			Sm VIII	635	Ce VII	633	P III	740	Y III	638	La VIII	632	U V	631
Sr La	TAP (4)	Multipoint	15/100	30	20	20	1/3	513				Y I	816	U II	631								
Si Ka	TAP (4)	Multipoint	15/20	40	20	20	1/2	501				Y I	638	Tb IV	814	Nd III	636	Er IV	805				
Al Ka	TAP (4)	Multipoint	15/20	20	20	20	2/2	501			740	Ti III	559	Yb I	817	Ho I	808						
As La	TAP (4)	Multipoint	15/100	40	20	20	1/2	562			558	Sm I	635	Nd IV	636								
Mg Ka	TAP (4)	Multipoint	15/20	30	20	20	1/2	502				U II	631										
Na Ka	TAP (4)	Multipoint	15/20	20	20	20	2/2	501				U III	631										
V Ka	LPET (5)	Linear	15/100	40	10	10	1/1	608															
W La	LPET (5)	Linear	15/100	40	10	10	1/1	596	739														
Sc Ka	LPET (5)	Linear	15/100	40	10	10	1/1	619	1116			Ca I	535										
Ta La	LPET (5)	Linear	15/100	40	10	10	1/1	601															
Bi Ma	LPET (5)	Linear	15/100	40	10	10	1/1	568				Ce II	1101										

[1] **See Full Standard List (Table S3) for standard number references**

Table S3: Full EPMA standard list

Full Standard List								
Ref. Num.	Mineral/ Composition	Manufacturer Information	Ref. Num.	Mineral/ Composition	Manufacturer Information	Ref. Num.	Mineral/ Composition	Manufacturer Information
501	Albite	Astimex	608	Vanadium	Astimex metal	815	Tm metal	Astimex REE block
502	Almandine Garnet	Astimex	616	Niobium	Astimex metal	816	Y metal	Astimex REE block
504	Apatite	Astimex	619	Scandium	Astimex metal	817	Yb metal	Astimex REE block
513	Celestite	Astimex	627	Pb Glass	NIST	1100	Lanthanum Phosphate	Smithsonian REEPO4 std
520	Crocoite	Astimex	628	Rare Earth Glass Standard	Drake and Weill glasses	1101	Cerium Phosphate	Smithsonian REEPO4 std
530	Marcasite	Astimex	629	Huttonite (ThSiO4)	DAS	1102	Praseodymium Phosphate	Smithsonian REEPO4 std
535	Plagioclase	Astimex	631	UO2	DAS	1103	Neodymium Phosphate	Smithsonian REEPO4 std
541	Sanidine	Astimex	632	La Glass	University Edinburgh	1104	Samarium Phosphate	Smithsonian REEPO4 std
545	45 Tugtupite (Na4BeAlSi4O12Cl)	Astimex	633	Ce Glass	University Edinburgh	1105	Europium Phosphate	Smithsonian REEPO4 std
551	51 Yittrium Al Garnet (Y3Al5O12)	Astimex	634	Gd Glass	University Edinburgh	1106	Gadolinium Phosphate	Smithsonian REEPO4 std
554	Barite	P&H	635	Sm Glass	University Edinburgh	1107	Terbium Phosphate	Smithsonian REEPO4 std
556	Chalcopyrite	P&H	636	Nd Glass	University Edinburgh	1108	Dysprosium Phosphate	Smithsonian REEPO4 std
557	Rhodonite	P&H	637	Pr Glass	University Edinburgh	1109	Holmium Phosphate	Smithsonian REEPO4 std
558	Wollastonite	P&H	638	Y2O3	University Edinburgh	1110	Erbium Phosphate	Smithsonian REEPO4 std
559	Rutile	P&H	739	CaWO4	Taylor Block	1111	Thulium Phosphate	Smithsonian REEPO4 std
560	Silver Telluride	P&H	740	GaP	Taylor Block	1112	Ytterbium Phosphate	Smithsonian REEPO4 std
562	Gallium Arsenide	P&H	804	Dy metal	Astimex REE block	1115	Yttrium Phosphate	Smithsonian REEPO4 std
568	Guajuatite Bi2Se3 Synthetic	P&H	805	Er metal	Astimex REE block	1116	Scandium Phosphate	Smithsonian REEPO4 std
596	Tungsten	Astimex metal	806	EuF3	Astimex REE block	2001	Apatite	Astimex Apatite
599	Zirconium	Astimex metal	808	Ho metal	Astimex REE block			
601	Tantalum	Astimex metal	814	Tb metal	Astimex REE block	2002	Apatite	P&H

Table S4: Full details of analytical set-up for LA-ICP-MS analysis of REE fluorocarbonates.

Analysis Details			
Mass	Element	Dwell Time (s)	Avg Detection Limit (ppm)
23	Na	0.005	64.3
27	Al	0.005	4.66
29	Si	0.005	1385
31	P	0.005	208
43	Ca	0.01	892
45	Sc	0.01	1.16
55	Mn	0.01	3.55
57	Fe	0.01	73.0
65	Cu	0.01	5.21
75	As	0.01	6.85
88	Sr	0.01	0.067
89	Y	0.01	0.041
90	Zr	0.01	0.076
93	Nb	0.01	0.019
137	Ba	0.01	0.245
139	La	0.01	0.013
141	Pr	0.01	0.013
146	Nd	0.01	0.050
147	Sm	0.01	0.051
153	Eu	0.01	0.038
157	Gd	0.01	0.177
159	Tb	0.01	0.014
163	Dy	0.01	0.034
165	Ho	0.01	0.008
166	Er	0.01	0.032
169	Tm	0.01	0.008
172	Yb	0.01	0.036
175	Lu	0.01	0.011
178	Hf	0.01	0.029
181	Ta	0.01	0.010
182	W	0.01	0.039
202	Hg	0.01	-
204	Pb	0.01	18.4
206	Pb	0.02	0.197
207	Pb	0.02	0.169
208	Pb	0.01	0.166
209	Bi	0.01	0.275
232	Th	0.03	0.009
238	U	0.03	0.008

Operating Conditions			
	Spot Size (um)	Hz	Fluence (J/cm^2)
Unknowns	9-29	5	3.5
Standards (GSD-1G, NIST-610)	51		

Table S5: Complete EPMA dataset for REE fluorocarbonates in weight percent (wt%).
Type bastnasite abbreviations: Mx-stby, Matrix-stubby; Mx-diss, Matrix-disseminated; Mx-f.g., Matrix-fine grained; CR, Clast Replacement; Irr., Irregular sulfide associated.

Sample	RX6709	RX6709	RX6709	RX6709	RX6710	RX6710	RX6710	RX6710	RX6710	RX6710	RX6710	RX6710	RX6710	RX6710	RX6710	RX6710	RX6710	RX6710	RX6710
Type	Mx-stby	Mx-stby	Mx-stby	Mx-stby	Mx-stby	Mx-stby	Mx-stby	Mx-stby	Mx-stby	Mx-stby	Mx-stby	Mx-stby	Mx-stby	Mx-stby	Mx-stby	Mx-stby	Mx-stby	Mx-stby	Mx-stby
Number	17306	17307	17308	17309	305	306	307	308	296	297	298	299	292	293	294	295	287	288	309
Ca	0.02	0.02	<0.008	<0.008	0.04	0.02	0.03	0.03	0.03	0.06	0.03	0.09	0.03	0.03	0.05	0.02	0.01	0.03	0.02
K	<0.008	0.01	0.01	<0.008	<0.008	<0.008	<0.008	<0.008	0.01	0.01	<0.008	<0.008	0.01	0.01	<0.008	0.01	0.02	0.02	<0.008
U	<0.02	<0.03	<0.03	<0.03	<0.02	<0.02	<0.02	<0.02	<0.02	<0.02	<0.02	<0.02	<0.02	<0.02	<0.02	<0.02	<0.02	<0.02	<0.03
La	16.80	21.30	16.30	20.90	15.40	15.80	14.20	14.90	17.30	20.00	17.30	15.50	18.70	17.70	17.60	18.70	17.90	14.10	14.60
Ce	37.30	38.00	36.70	35.10	32.50	33.90	30.90	32.10	34.50	23.80	33.20	33.20	35.10	33.90	34.40	34.60	33.80	32.10	33.20
F	7.60	7.30	7.30	7.40	7.30	7.40	7.30	7.20	7.30	7.40	7.40	7.20	7.70	7.40	7.40	7.30	7.40	7.30	7.40
Fe	0.06	0.15	0.07	0.10	0.49	<0.04	<0.04	<0.04	0.26	0.17	0.26	0.12	0.09	0.15	0.44	0.15	0.27	0.65	0.94
Ho	<0.09	<0.09	<0.09	<0.09	<0.09	<0.09	<0.09	<0.09	<0.09	<0.09	<0.09	<0.09	<0.09	<0.09	<0.09	<0.09	<0.09	<0.09	<0.09
Yb	<0.05	<0.05	<0.05	<0.05	<0.05	<0.05	<0.05	0.07	<0.05	<0.05	<0.05	<0.05	<0.05	<0.05	<0.05	<0.05	<0.05	<0.05	<0.05
Tm	<0.05	<0.05	<0.05	<0.05	<0.05	<0.05	<0.05	<0.05	<0.05	<0.05	<0.05	<0.05	<0.05	<0.05	<0.05	<0.05	<0.05	<0.05	<0.05
Er	0.06	<0.05	0.06	<0.05	0.08	0.06	0.09	0.14	<0.05	0.10	<0.05	0.11	<0.05	<0.05	<0.05	<0.05	<0.05	0.08	0.09
Gd	0.41	0.16	0.51	0.37	0.50	0.36	0.56	0.78	0.23	1.00	0.20	0.59	0.13	0.09	0.21	0.09	0.14	0.59	0.55
Dy	0.18	<0.05	0.22	0.20	0.24	0.08	0.29	0.42	<0.05	0.35	<0.05	0.27	<0.05	<0.05	<0.05	<0.05	<0.05	0.24	0.22
Tb	0.08	0.08	0.08	0.08	0.08	<0.05	0.08	0.11	<0.05	0.05	<0.05	0.06	<0.05	0.05	0.06	<0.05	<0.05	0.06	0.07
Sm	1.10	0.59	1.30	0.95	1.10	0.98	1.30	1.50	0.79	1.70	0.75	1.20	0.52	0.59	0.71	0.44	0.59	1.40	1.40
Eu	0.54	0.27	0.64	0.45	0.46	0.43	0.67	0.73	0.37	0.76	0.35	0.58	0.26	0.24	0.31	0.23	0.27	0.60	0.60
Nd	11.10	9.50	12.40	11.80	11.30	11.20	12.40	12.60	10.50	13.60	10.40	11.80	9.20	9.30	9.90	8.60	9.70	12.10	12.40
Pr	3.70	3.50	3.90	4.10	3.60	3.70	3.80	3.80	3.50	4.00	3.50	3.70	3.40	3.50	3.50	3.30	3.30	3.70	3.80
Na	<0.03	<0.03	<0.03	<0.03	<0.03	<0.03	<0.03	<0.03	<0.03	<0.03	<0.03	<0.03	<0.03	<0.03	<0.03	<0.03	<0.03	<0.03	<0.03
Si	<0.01	<0.01	<0.01	<0.01	<0.01	<0.01	<0.01	<0.01	<0.01	<0.01	<0.01	<0.01	<0.01	<0.01	<0.01	<0.01	<0.01	<0.01	<0.01
Al	<0.01	0.07	<0.01	<0.01	0.03	<0.01	<0.01	<0.01	<0.01	<0.01	<0.01	<0.01	<0.01	<0.01	<0.01	<0.01	<0.01	0.58	0.03
Sr	0.02	0.02	0.02	0.02	0.03	0.02	0.02	<0.01	0.05	0.02	0.02	0.04	0.02	0.02	0.02	0.03	0.03	0.21	0.04
As	<0.02	<0.02	<0.02	<0.02	<0.02	<0.02	<0.02	<0.02	<0.02	<0.02	<0.02	<0.02	<0.02	<0.02	<0.02	<0.02	<0.02	<0.02	<0.02
P	<0.01	<0.01	<0.01	<0.01	<0.01	<0.01	<0.01	<0.01	<0.01	<0.01	<0.01	<0.01	<0.01	<0.01	<0.01	<0.01	<0.01	<0.01	<0.01
S	0.07	0.04	0.03	<0.01	0.04	0.04	0.03	0.02	0.02	<0.01	0.06	0.03	0.05	0.05	0.03	0.02	0.03	0.10	0.03
Cl	0.02	0.02	<0.01	0.02	0.04	0.02	0.01	0.02	0.01	0.01	<0.01	0.01	0.01	0.02	<0.01	0.01	0.02	0.02	0.02
Th	<0.02	<0.02	<0.02	<0.02	0.02	<0.02	<0.02	<0.02	0.05	<0.02	<0.02	0.17	<0.02	<0.02	<0.02	<0.02	<0.02	<0.02	<0.02
Pb	<0.03	<0.03	<0.03	<0.03	<0.03	<0.03	<0.03	<0.03	<0.03	<0.03	<0.03	<0.03	<0.03	<0.03	<0.03	<0.03	<0.03	<0.03	<0.03
Y	0.35	0.07	0.50	0.41	0.70	0.34	0.95	1.20	0.19	1.00	0.15	0.85	0.07	0.08	0.14	0.04	0.05	0.73	0.70
Nb	<0.02	<0.02	<0.02	<0.02	<0.02	<0.02	<0.02	<0.02	<0.02	<0.02	<0.02	<0.02	<0.02	<0.02	<0.02	<0.02	<0.02	<0.02	<0.02
Zr	<0.02	<0.02	<0.02	<0.02	<0.02	<0.02	<0.02	<0.02	<0.02	<0.02	<0.02	<0.02	<0.02	<0.02	<0.02	<0.02	<0.02	<0.02	<0.02
Total	79.4	81.1	80.0	81.9	74.0	74.4	72.6	75.6	75.1	74.0	73.6	75.5	75.3	73.1	74.8	73.5	73.5	74.6	76.1
'<' indicates minimum detection limit																			
Total not including < values.																			

RX6710 Mx-stby	RX6710 Mx-stby	RX6728 Mx-stby	RX6728 Mx-stby	RX6728 Mx-stby	RX6728 Mx-stby	RX6728 Mx-stby	RX6728 Mx-stby	RX6728 Mx-stby	RX6728 Mx-stby	RX6728 Mx-stby	RX6728 Mx-stby	RX6728 Mx-stby	RX6728 Mx-stby	RX6728 Mx-stby	RX6728 Mx-stby	RX6728 Mx-stby	RX6728 Mx-stby	RX6728 Mx-stby	RX6728 Mx-stby	RX6728 Mx-stby
310	**311**	**268**	**269**	**270**	**271**	**272**	**273**	**258**	**259**	**260**	**261**	**247**	**248**	**249**	**250**	**251**	**252**	**253**	**254**	**255**
0.01	0.04	0.02	0.07	0.04	0.01	0.02	0.08	<0.008	<0.008	0.01	0.07	<0.008	0.02	0.02	0.03	0.05	<0.008	0.03	0.03	0.08
0.01	<0.008	<0.008	<0.008	<0.008	<0.008	<0.008	<0.008	<0.008	<0.008	0.01	0.01	<0.008	0.01	<0.008	<0.008	<0.008	<0.008	<0.008	0.01	<0.008
<0.02	<0.02	<0.03	<0.03	<0.02	<0.03	<0.02	<0.02	<0.02	<0.02	<0.02	<0.02	<0.02	<0.02	<0.02	<0.03	<0.02	<0.02	<0.02	<0.02	<0.02
15.20	18.90	15.40	17.20	17.80	15.30	18.10	15.50	14.10	14.90	15.20	17.30	18.80	17.60	17.30	16.20	16.90	15.80	17.90	18.90	16.70
33.90	34.10	34.50	33.80	33.00	33.80	34.70	32.30	33.00	33.20	33.90	33.40	35.80	34.20	33.00	34.60	32.50	33.70	36.00	35.20	33.30
7.30	7.30	7.20	7.30	7.60	7.40	7.30	7.40	7.20	7.00	7.00	7.30	7.30	7.30	7.00	7.30	7.40	7.10	7.10	7.20	7.80
0.35	0.69	0.56	0.17	0.18	0.09	0.12	0.23	<0.04	0.12	<0.04	0.07	<0.04	<0.04	<0.04	0.05	0.05	0.35	0.11	0.68	0.21
<0.09	<0.09	<0.09	<0.09	<0.09	<0.09	<0.09	<0.09	<0.09	<0.09	<0.09	<0.09	<0.09	<0.09	<0.09	<0.09	<0.09	<0.09	<0.09	<0.09	<0.09
<0.05	<0.05	<0.05	<0.05	<0.05	<0.05	<0.05	<0.05	<0.05	<0.05	<0.05	<0.05	<0.05	<0.05	<0.05	<0.05	<0.05	<0.05	<0.05	<0.05	<0.05
<0.05	<0.05	<0.05	<0.05	<0.05	<0.05	<0.05	<0.05	<0.05	<0.05	<0.05	<0.05	<0.05	<0.05	<0.05	<0.05	<0.05	<0.05	<0.05	<0.05	<0.05
<0.05	<0.05	0.08	0.08	<0.05	<0.05	<0.05	<0.05	0.11	0.07	<0.05	<0.05	0.05	<0.05	<0.05	0.10	<0.05	<0.05	<0.05	<0.05	<0.05
0.37	0.13	0.66	0.57	0.38	0.47	0.16	0.21	0.60	0.47	0.42	0.24	0.11	0.19	0.48	0.59	0.41	0.37	0.18	0.13	0.11
0.16	<0.05	0.24	0.22	0.07	0.15	<0.05	<0.05	0.26	0.15	0.13	0.06	<0.05	<0.05	0.19	0.27	0.10	0.12	<0.05	<0.05	<0.05
0.07	<0.05	0.07	0.07	0.05	<0.05	<0.05	<0.05	0.07	0.06	0.05	<0.05	<0.05	<0.05	<0.05	0.07	<0.05	<0.05	0.05	<0.05	<0.04
1.10	0.57	1.40	1.00	0.96	1.20	0.60	0.77	1.40	1.20	1.10	0.87	0.44	0.59	1.10	1.30	1.10	0.99	0.74	0.63	0.64
0.48	0.28	0.64	0.50	0.41	0.54	0.29	0.35	0.62	0.51	0.49	0.39	0.20	0.29	0.48	0.61	0.53	0.47	0.33	0.29	0.27
11.70	9.40	12.90	10.50	10.70	12.20	9.60	10.70	12.60	12.00	11.50	10.40	8.90	9.80	10.60	12.40	11.80	11.70	10.60	9.70	9.50
3.80	3.40	3.80	3.40	3.50	3.80	3.40	3.70	3.90	3.70	3.70	3.50	3.30	3.40	3.50	3.90	3.50	3.70	3.70	3.50	3.50
<0.03	<0.03	<0.03	<0.03	<0.03	<0.03	<0.03	<0.03	<0.03	<0.03	<0.03	<0.03	<0.03	<0.03	<0.03	<0.03	<0.03	<0.03	<0.03	<0.03	<0.03
<0.01	<0.01	<0.01	<0.01	<0.01	<0.01	<0.01	<0.01	<0.01	<0.01	<0.01	<0.01	<0.01	<0.01	<0.01	<0.01	<0.01	<0.01	<0.01	<0.01	<0.01
<0.01	<0.01	<0.01	<0.01	<0.01	<0.01	<0.01	<0.01	<0.01	<0.01	<0.01	<0.01	<0.01	<0.01	<0.01	<0.01	<0.01	<0.01	<0.01	<0.01	<0.01
<0.01	0.03	0.02	0.02	0.03	<0.01	0.02	0.02	0.02	0.02	0.02	0.02	0.03	0.03	0.03	<0.01	0.04	0.02	0.03	0.02	0.03
<0.02	<0.02	<0.02	<0.02	<0.02	<0.02	<0.02	<0.02	<0.02	<0.02	<0.02	<0.02	<0.02	<0.02	<0.02	<0.02	<0.02	<0.02	<0.02	<0.02	<0.02
<0.01	<0.01	<0.01	<0.01	<0.01	<0.01	<0.01	<0.01	<0.01	<0.01	<0.01	<0.01	<0.01	<0.01	<0.01	<0.01	<0.01	<0.01	<0.01	<0.01	<0.01
0.03	0.04	0.03	0.02	0.04	0.02	0.05	0.07	0.04	0.03	0.04	0.03	0.03	0.06	<0.01	0.03	0.02	0.02	0.03	0.06	0.09
0.02	<0.01	0.02	0.01	0.01	<0.01	0.01	0.01	0.02	<0.01	0.02	0.02	0.02	<0.01	<0.01	0.02	0.01	0.01	0.02	0.02	0.02
<0.02	<0.02	<0.02	<0.02	<0.02	<0.02	<0.02	<0.02	<0.02	<0.02	<0.02	<0.02	<0.02	<0.02	<0.02	<0.02	<0.02	<0.02	<0.02	<0.02	<0.02
<0.03	<0.03	<0.03	<0.03	<0.03	<0.03	<0.03	<0.03	<0.03	<0.03	<0.03	<0.03	<0.03	<0.03	<0.03	<0.03	<0.03	<0.03	<0.03	<0.03	<0.02
0.40	0.10	0.64	0.66	0.34	0.47	0.09	0.26	0.82	0.37	0.38	0.20	0.04	0.09	0.59	0.83	0.38	0.34	0.19	0.09	0.09
<0.02	<0.02	<0.02	<0.02	<0.02	<0.02	<0.02	<0.02	<0.02	<0.02	<0.02	<0.02	<0.02	<0.02	<0.02	<0.02	<0.02	<0.02	<0.02	<0.02	<0.02
<0.02	<0.02	<0.02	<0.02	<0.02	<0.02	<0.02	<0.02	<0.02	<0.02	<0.02	<0.02	<0.02	<0.02	<0.02	<0.02	<0.02	<0.02	<0.02	<0.02	<0.02
74.9	75.0	78.2	75.6	75.1	75.5	74.5	71.6	74.8	73.8	74.0	73.9	75.0	73.6	74.3	78.3	74.8	74.7	77.0	76.5	72.3

RX6728 Mx-stby	RX6728 Mx-stby	RX6728 Mx-stby	RX6728 Mx-stby	RX6728 Mx-stby	RX6728 Mx-stby	RX6711 Mx-diss	RX6711 Mx-diss	RX6711 Mx-diss	RX6711 Mx-diss	RX6712 Mx-diss	RX6712 Mx-diss	RX6715 Mx-diss	RX6715 Mx-diss	RX6715 Mx-diss	RX6715 Mx-diss	RX6723 Mx-diss	RX6723 Mx-diss	RX6723 Mx-diss	RX6723 Mx-diss
256	**257**	**235**	**236**	**237**	**238**	**17327**	**17328**	**17329**	**17330**	**496**	**497**	**17352**	**17354**	**17355**	**17357**	**477**	**478**	**488**	**489**
0.07	0.02	0.04	0.06	0.03	0.03	0.17	1.10	1.10	0.91	0.11	0.03	0.08	0.13	0.02	0.08	0.30	0.32	0.07	0.32
<0.009	<0.008	<0.008	0.01	<0.008	<0.008	0.02	0.06	0.08	0.09	0.03	0.06	0.12	0.07	0.08	0.13	0.14	0.03	0.01	0.01
<0.02	<0.02	<0.02	<0.02	<0.02	<0.02	<0.03	<0.03	<0.03	<0.03	<0.02	<0.02	<0.02	<0.03	0.08	<0.03	<0.02	<0.03	<0.02	<0.03
17.20	16.60	17.70	17.90	18.20	16.80	10.00	16.80	17.60	17.30	14.90	15.60	15.20	20.10	14.50	18.00	13.90	16.90	12.30	15.30
34.60	33.10	33.10	33.70	33.80	34.90	33.80	33.80	34.00	33.60	34.10	34.10	31.20	37.30	30.50	35.20	30.30	33.00	33.40	33.10
7.30	7.30	7.30	7.60	7.30	7.40	7.10	6.60	6.60	6.60	7.10	7.30	7.10	7.50	7.60	7.70	7.00	7.40	7.50	7.30
0.28	0.41	0.07	0.10	0.06	0.07	0.74	0.62	1.00	0.86	<0.04	0.05	1.00	0.84	0.88	1.30	0.49	0.57	<0.04	<0.04
<0.09	<0.09	<0.09	<0.09	<0.09	<0.09	<0.09	<0.09	<0.09	<0.09	<0.09	<0.09	<0.09	<0.09	<0.09	<0.09	<0.09	<0.09	<0.09	<0.09
<0.05	<0.05	<0.05	<0.05	<0.05	<0.05	<0.05	<0.05	<0.05	<0.05	<0.05	<0.05	<0.05	<0.05	<0.05	<0.05	<0.05	<0.05	<0.05	<0.05
<0.05	<0.05	<0.05	<0.05	<0.05	<0.05	<0.05	<0.05	<0.05	<0.05	<0.05	<0.05	<0.05	<0.05	<0.05	<0.05	<0.05	<0.05	<0.05	<0.05
<0.05	0.07	<0.05	<0.05	0.08	<0.05	0.14	0.06	0.09	<0.05	0.07	0.07	<0.05	<0.05	<0.05	<0.05	<0.05	<0.05	<0.05	0.16
0.33	0.55	0.43	0.29	0.32	0.22	1.20	0.43	0.30	0.32	0.46	0.41	0.12	0.46	0.40	0.38	0.65	0.47	0.96	0.95
0.08	0.18	0.11	0.06	<0.05	0.05	0.57	0.20	0.18	0.14	0.16	0.21	<0.04	0.20	0.16	0.10	0.18	0.13	0.30	0.45
0.07	0.07	<0.05	<0.05	<0.05	<0.05	0.17	0.07	0.09	0.06	0.06	0.07	<0.04	0.11	0.09	0.07	0.05	<0.05	0.07	0.12
0.91	1.00	1.10	0.81	0.89	0.74	1.90	0.89	0.76	0.84	0.98	0.90	0.59	0.95	1.00	1.00	1.40	1.00	1.80	1.40
0.42	0.47	0.49	0.39	0.38	0.31	0.60	0.42	0.37	0.37	0.56	0.50	0.26	0.48	0.48	0.50	0.54	0.43	0.67	0.55
11.30	10.60	11.20	10.70	10.60	10.50	16.20	10.20	8.90	9.70	10.10	9.40	7.30	10.40	10.90	9.50	11.60	10.50	14.60	11.90
3.80	3.60	3.60	3.40	3.50	3.70	4.60	3.40	3.20	3.20	3.50	3.50	2.20	3.70	3.60	3.00	3.40	3.50	4.30	3.50
<0.03	<0.03	<0.03	<0.03	<0.03	<0.03	<0.03	<0.03	0.08	0.06	<0.03	<0.03	<0.03	<0.03	<0.03	<0.03	<0.03	<0.03	<0.03	<0.03
<0.01	<0.01	<0.01	<0.01	<0.01	<0.01	<0.01	<0.01	<0.01	<0.01	<0.01	<0.01	<0.01	<0.01	<0.01	<0.01	<0.01	<0.01	<0.01	<0.01
<0.01	<0.01	<0.01	<0.01	<0.01	<0.01	0.04	0.01	0.02	0.03	<0.01	<0.01	<0.01	0.13	<0.01	0.11	0.22	0.03	<0.01	<0.01
0.03	0.02	0.03	0.02	0.04	0.02	<0.01	0.24	0.18	0.17	0.04	0.05	0.02	0.04	0.03	0.04	0.06	0.12	0.05	0.10
<0.02	<0.02	<0.02	<0.02	<0.02	<0.02	<0.02	<0.02	<0.02	<0.02	<0.02	<0.02	<0.02	<0.02	<0.02	<0.02	<0.02	<0.02	<0.02	<0.02
<0.01	<0.01	<0.01	<0.01	<0.01	<0.01	<0.01	<0.01	<0.01	<0.01	<0.01	<0.01	<0.01	<0.01	<0.01	<0.01	<0.01	<0.01	<0.01	<0.01
0.03	0.03	0.04	<0.01	0.02	0.02	<0.01	0.08	0.09	0.07	<0.01	<0.01	<0.01	<0.01	<0.01	<0.01	0.03	<0.01	<0.01	<0.01
0.01	0.01	0.02	0.01	0.02	0.02	0.02	0.07	0.08	0.06	0.02	0.01	0.02	0.04	<0.01	0.06	0.02	0.02	0.02	<0.01
<0.02	<0.02	<0.02	<0.02	<0.02	<0.02	0.26	1.30	1.20	0.93	0.17	0.47	0.30	0.37	0.43	0.31	0.36	0.37	0.07	0.56
<0.03	<0.03	<0.03	<0.03	<0.03	<0.03	<0.03	<0.03	0.06	0.03	<0.03	<0.03	0.04	<0.03	<0.03	<0.03	<0.03	<0.03	<0.03	0.03
0.42	0.50	0.35	0.34	0.22	0.16	1.50	0.89	0.86	0.65	0.28	0.53	0.12	0.20	0.27	0.15	0.45	0.36	0.64	1.00
<0.02	<0.02	<0.02	<0.02	<0.02	<0.02	<0.02	<0.02	<0.02	<0.02	<0.02	<0.02	<0.02	<0.02	<0.02	<0.02	<0.02	<0.02	<0.02	<0.02
<0.02	<0.02	<0.02	<0.02	<0.02	<0.02	<0.02	<0.02	<0.02	<0.02	<0.02	<0.02	<0.02	<0.02	<0.02	<0.02	<0.02	<0.02	<0.02	<0.02
76.9	74.5	75.6	75.4	75.5	74.9	79.0	77.2	76.8	76.0	72.6	73.3	65.7	83.0	71.0	77.6	71.1	75.2	76.8	76.8

RX6723 Mx-diss	RX6723 Mx-diss	RX6723 Mx-diss	RX6723 Mx-diss	RX6723 Mx-diss	RX6723 Mx-diss	RX6725 Mx-diss	RX6725 Mx-diss	RX6716 Mx-f.g.	RX6716 Mx-f.g.	RX6716 Mx-f.g.	RX6716 Mx-f.g.	RX6716 Mx-f.g.	RX6716 Mx-f.g.	RX6716 Mx-f.g.	RX6716 Mx-f.g.	RX6716 Mx-f.g.	RX6716 Mx-f.g.	RX6716 Mx-f.g.
490	**491**	**492**	**493**	**494**	**495**	**534**	**535**	**17331**	**17332**	**17333**	**17334**	**17335**	**17336**	**17337**	**17338**	**17339**	**17340**	**17341**
0.34	0.29	0.20	0.05	0.23	0.13	0.15	0.11	0.15	0.13	0.04	0.44	0.12	0.07	0.04	0.19	0.03	0.15	0.17
<0.008	0.01	<0.008	<0.008	<0.008	0.06	0.02	0.02	<0.008	0.02	<0.008	0.01	<0.008	0.03	<0.008	0.01	<0.008	0.02	0.02
0.03	<0.03	<0.03	<0.02	<0.02	<0.03	<0.02	<0.02	<0.03	<0.02	<0.02	<0.02	<0.02	<0.03	0.10	<0.02	<0.02	<0.03	<0.03
14.00	14.80	14.70	11.80	13.30	15.90	17.10	18.10	26.00	23.50	25.20	23.90	23.50	27.00	24.50	24.50	24.80	27.30	25.50
31.50	34.40	34.40	33.00	31.60	34.10	34.80	35.30	36.00	32.50	34.50	34.00	35.40	36.60	34.30	33.90	32.70	37.30	35.90
7.20	7.50	7.80	7.30	7.20	7.60	6.90	7.30	7.20	7.10	7.40	7.20	7.30	7.70	7.40	7.40	7.50	7.20	7.30
0.37	0.06	0.13	<0.04	<0.04	0.08	0.24	0.37	<0.04	0.19	<0.04	0.20	0.13	<0.04	<0.04	<0.04	0.16	0.05	<0.04
<0.09	<0.10	<0.09	<0.09	<0.09	<0.10	<0.09	<0.09	<0.09	<0.09	<0.09	<0.09	<0.09	<0.09	<0.09	<0.09	<0.09	<0.09	<0.09
<0.05	<0.05	<0.05	<0.05	<0.05	<0.05	<0.05	<0.05	<0.05	<0.05	<0.05	<0.05	<0.05	<0.05	<0.05	<0.05	<0.05	0.06	<0.05
<0.05	<0.05	<0.05	<0.05	<0.05	<0.05	<0.05	<0.05	<0.05	<0.05	<0.05	<0.05	<0.05	0.09	<0.05	<0.05	<0.05	0.05	<0.05
0.07	0.06	0.06	0.11	0.07	0.14	0.10	0.10	<0.05	<0.05	<0.05	0.06	<0.05	<0.05	<0.05	<0.05	<0.05	<0.05	<0.05
0.44	0.73	0.66	1.10	0.85	1.10	0.39	0.46	0.14	0.09	0.17	0.17	0.14	0.18	0.11	0.14	<0.08	0.18	0.17
0.19	0.25	0.22	0.54	0.37	0.52	0.25	0.24	0.05	<0.05	0.06	0.12	0.08	0.10	0.09	0.07	0.05	0.10	0.09
<0.04	0.08	0.07	0.12	0.09	0.14	0.09	0.07	0.08	0.05	0.08	0.08	0.06	0.11	0.08	0.07	0.06	0.10	0.10
0.85	1.40	1.30	1.80	1.50	1.50	0.85	0.73	0.30	0.28	0.36	0.46	0.37	0.41	0.35	0.37	0.32	0.41	0.34
0.33	0.53	0.51	0.65	0.53	0.59	0.37	0.38	0.23	0.20	0.24	0.26	0.22	0.29	0.23	0.18	0.23	0.25	0.19
9.60	12.80	12.50	14.40	12.60	12.20	9.10	9.00	6.30	5.90	6.10	6.40	6.40	6.90	6.20	6.10	5.90	6.80	6.50
3.20	3.80	3.90	4.20	3.90	3.90	3.40	3.30	2.60	2.50	2.60	2.80	2.80	2.90	2.60	2.60	2.50	2.90	2.70
<0.03	<0.03	<0.03	<0.03	<0.03	0.18	<0.03	<0.03	<0.03	<0.03	<0.03	<0.03	<0.03	<0.03	<0.03	<0.03	<0.03	<0.03	<0.03
<0.01	<0.01	<0.01	<0.01	<0.01	<0.01	<0.01	<0.01	<0.01	<0.01	<0.01	<0.01	<0.01	<0.01	<0.01	<0.01	<0.01	<0.01	<0.01
<0.01	<0.01	<0.01	<0.01	<0.01	0.29	<0.01	<0.01	<0.01	<0.01	<0.01	<0.01	<0.01	<0.01	<0.01	<0.01	<0.01	<0.01	<0.01
0.07	0.09	0.06	0.04	0.11	0.06	0.02	0.05	0.03	0.12	0.02	0.03	0.03	0.02	0.04	0.02	0.02	0.03	0.03
<0.02	<0.02	<0.02	<0.02	<0.02	<0.02	<0.02	<0.02	<0.02	<0.02	<0.02	<0.02	<0.02	<0.02	<0.02	<0.02	<0.02	<0.02	<0.02
<0.01	<0.01	<0.01	<0.01	<0.01	<0.01	<0.01	<0.01	<0.01	<0.01	<0.01	<0.01	<0.01	<0.01	<0.01	<0.01	<0.01	<0.01	<0.01
0.02	<0.01	0.02	<0.01	<0.01	<0.01	<0.01	<0.01	<0.01	<0.01	<0.01	<0.01	<0.01	<0.01	<0.01	0.02	<0.01	<0.01	<0.01
0.04	0.03	0.02	0.02	0.01	<0.01	<0.01	0.01	0.03	0.01	0.02	0.04	0.05	0.01	<0.01	0.08	0.03	0.03	0.04
0.71	0.33	0.25	0.16	0.09	0.31	0.22	0.21	<0.02	<0.02	<0.02	<0.02	<0.02	<0.02	<0.02	<0.02	<0.02	<0.02	<0.02
0.03	<0.03	<0.03	<0.03	<0.03	<0.03	<0.03	<0.03	<0.03	<0.03	<0.03	<0.03	<0.03	<0.03	<0.02	<0.03	<0.03	<0.03	<0.03
0.93	0.62	0.58	0.73	0.90	1.20	0.89	0.94	0.21	0.24	0.22	0.36	0.17	0.29	0.23	0.18	0.19	0.22	0.20
<0.02	<0.02	<0.02	<0.02	<0.02	<0.02	<0.02	<0.02	<0.02	<0.02	<0.02	<0.02	<0.02	<0.02	<0.02	<0.02	<0.02	<0.02	<0.02
<0.02	<0.02	<0.02	<0.02	<0.02	<0.02	<0.02	<0.02	<0.02	<0.02	<0.02	<0.02	<0.02	<0.02	<0.02	<0.02	<0.02	<0.02	<0.02
69.9	77.8	77.4	76.0	73.4	80.0	74.9	76.7	79.3	72.8	77.0	76.5	76.8	82.7	76.3	75.8	74.5	83.2	79.3

RX6716 Mx-f.g.	RX6716 Mx-f.g.	RX6716 Mx-f.g.	RX6716 Mx-f.g.	RX6716 Mx-f.g.	RX6716 Mx-f.g.	RX6716 Mx-f.g.	RX6716 Mx-f.g.	RX6717 Mx-f.g.	RX6717 Mx-f.g.	RX6717 Mx-f.g.	RX6717 Mx-f.g.	RX6717 Mx-f.g.	RX6718 Mx-f.g.	RX6718 Mx-f.g.	RX6718 Mx-f.g.	RX6718 Mx-f.g.	RX6718 Mx-f.g.	RX6718 Mx-f.g.
17342	**17343**	**17344**	**17345**	**17346**	**17347**	**17348**	**17349**	**17388**	**17389**	**17393**	**17394**	**17395**	**312**	**313**	**315**	**316**	**317**	**318**
0.27	0.13	0.03	0.01	0.16	0.22	0.16	0.10	0.29	0.42	0.17	0.42	0.38	0.42	0.37	0.36	0.43	0.42	0.41
<0.008	0.01	0.03	0.04	0.01	<0.008	<0.008	<0.008	0.01	0.01	<0.008	<0.008	<0.008	0.06	0.08	0.03	0.07	0.05	<0.008
<0.02	<0.02	<0.03	<0.03	<0.02	<0.02	<0.02	<0.02	<0.02	0.07	<0.03	<0.03	<0.03	0.13	0.05	<0.02	0.05	5.70	0.05
23.70	24.60	30.20	33.20	27.50	25.30	26.30	24.10	21.00	22.70	22.80	22.90	22.20	22.50	22.80	21.40	22.20	18.50	22.00
34.20	34.30	35.40	34.70	32.60	34.50	36.10	34.80	31.90	35.20	36.80	36.90	37.60	32.10	30.70	32.40	32.20	29.10	33.20
7.10	7.40	7.30	7.00	7.00	7.40	7.40	7.40	8.00	6.80	7.20	7.20	7.10	6.80	7.20	6.90	7.00	7.30	7.10
0.07	0.12	<0.04	<0.04	0.17	0.09	0.26	0.04	0.78	0.11	0.04	0.22	0.04	0.06	0.06	<0.04	0.13	0.82	<0.04
<0.09	<0.09	<0.10	<0.10	<0.09	<0.09	<0.09	<0.09	<0.09	<0.09	<0.09	<0.09	<0.09	<0.09	<0.09	<0.09	<0.09	<0.09	<0.09
<0.05	<0.05	<0.05	<0.05	<0.05	<0.05	<0.05	<0.05	<0.05	<0.05	<0.05	<0.05	<0.05	<0.05	0.06	<0.05	0.07	<0.05	<0.05
<0.05	<0.05	0.06	<0.05	<0.05	<0.05	<0.05	<0.05	<0.05	<0.05	<0.05	<0.05	<0.05	<0.05	<0.05	<0.05	0.08	<0.05	<0.05
0.06	<0.05	<0.05	<0.05	<0.05	<0.05	0.07	0.06	<0.05	0.09	0.06	0.05	<0.05	0.08	<0.05	0.09	0.10	0.09	0.07
0.16	0.18	0.14	<0.09	<0.08	0.12	0.18	0.18	0.18	0.34	0.22	0.22	0.16	0.25	0.34	0.31	0.32	0.26	0.33
0.12	0.07	<0.05	<0.05	<0.05	<0.05	0.09	0.09	0.13	0.18	0.12	0.12	0.09	0.12	0.18	0.16	0.09	0.12	0.16
0.10	0.05	0.07	0.06	<0.05	0.06	0.07	0.07	0.06	0.08	0.05	0.06	0.09	0.05	0.09	0.06	<0.04	<0.04	0.08
0.44	0.34	0.33	0.17	0.21	0.33	0.37	0.38	0.49	0.58	0.42	0.47	0.44	0.51	0.51	0.49	0.34	0.52	0.50
0.25	0.22	0.20	0.12	0.12	0.16	0.26	0.24	0.26	0.29	0.22	0.27	0.22	0.22	0.27	0.28	0.19	0.24	0.25
6.60	6.30	6.20	5.20	5.90	6.00	6.50	6.40	6.70	7.00	6.80	7.10	7.10	6.30	6.70	6.70	5.80	6.80	6.80
2.60	2.50	2.50	2.30	2.30	2.60	2.60	2.70	2.60	2.80	2.80	2.90	3.00	2.50	2.60	2.70	2.20	2.60	2.70
<0.03	<0.03	<0.03	<0.03	<0.03	<0.03	<0.03	<0.03	<0.03	<0.03	<0.03	<0.03	<0.03	<0.03	<0.03	<0.03	<0.03	<0.03	<0.03
<0.01	<0.01	<0.01	<0.01	<0.01	<0.01	<0.01	<0.01	<0.01	<0.01	<0.01	<0.01	<0.01	<0.01	<0.01	<0.01	<0.01	<0.01	<0.01
<0.01	<0.01	<0.01	<0.01	<0.01	<0.01	<0.01	<0.01	<0.01	<0.01	<0.01	<0.01	0.06	<0.01	0.17	<0.01	0.35	0.37	<0.01
0.02	0.04	0.03	0.03	0.05	0.02	0.03	0.04	0.06	0.07	0.08	0.06	0.05	0.07	0.07	0.07	0.07	0.10	0.08
<0.02	<0.02	<0.02	<0.02	<0.02	<0.02	<0.02	<0.02	<0.02	<0.02	<0.02	<0.02	<0.02	<0.02	<0.02	<0.02	<0.02	<0.02	<0.02
<0.01	<0.01	<0.01	<0.01	<0.01	<0.01	<0.01	<0.01	<0.01	<0.01	<0.01	<0.01	<0.01	<0.01	<0.01	<0.01	<0.01	<0.01	<0.01
<0.01	<0.01	<0.01	<0.01	<0.01	<0.01	<0.01	<0.01	0.02	0.02	<0.01	0.01	0.02	<0.01	<0.01	<0.01	0.01	0.05	<0.01
0.07	0.04	0.01	0.01	0.02	0.03	0.05	0.03	0.01	0.04	<0.01	0.04	0.05	0.04	0.03	0.03	0.03	0.05	0.04
<0.02	<0.02	<0.02	<0.02	<0.02	<0.02	<0.02	<0.02	0.02	<0.02	<0.02	<0.02	<0.02	0.04	0.07	0.05	<0.02	<0.02	0.12
<0.03	<0.03	<0.03	<0.03	<0.03	<0.03	<0.03	<0.03	<0.03	<0.03	<0.03	<0.03	<0.03	<0.02	<0.03	<0.03	<0.03	0.04	<0.03
0.27	0.26	0.11	0.04	0.06	0.23	0.20	0.38	0.62	0.79	0.52	0.55	0.36	0.65	0.66	0.73	0.60	0.68	0.73
<0.02	<0.02	<0.02	<0.02	<0.02	<0.02	<0.02	<0.02	<0.02	<0.02	<0.02	<0.02	<0.02	<0.02	<0.02	<0.02	<0.02	<0.02	<0.02
<0.02	<0.02	<0.02	<0.02	<0.02	<0.02	<0.02	<0.02	<0.02	<0.02	<0.02	<0.02	<0.02	<0.02	<0.02	<0.02	<0.02	<0.02	<0.02
76.0	76.6	82.6	82.9	76.1	77.1	80.6	77.0	73.1	77.6	78.3	79.5	79.0	72.9	73.0	72.8	72.3	73.8	74.6

RX6718 Mx-f.g.	RX6718 Mx-f.g.	RX6718 Mx-f.g.	RX6718 Mx-f.g.	RX6718 Mx-f.g.	RX6718 Mx-f.g.	RX6718 Mx-f.g.	RX6719 Mx-f.g.	RX6719 Mx-f.g.	RX6719 Mx-f.g.	RX6719 Mx-f.g.	RX6719 Mx-f.g.	RX6719 Mx-f.g.	RX6719 Mx-f.g.	RX6719 Mx-f.g.	RX6719 Mx-f.g.	RX6719 Mx-f.g.	RX6719 Mx-f.g.	RX6719 Mx-f.g.	RX6719 Mx-f.g.	RX6719 Mx-f.g.
319	**320**	**321**	**322**	**323**	**324**	**325**	**300**	**301**	**302**	**303**	**304**	**326**	**327**	**328**	**329**	**331**	**332**	**333**	**334**	**335**
0.40	0.34	0.38	0.44	0.47	0.40	0.47	0.74	0.77	0.59	0.76	0.57	0.75	0.81	0.69	0.75	0.54	0.53	0.64	0.90	0.61
<0.008	0.03	0.03	0.06	0.03	0.08	0.05	0.02	<0.008	<0.008	0.03	0.18	0.02	0.01	0.03	0.01	0.33	0.02	<0.008	0.38	0.52
0.06	0.05	0.06	<0.02	<0.03	<0.03	0.08	<0.02	<0.02	0.30	0.05	0.03	0.03	<0.03	0.07	<0.03	<0.02	0.04	<0.02	0.76	<0.02
22.30	23.70	22.20	21.60	22.80	22.10	22.10	23.00	22.90	22.10	20.90	20.30	25.20	24.50	22.70	23.70	21.00	22.80	23.70	19.70	20.00
32.60	34.20	33.40	32.50	35.30	35.30	32.90	32.60	32.60	31.50	32.10	28.20	35.00	34.90	32.00	33.80	29.40	31.90	33.70	27.90	28.00
7.10	6.80	7.00	7.00	7.00	7.10	7.00	7.20	7.90	7.30	7.30	6.70	6.10	6.20	6.20	6.80	7.50	7.20	7.00	7.60	7.70
<0.04	<0.04	<0.04	0.06	<0.04	0.08	0.18	0.11	0.04	0.37	0.08	<0.04	0.12	0.09	0.50	0.09	0.13	0.29	<0.04	2.10	0.52
<0.09	<0.09	<0.09	<0.09	<0.10	<0.10	<0.09	<0.09	<0.09	<0.09	<0.09	<0.09	<0.10	<0.09	<0.09	<0.09	<0.09	<0.09	<0.09	<0.09	<0.09
<0.05	<0.05	<0.05	<0.05	<0.05	<0.05	<0.05	<0.05	<0.05	<0.05	<0.05	<0.05	<0.05	<0.05	<0.05	<0.05	<0.05	<0.05	<0.05	<0.05	<0.05
<0.05	<0.05	<0.05	<0.05	<0.05	<0.05	<0.05	<0.05	<0.05	<0.05	<0.05	<0.05	<0.05	<0.05	<0.05	<0.05	<0.05	<0.05	<0.05	<0.05	<0.05
0.08	0.06	0.10	0.06	0.08	0.09	<0.05	0.07	<0.05	0.06	0.06	<0.05	<0.05	0.06	0.07	0.06	0.05	<0.05	<0.05	<0.05	<0.05
0.30	0.30	0.41	0.29	0.35	0.45	0.26	0.22	0.22	0.22	<0.08	0.15	0.24	0.22	0.17	0.24	0.21	0.23	0.24	0.17	0.20
0.15	0.14	0.17	0.15	0.18	0.20	0.12	0.09	0.08	0.08	0.07	0.07	0.07	0.08	0.05	0.07	0.08	0.10	0.08	0.09	0.10
0.08	0.06	0.07	0.06	0.07	0.08	0.05	0.07	<0.05	0.06	<0.05	<0.04	0.05	<0.05	<0.05	0.05	0.05	0.05	0.05	0.08	0.12
0.49	0.50	0.54	0.50	0.54	0.56	0.40	0.41	0.38	0.31	0.33	0.37	0.39	0.37	0.34	0.42	0.35	0.41	0.36	0.40	0.27
0.23	0.26	0.32	0.27	0.29	0.30	0.21	0.19	0.17	0.09	0.15	0.14	0.21	0.17	0.16	0.22	0.17	0.17	0.19	0.14	0.19
6.60	6.90	7.00	6.90	7.30	7.00	6.40	6.20	6.30	5.90	6.10	5.40	6.50	6.50	5.70	6.10	5.40	6.00	6.40	4.60	4.50
2.60	2.70	2.60	2.60	2.70	2.60	2.50	2.50	2.50	2.30	2.50	2.30	2.50	2.50	2.30	2.40	2.20	2.40	2.50	1.80	1.70
<0.03	<0.03	<0.03	<0.03	<0.03	<0.03	<0.03	<0.03	0.06	<0.03	0.08	0.43	<0.03	<0.03	<0.03	0.09	0.05	<0.03	0.05	0.08	0.15
<0.01	<0.01	<0.01	<0.01	<0.01	<0.01	<0.01	<0.01	<0.01	<0.01	<0.01	<0.01	<0.01	<0.01	<0.01	<0.01	<0.01	<0.01	<0.01	<0.01	<0.01
<0.01	<0.01	<0.01	0.06	<0.01	0.03	<0.01	<0.01	<0.01	<0.01	<0.01	<0.01	<0.01	<0.01	<0.01	<0.01	0.60	<0.01	<0.01	0.89	0.73
0.07	0.06	0.08	0.10	0.08	0.15	0.06	0.12	0.13	0.12	0.14	0.12	0.14	0.15	0.12	0.13	0.11	0.10	0.11	0.13	0.12
<0.02	<0.02	<0.02	<0.02	<0.02	<0.02	<0.02	<0.02	<0.02	<0.02	<0.02	<0.02	<0.02	<0.02	<0.02	<0.02	<0.02	<0.02	<0.02	<0.02	<0.02
<0.01	<0.01	<0.01	<0.01	<0.01	<0.01	<0.01	<0.01	<0.01	<0.01	<0.01	<0.01	<0.01	<0.01	<0.01	<0.01	<0.01	<0.01	<0.01	<0.01	<0.01
0.01	0.02	<0.01	0.02	<0.01	0.01	<0.01	0.01	0.03	0.02	0.03	0.02	0.03	0.02	0.12	0.02	<0.01	<0.01	0.01	<0.01	0.01
0.02	0.03	0.02	0.04	0.04	0.05	0.06	0.05	0.06	0.06	0.07	0.03	0.06	0.07	0.07	0.06	0.03	0.04	0.04	0.07	0.03
0.12	0.05	0.09	0.06	0.26	0.27	0.18	0.02	0.04	0.07	0.09	0.04	0.05	0.04	0.02	0.06	<0.02	0.02	0.04	<0.02	<0.02
<0.03	<0.03	<0.03	<0.03	<0.03	<0.03	<0.03	<0.03	<0.03	<0.03	<0.02	<0.02	<0.03	<0.03	<0.03	<0.03	<0.02	<0.03	<0.03	0.04	<0.02
0.74	0.75	0.73	0.72	0.73	0.91	0.63	0.53	0.49	0.63	0.45	0.36	0.55	0.52	0.44	0.47	0.54	0.63	0.50	0.55	0.49
<0.02	<0.02	<0.02	<0.02	<0.02	<0.02	<0.02	<0.02	<0.02	<0.02	<0.02	<0.02	<0.02	<0.02	<0.02	<0.02	<0.02	<0.02	<0.02	<0.02	<0.02
<0.02	<0.02	<0.02	<0.02	<0.02	<0.02	<0.02	<0.02	<0.02	<0.02	<0.02	<0.02	<0.02	<0.02	<0.02	<0.02	<0.02	<0.02	<0.02	<0.02	<0.02
74.0	77.0	75.2	73.5	78.2	77.8	73.7	74.2	74.7	72.1	71.3	65.4	78.0	77.2	71.8	75.5	68.7	72.9	75.6	68.4	66.0

RX6719 Mx-f.g.	RX6723 Mx-f.g.	RX6723 Mx-f.g.	RX6723 Mx-f.g.	RX6723 Mx-f.g.	RX6723 Mx-f.g.	RX6723 Mx-f.g.	RX6723 Mx-f.g.	RX6723 Mx-f.g.	RX6723 Mx-f.g.	RX6723 Mx-f.g.	RX6724 Mx-f.g.	RX6724 Mx-f.g.	RX6724 Mx-f.g.	RX6724 Mx-f.g.	RX6724 Mx-f.g.	RX6724 Mx-f.g.	RX6724 Mx-f.g.	RX6724 Mx-f.g.	RX6724 Mx-f.g.	RX6724 Mx-f.g.
337	**498**	**499**	**500**	**501**	**502**	**503**	**479**	**504**	**505**	**506**	**544**	**545**	**551**	**17475**	**17476**	**17477**	**552**	**553**	**554**	**555**
0.49	0.27	0.24	0.33	0.38	0.27	0.30	0.20	0.45	0.14	0.31	0.40	0.40	0.42	0.58	0.50	0.48	0.35	0.32	0.50	0.34
<0.008	<0.008	<0.008	<0.008	0.02	0.01	0.02	0.01	0.03	<0.009	0.02	0.05	0.04	0.05	0.01	0.02	0.01	<0.008	0.01	<0.008	0.02
0.07	0.05	<0.03	<0.03	<0.02	<0.03	<0.03	<0.03	0.04	<0.02	<0.02	<0.03	<0.02	<0.02	<0.02	<0.03	<0.03	<0.02	<0.02	<0.02	<0.02
23.90	14.00	14.80	14.60	13.20	16.10	15.70	13.50	15.60	13.80	15.60	23.00	23.50	18.70	19.70	20.70	19.30	21.50	29.60	24.20	25.10
33.50	33.40	34.70	34.60	32.00	34.50	32.80	33.40	31.80	33.30	33.50	31.60	31.40	35.00	34.00	36.60	38.90	31.10	18.80	31.70	30.20
7.00	7.20	7.40	7.20	7.10	7.40	7.30	7.30	7.10	7.30	7.30	7.10	7.20	7.10	7.40	7.50	7.50	7.10	7.00	7.20	6.90
0.06	0.14	0.12	0.06	0.19	<0.04	0.25	0.64	1.00	1.40	0.25	0.04	0.06	0.30	0.14	0.05	0.18	<0.04	0.20	<0.04	0.05
<0.09	<0.09	<0.09	<0.10	<0.09	<0.09	<0.09	<0.09	<0.09	<0.09	<0.09	<0.09	<0.09	<0.09	<0.09	<0.09	<0.09	<0.09	<0.09	<0.09	<0.09
<0.05	<0.05	<0.05	<0.05	<0.05	<0.05	<0.05	<0.05	0.07	<0.05	<0.05	<0.05	0.06	<0.05	<0.05	<0.05	<0.05	0.10	0.06	<0.05	<0.05
<0.05	<0.05	<0.05	<0.05	<0.05	<0.05	<0.05	<0.05	<0.05	<0.05	<0.05	<0.05	<0.05	<0.05	<0.05	<0.05	<0.05	<0.05	<0.05	<0.05	<0.05
0.05	0.16	0.10	0.09	0.07	0.12	0.11	0.08	0.14	0.06	0.08	0.11	0.12	0.09	0.12	0.10	0.09	0.09	0.10	0.11	0.08
0.21	1.20	0.76	0.83	0.88	0.83	0.74	0.89	0.79	0.80	0.85	0.31	0.33	0.28	0.28	0.33	0.31	0.35	0.48	0.37	0.38
0.06	0.62	0.26	0.28	0.28	0.32	0.30	0.29	0.39	0.26	0.33	0.20	0.21	0.18	0.20	0.24	0.26	0.15	0.16	0.22	0.20
0.07	0.12	0.10	0.09	0.06	0.08	0.08	0.08	0.10	0.08	0.12	0.07	0.07	0.05	0.05	0.10	0.10	0.05	0.06	0.05	0.05
0.38	1.70	1.40	1.50	1.60	1.30	1.20	1.70	1.30	1.40	1.40	0.50	0.55	0.41	0.50	0.50	0.52	0.56	0.83	0.49	0.57
0.16	0.63	0.55	0.56	0.59	0.52	0.49	0.62	0.43	0.51	0.55	0.23	0.22	0.19	0.22	0.21	0.25	0.25	0.41	0.23	0.26
6.30	13.10	12.80	13.20	13.00	11.80	10.80	13.50	10.50	12.80	11.80	6.70	6.60	5.40	6.50	5.90	6.00	7.20	10.40	6.40	7.10
2.50	3.80	3.90	3.90	3.70	3.60	3.50	3.90	3.30	3.90	3.70	2.70	2.60	2.10	2.50	2.30	2.30	2.70	3.70	2.50	2.80
0.04	<0.03	<0.03	<0.03	<0.03	<0.03	<0.03	<0.03	<0.03	<0.03	<0.03	<0.03	<0.03	<0.03	0.03	<0.03	<0.03	<0.03	<0.03	<0.03	<0.03
<0.01	<0.01	<0.01	<0.01	<0.01	<0.01	<0.01	<0.01	<0.01	<0.01	<0.01	<0.01	<0.01	<0.01	<0.01	<0.01	<0.01	<0.01	<0.01	<0.01	<0.01
<0.01	<0.01	<0.01	0.03	0.08	<0.01	<0.01	0.02	<0.01	0.05	<0.01	<0.01	<0.01	<0.01	<0.01	<0.01	<0.01	0.03	<0.01	<0.01	<0.01
0.12	0.06	0.08	0.06	0.08	0.11	0.13	0.05	0.04	0.03	0.10	0.04	0.05	0.05	0.05	0.06	0.06	0.04	0.04	0.05	0.04
<0.02	<0.02	<0.02	<0.02	<0.02	<0.02	<0.02	<0.02	<0.02	<0.02	<0.02	<0.02	<0.02	<0.02	<0.02	<0.02	<0.02	<0.02	<0.02	<0.02	<0.02
<0.01	<0.01	<0.01	<0.01	<0.01	<0.01	<0.01	<0.01	<0.01	<0.01	<0.01	<0.01	<0.01	<0.01	<0.01	<0.01	<0.01	<0.01	<0.01	<0.01	<0.01
0.02	0.02	0.02	0.02	0.03	<0.01	0.02	0.02	0.07	0.02	0.01	0.01	<0.01	0.02	<0.01	<0.01	0.04	<0.01	<0.01	<0.01	0.04
0.04	0.03	0.03	0.03	0.03	0.01	0.02	0.03	0.12	0.09	0.05	0.03	0.03	0.04	0.04	0.05	0.07	0.02	<0.01	0.03	0.02
<0.02	0.24	0.13	0.17	0.30	0.32	0.19	0.41	0.09	0.13	0.13	0.17	0.13	0.17	0.16	0.18	0.16	0.04	0.06	<0.02	0.04
<0.03	<0.03	<0.03	<0.03	<0.03	<0.03	<0.03	<0.03	<0.03	<0.03	<0.03	0.03	<0.03	0.05	0.03	<0.03	<0.03	<0.03	<0.03	<0.03	0.03
0.50	1.40	0.72	0.78	0.73	0.88	0.83	0.70	1.20	0.63	0.98	0.90	0.99	1.10	1.00	1.20	1.10	0.88	0.84	1.00	1.10
<0.02	<0.02	<0.02	<0.02	<0.02	<0.02	<0.02	<0.02	<0.02	<0.02	<0.02	<0.02	<0.02	<0.02	<0.02	<0.02	<0.02	<0.02	<0.02	<0.02	<0.02
<0.02	<0.02	<0.02	<0.02	<0.02	<0.02	<0.02	<0.02	<0.02	<0.02	<0.02	<0.02	<0.02	<0.02	<0.02	<0.02	<0.02	<0.02	<0.02	<0.02	<0.02
75.5	78.1	78.1	78.3	74.3	78.2	74.8	77.3	74.6	76.7	77.1	74.2	74.6	71.7	73.5	76.5	77.6	72.5	73.1	75.1	75.3

RX6724 Mx-f.g.	RX6724 Mx-f.g.	RX6724 Mx-f.g.	RX6724 Mx-f.g.	RX6726 Mx-f.g.	RX6726 Mx-f.g.	RX6726 Mx-f.g.	RX6726 Mx-f.g.	RX6727 Mx-f.g.	RX6727 Mx-f.g.	RX6727 Mx-f.g.	RX6727 Mx-f.g.	RX6727 Mx-f.g.	RX6727 Mx-f.g.	RX6727 Mx-f.g.	RX6727 Mx-f.g.	RX6727 Mx-f.g.	RX6727 Mx-f.g.	RX6727 Mx-f.g.	RX6727 Mx-f.g.	RX6727 Mx-f.g.
556	**557**	**558**	**559**	**17434**	**17435**	**17437**	**17440**	**274**	**275**	**276**	**277**	**278**	**279**	**280**	**281**	**282**	**283**	**284**	**285**	**286**
0.34	0.35	0.32	0.37	0.15	0.04	0.25	0.06	0.23	0.27	0.22	0.09	0.11	0.52	0.27	0.49	0.21	0.44	0.32	0.34	0.37
0.01	0.01	0.01	<0.008	0.02	0.04	0.01	0.02	0.03	0.06	0.02	0.04	0.01	0.02	<0.008	0.01	0.01	0.01	<0.008	0.01	0.01
<0.02	<0.02	<0.02	<0.02	<0.02	<0.02	<0.03	<0.03	0.03	<0.02	<0.02	<0.02	<0.02	<0.02	0.08	0.12	<0.02	0.15	<0.02	<0.02	<0.03
24.90	18.80	28.60	25.30	20.30	21.60	22.20	20.60	21.80	18.80	18.80	19.70	19.40	22.00	19.40	22.20	19.30	20.80	19.60	21.30	20.50
30.00	38.70	25.90	28.50	35.90	36.00	35.20	36.10	30.70	31.40	32.00	33.80	31.60	31.30	33.60	32.90	31.90	31.50	32.30	33.80	33.40
7.10	7.30	7.20	7.20	7.10	7.50	7.40	7.20	7.30	7.00	7.30	7.40	7.20	7.10	7.00	7.00	7.40	7.10	7.30	7.30	7.80
<0.04	<0.04	<0.04	<0.04	1.00	0.94	<0.04	0.67	<0.04	0.08	<0.04	<0.04	<0.04	1.70	0.39	0.25	0.35	0.52	1.20	0.35	0.35
<0.09	<0.09	<0.09	<0.09	<0.09	<0.09	<0.09	<0.09	<0.09	<0.09	<0.09	<0.09	<0.09	<0.09	<0.09	<0.09	<0.09	<0.09	<0.09	<0.09	<0.09
<0.05	<0.05	<0.05	0.10	<0.05	<0.05	<0.05	<0.05	<0.05	<0.05	<0.05	<0.05	<0.05	<0.05	<0.05	<0.05	0.06	<0.05	<0.05	<0.05	<0.05
<0.05	<0.05	<0.05	<0.05	<0.05	<0.05	<0.05	<0.05	<0.05	<0.05	<0.05	<0.05	<0.05	<0.05	<0.05	<0.05	<0.05	<0.05	<0.05	<0.05	<0.05
0.11	0.15	0.08	0.07	0.06	0.08	0.07	0.07	0.07	0.06	<0.05	0.10	0.08	<0.05	0.09	<0.05	0.05	<0.05	0.06	<0.05	0.08
0.37	0.43	0.44	0.34	0.30	0.27	0.24	0.34	0.31	0.25	0.35	0.35	0.34	0.18	0.42	0.25	0.32	0.28	0.24	0.27	0.32
0.18	0.25	0.19	0.15	0.20	0.12	0.08	0.07	0.10	0.14	0.14	0.18	0.17	0.09	0.20	0.10	0.15	0.17	0.12	0.13	0.16
<0.05	0.08	0.08	0.05	0.10	0.06	0.05	0.06	0.07	0.06	0.05	0.06	0.05	0.05	0.08	<0.05	0.05	0.06	0.06	0.06	0.06
0.60	0.49	0.60	0.59	0.78	0.76	0.54	0.76	0.54	0.57	0.70	0.64	0.63	0.43	0.69	0.48	0.62	0.53	0.59	0.59	0.61
0.29	0.22	0.33	0.28	0.38	0.38	0.27	0.41	0.30	0.32	0.39	0.38	0.41	0.22	0.44	0.29	0.38	0.30	0.31	0.33	0.32
7.50	5.70	7.80	7.60	8.90	8.60	7.90	8.90	7.00	7.40	7.60	7.50	7.20	6.80	7.90	7.10	7.60	7.10	7.30	7.40	7.40
2.90	2.10	3.20	2.90	3.20	3.10	2.90	3.20	2.60	2.70	2.90	2.90	2.70	2.60	2.90	2.60	2.80	2.60	2.80	2.90	2.80
<0.03	<0.03	<0.03	<0.03	<0.03	<0.03	<0.03	<0.03	<0.03	<0.03	<0.03	<0.03	<0.03	<0.03	<0.03	<0.03	<0.03	<0.03	<0.03	<0.03	<0.03
<0.01	<0.01	<0.01	<0.01	<0.01	<0.01	<0.01	<0.01	<0.01	<0.01	<0.01	<0.01	<0.01	<0.01	<0.01	<0.01	<0.01	<0.01	<0.01	<0.01	<0.01
<0.01	<0.01	<0.01	<0.01	<0.01	<0.01	<0.01	<0.01	<0.01	<0.01	<0.01	0.02	<0.01	0.04	<0.01	<0.01	0.04	<0.01	<0.01	<0.01	0.09
0.03	0.06	0.04	0.03	0.04	0.06	0.07	0.02	0.07	0.05	0.05	0.07	0.05	0.04	0.04	0.06	0.07	0.06	0.08	0.08	0.08
<0.02	<0.02	<0.02	<0.02	<0.02	<0.02	<0.02	<0.02	<0.02	<0.02	<0.02	<0.02	<0.02	<0.02	<0.02	<0.02	<0.02	<0.02	<0.02	<0.02	<0.02
<0.01	<0.01	<0.01	<0.01	<0.01	<0.01	<0.01	<0.01	<0.01	<0.01	<0.01	<0.01	<0.01	<0.01	<0.01	<0.01	<0.01	<0.01	<0.01	<0.01	<0.01
<0.01	0.02	0.02	0.02	<0.01	<0.01	<0.01	<0.01	0.01	<0.01	<0.01	<0.01	<0.01	0.04	<0.01	0.03	0.05	0.04	0.01	0.02	0.02
0.04	0.06	0.02	0.04	0.02	0.01	0.01	0.03	0.03	0.02	0.01	0.01	0.01	0.10	0.04	0.08	0.04	0.04	0.05	0.05	0.05
0.03	0.04	0.06	0.03	0.02	<0.02	<0.02	<0.02	<0.02	<0.02	<0.02	<0.02	<0.02	<0.02	<0.02	<0.02	<0.02	<0.02	<0.02	<0.02	<0.02
<0.03	0.03	0.03	<0.03	<0.03	<0.03	<0.03	<0.03	<0.03	<0.03	<0.03	<0.03	<0.03	<0.03	<0.03	<0.03	<0.03	<0.03	<0.03	<0.03	<0.03
1.10	1.20	0.94	0.88	0.52	0.36	0.25	0.41	0.56	0.48	0.51	0.71	0.84	0.54	0.64	0.52	0.54	0.56	0.52	0.50	0.59
<0.02	<0.02	<0.02	<0.02	<0.02	<0.02	<0.02	<0.02	<0.02	<0.02	<0.02	<0.02	<0.02	<0.02	<0.02	<0.02	<0.02	<0.02	<0.02	<0.02	<0.02
<0.02	<0.02	<0.02	<0.02	<0.02	<0.02	<0.02	<0.02	<0.02	<0.02	<0.02	<0.02	<0.02	<0.02	<0.02	<0.02	<0.02	<0.02	<0.02	<0.02	<0.02
75.5	76.0	75.9	74.5	79.0	79.9	77.4	78.9	71.8	69.7	71.0	74.0	70.8	73.8	74.2	74.5	71.9	72.3	72.9	75.4	75.0

RX6713 CR 17383	RX6713 CR 17384	RX6713 CR 17385	RX6713 CR 17386	RX6713 CR 17379	RX6713 CR 17380	RX6713 CR 17382	RX6713 CR 17363	RX6713 CR 17373	RX6713 CR 17374	RX6713 CR 17375	RX6713 CR 17376	RX6713 CR 17377	RX6713 CR 17378	RX6713 CR 17358	RX6713 CR 17359	RX6713 CR 17360	RX6714 CR 17316
0.32	0.33	0.21	0.36	0.34	0.24	0.62	0.25	0.34	0.30	0.27	0.39	0.30	0.08	0.08	0.36	0.05	0.26
0.01	0.01	0.02	0.03	<0.008	<0.008	0.23	0.02	0.05	<0.008	0.01	<0.008	<0.008	0.02	<0.008	0.01	0.01	0.13
<0.03	<0.03	<0.03	<0.02	0.08	<0.03	0.05	0.04	<0.02	<0.03	<0.02	<0.03	<0.02	<0.02	<0.03	<0.03	<0.03	0.13
18.00	18.70	18.80	18.40	18.00	21.50	18.00	16.70	18.70	19.80	20.50	19.80	19.30	20.50	19.50	20.80	14.00	17.90
33.60	33.90	33.90	34.00	33.70	33.90	28.20	33.70	34.10	35.00	36.00	35.20	34.70	32.70	36.40	35.80	33.20	37.60
7.50	7.50	7.20	7.00	7.10	7.40	6.80	7.40	7.20	7.50	7.30	7.20	7.40	7.20	7.30	7.10	7.50	7.00
0.26	0.37	0.41	0.64	<0.04	0.07	1.10	1.70	0.18	0.17	0.48	0.29	0.59	0.86	<0.04	0.10	<0.04	0.36
<0.09	<0.09	<0.09	<0.09	<0.09	<0.09	<0.09	<0.10	<0.09	<0.09	<0.09	<0.09	<0.10	<0.09	<0.10	<0.10	<0.09	<0.09
0.20	0.25	0.25	0.35	<0.05	<0.05	<0.05	<0.05	<0.05	<0.05	0.06	<0.05	<0.05	<0.05	<0.05	<0.05	<0.05	<0.05
<0.05	<0.05	<0.05	<0.05	<0.05	<0.05	<0.05	<0.05	<0.05	<0.05	<0.05	<0.05	<0.05	<0.05	<0.05	<0.05	<0.05	<0.05
<0.05	0.06	<0.05	0.08	0.07	0.09	<0.05	0.09	<0.05	<0.05	0.06	<0.05	<0.05	<0.05	0.08	0.07	0.06	0.08
0.73	0.64	0.64	0.54	0.50	0.56	0.35	0.83	0.66	0.51	0.66	0.43	0.47	0.31	0.54	0.60	1.80	0.45
0.31	0.26	0.26	0.35	0.22	0.25	0.13	0.36	0.21	0.19	0.27	0.18	0.17	0.15	0.22	0.27	0.43	0.20
0.12	0.10	0.10	0.12	0.10	0.07	<0.04	0.13	0.12	0.12	0.10	0.08	0.08	0.09	0.08	0.14	0.15	0.06
1.20	1.10	1.00	0.92	0.90	0.80	0.63	1.30	1.20	0.93	1.00	0.85	0.92	0.74	0.93	0.95	2.80	0.76
0.64	0.56	0.53	0.53	0.48	0.56	0.42	0.66	0.62	0.56	0.57	0.47	0.50	0.37	0.55	0.57	1.40	0.35
10.30	10.20	10.10	8.30	8.50	8.00	6.60	10.60	9.90	9.10	9.30	8.90	9.00	8.50	9.60	9.00	15.70	8.70
3.30	3.30	3.30	3.20	3.20	2.80	2.40	3.50	3.20	3.20	3.30	3.30	3.20	3.10	3.30	3.30	4.10	2.90
<0.03	<0.03	<0.03	<0.03	<0.03	<0.03	<0.03	<0.03	<0.03	<0.03	<0.03	<0.03	<0.03	<0.03	<0.03	<0.03	<0.03	<0.03
<0.01	<0.01	<0.01	<0.01	<0.01	<0.01	<0.01	<0.01	<0.01	<0.01	<0.01	<0.01	<0.01	<0.01	<0.01	<0.01	<0.01	<0.01
<0.01	<0.01	<0.01	0.02	<0.01	0.03	1.70	<0.01	<0.01	<0.01	<0.01	<0.01	<0.01	<0.01	<0.01	<0.01	<0.01	0.07
0.04	0.05	0.04	0.04	0.07	0.03	0.06	0.08	0.03	0.04	0.05	0.08	0.07	0.02	0.02	0.02	0.04	<0.01
<0.02	<0.02	<0.02	<0.02	<0.02	<0.02	<0.02	<0.02	<0.02	<0.02	<0.02	<0.02	<0.02	<0.02	<0.02	<0.02	<0.02	<0.02
<0.01	<0.01	<0.01	<0.01	<0.01	<0.01	<0.01	<0.01	<0.01	<0.01	<0.01	<0.01	<0.01	<0.01	<0.01	<0.01	<0.01	<0.01
<0.01	<0.01	<0.01	<0.01	<0.01	<0.01	0.02	1.10	<0.01	<0.01	0.01	0.02	0.01	<0.01	<0.01	0.03	<0.01	0.02
<0.01	0.03	0.04	0.05	<0.01	0.02	0.05	0.03	0.02	0.03	0.03	0.03	0.01	0.02	0.02	0.01	<0.01	0.04
0.26	0.28	0.22	<0.02	<0.02	<0.02	0.13	0.22	0.08	<0.02	<0.02	<0.02	<0.02	<0.02	<0.02	<0.02	0.10	<0.02
<0.03	<0.03	<0.03	<0.03	<0.03	<0.03	<0.02	<0.03	<0.03	<0.03	<0.03	<0.03	<0.03	<0.03	<0.03	<0.03	<0.03	<0.03
1.10	1.10	1.00	1.30	1.00	0.91	0.54	1.30	0.61	0.77	0.70	0.70	0.62	0.58	0.95	0.94	0.91	0.60
<0.02	<0.02	<0.02	<0.02	<0.02	<0.02	<0.02	<0.02	<0.02	<0.02	<0.02	<0.02	<0.02	<0.02	<0.02	<0.02	<0.02	<0.02
<0.02	<0.02	<0.02	<0.02	<0.02	<0.02	<0.02	<0.02	<0.02	<0.02	<0.02	<0.02	<0.02	<0.02	<0.02	<0.02	<0.02	<0.02
77.9	78.7	78.0	76.2	74.3	77.2	68.0	80.0	77.2	78.2	80.7	77.9	77.3	75.2	79.6	80.1	82.3	77.6

RX6714 CR	RX6714 CR	RX6714 CR	RX6714 CR	RX6717 CR	RX6717 CR	RX6717 CR	RX6717 CR	RX6717 CR	RX6717 CR	RX6720 CR	RX6720 CR	RX6720 CR	RX6720 CR	RX6720 CR	RX6720 CR
17317	**17318**	**17319**	**17320**	**17321**	**17390**	**17391**	**17392**	**17396**	**17397**	**17398**	**572**	**573**	**451**	**452**	**453**	**376**	**377**	**378**	**379**
0.10	0.33	0.23	0.15	0.09	0.39	0.45	0.50	0.50	0.36	0.48	0.31	0.22	0.58	0.15	0.63	0.36	0.45	0.49	0.35
0.03	0.03	0.02	<0.008	<0.008	0.01	0.01	<0.008	0.02	0.01	0.07	0.21	<0.008	0.01	<0.008	<0.008	0.01	<0.008	0.01	0.22
<0.03	<0.03	<0.03	<0.02	<0.03	0.03	<0.03	0.03	<0.03	<0.03	0.05	0.09	0.04	<0.03	<0.02	<0.03	<0.02	<0.02	<0.03	0.24
20.40	20.50	17.00	27.20	22.40	23.30	22.60	23.00	23.30	22.90	19.00	18.60	21.40	21.30	18.00	21.10	19.70	20.60	19.40	14.90
36.00	35.00	40.80	24.70	34.10	36.90	36.30	36.80	35.70	35.80	31.50	31.20	34.50	32.50	30.80	32.20	32.60	31.20	31.00	27.30
7.40	7.10	7.30	7.30	7.30	7.30	7.30	6.90	7.20	7.50	6.20	7.00	6.50	7.10	7.10	7.10	7.20	6.70	7.20	6.70
0.40	0.13	0.14	0.79	0.56	<0.04	0.10	0.12	<0.04	0.05	0.40	0.28	0.12	0.31	0.22	0.44	0.05	5.70	1.80	2.10
<0.10	<0.09	<0.09	<0.09	<0.09	<0.09	<0.09	<0.09	<0.10	<0.10	<0.09	<0.09	<0.10	<0.09	<0.09	<0.09	<0.09	<0.09	<0.09	<0.09
<0.05	<0.05	<0.05	<0.05	<0.05	<0.05	<0.05	<0.05	0.66	0.99	1.10	1.10	1.20	<0.05	<0.05	<0.05	<0.05	<0.05	<0.05	<0.05
<0.05	0.06	<0.05	<0.05	<0.05	<0.05	<0.05	<0.05	<0.05	<0.05	<0.05	<0.05	<0.05	<0.05	<0.05	<0.05	<0.05	<0.05	<0.05	<0.05
0.06	0.07	0.06	<0.05	0.05	0.06	0.07	<0.05	<0.05	<0.05	<0.05	0.07	<0.05	<0.05	<0.05	<0.05	0.06	<0.05	<0.05	<0.05
0.47	0.58	0.55	0.48	0.39	0.28	0.28	0.28	0.11	0.34	0.29	0.27	0.35	0.32	0.49	0.34	0.49	0.32	0.40	0.41
0.21	0.24	0.27	0.18	0.22	0.17	0.13	0.13	0.06	0.16	0.15	0.16	0.16	0.12	0.10	0.13	0.14	0.14	0.14	0.13
0.10	0.10	0.12	0.08	0.10	0.09	0.06	0.06	0.05	0.08	0.05	0.06	0.06	0.06	0.05	0.05	0.08	0.06	0.07	0.07
0.89	0.94	0.94	1.20	0.90	0.53	0.47	0.48	0.37	0.51	0.44	0.46	0.56	0.63	1.00	0.61	0.75	0.59	0.74	0.83
0.39	0.40	0.41	0.55	0.36	0.30	0.30	0.25	0.18	0.31	0.26	0.29	0.33	0.34	0.45	0.33	0.37	0.34	0.39	0.44
9.50	9.70	9.60	13.50	9.80	7.30	7.20	7.00	6.40	7.30	6.50	6.00	7.20	7.90	9.40	7.80	8.80	7.60	8.60	8.80
3.40	3.40	3.30	4.50	3.50	3.00	2.90	2.90	2.80	2.80	2.50	2.30	2.70	2.70	3.10	2.80	3.10	2.70	2.90	2.80
<0.03	<0.03	<0.03	<0.03	<0.03	<0.03	<0.03	<0.03	<0.03	<0.03	<0.03	<0.03	<0.03	<0.03	<0.03	<0.03	<0.03	<0.03	<0.03	<0.03
<0.01	<0.01	<0.01	<0.01	<0.01	<0.01	<0.01	<0.01	<0.01	<0.01	<0.01	<0.01	<0.01	<0.01	<0.01	<0.01	<0.01	<0.01	<0.01	<0.01
<0.01	<0.01	<0.01	<0.01	<0.01	<0.01	<0.01	<0.01	<0.01	<0.01	<0.01	1.50	<0.01	<0.01	<0.01	<0.01	<0.01	0.07	0.02	0.48
0.03	0.02	0.02	0.04	0.02	0.05	0.07	0.09	0.06	0.07	0.07	0.04	0.04	0.06	0.07	0.08	0.06	0.07	0.08	0.04
<0.02	<0.02	<0.02	<0.02	<0.02	<0.02	<0.02	<0.02	<0.02	<0.02	<0.02	<0.02	<0.02	<0.02	<0.02	<0.02	<0.02	<0.02	<0.02	<0.02
<0.01	<0.01	<0.01	<0.01	<0.01	<0.01	<0.01	<0.01	<0.01	<0.01	<0.01	<0.01	<0.01	<0.01	<0.01	<0.01	<0.01	<0.01	<0.01	<0.01
<0.01	<0.01	<0.01	<0.01	0.01	0.03	<0.01	0.03	<0.01	0.02	<0.01	<0.01	<0.01	0.03	<0.01	0.02	<0.01	<0.01	0.02	0.02
0.04	0.07	0.05	0.04	0.05	0.03	0.04	0.04	0.04	0.02	0.04	0.02	0.02	0.04	0.02	0.05	0.03	0.03	0.04	0.04
<0.02	<0.02	<0.02	<0.02	<0.02	<0.02	<0.02	<0.02	<0.02	0.16	0.10	0.18	0.16	0.34	0.97	0.35	0.41	0.30	0.35	0.31
<0.03	<0.03	<0.03	<0.03	<0.03	<0.03	<0.03	<0.03	<0.03	<0.03	<0.03	<0.03	<0.03	<0.03	0.04	<0.03	<0.03	<0.03	<0.03	<0.02
0.53	0.57	0.54	0.44	0.43	0.58	0.54	0.56	0.41	0.90	0.71	0.67	0.68	0.56	0.36	0.60	0.60	0.58	0.62	0.48
<0.02	<0.02	<0.02	<0.02	<0.02	<0.02	<0.02	<0.02	<0.02	<0.02	<0.02	<0.02	<0.02	<0.02	<0.02	<0.02	<0.02	<0.02	<0.02	<0.02
<0.02	<0.02	<0.02	<0.02	<0.02	<0.02	<0.02	<0.02	<0.02	<0.02	<0.02	<0.02	<0.02	<0.02	<0.02	<0.02	<0.02	<0.02	<0.02	<0.02
80.0	79.2	81.4	81.2	80.3	80.3	78.8	79.2	77.9	80.3	69.9	70.8	76.2	74.9	72.3	74.6	74.8	77.5	74.3	66.7

RX6720 CR 380	RX6720 CR 381	RX6720 CR 382	RX6720 CR 383	RX6723 CR 474	RX6723 CR 475	RX6723 CR 476	RX6726 CR 17442	RX6726 CR 17443	RX6726 CR 17444	RX6726 CR 17445	RX6726 CR 17446	RX6726 CR 17447	RX6726 CR 17448	RX6726 CR 17449	RX6726 CR 17450	RX6726 CR 17451	RX6726 CR 17452	RX6726 CR 17453
0.41	0.48	0.47	0.51	0.47	0.39	0.37	0.20	0.09	0.12	0.11	0.14	0.22	0.15	0.11	0.06	0.06	0.11	0.22
<0.008	<0.008	0.01	<0.008	0.01	<0.008	<0.008	0.02	<0.008	<0.008	0.01	<0.008	0.01	<0.008	<0.008	0.02	0.01	<0.008	<0.008
<0.02	<0.02	<0.03	<0.02	<0.03	<0.03	<0.03	<0.02	0.12	<0.03	0.02	<0.03	<0.02	<0.03	0.04	<0.03	<0.03	<0.03	<0.03
21.10	21.80	19.60	18.40	17.10	17.00	18.80	21.80	20.40	22.60	21.80	21.70	22.30	21.00	19.90	22.30	22.60	21.30	21.60
33.30	32.40	33.40	31.80	33.10	33.30	33.80	34.30	34.70	35.80	33.70	34.80	35.30	34.90	34.40	35.70	36.10	35.30	35.00
7.00	7.10	7.20	7.00	7.00	7.30	7.40	7.20	7.40	7.20	7.30	7.40	7.40	7.40	7.50	7.50	7.30	7.30	7.50
0.33	0.77	0.17	0.51	0.24	0.06	0.09	0.04	<0.04	<0.04	0.14	0.09	0.09	0.04	<0.04	<0.04	<0.04	<0.04	<0.04
<0.09	<0.09	<0.09	<0.09	<0.09	<0.09	<0.09	<0.09	<0.09	<0.09	<0.09	<0.09	<0.09	<0.09	<0.09	<0.09	<0.09	<0.09	<0.09
<0.05	<0.05	<0.05	<0.05	<0.05	<0.05	<0.05	<0.05	0.08	<0.05	<0.05	<0.05	<0.05	<0.05	<0.05	<0.05	<0.05	<0.05	<0.05
<0.05	<0.05	<0.05	<0.05	0.05	<0.05	<0.05	<0.05	<0.05	<0.05	<0.05	<0.05	<0.05	<0.05	<0.05	<0.05	<0.05	<0.05	<0.05
0.06	<0.05	0.08	<0.05	0.06	0.12	0.07	<0.05	0.18	0.09	0.06	0.05	<0.05	0.07	0.09	0.06	0.08	0.06	<0.05
0.29	0.27	0.54	0.46	0.49	0.67	0.47	0.13	0.40	0.24	0.31	0.23	0.09	0.30	0.45	0.24	0.26	0.27	0.26
0.11	0.12	0.14	0.15	0.11	0.27	0.19	0.07	0.26	0.13	0.18	0.10	0.07	0.19	0.24	0.11	0.11	0.11	0.09
0.06	0.06	0.08	0.07	0.06	0.08	0.05	0.05	0.07	0.06	0.07	0.06	0.05	0.05	0.08	0.06	0.08	0.05	<0.05
0.58	0.58	0.88	0.83	1.10	1.10	0.93	0.53	0.85	0.68	0.59	0.60	0.52	0.75	0.87	0.70	0.62	0.65	0.62
0.37	0.35	0.43	0.43	0.48	0.53	0.43	0.27	0.41	0.33	0.33	0.33	0.26	0.37	0.43	0.37	0.32	0.31	0.35
7.90	7.70	9.30	9.20	11.00	10.20	9.50	7.80	8.60	8.20	7.10	8.20	7.90	8.30	8.80	8.20	8.10	8.20	8.20
2.80	2.60	3.10	3.00	3.50	3.30	3.10	2.90	3.10	3.00	2.70	3.00	3.00	2.90	3.10	3.00	3.00	3.00	3.00
<0.03	<0.03	<0.03	<0.03	<0.03	<0.03	<0.03	<0.03	<0.03	<0.03	<0.03	<0.03	<0.03	<0.03	<0.03	<0.03	<0.03	<0.03	<0.03
<0.01	<0.01	<0.01	<0.01	<0.01	<0.01	<0.01	<0.01	<0.01	<0.01	<0.01	<0.01	<0.01	<0.01	<0.01	<0.01	<0.01	<0.01	<0.01
<0.01	<0.01	<0.01	<0.01	0.05	<0.01	<0.01	0.02	<0.01	<0.01	<0.01	<0.01	<0.01	<0.01	<0.01	0.02	<0.01	<0.01	<0.01
0.06	0.05	0.07	0.08	0.12	0.11	0.11	0.07	0.05	0.03	0.06	0.07	0.05	0.05	0.03	0.04	0.03	0.04	0.07
<0.02	<0.02	<0.02	<0.02	<0.02	<0.02	<0.02	<0.02	<0.02	<0.02	<0.02	<0.02	<0.02	<0.02	<0.02	<0.02	<0.02	<0.02	<0.02
<0.01	<0.01	<0.01	<0.01	<0.01	<0.01	<0.01	<0.01	<0.01	<0.01	<0.01	<0.01	<0.01	<0.01	<0.01	<0.01	<0.01	<0.01	<0.01
<0.01	0.02	0.02	0.02	0.03	<0.01	0.01	<0.01	<0.01	<0.01	<0.01	<0.01	<0.01	<0.01	<0.01	<0.01	<0.01	<0.01	<0.01
0.10	0.02	0.05	0.04	0.03	0.02	0.02	0.01	0.01	<0.01	0.02	<0.01	<0.01	0.03	0.03	0.02	0.02	0.04	0.02
0.29	0.31	0.36	0.40	0.48	0.35	0.29	<0.02	<0.02	<0.02	0.06	<0.02	<0.02	<0.02	<0.02	<0.02	<0.02	<0.02	<0.02
<0.03	<0.03	<0.03	<0.03	<0.03	<0.03	<0.03	<0.03	<0.03	<0.03	<0.03	<0.03	<0.03	<0.03	<0.03	<0.03	<0.03	<0.03	<0.03
0.52	0.53	0.70	0.64	0.53	0.72	0.62	0.25	0.91	0.51	0.60	0.35	0.19	0.57	0.86	0.36	0.45	0.37	0.26
<0.02	<0.02	<0.02	<0.02	<0.02	<0.02	<0.02	<0.02	<0.02	<0.02	<0.02	<0.02	<0.02	<0.02	<0.02	<0.02	<0.02	<0.02	<0.02
<0.02	<0.02	<0.02	<0.02	<0.02	<0.02	<0.02	<0.02	<0.02	<0.02	<0.02	<0.02	<0.02	<0.02	<0.02	<0.02	<0.02	<0.02	<0.02
75.3	75.2	76.6	73.5	76.0	75.5	76.3	75.7	77.6	79.0	75.2	77.1	77.4	77.1	76.9	78.8	79.1	77.1	77.2

RX6726 CR 17454	RX6726 CR 17455	RX6726 CR 17456	RX6726 CR 17457	RX6726 CR 17458	RX6726 CR 17459	RX6726 CR 17460	RX6726 CR 17461	RX6726 CR 17462	RX6726 CR 17464	RX6726 CR 17465	RX6727 CR 241	RX6727 CR 242	RX6727 CR 239	RX6727 CR 240	RX6728 CR 262	RX6728 CR 263	RX6728 CR 265	RX6728 CR 266	RX6728 CR 267
0.16	0.12	0.11	0.09	0.06	0.08	0.18	0.13	0.09	0.03	0.14	0.37	0.28	0.37	0.28	0.02	0.01	0.03	<0.008	0.04
<0.008	<0.008	0.02	0.02	0.01	<0.008	<0.008	0.01	<0.008	0.02	<0.008	0.02	0.02	0.03	0.01	0.01	<0.008	<0.008	0.01	0.02
0.06	<0.02	<0.02	<0.02	0.09	0.12	<0.02	0.05	<0.02	<0.02	<0.02	<0.03	<0.03	0.04	<0.02	<0.02	<0.02	<0.02	<0.02	<0.02
20.70	21.80	19.50	21.60	20.30	19.90	20.10	20.50	16.00	22.40	20.40	19.90	20.50	20.50	19.70	18.10	15.40	17.10	16.00	15.00
35.70	34.40	33.70	34.10	34.00	33.80	36.30	33.90	35.00	35.90	33.20	34.50	32.80	33.00	34.60	34.60	33.20	33.90	33.20	31.70
7.30	7.30	7.20	7.10	7.30	7.30	7.50	7.40	7.30	7.30	7.30	7.40	7.50	7.50	7.30	7.20	7.30	7.40	7.20	7.30
<0.04	<0.04	0.06	0.08	<0.04	<0.04	<0.04	0.06	<0.04	0.15	0.06	0.60	0.47	0.25	0.10	0.18	<0.04	0.15	0.16	0.19
<0.09	<0.09	<0.09	<0.09	<0.09	<0.09	<0.09	<0.09	<0.09	<0.09	<0.09	<0.09	<0.09	<0.09	<0.09	<0.09	<0.09	<0.09	<0.09	<0.09
<0.05	<0.05	<0.05	<0.05	<0.05	<0.05	<0.05	<0.05	<0.05	0.05	<0.05	<0.05	<0.05	<0.05	<0.05	<0.05	<0.05	<0.05	<0.05	0.07
<0.05	<0.05	<0.05	<0.05	<0.05	<0.05	<0.05	<0.05	<0.05	<0.05	<0.05	<0.05	<0.05	<0.05	<0.05	<0.05	<0.05	<0.05	<0.05	<0.05
0.07	0.08	0.09	<0.05	0.10	0.07	0.08	<0.05	<0.05	0.12	0.07	0.09	0.09	0.07	0.07	<0.05	<0.05	<0.05	<0.05	0.19
0.36	0.25	0.40	0.21	0.37	0.38	0.38	0.23	0.46	0.34	0.20	0.38	0.39	0.30	0.43	0.17	0.31	0.20	0.41	0.96
0.21	0.14	0.23	0.09	0.17	0.21	0.14	0.13	0.11	0.22	0.14	0.20	0.19	0.13	0.22	<0.05	0.09	<0.05	0.12	0.50
0.09	0.06	0.10	0.05	0.07	0.09	0.08	0.05	0.07	0.10	0.08	0.07	0.07	0.05	0.07	0.05	<0.05	<0.05	<0.05	0.11
0.86	0.64	0.90	0.51	0.77	0.82	0.88	0.67	1.00	0.76	0.65	0.64	0.61	0.58	0.71	0.61	1.00	0.67	1.10	1.30
0.44	0.29	0.44	0.28	0.35	0.42	0.42	0.33	0.46	0.40	0.32	0.40	0.33	0.32	0.39	0.29	0.50	0.33	0.50	0.65
9.00	8.00	8.90	7.50	8.30	8.60	9.10	8.30	9.70	8.30	8.20	7.90	7.60	7.30	8.40	9.40	11.20	10.30	11.90	12.20
3.10	3.00	3.10	2.80	3.00	3.20	3.20	3.10	3.40	3.10	3.00	2.90	2.80	2.70	3.10	3.40	3.60	3.50	3.70	3.80
<0.03	<0.03	<0.03	<0.03	<0.03	<0.03	<0.03	<0.03	<0.03	<0.03	<0.03	<0.03	<0.03	<0.03	<0.03	<0.03	<0.03	<0.03	<0.03	<0.03
<0.01	<0.01	<0.01	<0.01	<0.01	<0.01	<0.01	<0.01	<0.01	<0.01	<0.01	<0.01	<0.01	<0.01	<0.01	<0.01	<0.01	<0.01	<0.01	<0.01
<0.01	<0.01	0.02	<0.01	<0.01	<0.01	<0.01	<0.01	<0.01	<0.01	<0.01	0.02	<0.01	<0.01	<0.01	<0.01	<0.01	<0.01	<0.01	<0.01
0.02	0.04	0.04	0.07	0.04	0.04	0.02	0.05	0.02	0.04	0.05	0.08	0.06	0.08	0.05	0.03	0.02	0.03	<0.01	0.03
<0.02	<0.02	<0.02	<0.02	<0.02	<0.02	<0.02	<0.02	<0.02	<0.02	<0.02	<0.02	<0.02	<0.02	<0.02	<0.02	<0.02	<0.02	<0.02	<0.02
<0.01	<0.01	<0.01	<0.01	<0.01	<0.01	<0.01	<0.01	<0.01	<0.01	<0.01	<0.01	<0.01	<0.01	<0.01	<0.01	<0.01	<0.01	<0.01	<0.01
<0.01	<0.01	<0.01	<0.01	<0.01	<0.01	<0.01	<0.01	0.01	<0.01	<0.01	<0.01	0.05	0.05	0.01	0.09	0.02	0.04	0.02	0.02
0.01	<0.01	<0.01	0.02	0.02	<0.01	<0.01	<0.01	0.02	<0.01	<0.01	0.03	0.04	0.07	0.03	0.04	0.01	0.02	0.02	<0.01
<0.02	<0.02	<0.02	<0.02	<0.02	0.03	0.03	0.03	<0.02	<0.02	<0.02	0.06	0.03	<0.02	<0.02	<0.02	<0.02	<0.02	<0.02	0.04
<0.03	<0.03	<0.03	<0.02	<0.03	<0.03	<0.03	<0.03	<0.03	<0.03	<0.03	<0.03	<0.03	<0.03	<0.03	<0.03	<0.03	<0.03	<0.03	<0.03
0.57	0.62	0.74	0.21	0.62	0.59	0.31	0.37	0.17	0.70	0.66	0.70	0.79	0.54	0.78	0.07	0.23	0.22	0.34	1.70
<0.02	<0.02	<0.02	<0.02	<0.02	<0.02	<0.02	<0.02	<0.02	<0.02	<0.02	<0.02	<0.02	<0.02	<0.02	<0.02	<0.02	<0.02	<0.02	<0.02
<0.02	<0.02	<0.02	<0.02	<0.02	<0.02	<0.02	<0.02	<0.02	<0.02	<0.02	<0.02	<0.02	<0.02	<0.02	<0.02	<0.02	<0.02	<0.02	<0.02
78.7	76.7	75.6	74.7	75.6	75.7	78.7	75.3	73.8	79.9	74.5	76.3	74.6	73.9	76.3	74.3	72.9	73.9	74.7	75.8

RX6720 Irr.	RX6720 Irr.	RX6720 Irr.	RX6720 Irr.	RX6720 Irr.	RX6720 Irr.	RX6720 Irr.	RX6720 Irr.	RX6720 Irr.	RX6720 Irr.	RX6720 Irr.	RX6720 Irr.	RX6720 Irr.	RX6720 Irr.	RX6720 Irr.	RX6720 Irr.	RX6720 Irr.	RX6720 Irr.	RX6720 Irr.	RX6720 Irr.	RX6720 Irr.
374	**375**	**436**	**437**	**438**	**439**	**440**	**441**	**442**	**443**	**444**	**445**	**390**	**392**	**446**	**366**	**367**	**368**	**369**	**370**	**372**
0.18	0.23	0.25	0.53	0.08	0.34	0.28	0.69	0.29	0.28	0.62	0.50	0.26	0.45	0.36	0.22	0.11	0.55	0.14	0.26	0.22
0.02	<0.008	<0.008	0.01	<0.008	<0.008	<0.008	<0.008	<0.008	<0.008	<0.008	<0.008	<0.008	<0.008	<0.008	<0.008	<0.008	<0.008	<0.008	<0.008	<0.008
0.19	0.27	0.22	0.23	0.10	0.13	0.23	0.37	0.16	0.31	0.18	0.27	0.23	0.09	0.16	0.24	0.06	0.10	0.24	0.15	0.18
19.10	22.40	22.00	23.30	21.60	22.90	21.50	20.80	21.70	23.10	22.50	20.20	24.20	21.20	22.60	19.80	22.50	23.10	23.40	21.10	20.80
29.80	30.90	31.70	31.70	31.70	31.50	33.10	29.30	30.90	31.00	30.70	31.70	32.40	31.50	31.70	30.00	31.40	31.00	32.10	33.20	31.90
7.40	7.10	7.20	7.10	7.10	7.00	7.00	7.10	7.10	7.00	7.10	6.90	7.00	7.20	7.10	7.10	7.10	7.10	7.10	6.90	6.90
0.13	0.17	0.19	0.28	<0.04	0.19	0.24	0.06	0.15	0.07	0.12	0.26	<0.04	<0.04	0.25	<0.04	<0.04	<0.04	<0.04	0.44	0.06
<0.09	<0.09	<0.09	<0.09	<0.09	<0.09	<0.09	<0.09	<0.09	<0.09	<0.09	<0.09	<0.09	<0.09	<0.09	<0.09	<0.09	<0.09	<0.09	<0.09	<0.09
<0.05	<0.05	<0.05	<0.05	<0.05	<0.05	<0.05	0.09	<0.05	0.05	<0.05	<0.05	<0.05	<0.05	<0.05	<0.05	<0.05	<0.05	<0.05	<0.05	<0.05
<0.05	<0.05	<0.05	<0.05	<0.05	<0.05	<0.05	<0.05	<0.05	<0.05	<0.05	<0.05	<0.05	<0.05	<0.05	<0.05	<0.05	<0.05	<0.05	<0.05	<0.05
0.08	<0.05	0.07	0.09	0.07	0.08	0.07	0.12	<0.05	0.10	<0.05	0.08	0.08	0.07	0.05	0.09	0.08	0.05	0.09	0.07	0.08
0.31	0.25	0.26	0.23	0.32	0.21	0.34	0.32	0.23	0.26	0.15	0.39	0.21	0.38	0.24	0.35	0.28	0.22	0.24	0.40	0.42
0.12	0.12	0.10	0.09	0.14	0.06	0.17	0.20	0.09	0.12	0.05	0.17	0.08	0.13	0.10	0.20	0.13	0.05	0.12	0.19	0.24
0.05	<0.04	<0.05	0.07	<0.05	<0.05	<0.05	0.06	<0.05	0.06	<0.04	<0.05	<0.05	0.09	0.05	0.06	0.05	0.05	0.06	0.06	<0.05
0.63	0.46	0.46	0.42	0.64	0.40	0.61	0.53	0.50	0.40	0.35	0.61	0.41	0.70	0.51	0.48	0.50	0.47	0.49	0.70	0.71
0.31	0.21	0.23	0.20	0.32	0.19	0.32	0.25	0.21	0.17	0.14	0.30	0.18	0.29	0.23	0.22	0.24	0.20	0.21	0.35	0.33
7.80	6.80	7.10	7.00	7.90	7.10	7.80	7.20	7.40	6.80	6.60	8.10	6.80	7.90	7.20	6.90	7.10	6.80	7.00	8.40	8.10
2.70	2.60	2.60	2.50	2.80	2.50	2.90	2.50	2.70	2.50	2.40	3.00	2.50	2.80	2.60	2.50	2.60	2.50	2.60	3.00	2.90
<0.03	<0.03	<0.03	<0.03	<0.03	<0.03	<0.03	<0.03	<0.03	<0.03	<0.03	<0.03	<0.03	<0.03	<0.03	<0.03	<0.03	<0.03	<0.03	<0.03	<0.03
<0.01	<0.01	<0.01	<0.01	<0.01	<0.01	<0.01	<0.01	<0.01	<0.01	<0.01	<0.01	<0.01	<0.01	<0.01	<0.01	<0.01	<0.01	<0.01	<0.01	<0.01
<0.01	<0.01	<0.01	0.01	<0.01	<0.01	<0.01	0.02	<0.01	<0.01	<0.01	<0.01	<0.01	<0.01	<0.01	<0.01	<0.01	<0.01	<0.01	<0.01	<0.01
0.04	0.06	0.07	0.06	0.03	0.05	0.03	0.07	0.03	0.04	0.06	0.07	0.05	0.03	0.04	0.05	0.03	0.05	0.02	0.04	0.05
<0.02	<0.02	<0.02	<0.02	<0.02	<0.02	<0.02	<0.02	<0.02	<0.02	<0.02	<0.02	<0.02	<0.02	<0.02	<0.02	<0.02	<0.02	<0.02	<0.02	<0.02
<0.01	<0.01	<0.01	<0.01	<0.01	<0.01	<0.01	<0.01	<0.01	<0.01	<0.01	<0.01	<0.01	<0.01	<0.01	<0.01	<0.01	<0.01	<0.01	<0.01	<0.01
<0.01	<0.01	<0.01	<0.01	<0.01	<0.01	<0.01	0.03	<0.01	0.02	0.03	0.03	<0.01	<0.01	0.01	0.02	<0.01	<0.01	<0.01	0.01	<0.01
0.02	0.02	0.03	0.04	0.03	0.03	0.03	0.02	0.04	0.05	0.04	0.02	0.04	0.02	0.02	0.08	0.06	0.04	0.04	0.04	0.04
<0.02	<0.02	<0.02	<0.02	<0.02	<0.02	<0.02	<0.02	<0.02	<0.02	<0.02	<0.02	<0.02	<0.02	<0.02	<0.02	<0.02	<0.02	<0.02	<0.02	<0.02
<0.03	0.06	0.03	<0.03	<0.03	<0.03	<0.03	0.10	<0.03	0.07	<0.03	0.06	<0.03	<0.03	<0.03	0.05	<0.03	<0.03	0.03	<0.03	0.04
0.62	0.51	0.54	0.49	0.57	0.52	0.65	0.96	0.62	0.70	0.51	0.65	0.49	0.50	0.41	0.80	0.56	0.45	0.61	0.51	0.93
<0.02	<0.02	<0.02	<0.02	<0.02	<0.02	<0.02	<0.02	<0.02	<0.02	<0.02	<0.02	<0.02	<0.02	<0.02	<0.02	<0.02	<0.02	<0.02	<0.02	<0.02
<0.02	<0.02	<0.02	<0.02	<0.02	<0.02	<0.02	<0.02	<0.02	<0.02	<0.02	<0.02	<0.02	<0.02	<0.02	<0.02	<0.02	<0.02	<0.02	<0.02	<0.02
69.5	72.2	73.1	74.4	73.4	73.2	75.3	70.8	72.1	73.1	71.6	73.3	74.9	73.4	73.6	69.2	72.8	72.7	74.5	75.8	73.9

RX6720 Irr.	RX6720 Irr.	RX6720 Irr.	RX6720 Irr.	RX6720 Irr.	RX6720 Irr.	RX6720 Irr.	RX6720 Irr.	RX6720 Irr.	RX6720 Irr.	RX6720 Irr.	RX6720 Irr.	RX6720 Irr.	RX6720 Irr.	RX6720 Irr.	RX6720 Irr.	RX6720 Irr.	RX6720 Irr.	RX6720 Irr.	RX6720 Irr.	RX6720 Irr.	RX6720 Irr.
373	**433**	**434**	**435**	**425**	**426**	**427**	**428**	**430**	**431**	**432**	**384**	**386**	**387**	**388**	**422**	**423**	**424**	**447**	**448**	**450**
0.21	0.43	0.10	0.20	0.34	0.15	0.23	0.42	0.24	0.33	0.12	0.27	0.47	0.39	0.43	0.52	0.47	0.43	0.35	0.63	0.57
<0.008	<0.008	<0.008	<0.008	<0.008	<0.008	<0.008	<0.008	<0.008	0.01	<0.008	0.02	0.01	0.01	0.01	0.01	0.01	<0.008	<0.008	<0.008	0.02
0.09	0.12	<0.03	0.22	0.24	0.03	0.13	0.16	0.12	0.18	0.06	0.47	0.21	0.17	0.13	0.11	0.11	0.11	0.15	0.18	0.18
21.60	20.50	23.10	20.20	22.40	18.60	21.90	22.00	20.50	22.50	18.90	20.40	23.90	24.20	23.30	23.50	22.50	23.10	24.30	23.40	22.70
31.30	31.40	32.80	31.70	30.90	33.20	32.10	31.90	32.20	32.60	31.50	30.30	31.80	32.40	30.80	31.40	30.40	31.10	31.50	30.40	31.00
7.00	7.10	7.20	7.20	7.10	7.10	7.00	7.10	7.10	7.00	7.00	6.80	7.10	7.00	7.10	7.20	7.10	7.00	7.10	6.60	7.20
0.06	<0.04	<0.04	<0.04	0.06	<0.04	<0.04	0.07	0.79	0.80	0.07	1.90	4.00	0.25	0.32	0.09	0.36	<0.04	0.21	0.42	0.44
<0.09	<0.10	<0.10	<0.10	<0.09	<0.09	<0.09	<0.09	<0.09	<0.09	<0.09	<0.09	<0.09	<0.09	<0.09	<0.09	<0.09	<0.09	<0.09	<0.09	<0.09
<0.05	<0.05	<0.05	<0.05	<0.05	<0.05	<0.05	<0.05	<0.05	<0.05	<0.05	<0.05	<0.05	<0.05	<0.05	<0.05	<0.05	<0.05	0.07	0.07	<0.05
<0.05	<0.05	<0.05	<0.05	<0.05	<0.05	<0.05	<0.05	<0.05	<0.05	<0.05	<0.05	<0.05	<0.05	<0.05	<0.05	<0.05	<0.05	<0.05	<0.05	<0.05
0.06	<0.05	<0.05	<0.05	0.08	<0.05	0.07	0.07	0.10	0.07	<0.05	<0.05	0.07	<0.05	<0.05	0.06	0.05	0.07	<0.05	<0.05	<0.05
0.38	0.33	0.28	0.35	0.34	0.58	0.36	0.36	0.43	0.35	0.45	0.23	0.18	0.22	0.16	0.18	0.15	0.17	0.16	0.14	0.18
0.17	0.10	0.12	0.15	0.18	0.15	0.16	0.12	0.19	0.18	0.16	0.12	0.08	0.11	0.08	0.06	0.06	0.07	0.08	<0.05	0.07
0.05	<0.05	0.05	0.06	0.06	0.05	0.06	0.09	0.08	0.06	0.05	0.05	0.07	<0.05	0.05	0.05	<0.04	<0.05	0.06	0.06	<0.05
0.57	0.63	0.50	0.65	0.56	1.00	0.59	0.64	0.77	0.60	0.75	0.53	0.39	0.39	0.34	0.42	0.37	0.40	0.42	0.38	0.41
0.25	0.26	0.27	0.38	0.26	0.48	0.26	0.33	0.40	0.36	0.36	0.27	0.18	0.19	0.17	0.13	0.16	0.18	0.18	0.16	0.15
7.50	8.20	7.30	7.90	7.30	10.20	7.60	8.00	8.40	7.60	8.50	6.70	6.90	6.80	6.50	6.80	6.80	6.80	6.80	6.90	6.70
2.70	2.90	2.60	2.70	2.60	3.30	2.70	2.80	2.90	2.60	2.90	2.40	2.50	2.60	2.40	2.50	2.40	2.60	2.50	2.50	2.50
<0.03	<0.03	<0.03	<0.03	<0.03	<0.03	<0.03	<0.03	<0.03	<0.03	<0.03	<0.03	<0.03	<0.03	<0.03	<0.03	<0.03	<0.03	<0.03	<0.03	<0.03
<0.01	<0.01	<0.01	<0.01	<0.01	<0.01	<0.01	<0.01	<0.01	<0.01	<0.01	<0.01	<0.01	<0.01	<0.01	<0.01	<0.01	<0.01	<0.01	<0.01	<0.01
<0.01	<0.01	<0.01	<0.01	<0.01	<0.01	<0.01	<0.01	<0.01	<0.01	<0.01	0.06	0.08	<0.01	<0.01	<0.01	<0.01	<0.01	<0.01	<0.01	<0.01
0.05	0.05	0.04	0.07	0.04	0.04	0.05	0.06	0.05	0.04	0.02	0.04	0.04	0.05	0.05	0.07	0.04	0.07	0.06	0.06	0.08
<0.02	<0.02	<0.02	<0.02	<0.02	<0.02	<0.02	<0.02	<0.02	<0.02	<0.02	<0.02	<0.02	<0.02	<0.02	<0.02	<0.02	<0.02	<0.02	<0.02	<0.02
<0.01	<0.01	<0.01	<0.01	<0.01	<0.01	<0.01	<0.01	<0.01	<0.01	<0.01	<0.01	<0.01	<0.01	<0.01	<0.01	<0.01	<0.01	<0.01	<0.01	<0.01
<0.01	0.01	<0.01	<0.01	0.01	<0.01	<0.01	0.01	0.01	0.03	<0.01	<0.01	0.03	0.01	0.02	0.02	0.01	0.01	0.02	0.02	0.01
0.04	0.02	0.03	0.03	0.02	0.02	0.02	0.02	0.03	0.04	<0.01	0.03	0.11	0.04	0.03	0.03	0.02	0.04	<0.01	0.04	0.02
<0.02	<0.02	<0.02	<0.02	<0.02	<0.02	<0.02	<0.02	<0.02	<0.02	<0.02	<0.02	<0.02	<0.02	<0.02	<0.02	<0.02	<0.02	<0.02	<0.02	<0.02
<0.03	<0.03	<0.03	0.05	0.03	<0.03	<0.03	<0.03	<0.03	<0.03	<0.03	0.03	0.04	0.03	<0.03	<0.03	<0.03	<0.03	0.03	0.03	<0.03
0.60	0.56	0.55	0.65	0.68	0.50	0.64	0.47	0.79	0.69	0.58	0.50	0.56	0.55	0.59	0.47	0.48	0.53	0.46	0.48	0.49
<0.02	<0.02	<0.02	<0.02	<0.02	<0.02	<0.02	<0.02	<0.02	<0.02	<0.02	0.05	<0.02	<0.02	<0.02	<0.02	<0.02	<0.02	<0.02	<0.02	<0.02
<0.02	<0.02	<0.02	<0.02	<0.02	<0.02	<0.02	<0.02	<0.02	<0.02	<0.02	<0.02	<0.02	<0.02	<0.02	<0.02	<0.02	<0.02	<0.02	<0.02	<0.02
72.6	72.6	74.9	72.5	73.2	75.4	73.9	74.6	75.1	76.0	71.4	71.2	78.7	75.4	72.5	73.6	71.5	72.7	74.5	72.5	72.7

RX6721 Irr.	RX6721 Irr.	RX6721 Irr.	RX6721 Irr.	RX6721 Irr.	RX6721 Irr.	RX6721 Irr.	RX6721 Irr.	RX6721 Irr.	RX6721 Irr.	RX6721 Irr.	RX6721 Irr.	RX6721 Irr.	RX6721 Irr.	RX6721 Irr.	RX6721 Irr.	RX6721 Irr.	RX6721 Irr.
17400	**17401**	**17402**	**17403**	**17404**	**17405**	**17406**	**17407**	**17408**	**17409**	**17410**	**17411**	**17412**	**17415**	**17416**	**17417**	**17418**	**17419**
0.14	0.06	0.35	0.07	0.23	0.15	0.18	0.14	0.09	0.08	0.07	0.19	0.47	0.47	0.26	0.38	0.56	0.37
<0.008	0.01	<0.008	<0.008	0.01	<0.008	<0.008	<0.008	1.20	<0.008	<0.008	0.01	<0.008	<0.008	0.03	0.01	<0.008	0.01
0.06	0.09	0.14	0.13	0.06	0.06	0.08	0.05	<0.02	0.24	<0.02	0.24	0.13	0.18	0.11	0.24	0.12	0.26
25.60	19.10	24.30	23.60	25.20	25.50	24.90	25.10	24.80	24.70	22.10	25.20	24.60	22.00	21.20	19.40	22.20	24.80
34.60	34.10	33.30	32.40	34.70	34.50	33.70	33.60	33.40	33.30	33.80	33.70	33.60	33.70	30.10	30.00	32.90	33.40
7.00	7.40	7.10	7.20	7.30	7.40	7.40	7.30	7.10	7.40	7.50	7.30	7.50	7.30	7.60	7.40	7.10	7.20
<0.04	0.05	0.23	0.05	<0.04	0.06	0.29	0.13	1.10	0.19	0.28	0.15	0.11	0.36	0.46	1.20	0.61	0.40
<0.09	<0.09	<0.09	<0.09	<0.09	<0.09	<0.09	<0.09	0.13	<0.09	<0.09	<0.09	<0.09	<0.09	<0.09	<0.09	<0.09	<0.09
<0.05	<0.05	<0.05	<0.05	<0.05	<0.05	<0.05	<0.05	0.08	<0.05	<0.05	<0.05	<0.05	<0.05	<0.05	<0.05	<0.05	<0.05
<0.05	<0.05	<0.05	<0.05	0.05	<0.05	<0.05	<0.05	0.08	<0.05	<0.05	<0.05	<0.05	<0.05	<0.05	<0.05	<0.05	<0.05
0.06	0.05	<0.05	0.05	0.07	0.06	<0.05	<0.05	0.08	0.10	<0.05	0.06	<0.05	0.08	<0.05	<0.05	<0.05	0.07
0.24	0.70	0.25	0.17	0.28	0.27	0.21	0.19	<0.08	0.30	0.45	0.22	0.24	0.33	0.16	0.17	0.37	0.24
0.09	0.19	0.10	0.09	0.10	0.14	0.10	0.12	0.17	0.14	0.10	0.12	0.14	0.20	0.08	0.17	0.17	0.15
0.06	0.13	0.06	0.07	0.06	0.05	0.08	0.05	0.13	0.08	<0.04	0.08	0.09	0.09	0.08	0.11	0.07	0.07
0.46	1.10	0.47	0.41	0.49	0.47	0.46	0.43	0.55	0.48	0.63	0.43	0.48	0.65	0.40	0.59	0.66	0.50
0.19	0.46	0.21	0.16	0.21	0.21	0.16	0.19	0.24	0.19	0.29	0.19	0.17	0.29	0.20	0.29	0.31	0.20
7.00	10.60	7.20	7.00	7.20	7.30	7.10	7.00	7.20	6.90	7.70	7.00	7.10	7.70	6.40	7.00	7.80	7.10
2.60	3.50	2.70	2.60	2.60	2.70	2.70	2.70	2.80	2.70	2.50	2.70	2.70	2.80	2.40	2.60	2.80	2.60
<0.03	<0.03	<0.03	<0.03	<0.03	<0.03	<0.03	<0.03	<0.03	<0.03	<0.03	<0.03	<0.03	<0.03	<0.03	<0.03	<0.03	<0.03
<0.01	<0.01	<0.01	<0.01	<0.01	<0.01	<0.01	<0.01	<0.01	<0.01	<0.01	<0.01	<0.01	<0.01	<0.01	<0.01	<0.01	<0.01
<0.01	<0.01	<0.01	<0.01	<0.01	0.03	<0.01	<0.01	5.80	<0.01	0.01	<0.01	<0.01	<0.01	<0.01	<0.01	<0.01	<0.01
0.02	0.03	0.05	0.05	0.04	0.04	0.02	0.02	0.04	0.05	0.04	0.03	0.05	0.07	0.06	0.08	0.08	0.06
<0.02	<0.02	<0.02	<0.02	<0.02	<0.02	<0.02	<0.02	<0.02	<0.02	<0.02	<0.02	<0.02	<0.02	<0.02	<0.02	<0.02	<0.02
<0.01	<0.01	<0.01	<0.01	<0.01	<0.01	<0.01	<0.01	<0.01	<0.01	<0.01	<0.01	<0.01	<0.01	<0.01	<0.01	<0.01	<0.01
<0.01	<0.01	0.02	0.01	<0.01	<0.01	<0.01	<0.01	<0.01	<0.01	0.12	<0.01	<0.01	0.02	0.02	0.02	0.03	0.03
0.01	<0.01	0.01	0.02	0.01	0.03	0.01	0.04	0.03	0.01	0.01	<0.01	0.03	0.06	0.02	0.04	0.04	0.04
<0.02	<0.02	<0.02	<0.02	<0.02	<0.02	<0.02	<0.02	<0.02	<0.02	<0.02	<0.02	<0.02	0.07	0.12	0.13	0.02	<0.02
<0.03	<0.03	<0.03	<0.03	<0.03	<0.03	<0.03	<0.03	<0.03	0.05	<0.03	<0.03	<0.03	0.03	<0.02	0.04	<0.02	0.05
0.49	0.60	0.50	0.50	0.47	0.48	0.50	0.43	0.41	0.56	0.39	0.45	0.54	0.69	0.36	0.59	0.57	0.63
<0.02	<0.02	<0.02	<0.02	<0.02	<0.02	<0.02	<0.02	<0.02	<0.02	<0.02	<0.02	<0.02	<0.02	<0.02	<0.02	<0.02	<0.02
<0.02	<0.02	<0.02	<0.02	<0.02	<0.02	<0.02	<0.02	<0.02	<0.02	<0.02	<0.02	<0.02	<0.02	<0.02	<0.02	<0.02	<0.02
78.6	78.2	77.0	74.6	79.1	79.5	77.9	77.5	85.4	77.5	76.0	78.1	78.0	77.1	70.1	70.5	76.4	78.2

RX6721 Irr.	RX6721 Irr.	RX6721 Irr.	RX6721 Irr.	RX6721 Irr.	RX6722 Irr.	RX6722 Irr.	RX6722 Irr.	RX6722 Irr.	RX6722 Irr.	RX6722 Irr.	RX6722 Irr.	RX6722 Irr.	RX6722 Irr.	RX6722 Irr.	RX6722 Irr.	RX6722 Irr.	RX6722 Irr.	RX6722 Irr.	RX6714 Synchysite
17420	**17421**	**17422**	**17423**	**17424**	**465**	**466**	**462**	**463**	**464**	**454**	**455**	**456**	**457**	**458**	**459**	**460**	**461**	**467**	**17294**
1.20	0.46	0.41	0.59	0.44	0.20	0.12	0.29	0.32	0.17	0.58	0.30	0.33	0.29	0.36	0.22	0.29	0.10	0.10	12.60
0.02	<0.008	<0.008	0.01	<0.008	<0.008	0.01	0.01	0.01	<0.008	<0.008	<0.008	<0.008	0.02	<0.008	<0.008	0.01	<0.008	<0.008	0.10
0.21	0.08	0.11	0.19	0.22	<0.03	0.14	0.13	0.16	0.46	0.32	0.18	0.08	0.11	0.22	0.04	0.36	0.07	0.11	<0.02
25.00	26.10	22.90	22.10	25.60	20.70	23.60	23.90	24.70	18.60	22.90	23.80	23.20	20.30	21.70	23.10	19.80	21.50	19.60	11.10
33.00	32.50	33.00	32.00	34.00	32.20	31.10	31.00	31.70	31.30	31.00	32.20	32.90	29.70	31.90	31.30	32.40	32.00	32.10	23.50
7.30	6.90	7.30	7.10	7.30	7.20	7.20	7.20	7.20	7.00	6.90	7.60	7.20	7.00	7.10	6.90	6.90	7.20	7.30	3.60
2.80	0.04	0.44	1.50	0.08	0.17	0.17	<0.04	0.35	<0.04	<0.04	0.23	0.36	2.70	<0.04	0.11	<0.04	<0.04	0.30	0.14
<0.09	<0.09	<0.09	<0.09	<0.09	<0.09	<0.09	<0.09	<0.09	<0.09	<0.09	<0.09	<0.09	<0.09	<0.09	<0.09	<0.09	<0.09	<0.09	<0.09
<0.05	<0.05	<0.05	<0.05	<0.05	<0.05	<0.05	<0.05	0.06	<0.05	0.10	<0.05	<0.05	<0.05	0.08	<0.05	0.07	<0.05	<0.05	<0.05
<0.05	<0.05	<0.05	<0.05	<0.05	<0.05	<0.05	<0.05	<0.05	<0.05	<0.05	<0.05	<0.05	<0.05	<0.05	<0.05	<0.05	<0.05	<0.05	<0.05
0.06	0.06	0.07	<0.05	0.08	<0.05	0.07	0.09	0.06	0.11	0.13	0.08	0.09	0.05	0.16	0.07	0.13	0.09	0.08	0.13
0.25	0.23	0.30	0.24	0.22	0.54	0.29	0.20	0.27	0.47	0.28	0.27	0.37	0.30	0.41	0.33	0.60	0.39	0.44	0.61
0.12	0.12	0.12	0.16	0.13	0.21	0.11	0.13	0.14	0.25	0.15	0.13	0.14	0.13	0.23	0.15	0.29	0.22	0.26	0.39
0.08	0.07	0.09	0.06	0.06	0.08	0.05	0.06	0.05	0.09	0.06	0.06	0.07	0.06	0.07	0.07	0.09	0.08	0.09	0.08
0.47	0.52	0.57	0.59	0.46	0.90	0.52	0.45	0.41	0.81	0.48	0.48	0.58	0.62	0.56	0.57	0.92	0.62	0.73	0.92
0.22	0.25	0.26	0.28	0.24	0.42	0.21	0.21	0.19	0.39	0.21	0.22	0.21	0.27	0.26	0.26	0.46	0.29	0.31	0.40
6.70	6.70	7.40	7.40	6.80	8.80	7.10	6.80	6.80	8.30	6.90	6.90	7.70	7.30	7.60	7.10	8.80	7.70	8.70	7.90
2.60	2.50	2.80	2.80	2.60	3.00	2.50	2.50	2.50	2.80	2.60	2.50	2.70	2.50	2.70	2.60	2.90	2.80	2.90	2.50
<0.03	<0.03	<0.03	0.03	<0.03	<0.03	<0.03	<0.03	<0.03	<0.03	<0.03	<0.03	<0.03	<0.03	<0.03	<0.03	<0.03	<0.03	<0.03	<0.03
<0.01	<0.01	<0.01	<0.01	<0.01	<0.01	<0.01	<0.01	<0.01	<0.01	<0.01	<0.01	<0.01	<0.01	<0.01	<0.01	<0.01	<0.01	<0.01	<0.01
0.04	<0.01	<0.01	<0.01	<0.01	<0.01	<0.01	<0.01	<0.01	<0.01	<0.01	<0.01	<0.01	0.02	<0.01	<0.01	<0.01	<0.01	<0.01	<0.01
0.06	0.04	0.06	0.08	0.05	0.04	0.02	0.04	0.03	0.05	0.05	0.03	0.03	0.03	0.04	0.04	0.04	0.03	0.05	0.06
<0.02	<0.02	<0.02	<0.02	<0.02	<0.02	<0.02	<0.02	<0.02	<0.02	<0.02	<0.02	<0.02	<0.02	<0.02	<0.02	<0.02	<0.02	<0.02	<0.02
<0.01	<0.01	<0.01	<0.01	<0.01	<0.01	<0.01	<0.01	<0.01	<0.01	<0.01	<0.01	<0.01	<0.01	<0.01	<0.01	<0.01	<0.01	<0.01	<0.01
0.11	0.02	0.01	0.03	0.03	<0.01	0.01	<0.01	0.02	<0.01	0.02	<0.01	0.02	0.03	0.01	<0.01	0.01	<0.01	<0.01	<0.01
0.11	0.04	0.04	0.03	0.03	0.02	0.02	0.05	0.02	0.02	0.04	0.02	0.04	0.04	0.04	0.03	0.05	0.02	0.02	<0.009
<0.02	0.02	0.05	0.05	<0.02	<0.02	<0.02	<0.02	<0.02	<0.02	<0.02	<0.02	<0.02	<0.02	<0.02	<0.02	<0.02	<0.02	<0.02	<0.02
0.05	<0.03	<0.03	<0.03	0.07	<0.03	<0.03	0.04	0.03	0.12	0.07	0.05	<0.03	<0.03	<0.03	<0.03	0.03	<0.03	<0.03	<0.02
0.53	0.43	0.45	0.49	0.70	0.67	0.67	0.74	0.79	0.94	0.80	0.62	0.63	0.58	0.82	0.53	0.92	0.76	0.75	1.30
<0.02	<0.02	<0.02	<0.02	<0.02	<0.02	<0.02	<0.02	<0.02	<0.02	<0.02	<0.02	<0.02	<0.02	<0.02	<0.02	<0.02	<0.02	<0.02	<0.02
<0.02	<0.02	<0.02	<0.02	<0.02	<0.02	<0.02	<0.02	<0.02	<0.02	<0.02	<0.02	<0.02	<0.02	<0.02	<0.02	<0.02	<0.02	<0.02	<0.02
80.9	77.1	76.4	75.7	79.1	75.2	73.9	73.8	75.8	71.9	73.6	75.7	76.7	72.1	74.3	73.4	75.1	73.9	73.8	65.3

RX6714 Synchysite 17296	RX6714 Synchysite 17298	RX6714 Synchysite 17299	RX6714 Synchysite 17285	RX6714 Synchysite 17286	RX6714 Synchysite 17287	RX6714 Synchysite 17289	RX6714 Synchysite 17290	RX6714 Synchysite 17291	RX6714 Synchysite 17292	RX6726 Synchysite 17426	RX6726 Synchysite 17427	RX6726 Synchysite 17428	RX6726 Synchysite 17429	RX6726 Synchysite 17430	RX6726 Synchysite 17431
12.30	12.40	12.40	9.80	12.30	12.10	12.50	12.30	12.40	12.50	12.30	12.50	12.50	12.50	12.40	12.50
0.10	0.07	0.11	0.02	0.04	0.33	<0.008	<0.008	0.01	0.02	0.06	0.05	<0.008	<0.008	0.03	0.03
<0.02	<0.02	<0.02	<0.02	<0.02	<0.02	<0.02	0.03	<0.02	<0.02	<0.02	<0.02	<0.02	<0.02	<0.02	<0.02
11.00	11.10	11.00	8.40	7.90	10.80	10.50	12.90	10.50	7.80	9.30	8.90	9.00	10.10	8.90	9.20
22.80	23.10	23.30	23.60	24.40	24.10	25.40	28.20	23.30	24.00	23.70	22.60	22.90	23.90	22.90	23.60
3.40	3.80	3.80	5.20	3.50	2.60	3.70	3.60	3.60	3.60	3.70	3.80	3.50	3.40	3.40	3.70
0.23	0.10	0.12	0.08	0.13	0.18	<0.03	0.11	0.09	0.19	0.12	<0.03	<0.04	0.07	<0.03	0.04
<0.09	<0.09	<0.09	<0.09	<0.09	0.13	<0.09	<0.09	<0.09	<0.09	<0.09	<0.09	<0.09	<0.09	<0.09	<0.09
<0.05	<0.05	<0.05	<0.05	<0.05	<0.05	<0.05	<0.05	<0.05	<0.05	<0.05	<0.05	<0.05	<0.05	<0.05	<0.05
<0.05	<0.05	<0.05	<0.05	<0.05	<0.05	<0.05	<0.05	<0.05	<0.05	<0.05	<0.05	<0.05	<0.05	<0.05	<0.05
0.10	0.07	0.09	<0.05	<0.05	0.09	0.09	0.07	0.09	0.05	<0.05	<0.05	<0.05	<0.05	<0.05	<0.05
0.59	0.62	0.65	0.74	0.91	0.62	0.99	0.62	0.70	0.97	0.83	0.83	0.87	0.74	0.91	0.73
0.41	0.41	0.37	0.32	0.32	0.44	0.49	0.38	0.47	0.38	0.24	0.23	0.21	0.27	0.25	0.22
0.09	0.09	0.08	0.07	0.09	0.10	0.12	0.13	0.12	0.11	0.08	0.06	<0.04	0.08	0.09	0.09
0.90	0.93	0.97	1.10	1.30	1.10	1.20	1.00	1.00	1.40	1.30	1.40	1.50	1.20	1.50	1.20
0.41	0.43	0.44	0.51	0.56	0.51	0.62	0.46	0.49	0.59	0.61	0.68	0.72	0.60	0.74	0.59
7.90	7.90	8.00	8.60	9.50	8.30	9.40	8.80	8.10	9.80	9.10	10.20	10.40	8.40	10.00	9.70
2.50	2.50	2.50	2.50	2.70	2.50	2.80	2.90	2.50	2.80	2.80	2.90	2.80	2.60	2.80	2.80
<0.02	<0.03	<0.03	<0.03	<0.02	<0.03	<0.03	<0.03	<0.02	<0.03	<0.02	<0.03	<0.02	<0.02	<0.02	<0.03
<0.01	<0.01	<0.01	<0.01	<0.01	<0.01	<0.01	<0.01	<0.01	<0.01	<0.01	<0.01	<0.01	<0.01	<0.01	<0.01
0.02	<0.01	0.03	<0.01	<0.01	0.92	<0.01	<0.01	<0.01	<0.01	0.49	<0.01	<0.01	<0.01	<0.01	0.02
0.05	0.03	0.04	0.06	0.03	0.04	0.05	0.03	0.03	0.03	0.05	0.04	0.05	0.06	0.06	0.05
<0.02	<0.02	<0.02	<0.02	<0.02	<0.02	<0.02	<0.02	<0.02	<0.02	<0.02	<0.02	<0.02	<0.02	<0.02	<0.02
<0.01	<0.01	<0.01	<0.01	<0.01	<0.01	<0.01	<0.01	<0.01	<0.01	<0.01	<0.01	<0.01	<0.01	<0.01	<0.01
<0.01	<0.01	<0.01	<0.01	<0.01	0.01	<0.01	<0.01	<0.01	<0.01	<0.01	<0.01	<0.01	<0.01	<0.01	0.02
<0.009	0.02	0.01	0.03	<0.009	0.03	0.02	<0.009	0.03	0.02	<0.009	0.03	0.02	0.01	0.02	<0.009
<0.02	<0.02	<0.02	<0.02	<0.02	<0.02	<0.02	<0.02	<0.02	<0.02	<0.02	<0.02	<0.02	<0.02	<0.02	0.05
<0.02	<0.02	<0.02	<0.02	<0.02	<0.02	<0.02	<0.02	<0.02	<0.02	<0.02	<0.02	<0.02	<0.02	<0.02	<0.02
1.50	1.30	1.10	0.87	0.84	1.30	1.10	1.10	1.50	0.95	0.55	0.55	0.49	0.66	0.60	0.47
<0.02	<0.02	<0.02	<0.02	<0.02	<0.02	<0.02	<0.02	<0.02	<0.02	<0.02	<0.02	<0.02	<0.02	<0.02	<0.02
<0.02	<0.02	<0.02	<0.02	<0.02	<0.02	<0.02	<0.02	<0.02	<0.02	<0.02	<0.02	<0.02	<0.02	<0.02	<0.02
64.3	64.9	65.0	61.9	64.5	66.2	69.0	72.6	64.9	65.2	65.2	64.8	65.0	64.6	64.6	65.0

RX6726 Synchysite 17432	RX6726 Synchysite 17436	RX6726 Synchysite 17441	
12.60	12.50	12.70	
<0.008	0.02	0.01	
<0.02	<0.02	<0.02	
9.90	9.90	9.40	
23.50	23.80	22.70	
3.10	3.80	3.60	
0.05	0.04	0.05	
<0.09	<0.09	<0.09	
<0.05	<0.05	<0.05	
<0.05	<0.05	<0.05	
<0.05	<0.05	<0.05	
0.75	0.77	0.94	
0.29	0.29	0.33	
0.07	0.09	0.10	
1.10	1.20	1.40	
0.54	0.57	0.70	
8.60	8.50	9.10	
2.60	2.60	2.70	
<0.03	<0.02	<0.03	
<0.01	<0.01	<0.01	
<0.01	<0.01	<0.01	
0.05	0.07	0.06	
<0.02	<0.02	<0.02	
<0.01	<0.01	<0.01	
0.01	0.02	<0.01	
0.01	<0.009	0.01	
<0.02	<0.02	<0.02	
<0.02	<0.02	<0.02	
0.71	0.81	0.90	
<0.02	<0.02	<0.02	
<0.02	<0.02	<0.02	
63.9	65.0	64.7	

Table S6: Full LA-ICP-MS dataset for REE fluorocarbonates (in ppm).
Type bastnasite abbreviations: Mx-stby, Matrix-stubby; Mx-f.g., Matrix-fine grained; Irr., Irregular sulfide associated; CR, Clast Replacement.

RX Sample	RX6709	RX6709	RX6709	RX6709	RX6709	RX6709	RX6709	RX6709	RX6709	RX6709	RX6709	RX6709	RX6709	RX6709	RX6709	RX6709	RX6709	RX6709	RX6709	RX6709	RX6709	RX6709	RX6709	RX6709	RX6709	RX6709	RX6709	RX6709	RX6709	RX6709	RX6709
Type	Mx-Stby	Mx-Stby	Mx-Stby	Mx-Stby	Mx-Stby	Mx-Stby	Mx-Stby	Mx-Stby	Mx-Stby	Mx-Stby	Mx-Stby	Mx-Stby	Mx-Stby	Mx-Stby	Mx-Stby	Mx-Stby	Mx-Stby	Mx-Stby	Mx-Stby	Mx-Stby	Mx-Stby	Mx-Stby	Mx-Stby	Mx-Stby	Mx-Stby	Mx-Stby	Mx-Stby	Mx-Stby	Mx-Stby	Mx-Stby	Mx-Stby	Mx-Stby
Output #	**1_42**	**1_43**	**1_44**	**1_45**	**1_47**	**1_56**	**1_48**	**1_49**	**1_50**	**1_51**	**1_53**	**1_54**	**1_55**	**1_15**	**1_24**	**1_25**	**1_26**	**1_16**	**1_17**	**1_18**	**1_19**	**1_20**	**1_21**	**1_22**	**1_23**	**1_7**	**1_8**	**1_9**	**1_10**	**1_11**
La	198100	193200	186100	184000	202000	197600	185200	188700	182000	179400	195000	199000	195400	180700	202100	198100	182000	176900	178000	189900	171000	185300	169800	166800	192000	183000	211000	212200	174400	186000
Pr	39690	38520	36980	38200	36500	36960	35400	37400	36900	37000	37400	35600	36790	38500	40300	35670	38360	38000	36500	36800	36800	36000	37610	35000	35600	36500	35100	34590	38200	39500
Nd	114900	108800	113000	110100	106200	105400	104100	107800	100200	101100	105400	101900	102000	110500	119000	94500	119000	107500	101600	102900	100700	105100	109200	110000	98900	101600	102600	90100	106600	104900
Sm	10210	9130	8600	9730	8510	8970	9080	9040	8150	8470	9570	7680	8470	9930	10450	7230	10610	10550	9840	9170	10320	9270	10360	10000	8270	8640	8160	6320	10710	10130
Eu	3050	2653	2530	2780	2507	2760	2760	2730	2400	2620	2890	2380	2406	2988	3130	2070	3170	3300	3130	2730	2920	2770	3290	3080	2460	2670	2420	1656	3190	3220
Gd	3560	2930	2920	3180	2927	3178	3180	2990	2750	2900	3360	2717	2740	3550	3640	2310	3760	3880	3510	3080	3250	3370	3720	3460	2740	3020	2940	1751	3900	3680
Tb	314	261	251	283	245	278	279	268	228	267	302	230	233	324	302	188	333	351	343	277	312	305	358	330	231	298	243	113	355	345
Dy	1271	1027	1009	1153	945	1112	1120	1061	928	1020	1237	873	929	1480	1225	718	1400	1391	1470	1169	1210	1273	1500	1370	921	1200	990	400	1541	1484
Y	3170	2550	2430	2730	2500	3040	2740	2690	2280	2460	2930	2316	2270	3480	2930	1910	3320	3510	3620	3180	3180	3070	3770	3390	2370	2970	2540	912	4140	3560
Ho	175	140	133	160	123	154	153	142	131	145	164	118	127	190	163	99.3	193	198	208	164	186	176	215	196	120	166	134	41.2	223	197
Er	345	271	252	321	240	314	300	287	241	268	313	242	247	383	323	194	382	403	391	334	385	346	436	391	244	328	273	68.7	457	436
Tm	30.5	24.6	23.8	30.0	18.9	27.7	27.0	27.7	21.3	24.9	26.6	21.7	22.3	34.3	31.6	21.0	34.7	39.1	36.2	29.7	33.7	32.6	43.1	39.6	22.7	26.1	20.3	5.0	44.8	36.8
Yb	134	111	99.0	136	82.5	126	119	122	92.0	111	117	88.7	99.2	158	135	104	155	174	172	136	160	146	197	169	98.0	116	95.0	20.4	236	176
Lu	14.3	11.6	9.7	14.7	7.9	13.1	12.6	12.1	9.6	11.6	12.0	9.4	10.1	17.0	13.5	10.9	15.9	18.2	18.8	14.0	16.5	16.4	21.7	18.1	10.3	11.7	10.1	1.7	21.2	19.6
Ca	850	400	750	<267	700	2010	690	<256	<284	220	<309	290	460	<846	<1086	1660	<663	<697	<633	1270	<463	<1228	2200	<566	<696	<659	<630	<700	<653	<680
Sr	1900	1500	937	189	201	4560	487	224	567	127	182	201	610	1250	1260	2300	169	784	205	2710	270	180	1150	600	261	124	141	95.8	166	125
Ba	370	380	70.0	9.4	35.9	145	20.5	10.9	23.4	5.2	10.8	7.7	20.6	48.0	63.0	740	14.9	29.1	12.4	162	10.0	13.6	44.1	44.0	12.2	14.7	5.0	0.77	10.9	9.2
Cu	200	73.0	18.1	8.7	16.5	1500	16.6	9.7	28.8	71.0	10.8	13.4	73.0	149	280	1800	17.1	26.8	40.3	158	<3.7	140	51.0	36.0	28.5	<5.3	13.1	<3.7	12.0	21.9
Al	4950	4730	14600	182	4500	26600	1400	322	4000	136	890	820	2370	9100	9100	5800	1630	2070	184	7250	267	er	5900	1110	1200	1460	37.0	er	er	590
Fe	2550	2700	1080	107	12500	16000	2140	224	1010	44.0	348	83.0	850	1600	940	7100	193	er	120	3050	81.0	4100	13100	95.0	228	140	107	er	er	2800
Mn	1.3	2.2	<2.0	<1.0	3.1	46.0	1.3	<0.93	1.3	<0.95	<0.99	<1.0	<1.3	4.1	<4.7	12.3	<3.1	<2.7	<2.1	3.6	<2.1	er	27.0	<1.9	<3.0	<2.7	<2.5	<2.5	<2.2	5.0
P	2160	1530	820	77.0	<62.6	9200	446	119	286	63.0	75.0	95.0	450	1300	1160	3380	<143	630	<157	3100	<140	<298	1310	570	<155	<136	<141	<133	<152	<126
Na	220	236	460	<18.6	97.0	461	135	<16.8	129	<15.5	43.0	<14.5	84.0	270	550	130	76.0	69.0	<38.8	337	<42.1	<91.2	171	46.0	<45.0	73.0	68.0	<45.8	<46.6	<43.2
Nb	2.1	2.0	3.1	<0.001	28.1	1.6	140	0.75	4.2	0.09	0.32	10.4	<0.04	0.59	<0.001	250	0.26	1.0	<0.06	1.6	<0.001	<0.001	<0.18	er	er	<0.001	er	<0.07	er	<0.001
Sc	<0.44	<0.46	<0.61	<0.32	2.6	1.0	4.1	<0.35	<0.42	<0.33	<0.36	0.43	<0.40	<0.90	<1.6	4.0	<0.94	<0.75	<0.77	<1.1	<0.69	<1.4	<2.0	<0.68	<0.98	<0.81	<0.88	<0.78	<0.89	<0.92
Si	1220	1150	14900	<404	5700	13600	950	<389	2900	<311	1110	er	840	er	10800	<1038	2100	<925	<779	2100	<966	<1656	5800	<928	1660	2400	<957	<982	<1095	<933
W	0.98	0.70	er	<0.001	9.1	0.40	3.7	0.14	0.18	er	0.11	0.30	<0.08	<0.001	<0.001	7.5	<0.001	er	<0.13	0.48	<0.001	<0.001	er	<0.001	er	<0.16	<0.001	<0.001	er	<0.001
Zr	5.2	0.74	5.4	1.8	4.3	5.2	3.3	0.51	0.18	0.24	5.0	0.91	7.3	11.4	9.8	430	2.4	0.60	1.3	7.0	0.21	0.85	<0.31	0.15	2.9	0.85	0.27	0.21	0.40	0.22
As	465	401	398	429	397	508	403	396	371	379	393	378	392	431	475	412	422	439	415	468	410	411	475	435	390	417	373	380	443	448
Bi	0.89	0.59	0.27	0.11	0.87	2.2	0.98	0.26	0.37	0.15	<0.10	0.12	0.16	0.22	0.95	17.1	<0.28	0.31	0.20	4.3	0.58	<0.54	0.94	0.36	<0.26	<0.25	0.25	<0.15	0.44	<0.15
Hf	0.42	<0.001	<0.09	0.03	0.12	<0.07	0.53	er	<0.05	<0.001	0.18	0.14	0.15	0.23	<0.001	9.6	<0.001	<0.001	<0.001	0.23	er	<0.001	<0.001	<0.001	<0.001	<0.001	<0.001	<0.001	<0.001	<0.001
Ta	0.06	<0.02	0.23	<0.01	0.42	0.03	7.3	0.05	0.14	<0.001	<0.001	0.31	<0.001	er	<0.001	3.9	<0.001	0.06	<0.001	<0.001	<0.001	<0.001	<0.001	<0.001	<0.001	<0.001	<0.001	<0.001	<0.001	<0.001
Th	125	141	85.0	16.9	2313	348	244	52.0	123	39.6	140	72.0	73.0	65.0	127	54.0	16.7	35.5	26.0	84.0	5.3	12.5	9.2	7.6	46.9	25.2	120	35.9	33.4	11.2
U	12.6	4.5	5.3	8.7	13.1	7.1	8.6	0.99	3.1	3.7	10.8	3.4	13.2	24.8	8.3	930	8.9	8.0	14.7	12.7	2.7	4.1	2.7	0.63	8.5	3.2	15.1	0.31	2.0	1.4
Total Pb	29.8	25.3	15.9	7.0	221	62.6	37.8	8.1	13.7	6.4	16.2	8.2	13.3	17.4	29.6	97.5	8.4	14.8	9.9	39.3	10.5	7.9	24.3	11.4	11.3	6.7	14.1	4.4	12.0	7.1

'<' indicates minimum detection limit
'er' indicates values with too high analytical error

RX6709 Mx-Stby	RX6709 Mx-Stby	RX6709 Mx-Stby	RX6709 Mx-Stby	RX6709 Mx-Stby	RX6709 Mx-Stby	RX6709 Mx-Stby	RX6709 Mx-Stby	RX6709 Mx-Stby	RX6709 Mx-Stby	RX6709 Mx-Stby	RX6709 Mx-Stby	RX6709 Mx-Stby	RX6709 Mx-Stby	RX6709 Mx-Stby	RX6709 Mx-Stby	RX6709 Mx-Stby	RX6710 Mx-Stby	RX6710 Mx-Stby	RX6710 Mx-Stby	RX6710 Mx-Stby	RX6710 Mx-Stby	RX6710 Mx-Stby	RX6710 Mx-Stby	RX6710 Mx-Stby	RX6710 Mx-Stby	RX6710 Mx-Stby	RX6710 Mx-Stby	RX6710 Mx-Stby	RX6710 Mx-Stby	RX6710 Mx-Stby	RX6710 Mx-Stby
1_12	**1_13**	**1_14**	**1_1**	**1_2**	**1_3**	**1_4**	**1_5**	**1_6**	**1_28**	**1_32**	**1_37**	**1_38**	**1_39**	**1_40**	**1_41**	**1_57**	**1_58**	**1_59**	**1_60**	**1_61**	**1_62**	**1_63**	**1_64**	**1_65**	**1_66**	**1_67**	**1_68**	**1_70**	**1_71**	**1_72**
192000	166000	217500	190100	237000	182600	190000	179000	171000	210000	200100	196000	204300	182100	201000	188800	170300	160100	177200	167500	169300	177500	172300	176300	162400	173300	191000	169600	163400	184900	166000
37370	37100	35660	38370	40600	38200	37600	36400	39700	34100	36560	38000	37120	37720	38400	38840	32100	33800	32800	35110	34500	33170	32110	32300	34700	31800	32300	33960	33350	32400	33300
107100	109400	96300	111300	123500	100500	99400	111000	107700	92300	98300	111100	102100	108100	109600	109600	90400	105800	93300	102300	99650	94100	88800	88700	107500	83600	89400	101400	99500	90300	100900
9170	10810	7160	10240	9530	9700	8960	10190	9510	6510	8260	10980	8320	10130	9450	9830	7360	9740	7340	10360	9200	8050	7050	7020	11730	6140	7780	10100	10190	6900	9550
2700	3300	1900	3250	2490	2950	2600	2940	2900	1705	2420	3300	2320	3090	2760	3010	2060	3060	2110	3290	2960	2310	1926	1916	3770	1750	2320	3170	3240	1870	2950
3040	3810	2120	3840	3210	3260	3020	3990	3430	1849	2760	4110	2920	3490	3230	3410	2570	3570	2240	4400	3520	2657	2325	2270	5180	1830	2880	4390	4350	2190	3870
276	355	149	349	233	303	270	336	308	123	227	359	227	319	282	304	207	318	187	426	316	213	190	186	517	134	221	392	427	183	337
1157	1532	543	1640	872	1274	970	1360	1370	402	880	1530	885	1330	1130	1230	798	1306	703	1793	1290	811	726	673	2170	520	940	1565	1768	680	1360
2800	3970	1430	3920	1960	3240	2540	3540	3110	1010	2250	3810	2360	3310	2840	3140	2120	3330	1710	5110	3520	2120	1930	1810	6450	1110	2370	4630	4940	1860	3670
166	222	61.0	217	102	174	131	186	173	45.9	117	215	122	185	148	171	109	180	91.0	254	180	111	93.2	92.3	307	68.0	124	223	246	91.0	191
311	459	117	423	187	342	272	388	401	82.0	241	430	246	384	297	337	226	351	163	505	369	219	182	166	615	129	235	440	502	154	358
30.3	43.0	9.9	36.7	14.2	31.7	25.5	36.7	33.1	6.6	20.4	44.4	22.8	34.7	27.4	31.0	19.1	33.6	16.5	46.8	36.9	20.0	15.7	14.5	59.2	11.1	19.7	37.2	47.1	17.1	36.3
138	214	38.0	172	61.0	143	119	152	170	28.2	93.0	188	94.9	151	117	141	88.1	166	70.3	223	180	86.7	70.1	61.5	277	52.0	96.0	187	222	68.0	145
13.4	20.9	3.3	18.1	5.3	15.2	12.9	17.0	16.7	2.9	10.5	19.7	9.0	16.9	11.8	15.1	9.1	17.8	7.6	23.6	19.0	9.3	7.2	6.2	29.9	4.2	9.3	19.2	22.7	6.9	15.9
<591	<601	<1690	<710	<657	<851	440	<538	<636	<612	<1961	<520	<680	<788	<732	<762	338	346	274	900	295	224	187	487	790	<607	<466	1340	<895	<692	<582
145	133	300	257	86.0	337	124	120	84.0	119	1115	91.5	1240	1100	920	1012	83.3	165	113	970	114	63.4	83.0	268	400	71.1	105	1480	419	89.3	349
16.1	7.3	33.0	55.0	6.7	31.8	6.8	8.5	4.0	4.0	62.0	3.7	123	31.0	30.4	290	2.2	4.3	4.1	22.1	5.7	1.9	2.3	6.4	18.7	1.2	1.6	39.7	24.1	2.3	10.8
5.7	<4.2	250	62.0	10.2	153	5.4	26.0	<3.4	4.2	140	<3.6	103	135	38.0	16.4	34.0	148	73.0	189	5000	31.0	29.0	380	42.0	14800	74.0	77.0	340	<4.5	127
600	7.5	12700	15700	2400	7700	52.0	440	5.8	1150	11700	11.4	3380	1680	3930	9100	88.0	145	117	8200	64.0	8.9	129	1370	2240	28.0	9.4	7300	2840	930	980
1100	<52.1	66000	11800	2800	47000	<51.1	73.0	<46.5	410	35300	<58.3	290	1340	2610	1610	72.0	214	44.2	8200	172	186	430	1050	4700	280	530	8400	14000	1650	260
<2.5	<2.0	<5.5	3.1	6.7	3.4	<2.0	<2.0	<1.9	<2.6	17.4	<2.2	<2.7	<2.5	7.1	3.3	<0.48	<0.42	<0.36	1.8	0.67	<0.54	<0.50	0.50	3.4	<2.4	<2.2	4.9	<3.3	5.0	<2.5
<161	<151	720	290	<185	330	<129	<127	<126	<124	3100	<144	1690	920	910	870	104	370	180	3340	141	66.0	170	650	440	<145	<140	5500	1030	<149	1270
<41.6	<37.8	620	740	<46.3	383	<33.1	<46.7	<40.2	65.0	392	<49.5	168	108	218	227	15.2	23.4	23.0	99.0	21.0	<8.2	8.5	33.6	90.0	<39.1	<40.0	60.0	76.0	<41.8	<40.0
er	<0.001	7.4	2.1	<0.001	11.4	<0.001	<0.06	<0.001	0.27	9.5	<0.001	5.1	2.0	0.35	4.1	1.1	0.26	0.33	20.9	0.59	0.25	0.90	11.8	11.3	<0.001	0.47	24.3	23.9	er	<0.06
<0.70	<0.84	<2.1	<0.89	1.0	<0.88	<0.66	<0.90	<0.77	<0.96	<2.0	<0.85	<0.84	<1.0	<1.1	<1.1	<0.13	<0.15	<0.14	0.57	0.11	<0.16	<0.16	0.19	<0.94	<0.71	<0.73	<0.93	<0.94	<0.91	<0.91
<1073	<1082	16400	22500	er	9500	<696	<1042	<852	1360	12100	<899	<1060	<1341	2900	7800	188	<142	<168	4900	<154	<186	<215	1020	1830	<981	<808	1670	2800	<958	<904
<0.001	<0.001	er	<0.18	<0.001	1.2	<0.001	<0.001	<0.001	<0.16	1.4	<0.001	<0.001	<0.001	<0.001	0.40	0.08	0.21	er	2.9	0.19	er	er	0.37	1.1	<0.001	0.28	5.6	1.5	<0.001	er
0.56	0.16	2.7	0.86	er	7.0	0.38	0.54	0.22	<0.17	2.0	0.66	25.6	0.47	0.75	12.5	0.43	0.29	0.17	3.8	1.5	0.28	0.35	0.39	0.47	<0.11	er	0.32	1.3	0.11	0.15
425	423	381	429	464	439	500	435	395	347	401	449	464	446	432	425	350	402	354	441	383	377	350	348	420	326	428	444	399	334	409
<0.21	<0.17	1.9	1.5	<0.28	1.8	0.24	<0.20	0.15	1.6	1.9	<0.25	0.55	0.87	1.5	0.68	0.10	0.16	0.09	0.46	5.9	<0.03	0.05	0.13	0.50	4.3	0.32	0.55	0.78	0.36	0.33
<0.001	<0.001	<0.001	er	<0.001	er	<0.09	<0.001	<0.001	<0.001	<0.001	<0.001	er	<0.001	<0.001	0.65	<0.001	er	<0.001	0.18	0.11	0.04	<0.001	er	<0.001	<0.001	<0.001	<0.001	er	<0.001	<0.001
<0.001	<0.001	<0.08	er	<0.001	0.21	<0.001	er	er	<0.001	0.26	<0.001	0.39	0.06	<0.001	0.15	0.04	0.02	0.01	0.32	0.02	<0.001	<0.001	0.47	0.10	<0.001	<0.001	0.37	0.62	<0.001	er
66.0	0.14	137	124	213	47.0	89.0	13.8	0.42	450	135	26.9	122	47.7	117	122	327	255	22.3	681	205	20.4	304	235	1180	11.8	206	645	738	110	297
8.7	0.34	5.1	7.2	2.2	7.0	1.9	2.5	0.24	1.9	6.3	3.0	6.8	12.4	6.7	7.5	17.9	12.0	5.9	19.4	35.0	2.5	7.9	13.9	31.3	2.6	9.7	13.6	38.9	5.9	19.3
10.8	5.5	27.6	22.2	17.7	18.0	15.8	9.0	3.4	45.4	29.8	7.6	23.2	22.6	27.9	25.6	35.8	26.6	4.8	72.3	31.3	3.7	25.8	26.2	153	15.5	22.5	78.5	99.5	12.7	32.9

RX6710 Mx-Stby	RX6710 Mx-Stby	RX6710 Mx-Stby	RX6710 Mx-Stby	RX6710 Mx-Stby	RX6710 Mx-Stby	RX6710 Mx-Stby	RX6710 Mx-Stby	RX6710 Mx-Stby	RX6710 Mx-Stby	RX6710 Mx-Stby	RX6710 Mx-Stby	RX6710 Mx-Stby	RX6710 Mx-Stby	RX6710 Mx-Stby	RX6710 Mx-Stby	RX6710 Mx-Stby	RX6710 Mx-Stby	RX6710 Mx-Stby	RX6710 Mx-Stby	RX6710 Mx-Stby	RX6710 Mx-Stby	RX6710 Mx-Stby	RX6710 Mx-Stby	RX6710 Mx-Stby	RX6709 Mx-Stby	RX6709 Mx-Stby	RX6709 Mx-Stby	RX6709 Mx-Stby	RX6709 Mx-Stby	RX6709 Mx-Stby
1_84	**1_85**	**1_86**	**1_87**	**1_90**	**1_91**	**1_92**	**1_93**	**1_96**	**1_97**	**1_98**	**1_1**	**1_3**	**1_73**	**1_82**	**1_83**	**1_74**	**1_75**	**1_76**	**1_77**	**1_78**	**1_79**	**1_80**	**1_81**	**1_6**	**1_7**	**1_8**	**1_9**	**1_10**	**1_11**
199000	192700	189700	183300	162000	172500	160700	139700	168700	166400	189500	175400	173400	172500	163800	168400	170700	197200	165800	173400	165500	174100	158700	175800	187900	187400	182900	189100	187500	189600
32600	34200	34600	34000	30100	29380	30100	33780	34760	34440	32070	35570	31490	34100	33620	32400	32600	30800	33300	32700	32100	34300	33550	31670	36380	36960	36680	39020	36260	36540
98000	97600	98400	95600	87100	78000	88000	105500	103100	104700	90600	104500	88500	96500	97600	89400	89800	82000	98400	93100	88300	95700	99890	84700	103700	106300	109200	113100	105600	103400
7540	8600	8160	8500	7390	5780	7660	9930	9690	10930	7970	9960	7430	8420	8660	7580	7520	5520	8510	7790	7760	8200	9510	6520	9100	9900	9920	10290	9380	8780
1930	2610	2590	2710	2190	1549	2400	2507	2890	3540	2493	3000	2157	2455	2610	2180	2217	1456	2480	2270	2350	2350	2980	1800	2679	2979	3030	3074	2814	2640
2140	3050	3020	2980	2590	1654	2620	4340	3890	4430	3030	3930	2580	2868	3000	2640	2546	1470	2890	2520	2750	2700	3550	1970	2972	3305	3430	3545	3064	2805
178	241	259	234	215	114	218	427	336	427	284	326	229	245	270	223	211	93.2	253	236	240	216	322	153	261	298	305	328	269	247
720	950	1060	960	880	465	899	1898	1450	1863	1237	1310	946	972	1075	925	869	278	1046	860	970	850	1322	586	1057	1204	1307	1389	1145	1005
1370	2440	2980	2180	2260	1000	2100	6440	3980	5150	3350	3640	2740	2378	2790	2620	2120	664	2570	2140	2560	2150	3270	1440	2700	3081	3380	3730	2801	2682
77.0	120	147	110	119	48.0	120	274	192	263	164	173	127	129	150	129	116	29.0	140	112	135	114	180	72.1	145	165	177	192	155	140
101	219	294	203	246	88.0	234	544	363	531	349	338	236	259	301	278	216	44.4	282	224	261	221	342	144	293	327	370	373	308	305
12.9	19.5	25.2	14.9	22.8	8.2	21.5	50.3	29.4	49.4	30.8	25.3	17.3	22.2	28.0	32.1	19.5	3.0	23.0	21.7	23.2	21.0	29.6	12.2	27.0	30.8	33.8	31.6	28.5	31.2
40.6	91.0	121	69.0	109	41.7	102	222	130	228	142	142	79.8	103	125	230	83.8	13.9	112	109	99.0	109	130	57.1	123	144	161	130	134	163
3.7	8.6	12.3	7.5	11.2	3.2	11.4	25.2	14.2	24.0	14.1	13.1	7.3	10.7	13.9	20.5	8.7	1.0	10.7	11.3	10.8	11.2	13.2	5.6	12.3	14.7	16.2	12.6	13.3	18.6
<677	1100	1490	er	<595	<676	1150	2900	2550	2260	3100	880	<1909	620	550	377	260	158	422	337	310	510	910	459	421	294	206	389	500	639
256	350	1790	229	296	930	266	402	3200	3610	6500	860	3740	893	742	192	90.5	62.3	302	356	210	760	733	392	890	308	413	920	492	1433
4.7	12.8	53.0	31.0	18.3	1180	9.2	11.2	78.0	104	225	58.0	401	51.0	82.0	16.0	3.5	0.67	16.4	13.6	er	33.1	32.4	27.7	290	16.8	71.0	35.4	560	590
66.0	15.0	460	200	370	500	820	700	480	820	7200	182	740	221	551	190	7.0	0.82	740	74.0	500	26.7	470	18.8	253	5.5	1430	230	24.7	2480
420	1640	11500	43000	1490	3550	3100	7500	15500	12800	60300	7600	51900	7400	3210	417	880	0.60	800	722	430	1450	1550	970	4070	1500	1690	7010	1020	3210
er	590	58000	23000	303	1890	73000	23700	10700	6100	75000	46000	62800	3410	40500	1640	2200	<8.8	650	760	232	770	1050	431	1450	213	241	4780	480	923
<2.4	<2.8	14.5	26.0	<2.5	<2.0	<2.7	24.6	8.6	4.1	126	3.7	26.7	2.4	1.5	3.0	2.6	<0.44	0.52	<0.50	<0.38	<0.38	1.2	<0.43	na	na	na	na	na	na
370	370	5200	er	320	1570	600	<159	10600	10200	31400	2600	10500	983	1410	169	53.0	52.0	330	379	270	910	768	473	1175	362	387	1820	451	1480
57.0	165	290	750	52.0	128	125	330	210	222	800	280	2910	123	125	49.0	<8.3	<7.8	43.2	36.5	27.0	84.0	67.9	53.9	72.3	47.5	47.2	122	63.1	161
er	0.34	74.0	2.0	2.1	64.0	88.0	14.0	16.5	31.0	8.0	56.0	121	9.2	14.8	15.8	0.97	er	1.0	1.5	0.47	1.1	17.0	2.4	na	na	na	na	na	na
<0.68	<0.86	1.6	<1.0	<0.87	<0.85	<1.0	<0.79	<1.1	<1.0	<2.6	<1.3	<2.4	0.46	0.37	4.2	<0.15	<0.16	<0.18	<0.15	<0.14	0.31	0.95	0.12	na	na	na	na	na	na
<1000	1970	5500	64000	1470	1860	1580	7800	3000	2500	39600	6400	57000	7000	1840	820	640	<164	600	1010	147	310	304	370	1760	1120	980	3750	215	810
0.32	<0.001	0.75	0.23	<0.001	0.35	0.84	1.4	2.9	1.5	er	2.9	4.8	1.0	2.1	1.0	0.09	<0.001	0.09	0.19	er	0.23	1.7	0.36	0.12	0.14	0.05	0.05	0.18	0.43
0.55	<0.13	0.76	er	<0.16	0.27	1.7	1.5	1.6	1.2	3.1	2.5	60.0	0.75	0.48	1220	0.66	0.17	11.1	0.36	0.24	0.35	2.1	0.59	na	na	na	na	na	na
341	370	418	379	352	310	410	396	479	482	535	436	423	390	399	350	332	319	368	366	364	378	410	333	na	na	na	na	na	na
0.56	0.63	2.1	er	1.5	0.67	8.2	1.1	0.77	13.8	16.2	1.9	6.4	0.56	1.2	0.65	0.07	0.05	0.17	0.17	0.92	0.29	1.1	0.40	2.4	0.37	0.18	0.97	0.44	10.0
<0.001	<0.001	<0.001	<0.001	<0.001	<0.001	er	<0.12	<0.001	er	<0.43	<0.001	1.1	<0.001	<0.001	39.0	0.05	er	0.51	er	er	<0.02	0.15	0.06	na	na	na	na	na	na
er	<0.001	0.98	0.05	er	1.5	0.79	0.10	0.91	0.87	0.13	1.1	2.9	0.30	0.33	0.31	er	<0.001	0.03	0.04	er	0.02	0.82	0.07	na	na	na	na	na	na
454	205	417	154	310	124	186	4960	2070	728	481	1730	788	127	110	157	30.6	17.4	61.0	54.0	39.5	157	279	79.0	36.6	136	23.1	112	26.7	83.0
11.1	1.9	6.0	2.7	5.0	2.7	10.4	86.0	26.4	13.1	7.0	13.8	24.6	31.4	10.0	101	20.8	0.07	18.7	1.1	16.5	7.1	33.3	8.7	5.4	3.8	6.0	8.7	9.1	87.0
66.3	35.5	76.0	29.3	34.2	31.2	49.0	606	275	131	112	201	127	24.0	24.5	19.9	6.4	1.8	14.9	10.1	13.5	21.0	38.9	13.6	15.7	16.7	8.1	16.8	9.2	33.8

RX6728 Mx-Stby	RX6728 Mx-Stby	RX6728 Mx-Stby	RX6728 Mx-Stby	RX6728 Mx-Stby	RX6728 Mx-Stby	RX6728 Mx-Stby	RX6728 Mx-Stby	RX6728 Mx-Stby	RX6728 Mx-Stby	RX6728 Mx-Stby	RX6728 Mx-Stby	RX6728 Mx-Stby	RX6728 Mx-Stby	RX6728 Mx-Stby	RX6728 Mx-Stby	RX6728 Mx-Stby	RX6728 Mx-Stby	RX6728 Mx-Stby	RX6728 Mx-Stby	RX6728 Mx-Stby	RX6728 Mx-Stby	RX6728 Mx-Stby	RX6728 Mx-Stby	RX6728 Mx-Stby	RX6728 Mx-Stby	RX6728 Mx-Stby	RX6728 Mx-Stby	RX6728 Mx-Stby	RX6728 Mx-Stby	RX6728 Mx-Stby
1_193	**1_203**	**1_204**	**1_205**	**1_206**	**1_207**	**1_208**	**1_209**	**1_210**	**1_211**	**1_194**	**1_212**	**1_195**	**1_196**	**1_197**	**1_198**	**1_199**	**1_200**	**1_201**	**1_226**	**1_227**	**1_228**	**1_229**	**1_230**	**1_232**	**1_241**	**1_242**	**1_245**	**1_233**	**1_234**
160100	180300	179700	176700	172000	173000	195900	173000	175100	178300	177800	169000	213000	166700	170000	187000	205000	178000	165000	170300	174200	171200	163000	171600	169900	160000	170600	169000	174000	167000
33600	33400	34700	33500	32400	33800	34100	37300	33600	36000	33000	32600	34800	35900	31900	35300	34400	34200	36500	34900	33600	36700	35700	38070	38600	35500	39100	36800	36760	30700
100500	94800	93400	98500	92100	98500	88900	104200	95600	99810	88800	94200	105000	107000	83600	102500	90200	98300	112000	104300	101300	109200	94200	123200	108300	103000	105300	111500	114800	93900
9520	7950	8490	8460	7990	9270	7020	9590	9110	9170	7600	8930	9290	10070	6950	9090	7570	9400	13220	10430	9230	10770	9300	12540	11130	11340	10360	12370	12820	8260
3220	2380	2510	2530	2440	2810	1810	2970	2990	2760	2140	2990	2860	2980	1970	2750	2290	3210	4820	3530	2710	3560	2940	3990	3640	3810	3360	4090	4290	2330
3930	2690	2850	2950	2930	3250	1820	3670	3490	3440	2350	3980	3190	3620	2040	3110	2420	3770	5720	4150	3060	3770	3760	5010	4880	4500	4320	5170	5130	2370
360	200	223	257	258	284	114	303	304	312	187	305	272	273	148	254	189	351	561	407	251	320	313	468	450	414	392	489	485	192
1520	690	719	982	1020	1131	342	1240	1210	1270	720	1190	1040	1220	521	970	691	1430	2340	1510	990	1280	1310	2040	1860	1710	1680	2290	2016	620
4050	1760	1850	2540	3070	2840	739	2900	2910	3150	1910	3120	2450	2880	1180	2400	1850	3480	5760	3980	2760	2820	2900	5070	4440	4150	4750	5630	5200	1830
197	80.9	93.0	131	149	148	34.0	153	167	165	92.0	173	131	158	65.0	142	88.0	174	324	248	163	168	175	287	257	270	224	297	287	85.0
394	137	148	242	292	309	50.6	283	347	265	167	357	245	300	126	253	209	294	682	441	267	319	363	579	505	471	400	634	569	206
32.4	12.8	13.1	20.7	28.9	24.5	3.8	22.7	29.4	19.8	13.6	33.1	21.9	29.0	9.8	22.5	17.3	14.9	66.0	40.9	24.7	29.2	31.8	57.5	53.5	48.9	32.4	59.1	55.2	18.6
142	44.2	56.0	91.1	136	110	13.0	100	143	82.4	64.0	153	89.0	130	47.1	119	80.0	45.2	322	211	123	125	142	250	197	194	155	295	252	85.0
15.3	4.1	4.2	9.9	14.3	10.6	1.1	10.5	14.8	7.6	7.2	15.2	8.6	14.1	4.9	11.2	8.5	4.5	34.9	21.9	11.4	13.0	14.4	29.3	23.3	21.1	15.9	31.3	27.7	7.0
<537	<642	<570	<812	<801	<741	<734	<742	<661	<924	<681	1220	<805	<685	<808	<779	<815	2900	<1017	860	<745	<815	<548	<803	<701	<544	1360	<949	<882	<786
184	177	155	104	137	130	65.4	162	116	118	108	119	135	120	110	73.9	97.6	246	176	153	136	27.1	101	68.0	176	117	173	97.7	117	94.0
8.9	4.2	2.9	1.6	17.3	5.0	er	4.5	5.2	6.4	4.2	3.7	3.0	3.7	3.2	1.0	2.1	92.0	7.4	6.2	5.9	2.5	4.0	7000	4.3	5.0	16.5	3.1	6.0	4.1
248	<5.4	<4.0	12.1	191	19.0	<3.6	30.0	24.7	39.0	116	104	421	50.0	266	<4.7	531	14400	<4.0	75.0	402	636	184	<4.1	8.7	100	560	6.1	13.4	438
6.3	8.1	5.9	46.0	760	47.0	<4.2	12.4	12.4	2200	12.0	9.4	5.7	8.8	320	6.2	<5.1	40000	24.6	37.0	5.2	8.7	12.5	14.2	17.8	12.3	460	11.1	1480	4.9
<45.4	1450	<47.0	14100	3050	er	<54.3	er	350	28100	1320	67.0	<70.8	er	6500	<63.4	<78.9	2100	<63.1	7700	<64.8	<69.6	<59.9	300	<52.4	<54.3	10600	<75.4	4700	<50.4
<2.1	<2.8	<2.8	<3.0	6.5	<3.2	<3.0	<3.1	<3.0	7.3	<2.3	<2.4	<3.2	<3.3	<3.0	<2.9	<2.9	er	<3.3	<3.5	<2.8	<3.8	<2.4	<2.8	<2.6	<2.7	11.0	<3.3	13.5	<2.1
190	<202	<160	<201	200	310	<146	<165	<204	<239	550	<211	<257	<150	250	<175	520	<197	<200	270	240	<197	<145	<180	<163	<154	450	<217	<223	390
<48.4	<62.8	<54.6	<59.5	71.0	<66.6	<58.8	<55.3	<61.5	<78.0	<55.6	<38.8	<66.5	<66.7	<52.2	<61.8	<67.6	1360	<56.2	<67.2	<71.2	<62.5	<60.7	<64.5	<53.5	<60.1	161	<75.7	<70.9	49.0
<0.001	er	<0.001	0.89	<0.001	er	<0.001	er	<0.001	0.95	<0.001	<0.08	<0.001	<0.09	0.49	<0.001	er	er	<0.001	0.25	<0.001	<0.001	<0.08	<0.09	<0.001	<0.001	9.5	<0.10	<0.001	er
<0.89	<1.3	<0.82	<1.1	<0.90	<1.1	<1.0	<1.0	<0.99	<1.1	<0.91	<0.97	<0.90	<0.84	<0.97	<1.2	<1.1	er	<1.1	<1.0	<0.88	<0.86	<0.91	<1.2	<0.98	<0.87	<1.5	<1.4	<1.4	<0.89
<837	<1281	<1043	<1070	<1078	<1639	<1039	<1305	<1386	2800	<1203	<993	<1078	<1168	<1113	<1079	<1094	56000	<1122	<1591	<1267	<1508	<1179	<1156	<948	<990	<1808	<1282	2500	<929
<0.001	<0.001	<0.001	0.51	<0.001	er	<0.001	er	<0.001	0.48	<0.001	<0.001	<0.001	er	er	er	<0.001	er	<0.42	er	<0.001	<0.001	<0.001	<0.21	<0.18	<0.001	5.3	<0.001	<0.001	<0.17
er	<0.17	er	0.31	<0.20	er	0.22	<0.21	3.0	er	0.24	er	<0.001	0.15	er	<0.001	<0.001	0.19	<0.001	<0.16	0.22	er	0.09	<0.16	0.15	<0.22	13.3	0.12	0.14	er
366	350	344	353	325	378	324	410	380	367	318	371	411	409	305	344	329	346	427	377	358	421	345	465	395	434	426	408	426	296
0.18	<0.20	<0.17	er	er	1.2	<0.29	0.42	<0.28	3.0	0.40	<0.24	<0.28	<0.27	2.5	0.20	0.30	0.44	<0.27	1.1	<0.33	0.33	<0.29	0.33	0.62	0.16	4.0	0.28	0.67	<0.30
<0.001	<0.001	<0.001	<0.001	<0.001	<0.001	<0.001	er	er	<0.17	<0.001	<0.001	<0.001	<0.001	<0.001	<0.001	<0.001	<0.001	<0.001	<0.001	<0.001	<0.001	<0.001	<0.15	<0.001	er	er	<0.001	<0.001	<0.001
<0.001	<0.001	<0.04	<0.001	<0.001	<0.001	<0.001	<0.04	<0.001	<0.001	<0.001	<0.04	<0.001	<0.001	<0.001	<0.001	<0.001	<0.001	<0.001	<0.001	<0.001	<0.001	<0.001	<0.001	<0.04	<0.05	er	<0.001	<0.001	<0.001
128	11.7	3.5	49.0	302	36.0	128	49.0	42.1	134	60.0	23.4	19.5	14.0	43.9	48.0	75.8	219	13.3	135	106	34.9	32.6	34.9	32.0	62.0	290	139	47.0	81.0
7.1	2.0	0.49	5.9	7.8	2.9	0.23	6.2	5.3	18.9	3.0	3.5	1.8	0.29	3.3	4.4	0.35	33.2	2.6	13.3	5.2	6.4	0.25	4.8	12.5	3.1	1510	2.4	1.0	0.47
25.2	3.3	2.0	12.0	45.2	11.1	13.7	9.9	9.4	21.1	9.0	5.6	6.1	6.0	11.0	8.9	10.9	80.4	15.1	27.4	15.3	7.6	9.5	5.3	21.2	12.1	457	25.2	13.9	11.4

RX6728 Mx-Stby 1_235	RX6728 Mx-Stby 1_236	RX6728 Mx-Stby 1_237	RX6728 Mx-Stby 1_238	RX6728 Mx-Stby 1_239	RX6728 Mx-Stby 1_240	RX6728 Mx-Stby 1_213	RX6728 Mx-Stby 1_222	RX6728 Mx-Stby 1_223	RX6728 Mx-Stby 1_225	RX6728 Mx-Stby 1_214	RX6728 Mx-Stby 1_215	RX6728 Mx-Stby 1_216	RX6728 Mx-Stby 1_217	RX6728 Mx-Stby 1_218	RX6728 Mx-Stby 1_219	RX6727 Mx-f.g. 1_185	RX6727 Mx-f.g. 1_186	RX6727 Mx-f.g. 1_188	RX6727 Mx-f.g. 1_175	RX6727 Mx-f.g. 1_176	RX6727 Mx-f.g. 1_179	RX6714 Mx-f.g. 1_24	RX6714 Mx-f.g. 1_25	RX6714 Mx-f.g. 1_26	RX6714 Mx-f.g. 1_27	RX6716 Mx-f.g. 1_71	RX6716 Mx-f.g. 1_80	RX6716 Mx-f.g. 1_81
152000	173000	171100	171600	171000	168000	182000	174000	177900	171600	173000	175500	172000	172000	173200	193200	201100	204000	207200	214100	216400	260000	267000	252100	243000	256200	300600	240600	284100
37700	34100	34700	35360	39600	36900	34100	37800	35000	35380	33500	34820	36660	36700	36200	33500	26280	25970	27760	27250	28100	25100	31300	31700	35300	33500	26000	27770	25020
103500	101000	112000	100100	117700	112600	102500	104000	102700	103300	102000	103100	107800	102400	103000	97500	65800	67500	70500	68600	71100	58100	82400	87600	97900	95500	56800	68100	58900
11670	8850	9230	9370	13100	11450	9990	9390	9300	9380	9370	10300	11300	10160	11500	8250	5820	6060	6230	5740	6120	4320	6740	8650	8960	8430	3160	5260	3800
3770	2870	2870	2900	4130	3970	3300	3100	2850	3080	2920	3060	3500	3180	3600	2210	2326	2400	2416	2198	2433	1160	2170	2340	2910	2470	672	1511	905
4590	3200	3650	3330	5030	5000	3590	3410	3390	3580	3320	3710	4220	3640	4500	2860	2750	3000	3116	2580	2890	1850	3360	4340	4510	4600	1225	2570	1631
474	298	327	304	498	491	304	317	287	313	291	367	394	305	414	144	297	331	334	266	324	179	335	420	488	407	98.9	261	162
1900	1150	1250	1220	2160	2140	1069	1220	1170	1260	1200	1480	1620	1270	1690	540	1434	1677	1637	1217	1479	780	1550	1790	1916	1670	335	1286	740
5090	2830	3160	2820	4990	5600	2840	2690	2960	2990	3050	4020	4000	2970	3980	1180	4470	5220	4930	3720	4600	2430	3240	4300	4590	3880	1028	5210	2500
298	139	152	187	308	300	169	150	192	170	155	201	225	171	238	74.0	210	242	236	169	206	111	241	239	264	214	44.7	193	120
604	278	262	340	532	530	236	319	311	337	355	371	490	325	475	83.0	431	492	515	342	440	223	510	459	520	369	87.0	393	259
58.8	24.9	21.7	32.2	37.7	29.7	19.9	27.6	26.7	29.2	30.0	30.1	45.2	26.2	44.9	6.6	39.0	42.9	47.7	29.9	39.0	21.1	52.5	36.0	45.9	32.0	5.6	30.4	23.0
286	108	85.1	149	139	113	96.0	153	109	128	135	133	214	117	221	26.9	173	178	221	139	173	93.0	300	177	223	125	24.6	114	118
29.2	11.8	8.5	14.9	13.3	8.2	10.1	14.5	11.5	14.5	15.0	13.9	26.2	10.5	22.1	1.9	15.4	15.4	18.5	13.3	15.1	9.2	31.0	17.5	21.9	13.0	2.4	10.7	12.7
<716	<639	<781	<642	<1098	<813	<814	<867	<788	<1011	<674	1400	650	<846	1010	<885	5200	6400	4640	5400	2000	3360	2180	3380	3230	3230	<770	<1057	1510
74.0	172	166	130	77.0	117	134	65.8	103	110	116	190	104	131	154	94.2	982	2130	663	946	799	230	290	346	348	224	73.0	240	208
4.3	2.4	11.6	8.7	1.5	4.7	1.9	0.85	3.6	3.2	4.8	10.4	2.9	5.8	9.2	2.6	161	281	37.4	184	164	32.0	14.6	35.5	32.4	17.5	7.7	74.0	30.0
119	12.6	111	264	127	36.0	<4.6	6.3	<5.0	<5.0	34.0	17.0	<3.7	<5.6	7.0	er	101	2110	29.0	123	143	11.5	54.0	85.0	82.0	37.4	40.0	74.0	26.0
180	7.9	6.9	16.4	6.0	17.4	<5.8	4.8	24.1	25.8	12.8	155	12.7	16.3	22.6	er	11400	12000	1490	14000	13500	240	154	1690	430	46.0	6.6	4110	er
<44.8	<59.5	<67.7	<53.7	<72.1	2800	<55.6	96.0	2090	5300	<58.5	50000	410	250	490	er	3870	15200	er	2940	7500	2800	7800	1220	1520	2880	950	2120	3700
<2.8	<2.7	<3.2	<3.3	<3.5	<3.3	<3.2	<3.1	<3.5	<3.1	<2.6	er	<2.4	<3.3	<3.4	4.1	29.4	32.9	13.2	31.0	17.8	3.9	18.2	10.5	13.2	7.9	11.0	4.6	3.9
<162	<173	370	330	<205	<227	<199	<178	<198	<234	<155	520	<170	<188	<217	<208	1080	6900	<194	er	<347	<158	<164	810	<220	<230	<119	<225	<189
<57.0	<66.7	<66.5	<59.0	<69.9	120	<68.7	<69.1	<63.5	<77.2	<59.4	<85.4	<49.8	<66.8	<65.4	<67.5	<91.5	270	105	er	118	108	560	157	190	200	156	399	150
<0.08	er	er	<0.08	<0.001	<0.11	<0.09	<0.09	er	0.33	<0.001	2.2	0.06	<0.10	er	<0.001	8.6	16.2	14.0	1.1	6.4	3.6	14.5	12.1	9.0	14.9	<0.001	<0.001	1.3
<0.98	<1.0	<1.1	<0.94	<1.0	<1.1	<1.3	<0.89	<1.6	<1.4	<1.0	<1.3	<0.86	<1.3	<1.0	<1.2	<1.5	<2.3	<1.4	1.9	2.4	0.98	<1.0	<1.1	1.2	<1.3	<0.84	<1.3	<0.98
<1026	<1099	<1221	<1293	<1436	<1207	<1049	<1227	<1324	<1271	<1144	<1656	<1013	<1169	<997	<1317	68000	94000	<1346	98000	48000	<920	<1018	<1171	<900	<1310	<1386	6500	1900
<0.18	<0.001	<0.19	<0.001	<0.21	4.2	<0.001	<0.001	<0.001	er	<0.001	0.91	<0.001	<0.22	<0.001	<0.001	2.8	14.6	er	3.2	7.3	6.3	14.9	2.0	3.9	3.4	1.0	5.8	4.9
<0.001	<0.20	er	er	er	er	0.20	<0.15	0.16	er	0.25	<0.57	er	er	<0.001	er	0.79	0.26	0.51	<0.36	0.32	er	2.8	4.4	1.3	15.9	0.17	<0.001	0.25
453	368	390	427	465	422	376	367	364	372	408	386	379	381	377	338	299	447	246	271	250	214	366	453	435	373	227	348	238
<0.25	0.24	<0.28	<0.17	<0.26	<0.29	0.26	<0.19	0.34	1.5	<0.19	2.7	<0.21	<0.21	<0.23	<0.26	1.5	3.0	0.75	2.3	1.3	0.67	7.8	8.4	3.1	3.3	1.5	1.4	1.1
<0.001	<0.001	<0.001	<0.001	<0.001	<0.001	<0.001	<0.001	<0.001	<0.001	<0.001	<0.001	<0.001	<0.001	<0.001	<0.001	<0.001	<0.47	<0.001	<0.001	<0.001	<0.001	<0.001	<0.001	<0.001	er	<0.001	er	<0.001
<0.001	<0.001	<0.001	<0.001	<0.001	<0.001	<0.001	<0.001	<0.05	<0.001	<0.001	<0.001	<0.001	<0.001	<0.001	<0.001	0.10	0.10	0.24	<0.001	<0.07	<0.001	<0.001	<0.001	<0.001	<0.001	<0.001	<0.001	<0.001
39.7	2.4	227	45.1	183	216	32.0	25.7	86.0	27.5	17.2	151	50.1	33.0	14.9	79.0	130	136	250	93.3	102	57.2	5.3	28.9	43.1	33.7	0.88	5.9	3.9
2.0	0.17	12.0	1.1	34.3	34.4	3.2	1.2	6.3	5.1	2.1	19.1	6.4	6.2	3.6	0.78	195	355	249	338	307	390	660	383	551	274	8.7	113	168
7.0	4.1	26.1	14.8	28.7	34.9	8.5	4.6	15.1	9.8	5.5	34.1	10.1	8.7	12.3	12.6	114	200	97.8	180	166	95.9	496	297	359	191	5.8	79.0	67.3

RX6716 Mx-f.g.	RX6716 Mx-f.g.	RX6716 Mx-f.g.	RX6716 Mx-f.g.	RX6716 Mx-f.g.	RX6716 Mx-f.g.	RX6716 Mx-f.g.	RX6716 Mx-f.g.	RX6716 Mx-f.g.	RX6716 Mx-f.g.	RX6716 Mx-f.g.	RX6716 Mx-f.g.	RX6716 Mx-f.g.	RX6716 Mx-f.g.	RX6716 Mx-f.g.	RX6716 Mx-f.g.	RX6716 Mx-f.g.	RX6716 Mx-f.g.	RX6716 Mx-f.g.	RX6716 Mx-f.g.	RX6716 Mx-f.g.	RX6716 Mx-f.g.	RX6716 Mx-f.g.	RX6716 Mx-f.g.	RX6716 Mx-f.g.	RX6716 Mx-f.g.	RX6716 Mx-f.g.	RX6716 Mx-f.g.	RX6716 Mx-f.g.
1_82	**1_83**	**1_84**	**1_72**	**1_73**	**1_74**	**1_75**	**1_76**	**1_77**	**1_78**	**1_79**	**1_85**	**1_94**	**1_96**	**1_97**	**1_98**	**1_99**	**1_100**	**1_101**	**1_102**	**1_103**	**1_86**	**1_104**	**1_105**	**1_106**	**1_107**	**1_108**	**1_109**
250400	278300	230000	245000	292000	288000	284000	244000	243000	320000	232900	270800	260700	253000	246000	258000	238000	259000	284000	254000	310000	276000	237100	251800	252500	250000	250000	256800
26020	26020	27100	28600	25300	23400	25500	25700	25500	24600	26720	26070	26880	25300	25600	26700	25000	25410	25500	26070	25030	25700	26180	26690	26070	25600	24200	26510
62700	60600	62600	68500	65900	56600	60700	61400	65800	58800	65400	60900	63900	58500	61300	58300	58200	57200	60700	61300	55600	59300	62800	62300	61500	61300	58800	60100
4370	4250	4920	4610	4030	3230	4130	4290	4720	3320	5210	4090	4780	3910	4470	3720	3570	3730	3920	4340	3440	4110	4670	4420	4290	4330	3870	4290
1160	1159	1480	952	435	718	887	1130	1350	671	1603	1247	1550	1010	1390	1091	1083	1000	988	1298	871	1239	1498	1355	1310	1400	1156	1268
2000	1930	2370	2042	1620	1247	1680	1880	2330	1360	2470	1670	2330	1610	2045	1590	1560	1583	1510	1960	1190	1790	2250	1978	1958	1955	1756	1809
203	191	250	189	107	108	152	190	233	95.4	266	176	250	160	200	157	146	155	137	199	106	180	235	205	192	206	165	179
987	926	1275	832	349	423	675	910	1150	357	1283	801	1300	700	1026	705	640	667	593	917	420	772	1126	927	905	1028	792	848
3440	3310	4510	2850	1180	1380	2080	2950	4670	1170	5030	2520	4220	2100	3340	2034	2090	2100	1830	3150	1310	2500	3760	3660	3120	3300	2570	2660
151	142	194	124	39.1	62.6	103	128	188	46.6	203	122	189	104	153	108	105	103	85.9	139	59.4	120	179	154	131	153	120	126
329	310	395	236	55.9	124	217	278	353	83.0	428	241	405	220	302	226	204	207	163	261	117	258	335	305	271	332	235	242
32.3	26.9	33.2	19.3	3.8	11.6	20.3	23.8	26.7	6.7	34.4	21.6	36.1	17.2	24.4	19.3	16.2	17.2	13.8	18.8	9.1	23.2	25.5	24.6	22.3	28.0	19.6	20.0
148	122	144	78.0	12.6	49.7	90.8	110	101	28.8	146	87.5	150	75.0	91.0	76.5	65.9	68.5	52.7	72.4	41.4	99.4	102	95.0	79.0	111	78.2	79.2
16.7	12.2	14.4	8.4	1.2	5.1	8.9	10.4	10.7	2.6	14.9	8.6	14.6	6.3	8.1	7.8	5.7	6.8	5.9	7.4	3.5	9.2	10.3	9.2	8.5	11.0	7.7	7.3
2200	2520	1620	2300	<910	1670	1350	1500	1400	<782	1900	1920	2870	820	1560	1650	1940	<840	1260	<1215	1130	1420	1720	<1278	2360	2470	1730	2160
299	346	276	271	26.9	155	194	219	237	100	325	165	920	144	230	166	175	148	89.0	221	75.0	216	277	282	247	269	182	321
117	134	73.0	280	0.53	36.6	43.0	23.2	26.9	9.2	127	15.6	313	22.6	235	21.2	170	36.9	44.0	630	10.5	32.0	636	288	570	202	58.0	830
49.0	78.0	57.0	95.0	<5.7	20.1	33.0	17.6	610	14.9	282	15.2	301	16.3	18.2	15.2	32.0	<5.2	10.3	28.4	10.0	15.7	39.8	16.4	12.2	14.5	14.5	42.0
5600	3700	3400	15400	3.9	340	5200	256	890	23.0	13200	240	15700	79.0	9100	59.0	7900	1000	880	24600	<4.1	180	26200	9300	19600	7400	2210	29400
6740	590	2670	2160	<60.6	580	5800	1020	580	700	56000	2150	8100	500	2800	1150	2500	720	338	2480	340	1220	88000	1270	1860	6600	550	9000
14.3	6.7	4.8	<3.9	<2.9	13.9	7.0	6.0	4.5	15.8	11.5	7.7	<4.7	12.4	5.5	16.2	20.4	<3.0	9.2	8.5	7.2	12.0	12.0	8.4	9.0	<4.1	4.0	8.7
<255	<177	<178	<180	<174	<202	<165	<160	<165	<192	<297	<141	3710	<161	<176	<165	125	<160	<190	<360	<147	<201	<290	<300	<245	<226	<202	<266
870	590	470	1460	<40.0	640	530	168	119	101	1620	151	650	110	920	165	770	225	124	1840	71.0	176	1970	1150	1440	1030	310	2490
0.54	<0.09	0.22	er	<0.09	<0.001	1.1	er	er	er	9.9	<0.07	2.0	<0.001	0.69	er	<0.06	er	<0.09	<0.001	<0.001	<0.001	5.9	<0.001	0.10	0.26	<0.08	0.43
<1.3	<0.87	<1.2	<1.2	<1.1	<0.87	<1.0	<0.87	<0.75	<1.0	<1.6	<1.0	<1.5	<0.78	<1.0	<0.80	<0.68	<1.1	<1.0	<1.9	<0.91	<1.0	<1.7	<1.3	<1.1	<1.2	<0.72	<1.3
7500	4500	4200	20200	<1155	<1291	8000	<1043	<1040	1800	18400	<848	12500	<1031	11200	<1227	18000	2680	1700	35700	<1002	1200	35300	12000	27400	12800	2400	45000
3.3	0.68	2.1	0.89	<0.20	0.53	8.0	2.6	0.27	1.0	43.0	4.3	14.2	0.82	5.7	1.8	1.5	0.40	0.40	0.32	0.76	2.7	137	0.57	0.53	5.3	0.45	7.6
0.19	<0.16	er	er	<0.33	er	er	<0.14	0.11	<0.15	0.46	<0.13	<0.001	0.21	0.35	<0.16	er	0.19	0.12	er	0.26	<0.16	<0.37	er	<0.20	er	0.16	0.19
240	268	320	353	244	213	247	253	404	235	473	266	486	228	220	230	206	194	226	260	229	256	270	254	222	232	215	255
2.1	0.45	1.4	3.4	<0.16	<0.23	0.86	0.55	0.66	<0.19	1.5	0.48	1.9	0.41	0.69	1.2	0.61	0.52	0.32	0.85	<0.22	0.67	2.4	<0.35	0.75	0.45	0.32	0.98
<0.19	<0.001	<0.001	<0.001	<0.001	<0.001	<0.001	<0.001	<0.19	<0.001	<0.001	<0.001	<0.29	<0.001	<0.001	<0.15	<0.10	<0.001	<0.001	<0.001	<0.13	<0.001	<0.001	<0.001	<0.20	<0.001	<0.001	<0.001
<0.001	<0.001	<0.04	<0.001	<0.001	<0.001	<0.001	<0.001	<0.001	<0.04	<0.001	<0.001	<0.06	<0.001	<0.06	<0.001	<0.001	<0.001	<0.001	<0.08	<0.001	<0.001	<0.001	<0.001	<0.001	<0.001	<0.001	<0.001
4.7	3.2	4.2	3.6	1.3	1.4	1.7	1.9	5.1	0.49	5.5	1.2	9.4	1.6	3.0	0.32	0.52	0.95	1.1	1.4	0.25	1.1	1.5	1.1	1.1	3.2	1.0	0.64
111	100	228	63.2	7.4	19.2	132	160	87.0	36.3	182	102	215	69.6	142	82.0	39.6	76.0	26.9	80.0	52.0	110	142	76.3	91.3	128	84.5	71.3
72.4	51.3	130	51.2	5.2	11.9	60.3	90.0	57.5	16.5	137	49.7	150	42.9	95.0	40.8	21.8	41.8	17.3	53.7	17.6	62.1	98.4	49.0	57.5	71.4	53.4	63.5

RX6716 Mx-f.g.	RX6716 Mx-f.g.	RX6716 Mx-f.g.	RX6716 Mx-f.g.	RX6716 Mx-f.g.	RX6716 Mx-f.g.	RX6716 Mx-f.g.	RX6716 Mx-f.g.	RX6716 Mx-f.g.	RX6716 Mx-f.g.	RX6716 Mx-f.g.	RX6716 Mx-f.g.	RX6716 Mx-f.g.	RX6716 Mx-f.g.	RX6716 Mx-f.g.	RX6716 Mx-f.g.	RX6716 Mx-f.g.	RX6716 Mx-f.g.	RX6716 Mx-f.g.	RX6716 Mx-f.g.	RX6717 Mx-f.g.	RX6717 Mx-f.g.	RX6717 Mx-f.g.	RX6717 Mx-f.g.	RX6717 Mx-f.g.	RX6717 Mx-f.g.	RX6717 Mx-f.g.	RX6717 Mx-f.g.	RX6717 Mx-f.g.
1_110	**1_87**	**1_88**	**1_89**	**1_90**	**1_91**	**1_92**	**1_93**	**1_48**	**1_58**	**1_59**	**1_60**	**1_61**	**1_49**	**1_50**	**1_51**	**1_52**	**1_53**	**1_56**	**1_111**	**1_113**	**1_116**	**1_134**	**1_136**	**1_138**	**1_139**	**1_140**	**1_126**
265000	244700	260600	248100	259200	258200	258000	252000	257000	252000	281400	273300	241600	256000	269500	252000	261000	259400	215000	221400	210800	221300	239000	235600	239400	227800	232300	215000
26000	25320	26340	26320	25760	25300	25500	25200	25720	26390	25810	26260	27090	25450	26170	26000	26600	25870	29500	26570	27080	26820	31200	28720	28970	28860	29270	27250
61200	60700	61900	62200	59500	58700	57000	58600	60130	63100	59400	66300	67200	58400	60300	60200	59300	59710	74100	65090	66500	66900	75100	69800	69500	70200	73300	67730
3920	4440	4300	4490	4011	4090	3970	3910	4093	4800	3764	4070	5170	3843	3822	4240	4100	4170	6460	5690	5870	5840	5890	5660	5640	5650	6270	5880
1165	1394	1257	1428	1209	1206	1176	1197	1236	1540	1045	563	1527	1076	1097	1350	1205	1185	2253	1928	2072	2005	2090	1929	1768	1898	2086	1991
1733	2027	1890	2063	1699	1712	1640	1635	1814	2480	1544	1660	2410	1610	1583	1933	1850	1806	3180	3237	3304	3272	2940	2800	2734	2680	3120	3314
171	208	185	210	174	169	166	161	176	257	145	133	240	152	147	194	198	176	356	355	362	365	327	298	308	293	337	366
764	952	849	1025	794	760	723	762	800	1310	620	527	1130	687	636	879	888	802	2120	1764	1679	1805	1663	1438	1444	1410	1571	1781
2350	3370	3120	3650	2450	2334	2270	2840	2690	5000	2056	2040	4360	2100	1909	2730	2900	2680	6670	6570	6360	6650	5820	5170	5430	5200	5830	6604
112	143	134	155	120	113	117	114	115	202	99.6	63.2	171	101	92.3	134	139	126	270	275	258	277	262	216	233	218	244	281
224	276	285	299	230	222	226	226	237	397	220	122	338	190	168	249	285	255	518	584	513	594	582	464	546	484	517	603
18.5	20.8	19.3	22.4	17.5	17.7	20.7	18.9	17.8	29.1	18.0	9.9	25.7	14.6	13.0	21.0	22.9	21.2	38.5	59.4	48.0	57.0	54.1	46.2	53.1	46.4	48.5	57.8
83.3	79.6	73.3	84.0	65.3	66.4	72.0	82.4	70.1	115	75.5	31.0	108	52.3	47.5	83.4	85.5	72.4	142	304	228	285	306	233	261	253	249	291
7.0	6.9	7.1	7.9	6.6	6.1	7.1	7.1	6.1	10.3	9.2	3.0	10.3	5.1	4.5	7.3	8.3	7.1	12.4	34.3	28.7	34.9	32.5	28.0	33.2	30.1	29.8	34.6
1910	<1573	1280	1610	1280	2190	2970	2710	2500	<1014	1500	3070	2100	1670	1890	1650	1840	1900	9300	4860	4300	3600	5400	5300	8500	6400	7300	4230
178	321	144	252	188	247	217	184	217	258	93.0	100	243	179	113	187	173	273	624	751	1098	597	673	807	975	780	1046	685
62.0	980	44.0	407	97.0	238	135	56.0	400	75.0	23.4	110	169	64.0	11.1	45.0	19.0	2320	266	307	756	385	172	442	272	267	650	597
19.5	33.6	10.2	28.2	18.7	25.2	15.2	er	26.5	117	14.3	16.5	16.6	19.5	16.3	9.8	19.8	21.0	6500	<6.7	24.9	15.6	<4.1	<8.2	<5.6	10.4	310	86.3
2290	35600	1130	13100	5020	11200	2800	er	14300	6700	er	3000	7700	3080	640	1050	410	36600	3700	12500	48700	31900	4100	41000	2400	20800	36900	52900
400	8500	283	7500	1010	7200	2380	680	4830	850	er	920	16100	700	540	780	3700	3200	1200	3500	13800	19800	2300	18400	4450	12900	19900	18580
8.4	11.8	6.1	11.5	7.5	9.7	18.9	17.8	8.0	10.3	7.5	12.4	13.8	7.3	7.8	5.8	12.7	13.5	13.3	23.9	31.8	23.6	13.9	45.0	33.3	26.5	37.4	31.2
<194	<419	<172	<291	<259	<300	<197	<185	<282	<252	<189	<183	<312	<216	<201	<191	<173	<323	<211	<244	1300	<277	<203	<326	<203	<202	<367	121
490	3250	272	1540	518	1480	420	169	1280	820	215	420	880	332	166	133	180	2140	440	500	1270	900	137	950	245	770	1380	1201
<0.09	1.1	<0.001	0.79	<0.001	1.0	<0.001	0.13	0.27	<0.11	0.26	er	2.3	<0.001	er	er	1.4	er	0.28	0.62	1.7	2.6	er	7.5	0.89	6.1	6.3	17.3
<0.89	<1.8	<0.95	<1.5	<1.5	<1.4	<1.1	<0.95	<1.4	<1.4	<0.95	<0.99	<1.7	<1.3	<1.0	<0.85	<0.90	<2.3	<0.82	2.9	4.8	4.8	3.3	3.0	3.7	2.9	er	4.4
3500	56700	2500	19600	8600	13000	3700	<1255	19400	9800	<1260	5500	10700	4200	<1553	<1113	<999	53000	8800	20600	92000	45300	5200	68000	3500	31100	58000	71700
0.58	4.4	er	4.7	0.24	7.2	1.8	0.87	4.5	<0.25	2.4	1.3	18.1	0.60	0.44	2.7	23.0	er	0.98	0.57	2.0	9.0	er	2.5	0.74	1.7	er	4.8
0.30	<0.32	<0.16	<0.22	<0.21	er	er	er	0.56	0.19	er	<0.001	er	er	0.34	0.28	0.25	<0.30	0.20	0.60	2.6	0.86	0.26	0.58	0.25	er	0.53	3.8
244	259	245	251	221	227	226	222	231	215	207	239	237	213	221	270	240	214	324	244	254	244	292	232	255	274	347	262
0.33	0.57	<0.21	0.47	0.43	0.35	0.31	0.43	1.1	0.72	0.46	0.42	2.8	0.63	<0.39	0.79	0.72	0.53	1.5	<0.17	0.50	1.3	1.0	1.1	<0.39	1.1	0.71	0.24
<0.001	<0.001	<0.001	<0.21	<0.001	<0.001	<0.001	<0.15	<0.001	<0.18	<0.001	<0.16	<0.001	<0.001	<0.17	<0.001	<0.001	<0.001	<0.001	<0.20	<0.001	<0.001	<0.15	<0.001	<0.17	er	er	0.27
<0.001	<0.001	<0.001	<0.001	<0.001	<0.001	<0.001	<0.001	<0.001	<0.001	<0.001	<0.05	<0.07	<0.001	<0.001	<0.04	<0.001	<0.001	<0.001	0.14	<0.001	er	<0.06	0.68	er	0.23	0.22	1.1
0.50	1.1	0.78	1.3	0.37	0.54	0.41	0.79	0.62	7.4	6.9	2.4	10.3	0.45	0.23	1.2	1.1	1.4	12.5	304	455	471	900	570	494	834	713	463
34.6	78.4	22.6	50.9	50.4	65.2	79.0	67.0	99.0	85.0	59.9	25.0	135	39.4	23.0	106	103	81.0	317	528	352	430	596	611	577	663	598	542
18.5	61.0	12.5	41.3	34.5	48.3	46.0	35.9	68.1	61.1	24.7	13.0	91.3	24.4	11.8	68.0	57.7	55.6	134	277	235	236	359	416	324	466	479	239

RX6717 Mx-f.g.	RX6717 Mx-f.g.	RX6717 Mx-f.g.	RX6717 Mx-f.g.	RX6717 Mx-f.g.	RX6718 Mx-f.g.	RX6718 Mx-f.g.	RX6718 Mx-f.g.	RX6718 Mx-f.g.	RX6718 Mx-f.g.	RX6718 Mx-f.g.	RX6718 Mx-f.g.	RX6718 Mx-f.g.	RX6718 Mx-f.g.	RX6718 Mx-f.g.	RX6718 Mx-f.g.	RX6718 Mx-f.g.	RX6718 Mx-f.g.	RX6718 Mx-f.g.	RX6719 Mx-f.g.	RX6719 Mx-f.g.	RX6719 Mx-f.g.	RX6723 Mx-f.g.	RX6723 Mx-f.g.	RX6723 Mx-f.g.	RX6723 Mx-f.g.	RX6723 Mx-f.g.	RX6723 Mx-f.g.	RX6723 Mx-f.g.	RX6723 Mx-f.g.	RX6723 Mx-f.g.
1_127	**1_128**	**1_130**	**1_131**	**1_132**	**1_6**	**1_9**	**1_10**	**1_11**	**1_145**	**1_146**	**1_149**	**1_150**	**1_151**	**1_1**	**1_12**	**1_13**	**1_14**	**1_19**	**1_23**	**1_27**	**1_89**	**1_91**	**1_93**	**1_94**	**1_95**	**1_96**	**1_97**	**1_100**	**1_102**
210600	223800	225400	237200	239000	211100	209000	208500	212700	213500	222900	226500	218800	224800	225600	211500	231000	225600	239400	229700	231600	204000	183800	138900	146400	149900	148100	144700	147900	147000
27730	28950	29430	29360	28600	24260	25130	24990	25160	26070	26000	25530	25620	26130	25600	27320	26270	26310	24130	23190	22990	32500	31310	37600	37870	37200	37400	37960	37400	35950
70470	72000	73900	69400	69300	59300	62620	62610	63270	64100	65800	66200	63500	64400	63600	70300	65700	64300	55000	54600	56100	87100	87200	129100	123100	119600	125100	128300	126700	116600
6331	6220	6320	5610	5130	5100	5485	5477	5559	5760	5810	5570	5630	5510	5510	6950	5990	5840	4270	4270	4180	9620	9410	16550	14510	14230	15370	16240	15730	14530
2205	2242	2265	1740	1490	1633	1711	1718	1776	2030	2023	1860	1857	1687	1881	2830	2049	1973	834	916	897	2942	3038	4470	4054	3980	4410	4822	4505	4170
3673	3230	3110	2719	2570	2669	3008	2954	3064	3250	3095	3150	2956	2876	2920	4470	3242	3166	2033	2215	2160	4470	4780	7540	7340	7390	7450	8420	7500	7290
405	348	352	294	284	296	334	320	338	352	344	333	328	314	326	576	367	343	197	217	210	468	501	676	681	735	671	781	699	735
1936	1615	1695	1436	1530	1406	1632	1551	1631	1681	1662	1620	1619	1492	1600	3500	1744	1656	886	1025	973	2028	2170	2634	2682	2980	2760	3060	2743	3020
6990	5430	6080	5210	4890	5790	6661	6101	6671	6340	6280	6380	6560	5960	6020	11800	6580	6350	4090	5260	4430	5130	5450	6060	6420	7390	6320	6850	6440	7410
296	244	265	226	195	219	259	245	261	256	258	250	260	229	244	593	260	264	140	162	161	289	312	328	340	384	326	367	333	421
592	484	586	484	449	496	573	538	566	542	568	529	563	523	539	1770	590	576	330	400	382	560	547	550	580	735	565	594	571	789
51.7	42.4	55.2	48.1	49.1	50.1	56.2	52.6	55.8	52.1	53.4	54.0	54.4	51.9	55.3	228	58.0	57.3	37.5	44.4	47.3	44.6	45.4	39.6	44.3	52.4	42.3	44.6	45.2	65.5
240	215	272	257	268	268	279	270	282	259	274	288	282	279	281	1420	280	297	209	239	280	193	172	166	187	200	169	166	170	275
27.4	25.1	29.9	30.7	28.9	30.8	33.0	31.1	34.4	31.0	33.0	34.1	32.0	32.3	35.7	152	32.6	35.4	27.2	31.1	32.0	17.5	16.2	15.6	18.5	18.0	14.2	15.6	15.2	25.5
3440	3900	3560	5300	6800	5600	5530	5230	5130	3700	5100	3700	7000	5000	6000	278000	5790	4800	9500	9950	9100	6000	5700	5200	4600	4400	3900	4300	3000	5600
838	913	688	770	725	1077	1224	1293	1020	972	842	839	1411	975	799	3730	909	836	1315	1539	1488	1523	1460	822	889	957	890	838	797	623
806	1000	204	187	161	413	1011	1043	711	840	299	780	1134	591	354	9500	268	311	258	620	990	28.0	29.4	93.0	65.9	53.0	62.0	66.0	72.0	86.0
11.0	<10.2	<7.2	<5.1	<4.3	21.6	11.0	18.5	11.9	11.6	5.7	<5.8	16.0	<8.1	<7.6	72.0	7.8	<8.8	120	23000	59.0	175	13.7	22.6	<7.5	33.0	24.2	11.5	91.0	93.0
48300	39900	19200	2410	350	22300	53500	70700	42700	28700	9800	50000	44500	32900	16300	32700	10600	14200	2530	19100	47000	430	271	22700	2260	1180	9600	17600	24400	32000
28700	13300	25900	9700	1000	5870	12980	15710	10430	7700	3200	9500	15000	6670	4100	43200	3340	4360	1730	18400	27100	93000	2010	5000	2440	2260	5700	6400	12300	11000
54.4	22.7	14.6	19.0	20.4	39.9	49.9	53.7	42.2	35.7	21.4	39.7	59.9	31.8	30.1	590	24.1	26.9	49.5	118	142	15.8	8.8	14.8	11.9	12.2	15.7	15.8	12.8	13.1
945	550	<269	<212	<120	600	136	1110	69.0	<312	<225	<304	<442	<297	310	<581	<272	<293	<246	550	<345	<224	<190	320	<259	<152	740	<339	<389	490
950	1340	510	164	138	910	1729	1994	1219	1300	590	1290	2360	871	670	3370	620	610	341	1130	2330	237	169	310	190	167	218	530	344	770
3.8	0.68	4.9	0.62	<0.07	er	1.0	5.4	1.6	0.18	0.16	er	9.2	0.14	<0.001	1620	0.13	1.7	<0.001	8.7	8.8	150	2.6	3.2	3.7	6.2	8.9	6.4	9.7	5.8
3.1	4.0	3.3	3.4	2.5	3.1	5.3	5.2	4.3	4.1	2.0	5.6	9.0	4.2	3.4	71.0	2.9	3.1	10.6	15.0	19.2	<1.4	<1.3	2.1	<1.5	1.1	<1.4	<1.4	<2.0	<1.6
61700	78000	40800	3500	<1037	38900	74500	98100	58800	60200	20100	73000	71100	51900	29000	64000	16900	20700	14000	39200	90000	<1493	<1427	36800	10300	1400	22700	29300	38300	53000
2.3	0.95	4.1	1.0	er	er	0.94	2.4	0.99	<0.001	er	<0.34	6.9	<0.001	<0.31	609	er	0.41	0.74	45.0	58.0	380	2.7	3.6	3.6	5.0	4.8	8.7	6.9	21.5
1.4	0.29	0.41	0.79	0.43	0.76	1.3	6.7	17.6	er	<0.18	<0.51	11.0	0.44	0.29	870	<0.22	1.2	0.21	14.1	110	4.4	12.6	6.2	0.20	1.4	0.51	1.0	0.43	1.9
269	312	303	274	271	231	255	258	243	275	260	289	231	237	276	262	259	239	228	229	227	396	360	534	479	472	530	505	534	534
0.18	0.94	0.25	0.23	<0.17	<0.48	0.10	0.12	0.05	0.56	0.43	<0.35	<0.51	<0.30	1.0	1.5	0.53	0.45	1.5	16.0	21.0	0.55	0.66	1.1	0.80	1.2	0.93	4.1	<0.48	0.58
0.14	<0.33	<0.001	<0.001	<0.001	er	0.15	0.30	0.69	<0.001	<0.001	<0.24	er	<0.24	<0.22	35.7	<0.21	er	<0.001	0.65	9.0	<0.18	0.70	0.15	<0.28	<0.001	er	<0.001	<0.27	<0.001
0.21	<0.14	0.20	<0.001	<0.001	er	0.07	0.25	0.44	er	<0.05	<0.001	1.8	er	<0.07	102	er	er	<0.001	0.17	0.36	0.10	er	er	er	<0.001	<0.06	0.07	er	<0.001
466	374	522	261	496	421	529	408	479	638	762	729	750	560	861	909	765	701	471	628	253	2870	2920	2291	2046	2740	2280	3210	2410	2600
345	558	508	522	538	646	720	1280	986	608	798	719	1810	539	618	117000	881	855	379	5700	7200	504	274	324	228	309	179	262	233	846
169	379	292	255	241	403	380	363	337	446	487	360	671	313	455	4224	553	500	333	1133	1368	461	409	357	368	425	354	501	392	541

RX6723 Mx-f.g.	RX6724 Mx-f.g.	RX6724 Mx-f.g.	RX6724 Mx-f.g.	RX6724 Mx-f.g.	RX6724 Mx-f.g.	RX6724 Mx-f.g.	RX6724 Mx-f.g.	RX6724 Mx-f.g.	RX6724 Mx-f.g.	RX6724 Mx-f.g.	RX6724 Mx-f.g.	RX6724 Mx-f.g.	RX6724 Mx-f.g.	RX6724 Mx-f.g.	RX6724 Mx-f.g.	RX6724 Mx-f.g.	RX6724 Mx-f.g.	RX6724 Mx-f.g.	RX6724 Mx-f.g.	RX6724 Mx-f.g.	RX6724 Mx-f.g.	RX6724 Mx-f.g.	RX6724 Mx-f.g.	RX6724 Mx-f.g.	RX6720 Irr.	RX6720 Irr.	RX6720 Irr.	RX6720 Irr.	RX6720 Irr.	RX6721 Irr.	RX6721 Irr.
1_103	**1_105**	**1_106**	**1_109**	**1_118**	**1_119**	**1_120**	**1_121**	**1_122**	**1_124**	**1_125**	**1_110**	**1_111**	**1_112**	**1_113**	**1_114**	**1_115**	**1_116**	**1_117**	**1_126**	**1_127**	**1_128**	**1_130**	**1_131**	**1_1**	**1_2**	**1_3**	**1_4**	**1_5**	**1_39**	**1_40**
144000	231000	239200	277000	203500	292000	210000	311000	212800	187200	171400	287000	246000	239500	227900	273000	198800	254000	209900	102800	169000	122600	174200	202400	218100	222300	213100	225100	219300	234300	232800
36000	24200	24690	29300	22960	31800	24670	32240	23140	20760	19770	32100	27300	26570	24520	30500	21750	28000	23480	11760	17900	13860	19310	22020	27150	26110	27160	25880	25990	29400	29130
117800	59500	59900	70400	55400	75300	60400	80100	57600	51000	49100	77100	67900	64200	61000	71200	53300	67500	57000	29140	44200	34970	46700	55300	74300	70900	77900	70100	70200	86900	86600
14080	5450	5220	6360	4970	6890	5590	6980	5200	4670	4510	7020	6050	5980	5550	6430	4910	6380	5030	2856	3930	3200	4310	4990	7450	6650	7660	6220	6300	8370	8520
4190	1330	1350	1650	1392	1900	1554	2140	1356	1290	1267	1880	1633	1557	1510	1677	1402	1725	1358	849	1106	964	1147	1328	2217	2071	2420	1859	1860	2420	2510
7910	2870	2860	3670	2829	3740	3070	3959	2884	2693	2574	3800	3530	3290	3206	3670	2890	3370	2836	1683	2240	1917	2430	2704	3705	3410	3940	3141	3160	4610	4510
819	344	340	425	335	468	353	449	346	319	319	446	402	401	398	442	349	394	341	233	265	238	295	336	369	360	396	327	343	392	400
3510	1800	1757	2130	1716	2163	1963	2400	1897	1744	1712	2230	2038	2057	2083	2350	1903	2110	1762	1372	1550	1473	1649	1822	1652	1683	1796	1561	1635	1530	1410
8370	8100	7630	9540	8150	10060	9720	10850	9430	8090	8030	10360	9590	10460	10600	10220	9390	10370	8300	6950	7540	7050	8110	8650	5540	5720	5820	5420	5680	5290	4850
456	271	283	339	292	363	333	380	321	288	291	367	338	357	364	372	325	348	302	259	276	261	299	319	244	263	263	245	262	226	184
809	669	690	857	721	888	835	895	801	711	732	851	827	863	898	920	808	810	733	710	727	703	774	808	534	599	561	578	594	377	342
60.5	90.0	84.5	99.7	75.9	99.3	90.4	99.8	83.6	82.8	80.8	93.6	85.1	96.4	101	106	83.9	85.9	84.1	84.8	89.3	83.8	93.6	95.8	55.0	60.6	56.7	62.2	61.3	33.3	31.0
223	491	455	620	395	555	437	549	396	421	381	483	436	495	507	602	446	446	433	430	535	446	528	516	286	315	302	324	299	158	134
18.4	58.9	55.3	62.4	41.7	65.1	48.2	62.5	43.3	41.9	41.8	56.1	47.5	59.4	59.0	72.3	46.5	46.4	47.6	41.1	52.1	40.6	54.3	56.9	30.5	32.9	32.6	35.5	30.2	18.0	14.1
5500	4160	5800	4810	5500	4700	4910	5700	3630	4900	3900	4900	4800	3500	5200	5100	5800	3800	6200	5300	7000	4500	3900	6600	2810	2580	2600	2670	2010	2950	<1004
869	425	533	438	725	473	588	519	475	772	711	495	582	508	497	448	698	413	729	1320	2940	759	555	735	317	286	291	279	260	282	217
22.9	43.3	136	40.3	294	75.0	96.0	59.3	96.0	568	570	89.0	72.0	196	67.9	41.4	192	133	285	382	560	297	126	102	17.1	39.0	10.8	6.8	150	16.9	31.4
100	159	371	710	28.9	510	174	164	61.0	<18.9	er	23.7	270	199	173	360	12.5	61.0	24.7	er	52.0	<5.9	61.0	30.1	45.5	11.1	5.7	13.9	156	4.7	<6.0
490	68.0	8500	29.6	25700	1050	2890	650	5100	64500	71000	5600	1350	13000	4230	1590	13000	14600	28500	37000	78000	35500	15400	5800	1120	188	1540	77.9	1110	1880	10900
2640	1270	2250	650	7700	1870	2360	3930	2020	61000	6470	18400	3580	11200	12400	2170	1950	13600	24100	9300	26600	9100	6180	5210	2940	3090	2250	3460	2270	1310	22000
8.7	12.4	18.7	18.7	30.7	15.4	23.8	21.2	18.9	54.6	35.2	20.2	16.5	26.8	20.3	10.3	34.2	15.3	44.0	28.7	42.0	23.2	25.6	25.1	na	na	na	na	na	4.1	13.7
<263	<158	290	<232	370	<237	<205	<269	<224	<710	<478	<221	<263	<244	<307	<270	<274	<281	<354	3700	9700	600	350	<289	84.9	83.0	79.9	81.4	75.0	<230	<289
190	170	560	268	536	477	247	333	296	1490	1750	433	300	640	526	264	372	600	690	1380	2340	910	400	304	148	154	115	125	183	94.0	148
4.9	er	0.09	0.22	1.6	<0.001	0.86	0.34	0.16	22.4	4.3	6.2	0.15	6.3	1.9	<0.12	6.2	0.26	4.5	1.6	10.8	0.71	2.3	13.5	na	na	na	na	na	0.61	6.2
<1.2	2.3	3.2	1.8	4.4	2.2	1.5	<1.7	1.8	6.6	6.6	3.4	1.4	3.5	2.5	2.2	3.9	3.7	3.7	4.3	6.0	2.8	4.2	4.4	na	na	na	na	na	<1.1	2.2
<1528	<887	15100	<1098	35900	<1777	3200	<1713	5400	93000	99700	7500	<1334	15000	7300	1740	20700	25000	42200	52000	96000	52400	28000	7900	1460	360	2320	141	1640	2800	16600
6.6	0.19	1.0	<0.24	0.66	er	0.50	0.64	0.20	5.2	er	4.9	0.56	4.0	3.9	0.25	0.43	1.6	3.3	0.69	2.6	0.63	1.3	10.8	6.1	5.0	3.4	4.3	10.3	1.0	2.3
2.5	er	43.0	0.58	5.0	<0.20	0.20	0.42	0.32	22.3	0.49	0.84	0.37	er	<0.25	<0.20	2.9	0.28	2.2	4.1	20.9	3.5	6.8	43.0	na	na	na	na	na	<0.16	0.10
467	238	255	279	212	293	227	292	218	210	183	319	266	256	243	295	206	255	217	159	346	113	198	207	na	na	na	na	na	303	354
1.1	4.8	3.8	53.1	2.7	17.0	10.4	3.8	2.6	4.9	2.6	23.1	4.2	16.0	4.9	29.0	3.5	3.9	2.6	20.1	44.5	19.4	33.1	2.2	0.78	0.63	0.71	1.4	0.60	0.34	0.61
er	<0.001	0.55	<0.17	<0.001	<0.001	<0.001	er	<0.001	er	<0.001	er	<0.001	er	<0.001	<0.001	<0.001	<0.001	<0.001	<0.001	er	er	er	1.6	na	na	na	na	na	<0.001	<0.001
er	<0.001	<0.08	<0.05	<0.09	<0.06	er	<0.001	<0.001	0.91	er	er	<0.001	0.08	<0.001	<0.001	0.33	<0.001	<0.08	0.08	0.69	er	0.10	0.38	na	na	na	na	na	<0.001	<0.001
3760	1135	1135	468	556	646	683	841	633	548	567	666	684	636	561	358	469	617	534	2026	1594	1729	1575	1937	123	65.6	74.0	14.5	13.8	2.0	1.5
384	109	169	178	159	184	167	198	125	174	109	274	205	232	187	252	205	164	206	172	376	137	283	155	1518	1632	1680	1738	1860	1070	781
566	668	672	668	628	892	876	1027	597	705	584	769	766	943	1101	485	717	760	738	507	1085	508	815	807	474	470	505	516	491	459	422

RX6721 Irr.	RX6721 Irr.	RX6721 Irr.	RX6721 Irr.	RX6721 Irr.	RX6721 Irr.	RX6721 Irr.	RX6721 Irr.	RX6721 Irr.	RX6721 Irr.	RX6721 Irr.	RX6721 Irr.	RX6721 Irr.	RX6721 Irr.	RX6721 Irr.	RX6721 Irr.	RX6721 Irr.	RX6721 Irr.	RX6721 Irr.	RX6721 Irr.	RX6721 Irr.	RX6721 Irr.	RX6721 Irr.	RX6721 Irr.	RX6721 Irr.	RX6721 Irr.	RX6721 Irr.	RX6721 Irr.	RX6721 Irr.	RX6721 Irr.	RX6721 Irr.	RX6721 Irr.
1_41	**1_45**	**1_46**	**1_47**	**1_48**	**1_31**	**1_49**	**1_50**	**1_51**	**1_53**	**1_32**	**1_34**	**1_35**	**1_36**	**1_37**	**1_38**	**1_54**	**1_63**	**1_64**	**1_65**	**1_66**	**1_55**	**1_56**	**1_57**	**1_58**	**1_59**	**1_60**	**1_61**	**1_67**	**1_69**	**1_70**
251000	271000	240000	267000	248000	259000	262000	237300	228100	255800	252000	245200	259500	258000	259000	263000	224100	241000	246100	245000	265000	233500	217000	236000	251400	253000	230000	218800	240400	234700	251900
27600	25100	26400	26070	27420	28600	24600	27940	28440	26170	25700	26560	25810	25400	26260	26390	26970	26300	27400	25800	26400	26180	27210	27800	25520	24000	27600	28170	25740	25520	25460
72500	64700	73100	71300	75300	68400	67400	78100	78900	65500	65100	71700	67300	66100	68800	68500	68700	66800	70200	67500	72300	66900	74000	78000	65200	64400	71400	82000	67600	67500	65900
5750	4670	5660	5290	7300	5210	5090	7330	7670	4940	4960	6000	4800	4900	4910	4940	6340	5760	5420	5970	6550	5550	7090	6950	5190	4720	7330	8500	6000	5820	5690
1410	870	1520	1220	1600	1020	1080	2000	2270	1057	1028	1632	980	1027	1123	1171	1831	1464	1434	1501	1928	1493	2365	1990	1153	971	1910	2670	1701	1657	1677
2960	2270	2900	2760	3440	2410	2450	3770	4030	2490	2280	3220	2271	2353	2190	2540	3010	2920	3060	3038	3490	2720	3470	3740	2656	2466	3770	4700	3152	3050	2956
259	218	279	240	311	229	227	326	348	289	232	290	219	225	197	245	321	303	306	314	403	283	363	379	272	260	449	455	314	296	294
1124	1054	1283	1157	1235	1120	1030	1235	1376	1330	1100	1168	1029	1020	882	1129	1500	1535	1454	1623	1893	1389	1576	1874	1397	1370	1640	1840	1370	1416	1312
4260	4470	4690	4490	4830	4540	4150	4420	4410	6000	4240	3970	3980	3860	3300	4010	5290	6240	5880	6170	6420	5370	5370	6800	6890	7370	6740	6040	4940	5190	4540
185	185	186	182	183	185	166	168	173	242	168	160	164	156	127	175	242	273	264	269	309	229	234	292	261	252	259	259	214	218	203
378	438	412	436	392	426	391	330	312	630	414	309	370	376	284	418	533	648	622	656	717	566	478	721	715	757	646	503	478	530	427
34.8	47.9	38.2	45.4	41.3	43.6	38.5	30.1	26.6	65.0	41.6	25.6	39.6	35.8	26.8	36.6	56.5	79.7	72.3	68.6	75.7	63.0	43.3	81.7	89.3	91.9	71.6	48.0	52.0	56.6	46.5
163	231	194	229	210	236	198	140	105	440	228	127	188	166	131	172	290	435	407	365	384	344	230	437	588	623	395	245	265	308	228
15.7	26.4	19.1	25.9	23.4	26.1	22.4	15.9	12.5	54.0	21.6	14.3	19.8	17.9	14.3	17.7	31.2	51.3	52.5	45.6	46.2	39.7	25.5	56.8	80.6	90.0	51.2	26.9	33.1	39.6	27.2
9800	1620	2150	2130	2200	1980	2810	2000	<1067	<1398	er	3100	2600	1440	106000	1890	2080	2400	4400	4100	3210	5100	4700	4050	7100	4800	3040	2620	6400	7100	6200
240	251	288	285	304	321	273	296	342	348	318	223	305	274	195	232	316	334	367	311	313	329	430	373	424	355	318	389	778	872	738
7.4	13.4	56.0	5.0	15.9	8.5	19.8	47.0	83.0	99.0	83.0	55.0	65.0	24.5	10.9	22.2	6.6	14.5	8.1	10.9	7.7	8.1	119	5.2	11.7	9.4	9.3	33.3	107	205	93.0
11.9	<5.0	130	4.8	9.6	<4.1	140	235	117	73.0	203	177	168	16.7	<7.1	<5.4	<5.2	24.0	<3.7	12.2	6.5	9.5	240	7.6	11.5	19.3	6.2	94.0	21.5	411	25.0
42.0	33.7	11000	55.0	246	48.0	11900	22500	34100	47000	41000	26900	25000	3300	530	4700	52.4	880	61.0	91.0	84.0	190	33400	71.0	89.0	59.0	53.1	6400	15200	45300	4040
1750	690	8800	4400	3220	550	4400	11500	10300	49000	11000	8100	10600	5500	11700	25100	5000	1650	3120	7700	5300	9500	9800	1280	3930	3020	1230	4200	13140	42100	8930
7.9	6.5	20.0	4.8	<3.4	4.8	13.5	15.3	22.4	20.6	29.0	27.8	18.3	11.8	er	7.9	7.3	3.5	5.5	6.5	9.9	10.6	24.5	5.5	9.5	7.9	5.0	8.1	28.4	50.0	26.6
<226	190	<190	<206	<226	<183	<194	<245	<271	1100	<239	<286	<276	240	<307	<200	<188	<155	250	<197	<277	180	<285	<178	<243	420	230	<234	<280	560	<265
147	209	197	131	117	139	370	227	293	480	550	184	240	111	280	186	146	127	182	216	155	241	470	227	233	230	83.0	149	617	1100	456
2.6	<0.16	0.84	10.2	0.47	<0.08	1.9	1.1	2.3	7.3	0.63	0.60	0.76	1.0	23.7	4.3	0.32	0.22	1.1	1.0	2.1	3.3	0.90	0.93	3.4	1.0	0.26	0.91	3.5	6.6	2.6
<1.0	<0.88	<1.1	<1.1	<0.99	<1.1	<1.1	1.9	1.7	5.0	5.4	er	5.8	<0.97	er	<1.1	<1.2	<0.87	<0.90	<1.2	1.6	<1.3	er	<0.90	<1.3	0.87	<0.99	<1.3	2.9	4.6	2.2
<1343	<1165	14200	<1366	<1154	<1090	8200	36000	45000	87000	69000	56000	40000	5200	3600	9700	<1424	1200	<967	<1127	<1117	<1323	54000	<944	<1459	<775	<1053	9300	23800	80000	5800
1.4	0.29	3.2	5.6	4.7	0.53	2.3	0.83	2.1	11.1	1.4	1.3	5.5	5.4	9.9	5.1	3.5	2.9	4.6	13.8	8.5	12.2	2.8	2.2	5.9	2.0	2.9	2.7	10.4	33.0	10.5
er	er	<0.18	er	<0.25	er	0.26	0.19	<0.48	<0.23	<0.17	<0.31	er	<0.16	er	<0.17	er	er	0.16	er	<0.18	<0.17	er	<0.18	er	<0.12	<0.32	<0.28	0.84	0.69	0.35
316	246	249	283	340	270	254	285	298	318	263	308	280	251	289	283	297	268	249	275	302	271	262	309	275	254	279	311	270	293	263
0.50	<0.18	1.6	0.29	<0.28	0.37	1.1	6.9	2.9	4.6	4.7	3.9	1.8	0.55	3.3	1.1	0.55	1.6	1.3	0.98	1.6	1.7	0.90	1.5	0.88	0.67	0.47	1.4	2.5	7.4	2.3
<0.15	<0.001	<0.001	<0.001	<0.001	<0.001	<0.001	<0.001	<0.20	<0.31	<0.16	<0.001	<0.001	<0.001	<0.001	<0.001	<0.001	<0.001	<0.001	<0.001	<0.17	<0.001	<0.001	<0.001	<0.001	<0.11	<0.001	<0.19	<0.001	<0.001	<0.001
er	<0.001	<0.001	<0.001	<0.05	<0.001	<0.001	<0.001	<0.001	<0.07	<0.001	<0.06	<0.001	<0.001	<0.001	<0.001	<0.05	<0.04	er	<0.001	<0.001	<0.001	<0.06	<0.04	<0.001	er	<0.001	er	<0.001	<0.09	<0.06
2.8	2.3	1.4	1.5	1.7	1.8	1.2	1.2	1.7	1.7	2.4	1.5	2.7	3.4	1.8	1.4	13.8	9.9	11.2	6.3	1.5	4.8	158	28.1	60.0	19.1	325	301	619	501	597
1170	1581	1420	1540	1420	1580	1670	980	950	2080	1710	1100	1256	1270	811	1550	1417	2080	2380	1770	2160	1500	1138	2610	2850	2590	1390	1320	2063	2457	1821
470	712	666	713	651	704	764	476	550	822	825	502	694	543	254	681	670	919	1068	794	987	751	624	1185	1354	1099	626	638	987	1103	859

RX6721 Irr.	RX6722 Irr.	RX6722 Irr.	RX6722 Irr.	RX6722 Irr.	RX6722 Irr.	RX6722 Irr.	RX6722 Irr.	RX6722 Irr.	RX6722 Irr.	RX6722 Irr.	RX6722 Irr.	RX6713 CR	RX6713 CR	RX6713 CR	RX6713 CR	RX6713 CR	RX6713 CR	RX6713 CR	RX6713 CR	RX6714 CR	RX6714 CR	RX6714 CR	RX6714 CR	RX6714 CR	RX6714 CR	RX6714 CR	RX6714 CR	RX6714 CR	RX6714 CR	RX6714 CR	RX6714 CR
1_71	**1_81**	**1_73**	**1_78**	**1_82**	**1_83**	**1_84**	**1_85**	**1_86**	**1_87**	**1_88**	**1_8**	**1_9**	**1_10**	**1_11**	**1_4**	**1_5**	**1_6**	**1_7**	**1_21**	**1_22**	**1_23**	**1_28**	**1_12**	**1_13**	**1_14**	**1_15**	**1_16**	**1_17**	**1_44**	**1_45**
239800	222800	216600	220000	245000	233000	236700	243000	239000	229700	244300	192000	222000	199000	187000	207400	180400	225000	206900	265000	278000	290000	234000	159000	186000	190900	205000	182100	185000	328000	395000
25600	24990	27230	27270	25970	26700	25470	26050	28600	25960	25460	28400	38200	35000	41300	32700	36030	32900	31990	27100	25200	26000	29600	30000	29300	33200	30700	29100	31600	45300	58100
66300	68200	77400	78800	70700	69200	67700	70400	72600	71350	67500	81200	75500	83100	99500	91100	116400	94000	90400	66900	64400	68500	85600	79900	85100	92400	83900	84300	88200	131000	163000
5710	6350	8170	8020	6170	6550	5710	6690	6300	6950	5860	9250	7640	11040	13290	10350	16800	10720	10250	4750	5300	5520	8990	8640	8150	9330	8240	8540	8650	10820	12800
1649	2030	2692	2610	1822	1810	1587	2073	1943	2162	1638	4000	3523	4070	5360	4510	7200	4550	4400	1647	1790	1697	2770	2770	2540	2857	2550	2695	2580	3200	3540
2987	3520	4660	4230	3290	3140	3151	3810	3700	3710	3040	5400	4490	6850	7920	6100	9820	6170	5750	2280	2550	2660	4570	4710	4500	4970	4360	4560	4570	4750	4390
299	427	454	429	353	343	343	435	383	386	315	539	438	733	801	623	830	568	552	187	229	222	476	496	464	532	451	454	462	468	416
1345	2280	1822	1850	1598	1680	1738	2151	1748	1653	1558	2070	1964	3150	3290	2670	2960	2131	2104	644	851	769	2000	2070	1950	2280	1950	1940	2120	1963	1580
4800	6410	5630	5900	5410	6010	6650	6850	6180	5320	5670	7390	7590	11590	10680	7830	9300	8320	6770	842	1162	1271	4660	4850	4900	5470	4600	4100	4870	4450	3520
208	346	238	249	248	273	301	316	280	228	254	265	284	430	460	341	370	319	251	70.6	105	84.9	256	268	246	293	270	249	276	270	233
462	1010	424	507	542	601	752	784	654	470	600	441	547	839	809	735	625	488	418	110	169	137	408	427	421	475	459	394	436	503	372
47.3	124	37.8	46.7	55.9	67.1	84.2	82.7	71.8	46.4	62.7	29.5	51.4	67.8	67.0	66.6	53.3	39.8	31.1	7.6	10.7	8.7	33.9	32.5	32.2	34.2	33.8	31.4	32.9	46.4	30.5
249	690	174	239	274	359	490	461	350	231	360	101	223	330	277	404	215	154	114	27.5	32.7	31.8	152	121	140	133	153	117	146	232	133
29.0	75.0	18.0	24.8	33.0	45.7	56.1	54.6	44.5	27.5	42.2	9.7	26.1	29.4	30.8	36.1	22.3	14.7	12.4	2.0	3.0	2.5	12.7	11.0	14.3	12.7	14.5	11.5	11.5	25.5	14.0
6700	10900	4100	143000	3280	3760	9000	39900	4540	8900	12700	2410	3070	3740	6100	5000	4300	3080	4790	1230	<687	1060	2700	5300	2180	1940	4500	1870	4100	2190	<1244
759	1470	702	575	384	362	514	1270	491	488	409	262	434	358	752	407	597	338	730	149	123	122	272	248	262	216	284	199	300	352	215
127	970	111	217	21.9	27.0	149	600	18.0	108	21.0	18.6	60.6	15.0	39.0	1100	140	31.4	114	1.1	<0.46	3.1	320	18.7	47.8	22.0	37.2	21.0	26.9	21.7	34.9
64.0	18.0	214	30200	23.6	<5.8	21400	14800	12.3	<8.3	127	6.6	9.0	<4.3	<4.0	2700	<8.3	5.4	<6.6	<4.2	<4.0	<5.8	96.0	65.0	65.8	39.9	51.0	26.9	31.7	128	50.0
7400	39500	3530	2270	169	313	356	440	209	10500	112	2560	161	er	40.3	32000	10600	208	12100	<3.4	<3.3	<4.9	21000	14.8	840	47.0	35.5	145	79.0	82.0	30.5
14000	84000	7900	35300	3880	2020	33600	23300	3160	39000	6310	5000	2100	1350	2430	71000	4870	4020	13200	<61.4	<74.5	<65.4	88000	1830	2490	3310	2090	7800	710	8800	7400
26.3	1800	36.7	188	12.6	9.6	147	253	13.5	47.0	19.3	5.6	12.1	9.0	13.8	450	26.7	6.6	20.9	<3.1	<2.4	3.7	30.0	11.3	18.4	12.9	15.7	16.0	12.4	14.9	14.3
<274	<642	<304	<383	<204	<214	<337	<272	<194	<307	<241	er	<218	<178	<189	<271	<396	<217	<238	<179	<161	<209	<172	<150	<152	<188	<166	<197	<181	<219	<231
560	1620	376	335	236	207	216	480	293	380	223	93.0	198	146	376	1620	428	107	219	<47.0	<51.7	<50.6	770	306	330	354	292	375	179	291	177
3.8	79.0	0.42	10.7	<0.001	er	7.1	18.7	<0.001	0.87	0.84	1.1	0.33	er	er	160	22.0	4.3	2.0	<0.001	<0.001	<0.001	560	14.4	28.3	28.8	26.3	23.3	19.9	8.1	2.7
<1.2	12.8	<1.5	2.8	<0.92	<1.2	3.6	4.2	<1.2	2.8	<1.3	1.8	<1.2	<0.81	<1.0	37.0	13.9	1.5	9.4	<0.85	<0.99	<1.2	1.4	<0.93	<0.80	<1.2	<0.98	<1.2	<0.90	<1.3	<1.3
11800	98000	7700	7100	<1360	<1717	<2252	<1807	<1051	18000	<1465	3400	<15824	<1006	<1238	56000	18400	<1686	16500	<1007	<1099	<1430	20000	<1257	2450	<1246	<1107	<1018	<1043	<1835	<1481
13.2	460	6.7	75.0	3.3	2.9	92.0	139	2.8	145	13.9	er	<0.20	0.36	0.73	159	1.3	2.2	1.4	er	<0.001	er	189	3.1	4.7	4.7	4.8	8.9	1.4	15.0	8.8
0.74	<0.001	<0.001	<0.001	er	er	<0.26	er	<0.001	er	0.15	0.37	0.46	<0.19	0.69	155	1.9	0.22	0.29	er	<0.14	<0.21	16.4	8.4	4.2	1.2	2.3	1.6	6.6	4.0	2.3
265	412	282	339	268	277	314	338	257	320	800	307	288	332	400	454	515	390	351	262	223	259	470	368	336	394	374	357	358	523	598
2.3	5.5	1.6	37.9	0.33	0.50	52.0	28.0	0.42	0.56	214	<0.09	<0.19	0.35	<0.25	7.6	0.55	<0.14	0.29	0.67	0.50	<0.24	5.8	4.0	3.4	2.8	5.0	3.1	2.7	4.4	4.1
<0.001	<0.001	<0.001	<0.001	<0.001	<0.001	<0.001	<0.21	<0.001	<0.001	<0.001	<0.001	<0.001	<0.001	er	1.6	er	<0.17	<0.001	<0.001	<0.001	<0.001	<0.13	0.19	er	<0.001	er	<0.001	<0.001	er	<0.001
er	<0.001	<0.001	<0.001	<0.001	<0.001	<0.001	<0.001	<0.001	<0.001	<0.001	er	er	<0.001	<0.001	1.8	0.21	er	<0.06	<0.001	<0.001	<0.001	er	<0.001	<0.001	<0.001	<0.001	<0.001	<0.001	<0.001	<0.001
460	0.71	2.5	0.78	1.3	1.1	0.88	1.5	1.0	1.1	0.92	310	165	750	5290	1210	1460	168	650	1.9	2.0	2.7	22.8	30.9	26.1	33.6	24.4	17.0	31.9	9.3	5.3
1896	97000	1161	11200	1350	1490	10100	26400	1740	2120	2560	222	316	82.0	420	71000	1040	336	267	1.5	1.5	2.2	419	188	232	278	290	247	215	505	202
851	3581	526	580	625	771	2151	1876	818	549	1022	88.0	114	77.7	404	2836	580	120	199		0.96	5.8	367	136	224	161	247	182	166	299	173

RX6714 CR	RX6714 CR	RX6714 CR	RX6714 CR	RX6714 CR	RX6714 CR	RX6714 CR	RX6714 CR	RX6714 CR	RX6714 CR	RX6714 CR	RX6714 CR	RX6714 CR	RX6714 CR	RX6714 CR	RX6714 CR	RX6716 CR	RX6716 CR	RX6716 CR	RX6716 CR	RX6716 CR	RX6716 CR	RX6716 CR	RX6716 CR	RX6726 CR	RX6726 CR	RX6726 CR	RX6726 CR	RX6726 CR	RX6726 CR	RX6726 CR	RX6726 CR
1_29	1_38	1_39	1_40	1_41	1_42	1_43	1_30	1_31	1_32	1_33	1_34	1_35	1_36	1_37	1_62	1_63	1_64	1_65	1_66	1_69	1_46	1_47	1_151	1_160	1_152	1_153	1_154	1_155	1_156	1_157
244100	265800	302000	214000	317000	215000	303000	243000	264300	236000	259000	270000	170000	232000	277000	244500	248100	255800	255800	368000	245600	262000	260900	215000	221000	222200	260000	221600	195600	226000	231100
37300	26920	39900	29800	40000	31400	26300	35280	29400	34200	31900	33890	35360	34740	29600	26940	26960	26350	26100	21800	27800	24500	25370	29900	30400	28740	30600	30150	29000	30400	29690
103000	72100	109600	80600	107000	91400	72600	96900	80200	93600	86200	92900	109600	94400	71500	64400	63600	60500	61400	43200	65300	58100	60300	75500	77800	75300	78300	80200	82400	77600	75200
9600	6350	9540	7170	8100	8120	5850	8160	7390	8980	8400	9030	13460	8810	5540	4780	4740	4130	4360	1864	4980	3720	3980	6480	7800	6900	7550	7450	7720	7120	6940
2980	2060	2860	2080	2210	2540	1360	2500	1786	2760	2170	2690	4760	2670	1140	1528	1508	1279	1360	347	1608	1056	1131	2340	2400	2340	2632	2495	2760	2380	2240
4752	3320	4620	3760	3180	4260	2810	4190	3920	4540	3990	4480	8830	4240	2540	2216	2227	1775	1939	627	2330	1534	1572	2950	2710	2770	3460	2940	3490	2920	2670
480	308	450	363	267	384	227	393	327	449	401	424	1106	455	231	233	230	178	192	41.4	245	150	171	277	282	300	365	296	343	302	282
1967	1195	1860	1640	996	1590	900	1650	1183	1990	1670	1933	5060	1788	943	1089	1071	824	923	153	1206	640	638	1370	1260	1390	1660	1345	1354	1451	1390
4590	2310	4260	4330	1910	3480	2460	3840	4370	4450	3460	3934	14100	4410	3030	3940	3870	2344	3290	378	4140	1947	2000	4950	3760	4830	5060	3850	4410	4340	3980
268	154	261	236	121	212	108	232	158	265	204	270	646	233	126	171	166	122	144	19.2	183	92.6	94.8	230	190	227	248	201	196	223	195
455	243	456	502	208	350	173	413	248	447	349	495	1020	434	230	323	333	241	271	36.7	355	175	179	587	452	572	575	482	302	520	610
37.6	17.1	37.4	45.0	17.1	27.5	13.5	37.3	21.0	35.5	29.2	45.6	74.4	33.9	18.8	25.1	24.6	20.5	20.9	2.7	28.8	13.5	14.1	78.0	50.9	69.5	60.2	52.8	29.1	56.9	56.4
175	61.5	205	240	70.3	118	51.4	158	94.8	147	117	221	254	153	67.1	97.8	88.6	81.4	79.3	11.4	101	49.9	54.7	434	280	380	306	281	164	325	368
17.6	6.0	18.8	26.1	6.8	11.5	5.3	17.1	11.1	16.3	10.7	24.8	17.1	16.6	5.1	9.1	8.9	8.0	7.1	1.1	9.1	4.9	5.1	49.2	29.6	37.0	32.8	32.4	16.0	34.4	36.4
2900	1840	2030	2570	2950	3200	1750	2360	3690	1430	3800	3960	175000	3280	1110	2300	<1359	1400	1410	<932	1480	2550	1800	2350	<729	2300	1350	1720	1450	1200	1200
416	115	293	293	174	231	152	414	212	232	246	349	540	411	40.6	386	261	206	220	24.1	319	144	145	425	214	368	399	317	151	349	330
54.0	4.7	66.9	16.2	22.1	13.5	7.6	55.3	<0.77	14.3	24.1	22.8	22.9	61.1	1.6	1560	587	54.0	360	5.8	380	35.1	31.1	0.57	er	10.0	4.6	8.4	0.89	0.68	1.1
41.1	9.8	80.0	63.0	39.6	43.1	12.6	43.3	17.0	76.0	49.7	60.0	<10.6	99.0	7.3	1950	336	19.6	820	<4.2	272	33.4	53.0	<5.4	4.6	230	188	51.0	12900	11.6	11.9
550	99.0	3010	26.8	5.3	13.7	6.0	156	7.6	30.9	138	59.0	2280	16.1	<4.4	54900	18200	1970	12500	72.0	20200	6400	142	162	160	12400	er	4600	er	166	174
790	6300	2180	1610	540	2400	940	410	310	4000	3430	2890	280	370	270	4450	1960	560	1740	<66.4	1390	6100	580	460	<66.6	1850	3420	1180	150	1210	2180
13.1	15.2	8.8	6.6	33.9	9.9	5.7	16.7	3.8	8.1	13.3	11.9	74.0	16.2	<3.1	<7.4	<4.6	5.6	7.4	<3.0	7.2	12.1	17.5	<3.4	<3.0	<3.2	5.3	3.8	14.0	<3.0	<3.0
<213	<221	<215	<168	<257	<134	<182	<180	<197	<172	<201	<210	<440	<190	<209	<401	<253	<191	<245	<216	<258	<245	<193	<211	<154	<232	<278	<243	<219	<173	<196
187	200	299	236	660	144	98.0	181	81.0	263	236	213	<131	160	<63.4	3740	1630	320	1310	<63.6	1640	127	103	<58.6	<61.0	er	<75.5	<66.4	<58.3	<67.0	<78.2
7.2	2.3	8.2	5.1	0.28	4.5	1.4	6.1	er	12.0	16.0	7.3	2.5	4.7	0.20	er	<0.001	er	er	<0.001	<0.001	0.39	<0.001	0.37	<0.001	0.27	2.4	0.58	<0.13	2.7	0.89
<1.0	<1.1	<1.4	<1.0	<1.2	1.2	<0.82	<0.92	<1.1	<1.2	<1.3	<1.5	<2.3	<1.2	<0.92	<2.6	<1.7	<1.1	<1.4	<1.1	<1.2	<1.2	<1.1	<1.1	<0.95	<1.1	<1.4	1.9	<1.0	<1.2	<1.1
<1170	<1235	3930	<1092	<1433	<1166	<1185	<922	<880	<1353	<1370	<1380	4300	<1350	<1185	83000	26100	2500	18700	<1081	27000	9700	<1461	<1258	<1200	24000	<1492	10900	<1132	<1511	1660
1.7	5.7	4.8	1.2	1.6	3.5	0.85	1.4	0.28	3.9	6.5	4.7	er	1.5	0.39	<0.001	er	0.40	1.4	<0.29	<0.001	2.1	0.69	0.22	<0.19	1.2	10.9	0.82	er	1.2	2.4
0.76	0.64	1.1	1.6	0.29	5.2	2.1	0.65	<0.16	8.9	5.4	4.9	212	1.0	0.10	<0.001	0.30	er	er	er	er	<0.16	er	<0.16	<0.14	er	3.3	0.20	0.24	0.28	0.38
474	286	522	328	412	403	260	406	367	381	359	450	457	508	292	335	268	226	272	162	284	196	236	265	280	287	301	338	325	266	291
3.6	2.1	4.2	4.8	0.93	5.1	1.3	2.1	0.56	7.1	7.4	3.8	0.76	2.7	0.74	<0.33	0.49	0.54	<0.24	<0.43	0.51	<0.24	0.32	0.52	<0.12	0.43	0.66	0.64	2.2	0.35	0.23
<0.001	<0.001	<0.18	<0.001	<0.26	er	er	<0.001	<0.001	<0.001	<0.17	0.15	1.2	<0.001	<0.001	<0.61	<0.001	<0.001	<0.001	<0.001	<0.001	<0.001	<0.001	<0.001	<0.001	er	er	<0.001	<0.001	<0.001	<0.001
<0.001	<0.001	<0.001	er	<0.001	<0.05	<0.001	<0.001	<0.001	<0.001	<0.001	<0.001	<0.10	<0.001	<0.05	<0.001	<0.06	<0.001	<0.001	<0.001	<0.06	<0.001	<0.05	<0.001	<0.001	<0.05	<0.001	<0.001	<0.001	<0.001	<0.001
10.3	1.8	11.4	6.3	5.4	10.6	5.0	10.4	0.95	6.6	7.7	40.7	2.2	12.8	0.63	2.2	2.3	0.89	1.0	0.08	2.1	0.40	0.22	384	381	322	317	338	211	374	447
283	113	421	530	70.4	229	77.0	256	13.6	436	284	502	72.0	231	24.3	84.2	139	94.0	58.6	30.0	97.0	27.1	23.9	230	216	206	452	478	213	378	445
240	77.7	304	392	72.3	148	52.6	232	10.2	256	249	342	7.9	267	22.7	78.7	90.7	57.6	48.4	13.3	58.4	18.0	16.5	170	125	130	234	266	101	233	285

RX6726 CR	RX6726 CR	RX6726 CR	RX6726 CR	RX6726 CR	RX6726 CR	RX6726 CR	RX6726 CR	RX6726 CR	RX6726 CR	RX6726 CR	RX6726 CR	RX6726 CR	RX6726 CR	RX6726 CR	RX6726 CR	RX6726 CR	RX6726 CR	RX6726 CR	RX6726 CR	RX6726 CR	RX6726 CR	RX6726 CR	RX6726 CR	RX6726 CR	RX6726 CR	RX6726 CR	RX6726 CR	RX6726 CR	RX6726 CR	RX6726 CR	RX6726 CR
1_158	**1_159**	**1_134**	**1_143**	**1_144**	**1_145**	**1_146**	**1_147**	**1_148**	**1_149**	**1_150**	**1_135**	**1_136**	**1_137**	**1_138**	**1_139**	**1_140**	**1_141**	**1_142**	**1_161**	**1_170**	**1_171**	**1_172**	**1_173**	**1_174**	**1_162**	**1_163**	**1_164**	**1_165**	**1_166**	**1_167**
246000	226500	226000	231000	215100	219000	223000	228000	217000	208000	215200	206000	227000	215000	211700	261000	226000	219000	217000	205000	221000	244000	207200	213000	234000	236000	229000	251000	222000	231000	223000
31700	30200	29150	29700	28850	28200	30700	28200	29580	26700	29600	27900	29300	28500	28800	29800	31100	29000	28600	30200	29500	27200	30300	28400	29800	30500	29200	31500	30900	29500	29470
76400	84900	78800	81700	77100	79000	75100	75100	78300	68900	82600	70900	68900	75000	75600	74500	79200	77700	78500	83600	77400	71300	82700	76100	74700	79400	75100	84500	80400	80800	75800
6650	7520	7320	6850	7080	7550	7210	6610	6530	5290	7550	6300	6380	6540	6440	6040	7770	7740	7410	7710	6840	5970	7780	6500	7010	6740	6460	7170	7830	8620	6860
2200	2470	2500	2230	2480	2490	2230	2200	2248	1700	2456	2270	2300	2200	2270	1970	2780	2900	2770	2570	2120	1950	2630	2070	2130	2300	2122	2470	2744	2760	2459
2700	3120	3140	2750	2920	2760	2510	2450	2679	1900	3000	2750	2420	2510	2690	2300	3220	3340	3270	3510	2650	2220	3560	2430	2690	2560	2530	2820	3290	3550	2710
241	311	313	268	290	269	271	260	252	195	298	273	245	247	274	238	351	357	365	316	271	228	319	219	258	225	253	273	335	405	283
1019	1380	1461	1285	1270	1186	1290	1130	1095	737	1241	1320	1230	1173	1137	1170	1740	1701	1840	1190	1330	1180	1285	1100	1250	1055	1125	1260	1498	2130	1310
2720	4170	4990	4030	3520	3360	4220	3520	2970	2120	3680	3800	3400	3520	3300	3010	5270	5010	5950	3120	4010	3980	3400	3140	3670	3480	3930	3650	4690	6530	4450
151	206	249	191	185	178	193	175	160	118	187	205	168	178	166	146	280	269	300	149	210	180	159	150	187	171	178	180	239	356	209
317	471	631	501	400	408	506	403	355	248	421	532	424	437	402	351	695	641	790	257	500	483	322	355	422	404	449	438	568	935	511
34.7	55.4	78.7	57.3	43.7	46.3	57.6	45.0	38.2	28.0	48.1	61.2	52.9	49.0	45.7	37.3	77.4	70.1	98.0	22.5	56.5	62.2	26.7	35.2	45.8	44.8	50.0	51.4	61.1	108	61.2
192	318	417	298	231	236	332	229	211	164	253	341	265	297	251	185	442	390	464	100	304	333	139	198	234	268	270	269	337	617	358
19.2	35.4	43.9	32.1	23.2	29.1	34.8	24.3	24.3	20.6	27.1	39.1	26.4	27.3	28.6	18.9	52.3	44.1	45.8	10.7	30.3	34.2	14.1	19.9	24.1	30.7	26.7	27.8	32.5	60.8	30.2
1570	1730	910	<1032	er	2240	2110	1580	1930	1630	1870	1860	1180	1480	2120	1840	1360	1510	<899	1290	1620	1510	1310	920	2900	2420	790	2440	<903	<844	er
319	271	313	361	267	340	374	356	315	271	287	351	335	354	305	328	283	303	277	151	260	394	218	214	349	429	324	401	296	197	276
0.92	1.0	er	10.9	10.4	1.4	1.4	1.2	3.2	0.55	4.3	1.4	<0.40	<0.98	3.0	<0.47	1.4	0.75	<0.50	17.1	2.1	<0.001	120	<0.39	1.1	0.51	<0.001	er	1.3	<0.001	95.0
<5.8	2600	<5.0	er	230	10.7	7.0	<4.4	11.7	<3.6	22.6	4.3	<3.2	33.0	25.0	8.0	<4.6	41.4	<4.3	19.9	<4.2	<3.4	41.0	<3.1	8.3	5.2	<4.0	<5.2	6.5	<6.3	330
141	160	29.5	er	9400	183	37.0	280	265	97.0	156	155	120	99.0	800	14.9	84.0	362	680	2410	1300	22.7	2090	99.0	103	141	690	er	195	520	43000
2380	3600	560	er	10100	1020	1430	3030	1160	<47.5	<67.8	910	210	117	263	156	590	120	256	3140	880	<51.2	860	55.0	610	610	172	<72.8	410	233	3600
4.2	6.3	<3.7	<3.7	10.3	6.1	<3.1	2.7	5.4	2.9	<3.6	<2.6	<2.3	<3.1	4.2	<2.9	<3.5	<3.2	<3.3	<4.3	6.1	<2.4	<3.4	<2.4	<3.1	<3.1	<2.8	3.7	<2.7	3.1	er
<203	<252	<184	<189	<233	<222	<163	<201	<255	<135	<245	<138	<163	<178	<181	<165	<196	<160	<191	<278	<208	<128	260	<144	<200	<204	<174	<178	<227	<209	<226
<69.4	102	<69.6	<60.6	890	<70.2	<47.9	<49.2	147	<55.9	<80.5	<51.1	<42.2	<65.5	<47.6	<58.2	166	<60.4	<54.0	er	<51.8	<51.1	109	<49.7	<63.6	104	<49.6	<59.7	<65.5	<84.5	530
1.4	1.9	er	er	7.8	0.21	2.4	2.4	0.76	<0.001	<0.001	1.1	er	er	er	er	0.47	er	0.11	1.8	<0.08	<0.001	0.07	<0.001	0.19	0.17	0.10	<0.001	0.46	er	er
<1.1	<1.1	<1.1	<1.2	<1.1	<1.1	<0.96	<1.1	<0.94	<0.69	<1.2	<0.74	<1.0	<0.93	<0.91	<0.86	<1.1	<0.85	<1.0	<1.4	<0.83	<0.87	<1.5	<0.87	<1.1	<1.2	<1.4	1.1	<1.0	<0.93	<1.3
<1269	<1380	<1166	er	34000	<1139	<859	<1102	<1160	<1000	<1605	<860	<1112	<1329	<913	<1063	<1037	<1016	<1234	37400	2800	<1046	3760	<946	<1131	<1280	1290	<967	<1158	1860	73000
2.1	6.7	<0.42	er	20.0	2.8	2.3	4.3	3.1	<0.001	<0.001	1.7	er	<0.001	er	er	0.26	er	0.23	3.1	<0.001	<0.001	2.6	<0.001	1.5	0.99	<0.26	<0.001	0.86	er	er
<0.17	0.12	<0.22	<0.18	0.54	<0.17	0.12	2.8	<0.16	er	er	0.67	0.22	er	<0.13	0.13	0.22	<0.001	<0.15	er	er	er	0.20	<0.001	0.42	0.23	<0.001	<0.14	0.30	er	0.23
318	308	342	327	337	295	284	298	298	253	299	275	284	274	281	282	308	299	302	319	297	257	302	274	242	295	284	340	345	282	275
<0.24	1.1	0.30	<0.27	1.3	0.20	1.5	0.38	0.74	0.25	<0.28	0.41	<0.19	0.37	0.70	0.23	0.42	0.21	<0.25	0.65	<0.19	<0.17	<0.28	<0.13	0.56	<0.29	<0.24	0.72	0.69	<0.34	<0.31
<0.001	<0.16	<0.001	<0.001	<0.001	<0.001	<0.17	er	<0.001	<0.001	<0.001	<0.11	<0.001	<0.20	<0.001	<0.001	<0.001	<0.001	<0.001	<0.001	<0.001	<0.001	<0.001	<0.001	<0.001	er	<0.001	er	<0.001	<0.001	<0.001
<0.001	<0.05	<0.001	<0.001	<0.001	<0.001	<0.001	<0.001	<0.001	<0.03	<0.001	<0.03	<0.001	<0.001	<0.001	er	er	<0.001	<0.04	<0.001	<0.001	<0.001	<0.001	<0.001	<0.001	<0.05	<0.04	<0.001	er	<0.001	<0.001
371	260	225	180	192	237	222	242	270	271	266	181	214	200	278	146	225	227	344	418	312	413	394	260	268	543	235	323	346	453	272
261	398	580	296	212	328	271	238	317	286	237	479	498	281	359	221	715	336	236	108	202	305	125	139	282	402	104	323	366	389	237
167	225	265	150	114	178	156.5542	142.12	191.73	135.5262	96.53673	185.04	232.3376	146.75	165.7197	102.307	337.1546	179.09	145.93	78.637	112.81	196.24	106.58	76.396	161.19	229.05	69.541	162.48	226.85	217.72	123.25

RX6726 CR	RX6726 CR	RX6714 Synchysite	RX6714 Synchysite	RX6714 Synchysite	RX6714 Synchysite	RX6714 Synchysite	RX6714 Synchysite
1_168	1_169	1_3	1_4	1_5	1_6	1_7	1_2
210600	223400	115000	118400	123000	117200	119600	114200
31150	30390	25340	26100	25100	26140	25740	21700
85500	81800	78200	79000	75000	80900	83500	62400
7910	7980	9340	10000	8720	10460	9740	6550
2820	2670	3320	3540	2940	3680	3362	2110
4030	3350	5970	6190	5360	6550	6200	3680
429	352	733	766	630	835	763	376
1830	1670	3510	3860	2860	3630	3890	1630
4360	3860	9820	11460	8000	10270	11310	3430
248	210	452	509	359	463	545	189
469	402	751	1003	544	723	851	297
36.2	38.8	52.7	74.0	33.6	49.7	68.1	21.5
145	197	202	290	128	161	209	75.0
12.5	22.0	12.6	26.2	10.4	8.0	16.5	5.9
<863	1560	142000	130000	94000	125000	155000	20200
176	270	508	368	248	335	890	214
33.0	3.3	24.0	690	er	60.0	112	22.9
75.0	310	<16.9	85.0	<18.6	27.0	33.0	13.5
5800	129	er	45000	er	11000	18800	345
9600	3270	570	4400	<231	1300	1290	1610
<3.6	9.3	57.0	78.5	44.0	40.0	53.6	18.6
<183	<213	<671	<1123	<600	<734	5900	<167
69.0	<74.7	<189	<290	<166	<170	<233	59.0
3.1	0.69	2.0	4.4	er	er	0.66	7.4
1.4	<0.93	<2.8	<6.3	<3.2	<3.0	<5.7	<1.2
11600	<1393	er	57000	<3548	9900	23000	<1242
18.9	3.0	<0.69	er	<0.001	<0.70	er	0.73
0.94	<0.18	228	690	<0.48	<0.74	108	4.5
299	313	360	400	270	318	451	270
0.78	1.1	<0.72	<1.3	<0.61	<0.63	1.5	1.5
<0.001	<0.001	3.3	10.4	<0.001	<0.001	1.4	er
er	<0.001	<0.001	<0.001	<0.001	<0.21	<0.001	<0.001
203	475	8.3	14.4	17.9	29.5	23.1	27.7
60.0	344	44.8	114	29.0	42.4	39.6	104
43.034	213.78	9.7567621	26.533017	2.9610292	11.643124	21.604097	69.455472

SUPPLEMENTARY MATERIAL B

APPENDIX FOR CHAPTER 3

Rare earth element phosphates from the Olympic Dam Cu-U-Au-Ag deposit, South Australia: Recognizing temporal-spatial controls on REE mineralogy in an evolved IOCG systems

INCLUDES:

APPENDIX 1: WHOLE ROCK ASSAY AND XRD DATA FOR SAMPLE SUITE

APPENDIX 2A: SAMPLE DESCRIPTION TABLE

APPENDIX 2B: SAMPLE DESCRIPTION FIGURE

APPENDIX 3A: EPMA STANDARD LIST

APPENDIX 3B: EPMA SET UP DETAILS

APPENDIX 4: COMPLETE EPMA DATASET FOR FLORENCITE

APPENDIX 1. Whole rock assays and XRD data for sample suite §

	Sample	RX6709	RX6710	RX6711	RX6728	RX6714	RX6723	RX6716	RX6727	RX6712
	Mine area	FN	FN	FN	FN	C	E	DSE	DSE	B
Element	Units									
Fe	wt.%	23.3	24.9	17.8	48.3	31.1	13.7	27.9	13.2	9.69
Al	wt.%	4.47	4.96	14.3	2.71	7.62	6.80	3.95	5.9	7.58
Si	wt.%	3.84	4.66	14.7	2.33	8.69	24.5	5.27	13.6	27.2
K	wt.%	0.81	1.13	5.13	0.37	3.27	3.49	1.28	2.67	3.71
S	wt.%	0.36	0.22	0.21	1.10	0.08	0.59	0.14	3.63	0.14
P	wt.%	0.23	0.39	0.47	0.26	0.51	0.16	0.18	0.39	0.09
Ca	wt.%	0.21	0.12	0.08	0.09	0.21	0.80	0.15	0.55	0.07
Ti	wt.%	0.11	0.13	0.06	0.02	0.01	0.11	0.03	0.10	0.18
Na	wt.%	0.11	0.18	0.18	0.05	0.11	0.05	0.22	0.03	0.09
Mg	wt.%	0.09	0.08	0.29	0.14	0.24	0.41	0.09	0.12	0.31
CO_2	wt.%	8.97	7.56	0.28	2.14	2.73	3.70	7.18	3.36	1.08
Cl	wt.%	0.03	0.03	0.04	0.06	0.06	0.03	0.07	0.04	0.08
Y	ppm	1229	1430	89	544	539	109	2137	729	222
La	ppm	71835	66071	5292	17635	28598	3260	80434	33896	9304
Ce	ppm	139173	122126	6720	33524	41422	5941	114351	53284	14370
Pr	ppm	14655	13314	610	3453	3893	704	9481	4506	1395
Nd	ppm	45546	39469	1348	10424	10019	1911	23996	11563	3272
Sm	ppm	3989	3818	139	1083	1033	294	1935	1053	434
Eu	ppm	1154	1187	40.4	356	285	81	551	392	186
Gd	ppm	1335	1359	59.0	466	483	128	893	501	212
Tb	ppm	131	140	5.90	51.2	54.3	11.3	111	58.6	23.0
Dy	ppm	485	534	25.3	206	224	41.8	526	256	94.6
Ho	ppm	62.6	69.4	3.72	26.7	26.9	5.16	74.4	31.9	12.5
Er	ppm	138	157	9.03	53.3	50.8	10.4	171	69.9	23.4
Tm	ppm	13.5	14.4	1.16	5.14	4.78	1.26	16.0	6.58	2.33
Yb	ppm	58.9	70.4	6.46	23.1	20.6	7.30	66.1	29.0	11.5
Lu	ppm	6.38	7.38	0.89	2.54	2.25	0.88	7.25	2.83	1.26
Ag	ppm	0.32	0.17	0.16	0.74	3.40	5.37	2.30	26.5	1.04
As	ppm	60.1	75.8	44.3	68.2	328	57.4	141	60.0	517
Ba	ppm	9258	3957	6109	37161	2715	1899	2429	26519	4950
Be	ppm	1.10	1.40	2.00	1.10	3.70	1.60	1.10	2.10	3.80
Bi	ppm	4.00	3.94	3.39	8.08	11.1	3.93	8.75	10.7	3.83
Cd	ppm	<0.02	<0.02	0.05	<0.02	<0.02	0.02	0.03	<0.02	<0.02
Co	ppm	30.9	25.4	45.4	50.5	21.0	6.20	8.30	8.60	19.6
Cr	ppm	39.0	35.0	69.0	49.0	42.0	165	60.0	55.0	115
Cs	ppm	4.36	4.83	1.84	0.52	1.8	2.53	3.63	2.64	9.13
Cu	ppm	1536	1631	826	3425	646	21286	1412	90726	370
F	ppm	35964	32307	2968	9438	12580	-	-	18248	5878
Hf	ppm	6.10	6.30	2.60	1.00	0.90	5.50	2.10	3.30	6.30
In	ppm	0.04	0.05	0.03	0.22	0.19	0.01	0.16	0.04	0.05
Li	ppm	29.0	20.0	210	20.0	30.0	22.0	41.0	24.0	24.0
Mo	ppm	216	572	46.0	397	80.0	20.0	58.0	38.0	69.0
Nb	ppm	51.8	76.1	50.8	81.5	121.0	174.2	58.1	163.6	40.0
Ni	ppm	<1	<1	2.00	6.00	3.00	2.00	<1	1.00	3.00
Pb	ppm	19.0	24.0	14.0	47.0	120	30.0	74.0	43.0	75.0
Rb	ppm	27.8	35.8	169	15.1	152.2	142	57.9	105.5	179.2
Re	ppm	0.043	0.041	0.008	0.015	0.012	0.01	0.058	0.009	0.004
Sb	ppm	2.90	3.10	3.00	3.50	27.2	6.90	14.5	5.80	7.20
Sc	ppm	25.0	25.0	2.00	6.00	14.0	5.00	11.0	18.0	10.0
Se	ppm	39.1	44.5	3.30	26.1	20.2	7.60	36.1	28.3	9.5
Sn	ppm	6.00	9.00	35.0	9.00	340	40.0	77.0	22.0	42.0
Sr	ppm	1104	1767	2404	1308	603	340	621	870	296
Ta	ppm	2.30	2.20	0.70	1.30	0.7	2.60	0.20	5.70	1.80
Te	ppm	1.03	1.77	2.71	3.45	7.7	5.76	3.56	6.02	1.60
Th	ppm	46.3	55.7	105	47.7	7.3	68.3	24.1	37.5	57.2
Tl	ppm	0.14	0.15	0.96	0.09	1.99	0.49	0.40	0.26	2.28
U_3O_8	ppm	43.6	81.8	65.7	154	134	175	133	102	96.3
V	ppm	137	135	40.0	74.0	109	24.0	119	86.0	61.0
W	ppm	6.00	10.0	40.0	22.0	333	136	189	79.0	180
Zn	ppm	102	126	56.0	164	140	31.0	38.0	42.0	147
Zr	ppm	193	191	78.0	21.0	24.0	159	42.0	85.0	199
Au	ppb	28.0	54.0	4143	59.0	6409	602	12690	653	2526
Total	wt.%	75	73	56	70	65	58	71	68	55

XRD Data		RX6709	RX6710	RX6711	RX6728	RX6714	RX6723	RX6716	RX6727	RX6712
Hem	wt.%	32	38	20	72	47	20	46	16	11
Quartz	wt.%	-	-	-	-	-	39	2	14	39
Chlorite	wt.%	10	6	9	6	-	-	-	-	-
Fluorite	wt.%	-	-	-	-	-	1	-	1	-
Barite	wt.%	2	1	1	7	0	-	-	4	1
Florencite	wt.%	3	4	4	1	4	1	1	2	1
Bastnasite	wt.%	44	36	1	9	11	1	37	14	4
Sericite	wt.%	8	15	65	4	38	35	14	39	45
Chalcopyrite	wt.%	-	-	-	-	-	-	-	-	-
Bornite	wt.%	2	-	-	-	-	1	-	2	-
Chalcocite	wt.%	-	-	-	-	-	3	-	8	-

§ core samples for analysis from equivelent depth of study of studied samples with florencite analysis or observed florencite.

*DL- detection limit

** Assay methods: FB6/MS:Lithium metaborate/tetraborate fusion analysed by Inductively Coupled Plasma (ICP)-Mass Spectrometry (MS). FB6/OE: Lithium metabor
Hydrofluoric, Nitric, Perchloric and Hydrochloric acids in Teflon Beakers analysed by ICP-MS. 4A/OE: Multi-acid digest including Hydrofluoric, Nitric, Perchloric and H
Spectrometry. FA25: 25g Fire Assay. FC7: Carbonate Fusion/SIE.

***XRD sericite includes Muscovite-1M and -2M1 and chlorite includes chamosite.

RX6715	RX6713	RX6720	RX6721	RX6726	RX6724		
B	DNW	DNW	DNW	H	FNW (dyke)	DL*	Method**
22.0	13.6	43.6	25.6	17.2	3.95	0.01	FB6/OE
2.54	5.95	1.60	0.84	6.01	15.1	0.01	FB6/OE
15.0	21.3	3.0	2.4	17.6	16.6	0.01	FB6/OE
1.12	3.08	0.72	0.34	2.91	6.47	0.01	FB6/OE
3.45	2.08	2.20	2.30	1.63	0.02	0.01	CSA
0.09	0.20	0.09	0.06	0.18	0.03	0.01	FB6/OE
0.05	3.99	10.69	18.36	0.10	0.11	0.01	FB6/OE
0.11	0.18	0.01	0.01	0.17	0.27	0.005	FB6/OE
0.04	0.06	0.02	0.02	0.07	0.22	0.01	FB6/OE
0.29	0.12	0.03	0.02	0.55	0.09	0.01	FB6/OE
1.34	0.34	0.45	3.69	2.39	3.75	0.05	CSA
0.08	0.06	0.03	0.03	0.07	0.03	0.02	CL1/COL
196	279	203	1202	472	1360	0.5	FB6/MS
11383	3175	4176	39419	22543	41567	50	FB6/OE
18181	5112	5830	56390	35122	55803	100	FB6/OE
1731	505	550	4609	3026	4883	0.05	FB6/MS
4203	1225	1323	12814	8023	12426	0.1	FB6/MS
512	174	146	1256	860	1150	0.05	FB6/MS
167	67.7	45.2	361	286	298	0.05	FB6/MS
222	100	73.6	633	392	600	0.05	FB6/MS
22.4	13.1	8.03	72.7	43.4	73.3	0.02	FB6/MS
90.4	66.9	37.2	336	167	342	0.05	FB6/MS
11.1	11.7	5.93	46.4	20.6	49.2	0.02	FB6/MS
21.6	33.8	15.5	128	40.8	127	0.05	FB6/MS
2.21	4.87	2.14	15.1	4.29	14.2	0.05	FB6/MS
10.9	35.1	13.8	96.6	22.2	76.0	0.05	FB6/MS
1.45	4.60	1.81	12.7	2.50	8.61	0.02	FB6/MS
4.26	7.89	4.33	10.1	10.38	0.26	0.05	4A/MS
84.7	63.2	31.8	66.0	75.2	62.6	0.5	4A/MS
106655	7624	1315	1842	1352	1153	50	FB6/OE
1.20	3.90	1.10	1.20	2.00	1.90	0.5	FB6/MS
1.67	13.5	3.67	20.8	12.6	2.53	0.01	4A/MS
0.05	0.06	<0.02	<0.02	0.02	0.14	0.02	4A/MS
11.8	41.1	14.1	29.2	13.0	11.0	0.1	4A/MS
124	124	42.0	78.0	76.0	39.0	20	FB6/OE
1.00	2.73	0.53	0.42	2.3	2.52	0.05	FB6/MS
18112	44204	20553	29332	51208	105	1	4A/OE
5728	34010	80243	90612	12511	17811	50	FC7/SIE
4.70	7.20	0.80	1.20	6.90	17.5	0.1	FB6/MS
0.06	0.16	0.04	0.09	0.04	0.25	0.01	4A/MS
14.0	42.0	7.00	17.0	22	62.0	1	4A/OE
30.0	136	84.0	57.0	65.0	3.00	1	FB6/MS
43.0	57.5	339.1	809.1	101.0	52.4	0.1	FB6/MS
<1	7	2	<1	<1	<1	1	4A/OE
99.0	140	96.0	213	29.0	63.0	5	4A/OE
51.3	109.2	33.9	16.7	121	203	0.1	FB6/MS
0.006	0.397	0.083	0.563	0.01	0.01	0.002	4A/MS
6.00	8.00	6.60	7.00	7.30	2.20	0.5	FB6/MS
4.00	8.00	<2	12.0	12.0	28.0	2	FB6/OE
11.7	10.4	5.70	26.0	17.6	24.2	0.5	4A/MS
51.0	16.0	157	89.0	97.0	16.0	1	FB6/MS
1161	588	180	196	369	228	20	FB6/OE
1.30	2.80	0.40	2.30	3.60	5.50	0.1	FB6/MS
2.98	0.98	5.99	12.3	6.51	1.62	0.05	4A/MS
86.7	102	27.6	32.6	70.4	158	0.05	FB6/MS
0.81	0.88	0.21	0.15	0.58	0.91	0.02	4A/MS
494	1485	718	1249	71.5	296	0.5	FB6/MS
80.0	39.0	49.0	100	66.0	78.0	20	FB6/OE
145	18.0	544	66.0	296	16.0	1	FB6/MS
76.0	63.0	13.0	8.00	318	46.0	1	4A/OE
142	244	14.0	8.00	205	534	1	FB6/MS
2380	345	1794	4876	2236	45.0	1	FA25/MS
63	61	74	78	63	61		

RX6715	RX6713	RX6720	RX6721	RX6726	RX6724
33	15	60	32	22	5
30	32	3	3	21	-
1	0	-	-	1	-
-	8	21	33	-	-
19	1	-	-	-	-
0	1	0	-	1	-
5	1	1	15	9	17
12	34	9	7	41	78
-	-	5	3	-	-
-	8	1	6	1	-
-	-	-	-	4	-

rate/tetraborate fusion analysed by ICP-Optical Emission (OE). 4A/MS: Multi-acid digest including Hydrochloric acids in Teflon Beakers analysed by ICP-OE. CSA: Induction Furnace Analysed by Infrared

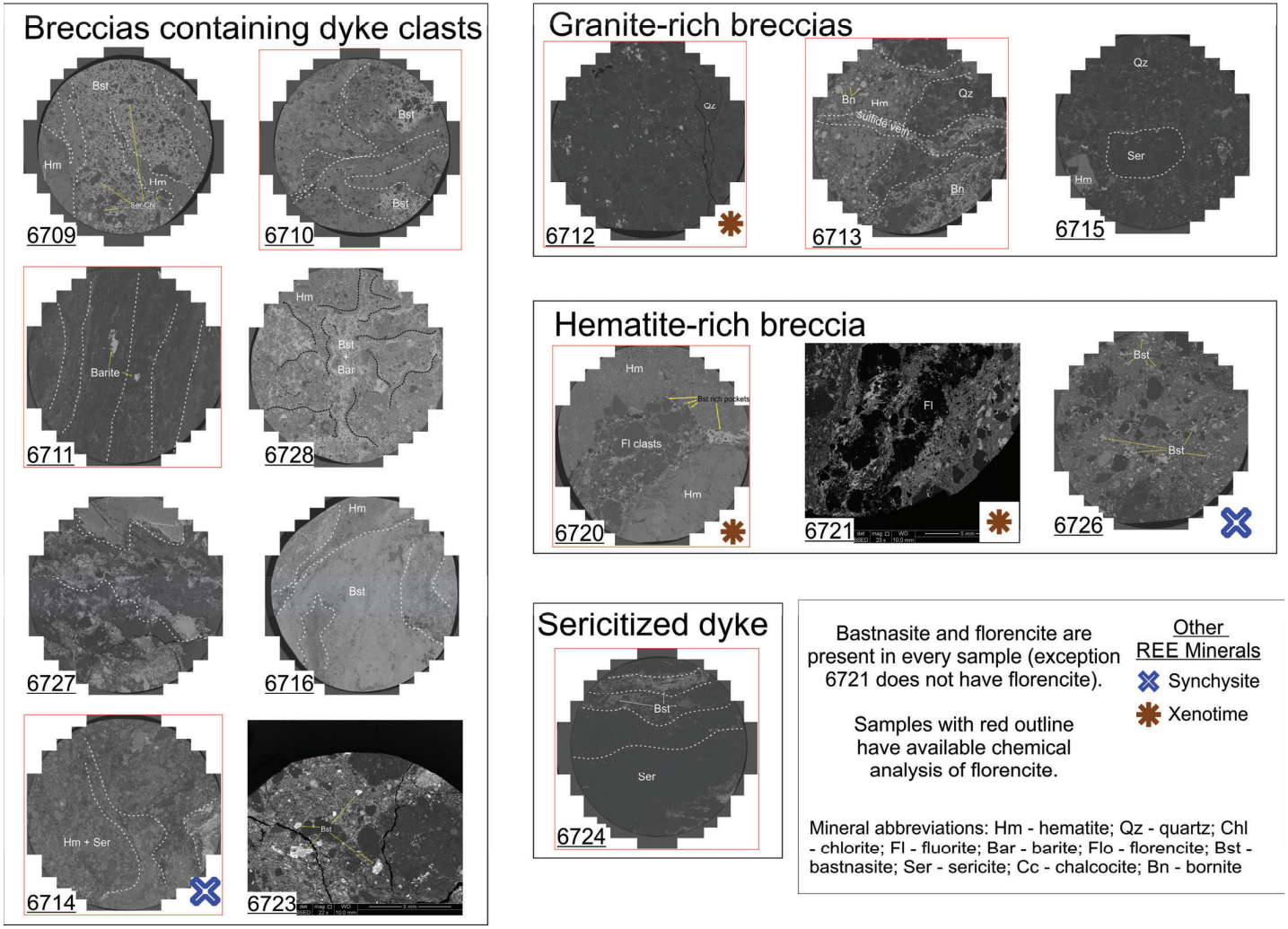
APPENDIX 2a. Summary description table of samples in this study.

Lithology	Sample location				Brief sample description[1]	REE Minerals			
	Area	Drill hole	Sample no.	Core depth (m)		Bst	Synch	Flo	Xeno
Breccias containing dike clasts	NW arm	RU34- 3829	RX6709	72.8-73.0	Strong Bst matrix zone with clasts of Ser and Chl. Around Bst zones are Hm dominate zones with Hm as matrix and clasts with Ser-Chl. Rt and Zr present.	X		X	
			RX6710	73.6-73.7	Hm is the major mineral, present in clasts and with strong lineaments in matrix. Distinct zones with abundant angular-rounded clasts of Ser-Chl. Zr present.	X		**x**	
			RX6711	74.7-74.8	Strong foliation across the sample. More fine grained sample of mostly Ser with Chl, few and small clasts, mostly composed of Hm. Flo occurs along "pressure shadows" around mineral grains. Rt and Zr present.	x		**X**	
		RU41- 2571	RX6728	174.8-174.9	Mostly Hm with "crackle" Bar veinlets with Bst around clasts and Hm. Some clasts of Hm, Qz, and Ser.	X		x	
	East edge	RU33- 159	**RX6714**	66.3-66.4	Sample dominated by Hm as clasts and matrix with Ser. Hm makes rounded thick rims around cores of Ser and Bar. Bst concentrated in light-colored zone on edge.	X	x	**X**	
		RU37- 7354	RX6723	4.3-4.4	Bst occurs as blades in the matrix, both disseminated and abundant in distinct zones, and in relict clasts. Abundant clasts of mostly Qz in sample, rounded - angular, all sizes. Orange areas on hand sample are mostly Qz+Hm.	X		x	
	Central	RU34- 454	RX6716	82.9-83.0	Very abundant Bst throughout sample, concentrated in more fine-grained conduit, as matrix and clast replacement. Around Bst zone is mostly Hm as clasts and matrix.	X		x	
		RU45- 2661	RX6727	51.8-51.9	Chaotic sample with blocky zones of fine grained Ser and Hm matrix. Other areas of breccia conduits with abundant clasts of Qz, Hm, sulfides, and Bar.	X		x	
Granite-rich breccias	East edge	RU3-558	**RX6712**	23.7-23.8	Clasts are mostly Qz with some Bar and Hm, rounded to angular. Ser matrix. Rt and Zr present.	X		**X**	x
		RU4-105	RX6715	12.2-12.3	Abundant clasts, rounded to angular, matrix supported heterolithic breccia but clasts mostly of Qz and Hm, matrix is microbreccia and Ser.	x		x	
	Central	RU3-954	**RX6713**	70.1-70.2	Hm abundant as matrix and clasts. Other clats of sulfide, Qz, and Ser. Bn vein. Lacking pervasive disseminated bst in the matrix, Flo is present instead. Rt present.	X		**X**	
Hematite-rich breccia	Central	RU40-1407	**RX6720**	19.0-19.2	Primarly composed of coarse-grained Hm with a range of textures. Cluster of clasts of rounded to angular Fl and minor Qz and Cp/Bn. Bst matrix in distinct veinlet zone with Cp and Bn.	X		**X**	x
			RX6721	19.4-19.5	Strong linear zones from veins of Hm and Ser with Cp-Bn between bands of Fl clasts with matrix of Ser, Hm, Bst, and Cp-Bn.	X			x
		RU38-2685	RX6726	77.1-77.3	Clasts of mostly Qz, Ser, Hm, and Bst. Microbreccia matrix of fine-grained Hm blades and Ser with veinlets and lineation around clasts. Rt and Zr are present.	X	x	x	
Sericitized dike	NW arm	RU41-5181	**RX6724**	183.7-183.8	Bst in disntinct zones in darker red areas. Fine grained Bst in matrix to massive clumps. Clumps are dirty with possible faint zoning from inclusions of Hm and Ser but mostly irregular. Some distinct zones of Flo with distinct hexagonal textures with Ser in shape.Fine grained irregluar Bst in Ser around Flo.	X		**X**	

[1] mineral abbreviations: Hm - hematite; Qz - quartz; Chl - chlorite; Fl - fluorite; Bar - barite; Flo - florencite; Bst - bastnasite; Ser - sericite; Cp - chalcopyrite; Bn - bornite; Cc - chalcocite; Rt - rutile; Zr - zircon. XRD analysis of major minerals of sample areas are included in Supplementary Table S1. X - major, x - minor.

Bolded samples have florencite analysis avaiable.

APPENDIX 2b: Sample description figure. Backscatter electron scans of sample blocks with florencite, illustrating macroscopic textures and dominant mineralogy. Symbols indicate presence of other REE minerals, synchysite, and xenotime.



APPENDIX 3A: FULL EPMA STANDARD LIST

Full Standard List								
Ref. Num.	**Mineral/ Composition**	**Manufacturer Information**	**Ref. Num.**	**Mineral/ Composition**	**Manufacturer Information**	**Ref. Num.**	**Mineral/ Composition**	**Manufacturer Information**
501	Albite	Astimex	608	Vanadium	Astimex metal	815	Tm metal	Astimex REE block
502	Almandine Garnet	Astimex	616	Niobium	Astimex metal	816	Y metal	Astimex REE block
504	Apatite	Astimex	619	Scandium	Astimex metal	817	Yb metal	Astimex REE block
513	Celestite	Astimex	627	Pb Glass	NIST	1100	Lanthanum Phosphate	Smithsonian REEPO4 std
520	Crocoite	Astimex	628	Rare Earth Glass Standard	Drake and Weill glasses	1101	Cerium Phosphate	Smithsonian REEPO4 std
530	Marcasite	Astimex	629	Huttonite (ThSiO4)	DAS	1102	Praseodymium Phosphate	Smithsonian REEPO4 std
535	Plagioclase	Astimex	631	UO2	DAS	1103	Neodymium Phosphate	Smithsonian REEPO4 std
541	Sanidine	Astimex	632	La Glass	University Edinburgh	1104	Samarium Phosphate	Smithsonian REEPO4 std
545	45 Tugtupite (Na4BeAlSi4O12Cl)	Astimex	633	Ce Glass	University Edinburgh	1105	Europium Phosphate	Smithsonian REEPO4 std
551	51 Yittrium Al Garnet (Y3Al5O12)	Astimex	634	Gd Glass	University Edinburgh	1106	Gadolinium Phosphate	Smithsonian REEPO4 std
554	Barite	P&H	635	Sm Glass	University Edinburgh	1107	Terbium Phosphate	Smithsonian REEPO4 std
556	Chalcopyrite	P&H	636	Nd Glass	University Edinburgh	1108	Dysprosium Phosphate	Smithsonian REEPO4 std
557	Rhodonite	P&H	637	Pr Glass	University Edinburgh	1109	Holmium Phosphate	Smithsonian REEPO4 std
558	Wollastonite	P&H	638	Y2O3	University Edinburgh	1110	Erbium Phosphate	Smithsonian REEPO4 std
559	Rutile	P&H	739	CaWO4	Taylor Block	1111	Thulium Phosphate	Smithsonian REEPO4 std
560	Silver Telluride	P&H	740	GaP	Taylor Block	1112	Ytterbium Phosphate	Smithsonian REEPO4 std
562	Gallium Arsenide	P&H	804	Dy metal	Astimex REE block	1115	Yttrium Phosphate	Smithsonian REEPO4 std
568	Guajuatite Bi2Se3 Synthetic	P&H	805	Er metal	Astimex REE block	1116	Scandium Phosphate	Smithsonian REEPO4 std
596	Tungsten	Astimex metal	806	EuF3	Astimex REE block	2001	Apatite	Astimex Apatite
599	Zirconium	Astimex metal	808	Ho metal	Astimex REE block			
601	Tantalum	Astimex metal	814	Tb metal	Astimex REE block	2002	Apatite	P&H

APPENDIX 3B: FULL DETAILS OF ANALYTICAL SET-UP FOR EPMA ANALYSIS; ELEMENTS ANALYZED, PEAK/BACKGROUND POSITIONS, COUNT TIMES, STANDARDS, ELEMENTAL OVERLAP CORRECTIONS USED IN REE MINERAL PACKAGE.

Element and Line	Diffracting Crystal (Sp#)	Background type/fit	kV/nA	Peak Count Time	Bkgd Count Times		# bkgd points acquired (Lo/Hi)	Standards[1]				Overplaping element and order with their overlap correction standard											
					Lo	Hi		Primary standards	Secondary standards 1	Secondary standards 2	Interference standards	Interfering line	Int std	Interfering line	Int std	Interfering line	Int std	Interfering line	Int std	Interfering line	Int std	Interfering line	Int std
Cu Ka	LLIF (3)	Shared	15/20	20	10	10	1/3	556				Tm I	815	Tb I	814	Er I	805						
Ho Lb	LLIF (3)	Shared	15/100	40	10	10	4/8	1109	808			Y II	816	Yb I	817	Sm I	635	Eu I	806	Th II	629		
Yb La	LLIF (3)	Shared	15/100	40	10	10	4/12	1112	817			Y II	816	Ho I	808	Dy I	804	Tb I	814				
Tm La	LLIF (3)	Shared	15/100	40	10	10	7/12	1111	815			Dy I	804	Sm I	635								
Er La	LLIF (3)	Shared	15/100	40	10	10	5/8	1110	805			Tb I	814										
Gd Lb	LLIF (3)	Shared	15/100	40	10	10	7/8	634	1106			U II	631	Ho I	808								
Dy La	LLIF (3)	Shared	15/100	40	10	10	8/6	1108	804			Th II	629	Eu I	806	Pb II	627	Yb I	817				
Fe Ka	LLIF (3)	Shared	15/20	20	10	10	8/6	502				Th II	629										
Tb La	LLIF (3)	Shared	15/100	40	10	10	8/6	1107	814			Pb II	627	Pr I	637	Sm I	635						
Sm Lb	LLIF (3)	Shared	15/100	40	10	10	12/9	635	1104			Tb I	814	Nd I	636								
Mn Ka	LLIF (3)	Shared	15/20	20	10	10	12/6	557				As II	562										
Eu La	LLIF (3)	Shared	15/100	40	10	10	3/6	1105	806			Pr I	637	Nd I	636								
Nd Lb	LLIF (3)	Shared	15/100	40	10	10	4/3	636	1103			U II	631										
Pr Lb	LLIF (3)	Shared	15/100	40	10	10	4/1	637	1102			U III	631										
Ce La	PET (1)	Linear	15/100	20	40	40	1/1	633	1101			Y III	816	Yb II	817	Tm II	815						
La La	PET (1)	Linear	15/100	20	40	40	1/1	632	1100			Nd I	636	Tm II	815								
Ti Ka	PET (1)	Multipoint	15/20	30	20	20	2/2	559				U III	631										
Ba La	PET (1)	Multipoint	15/100	20	20	20	1/2	554			816	Ti I	559	U III	631	Pr I	637						
Te La	PET (1)	Multipoint	15/100	20	20	20	2/2	560				Sm II	635	U I	631								
Ca Ka	PET (1)	Multipoint	15/20	20	20	20	2/2	535				Y IV	816	Yb II	817	Th III	629	Dy II	804	Tb II	814		
U Mb	LPET (1)	Multipoint	15/100	60	20	20	2/2	631				K I	541	Th I	629	Ho II	808	Gd II	634				
K Ka	LPET (1)	Multipoint	15/20	20	20	20	2/2	541				U I	631										
Th Ma	LPET (5)	Linear	15/100	60	40	40	1/1	629				Gd II	634	Y V	816								
Cl Ka	LPET (5)	Linear	15/20	15	40	40	1/2	545				Ce II	633	Nd II	636	Er III	805	Ho III	808				
Pb Mb	LPET (5)	Multipoint	15/100	100	30	30	3/2	627	520			U I	631	S I	530	Ce II	633	Y VI	638				
S Ka	LPET (5)	Multipoint	15/20	20	20	20	1/2	513				Nd II	636	La II	632								
Nb La	LPET (5)	Multipoint	15/100	20	10	20	1/2	616				Mn III	557										
Zr La	LPET (5)	Multipoint	15/100	30	20	20	2/1	599				Nd III	636	P I	740	Tb IV	814						
P Ka	LPET (5)	Multipoint	15/20	15	20	20	2/2	504				Ca II	558	Cu IV	556	Tm IV	815	Gd III	1106	Ce III	1101		
Y La	LPET (5)	Multipoint	15/100	40	20	20	2/2	628	1115	638		La III	632	Ho IV	808								
F Ka	PC0 (2)	Multipoint	15/20	20	40	40	4/4	2001	2002			Sm VIII	635	Ce VII	633	P III	740	Y III	638	La VIII	632	U V	631
Sr La	TAP (4)	Multipoint	15/100	30	20	20	1/3	513				Y I	816	U II	631								
Si Ka	TAP (4)	Multipoint	15/20	40	20	20	1/2	501				Y I	638	Tb IV	814	Nd III	636	Er IV	805				
Al Ka	TAP (4)	Multipoint	15/20	20	20	20	2/2	501			740	Ti III	559	Yb I	817	Ho I	808						
As La	TAP (4)	Multipoint	15/100	40	20	20	1/2	562			558	Sm I	635	Nd IV	636								
Mg Ka	TAP (4)	Multipoint	15/20	30	20	20	1/2	502				U II	631										
Na Ka	TAP (4)	Multipoint	15/20	20	20	20	2/2	501				U III	631										
V Ka	LPET (5)	Linear	15/100	40	10	10	1/1	608															
W La	LPET (5)	Linear	15/100	40	10	10	1/1	596	739														
Sc Ka	LPET (5)	Linear	15/100	40	10	10	1/1	619	1116			Ca I	535										
Ta La	LPET (5)	Linear	15/100	40	10	10	1/1	601															
Bi Ma	LPET (5)	Linear	15/100	40	10	10	1/1	568				Ce II	1101										

[1] See Full Standard List (Appendix 3A) for standard number references

APPENDIX 4. COMPLETE EPMA DATASET FOR FLORENCITE

	RX6710 (n=6)											
wt.%	1	2	3	4	5	6	*median*	*mean*	*min*	*max*	*2stddv*	*AvgDL*
La_2O_3	11.6	11.8	11.5	11.5	11.2	9.8	*11.5*	*11.2*	*9.8*	*11.8*	*1.3*	0.01
Ce_2O_3	9.2	10.7	9.9	9.3	9.8	9.8	*9.8*	*9.8*	*9.2*	*10.7*	*1.0*	0.02
Pr_2O_3	0.38	0.36	0.49	0.36	0.47	0.47	*0.42*	*0.42*	*0.36*	*0.49*	*0.1*	0.07
Nd_2O_3	0.41	0.64	0.61	0.54	0.63	0.68	*0.62*	*0.58*	*0.41*	*0.68*	*0.2*	0.06
Sm_2O_3	-	-	-	-	-	-	-	-	-	-	-	0.07
Eu_2O_3	-	0.05	-	-	-	-	*0.05*	*0.05*	*0.05*	*0.05*	-	0.04
Gd_2O_3	-	-	-	-	-	-	-	-	-	-	-	0.07
Tb_2O_3	0.04	-	-	0.05	-	-	*0.04*	*0.04*	*0.04*	*0.05*	*0.01*	0.04
Dy_2O_3	-	-	-	-	-	-	-	-	-	-	-	0.04
Ho_2O_3	-	0.09	-	-	-	-	*0.09*	*0.09*	*0.09*	*0.09*	-	0.09
Er_2O_3	-	-	-	-	-	-	-	-	-	-	-	0.04
Yb_2O_3	-	-	-	-	0.05	0.05	*0.05*	*0.05*	*0.05*	*0.05*	*0.00*	0.05
Y_2O_3	-	-	-	-	-	-	-	-	-	-	-	0.02
$\sum REY_2O_3$	*21.6*	*23.7*	*22.5*	*21.8*	*22.2*	*20.8*	*22.0*	*22.1*	*20.8*	*23.7*	*1.74*	
CaO	0.16	0.17	0.11	0.22	0.22	0.46	*0.19*	*0.22*	*0.11*	*0.46*	*0.2*	0.01
SrO	3.45	3.58	3.73	3.27	3.37	3.23	*3.41*	*3.44*	*3.23*	*3.73*	*0.3*	0.01
PbO	-	-	-	-	-	-	-	-	-	-	-	0.02
ThO_2	0.02	-	-	-	0.02	-	*0.02*	*0.02*	*0.02*	*0.02*	*0.01*	0.02
UO_2	-	0.02	-	-	0.02	0.03	*0.02*	*0.03*	*0.02*	*0.03*	*0.01*	0.02
Na_2O	-	0.05	-	-	0.03	0.05	*0.05*	*0.05*	*0.03*	*0.05*	*0.02*	0.02
K_2O	0.05	0.23	0.01	0.08	0.11	0.20	*0.10*	*0.12*	*0.01*	*0.23*	*0.15*	0.01
Al_2O_3	28.9	30.5	30.2	29.4	30.7	29.2	*29.8*	*29.8*	*28.9*	*30.7*	*1.4*	0.02
FeO	0.31	0.66	1.31	0.90	1.51	1.61	*1.10*	*1.05*	*0.31*	*1.61*	*0.9*	0.04
P_2O_5	24.6	23.1	24.8	24.8	24.3	23.5	*24.5*	*24.2*	*23.1*	*24.8*	*1.3*	0.02
SO_3	3.57	3.50	3.81	3.68	3.48	3.68	*3.62*	*3.62*	*3.48*	*3.81*	*0.2*	0.03
As_2O_5	0.11	0.06	0.06	0.07	0.09	0.05	*0.07*	*0.07*	*0.05*	*0.11*	*0.04*	0.02
Nb_2O_5	-	0.02	-	0.23	-	-	*0.12*	*0.12*	*0.02*	*0.23*	*0.21*	0.02
SiO_2	-	0.04	-	-	-	-	*0.04*	*0.04*	*0.04*	*0.04*	-	0.02
F	0.15	0.21	0.05	0.11	0.07	0.16	*0.13*	*0.12*	*0.05*	*0.21*	*0.1*	0.02
Cl	0.06	0.11	0.05	0.03	0.11	0.05	*0.06*	*0.07*	*0.03*	*0.11*	*0.1*	0.01
Total	*83.0*	*86.0*	*86.6*	*84.6*	*86.2*	*83.0*	*85.3*	*84.9*	*83.0*	*86.6*	*2.95*	
apfu												
La	0.38	0.38	0.37	0.37	0.36	0.33	*0.37*	*0.37*	*0.33*	*0.38*	*0.04*	
Ce	0.30	0.35	0.31	0.30	0.31	0.32	*0.31*	*0.32*	*0.30*	*0.35*	*0.03*	
Pr	0.01	0.01	0.02	0.01	0.01	0.02	*0.01*	*0.01*	*0.01*	*0.02*	*0.00*	
Nd	0.01	0.02	0.02	0.02	0.02	0.02	*0.02*	*0.02*	*0.01*	*0.02*	*0.01*	
Sm	-	-	-	-	-	-	-	-	-	-	-	
Eu	-	0.00	-	-	-	-	*0.00*	*0.00*	*0.00*	*0.00*	-	
Gd	-	-	-	-	-	-	-	-	-	-	-	
Tb	0.00	-	-	0.00	-	-	*0.00*	*0.00*	*0.00*	*0.00*	*0.00*	
Dy	-	-	-	-	-	-	-	-	-	-	-	
Ho	-	0.00	-	-	-	-	*0.00*	*0.00*	*0.00*	*0.00*	-	
Er	-	-	-	-	-	-	-	-	-	-	-	
Yb	-	-	-	-	0.00	0.00	*0.00*	*0.00*	*0.00*	*0.00*	*0.00*	
Y	-	-	-	-	-	-	-	-	-	-	-	
$\sum REY$	*0.71*	*0.77*	*0.72*	*0.70*	*0.71*	*0.69*	*0.71*	*0.72*	*0.69*	*0.77*	*0.05*	
Ca	0.02	0.02	0.01	0.02	0.02	0.04	*0.02*	*0.02*	*0.01*	*0.04*	*0.02*	
Sr	0.18	0.18	0.19	0.17	0.17	0.17	*0.17*	*0.18*	*0.17*	*0.19*	*0.02*	
Pb	-	-	-	-	-	-	-	-	-	-	-	
Th	0.00	-	-	-	0.00	-	*0.00*	*0.00*	*0.00*	*0.00*	*0.00*	
U	-	0.00	-	-	0.00	0.00	*0.00*	*0.00*	*0.00*	*0.00*	*0.00*	
Na	-	0.01	-	-	0.01	0.01	*0.01*	*0.01*	*0.01*	*0.01*	*0.00*	
K	0.01	0.03	0.00	0.01	0.01	0.02	*0.01*	*0.01*	*0.00*	*0.03*	*0.02*	
Total (D)	*0.91*	*1.00*	*0.92*	*0.90*	*0.92*	*0.94*	*0.92*	*0.93*	*0.90*	*1.00*	*0.07*	
Al	3.05	3.18	3.09	3.06	3.15	3.10	*3.09*	*3.11*	*3.05*	*3.18*	*0.10*	
Fe	0.02	0.05	0.09	0.07	0.11	0.12	*0.08*	*0.08*	*0.02*	*0.12*	*0.07*	
Total (G)	*3.08*	*3.23*	*3.18*	*3.12*	*3.26*	*3.23*	*3.20*	*3.18*	*3.08*	*3.26*	*0.13*	
P	1.87	1.73	1.82	1.85	1.79	1.79	*1.81*	*1.81*	*1.73*	*1.87*	*0.09*	
S	0.20	0.19	0.21	0.20	0.19	0.21	*0.20*	*0.20*	*0.19*	*0.21*	*0.01*	
As	0.01	0.00	0.00	0.00	0.00	0.00	*0.00*	*0.00*	*0.00*	*0.01*	*0.00*	
Nb	-	0.00	-	0.01	-	-	*0.01*	*0.01*	*0.00*	*0.01*	*0.01*	
Si	-	0.00	-	-	-	-	*0.00*	*0.00*	*0.00*	*0.00*	-	
Total (T)	*2.07*	*1.93*	*2.03*	*2.07*	*1.98*	*2.00*	*2.02*	*2.02*	*1.93*	*2.07*	*0.10*	
O	8.00	8.00	8.00	8.00	8.00	8.00	*8.00*	*8.00*	*8.00*	*8.00*	-	
F=O	0.04	0.06	0.01	0.03	0.02	0.04	*0.04*	*0.04*	*0.01*	*0.06*	*0.03*	
OH	5.96	5.94	5.99	5.97	5.98	5.96	*5.96*	*5.96*	*5.94*	*5.99*	*0.03*	
% Flor-La	*53.9*	*50.0*	*51.2*	*53.0*	*50.8*	*47.1*	*51.0*	*51.0*	*47.1*	*53.9*	*4.3*	
% Flor-Ce	*42.4*	*45.3*	*43.7*	*42.4*	*44.2*	*46.9*	*43.9*	*44.1*	*42.4*	*46.9*	*3.2*	
% Flor-Nd	*1.83*	*2.64*	*2.62*	*2.39*	*2.75*	*3.18*	*2.63*	*2.57*	*1.83*	*3.18*	*0.81*	
cation sum	*6.06*	*6.17*	*6.13*	*6.09*	*6.17*	*6.17*	*6.15*	*6.13*	*6.06*	*6.17*	*0.08*	

	RX6711 (n=6)												RX6712 (n=1)	
	1	2	3	4	5	6	*median*	*mean*	*min*	*max*	*2stddv*	*AvgDL*	1	*DL*
La_2O_3	9.7	7.0	10.6	6.9	6.8	10.1	*8.3*	*8.5*	*6.8*	*10.6*	*3.3*	0.01	14.4	0.02
Ce_2O_3	9.5	6.3	10.1	6.2	6.6	9.7	*8.1*	*8.1*	*6.2*	*10.1*	*3.4*	0.01	10.9	0.02
Pr_2O_3	0.41	0.28	0.34	-	0.25	0.42	*0.34*	*0.34*	*0.25*	*0.42*	*0.1*	0.07	0.39	0.07
Nd_2O_3	0.78	0.22	0.61	0.10	0.40	0.79	*0.50*	*0.48*	*0.10*	*0.79*	*0.5*	0.06	0.31	0.07
Sm_2O_3	-	-	0.02	-	-	-	*0.02*	*0.02*	*0.02*	*0.02*	-	0.07	-	0.08
Eu_2O_3	-	-	-	-	-	-	-	-	-	-	-	0.04	-	0.04
Gd_2O_3	-	-	-	-	-	-	-	-	-	-	-	0.07	-	0.07
Tb_2O_3	0.04	-	0.04	-	-	-	*0.04*	*0.04*	*0.04*	*0.04*	*0.00*	0.04	-	0.04
Dy_2O_3	-	-	-	-	-	-	-	-	-	-	-	0.04	-	0.04
Ho_2O_3	-	0.16	0.10	0.08	0.27	0.08	*0.10*	*0.14*	*0.08*	*0.27*	*0.1*	0.08	-	0.09
Er_2O_3	-	-	-	-	-	-	-	-	-	-	-	0.04	-	0.05
Yb_2O_3	-	0.11	0.03	-	0.05	0.06	*0.06*	*0.06*	*0.03*	*0.11*	*0.1*	0.05	0.05	0.05
Y_2O_3	-	-	-	-	-	-	-	-	-	-	-	0.02	-	0.02
$\sum REY_2O_3$	*20.4*	*14.0*	*21.8*	*13.2*	*14.4*	*21.2*	*17.4*	*17.5*	*13.2*	*21.8*	*7.4*		*26.0*	
CaO	0.18	0.14	0.16	0.16	0.17	0.16	*0.16*	*0.16*	*0.14*	*0.18*	*0.0*	0.01	0.12	0.01
SrO	6.14	5.42	5.16	4.89	5.40	6.72	*5.41*	*5.62*	*4.89*	*6.72*	*1.2*	0.01	0.82	0.01
PbO	-	-	0.02	0.05	-	0.02	*0.02*	*0.03*	*0.02*	*0.05*	*0.0*	0.02	-	0.02
ThO_2	0.02	-	-	0.04	0.03	-	*0.03*	*0.03*	*0.02*	*0.04*	*0.0*	0.02	-	0.02
UO_2	-	-	-	-	0.02	-	*0.02*	*0.02*	*0.02*	*0.02*	-	0.02	-	0.02
Na_2O	-	-	-	-	-	-	-	-	-	-	-	0.02	-	0.03
K_2O	0.06	0.04	0.06	0.05	0.07	0.04	*0.06*	*0.06*	*0.04*	*0.07*	*0.0*	0.01	0.03	0.01
Al_2O_3	31.6	28.7	32.3	30.7	28.9	33.6	*31.2*	*31.0*	*28.7*	*33.6*	*3.5*	0.02	30.3	0.02
FeO	1.19	0.97	1.39	0.80	0.93	1.61	*1.08*	*1.15*	*0.80*	*1.61*	*0.6*	0.04	0.19	0.04
P_2O_5	19.1	20.8	19.3	20.7	20.4	19.0	*19.8*	*19.9*	*19.0*	*20.8*	*1.6*	0.02	21.0	0.02
SO_3	5.80	5.15	5.33	5.30	5.51	5.92	*5.42*	*5.50*	*5.15*	*5.92*	*0.6*	0.03	0.88	0.03
As_2O_5	0.11	0.22	0.24	0.13	0.18	0.07	*0.16*	*0.16*	*0.07*	*0.24*	*0.1*	0.02	3.50	0.02
Nb_2O_5	-	0.04	0.02	-	-	-	*0.03*	*0.03*	*0.02*	*0.04*	*0.0*	0.02	0.02	0.02
SiO_2	-	-	-	-	-	-	-	-	-	-	-	0.02	-	0.02
F	0.12	0.18	0.09	0.25	0.17	0.11	*0.14*	*0.15*	*0.09*	*0.25*	*0.1*	0.02	0.11	0.02
Cl	0.02	0.04	0.04	0.02	0.04	0.01	*0.03*	*0.03*	*0.01*	*0.04*	*0.0*	0.01	0.06	0.01
Total	*84.8*	*75.8*	*85.9*	*76.3*	*76.2*	*88.4*	*80.6*	*81.2*	*75.8*	*88.4*	*10.5*		*83.1*	
apfu														
La	0.33	0.25	0.35	0.24	0.24	0.33	*0.29*	*0.29*	*0.24*	*0.35*	*0.10*		0.49	
Ce	0.32	0.22	0.34	0.21	0.23	0.31	*0.27*	*0.27*	*0.21*	*0.34*	*0.10*		0.37	
Pr	0.01	0.01	0.01	-	0.01	0.01	*0.01*	*0.01*	*0.01*	*0.01*	*0.00*		0.01	
Nd	0.03	0.01	0.02	0.00	0.01	0.03	*0.02*	*0.02*	*0.00*	*0.03*	*0.02*		0.01	
Sm	-	-	0.00	-	-	-	*0.00*	*0.00*	*0.00*	*0.00*	-		-	
Eu	-	-	-	-	-	-	-	-	-	-	-		-	
Gd	-	-	-	-	-	-	-	-	-	-	-		-	
Tb	0.00	-	0.00	-	-	-	0.00	0.00	0.00	0.00	0.00		-	
Dy	-	-	-	-	-	-	-	-	-	-	-		-	
Ho	-	0.00	0.00	0.00	0.01	0.00	*0.00*	*0.00*	*0.00*	*0.00*	*0.01*	*0.00*	-	
Er	-	-	-	-	-	-	-	-	-	-	-		-	
Yb	-	-	-	0.00	0.00	0.00	*0.00*	*0.00*	*0.00*	*0.00*	*0.00*	*0.00*	0.00	
Y	-	-	-	-	-	-	-	-	-	-	-		-	
$\sum REY$	*0.69*	*0.50*	*0.72*	*0.46*	*0.51*	*0.69*	*0.60*	*0.59*	*0.46*	*0.72*	*0.22*		*0.89*	
Ca	0.02	0.01	0.02	0.02	0.02	0.02	*0.02*	*0.02*	*0.01*	*0.02*	*0.00*		0.01	
Sr	0.33	0.30	0.27	0.27	0.30	0.34	*0.30*	*0.30*	*0.27*	*0.34*	*0.05*		0.04	
Pb	-	-	0.00	0.00	-	0.00	*0.00*	*0.00*	*0.00*	*0.00*	*0.00*		-	
Th	0.00	-	-	0.00	0.00	-	*0.00*	*0.00*	*0.00*	*0.00*	*0.00*		-	
U	-	-	-	-	0.00	-	0.00	0.00	0.00	0.00	-		-	
Na	-	-	-	-	-	-	-	-	-	-	-		-	
K	0.01	0.01	0.01	0.01	0.01	0.00	*0.01*	*0.01*	*0.00*	*0.01*	*0.00*		0.00	
Total (D)	*1.04*	*0.82*	*1.02*	*0.75*	*0.84*	*1.05*	*0.93*	*0.92*	*0.75*	*1.05*	*0.24*		*0.95*	
Al	3.41	3.27	3.45	3.41	3.29	3.49	*3.41*	*3.39*	*3.27*	*3.49*	*0.17*		3.33	
Fe	0.09	0.08	0.11	0.06	0.08	0.12	*0.08*	*0.09*	*0.06*	*0.12*	*0.04*		0.01	
Total (G)	*3.50*	*3.34*	*3.55*	*3.47*	*3.36*	*3.61*	*3.49*	*3.47*	*3.34*	*3.61*	*0.19*		*3.35*	
P	1.48	1.70	1.48	1.65	1.67	1.42	*1.57*	*1.57*	*1.42*	*1.70*	*0.22*		1.66	
S	0.33	0.31	0.30	0.31	0.33	0.33	*0.32*	*0.32*	*0.30*	*0.33*	*0.02*		0.05	
As	0.01	0.01	0.01	0.01	0.01	0.00	*0.01*	*0.01*	*0.00*	*0.01*	*0.01*		0.20	
Nb	-	0.00	0.00	-	-	-	*0.00*	*0.00*	*0.00*	*0.00*	*0.00*		0.00	
Si	-	-	-	-	-	-	-	-	-	-	-		-	
Total (T)	*1.82*	*2.03*	*1.79*	*1.97*	*2.01*	*1.75*	*1.90*	*1.89*	*1.75*	*2.03*	*0.22*		*1.91*	
O	8.00	8.00	8.00	8.00	8.00	8.00	*8.00*	*8.00*	*8.00*	*8.00*	-		8.00	
F=O	0.04	0.06	0.02	0.07	0.05	0.03	*0.04*	*0.04*	*0.02*	*0.07*	*0.03*		0.03	
OH	5.96	5.94	5.98	5.93	5.95	5.97	*5.96*	*5.95*	*5.93*	*5.98*	*0.03*		5.97	
% Flor-La	*47.7*	*49.9*	*48.7*	*52.2*	*47.8*	*48.0*	*48.3*	*49.1*	*47.7*	*52.2*	*3.22*		*55.3*	
% Flor-Ce	*46.3*	*44.9*	*46.2*	*46.5*	*45.8*	*45.7*	*46.0*	*45.9*	*44.9*	*46.5*	*1.05*		*41.7*	
% Flor-Nd	*3.70*	*1.51*	*2.70*	*0.71*	*2.70*	*3.64*	*2.70*	*2.49*	*0.71*	*3.70*	*2.16*		*1.14*	
cation sum	*6.36*	*6.19*	*6.36*	*6.20*	*6.21*	*6.42*	*6.29*	*6.29*	*6.19*	*6.42*	*0.19*		*6.21*	

	RX6713 (n=9)													
	1	2	3	4	5	6	7	8	9	*median*	*mean*	*min*	*max*	*2stddv*	*AvgDL*
La_2O_3	4.0	10.7	10.7	10.9	12.1	10.9	11.4	11.1	11.3	*10.9*	*10.3*	*4.0*	*12.1*	*4.6*	0.01
Ce_2O_3	13.1	13.0	14.1	13.9	13.9	14.6	14.9	14.7	15.0	*14.1*	*14.1*	*13.0*	*15.0*	*1.4*	0.02
Pr_2O_3	0.66	0.67	0.77	0.73	0.67	0.91	0.82	0.84	0.82	*0.77*	*0.77*	*0.66*	*0.91*	*0.2*	0.07
Nd_2O_3	1.06	1.00	1.27	1.23	1.07	1.52	1.38	1.55	1.63	*1.27*	*1.30*	*1.00*	*1.63*	*0.4*	0.06
Sm_2O_3	-	-	-	-	-	-	-	-	0.10	*0.10*	*0.10*	*0.10*	*0.10*	-	0.07
Eu_2O_3	-	-	-	-	-	-	0.04	-	0.11	*0.07*	*0.07*	*0.04*	*0.11*	*0.08*	0.04
Gd_2O_3	-	-	-	-	-	-	-	-	-	-	-	-	-	-	0.08
Tb_2O_3	-	-	-	-	-	-	0.05	0.05	0.05	*0.05*	*0.05*	*0.05*	*0.05*	*0.00*	0.04
Dy_2O_3	-	-	-	-	-	-	-	-	0.06	*0.06*	*0.06*	*0.06*	*0.06*	-	0.04
Ho_2O_3	-	-	-	-	-	-	-	0.09	-	0.09	0.09	0.09	0.09	-	0.09
Er_2O_3	-	-	-	-	-	-	-	-	-	-	-	-	-	-	0.05
Yb_2O_3	-	-	0.12	0.05	0.11	0.12	0.31	0.23	-	*0.12*	*0.16*	*0.05*	*0.31*	*0.2*	0.05
Y_2O_3	0.02	0.02	-	0.02	-	-	-	-	0.02	*0.02*	*0.02*	*0.02*	*0.02*	*0.0*	0.02
$\sum REY_2O_3$	*18.9*	*25.3*	*26.9*	*26.8*	*27.9*	*28.0*	*28.9*	*28.6*	*29.1*	*27.9*	*26.7*	*18.9*	*29.1*	*6.0*	
CaO	0.60	0.34	0.36	0.22	0.28	0.19	0.35	0.42	2.64	*0.35*	*0.60*	*0.19*	*2.64*	*1.5*	0.01
SrO	0.62	1.77	1.83	1.76	1.74	1.51	1.97	2.19	1.94	*1.77*	*1.70*	*0.62*	*2.19*	*0.8*	0.01
PbO	-	-	-	-	0.02	-	-	-	-	*0.02*	*0.02*	*0.02*	*0.02*	-	0.02
ThO_2	-	-	-	-	-	-	-	-	-	-	-	-	-	-	0.02
UO_2	0.53	0.10	0.07	-	0.09	0.03	-	-	-	*0.09*	*0.16*	*0.03*	*0.53*	*0.4*	0.02
Na_2O	-	-	-	-	-	-	0.08	-	0.03	*0.05*	*0.05*	*0.03*	*0.08*	*0.1*	0.03
K_2O	0.62	0.43	0.14	0.03	0.14	0.10	1.15	0.02	0.47	*0.14*	*0.34*	*0.02*	*1.15*	*0.7*	0.01
Al_2O_3	27.1	32.1	30.3	31.5	29.9	30.9	33.1	31.8	30.4	*30.9*	*30.8*	*27.1*	*33.1*	*3.2*	0.02
FeO	1.64	1.58	1.80	2.80	1.67	5.03	5.19	2.26	1.88	*1.88*	*2.65*	*1.58*	*5.19*	*2.7*	0.04
P_2O_5	18.7	19.4	20.4	20.7	20.7	18.9	15.6	20.2	16.8	*19.4*	*19.0*	*15.6*	*20.7*	*3.4*	0.02
SO_3	1.57	1.63	1.32	0.91	1.45	1.47	2.07	1.62	1.30	*1.47*	*1.48*	*0.91*	*2.07*	*0.6*	0.03
As_2O_5	-	-	0.02	0.04	0.02	-	0.04	0.05	-	*0.04*	*0.03*	*0.02*	*0.05*	*0.02*	0.02
Nb_2O_5	0.02	0.02	-	0.02	-	-	-	-	-	*0.02*	*0.02*	*0.02*	*0.02*	*0.00*	0.02
SiO_2	-	0.14	-	-	-	-	2.83	-	-	*1.49*	*1.49*	*0.14*	*2.83*	*2.7*	0.02
F	0.43	0.16	0.18	0.12	0.22	0.06	-	0.13	0.73	*0.17*	*0.25*	*0.06*	*0.73*	*0.4*	0.02
Cl	0.08	0.06	0.05	0.03	0.03	0.02	0.03	0.02	0.07	*0.03*	*0.04*	*0.02*	*0.08*	*0.0*	0.01
Total	*70.8*	*83.0*	*83.4*	*84.9*	*84.1*	*86.2*	*91.3*	*87.2*	*85.4*	*84.9*	*84.0*	*70.8*	*91.3*	*10.5*	
apfu															
La	0.15	0.37	0.37	0.37	0.42	0.37	0.38	0.37	0.40	*0.37*	*0.36*	*0.15*	*0.42*	*0.15*	
Ce	0.51	0.44	0.48	0.47	0.48	0.50	0.49	0.49	0.52	*0.49*	*0.49*	*0.44*	*0.52*	*0.04*	
Pr	0.03	0.02	0.03	0.02	0.02	0.03	0.03	0.03	0.03	*0.03*	*0.03*	*0.02*	*0.03*	*0.01*	
Nd	0.04	0.03	0.04	0.04	0.04	0.05	0.04	0.05	0.06	*0.04*	*0.04*	*0.03*	*0.06*	*0.01*	
Sm	-	-	-	-	-	-	-	-	0.00	*0.00*	*0.00*	*0.00*	*0.00*	-	
Eu	-	-	-	-	-	-	0.00	-	0.00	0.00	0.00	0.00	0.00	0.00	
Gd	-	-	-	-	-	-	-	-	-	-	-	-	-	-	
Tb	-	-	-	-	-	-	0.00	0.00	0.00	0.00	0.00	0.00	0.00	0.00	
Dy	-	-	-	-	-	-	-	-	0.00	0.00	0.00	0.00	0.00	-	
Ho	-	-	-	-	-	-	-	0.00	-	0.00	0.00	0.00	0.00	-	
Er	-	-	-	-	-	-	-	-	-	-	-	-	-	-	
Yb	-	-	0.00	0.00	0.00	0.00	0.01	0.01	-	*0.00*	*0.00*	*0.00*	*0.01*	*0.00*	
Y	0.00	0.00	-	0.00	-	-	-	-	0.00	*0.00*	*0.00*	*0.00*	*0.00*	*0.00*	
$\sum REY$	*0.73*	*0.87*	*0.93*	*0.90*	*0.96*	*0.96*	*0.95*	*0.95*	*1.02*	*0.95*	*0.92*	*0.73*	*1.02*	*0.16*	
Ca	0.07	0.03	0.04	0.02	0.03	0.02	0.03	0.04	0.27	*0.03*	*0.06*	*0.02*	*0.27*	*0.15*	
Sr	0.04	0.10	0.10	0.09	0.09	0.08	0.10	0.12	0.11	*0.10*	*0.09*	*0.04*	*0.12*	*0.04*	
Pb	-	-	-	-	0.00	-	-	-	-	0.00	0.00	0.00	0.00	-	
Th	-	-	-	-	-	-	-	-	-	-	-	-	-	-	
U	0.01	0.00	0.00	-	0.00	0.00	-	-	-	*0.00*	*0.00*	*0.00*	*0.01*	*0.01*	
Na	-	-	-	-	-	-	0.01	-	0.01	*0.01*	*0.01*	*0.01*	*0.01*	*0.01*	
K	0.08	0.05	0.02	0.00	0.02	0.01	0.13	0.00	0.06	*0.02*	*0.04*	*0.00*	*0.13*	*0.08*	
Total (D)	*0.93*	*1.05*	*1.08*	*1.02*	*1.10*	*1.07*	*1.23*	*1.11*	*1.46*	*1.08*	*1.12*	*0.93*	*1.46*	*0.28*	
Al	3.37	3.53	3.36	3.41	3.31	3.41	3.51	3.41	3.42	*3.41*	*3.41*	*3.31*	*3.53*	*0.13*	
Fe	0.14	0.12	0.14	0.22	0.13	0.39	0.39	0.17	0.15	*0.15*	*0.21*	*0.12*	*0.39*	*0.20*	
Total (G)	*3.51*	*3.66*	*3.50*	*3.63*	*3.44*	*3.80*	*3.90*	*3.59*	*3.57*	*3.59*	*3.62*	*3.44*	*3.90*	*0.28*	
P	1.67	1.54	1.62	1.61	1.64	1.50	1.18	1.56	1.36	*1.56*	*1.52*	*1.18*	*1.67*	*0.30*	
S	0.10	0.10	0.08	0.05	0.08	0.09	0.12	0.09	0.08	*0.09*	*0.09*	*0.05*	*0.12*	*0.03*	
As	-	-	0.00	0.00	0.00	-	0.00	0.00	-	*0.00*	*0.00*	*0.00*	*0.00*	*0.00*	
Nb	0.00	0.00	-	0.00	-	-	-	-	-	0.00	0.00	0.00	0.00	0.00	
Si	-	0.01	-	-	-	-	0.25	-	-	*0.13*	*0.13*	*0.01*	*0.25*	*0.24*	
Total (T)	*1.77*	*1.65*	*1.70*	*1.67*	*1.72*	*1.58*	*1.56*	*1.65*	*1.43*	*1.65*	*1.64*	*1.43*	*1.77*	*0.19*	
O	8.00	8.00	8.00	8.00	8.00	8.00	8.00	8.00	9.00	*8.00*	*8.11*	*8.00*	*9.00*	*0.63*	
F=O	0.14	0.05	0.05	0.04	0.06	0.02	-	0.04	0.22	*0.05*	*0.08*	*0.02*	*0.22*	*0.13*	
OH	5.86	5.95	5.95	5.96	5.94	5.98	6.00	5.96	5.78	*5.95*	*5.93*	*5.78*	*6.00*	*0.13*	
% Flor-La	*21.1*	*42.3*	*39.8*	*40.9*	*43.6*	*39.0*	*39.6*	*39.1*	*39.2*	*39.6*	*38.3*	*21.1*	*43.6*	*12.5*	
% Flor-Ce	*69.4*	*51.1*	*52.0*	*51.7*	*49.7*	*51.9*	*51.6*	*51.4*	*51.4*	*51.6*	*53.4*	*49.7*	*69.4*	*11.4*	
% Flor-Nd	*5.46*	*3.83*	*4.59*	*4.47*	*3.73*	*5.28*	*4.67*	*5.31*	*5.47*	*4.67*	*4.76*	*3.73*	*5.47*	*1.3*	
cation sum	*6.22*	*6.35*	*6.29*	*6.32*	*6.26*	*6.46*	*6.69*	*6.35*	*6.47*	*6.35*	*6.38*	*6.22*	*6.69*	*0.3*	

- indicates below detection limit
Flor = florencite
REY = REE + Y
AvgDL = Average detection limit for that element in that sample

RX6714 (n=4)

1	2	3	4	median	mean	min	max	2stddv	AvgDL
13.3	14.6	13.0	14.7	14.0	13.9	13.0	14.7	1.6	0.02
13.7	14.5	12.7	14.0	13.8	13.7	12.7	14.5	1.3	0.02
0.66	0.31	0.39	0.42	0.41	0.44	0.31	0.66	0.3	0.07
1.47	0.44	0.38	0.67	0.56	0.74	0.38	1.47	0.9	0.06
-	-	-	-	-	-	-	-	-	0.07
-	-	-	-	-	-	-	-	-	0.04
-	-	-	-	-	-	-	-	-	0.08
-	-	-	-	-	-	-	-	-	0.04
-	-	-	-	-	-	-	-	-	0.04
-	-	-	-	-	-	-	-	-	0.09
-	-	-	-	-	-	-	-	-	0.05
-	0.22	0.22	-	0.22	0.22	0.22	0.22	0.0	0.05
0.02	0.04	0.02	0.03	0.03	0.03	0.02	0.04	0.0	0.02
29.1	30.1	26.7	29.8	29.5	28.9	26.7	30.1	2.7	
0.33	0.22	0.24	0.34	0.29	0.28	0.22	0.34	0.1	0.01
1.28	0.98	1.20	1.14	1.17	1.15	0.98	1.28	0.2	0.01
-	0.03	-	0.02	0.02	0.02	0.02	0.03	0.0	0.02
-	-	-	-	-	-	-	-	-	0.02
0.23	0.10	0.06	-	0.10	0.13	0.06	0.23	0.2	0.02
0.12	0.04	0.02	0.07	0.06	0.07	0.02	0.12	0.1	0.02
0.16	0.20	0.29	0.05	0.18	0.17	0.05	0.29	0.2	0.01
30.4	29.2	31.5	29.8	30.1	30.2	29.2	31.5	1.7	0.02
1.53	0.64	0.89	4.13	1.21	1.80	0.64	4.13	2.8	0.04
17.5	19.3	19.4	18.9	19.1	18.8	17.5	19.4	1.6	0.02
1.24	1.11	0.97	1.05	1.08	1.09	0.97	1.24	0.2	0.03
0.70	0.78	0.44	0.49	0.59	0.60	0.44	0.78	0.3	0.02
-	-	-	0.02	0.02	0.02	0.02	0.02	-	0.02
-	-	0.50	-	0.50	0.50	0.50	0.50	-	0.02
0.14	0.16	0.29	0.36	0.23	0.24	0.14	0.36	0.2	0.02
0.06	0.08	0.03	0.06	0.06	0.06	0.03	0.08	0.04	0.01
82.8	82.9	82.5	86.3	82.8	83.6	82.5	86.3	3.1	
0.48	0.52	0.45	0.51	0.50	0.49	0.45	0.52	0.06	
0.49	0.51	0.44	0.48	0.49	0.48	0.44	0.51	0.06	
0.02	0.01	0.01	0.01	0.01	0.02	0.01	0.02	0.01	
0.05	0.02	0.01	0.02	0.02	0.03	0.01	0.05	0.03	
-	-	-	-	-	-	-	-	-	
-	-	-	-	-	-	-	-	-	
-	-	-	-	-	-	-	-	-	
-	-	-	-	-	-	-	-	-	
-	-	-	-	-	-	-	-	-	
-	-	-	-	-	-	-	-	-	
-	-	-	-	-	-	-	-	-	
-	0.01	0.01	-	0.01	0.01	0.01	0.01	0.00	
0.00	0.00	0.00	0.00	0.00	0.00	0.00	0.00	0.00	
1.05	1.07	0.92	1.03	1.04	1.02	0.92	1.07	0.12	
0.04	0.02	0.02	0.03	0.03	0.03	0.02	0.04	0.01	
0.07	0.06	0.07	0.06	0.06	0.06	0.06	0.07	0.01	
-	0.00	-	0.00	0.00	0.00	0.00	0.00	0.00	
-	-	-	-	-	-	-	-	-	
0.01	0.00	0.00	-	0.00	0.00	0.00	0.01	0.00	
0.02	0.01	0.00	0.01	0.01	0.01	0.00	0.02	0.01	
0.02	0.02	0.03	0.01	0.02	0.02	0.01	0.03	0.02	
1.20	1.19	1.05	1.15	1.17	1.15	1.05	1.20	0.12	
3.51	3.34	3.49	3.31	3.41	3.41	3.31	3.51	0.18	
0.13	0.05	0.07	0.33	0.10	0.14	0.05	0.33	0.22	
3.64	3.39	3.56	3.63	3.60	3.55	3.39	3.64	0.20	
1.45	1.59	1.55	1.51	1.53	1.52	1.45	1.59	0.10	
0.08	0.07	0.06	0.06	0.06	0.07	0.06	0.08	0.01	
0.04	0.05	0.03	0.03	0.03	0.04	0.03	0.05	0.02	
-	-	-	0.00	0.00	0.00	0.00	0.00	-	
-	-	0.05	-	0.05	0.05	0.05	0.05	-	
1.57	1.70	1.67	1.60	1.64	1.64	1.57	1.70	0.11	
8.00	8.00	8.00	8.00	8.00	8.00	8.00	8.00	-	
0.04	0.05	0.09	0.11	0.07	0.07	0.04	0.11	0.05	
5.96	5.95	5.91	5.89	5.93	5.93	5.89	5.96	0.05	
45.8	48.8	48.9	49.6	48.9	48.3	45.8	49.6	2.9	
46.9	47.9	47.5	46.6	47.2	47.2	46.6	47.9	1.0	
4.90	1.42	1.38	2.20	1.81	2.47	1.38	4.90	2.9	
6.41	6.28	6.29	6.38	6.33	6.34	6.28	6.41	0.1	

RX6720 (n=3)

1	2	3	median	mean	min	max	2stddv	AvgDL
11.2	11.3	11.2	11.2	11.2	11.2	11.3	0.1	0.01
11.1	11.1	11.7	11.1	11.3	11.1	11.7	0.5	0.02
0.56	0.46	0.42	0.46	0.48	0.42	0.56	0.1	0.07
0.84	0.70	0.69	0.70	0.74	0.69	0.84	0.1	0.06
-	-	-	-	-	-	-	-	0.07
0.04	0.04	0.05	0.04	0.04	0.04	0.05	0.0	0.04
-	-	-	-	-	-	-	-	0.07
-	-	-	-	-	-	-	-	0.04
-	-	-	-	-	-	-	-	0.04
-	-	-	-	-	-	-	-	0.09
-	0.05	-	0.05	0.05	0.05	0.05	-	0.04
-	-	-	-	-	-	-	-	0.05
0.04	0.02	-	0.03	0.03	0.02	0.04	0.0	0.02
23.8	23.6	24.0	23.8	23.8	23.6	24.0	0.3	
0.21	0.25	0.24	0.24	0.23	0.21	0.25	0.0	0.01
2.17	2.19	2.59	2.19	2.32	2.17	2.59	0.4	0.01
-	0.02	0.02	0.02	0.02	0.02	0.02	0.01	0.02
-	0.02	-	0.02	0.02	0.02	0.02	-	0.02
-	-	-	-	-	-	-	-	0.02
-	-	0.02	0.02	0.02	0.02	0.02	-	0.02
0.02	0.02	0.01	0.02	0.02	0.01	0.02	0.0	0.01
29.6	27.1	27.6	27.6	28.1	27.1	29.6	2.1	0.02
1.47	2.08	1.61	1.61	1.72	1.47	2.08	0.5	0.04
25.7	25.7	25.6	25.7	25.7	25.6	25.7	0.1	0.02
1.73	1.80	1.74	1.74	1.76	1.73	1.80	0.1	0.03
0.06	0.04	0.02	0.04	0.04	0.02	0.06	0.0	0.02
-	-	-	-	-	-	-	-	0.02
-	-	-	-	-	-	-	-	0.02
0.18	0.21	0.16	0.18	0.18	0.16	0.21	0.0	0.02
0.03	0.03	0.03	0.03	0.03	0.03	0.03	0.0	0.01
85.0	83.1	83.6	83.6	83.9	83.1	85.0	1.6	
0.36	0.38	0.37	0.37	0.37	0.36	0.38	0.01	
0.36	0.37	0.39	0.37	0.37	0.36	0.39	0.02	
0.02	0.02	0.01	0.02	0.02	0.01	0.02	0.00	
0.03	0.02	0.02	0.02	0.02	0.02	0.03	0.00	
-	-	-	-	-	-	-	-	
0.00	0.00	0.00	0.00	0.00	0.00	0.00	0.00	
-	-	-	-	-	-	-	-	
-	-	-	-	-	-	-	-	
-	-	-	-	-	-	-	-	
-	-	-	-	-	-	-	-	
-	-	-	-	-	-	-	-	
-	0.00	-	0.00	0.00	0.00	0.00	-	
-	-	-	-	-	-	-	-	
0.00	0.00	0.00	0.00	0.00	0.00	0.00	0.00	
0.77	0.78	0.80	0.78	0.78	0.77	0.80	0.02	
0.02	0.02	0.02	0.02	0.02	0.02	0.02	0.00	
0.11	0.11	0.14	0.11	0.12	0.11	0.14	0.02	
-	0.00	0.00	0.00	0.00	0.00	0.00	0.00	
-	0.00	-	0.00	0.00	0.00	0.00	-	
-	-	-	-	-	-	-	-	
0.00	0.00	0.00	0.00	0.00	0.00	0.00	0.00	
0.00	0.00	-	0.00	0.00	0.00	0.00	-	
0.11	0.16	0.12	0.12	0.13	0.11	0.16	0.04	
3.17	3.05	3.05	3.05	3.09	3.05	3.17	0.11	
1.91	1.97	1.95	1.95	1.94	1.91	1.97	0.05	
0.10	0.10	0.10	0.10	0.10	0.10	0.10	0.01	
0.00	0.00	0.00	0.00	0.00	0.00	0.00	0.00	
-	-	-	-	-	-	-	-	
-	-	-	-	-	-	-	-	
2.01	2.07	2.05	2.05	2.04	2.01	2.07	0.05	
8.00	8.00	8.00	8.00	8.00	8.00	8.00	-	
0.05	0.06	0.04	0.05	0.05	0.04	0.06	0.01	
5.95	5.94	5.96	5.95	5.95	5.94	5.96	0.01	
47.1	48.0	46.8	47.1	47.3	46.8	48.0	1.01	
46.7	46.6	48.3	46.7	47.2	46.6	48.3	1.59	
3.45	2.89	2.78	2.89	3.04	2.78	3.45	0.59	
6.07	6.05	6.06	6.06	6.06	6.05	6.07	0.02	

RX6724 (n=7)

1	2	3	4	5	6	7	median	mean	min	max	2stddv	AvgDL
12.8	14.0	13.1	14.3	13.3	13.9	11.9	13.3	13.3	11.9	14.3	1.5	0.01
9.2	10.9	10.7	11.2	9.7	11.0	8.8	10.7	10.2	8.8	11.2	1.8	0.02
0.20	0.29	0.35	0.30	0.26	0.30	0.23	0.29	0.28	0.20	0.35	0.1	0.07
0.26	0.40	0.37	0.32	0.34	0.41	0.28	0.34	0.34	0.26	0.41	0.1	0.06
-	-	-	-	-	-	-	-	-	-	-	-	0.08
-	-	-	-	-	0.04	-	0.04	0.04	0.04	0.04	-	0.04
-	-	-	-	-	-	-	-	-	-	-	-	0.08
-	-	-	-	-	-	-	-	-	-	-	-	0.04
-	-	-	-	-	-	-	-	-	-	-	-	0.04
-	-	-	-	-	-	-	-	-	-	-	-	0.09
-	-	-	-	-	-	-	-	-	-	-	-	0.05
-	0.05	-	-	-	-	-	0.05	0.05	0.05	0.05	-	0.05
-	0.11	0.03	-	-	-	-	0.07	0.07	0.03	0.11	0.1	0.02
22.5	25.8	24.5	26.1	23.6	25.6	21.2	24.5	24.2	21.2	26.1	3.4	
0.27	0.26	0.24	0.14	0.16	0.31	0.20	0.24	0.23	0.14	0.31	0.1	0.01
3.19	3.41	2.68	3.72	2.56	2.82	3.05	3.05	3.06	2.56	3.72	0.8	0.01
0.12	0.03	0.09	0.04	-	0.02	0.03	0.04	0.05	0.02	0.12	0.1	0.02
-	-	-	-	-	-	-	-	-	-	-	-	0.02
0.11	0.06	0.03	0.02	0.05	0.07	0.07	0.06	0.06	0.02	0.11	0.1	0.02
-	-	0.02	-	0.02	-	-	0.02	0.02	0.02	0.02	0.0	0.02
0.25	0.16	0.28	0.12	0.59	0.29	0.41	0.28	0.30	0.12	0.59	0.3	0.01
33.3	29.9	29.6	30.1	30.7	31.6	29.4	30.1	30.7	29.4	33.3	2.6	0.02
0.20	0.99	3.58	0.99	0.83	0.52	1.35	0.99	1.21	0.20	3.58	2.1	0.04
20.0	23.4	22.6	24.0	21.2	23.2	23.2	23.2	22.5	20.0	24.0	2.6	0.02
2.60	3.18	2.70	3.25	2.93	2.96	2.96	2.96	2.94	2.60	3.25	0.4	0.03
0.11	0.08	0.07	0.06	0.08	0.11	0.06	0.08	0.08	0.06	0.11	0.0	0.02
-	-	-	-	0.03	-	-	0.03	0.03	0.03	0.03	-	0.02
0.65	0.04	0.46	-	1.68	0.44	2.25	0.56	0.92	0.04	2.25	1.6	0.02
0.44	0.30	0.13	0.10	0.15	0.30	0.22	0.22	0.23	0.10	0.44	0.2	0.02
0.03	0.01	0.07	0.10	0.03	0.02	0.01	0.03	0.04	0.01	0.10	0.1	0.01
83.8	87.6	87.1	88.7	84.7	88.3	84.4	87.1	86.4	83.8	88.7	3.7	
0.42	0.45	0.43	0.46	0.44	0.44	0.39	0.44	0.43	0.39	0.46	0.04	
0.30	0.35	0.35	0.36	0.32	0.35	0.28	0.35	0.33	0.28	0.36	0.05	
0.01	0.01	0.01	0.01	0.01	0.01	0.01	0.01	0.01	0.01	0.01	0.00	
0.01	0.01	0.01	0.01	0.01	0.01	0.01	0.01	0.01	0.01	0.01	0.00	
-	-	-	-	-	-	-	-	-	-	-	-	
-	-	-	-	-	0.00	-	0.00	0.00	0.00	0.00	-	
-	-	-	-	-	-	-	-	-	-	-	-	
-	-	-	-	-	-	-	-	-	-	-	-	
-	-	-	-	-	-	-	-	-	-	-	-	
-	-	-	-	-	-	-	-	-	-	-	-	
-	-	-	-	-	-	-	-	-	-	-	-	
-	0.01	0.00	-	-	-	-	0.00	0.00	0.00	0.00	-	
0.74	0.83	0.80	0.84	0.78	0.81	0.69	0.80	0.78	0.69	0.84	0.10	
0.03	0.02	0.02	0.01	0.02	0.03	0.02	0.02	0.02	0.01	0.03	0.01	
0.17	0.17	0.14	0.19	0.13	0.14	0.16	0.16	0.16	0.13	0.19	0.04	
0.00	0.00	0.00	0.00	-	0.00	0.00	0.00	0.00	0.00	0.00	0.00	
-	-	-	-	-	-	0.00	0.00	0.00	0.00	0.00	-	
0.00	0.00	0.00	0.00	0.00	0.00	0.00	0.00	0.00	0.00	0.00	0.00	
-	-	-	-	0.00	-	-	0.00	0.00	0.00	0.00	-	
0.03	0.02	0.03	0.01	0.07	0.03	0.05	0.03	0.03	0.01	0.07	0.03	
0.97	1.05	1.00	1.05	1.00	1.02	0.91	1.00	1.00	0.91	1.05	0.09	
3.53	3.09	3.11	3.09	3.25	3.21	3.05	3.11	3.19	3.05	3.53	0.31	
0.02	0.07	0.27	0.07	0.06	0.04	0.10	0.07	0.09	0.02	0.27	0.15	
3.55	3.19	3.37	3.16	3.31	3.25	3.15	3.25	3.28	3.15	3.55	0.26	
1.52	1.73	1.70	1.77	1.61	1.70	1.72	1.70	1.68	1.52	1.77	0.16	
0.15	0.17	0.15	0.18	0.16	0.16	0.16	0.16	0.16	0.15	0.18	0.02	
0.01	0.00	0.00	0.00	0.00	0.01	0.00	0.00	0.00	0.00	0.01	0.00	
-	-	-	-	0.00	-	-	0.00	0.00	0.00	0.00	-	
0.06	0.00	0.04	-	0.15	0.04	0.20	0.05	0.08	0.00	0.20	0.14	
1.73	1.92	1.89	1.95	1.93	1.90	2.09	1.92	1.92	1.73	2.09	0.19	
12.00	8.00	8.00	8.00	8.00	8.00	8.00	8.00	8.57	8.00	12.00	2.80	
0.12	0.08	0.04	0.03	0.04	0.08	0.06	0.06	0.06	0.03	0.12	0.06	
5.88	5.92	5.96	5.97	5.96	5.92	5.94	5.94	5.94	5.88	5.97	0.06	
56.8	54.3	53.5	54.8	56.5	54.2	56.3	54.8	55.2	53.5	56.8	2.4	
40.7	42.0	43.1	42.6	40.8	42.7	41.1	42.0	41.9	40.7	43.1	1.8	
1.10	1.48	1.44	1.19	1.39	1.57	1.29	1.39	1.35	1.10	1.57	0.3	
6.25	6.16	6.27	6.17	6.24	6.17	6.15	6.17	6.20	6.15	6.27	0.1	

SUPPLEMENTARY MATERIAL C

APPENDIX FOR CHAPTER 4

Uptake of trace elements by baryte during copper ore processing: a case study from Olympic Dam, South Australia

INCLUDES:

APPENDIX A: ANALYTICAL SET UP FOR LA-ICP-MS OF BARYTE

Appendix A: Analytical set-up for LA-ICP-MS analysis of baryte				
Baryte Operating Conditions				
		Spot Size (um)	Hz	Fluence (J/cm^2)
Unknowns		9-43	5	3.5
Standards (GSD-1G, NIST-610)		51		
Baryte Analysis Details				
Mass	Element	Dwell Time (s)	Avg Limit of Detection (ppm)	
			grains	veins
23	Na	0.005	68.7	6.46
27	Al	0.005	6.57	0.55
29	Si	0.005	1325	98.8
31	P	0.005	204	10.5
43	Ca	0.01	1024	59.9
57	Fe	0.01	66.8	7.49
65	Cu	0.01	5.09	0.34
85	Rb	0.01	0.80	0.12
88	Sr	0.01	0.18	1.71
89	Y	0.01	0.04	0.01
133	Cs	0.01	0.32	0.05
137	Ba	0.01	-	-
139	La	0.01	0.04	0.01
140	Ce	0.01	0.03	0.01
141	Pr	0.01	0.11	0.00
143	Nd	0.01	0.17	0.04
146	Nd	0.01	0.16	0.03
147	Sm	0.01	0.21	0.04
151	Eu	0.01	0.22	0.06
153	Eu	0.01	0.26	0.08
157	Gd	0.01	0.57	0.12
159	Tb	0.01	0.02	0.00
163	Dy	0.01	0.11	0.02
165	Ho	0.01	0.02	0.00
166	Er	0.01	0.07	0.01
169	Tm	0.01	0.03	0.01
172	Yb	0.01	0.17	0.02
175	Lu	0.01	0.04	0.01
182	W	0.01	0.14	0.02
202	Hg	0.01	-	-
204	Pb	0.01	17.9	1.44
206	Pb	0.02	0.52	0.05
207	Pb	0.02	0.47	0.04
208	Pb	0.01	0.41	0.03
209	Bi	0.03	0.10	0.01
226	Ra	0.03	0.00	0.00
232	Th	0.03	0.03	0.004
238	U	0.02	0.10	0.005

SUPPLEMENTARY MATERIAL D

APPENDIX FOR CHAPTER 5

Mineralogy and geochemistry of fluorite in the Olympic Dam Cu-U-Au-Ag deposit, South Australia

INCLUDES:

APPENDIX A: LA-ICP-MS SET UP DETAILS

APPENDIX B: COMPLETE LA-ICP-MS

APPENDIX C: EPMA METHODOLOGY AND SET UP DETAILS

APPENDIX D: COMPLETE EPMA DATASET

Appendix A: Full details of analytical set-up for LA-ICP-MS analysis of fluorite.

Fluorite Analysis Details: Veins			Fluorite Analysis Details: Grains		
Mass	Element	Dwell Time (s)	Mass	Element	Dwell Time (s)
9	Be	0.01			
23	Na	0.005	23	Na	0.005
24	Mg	0.01			
27	Al	0.005	27	Al	0.005
29	Si	0.005	29	Si	0.005
31	P	0.005	31	P	0.005
43	Ca	0.01	43	Ca	0.01
39	K	0.005			
45	Sc	0.01			
49	Ti	0.01			
51	V	0.01			
52	Cr	0.01			
55	Mn	0.01			
57	Fe	0.01	57	Fe	0.01
60	Ni	0.01			
65	Cu	0.01	65	Cu	0.01
66	Zn	0.01			
85	Rb	0.01	85	Rb	0.01
88	Sr	0.01	88	Sr	0.01
89	Y	0.01	89	Y	0.01
90	Zr	0.01			
93	Nb	0.01			
107	Ag	0.01			
			133	Cs	0.01
137	Ba	0.01	137	Ba	0.01
139	La	0.01	139	La	0.01
140	Ce	0.01	140	Ce	0.01
141	Pr	0.01	141	Pr	0.01
146	Nd	0.01	146	Nd	0.01
147	Sm	0.01	147	Sm	0.01
153	Eu	0.01	153	Eu	0.01
157	Gd	0.01	157	Gd	0.01
159	Tb	0.01	159	Tb	0.01
163	Dy	0.01	163	Dy	0.01
165	Ho	0.01	165	Ho	0.01
166	Er	0.01	166	Er	0.01
169	Tm	0.01	169	Tm	0.01
172	Yb	0.01	172	Yb	0.01
175	Lu	0.01	175	Lu	0.01
			182	W	0.01
201	Hg	0.01			
202	Hg	0.01	202	Hg	0.01
203	Tl	0.01			
204	Pb	0.01	204	Pb	0.01
205	Tl	0.01			
206	Pb	0.02	206	Pb	0.02
207	Pb	0.02	207	Pb	0.02
208	Pb	0.01	208	Pb	0.01
209	Bi	0.01	209	Bi	0.03
232	Th	0.01	232	Th	0.03
235	U	0.01			
238	U	0.01	238	U	0.02

Due to the size restrictions of the fluorite in grains, certain elements were not included in analysis in order to shorten sweep time

Fluorite Operating Conditions			
	Spot Size (um)	Hz	Fluence (J/cm^2)
Unknowns	9-43	5	10
Standards (GSD-	51		3.5

Analysis timing	
Delay	20 seconds
Cleaning	5 pulses
Background collection	30 seconds
Ablation time	40 seconds
Delay	2 seconds

Appendix B: Complete LA-ICP-MS dataset for fluorite veins, by sample and color, and ore feed grains.

Sample 5; purple

n=73	1	2	3	4	5	6	7	8	9	10	11	12	13	14	15	16	17	18	19	20	21	22
Y	259	198	225	262	111	148	281	216	256	143	265	240	88.0	117	219	229	206	77.0	131	239	169	191
La	1.9	3.8	19.9	3.1	15.9	3.6	5.0	3.6	5.8	7.1	6.5	15.6	4.4	5.7	2.4	3.8	4.7	25.6	14.4	2.6	18.3	10.9
Ce	5.1	9.6	52.0	8.3	39.2	10.5	13.5	10.5	15.4	19.8	15.2	22.9	10.1	19.5	7.6	15.5	11.0	32.4	24.1	7.2	29.0	15.8
Pr	0.89	1.6	7.3	1.6	7.2	1.7	2.7	2.1	2.6	3.2	2.4	3.0	1.6	3.0	1.4	2.9	1.5	4.3	3.3	1.2	3.7	2.4
Nd	4.9	8.3	32.4	8.2	30.8	10.6	13.1	12.7	15.4	17.0	12.3	16.7	9.3	12.5	7.4	17.3	7.3	14.7	14.2	5.5	16.9	10.3
Sm	2.7	4.4	7.4	3.6	6.5	3.0	6.3	4.4	5.4	4.8	6.3	7.7	2.4	3.7	2.6	5.9	3.0	4.4	5.1	3.0	5.8	3.7
Eu	1.6	1.9	2.1	2.0	1.2	1.0	2.9	1.8	2.1	1.5	2.5	3.1	0.97	1.7	1.2	1.9	1.6	1.3	2.1	1.7	2.4	1.6
Gd	6.9	8.8	7.8	8.7	5.4	4.3	14.2	5.6	9.4	6.8	13.4	16.4	3.4	5.0	4.8	7.2	8.1	7.3	10.7	7.1	10.4	8.7
Tb	1.4	1.5	1.0	1.6	0.59	0.72	2.0	1.3	1.5	0.88	2.3	2.2	0.47	0.85	0.95	1.0	1.4	1.0	1.8	1.3	1.8	1.3
Dy	9.9	9.3	6.2	10.0	3.9	4.9	13.9	7.6	9.9	5.3	14.6	13.0	2.9	6.8	6.9	7.2	10.0	5.4	9.7	10.2	11.1	9.2
Ho	2.3	2.1	1.5	2.4	0.75	0.96	2.8	1.5	2.2	1.0	2.8	2.4	0.63	1.5	1.6	1.7	2.2	0.81	1.7	2.2	2.0	2.0
Er	7.5	6.0	4.3	6.6	2.1	3.1	8.3	4.6	6.3	3.1	7.9	6.3	1.8	5.0	5.0	5.0	6.9	2.0	4.5	6.5	6.0	6.1
Tm	0.92	0.78	0.60	0.82	0.29	0.38	0.91	0.61	0.75	0.40	1.0	0.75	0.17	0.66	0.63	0.55	0.85	0.28	0.62	0.89	0.65	0.77
Yb	5.3	4.1	3.8	5.5	1.9	2.0	5.8	3.5	4.1	2.3	5.5	4.4	1.0	4.0	3.7	3.2	4.6	1.5	3.4	4.9	4.1	4.3
Lu	0.57	0.52	0.40	0.59	0.21	0.30	0.76	0.39	0.57	0.28	0.65	0.50	0.14	0.50	0.34	0.44	0.62	0.23	0.42	0.62	0.55	0.52
∑REE	52.0	62.9	147	63.1	116	47.1	92.1	60.2	81.4	73.5	93.4	115	39.4	70.2	46.5	73.7	63.9	101	96.0	54.9	113	77.6
Th	0.08	0.03	<LOD	<LOD	<LOD	0.02	0.03	0.04	0.13	0.05	0.02	0.14	0.03	0.05	0.08	0.02	<LOD	0.04	0.01	0.06	0.05	0.14
U	<LOD	<LOD	<LOD	<LOD	<LOD	<LOD	<LOD	<LOD	<LOD	<LOD	<LOD	0.05	<LOD	0.01	<LOD	<LOD	<LOD	<LOD	<LOD	<LOD	0.03	0.06
Pb	0.09	0.19	0.29	0.16	0.33	0.12	0.40	0.16	0.25	0.22	0.32	3.7	0.47	0.46	2.1	<LOD	<LOD	0.74	0.46	0.28	0.70	6.0
Fe	209	261	255	219	233	222	201	214	202	240	410	6100	226	852	188	191	192	181	219	194	530	4950
Sr	59.5	101	28.8	101	<LOD	12.8	64.1	24.7	38.1	24.3	58.5	286	26.4	97.0	75.0	30.1	84.6	108	277	82.5	340	<LOD
Ba	0.16	0.13	<LOD	0.40	4.2	1.2	<LOD	1.2	<LOD	<LOD	2.0	3500	346	<LOD	11.9	<LOD	0.93	14.0	1.3	4.3	15.8	18.4
Na	209	451	682	1000	530	97.0	674	319	<LOD	540	770	3090	279	250	940	228	240	1210	943	438	3040	<LOD
Al	<LOD	1.4	2.3	<LOD	<LOD	1.2	<LOD	1.9	1.3	0.71	11.9	620	5.9	0.65	<LOD	<LOD	<LOD	5.1	7.8	0.99	132	537
Si	327	<LOD	<LOD	<LOD	<LOD	<LOD	<LOD	209	<LOD	266	<LOD	1460	229	164	165	198	<LOD	173	170	<LOD	398	840
P	17.5	<LOD	21.0	<LOD	<LOD	<LOD	25.8	<LOD	<LOD	21.0	23.0	42.5	27.6	41.7	19.0	19.0	19.0	20.5	20.4	<LOD	26.7	28.4
K	<LOD	18.2	95.0	98.0	165	<LOD	33.0	31.0	55.0	128	56.0	490	28.1	9.0	116	13.5	<LOD	155	58.0	17.3	333	<LOD
Sc	0.31	0.57	0.35	<LOD	<LOD	<LOD	0.37	0.24	0.31	0.30	<LOD	0.40	0.30	0.60	<LOD	<LOD	<LOD	<LOD	<LOD	<LOD	<LOD	<LOD
Ti	<LOD	<LOD	<LOD	<LOD	<LOD	<LOD	<LOD	<LOD	<LOD	0.82	<LOD	3.0	<LOD	<LOD	2.3	2.6	3.2	2.9	2.0	<LOD	4.0	10.0
V	<LOD	<LOD	<LOD	<LOD	<LOD	<LOD	<LOD	<LOD	<LOD	<LOD	<LOD	0.89	<LOD	<LOD	<LOD	<LOD	<LOD	<LOD	<LOD	<LOD	0.22	1.3
Cr	<LOD	<LOD	<LOD	<LOD	<LOD	<LOD	<LOD	<LOD	<LOD	<LOD	<LOD	<LOD	<LOD	<LOD	<LOD	<LOD	<LOD	<LOD	<LOD	<LOD	<LOD	<LOD
Mn	<LOD	0.93	0.86	1.6	4.1	<LOD	1.9	0.89	<LOD	<LOD	0.82	19.0	1.6	5760	0.97	<LOD	<LOD	4.0	1.9	0.63	3.1	3.0
Ni	<LOD	0.05	0.18	<LOD	<LOD	<LOD	<LOD	0.10	<LOD	<LOD	0.33	<LOD	<LOD	0.09	0.17	<LOD	0.12	0.15	<LOD	<LOD	0.05	<LOD
Cu	<LOD	<LOD	0.45	0.47	0.57	0.49	1.1	<LOD	6.2	0.51	<LOD	0.76	1.4	2.6	0.29	<LOD	0.31	0.42	<LOD	0.64	0.69	2.0
Zn	<LOD	<LOD	1.2	<LOD	1.1	<LOD	0.65	<LOD	<LOD	<LOD	0.69	10.4	0.83	0.44	6.8	<LOD	<LOD	2.0	0.90	0.91	1.7	<LOD
Rb	0.14	<LOD	0.32	0.38	0.63	<LOD	0.13	0.13	0.29	0.45	0.26	2.2	0.16	<LOD	0.54	<LOD	<LOD	0.71	0.21	0.21	1.5	<LOD
Zr	<LOD	<LOD	<LOD	<LOD	<LOD	<LOD	<LOD	<LOD	<LOD	0.01	0.01	0.49	<LOD	<LOD	<LOD	<LOD	<LOD	<LOD	<LOD	<LOD	0.19	0.46
Nb	<LOD	<LOD	<LOD	<LOD	<LOD	<LOD	<LOD	<LOD	<LOD	<LOD	<LOD	0.26	<LOD	<LOD	<LOD	<LOD	<LOD	<LOD	<LOD	<LOD	0.07	0.16
Ag	<LOD	<LOD	<LOD	<LOD	<LOD	<LOD	<LOD	<LOD	<LOD	<LOD	<LOD	<LOD	<LOD	0.04	0.09	<LOD	<LOD	0.10	<LOD	<LOD	<LOD	<LOD
Bi	<LOD	<LOD	<LOD	<LOD	<LOD	<LOD	<LOD	0.02	<LOD	<LOD	<LOD	<LOD	<LOD	<LOD	<LOD	<LOD	<LOD	<LOD	<LOD	<LOD	<LOD	<LOD

23	24	25	26	27	28	29	30	31	32	33	34	35	36	37	38	39	40	41	42	43	44	45
190	220	252	211	132	179	115	127	188	224	149	168	175	137	190	130	73.0	117	148	250	182	181	229
5.2	11.2	3.6	9.7	79.0	51.9	32.6	22.7	17.9	19.9	7.5	6.0	2.2	17.4	8.0	4.6	29.3	11.8	8.0	2.0	3.9	7.7	2.2
13.1	17.5	10.8	25.9	95.6	89.5	65.3	42.5	36.4	42.1	18.0	16.0	7.3	35.3	18.7	10.1	39.2	19.3	14.9	5.7	10.3	16.7	6.6
2.3	2.5	1.8	4.2	10.0	10.6	7.7	6.2	6.2	5.5	3.1	2.9	1.2	4.6	3.0	1.5	4.5	2.7	2.3	0.94	1.7	2.3	1.1
11.0	11.4	9.4	21.2	36.5	44.5	37.3	24.1	28.4	26.7	15.3	16.1	7.0	19.9	13.7	7.4	17.7	11.5	10.2	5.7	9.1	11.6	6.4
3.8	3.2	4.1	6.2	6.0	10.2	7.4	5.0	6.3	6.8	4.2	4.3	2.4	5.4	4.9	2.5	4.4	4.3	4.0	2.6	4.0	4.5	3.2
1.4	1.8	1.9	2.0	1.4	3.0	1.6	1.3	1.6	2.1	1.3	1.3	1.1	1.7	2.5	0.99	1.4	1.5	1.7	1.5	2.1	1.9	1.7
4.7	7.1	8.0	9.5	5.1	11.4	6.3	4.6	6.5	8.2	5.9	5.9	5.1	7.9	8.4	4.0	7.7	7.6	7.5	7.0	7.5	9.0	7.6
0.89	1.2	1.5	1.3	0.68	1.6	0.65	0.59	0.87	1.4	0.79	0.98	0.87	1.2	1.5	0.70	1.0	1.2	1.2	1.2	1.2	1.5	1.5
5.4	8.4	10.0	8.4	4.5	9.1	3.8	3.8	6.0	8.3	5.1	6.1	5.6	7.5	9.1	4.3	5.0	7.9	7.7	9.7	9.1	9.6	10.3
1.2	2.0	2.1	1.7	0.99	1.7	0.70	0.84	1.3	2.0	1.2	1.3	1.5	1.4	2.0	1.1	0.82	1.3	1.6	2.2	1.9	2.2	2.4
4.2	6.2	6.9	4.9	3.0	4.7	2.3	2.7	4.2	5.9	3.2	3.8	4.6	4.1	5.0	2.8	2.2	3.8	4.4	7.1	6.1	5.9	6.9
0.57	0.72	0.91	0.66	0.41	0.60	0.25	0.34	0.52	0.74	0.33	0.45	0.51	0.54	0.69	0.38	0.25	0.55	0.58	0.81	0.63	0.72	0.89
3.0	4.2	4.7	3.7	2.3	3.7	1.5	2.1	3.5	4.4	2.8	3.2	3.3	3.0	4.3	2.4	1.6	3.0	2.6	4.6	4.1	4.6	5.1
0.39	0.53	0.62	0.41	0.32	0.42	0.22	0.27	0.45	0.54	0.28	0.31	0.34	0.34	0.51	0.26	0.18	0.35	0.38	0.63	0.47	0.50	0.55
57.2	77.9	66.3	99.7	246	243	168	117	120	134	68.9	68.6	42.9	110	82.2	43.0	115	76.8	67.0	51.6	62.1	78.7	56.5
0.04	0.06	<LOD	<LOD	0.44	0.46	0.15	0.16	0.11	0.18	0.06	0.07	0.10	<LOD	0.06	0.07	0.02	<LOD	0.01	0.06	0.03	0.05	0.03
0.01	0.01	<LOD	<LOD	0.32	0.24	0.07	0.03	0.03	0.11	<LOD	<LOD	0.01	<LOD	<LOD	<LOD	<LOD	0.01	<LOD	<LOD	<LOD	<LOD	<LOD
1.4	0.89	0.19	<LOD	1.2	4.1	0.70	0.71	1.4	6.0	<LOD	0.43	<LOD	<LOD	0.21	0.44	0.65	<LOD	0.21	<LOD	0.20	0.09	<LOD
506	386	173	187	9740	1660	840	440	580	5500	251	185	175	199	177	182	<LOD	176	170	159	201	197	181
53.6	67.4	52.5	66.2	35.7	168	<LOD	24.4	50.0	220	20.6	19.3	26.0	86.9	110	58.1	317	205	140	73.0	125	192	70.0
17.2	20.1	<LOD	0.60	41.8	87.0	20.8	9.7	9.6	530	<LOD	18.2	<LOD	3.1	0.34	3.9	1220	<LOD	<LOD	0.53	2.6	1.1	<LOD
1180	1280	713	237	108	2090	<LOD	429	1370	8500	420	452	221	402	457	307	1160	512	399	230	376	513	237
17.4	186	1.1	1.4	3870	1150	361	130	123	181	6.8	8.4	0.85	11.2	1.8	1.2	3.6	2.7	1.8	0.76	3.7	5.2	<LOD
150	333	257	<LOD	4850	1440	770	320	212	427	170	195	195	185	<LOD	126	225	<LOD	146	<LOD	<LOD	136	207
22.1	21.4	19.7	16.2	92.0	70.0	<LOD	27.7	38.3	48.4	<LOD	<LOD	28.8	24.9	22.3	26.5	30.9	23.0	18.2	15.0	18.2	23.2	13.0
101	165	42.6	7.6	1740	640	158	155	310	1060	34.9	46.8	11.8	56.5	80.0	23.9	84.0	<LOD	8.2	4.4	11.3	21.1	<LOD
<LOD	<LOD	<LOD	<LOD	0.22	0.19	<LOD	<LOD	0.09	<LOD	<LOD	<LOD	<LOD	<LOD	<LOD	<LOD	0.19	<LOD	<LOD	<LOD	<LOD	<LOD	<LOD
<LOD	1.6	<LOD	<LOD	40.2	13.5	4.9	4.9	3.0	4.4	<LOD	1.2	<LOD	1.7	<LOD	1.2	0.76	<LOD	<LOD	1.4	<LOD	2.2	<LOD
<LOD	0.08	<LOD	<LOD	1.8	0.56	0.30	0.21	0.19	0.64	<LOD	0.07	<LOD	<LOD	<LOD	<LOD	<LOD	<LOD	<LOD	<LOD	<LOD	<LOD	<LOD
<LOD	<LOD	<LOD	<LOD	1.8	1.2	<LOD	<LOD	0.54	<LOD	<LOD	<LOD	<LOD	<LOD	<LOD	<LOD	<LOD	<LOD	<LOD	<LOD	<LOD	<LOD	<LOD
3.5	5.8	2.1	0.83	10.8	5.6	1.7	4.0	11.0	42.0	1.6	1.8	0.55	3.6	3.7	0.57	2.2	<LOD	0.45	<LOD	<LOD	<LOD	<LOD
0.18	<LOD	<LOD	<LOD	1.7	<LOD	<LOD	0.10	0.10	0.21	0.10	0.30	<LOD	0.32	<LOD	0.13	0.21	<LOD	0.15	0.19	0.12	0.10	<LOD
1.8	0.86	<LOD	<LOD	6.4	<LOD	<LOD	0.58	0.67	0.42	<LOD	<LOD	0.72	0.56	0.69	0.60	<LOD	0.87	1.0	<LOD	<LOD	0.16	<LOD
2.6	1.7	0.50	<LOD	1.5	8.5	1.1	0.68	2.5	24.0	<LOD	0.62	<LOD	0.51	7.6	1.2	2.8	0.77	0.79	<LOD	0.42	1.4	<LOD
0.41	0.84	0.19	0.12	8.4	2.8	0.98	0.79	1.2	3.8	0.16	0.24	0.15	0.18	0.33	0.15	0.45	<LOD	<LOD	<LOD	<LOD	0.09	<LOD
0.01	0.08	<LOD	<LOD	2.1	0.72	0.47	0.20	0.16	0.43	<LOD	<LOD	<LOD	<LOD	<LOD	<LOD	<LOD	<LOD	<LOD	<LOD	<LOD	<LOD	<LOD
<LOD	0.02	<LOD	<LOD	1.1	0.27	0.24	0.06	0.02	0.19	<LOD	<LOD	<LOD	<LOD	<LOD	<LOD	<LOD	<LOD	<LOD	<LOD	<LOD	<LOD	<LOD
<LOD	<LOD	<LOD	<LOD	<LOD	<LOD	<LOD	0.08	0.07	0.10	<LOD	<LOD	<LOD	0.16	0.15	<LOD	<LOD	<LOD	<LOD	<LOD	<LOD	0.10	0.11
<LOD	0.03	<LOD	<LOD	0.04	<LOD	<LOD	<LOD	0.01	0.01	<LOD	<LOD	<LOD	0.05	<LOD	<LOD	<LOD	<LOD	0.02	<LOD	<LOD	<LOD	<LOD

46	47	48	49	50	51	52	53	54	55	56	57	58	59	60	61	62	63	64	65	66	67	68
226	111	205	231	233	181	123	219	84.0	114	113	192	266	253	181	107	232	188	158	232	267	243	279
5.0	6.7	2.1	2.1	5.3	13.4	9.9	16.1	3.8	6.4	2.9	3.8	5.6	8.5	13.3	7.5	61.6	21.7	9.4	10.3	4.1	2.8	2.1
11.0	13.1	5.8	6.0	12.5	31.3	22.0	36.6	10.6	18.2	7.5	10.8	17.0	21.5	28.9	15.0	132	46.1	20.8	24.0	8.7	8.6	5.8
2.6	1.8	0.93	1.1	2.3	4.8	3.7	5.9	1.9	3.7	1.5	2.1	2.7	3.9	4.5	2.5	20.3	7.4	3.1	4.2	1.7	1.7	1.5
10.4	8.6	5.9	5.2	11.0	24.1	17.4	28.3	8.9	19.1	7.8	12.6	15.8	21.2	22.9	12.2	102	35.4	17.8	19.7	9.8	9.2	7.5
4.0	3.2	2.4	2.2	4.9	5.8	3.4	8.8	1.9	4.2	2.2	3.7	5.6	7.6	9.1	3.7	30.6	9.7	5.5	5.9	5.6	3.7	4.4
1.7	0.94	1.2	1.2	2.1	1.7	1.1	2.9	0.65	1.2	0.84	1.3	2.1	2.7	2.8	0.97	8.4	2.8	1.8	2.2	2.5	1.8	2.2
7.8	4.4	5.6	5.3	9.6	7.5	4.6	12.7	2.6	5.0	3.4	6.2	8.9	10.5	13.8	5.5	33.7	12.6	9.1	9.8	14.1	8.1	11.6
1.4	0.68	1.0	1.0	1.7	0.90	0.55	2.1	0.40	0.51	0.57	0.96	1.4	1.7	1.9	0.72	4.4	1.5	1.2	1.4	2.4	1.4	2.2
9.3	4.6	7.0	7.1	10.7	6.1	3.7	13.1	2.3	3.1	3.5	6.3	8.4	10.0	9.9	3.7	19.8	7.7	6.5	9.3	15.3	8.8	12.4
2.1	0.99	1.6	1.7	2.2	1.3	0.88	2.5	0.59	0.68	0.96	1.5	2.1	2.3	1.9	0.75	2.9	1.5	1.2	1.9	3.0	2.2	2.5
5.9	2.9	5.4	5.6	6.7	3.8	2.4	7.1	1.8	2.3	2.8	4.5	6.0	6.4	4.7	2.2	7.0	4.2	3.9	5.9	8.1	6.6	7.5
0.70	0.37	0.60	0.61	0.80	0.48	0.37	0.92	0.24	0.27	0.32	0.51	0.80	0.86	0.62	0.24	0.70	0.53	0.43	0.76	0.98	0.87	0.90
4.2	2.2	3.3	3.8	4.9	3.1	2.2	5.7	1.3	1.6	2.2	3.2	4.5	5.0	3.6	1.6	3.2	3.2	2.8	4.2	5.8	4.5	5.3
0.55	0.25	0.39	0.50	0.63	0.41	0.24	0.67	0.12	0.14	0.21	0.42	0.56	0.49	0.37	0.19	0.42	0.40	0.38	0.49	0.64	0.48	0.56
66.6	50.8	43.3	43.3	75.4	105	72.4	143	37.0	66.3	36.6	57.9	81.4	103	118	56.8	427	155	83.8	100	82.6	60.6	66.4
0.05	0.05	0.04	<LOD	0.01	<LOD	0.01	0.06	0.04	0.08	0.04	0.06	0.06	0.12	0.08	<LOD	0.04	0.01	0.03	0.03	0.02	0.01	0.03
<LOD	0.01	<LOD	<LOD	<LOD	<LOD	0.04	3.6	0.04	0.01	<LOD	<LOD	<LOD	<LOD	<LOD	<LOD	0.01	<LOD	0.05	<LOD	<LOD	<LOD	<LOD
<LOD	10.1	<LOD	<LOD	0.28	0.98	0.34	0.28	<LOD	0.42	0.19	0.12	<LOD	0.40	<LOD	1.2	<LOD	0.33	0.36	0.59	2.1	<LOD	0.39
174	374	161	176	165	178	181	175	560	159	173	168	151	198	155	178	190	169	152	135	343	161	192
56.8	320	37.2	42.0	115	42.0	27.5	33.3	15.6	9.4	18.8	32.0	15.3	40.1	24.9	39.6	52.8	82.0	28.3	48.1	204	<LOD	35.2
0.58	230	77.0	138	<LOD	156	<LOD	7.8	2.7	0.78	2.5	8.7	<LOD	46.0	<LOD	16.6	4.9	15.2	2.6	14.1	2590	<LOD	14.4
335	6600	<LOD	240	1340	638	146	281	101	126	208	1330	197	1380	226	1490	930	2040	326	559	1650	<LOD	740
1.7	22.1	<LOD	1.6	0.71	3.9	<LOD	5.5	11.0	<LOD	1.0	0.75	1.0	1.8	2.2	1.7	6.7	3.8	1.5	1.2	10.2	<LOD	1.4
146	171	177	<LOD	174	196	<LOD	<LOD	128	<LOD	<LOD	<LOD	222	175	235	240	<LOD	182	240	<LOD	<LOD	184	<LOD
20.7	28.8	<LOD	<LOD	13.9	33.8	22.7	43.0	14.9	14.4	19.2	23.5	23.8	29.5	19.3	32.2	113	49.1	30.0	25.2	35.4	12.8	27.0
20.8	560	<LOD	17.2	51.0	64.6	14.4	19.9	20.6	14.6	20.8	102	15.7	95.0	18.2	186	66.0	117	77.6	47.5	153	<LOD	67.0
<LOD	0.60	<LOD	1.2	<LOD	<LOD	<LOD	<LOD	<LOD	<LOD	<LOD	<LOD	1.4	1.2	<LOD	<LOD	<LOD	<LOD	<LOD	1.9	1.3	1.0	<LOD
<LOD	0.05	<LOD	<LOD	<LOD	<LOD	<LOD	<LOD	<LOD	<LOD	<LOD	<LOD	<LOD	<LOD	0.03	<LOD	<LOD	<LOD	<LOD	<LOD	0.11	0.04	<LOD
<LOD	0.53	<LOD	<LOD	0.61	<LOD	<LOD	<LOD	<LOD	<LOD	<LOD	<LOD	<LOD	<LOD	<LOD	<LOD	<LOD	<LOD	<LOD	<LOD	<LOD	<LOD	<LOD
0.54	12.8	<LOD	1.2	1.3	2.9	0.96	1.2	1.1	0.87	0.91	0.98	0.55	0.45	0.68	3.3	0.89	1.3	1.0	0.89	6.2	<LOD	0.09
<LOD	0.13	0.17	<LOD	<LOD	<LOD	<LOD	<LOD	0.02	0.08	0.13	<LOD	0.09	<LOD	<LOD	0.24	0.11	0.26	0.07	<LOD	0.47	<LOD	1.1
0.40	1.4	<LOD	<LOD	2.3	1.9	0.60	0.55	0.18	<LOD	0.53	<LOD	0.41	4.9	<LOD	0.37	0.76	3.5	<LOD	0.21	1.1	<LOD	1.1
<LOD	23.0	<LOD	<LOD	0.50	1.9	<LOD	0.90	1.7	<LOD	<LOD	0.50	<LOD	<LOD	<LOD	1.4	0.37	2.2	0.83	1.4	5.7	<LOD	0.43
<LOD	2.7	<LOD	0.11	0.24	0.32	<LOD	0.10	0.17	<LOD	0.21	0.50	<LOD	0.15	0.07	1.0	0.27	0.37	0.15	0.18	0.88	<LOD	0.49
<LOD	0.04	<LOD	<LOD	0.01	0.01	<LOD	0.10	<LOD	<LOD	<LOD	<LOD	<LOD	<LOD	<LOD	<LOD	<LOD	<LOD	<LOD	<LOD	0.03	<LOD	<LOD
<LOD	<LOD	<LOD	<LOD	<LOD	<LOD	<LOD	<LOD	<LOD	<LOD	<LOD	<LOD	<LOD	<LOD	<LOD	<LOD	<LOD	<LOD	<LOD	<LOD	<LOD	<LOD	<LOD
<LOD	<LOD	0.09	<LOD	<LOD	<LOD	0.01	0.01	<LOD	<LOD	0.03	<LOD	<LOD	<LOD	<LOD	<LOD	<LOD	<LOD	<LOD	<LOD	<LOD	<LOD	<LOD

69	70	71	72	73	*AVG*	*MIN*	*MAX*	AVG LOD
306	271	152	260	331	*192*	*73.0*	*331*	33.60
3.6	2.5	2.9	1.9	40.4	*8.3*	*1.9*	*79.0*	1.30
8.2	7.6	7.7	5.2	51.5	*18.2*	*5.1*	*132*	2.80
1.7	1.4	1.4	1.1	5.5	*2.9*	*0.89*	*20.3*	0.44
10.3	9.8	7.9	7.5	21.6	*14.1*	*4.9*	*102*	2.20
8.1	6.6	3.2	4.9	8.8	*4.7*	*1.9*	*30.6*	0.75
3.9	2.8	1.3	2.4	3.8	*1.8*	*0.65*	*8.4*	0.29
19.9	14.4	6.7	13.3	18.4	*8.0*	*2.6*	*33.7*	1.30
3.1	2.4	1.2	2.1	3.2	*1.3*	*0.40*	*4.4*	0.22
19.9	14.4	6.8	14.3	20.5	*8.1*	*2.3*	*20.5*	1.40
3.6	3.2	1.4	2.8	3.8	*1.7*	*0.59*	*3.8*	0.30
10.4	8.0	4.2	7.5	11.1	*5.1*	*1.8*	*11.1*	0.90
1.2	1.1	0.50	0.94	1.3	*0.63*	*0.17*	*1.3*	0.11
6.7	5.9	2.9	5.2	8.1	*3.7*	*1.0*	*8.1*	0.66
0.84	0.65	0.35	0.58	0.91	*0.44*	*0.12*	*0.91*	0.08
101	80.8	48.4	69.6	199	*80.6*	*36.6*	*427*	<LOD
0.01	<LOD	<LOD	0.04	0.26	*0.06*	*<LOD*	*0.46*	0.02
<LOD	<LOD	0.01	<LOD	0.33	*0.05*	*<LOD*	*3.6*	0.01
<LOD	<LOD	0.16	0.26	1.2	*0.58*	*<LOD*	*10.1*	<LOD
174	165	208	<LOD	7600	*247*	*<LOD*	*9740*	49.10
45.1	48.1	91.0	39.0	56.6	*67.5*	*<LOD*	*340*	10.60
<LOD	7.1	1550	<LOD	11.2	*32.1*	*<LOD*	*3500*	3.60
550	687	<LOD	437	686	*630*	*<LOD*	*8500*	85.30
1.8	1.3	6.8	1.0	365	*19.7*	*<LOD*	*3870*	0.18
203	<LOD	176	<LOD	950	*250*	*<LOD*	*4850*	7.40
30.0	30.8	<LOD	21.8	88.0	*25.7*	*<LOD*	*113*	14.20
44.6	43.1	7.1	12.6	180	*72.2*	*<LOD*	*1740*	11.30
0.16	<LOD	0.14	<LOD	0.21	*0.28*	*<LOD*	*0.60*	0.19
<LOD	<LOD	1.8	1.9	33.0	*2.6*	*<LOD*	*40.2*	1.40
<LOD	<LOD	<LOD	<LOD	1.6	*0.45*	*<LOD*	*1.8*	0.06
<LOD	<LOD	<LOD	<LOD	1.6	*1.0*	*<LOD*	*1.8*	0.97
1.8	<LOD	<LOD	0.77	2.4	*2.2*	*<LOD*	*5760*	0.63
0.18	0.34	0.09	<LOD	0.17	*0.16*	*<LOD*	*1.7*	0.13
<LOD	<LOD	9.4	<LOD	6.0	*1.1*	*<LOD*	*9.4*	0.43
<LOD	<LOD	0.63	0.72	1.3	*1.6*	*<LOD*	*24.0*	0.48
<LOD	0.29	<LOD	0.08	0.91	*0.42*	*<LOD*	*8.4*	0.10
<LOD	0.01	<LOD	<LOD	0.60	*0.19*	*<LOD*	*2.1*	0.02
<LOD	<LOD	<LOD	<LOD	3.3	*0.20*	*<LOD*	*3.3*	0.01
<LOD	<LOD	<LOD	<LOD	<LOD	*0.10*	*<LOD*	*0.16*	0.10
<LOD	<LOD	0.03	<LOD	0.02	*0.02*	*<LOD*	*0.05*	0.03

Sample 6; purple

n=47	1	2	3	4	5	6	7	8	9	10	11	12
Y	83.6	97.0	42.6	121	187	245	174	206	184	243	149	218
La	12.2	13.0	7.1	3.0	2.7	1.6	1.9	1.6	1.6	1.4	1.7	1.7
Ce	22.7	29.0	16.1	6.0	6.8	4.8	5.1	4.8	4.7	4.9	3.2	5.2
Pr	3.4	4.4	2.7	1.0	1.1	0.92	0.98	0.79	0.85	0.94	0.53	1.0
Nd	13.8	21.6	12.4	5.9	6.2	6.2	5.0	4.9	5.1	6.7	2.7	5.0
Sm	2.9	4.3	2.0	2.0	3.3	3.6	2.8	2.7	3.2	3.3	1.8	3.1
Eu	0.85	1.2	0.43	1.2	1.4	1.6	1.2	1.2	1.3	1.6	0.91	1.3
Gd	4.5	4.6	1.9	5.0	7.0	7.8	6.9	7.3	6.5	8.2	5.3	7.3
Tb	0.61	0.52	0.16	0.93	1.2	1.6	1.0	1.2	1.1	1.5	0.97	1.3
Dy	3.3	2.9	0.91	5.5	8.4	8.9	7.0	8.9	7.5	10.4	5.6	8.5
Ho	0.73	0.71	0.23	1.2	1.8	1.9	1.4	1.9	1.5	2.3	1.2	1.8
Er	2.0	1.8	0.72	3.3	4.8	5.9	3.8	4.9	4.1	5.7	3.7	5.4
Tm	0.22	0.20	0.07	0.38	0.55	0.60	0.45	0.58	0.43	0.66	0.43	0.64
Yb	1.3	1.4	0.48	2.2	2.9	4.0	2.6	3.0	3.0	4.1	2.4	3.4
Lu	0.16	0.14	0.06	0.27	0.35	0.51	0.35	0.42	0.26	0.46	0.30	0.41
∑REE	68.6	85.8	45.2	38.0	48.5	50.0	40.5	44.1	40.9	52.0	30.7	45.9
Th	0.08	0.15	0.50	0.36	0.52	0.37	0.36	0.35	0.34	0.43	0.45	0.39
U	<LOD	<LOD	<LOD	<LOD	<LOD	<LOD	<LOD	<LOD	<LOD	<LOD	<LOD	<LOD
Pb	0.97	0.85	0.44	<LOD	0.50	0.62	<LOD	<LOD	<LOD	<LOD	<LOD	<LOD
Fe	153	197	149	150	146	160	149	155	173	159	157	142
Sr	<LOD	40.5	10.7	35.8	68.9	76.4	<LOD	52.2	62.7	61.2	26.0	61.5
Ba	<LOD	12.9	2.4	7.4	22.4	1.8	<LOD	0.71	0.10	0.26	<LOD	<LOD
Na	643	172	92.0	96.0	210	447	<LOD	172	174	178	60.1	168
Al	3.5	2.6	<LOD	0.48	1.5	1.4	0.76	0.57	0.69	1.4	<LOD	<LOD
Si	<LOD	224	210	<LOD	192	188	187	208	224	164	174	153
P	24.6	21.2	<LOD	<LOD	21.2	19.8	16.2	21.1	18.5	25.3	16.8	25.6
K	111	27.2	10.5	4.5	13.1	49.0	<LOD	<LOD	6.3	<LOD	<LOD	3.6
Sc	0.22	<LOD	<LOD	<LOD	<LOD	<LOD	<LOD	<LOD	<LOD	<LOD	<LOD	<LOD
Ti	<LOD	2.2	2.2	<LOD	<LOD	1.8	<LOD	2.4	1.2	1.1	1.7	<LOD
V	<LOD	<LOD	<LOD	<LOD	<LOD	0.03	<LOD	<LOD	<LOD	0.02	<LOD	<LOD
Cr	<LOD	<LOD	<LOD	0.61	<LOD	<LOD	<LOD	<LOD	<LOD	<LOD	<LOD	<LOD
Mn	7.3	2.0	0.76	0.35	1.1	2.0	1.2	<LOD	<LOD	<LOD	<LOD	<LOD
Ni	<LOD	0.18	<LOD	0.18	0.10	<LOD	0.18	0.24	0.17	<LOD	0.14	0.03
Cu	<LOD	<LOD	<LOD	<LOD	1.2	<LOD	0.58	<LOD	<LOD	<LOD	<LOD	<LOD
Zn	1.7	1.9	0.72	<LOD	0.34	0.98	<LOD	<LOD	<LOD	<LOD	<LOD	<LOD
Rb	0.49	<LOD	<LOD	0.13	0.17	0.21	<LOD	0.17	<LOD	<LOD	<LOD	0.10
Zr	<LOD	<LOD	<LOD	<LOD	<LOD	<LOD	<LOD	<LOD	<LOD	0.01	<LOD	<LOD
Nb	<LOD	<LOD	<LOD	<LOD	<LOD	<LOD	<LOD	<LOD	<LOD	<LOD	<LOD	<LOD
Ag	<LOD	<LOD	<LOD	<LOD	0.10	<LOD	<LOD	<LOD	<LOD	<LOD	<LOD	<LOD
Bi	0.07	<LOD	<LOD	<LOD	0.02	<LOD	<LOD	<LOD	0.03	<LOD	<LOD	<LOD

13	14	15	16	17	18	19	20	21	22	23	24	25	26	27	28	29	30	31	32	33	34	35
180	147	98.9	187	215	269	196	236	73.9	57.2	109	144	130	77.0	166	419	194	285	264	171	124	148	137
1.1	1.0	3.2	0.95	1.1	1.2	1.2	1.0	5.1	5.9	4.9	8.3	9.4	5.5	1.3	9.8	10.8	14.1	12.4	4.6	7.0	6.4	4.5
3.1	3.3	8.2	2.9	3.7	3.5	3.3	3.0	11.5	13.1	10.2	18.7	21.0	11.9	3.4	16.6	22.8	35.7	35.5	14.9	29.4	23.0	9.2
0.66	0.57	1.4	0.53	0.57	0.71	0.59	0.66	1.7	2.2	1.5	3.1	3.0	2.1	0.61	2.9	3.2	6.6	6.2	2.8	5.4	4.4	1.5
3.5	3.3	7.5	3.6	3.7	4.9	4.1	3.6	8.7	11.1	7.1	14.0	16.3	10.9	3.7	14.8	17.2	32.0	31.8	14.3	30.8	24.4	8.0
2.3	1.9	2.1	2.2	2.2	2.6	2.7	2.9	2.3	1.9	2.4	4.4	4.1	2.3	2.8	13.7	7.0	9.7	9.0	4.8	6.4	5.9	2.7
1.1	0.96	0.80	0.92	1.3	1.4	1.4	1.5	0.51	0.48	0.82	1.2	1.2	0.66	1.3	5.9	2.5	3.5	3.1	1.6	1.7	1.9	0.96
5.4	5.5	3.8	6.6	5.8	7.8	7.4	8.3	2.7	1.9	4.4	4.9	4.1	2.6	7.1	35.4	12.7	12.2	12.3	7.0	6.1	6.7	4.4
0.99	0.81	0.59	0.94	1.1	1.3	1.3	1.4	0.32	0.21	0.76	0.69	0.63	0.36	1.2	5.8	1.9	1.5	1.3	0.87	0.59	0.83	0.78
6.4	5.4	3.3	6.8	8.1	9.0	8.3	9.4	2.4	1.2	4.4	4.6	4.0	2.3	7.1	33.3	11.4	8.9	8.7	5.7	3.8	5.1	4.8
1.4	1.1	0.72	1.5	1.8	1.9	1.7	1.9	0.46	0.31	0.90	0.93	0.80	0.48	1.5	5.8	2.0	2.0	1.9	1.4	0.68	1.1	1.0
3.6	3.0	1.8	3.5	4.7	6.2	5.2	5.7	1.4	0.96	2.4	2.6	2.4	1.4	4.2	14.8	5.1	6.1	5.7	4.2	2.1	3.3	2.9
0.45	0.33	0.19	0.42	0.53	0.59	0.64	0.65	0.16	0.10	0.29	0.31	0.29	0.13	0.47	1.9	0.63	0.92	0.83	0.41	0.23	0.32	0.34
2.6	1.8	1.4	2.8	3.1	3.9	3.9	3.9	0.96	0.57	1.9	2.2	1.9	0.90	2.4	11.3	3.8	4.8	4.9	3.0	1.6	2.1	2.0
0.31	0.27	0.14	0.36	0.37	0.48	0.40	0.47	0.13	0.08	0.24	0.27	0.20	0.10	0.29	1.4	0.43	0.75	0.68	0.36	0.15	0.25	0.23
32.7	29.1	35.1	34.1	37.9	45.6	42.2	44.5	38.3	40.1	42.1	66.2	69.3	41.7	37.3	173	101	139	134	65.9	95.9	85.5	43.3
0.13	0.10	0.17	0.17	0.25	0.23	0.32	0.34	0.11	0.30	0.11	0.17	0.16	0.28	0.14	0.04	0.06	0.94	0.84	0.58	0.90	0.69	0.59
<LOD	<LOD	<LOD	<LOD	<LOD	<LOD	<LOD	<LOD	<LOD	<LOD	<LOD	<LOD	<LOD	<LOD	<LOD	<LOD	<LOD	<LOD	<LOD	<LOD	<LOD	<LOD	<LOD
<LOD	<LOD	0.95	0.21	0.10	0.14	0.25	<LOD	0.09	<LOD	<LOD	<LOD	<LOD	<LOD	<LOD	2.6	0.61	3.0	0.68	0.67	<LOD	1.0	4.9
136	157	171	132	172	147	137	138	166	147	129	140	149	150	147	224	139	160	157	148	141	142	164
39.0	34.4	50.0	39.5	37.0	40.3	49.4	50.2	19.5	6.6	36.0	27.3	25.9	10.6	35.4	188	162	144	97.6	66.3	59.5	65.0	133
<LOD	0.15	4.8	2.6	0.74	1.2	3.4	<LOD	0.32	0.15	<LOD	0.10	<LOD	2.8	<LOD	<LOD	<LOD	41.0	7.7	15.8	35.0	18.9	207
96.8	75.0	397	122	182	105	217	198	194	58.9	82.0	42.1	17.7	104	1260	894	640	487	714	680	1170	1960
<LOD	<LOD	<LOD	<LOD	<LOD	<LOD	0.97	1.2	0.99	0.68	0.88	1.2	<LOD	0.34	5.1	4.4	2.9	3.7	1.7	<LOD	1.4	0.69
153	<LOD	206	<LOD	221	186	243	179	151	167	184	182	180	<LOD	163	190	178	<LOD	<LOD	<LOD	205	<LOD
17.0	19.3	16.5	<LOD	10.0	<LOD	<LOD	20.9	<LOD	25.9	23.8	26.5	17.8	<LOD	119	60.6	28.8	43.0	29.0	26.0	22.0	15.0
<LOD	<LOD	66.0	7.1	11.7	<LOD	7.0	4.5	41.5	<LOD	11.4	<LOD	<LOD	<LOD	79.0	26.1	55.0	39.7	83.0	72.0	107	190
<LOD	<LOD	<LOD	<LOD	0.73	1.7	1.6	1.0	<LOD	<LOD	<LOD	<LOD	<LOD	<LOD	<LOD	<LOD	1.4	2.0	<LOD	<LOD	1.5	1.1
<LOD	1.4	<LOD	<LOD	<LOD	0.02	<LOD	<LOD	<LOD	<LOD	<LOD	<LOD	<LOD	<LOD	<LOD	<LOD	<LOD	<LOD	<LOD	<LOD	<LOD	<LOD	<LOD
<LOD	0.05	<LOD	<LOD	0.65	<LOD	<LOD	<LOD	<LOD	<LOD	<LOD	<LOD	<LOD	<LOD	<LOD	<LOD	0.91	<LOD	<LOD	<LOD	<LOD	<LOD	<LOD
<LOD	<LOD	1.7	<LOD	<LOD	<LOD	<LOD	<LOD	<LOD	<LOD	<LOD	<LOD	<LOD	<LOD	2.2	<LOD	<LOD	<LOD	<LOD	0.88	<LOD	0.89	2.2
<LOD	0.05	0.24	0.19	<LOD	<LOD	<LOD	<LOD	0.26	<LOD	<LOD	<LOD	<LOD	<LOD	<LOD	1.6	1.1	2.5	<LOD	<LOD	0.85	1.0	0.74
<LOD	<LOD	0.79	<LOD	0.49	<LOD	0.83	<LOD	0.22	<LOD	<LOD	<LOD	<LOD	<LOD	<LOD	30.2	<LOD	4.3	1.5	1.9	1.0	4.7	12.7
<LOD	<LOD	1.2	<LOD	0.15	<LOD	0.12	0.16	0.12	<LOD	<LOD	<LOD	<LOD	<LOD	0.12	0.34	<LOD	0.32	<LOD	0.34	0.39	0.51	1.0
<LOD	<LOD	0.28	<LOD	<LOD	<LOD	<LOD	<LOD	0.01	<LOD	<LOD	<LOD	<LOD	<LOD	<LOD	<LOD	<LOD	<LOD	<LOD	<LOD	<LOD	<LOD	<LOD
<LOD	<LOD	<LOD	<LOD	<LOD	<LOD	<LOD	<LOD	<LOD	<LOD	<LOD	<LOD	<LOD	<LOD	<LOD	<LOD	<LOD	<LOD	<LOD	<LOD	<LOD	<LOD	<LOD
<LOD	<LOD	<LOD	<LOD	0.09	<LOD	0.08	0.08	<LOD	<LOD	0.10	<LOD	0.04	<LOD	<LOD	0.02	0.52	<LOD	0.03	<LOD	<LOD	<LOD	0.01

36	37	38	39	40	41	42	43	44	45	46	47	*AVG*	*MIN*	*MAX*	AVG LOD
68.7	93.3	127	111	100	90.0	110	103	115	140	203	124	*151*	*42.6*	*419*	24.20
16.1	24.5	17.0	9.0	3.7	4.3	7.2	3.4	19.3	23.3	1.2	6.2	*5.6*	*0.95*	*24.5*	0.84
30.5	47.7	32.9	16.9	8.4	9.8	13.6	8.1	37.3	48.9	3.6	12.1	*13.1*	*2.9*	*48.9*	2.0
4.0	6.1	4.8	2.3	1.4	1.5	2.2	1.4	5.4	6.5	0.60	2.2	*2.1*	*0.53*	*6.6*	0.32
17.4	24.9	20.3	11.7	7.6	7.5	11.0	7.6	21.8	28.0	3.9	9.2	*10.5*	*2.7*	*32.0*	1.70
3.2	4.4	4.3	2.6	2.7	2.1	4.6	1.8	3.7	3.9	2.8	3.5	*3.2*	*1.8*	*13.7*	0.54
0.65	0.93	1.3	0.96	0.84	0.66	1.6	0.60	0.97	1.0	1.2	1.0	*1.2*	*0.43*	*5.9*	0.17
2.9	4.6	5.5	5.2	4.5	4.0	9.5	2.5	3.4	4.1	7.0	5.7	*5.8*	*1.9*	*35.4*	0.92
0.45	0.67	0.80	0.77	0.72	0.58	1.2	0.46	0.58	0.62	1.2	0.89	*0.91*	*0.16*	*5.8*	0.14
2.3	3.8	4.7	4.7	4.7	3.5	7.2	3.3	3.9	4.6	7.3	5.0	*5.8*	*0.91*	*33.3*	0.91
0.52	0.67	1.1	0.90	0.83	0.66	1.4	0.75	0.91	1.1	1.7	1.1	*1.2*	*0.23*	*5.8*	0.20
1.4	2.0	3.1	2.6	2.5	1.7	3.2	2.2	2.9	4.0	4.4	2.6	*3.4*	*0.72*	*14.8*	0.53
0.16	0.24	0.37	0.28	0.22	0.20	0.38	0.31	0.38	0.48	0.49	0.30	*0.39*	*0.07*	*1.9*	0.06
1.2	1.7	2.4	1.6	1.4	1.1	2.7	1.7	2.4	3.2	2.7	1.8	*2.4*	*0.48*	*11.3*	0.42
0.15	0.24	0.31	0.19	0.15	0.15	0.26	0.22	0.40	0.47	0.32	0.23	*0.29*	*0.06*	*1.4*	0.04
80.8	122	98.8	59.6	39.7	37.8	65.9	34.3	103	130	38.3	51.9	*57.0*	*29.1*	*173*	<LOD
<LOD	0.09	0.19	0.15	0.33	0.23	0.36	<LOD	0.05	0.05	0.42	0.42	*0.29*	*<LOD*	*0.94*	0.04
<LOD	<LOD	0.11	<LOD	<LOD	<LOD	<LOD	0.16	<LOD	0.01	<LOD	<LOD	*0.04*	*<LOD*	*0.16*	0.01
2.0	<LOD	0.71	<LOD	0.44	3.1	<LOD	0.78	0.94	0.85	<LOD	0.36	*0.89*	*<LOD*	*4.9*	<LOD
170	<LOD	2600	<LOD	145	158	139	4300	<LOD	156	128	143	*152*	*<LOD*	*4300*	27.0
182	38.3	95.0	27.2	55.2	130	163	19.4	42.7	36.5	28.6	63.8	*55.5*	*<LOD*	*188*	9.10
<LOD	<LOD	3600	<LOD	3.2	27.0	<LOD	5.5	6.1	8.8	<LOD	23.0	*8.6*	*<LOD*	*3600*	1.40
<LOD	<LOD	477	163	369	1700	455	181	271	283	149	240	*289*	*<LOD*	*1960*	57.10
4.4	6.6	11.5	<LOD	<LOD	0.33	2.2	22.6	8.0	9.1	0.33	0.81	*2.2*	*<LOD*	*22.6*	0.58
<LOD	<LOD	<LOD	172	<LOD	61.0	<LOD	151	183	<LOD	<LOD	<LOD	*184*	*<LOD*	*243*	142
36.0	73.0	46.5	29.8	<LOD	8.3	<LOD	37.9	82.0	78.5	<LOD	<LOD	*28.0*	*<LOD*	*119*	13.20
<LOD	<LOD	53.9	27.2	79.8	89.0	19.0	35.8	33.8	30.7	<LOD	15.7	*38.1*	*<LOD*	*190*	6.50
<LOD	<LOD	<LOD	<LOD	<LOD	<LOD	<LOD	<LOD	<LOD	<LOD	<LOD	<LOD	*0.16*	*<LOD*	*0.22*	0.16
<LOD	<LOD	1.6	1.3	<LOD	0.79	<LOD	1.2	<LOD	<LOD	<LOD	<LOD	*1.5*	*<LOD*	*2.4*	1.30
<LOD	<LOD	0.45	<LOD	<LOD	<LOD	0.04	0.30	<LOD	0.03	<LOD	<LOD	*0.12*	*<LOD*	*0.45*	0.05
<LOD	<LOD	<LOD	<LOD	<LOD	<LOD	<LOD	<LOD	<LOD	<LOD	<LOD	<LOD	*0.72*	*<LOD*	*0.91*	0.87
4.6	<LOD	2.1	2.0	1.7	4.7	<LOD	1.5	1.6	1.1	<LOD	0.72	*1.7*	*<LOD*	*7.3*	0.53
<LOD	<LOD	<LOD	<LOD	0.24	0.10	<LOD	0.07	<LOD	0.22	<LOD	0.25	*0.16*	*<LOD*	*0.25*	0.15
1.3	<LOD	<LOD	<LOD	<LOD	0.47	<LOD	1.1	1.2	0.41	<LOD	<LOD	*0.94*	*<LOD*	*2.5*	0.43
<LOD	<LOD	2.1	<LOD	0.85	20.0	<LOD	1.4	1.6	1.8	<LOD	1.2	*2.3*	*<LOD*	*30.2*	0.49
0.98	<LOD	0.20	0.12	0.27	0.67	0.12	0.15	<LOD	<LOD	<LOD	0.07	*0.25*	*<LOD*	*1.0*	0.11
<LOD	<LOD	0.50	<LOD	<LOD	<LOD	<LOD	<LOD	<LOD	<LOD	<LOD	<LOD	*0.10*	*<LOD*	*0.50*	0.01
<LOD	<LOD	0.18	<LOD	<LOD	<LOD	<LOD	<LOD	<LOD	<LOD	<LOD	<LOD	*0.09*	*<LOD*	*0.18*	0.01
<LOD	<LOD	<LOD	<LOD	<LOD	0.11	<LOD	<LOD	<LOD	<LOD	<LOD	<LOD	*0.10*	*<LOD*	*0.52*	0.10
<LOD	<LOD	0.08	<LOD	<LOD	<LOD	<LOD	<LOD	<LOD	<LOD	<LOD	<LOD	*0.04*	*<LOD*	*0.08*	0.03

Sample 7a; purple

n=30	1	2	3	4	5
Y	133	167	207	104	192
La	12.1	3.7	3.2	2.0	5.4
Ce	24.4	9.0	10.2	8.7	25.9
Pr	3.6	1.4	1.9	2.0	4.4
Nd	16.4	7.9	10.3	9.9	24.3
Sm	5.3	3.6	4.7	2.9	6.9
Eu	1.6	1.6	2.0	0.83	2.5
Gd	8.3	7.3	9.1	3.5	7.0
Tb	1.2	1.1	1.5	0.36	1.0
Dy	7.3	8.1	10.0	2.2	5.9
Ho	1.4	1.8	2.1	0.59	1.3
Er	3.5	5.2	5.7	1.6	3.9
Tm	0.44	0.58	0.70	0.23	0.41
Yb	2.9	3.9	4.1	1.2	2.7
Lu	0.32	0.45	0.45	0.15	0.30
∑REE	88.7	55.4	65.8	36.2	91.9
Th	0.04	0.02	0.51	0.19	0.16
U	<LOD	<LOD	<LOD	<LOD	<LOD
Pb	2.3	<LOD	0.31	<LOD	7.9
Fe	119	118	119	139	115
Sr	98.0	79.0	122	<LOD	51.1
Ba	0.99	0.30	0.90	122	61.0
Na	4730	766	3100	<LOD	3150
Al	1.8	0.93	1.3	0.89	0.43
Si	231	150	<LOD	135	<LOD
P	32.6	33.5	32.0	<LOD	16.8
K	478	64.4	254	<LOD	234
Sc	<LOD	<LOD	<LOD	<LOD	<LOD
Ti	<LOD	1.4	<LOD	1.6	0.94
V	<LOD	<LOD	<LOD	<LOD	<LOD
Cr	<LOD	<LOD	<LOD	<LOD	<LOD
Mn	2.9	<LOD	1.7	<LOD	4.3
Ni	0.12	0.08	<LOD	<LOD	<LOD
Cu	<LOD	<LOD	<LOD	<LOD	<LOD
Zn	17.8	<LOD	1.3	<LOD	17.8
Rb	1.7	<LOD	0.98	<LOD	0.93
Zr	<LOD	<LOD	<LOD	<LOD	<LOD
Nb	<LOD	<LOD	<LOD	<LOD	<LOD
Ag	<LOD	<LOD	0.14	<LOD	<LOD
Bi	0.06	0.05	<LOD	<LOD	<LOD

6	7	8	9	10	11	12	13	14	15	16	17	18	19	20	21	22	23	24	25	26	27	28
100	112	70.0	212	165	153	113	254	226	177	247	250	225	238	276	204	219	270	261	262	343	394	
4.1	16.4	26.2	0.99	1.8	2.4	12.6	1.1	2.0	2.1	2.8	1.7	1.7	3.3	63.7	29.0	10.1	4.4	4.5	6.0	2.2	1.8	
14.0	27.9	38.7	3.4	4.9	5.9	22.6	3.9	6.7	5.8	7.8	5.9	7.4	8.8	71.1	49.3	24.0	11.9	12.1	16.9	7.5	6.4	
2.6	3.6	4.2	0.63	0.76	0.90	3.1	0.64	1.1	0.96	1.5	1.0	1.3	1.5	8.3	6.7	3.5	1.9	2.0	2.4	1.4	1.2	
12.9	14.7	15.4	3.1	4.8	4.7	13.6	4.1	4.9	5.3	7.1	4.5	6.3	8.7	24.1	29.9	17.4	9.2	9.3	11.5	8.2	7.1	
2.8	5.3	4.0	1.8	2.4	2.3	4.1	2.1	2.2	1.9	3.5	2.9	3.1	3.9	5.3	11.0	7.7	4.8	4.9	5.2	5.0	3.7	
0.84	1.6	0.97	1.3	1.4	1.1	1.6	1.4	1.3	1.2	1.9	1.3	1.9	2.1	2.5	3.8	2.6	2.1	2.2	2.4	2.2	2.3	
2.9	6.9	4.6	5.0	6.0	5.3	7.9	5.5	5.8	5.4	8.4	5.7	9.3	8.9	10.5	20.3	14.0	10.2	9.6	10.0	11.1	9.0	
0.41	0.97	0.59	0.96	1.1	0.92	1.2	1.1	1.1	1.0	1.5	1.3	1.6	1.5	1.8	3.0	2.0	1.5	1.4	1.7	2.3	1.9	
2.3	7.1	3.2	7.7	8.8	6.9	7.6	9.0	8.3	7.7	11.4	9.4	11.7	11.5	13.6	14.5	11.9	11.1	10.6	12.8	14.9	14.5	
0.73	1.3	0.51	1.9	1.8	1.6	1.4	2.1	2.0	1.6	2.4	1.8	2.3	2.2	3.2	2.6	2.2	2.4	2.4	2.3	3.1	3.3	
1.7	3.1	1.4	5.4	5.0	4.7	4.0	6.6	6.6	5.1	7.3	6.8	7.9	7.8	9.9	6.9	6.5	7.3	7.4	7.3	10.6	10.9	
0.24	0.42	0.13	0.59	0.69	0.56	0.53	0.76	0.65	0.60	0.97	0.85	1.0	0.91	1.3	0.89	0.82	0.87	0.97	0.91	1.5	1.3	
1.3	2.8	0.92	4.1	3.8	3.5	3.0	5.1	3.9	3.8	5.4	4.5	5.4	5.1	7.3	5.1	5.1	5.3	6.5	5.1	7.6	8.2	
0.13	0.38	0.10	0.42	0.48	0.38	0.36	0.57	0.38	0.42	0.73	0.45	0.59	0.58	0.90	0.60	0.63	0.68	0.57	0.67	1.1	1.1	
47.0	92.4	101	37.2	43.7	41.2	83.5	44.0	46.9	42.8	62.8	48.0	61.6	66.8	224	184	108	73.9	74.4	85.3	78.6	72.7	
27.6	92.4	101	37.2	43.7	41.2	83.5	44.0	46.9	42.8	62.8	48.0	61.6	66.8	224	184	108	73.9	74.4	85.3	78.6	72.7	
0.13	0.01	0.04	0.23	0.30	0.29	<LOD	0.19	0.12	0.11	0.09	0.05	0.08	0.11	1.0	0.04	<LOD	0.02	<LOD	0.03	0.01	0.08	
<LOD	<LOD	<LOD	<LOD	<LOD	<LOD	<LOD	<LOD	<LOD	<LOD	<LOD	<LOD	<LOD	<LOD	0.83	<LOD	<LOD	<LOD	<LOD	<LOD	<LOD	<LOD	
<LOD	0.74	1.8	<LOD	<LOD	0.72	<LOD	<LOD	<LOD	<LOD	<LOD	<LOD	<LOD	<LOD	0.98	1.5	0.27	<LOD	<LOD	0.49	<LOD	<LOD	
122	125	156	122	138	128	130	135	128	130	126	130	153	131	<LOD	<LOD	113	104	106	131	110	150	
24.6	375	346	40.3	52.5	63.4	255	50.1	70.7	61.3	104	67.0	74.0	82.0	99.0	820	162	105	86.4	120	72.0	63.8	
<LOD	1.2	1550	<LOD	<LOD	2.5	<LOD	0.40	0.26	<LOD	0.02	<LOD	2.8	0.31	480	<LOD	0.34	0.39	5.2	2.1	5.4	2.6	
239	947	1600	107	132	1290	452	179	168	150	299	171	216	388	610	7300	1570	472	295	720	274	350	
0.84	10.6	9.9	0.54	0.68	0.92	5.8	<LOD	0.56	<LOD	0.99	<LOD	1.7	0.96	882	10.0	1.7	0.98	<LOD	0.94	2.1	0.93	
<LOD	<LOD	191	<LOD	<LOD	142	176	<LOD	182	<LOD	<LOD	<LOD	<LOD	<LOD	1100	120	<LOD	<LOD	<LOD	<LOD	<LOD	<LOD	
<LOD	53.0	53.1	13.2	<LOD	15.3	35.0	<LOD	18.4	9.6	30.8	<LOD	<LOD	14.6	69.0	32.8	24.7	<LOD	<LOD	<LOD	16.0	38.0	
28.0	43.6	106	<LOD	<LOD	62.0	7.6	<LOD	<LOD	<LOD	<LOD	<LOD	<LOD	8.6	352	409	46.7	<LOD	<LOD	25.8	<LOD	<LOD	
<LOD	<LOD	<LOD	<LOD	<LOD	<LOD	<LOD	<LOD	<LOD	<LOD	<LOD	<LOD	<LOD	<LOD	3.0	<LOD	<LOD	<LOD	<LOD	<LOD	0.14	<LOD	
<LOD	<LOD	1.3	<LOD	<LOD	0.07	<LOD	<LOD	<LOD	1.9	<LOD	1.1	<LOD	<LOD	18.6	0.56	0.96	<LOD	<LOD	<LOD	2.7	1.3	
<LOD	<LOD	0.85	<LOD	<LOD	<LOD	<LOD	<LOD	<LOD	<LOD	<LOD	<LOD	<LOD	<LOD	1.3	<LOD	<LOD	<LOD	<LOD	<LOD	0.18	<LOD	
<LOD	2.6	3.0	<LOD	<LOD	<LOD	<LOD	<LOD	<LOD	<LOD	<LOD	<LOD	0.29	<LOD	<LOD	<LOD	0.62	<LOD	<LOD	1.2	0.70	<LOD	
<LOD	0.03	<LOD	<LOD	<LOD	<LOD	<LOD	0.11	<LOD	<LOD	0.10	0.23	0.29	0.45	<LOD	<LOD	<LOD	0.35	<LOD	<LOD	0.20	<LOD	
<LOD	1.9	4.8	<LOD	<LOD	1.4	<LOD	<LOD	<LOD	<LOD	<LOD	<LOD	0.69	0.38	<LOD	4.7	1.2	<LOD	<LOD	0.92	0.82	<LOD	
<LOD	0.18	0.51	<LOD	<LOD	0.24	0.09	<LOD	<LOD	<LOD	<LOD	<LOD	<LOD	<LOD	1.7	2.1	<LOD	0.09	<LOD	0.19	<LOD	<LOD	
<LOD	<LOD	<LOD	<LOD	<LOD	<LOD	<LOD	<LOD	<LOD	<LOD	<LOD	<LOD	<LOD	<LOD	1.4	<LOD	<LOD	<LOD	<LOD	<LOD	<LOD	<LOD	
<LOD	<LOD	<LOD	<LOD	<LOD	<LOD	<LOD	<LOD	<LOD	<LOD	<LOD	<LOD	0.16	<LOD	0.99	<LOD	<LOD	<LOD	<LOD	<LOD	<LOD	0.16	
<LOD	<LOD	<LOD	<LOD	<LOD	<LOD	<LOD	<LOD	<LOD	<LOD	<LOD	<LOD	<LOD	<LOD	0.10	<LOD	0.15	<LOD	<LOD	0.12	<LOD	0.07	
<LOD	<LOD	0.04	<LOD	<LOD	<LOD	0.02	<LOD	<LOD	<LOD	0.12	<LOD	<LOD	<LOD	0.05	0.01	<LOD	<LOD	<LOD	<LOD	<LOD	<LOD	

Sample 7b; purple

29	30	*AVG*	*MIN*	*MAX*	AVG LOD	n=40	1	2	3	4	5	6	7	8	9	10	11	12	13	14	15
193	198	*199*	*70.0*	*394*	30.3	Y	260	199	194	120	125	222	225	150	146	128	178	194	141	149	207
2.4	8.6	*4.9*	*0.99*	*63.7*	0.99	La	1.1	1.0	1.4	29.9	7.0	1.5	7.0	9.3	4.9	2.5	1.3	0.83	1.0	8.5	1.3
6.3	20.9	*12.6*	*3.4*	*71.1*	2.30	Ce	4.5	3.7	5.1	42.5	11.6	5.0	11.9	18.1	10.5	5.0	3.3	2.3	2.2	16.9	3.8
0.86	3.1	*2.0*	*0.63*	*8.3*	0.39	Pr	0.72	0.65	0.83	4.8	1.6	0.76	1.4	2.2	1.5	0.73	0.55	0.39	0.44	2.4	0.69
6.4	14.3	*9.7*	*3.1*	*29.9*	1.90	Nd	5.0	3.4	3.8	19.2	7.0	4.0	6.8	11.1	7.8	3.7	3.1	2.6	2.3	11.4	3.7
2.9	6.9	*3.9*	*1.8*	*11.0*	0.78	Sm	2.4	2.1	1.9	4.4	2.7	1.8	2.8	3.7	2.5	1.9	1.8	1.9	1.2	3.3	2.0
1.6	2.4	*1.7*	*0.59*	*3.8*	0.27	Eu	1.3	1.3	1.2	1.6	1.2	1.2	1.5	1.5	1.4	0.85	1.0	1.1	0.77	1.2	1.1
7.2	11.4	*7.7*	*2.6*	*20.3*	1.20	Gd	7.7	5.2	4.8	6.0	6.1	4.8	6.0	6.7	5.9	4.5	5.2	4.4	3.5	6.3	5.0
1.3	1.9	*1.3*	*0.34*	*3.0*	0.21	Tb	1.4	1.0	0.92	0.84	1.1	1.1	1.2	1.3	0.98	0.71	1.1	1.0	0.75	1.1	1.1
9.0	11.7	*9.3*	*2.2*	*14.9*	1.40	Dy	10.0	7.1	6.6	5.0	6.6	7.7	8.8	7.7	6.8	5.4	7.3	7.3	5.9	6.4	8.5
1.9	2.2	*1.9*	*0.51*	*3.3*	0.31	Ho	3.0	1.7	1.7	0.96	1.4	1.8	1.9	1.6	1.4	1.2	1.5	1.7	1.3	1.3	2.0
5.6	7.0	*5.8*	*1.4*	*10.9*	0.90	Er	6.9	5.1	5.3	2.4	3.6	5.9	6.1	4.2	4.3	3.5	4.6	5.4	3.9	3.6	6.0
0.76	0.93	*0.71*	*0.13*	*1.5*	0.12	Tm	0.93	0.57	0.52	0.28	0.43	0.67	0.74	0.54	0.51	0.37	0.57	0.62	0.44	0.50	0.70
4.1	4.9	*4.2*	*0.92*	*8.2*	0.71	Yb	4.6	3.4	3.3	1.8	2.7	4.1	4.3	3.0	2.9	2.4	3.9	3.8	2.7	2.9	4.4
0.49	0.69	*0.49*	*0.10*	*1.1*	0.08	Lu	0.53	0.42	0.36	0.17	0.34	0.52	0.54	0.36	0.36	0.24	0.44	0.44	0.30	0.33	0.63
50.7	96.8	*67.3*	*27.6*	*224*	<LOD	∑REE	50.2	36.6	37.7	120	53.4	40.9	60.9	71.3	51.7	33.0	35.7	33.6	26.8	66.1	40.8
0.12	0.06	*0.11*	*<LOD*	*1.0*	0.02	Th	0.46	0.35	0.31	0.02	0.08	0.14	0.12	0.04	0.06	0.09	0.08	0.12	0.06	0.06	0.07
<LOD	<LOD	*0.28*	*<LOD*	*0.83*	0.01	U	<LOD	<LOD	0.49	<LOD	<LOD	0.01	<LOD	<LOD	<LOD	<LOD	<LOD	<LOD	<LOD	<LOD	<LOD
<LOD	<LOD	*1.9*	*<LOD*	*42.8*	<LOD	Pb	0.22	<LOD	0.49	4.2	0.28	0.19	1.4	9.5	0.64	1.4	0.92	0.68	0.32	<LOD	0.21
135	124	*128*	*<LOD*	*170*	49.7	Fe	166	127	126	210	133	132	125	138	122	127	171	130	119	130	131
69.6	228	*118*	*<LOD*	*820*	28.9	Sr	66.0	44.0	80.6	227	86.1	54.2	239	315	96.1	91.0	44.5	36.7	26.4	31.7	46.2
2.7	0.21	*33.2*	*<LOD*	*1550*	15.2	Ba	0.87	<LOD	0.80	<LOD	<LOD	0.20	0.93	9.4	0.51	7.9	2.9	2.3	0.55	0.67	3.9
351	659	*767*	*<LOD*	*7300*	138	Na	127	108	210	7100	349	189	2520	6200	532	1170	800	670	231	163	420
<LOD	4.8	*2.3*	*<LOD*	*882*	0.91	Al	1.4	<LOD	<LOD	6.0	1.3	1.3	5.2	4.1	1.7	3.4	<LOD	0.62	1.5	<LOD	1.1
<LOD	<LOD	*167*	*<LOD*	*1100*	135	Si	81.0	218	<LOD	98.0	146	<LOD	130	137	191	<LOD	<LOD	<LOD	<LOD	179	190
18.4	35.0	*27.2*	*<LOD*	*69.0*	13.5	P	11.6	18.0	<LOD	52.0	33.0	<LOD	18.6	24.0	21.0	<LOD	15.3	17.5	15.6	22.5	20.8
11.7	10.3	*142*	*<LOD*	*960*	13.5	K	3.9	4.0	9.3	341	20.6	<LOD	184	570	39.5	83.0	60.0	53.0	22.4	23.2	26.3
<LOD	<LOD	*1.6*	*<LOD*	*3.0*	0.16	Sc	<LOD	<LOD	<LOD	<LOD	<LOD	<LOD	<LOD	<LOD	<LOD	<LOD	<LOD	<LOD	<LOD	<LOD	<LOD
<LOD	<LOD	*1.5*	*<LOD*	*18.6*	1.40	Ti	<LOD	<LOD	<LOD	0.84	0.80	<LOD	<LOD	<LOD	<LOD	<LOD	<LOD	<LOD	<LOD	<LOD	1.4
<LOD	<LOD	*0.13*	*<LOD*	*0.18*	0.06	V	0.03	<LOD	<LOD	0.03	<LOD	<LOD	<LOD	<LOD	<LOD	<LOD	<LOD	0.05	<LOD	<LOD	<LOD
<LOD	<LOD	*1.5*	*<LOD*	*3.0*	0.89	Cr	<LOD	<LOD	<LOD	<LOD	<LOD	<LOD	<LOD	<LOD	<LOD	<LOD	<LOD	<LOD	<LOD	<LOD	<LOD
0.69	<LOD	*2.1*	*<LOD*	*37.0*	7.40	Mn	<LOD	<LOD	2.0	9.8	0.90	<LOD	2.6	2.8	1.4	0.89	1.7	2.0	1.2	0.65	<LOD
0.19	<LOD	*0.17*	*<LOD*	*0.35*	0.15	Ni	0.28	<LOD	0.12	0.11	<LOD	<LOD	0.08	0.08	0.09	0.18	<LOD	0.25	<LOD	<LOD	0.16
<LOD	<LOD	*0.97*	*<LOD*	*2.8*	0.43	Cu	0.58	<LOD	<LOD	0.78	<LOD	0.32	<LOD	0.37	0.82	<LOD	1.3	<LOD	<LOD	<LOD	<LOD
0.98	<LOD	*4.5*	*<LOD*	*112*	1.30	Zn	0.79	<LOD	<LOD	16.2	<LOD	<LOD	7.2	51.0	1.7	3.3	1.4	0.83	<LOD	<LOD	0.98
0.10	<LOD	*0.80*	*<LOD*	*5.2*	0.13	Rb	0.08	<LOD	<LOD	1.7	0.12	<LOD	0.82	2.7	0.24	0.53	0.36	0.34	0.14	0.13	0.18
<LOD	<LOD	*0.28*	*<LOD*	*1.4*	0.01	Zr	0.08	<LOD	<LOD	<LOD	<LOD	<LOD	<LOD	<LOD	<LOD	<LOD	<LOD	<LOD	<LOD	<LOD	<LOD
<LOD	<LOD	*0.99*	*<LOD*	*0.99*	0.01	Nb	<LOD	<LOD	<LOD	<LOD	<LOD	<LOD	<LOD	<LOD	<LOD	<LOD	<LOD	<LOD	<LOD	<LOD	<LOD
0.16	<LOD	*0.14*	*<LOD*	*0.20*	0.11	Ag	<LOD	<LOD	<LOD	0.24	0.09	<LOD	0.10	0.24	<LOD	<LOD	<LOD	<LOD	<LOD	<LOD	<LOD
<LOD	<LOD	*0.04*	*<LOD*	*0.07*	0.03	Bi	0.04	<LOD	<LOD	<LOD	<LOD	<LOD	<LOD	<LOD	<LOD	<LOD	<LOD	<LOD	0.06	<LOD	<LOD

16	17	18	19	20	21	22	23	24	25	26	27	28	29	30	31	32	33	34	35	36	37	38
198	146	118	152	171	268	193	189	154	132	115	125	305	136	140	244	202	352	276	325	279	332	182
3.8	3.9	1.5	5.7	3.5	19.0	8.4	7.2	13.6	29.3	12.8	3.8	3.3	11.8	17.3	8.9	19.7	3.2	7.1	3.8	5.5	4.2	9.9
8.4	17.5	6.8	22.6	11.4	38.9	18.8	18.1	30.6	54.2	22.7	9.6	10.1	23.0	29.8	22.5	39.0	9.5	19.8	11.9	13.4	12.8	22.1
1.1	3.2	1.3	4.3	2.2	5.9	2.8	3.0	4.3	7.0	3.0	1.5	1.5	3.1	4.2	3.4	5.8	2.0	3.6	2.1	2.5	2.8	3.2
5.9	17.9	7.5	25.7	10.4	28.5	15.2	14.4	21.7	30.2	14.1	7.6	8.1	15.3	18.6	18.3	28.2	10.8	19.7	13.0	13.2	14.0	16.4
2.3	5.4	1.9	6.1	4.1	7.9	5.9	4.2	5.9	8.7	4.5	2.5	3.9	5.1	6.3	7.8	10.6	5.3	7.2	5.8	5.9	6.9	7.2
1.1	1.6	0.74	1.7	1.7	2.9	2.3	1.6	1.7	2.6	1.5	0.75	2.0	1.6	1.9	3.0	3.2	2.5	2.5	2.8	2.5	2.8	2.2
4.6	4.7	2.9	5.6	6.4	12.3	10.8	6.3	7.8	12.4	8.2	3.7	9.0	8.1	10.1	14.7	17.8	11.0	11.9	12.0	11.8	12.3	12.1
0.94	0.64	0.41	0.60	1.0	1.8	1.6	0.90	1.0	1.6	1.3	0.50	1.6	1.1	1.3	2.3	2.3	1.9	1.7	1.9	1.9	2.0	1.8
7.1	3.5	2.9	3.6	6.3	11.1	10.6	6.8	6.1	8.2	6.5	3.7	11.9	6.5	7.5	13.6	13.1	14.6	9.8	13.5	13.2	14.2	9.2
1.4	0.75	0.60	0.85	1.4	2.3	2.0	1.5	1.3	1.4	1.2	0.87	2.7	1.2	1.3	2.6	2.1	3.2	2.3	3.1	2.9	3.0	1.7
4.8	2.6	2.0	2.5	4.4	7.0	5.7	4.6	3.8	3.3	3.5	2.4	9.0	3.2	3.4	7.1	5.5	9.9	7.1	8.4	9.0	9.5	4.5
0.63	0.32	0.20	0.26	0.46	0.83	0.72	0.63	0.42	0.44	0.39	0.30	1.1	0.40	0.40	0.90	0.72	1.2	0.85	1.0	1.1	1.0	0.54
3.2	2.2	1.3	1.7	2.8	5.3	3.9	3.5	2.8	2.7	2.5	1.7	7.0	2.6	2.5	5.0	4.6	7.1	5.2	5.8	6.4	6.8	3.5
0.32	0.19	0.13	0.19	0.34	0.64	0.53	0.45	0.32	0.30	0.33	0.21	0.85	0.35	0.35	0.57	0.61	0.83	0.60	0.69	0.78	0.81	0.41
45.6	64.3	30.1	81.4	56.4	144	89.2	73.3	101	162	82.3	39.1	72.0	83.4	105	111	153	82.8	99.4	85.6	90.1	93.1	94.5
0.06	0.21	0.15	0.26	0.36	0.02	<LOD	0.01	0.02	<LOD	<LOD	0.13	0.15	0.10	<LOD	0.05	0.07	0.10	0.07	0.09	0.11	0.06	<LOD
<LOD	<LOD	<LOD	<LOD	<LOD	<LOD	<LOD	<LOD	<LOD	0.01	<LOD	<LOD	<LOD	0.01	0.01	0.01	0.01	<LOD	<LOD	<LOD	<LOD	<LOD	0.03
1.3	0.64	<LOD	1.0	0.67	<LOD	4.8	2.4	1.2	1.0	0.13	12.7	0.58	6.3	1.5	0.46	2.6	3.6	<LOD	<LOD	0.07	<LOD	0.58
154	111	137	171	132	138	132	149	160	141	<LOD	148	131	138	134	102	137	760	138	130	145	131	125
270	27.6	<LOD	29.1	98.6	248	190	238	89.0	243	105	129	54.8	302	188	104	170	<LOD	66.2	57.3	44.3	54.4	70.8
41.0	1.7	<LOD	2.4	<LOD	<LOD	16.0	59.0	5.6	5.8	0.33	33.5	<LOD	62.0	7.6	1.8	7.0	22.0	1.0	<LOD	0.15	1.0	1.2
9100	430	<LOD	543	1220	<LOD	4800	8600	3320	5030	995	6400	892	7700	1559	1570	3140	<LOD	588	709	529	614	770
0.76	<LOD	<LOD	<LOD	1.5	16.3	3.3	6.2	1.4	5.8	<LOD	0.84	1.7	5.8	3.4	2.0	9.0	2.7	7.5	<LOD	1.9	2.3	5.8
153	<LOD	<LOD	124	226	202	169	168	181	70.0	<LOD	201	348	171	145	<LOD	164	278	480	<LOD	69.0	141	135
11.5	16.7	22.0	17.3	43.8	134	42.9	37.3	32.3	124	30.6	33.9	36.2	50.9	45.8	54.4	159	52.4	1870	<LOD	48.7	66.0	85.0
500	35.6	<LOD	41.4	105	<LOD	360	471	372	264	43.2	520	75.4	530	108	59.0	210	<LOD	25.2	23.1	8.8	13.5	39.0
<LOD	<LOD	<LOD	<LOD	<LOD	<LOD	<LOD	<LOD	<LOD	<LOD	<LOD	<LOD	<LOD	<LOD	<LOD	<LOD	<LOD	<LOD	1.3	<LOD	<LOD	<LOD	<LOD
0.80	<LOD	<LOD	0.82	<LOD	<LOD	0.81	0.68	<LOD	5.8	<LOD	0.95	<LOD	0.60	1.3	2.6	<LOD	<LOD	3.2	<LOD	<LOD	<LOD	<LOD
0.02	<LOD	<LOD	<LOD	<LOD	<LOD	<LOD	<LOD	<LOD	<LOD	<LOD	<LOD	0.03	<LOD	<LOD	<LOD	0.03	<LOD	0.11	<LOD	<LOD	<LOD	<LOD
<LOD	<LOD	<LOD	<LOD	<LOD	0.54	<LOD	0.43	<LOD	<LOD	<LOD	<LOD	<LOD	<LOD	<LOD	<LOD	<LOD	<LOD	7.5	<LOD	<LOD	<LOD	<LOD
2.9	1.5	<LOD	0.69	0.74	<LOD	4.8	9.3	7.9	2.5	0.94	5.7	1.2	12.5	4.3	0.86	3.0	5.3	20.0	<LOD	<LOD	<LOD	1.3
0.11	0.31	<LOD	0.18	0.03	<LOD	<LOD	0.15	<LOD	0.10	<LOD	0.03	0.40	<LOD	<LOD	<LOD	0.16	<LOD	0.63	<LOD	0.24	0.15	0.25
0.20	<LOD	<LOD	0.50	<LOD	<LOD	0.38	<LOD	0.26	0.16	<LOD	0.91	<LOD	0.52	0.62	<LOD	8.1	0.62	0.57	<LOD	0.30	<LOD	<LOD
24.0	1.8	<LOD	2.4	7.2	<LOD	8.0	9.5	1.8	10.0	0.41	31.0	2.2	37.0	3.5	2.4	10.3	<LOD	<LOD	<LOD	1.2	0.86	2.2
2.2	<LOD	<LOD	0.24	0.39	<LOD	1.4	1.8	1.2	0.98	0.18	2.8	0.47	2.3	0.46	0.30	0.94	<LOD	0.19	0.17	<LOD	<LOD	0.12
<LOD	0.02	<LOD	<LOD	<LOD	<LOD	<LOD	<LOD	<LOD	<LOD	<LOD	<LOD	<LOD	<LOD	<LOD	<LOD	<LOD	<LOD	<LOD	<LOD	<LOD	<LOD	0.04
<LOD	<LOD	<LOD	<LOD	<LOD	<LOD	<LOD	<LOD	<LOD	<LOD	<LOD	<LOD	<LOD	<LOD	<LOD	<LOD	<LOD	<LOD	<LOD	<LOD	<LOD	<LOD	<LOD
<LOD	<LOD	<LOD	<LOD	<LOD	<LOD	0.13	0.05	0.11	0.21	0.09	<LOD	0.23	0.12	<LOD	<LOD	<LOD	<LOD	0.18	<LOD	0.07	0.10	<LOD
<LOD	<LOD	<LOD	<LOD	<LOD	<LOD	0.01	<LOD	<LOD	0.01	0.07	0.03	<LOD	<LOD	<LOD	<LOD	<LOD	<LOD	<LOD	<LOD	<LOD	<LOD	<LOD

						Sample 7c, white														
39	**40**	***AVG***	***MIN***	***MAX***	**AVG LOD**	**n=39**	**1**	**2**	**3**	**4**	**5**	**6**	**7**	**8**	**9**	**10**	**11**	**12**	**13**	**14**	**15**
215	179	*187*	*115*	*352*	30.2	Y	236	273	244	226	305	221	234	227	251	229	217	212	258	226	207
11.1	26.4	*6.7*	*0.83*	*29.9*	0.81	La	0.17	0.15	0.16	0.13	0.23	0.18	0.14	0.15	0.13	0.14	0.09	0.07	0.17	0.10	0.09
25.5	57.3	*15.6*	*2.2*	*57.3*	1.90	Ce	0.96	1.2	0.94	0.89	1.4	1.1	1.0	0.88	1.0	0.70	0.64	0.65	1.2	0.67	0.42
4.0	8.0	*2.4*	*0.39*	*8.0*	0.28	Pr	0.27	0.28	0.27	0.21	0.29	0.23	0.24	0.25	0.28	0.21	0.17	0.16	0.21	0.19	0.16
19.5	37.1	*12.2*	*2.3*	*37.1*	1.50	Nd	1.8	2.2	1.9	1.9	3.0	1.7	1.9	1.8	1.7	1.7	1.3	1.4	1.8	1.8	1.3
7.2	11.4	*4.4*	*1.2*	*11.4*	0.59	Sm	1.8	2.0	1.8	1.5	2.2	1.4	1.7	1.4	1.7	1.8	1.6	1.2	1.5	1.6	1.5
2.6	3.2	*1.7*	*0.74*	*3.2*	0.23	Eu	1.6	1.9	1.7	1.6	2.1	1.5	1.4	1.4	1.5	1.5	1.4	1.1	1.1	1.8	1.3
14.0	15.6	*7.9*	*2.9*	*17.8*	1.10	Gd	6.0	6.6	6.0	5.5	7.1	5.2	5.4	5.6	5.6	5.1	4.4	4.4	4.4	5.4	4.2
2.1	2.0	*1.3*	*0.41*	*2.3*	0.18	Tb	1.4	1.5	1.4	1.3	1.6	1.2	1.2	1.3	1.3	1.3	1.2	1.1	1.1	1.2	1.0
11.2	10.5	*8.2*	*2.9*	*14.6*	1.30	Dy	11.2	10.8	10.7	9.6	14.3	8.4	8.6	9.4	11.3	9.5	8.8	8.6	8.6	11.5	8.2
2.3	1.8	*1.7*	*0.60*	*3.2*	0.26	Ho	2.3	2.5	2.3	2.2	3.8	2.0	2.1	2.0	2.2	2.1	1.9	1.9	2.1	2.1	1.9
6.5	4.9	*5.0*	*2.0*	*9.9*	0.79	Er	6.6	6.6	6.4	5.2	7.8	5.8	5.6	5.4	6.1	6.2	5.0	4.9	5.7	5.2	5.0
0.79	0.60	*0.60*	*0.20*	*1.2*	0.10	Tm	0.61	0.73	0.63	0.65	0.78	0.53	0.63	0.62	0.70	0.59	0.53	0.48	0.65	0.71	0.50
4.8	3.9	*3.6*	*1.3*	*7.1*	0.58	Yb	2.6	3.8	3.1	2.6	4.0	3.0	3.0	3.2	3.1	2.9	2.4	2.5	3.1	2.9	2.7
0.58	0.46	*0.43*	*0.13*	*0.85*	0.07	Lu	0.30	0.32	0.35	0.33	0.40	0.29	0.29	0.34	0.32	0.27	0.26	0.27	0.25	0.29	0.28
112	183	*72.7*	*26.8*	*183*	<LOD	∑REE	37.6	40.6	37.6	33.5	49.0	32.6	33.2	33.6	37.1	34.0	29.7	28.8	31.7	35.3	28.6
0.04	<LOD	*0.10*	*<LOD*	*0.46*	0.02	Th	0.09	0.06	<LOD	0.07	0.18	0.09	0.10	0.08	0.06	0.05	0.07	0.05	0.17	0.05	0.04
0.01	0.03	*0.009*	*<LOD*	*0.49*	0.00	U	<LOD	<LOD	<LOD	<LOD	<LOD	<LOD	<LOD	0.001	<LOD	<LOD	<LOD	<LOD	<LOD	<LOD	<LOD
<LOD	0.04	*1.3*	*<LOD*	*12.7*	<LOD	Pb	<LOD	0.27	0.15	<LOD	0.04	<LOD	<LOD	0.15	<LOD	<LOD	<LOD	<LOD	<LOD	<LOD	<LOD
140	137	*137*	*102*	*760*	24.0	Fe	155	147	129	150	193	142	152	151	164	125	162	124	167	176	140
59.6	133	*109*	*<LOD*	*315*	11.8	Sr	13.2	27.2	22.5	14.7	16.9	12.8	14.5	17.1	14.2	11.8	12.9	11.4	14.1	10.6	7.7
<LOD	0.77	*5.5*	*<LOD*	*62.0*	0.37	Ba	0.59	1.9	1.2	1.5	2.0	0.11	0.40	0.36	0.36	<LOD	0.03	<LOD	0.72	0.19	0.85
741	1355	*1791*	*<LOD*	*9100*	129	Na	56.0	550	504	<LOD	54.0	34.2	39.9	326	49.0	35.1	<LOD	26.7	34.0	24.5	20.3
2.2	7.2	*3.2*	*<LOD*	*16.3*	0.60	Al	<LOD	<LOD	<LOD	<LOD	0.39	0.46	<LOD	<LOD	<LOD	<LOD	<LOD	<LOD	<LOD	0.36	<LOD	0.38
<LOD	<LOD	*166*	*<LOD*	*4800*	114	Si	235	252	323	248	<LOD	174	222	175	100	<LOD	<LOD	<LOD	152	<LOD	156
68.0	181	*42.8*	*<LOD*	*1870*	12.3	P	<LOD	<LOD	27.9	13.4	24.0	17.1	<LOD	11.5	<LOD	<LOD	<LOD	20.2	13.0	<LOD	<LOD
<LOD	47.4	*126*	*<LOD*	*570*	10.0	K	<LOD	46.5	53.4	<LOD	<LOD	<LOD	<LOD	45.0	<LOD	<LOD	<LOD	<LOD	2.4	4.5	2.9
0.12	0.18	*0.46*	*<LOD*	*1.3*	0.13	Sc	<LOD	<LOD	<LOD	<LOD	<LOD	<LOD	<LOD	<LOD	<LOD	<LOD	<LOD	<LOD	<LOD	<LOD	<LOD
<LOD	<LOD	*1.1*	*<LOD*	*3.2*	1.10	Ti	<LOD	0.89	<LOD	<LOD	<LOD	<LOD	<LOD	<LOD	0.77	<LOD	<LOD	<LOD	<LOD	<LOD	<LOD
<LOD	<LOD	*0.04*	*<LOD*	*0.11*	0.04	V	<LOD	<LOD	<LOD	<LOD	0.04	<LOD	<LOD	<LOD	<LOD	<LOD	<LOD	<LOD	<LOD	<LOD	<LOD
<LOD	<LOD	*2.8*	*<LOD*	*7.5*	0.71	Cr	<LOD	<LOD	<LOD	<LOD	<LOD	<LOD	<LOD	<LOD	<LOD	<LOD	<LOD	<LOD	<LOD	<LOD	<LOD
<LOD	0.57	*2.8*	*<LOD*	*20.0*	0.53	Mn	<LOD	1.0	<LOD	<LOD	<LOD	<LOD	<LOD	<LOD	<LOD	<LOD	<LOD	<LOD	<LOD	<LOD	<LOD
0.05	0.19	*0.16*	*<LOD*	*0.63*	0.11	Ni	<LOD	0.19	<LOD	<LOD	<LOD	<LOD	0.12	<LOD	0.11	<LOD	0.14	<LOD	<LOD	<LOD	<LOD
<LOD	0.16	*0.54*	*<LOD*	*8.1*	0.33	Cu	<LOD	<LOD	<LOD	<LOD	0.30	<LOD	<LOD	<LOD	<LOD	<LOD	<LOD	<LOD	0.27	<LOD	<LOD
<LOD	0.32	*6.3*	*<LOD*	*51.0*	0.57	Zn	<LOD	0.59	0.94	0.31	<LOD	<LOD	<LOD	0.40	0.36	<LOD	<LOD	<LOD	0.30	<LOD	<LOD
<LOD	0.10	*0.65*	*<LOD*	*2.8*	0.11	Rb	<LOD	0.28	0.31	<LOD	<LOD	<LOD	<LOD	0.20	<LOD	<LOD	<LOD	<LOD	<LOD	<LOD	<LOD
<LOD	<LOD	*0.02*	*<LOD*	*0.08*	0.01	Zr	<LOD	<LOD	<LOD	<LOD	<LOD	<LOD	<LOD	<LOD	<LOD	<LOD	<LOD	<LOD	<LOD	<LOD	<LOD
<LOD	<LOD	*<LOD*	*<LOD*	*<LOD*	0.01	Nb	<LOD	<LOD	<LOD	<LOD	<LOD	<LOD	<LOD	<LOD	<LOD	<LOD	<LOD	<LOD	<LOD	<LOD	<LOD
<LOD	0.20	*0.14*	*<LOD*	*0.24*	0.10	Ag	<LOD	<LOD	<LOD	<LOD	0.12	<LOD	<LOD	<LOD	<LOD	<LOD	<LOD	<LOD	<LOD	<LOD	<LOD
<LOD	<LOD	*0.04*	*<LOD*	*0.07*	0.03	Bi	<LOD	<LOD	<LOD	<LOD	<LOD	<LOD	<LOD	<LOD	<LOD	<LOD	<LOD	<LOD	<LOD	<LOD	<LOD

16	17	18	19	20	21	22	23	24	25	26	27	28	29	30	31	32	33	34	35	36	37	38
204	215	216	196	197	204	193	245	208	195	227	208	196	226	246	245	290	305	406	233	254	248	350
0.07	0.05	0.12	0.12	0.21	0.21	0.26	0.16	0.39	0.14	0.47	0.14	0.17	0.12	0.22	0.21	0.22	0.25	0.18	0.13	0.53	0.33	10.0
0.47	0.55	0.88	1.1	1.1	1.3	1.5	0.97	2.3	0.79	1.5	0.93	1.0	1.0	1.3	1.3	1.3	1.7	1.7	0.74	1.7	1.1	27.9
0.15	0.14	0.23	0.35	0.27	0.29	0.36	0.24	0.37	0.26	0.33	0.26	0.22	0.27	0.34	0.39	0.48	0.33	0.50	0.17	0.37	0.23	4.5
1.4	1.6	2.0	3.0	1.5	2.1	2.3	2.1	2.4	2.0	1.7	2.1	2.6	2.8	2.9	2.9	3.0	2.9	3.7	1.7	2.0	1.6	22.6
1.2	1.6	1.5	2.0	1.6	1.8	1.8	2.2	1.6	1.6	1.7	2.1	2.4	1.9	2.3	2.5	3.4	2.9	3.8	1.5	1.3	0.86	7.5
1.2	1.4	1.7	1.6	1.6	1.4	1.6	2.1	1.1	1.5	1.8	1.7	1.7	2.0	1.9	2.2	3.0	2.2	3.0	1.8	1.1	0.79	2.7
4.5	5.6	5.5	7.2	5.6	5.6	5.0	6.7	3.9	5.9	6.3	6.1	7.0	7.2	8.2	7.7	10.3	9.8	16.3	6.2	4.2	3.5	10.2
1.3	1.2	1.5	1.9	1.2	1.3	1.1	1.5	0.80	1.4	1.7	1.4	1.5	1.5	1.6	1.7	2.3	2.0	2.4	1.4	1.1	0.86	1.7
8.2	10.7	9.6	11.1	8.5	9.6	8.3	12.1	7.0	9.8	9.8	10.7	9.4	11.2	12.3	13.2	17.6	15.2	19.9	10.6	8.5	9.2	13.8
1.9	1.9	2.3	2.4	2.0	2.0	2.0	2.3	1.7	2.2	2.1	2.3	2.3	2.6	2.6	2.7	3.1	3.3	4.6	2.6	2.2	2.7	3.2
5.7	5.5	5.9	7.0	5.7	5.8	5.9	7.0	4.9	5.3	7.7	6.7	6.7	7.2	7.1	7.8	9.7	9.6	12.4	6.7	7.0	8.8	12.0
0.55	0.66	0.57	0.76	0.59	0.66	0.62	0.66	0.50	0.59	0.79	0.71	0.61	0.67	0.77	0.86	1.1	1.2	1.5	0.69	0.89	1.1	1.7
2.5	3.1	3.0	3.7	2.9	2.8	3.2	3.5	2.5	2.7	3.6	2.8	3.5	3.3	4.1	4.0	6.0	6.3	6.5	2.8	4.0	6.4	8.5
0.27	0.36	0.30	0.39	0.32	0.31	0.28	0.32	0.29	0.28	0.31	0.37	0.41	0.39	0.40	0.44	0.56	0.72	0.82	0.36	0.49	0.70	1.1
29.4	34.3	35.0	42.6	33.0	34.9	34.3	41.9	29.7	34.3	39.8	38.3	39.5	42.1	46.0	47.9	61.9	58.3	77.3	37.4	35.3	38.2	127
0.04	0.03	0.06	0.18	0.05	0.09	0.07	0.05	0.20	0.04	0.06	0.04	0.07	0.08	0.09	0.11	0.15	0.12	0.19	<LOD	0.06	0.07	<LOD
<LOD	<LOD	<LOD	<LOD	<LOD	<LOD	0.002	<LOD	<LOD	<LOD	0.02	<LOD	<LOD	<LOD	0.001	<LOD	<LOD	<LOD	0.006	<LOD	0.02	0.02	<LOD
0.21	<LOD	0.18	<LOD	<LOD	<LOD	<LOD	<LOD	0.22	<LOD	<LOD	0.69	0.92	2.6	<LOD	<LOD	0.88	2.1	<LOD	0.11	<LOD	0.40	0.49
139	124	113	145	159	140	151	156	157	136	153	126	141	127	134	157	175	122	167	132	139	2610	139
12.3	11.0	14.5	13.5	13.2	54.0	<LOD	15.1	17.4	20.8	14.6	59.9	43.2	52.5	17.9	25.8	27.6	46.7	23.1	19.0	29.1	43.0	26.0
5.8	<LOD	32.0	1.4	<LOD	1.4	<LOD	0.22	0.45	1.5	2.5	3.4	12.2	29.8	<LOD	24.0	0.95	4.4	0.73	3.1	4.4	10.4	0.56
129	<LOD	45.0	36.0	67.0	2260	<LOD	50.6	134	299	<LOD	2260	680	1200	160	106	290	1230	<LOD	231	185	630	459
<LOD	<LOD	1.5	<LOD	0.68	<LOD	<LOD	<LOD	<LOD	<LOD	0.47	<LOD	<LOD	<LOD	0.73	0.87	1.1	0.69	1.8	<LOD	0.93	1340	0.90
140	<LOD	420	<LOD	<LOD	171	<LOD	111	<LOD	<LOD	<LOD	205	290	190	127	173	<LOD	<LOD	<LOD	<LOD	<LOD	1720	<LOD
9.5	<LOD	<LOD	<LOD	<LOD	21.4	<LOD	13.4	20.8	13.9	17.2	<LOD	25.0	<LOD	17.3	24.5	24.1	26.0	56.0	<LOD	32.0	40.0	73.0
8.8	<LOD	<LOD	<LOD	164	<LOD	<LOD	<LOD	6.8	14.1	<LOD	143	100	93.0	<LOD	6.8	10.6	149	<LOD	9.9	5.8	95.0	41.0
<LOD	<LOD	<LOD	<LOD	<LOD	<LOD	<LOD	<LOD	<LOD	<LOD	<LOD	0.19	<LOD	<LOD	<LOD	<LOD	<LOD	0.18	<LOD	<LOD	<LOD	<LOD	1.9
<LOD	<LOD	<LOD	<LOD	1.3	<LOD	<LOD	0.81	<LOD	<LOD	<LOD	<LOD	<LOD	<LOD	<LOD	<LOD	<LOD	<LOD	<LOD	1.5	<LOD	0.98	<LOD
<LOD	<LOD	<LOD	<LOD	<LOD	<LOD	<LOD	<LOD	<LOD	<LOD	<LOD	<LOD	<LOD	<LOD	<LOD	<LOD	<LOD	<LOD	<LOD	<LOD	<LOD	0.70	<LOD
<LOD	<LOD	<LOD	<LOD	<LOD	<LOD	<LOD	<LOD	<LOD	<LOD	<LOD	<LOD	<LOD	<LOD	<LOD	<LOD	<LOD	<LOD	<LOD	<LOD	<LOD	<LOD	<LOD
0.47	<LOD	0.22	<LOD	<LOD	0.21	<LOD	0.12	0.84	<LOD	<LOD	1.1	2.5	4.8	<LOD	<LOD	0.51	1.6	<LOD	<LOD	0.83	8.7	1.4
<LOD	<LOD	<LOD	<LOD	<LOD	<LOD	<LOD	0.19	0.46	<LOD	<LOD	4.6	3.8	2.7	0.46	0.38	2.0	4.5	<LOD	<LOD	<LOD	2.4	<LOD
0.60	<LOD	<LOD	<LOD	<LOD	<LOD	<LOD	<LOD	<LOD	0.69	<LOD	0.64	0.42	0.42	<LOD	<LOD	<LOD	0.69	<LOD	<LOD	0.55	7.0	1.6
<LOD	<LOD	<LOD	<LOD	<LOD	0.96	<LOD	<LOD	0.15	<LOD	<LOD	<LOD	<LOD	<LOD	<LOD	0.08	<LOD	<LOD	<LOD	<LOD	<LOD	0.50	0.23
<LOD	<LOD	<LOD	<LOD	<LOD	<LOD	<LOD	<LOD	<LOD	<LOD	0.002	<LOD	<LOD	<LOD	0.005	<LOD	<LOD	<LOD	<LOD	<LOD	<LOD	0.10	<LOD
<LOD	0.005	<LOD	<LOD	<LOD	<LOD	<LOD	<LOD	<LOD	<LOD	<LOD	<LOD	<LOD	<LOD	<LOD	<LOD	<LOD	<LOD	<LOD	<LOD	<LOD	<LOD	<LOD
<LOD	<LOD	0.10	<LOD	<LOD	<LOD	<LOD	<LOD	<LOD	<LOD	<LOD	<LOD	<LOD	<LOD	<LOD	<LOD	<LOD	<LOD	<LOD	<LOD	<LOD	<LOD	<LOD
<LOD	<LOD	<LOD	<LOD	<LOD	<LOD	<LOD	<LOD	<LOD	<LOD	<LOD	<LOD	<LOD	<LOD	<LOD	<LOD	<LOD	<LOD	<LOD	<LOD	<LOD	<LOD	<LOD

					Sample RX11077; green															
39	*AVG*	*MIN*	*MAX*	AVG LOD	n=55	1	2	3	4	5	6	7	8	9	10	11	12	13	14	15	16
127	*231*	*127*	*406*	39.5	Y	721	925	630	620	468	992	921	881	784	870	774	726	273	645	834	851
11.2	*0.18*	*0.05*	*11.2*	0.04	La	21.0	24.2	18.7	17.0	13.4	21.4	22.4	18.9	26.2	23.0	24.3	21.0	7.0	18.1	25.8	23.4
23.5	*1.1*	*0.42*	*27.9*	0.18	Ce	95.8	117	89.5	77.9	60.8	102	110	95.5	125	110	115	98.4	32.3	87.4	125	112
3.8	*0.27*	*0.14*	*4.5*	0.05	Pr	18.8	22.3	17.4	15.4	11.5	20.2	20.8	18.8	24.2	21.9	22.1	19.3	6.7	17.3	24.6	21.5
17.3	*2.1*	*1.3*	*22.6*	0.33	Nd	94.4	111	89.7	73.5	56.8	105	109	92.1	121	111	112	96.3	30.4	89.2	116	109
6.3	*1.9*	*0.86*	*7.5*	0.34	Sm	18.8	21.6	17.3	14.7	11.3	20.0	20.9	18.8	23.5	20.2	21.4	18.5	5.7	18.2	23.9	23.0
1.9	*1.6*	*0.79*	*3.0*	0.26	Eu	8.9	10.5	8.0	6.8	5.1	9.5	10.0	9.5	11.0	10.0	10.3	8.7	2.5	7.8	11.0	10.3
8.8	*6.0*	*3.5*	*16.3*	0.95	Gd	24.2	29.3	21.5	19.3	13.7	27.7	29.6	25.3	30.0	27.3	28.9	23.3	7.1	21.9	29.6	29.0
1.1	*1.4*	*0.80*	*2.4*	0.23	Tb	4.5	5.4	4.2	3.4	2.7	5.4	5.1	4.7	5.2	4.9	4.8	4.5	1.3	4.0	5.4	5.3
6.6	*10.2*	*6.6*	*19.9*	1.70	Dy	29.2	36.9	25.0	23.7	17.2	37.0	34.8	32.6	32.6	33.2	31.3	29.3	8.9	24.3	33.0	33.5
1.3	*2.3*	*1.3*	*4.6*	0.40	Ho	6.4	8.2	5.8	5.3	4.2	8.2	7.9	7.4	6.9	7.6	6.7	6.2	2.1	5.5	7.4	7.4
4.1	*6.4*	*4.1*	*12.4*	1.10	Er	15.9	20.2	14.1	13.3	9.9	19.8	19.7	20.5	17.1	19.3	17.0	15.4	5.1	13.2	17.5	18.1
<LOD	*0.69*	*0.48*	*1.7*	0.12	Tm	1.7	2.3	1.5	1.4	1.1	2.3	2.0	2.1	1.8	2.4	2.0	1.7	0.62	1.5	1.9	2.0
3.0	*3.4*	*2.4*	*8.5*	0.53	Yb	10.0	13.6	8.8	8.7	7.0	15.0	13.1	12.7	10.8	14.1	11.7	10.1	3.7	8.9	11.5	11.9
0.42	*0.36*	*0.25*	*1.1*	0.06	Lu	1.0	1.4	0.92	0.92	0.70	1.7	1.3	1.4	1.1	1.5	1.2	1.1	0.38	0.92	1.2	1.3
89.2	*38.5*	*28.6*	*127*	<LOD	∑REE	351	425	322	281	215	395	406	360	437	406	409	354	114	318	433	408
<LOD	*0.08*	*<LOD*	*0.20*	0.02	Th	0.82	0.97	0.80	0.85	0.68	0.95	1.1	0.71	0.67	0.69	0.74	0.74	0.50	0.74	0.78	0.75
0.01	*0.009*	*<LOD*	*0.02*	0.00	U	<LOD	<LOD	0.09	<LOD	0.007	<LOD	<LOD	0.08	0.005	0.002	0.004	<LOD	<LOD	0.005	0.47	0.01
<LOD	*0.52*	*<LOD*	*2.6*	<LOD	Pb	4.8	4.8	2.8	24.0	27.3	5.4	0.83	3.5	2.8	1.7	0.13	2.2	5.5	9.7	6.3	0.53
120	*146*	*113*	*2610*	27.5	Fe	103	102	89.0	115	117	94.0	95.6	117	112	87.4	85.7	93.9	89.2	116	108	97.0
47.4	*21.0*	*<LOD*	*59.9*	3.50	Sr	45.1	77.3	36.8	46.6	59.2	50.0	49.8	65.2	49.9	54.8	41.8	49.2	40.6	57.6	49.3	44.5
2.0	*2.4*	*<LOD*	*32.0*	0.19	Ba	4.0	8.0	2.4	3.1	7.1	0.34	10.6	4.8	2.5	2.9	0.11	1.7	3.7	3.7	19.7	<LOD
849	*268*	*<LOD*	*2260*	35.2	Na	390	750	108	501	286	310	400	2090	126	634	28.5	193	3800	324	789	46.1
2.5	*0.95*	*<LOD*	*1340*	0.51	Al	<LOD	<LOD	<LOD	<LOD	<LOD	<LOD	<LOD	<LOD	<LOD	<LOD	<LOD	<LOD	<LOD	<LOD	<LOD	<LOD
<LOD	*202*	*<LOD*	*1720*	146	Si	204	337	362	317	272	260	293	270	282	234	291	260	267	210	297	366
63.9	*23.5*	*<LOD*	*73.0*	13.2	P	16.2	20.1	29.9	20.4	19.2	<LOD	20.1	19.9	<LOD	<LOD	16.0	12.8	16.0	22.0	18.1	15.9
42.4	*42.7*	*<LOD*	*164*	4.60	K	66.0	55.0	22.2	155	145	41.0	18.0	135	61.0	41.2	<LOD	81.0	280	122	48.9	10.1
<LOD	*0.18*	*<LOD*	*0.19*	0.16	Sc	<LOD	<LOD	<LOD	<LOD	<LOD	<LOD	<LOD	<LOD	<LOD	<LOD	<LOD	<LOD	<LOD	<LOD	<LOD	<LOD
<LOD	*1.2*	*<LOD*	*1.9*	1.30	Ti	<LOD	<LOD	<LOD	<LOD	<LOD	<LOD	<LOD	<LOD	<LOD	<LOD	<LOD	<LOD	<LOD	<LOD	<LOD	<LOD
<LOD	*0.37*	*<LOD*	*0.70*	0.06	V	<LOD	<LOD	<LOD	<LOD	<LOD	<LOD	<LOD	<LOD	<LOD	<LOD	<LOD	<LOD	0.05	<LOD	<LOD	<LOD
<LOD	*<LOD*	*<LOD*	*<LOD*	0.92	Cr	<LOD	<LOD	<LOD	<LOD	<LOD	<LOD	<LOD	<LOD	<LOD	<LOD	<LOD	<LOD	<LOD	<LOD	<LOD	<LOD
0.94	*1.5*	*<LOD*	*8.7*	0.56	Mn	2.6	6.2	3.2	22.8	44.0	1.0	0.34	1.2	12.3	1.7	<LOD	3.1	4.0	17.6	4.4	1.1
0.17	*0.15*	*<LOD*	*2.4*	0.15	Ni	0.15	<LOD	0.24	<LOD	<LOD	<LOD	<LOD	<LOD	0.15	0.23	0.17	<LOD	<LOD	0.11	<LOD	0.21
<LOD	*0.37*	*<LOD*	*0.60*	0.43	Cu	0.61	1.7	4.2	2.9	7.7	0.24	<LOD	21.5	0.64	<LOD	0.95	0.72	4.8	4.7	0.93	<LOD
0.53	*1.5*	*<LOD*	*7.0*	0.40	Zn	3.4	3.8	1.8	11.5	13.8	1.2	1.2	4.6	2.4	1.5	<LOD	4.5	5.6	3.8	<LOD	<LOD
0.18	*0.36*	*<LOD*	*0.96*	0.10	Rb	0.23	0.27	<LOD	0.66	0.49	0.26	0.11	0.55	0.22	0.16	<LOD	0.31	0.74	0.52	0.12	<LOD
<LOD	*0.02*	*<LOD*	*0.10*	0.01	Zr	<LOD	<LOD	<LOD	<LOD	0.02	<LOD	<LOD	0.10	0.02	<LOD	<LOD	<LOD	<LOD	<LOD	0.06	<LOD
<LOD	*0.004*	*<LOD*	*0.005*	0.01	Nb	<LOD	<LOD	<LOD	<LOD	<LOD	<LOD	<LOD	<LOD	<LOD	<LOD	<LOD	<LOD	<LOD	<LOD	<LOD	<LOD
<LOD	*0.11*	*<LOD*	*0.12*	0.11	Ag	<LOD	<LOD	<LOD	<LOD	<LOD	<LOD	<LOD	<LOD	<LOD	<LOD	<LOD	<LOD	<LOD	<LOD	<LOD	<LOD
<LOD	*<LOD*	*<LOD*	*<LOD*	0.04	Bi	<LOD	<LOD	<LOD	<LOD	<LOD	<LOD	<LOD	2.4	<LOD	<LOD	<LOD	<LOD	<LOD	<LOD	<LOD	<LOD

17	18	19	20	21	22	23	24	25	26	27	28	29	30	31	32	33	34	35	36	37	38	39
860	274	758	645	759	856	653	882	845	790	1064	884	879	955	1047	1021	616	809	843	856	856	828	860
28.6	7.9	23.0	20.2	26.0	24.9	28.4	22.3	24.3	22.9	21.2	22.4	22.1	24.9	23.2	25.9	27.5	24.2	26.3	26.1	26.4	24.5	25.6
138	36.5	110	82.0	123	117	106	105	116	109	99.1	104	108	125	119	119	110	118	126	123	123	116	125
27.2	7.0	21.3	15.0	23.3	22.2	18.5	20.3	21.5	20.5	19.2	20.0	20.6	24.6	21.1	23.8	20.0	22.1	23.6	23.7	24.0	22.7	24.1
131	34.5	105	71.5	120	110	91.6	101	111	105	99.6	101	105	125	109	117	96.9	117	120	116	120	114	116
25.3	6.5	20.3	14.3	22.4	22.1	17.6	20.4	21.4	20.1	20.1	19.4	20.0	24.7	21.0	25.2	18.5	21.6	23.9	23.0	23.5	21.5	24.1
11.9	3.0	9.4	6.2	10.9	10.7	8.1	9.4	9.8	9.4	8.9	9.0	9.9	11.2	10.0	11.8	8.9	10.5	11.0	11.2	11.5	10.3	10.9
32.3	8.2	26.4	19.3	27.4	29.4	23.0	26.5	27.2	26.2	26.3	25.5	26.7	32.2	29.4	32.7	23.9	28.4	30.8	32.4	30.6	28.3	30.6
5.4	1.5	4.6	3.5	4.9	5.4	4.2	5.0	4.9	4.6	5.5	4.7	4.9	5.5	5.6	5.7	4.3	5.0	5.5	5.5	5.3	5.0	5.4
36.0	9.8	30.5	25.0	31.2	33.8	26.8	33.2	33.6	30.7	36.0	31.6	32.6	38.8	39.6	42.0	29.4	33.1	35.8	35.9	37.0	33.5	35.1
7.9	2.1	6.7	5.7	6.9	7.3	6.1	7.6	7.3	7.1	9.2	7.4	7.3	8.4	9.2	8.9	5.8	7.0	7.8	7.9	8.0	7.4	7.9
19.0	5.9	16.3	15.6	16.3	18.1	14.9	19.5	18.5	18.4	23.9	19.4	18.9	20.6	23.9	21.7	14.3	18.3	19.3	19.1	18.2	18.1	19.4
2.0	0.62	1.7	1.9	1.7	2.0	1.6	2.1	2.1	2.1	2.9	2.2	2.1	2.2	2.6	2.5	1.6	1.9	2.0	2.1	2.0	2.1	2.1
12.8	3.5	10.3	10.8	10.3	12.2	10.0	12.7	12.5	11.7	17.4	13.7	11.9	12.3	16.2	14.3	9.3	11.6	11.9	12.9	12.2	11.0	12.9
1.3	0.42	1.1	1.2	1.1	1.2	1.1	1.5	1.3	1.3	1.8	1.5	1.3	1.3	1.6	1.6	0.98	1.3	1.3	1.4	1.3	1.2	1.3
478	127	387	292	425	417	358	386	412	389	391	382	391	456	431	452	372	419	446	440	443	415	441
0.82	0.46	0.89	0.54	0.67	0.76	0.62	0.82	0.85	0.68	1.1	0.75	0.87	1.0	1.0	1.0	0.65	0.68	0.87	0.70	0.79	0.67	0.75
<LOD	0.21	0.15	0.15	0.10	<LOD	0.03	<LOD	0.02	0.02	<LOD	<LOD	0.03	<LOD	<LOD	<LOD	<LOD	0.004	<LOD	<LOD	<LOD	<LOD	<LOD
1.8	9.0	3.1	3.7	0.39	0.27	0.67	55.4	<LOD	0.71	0.17	5.5	3.0	<LOD	<LOD	0.07	<LOD	0.05	<LOD	0.08	0.08	<LOD	<LOD
92.8	82.0	90.8	97.3	82.0	101	88.0	105	85.0	117	83.1	90.7	82.6	81.3	83.5	109	59.8	71.4	69.6	66.0	69.9	69.3	61.7
46.3	33.2	44.3	37.3	39.6	43.4	34.9	79.1	40.6	38.1	43.9	44.2	46.2	44.7	51.2	50.7	31.7	56.8	41.7	44.8	43.4	42.0	42.8
0.43	4.6	2.1	0.46	0.17	0.14	0.24	6.5	0.08	0.06	0.86	1.4	1.1	1.2	<LOD	<LOD	<LOD	9.9	<LOD	<LOD	3.3	<LOD	<LOD
147	750	349	132	31.9	93.0	66.0	308	54.0	60.0	151	88.0	100	62.0	31.1	28.3	11.6	490	24.7	43.3	161	21.7	19.6
<LOD	<LOD	<LOD	<LOD	<LOD	<LOD	<LOD	<LOD	<LOD	1.1	<LOD	<LOD	<LOD	<LOD	<LOD	1.5	<LOD	<LOD	<LOD	<LOD	<LOD	<LOD	<LOD
345	303	389	236	274	262	255	283	281	290	350	293	275	263	305	350	281	317	327	298	286	257	254
14.1	24.5	13.2	20.3	21.3	<LOD	14.8	<LOD	10.2	23.7	13.7	16.0	17.0	<LOD	14.3	27.0	15.5	12.4	12.6	<LOD	14.7	<LOD	25.0
36.9	160	47.0	14.1	<LOD	<LOD	<LOD	246	<LOD	<LOD	18.1	28.2	24.3	<LOD	<LOD	<LOD	<LOD	27.9	<LOD	<LOD	6.2	<LOD	<LOD
<LOD	<LOD	<LOD	0.12	<LOD	<LOD	<LOD	0.12	<LOD	<LOD	<LOD	0.44	<LOD	<LOD	<LOD	<LOD	<LOD	<LOD	<LOD	<LOD	<LOD	<LOD	<LOD
<LOD	<LOD	<LOD	<LOD	<LOD	<LOD	<LOD	<LOD	<LOD	<LOD	0.13	<LOD	<LOD	<LOD	<LOD	<LOD	<LOD	<LOD	<LOD	<LOD	<LOD	0.40	<LOD
<LOD	<LOD	<LOD	<LOD	<LOD	<LOD	<LOD	<LOD	<LOD	<LOD	<LOD	<LOD	<LOD	<LOD	<LOD	<LOD	<LOD	<LOD	<LOD	<LOD	<LOD	<LOD	1.1
6.0	5.0	2.5	2.8	0.50	0.80	4.0	35.7	<LOD	5.5	0.63	9.1	3.4	<LOD	<LOD	0.15	<LOD	<LOD	<LOD	<LOD	0.11	<LOD	<LOD
<LOD	0.16	<LOD	0.13	<LOD	<LOD	<LOD	<LOD	<LOD	0.25	0.16	<LOD	<LOD	<LOD	0.52	<LOD	0.92	<LOD	<LOD	<LOD	0.39	<LOD	<LOD
1.7	3.2	0.71	12.3	1.2	<LOD	<LOD	13.9	0.24	<LOD	<LOD	2.7	2.0	<LOD	<LOD	<LOD	<LOD	0.31	<LOD	<LOD	<LOD	<LOD	<LOD
1.7	6.9	3.6	1.5	<LOD	<LOD	<LOD	27.5	<LOD	<LOD	0.10	5.3	2.8	<LOD	<LOD	<LOD	0.92	<LOD	<LOD	<LOD	<LOD	<LOD	<LOD
<LOD	0.70	0.12	<LOD	<LOD	<LOD	<LOD	1.1	<LOD	<LOD	0.01	0.11	0.14	<LOD	<LOD	0.009	<LOD	<LOD	<LOD	<LOD	<LOD	<LOD	<LOD
<LOD	<LOD	<LOD	<LOD	0.06	<LOD	<LOD	0.03	<LOD	0.009	0.005	<LOD	0.02	<LOD	<LOD	<LOD	<LOD	<LOD	<LOD	<LOD	<LOD	<LOD	<LOD
<LOD	<LOD	<LOD	<LOD	<LOD	<LOD	<LOD	<LOD	<LOD	<LOD	<LOD	<LOD	<LOD	<LOD	<LOD	<LOD	<LOD	<LOD	<LOD	<LOD	<LOD	<LOD	<LOD
<LOD	<LOD	<LOD	<LOD	<LOD	<LOD	<LOD	<LOD	<LOD	<LOD	<LOD	<LOD	0.07	<LOD	<LOD	<LOD	<LOD	0.07	<LOD	<LOD	<LOD	<LOD	<LOD
<LOD	<LOD	0.35	<LOD	<LOD	0.04	<LOD	<LOD	<LOD	0.04	<LOD	<LOD	<LOD	<LOD	<LOD	<LOD	<LOD	<LOD	<LOD	<LOD	<LOD	<LOD	<LOD

																				Sample RX11078	
40	41	42	43	44	45	46	47	48	49	50	51	52	53	54	55	*AVG*	*MIN*	*MAX*	AVG LOD	n=122	1
731	754	797	407	241	1002	491	1011	974	723	970	719	1010	621	318	724	791	241	1064	0.009	Y	210
24.8	25.3	26.3	4.6	28.8	21.3	18.1	22.3	24.3	14.8	24.4	17.3	24.6	29.4	8.1	19.3	22.8	4.6	29.4	0.007	La	30.1
121	123	130	22.8	119	97.4	83.9	108	116	69.3	114	80.1	115	98.5	34.5	85.5	107	22.8	138	0.007	Ce	154
22.8	23.4	25.3	4.2	23.9	18.4	16.7	20.8	22.4	13.4	20.8	16.3	21.5	16.4	6.4	16.0	20.4	4.2	27.2	0.005	Pr	29.4
117	121	127	26.3	120	96.4	87.3	103	111	66.9	107	76.9	110	75.7	32.4	79.7	102	26.3	131	0.03	Nd	152
21.3	22.2	23.6	4.7	18.2	19.2	15.5	21.7	21.8	13.4	21.2	14.5	22.9	15.1	6.3	16.4	19.9	4.7	25.3	0.04	Sm	23.1
10.2	10.2	10.5	2.5	7.7	9.0	8.0	10.5	10.8	6.8	10.2	7.3	10.2	6.9	3.0	7.3	9.4	2.5	11.9	0.01	Eu	10.1
27.4	29.0	28.7	8.3	19.2	25.7	20.2	30.4	30.1	19.1	28.8	21.0	30.1	19.6	8.1	21.4	26.1	7.1	32.7	0.03	Gd	22.7
4.8	5.1	5.2	1.6	2.4	5.0	3.3	5.6	5.5	3.6	5.3	3.9	5.5	3.8	1.5	3.8	4.7	1.3	5.7	0.005	Tb	2.7
32.1	31.6	34.4	11.5	11.6	37.1	21.6	40.7	37.0	25.5	35.5	26.6	37.7	25.6	11.0	27.5	31.3	8.9	42.0	0.02	Dy	12.7
6.8	7.1	7.1	2.8	2.0	8.4	4.5	9.2	8.6	6.0	8.1	6.5	8.9	5.6	2.5	6.2	7.0	2.0	9.2	0.006	Ho	2.1
16.1	16.5	17.0	6.5	4.4	23.2	10.2	22.3	20.3	15.3	20.5	15.6	22.0	14.1	6.7	16.0	17.3	4.4	23.9	0.02	Er	4.3
1.8	1.8	2.1	0.87	0.41	2.7	1.2	2.5	2.4	1.7	2.4	1.7	2.3	1.5	0.72	1.7	1.9	0.41	2.9	0.005	Tm	0.48
10.0	10.8	12.8	5.9	2.3	17.0	6.5	14.8	13.5	10.6	14.2	10.8	14.6	9.5	4.5	10.5	11.4	2.3	17.4	0.02	Yb	2.5
1.1	1.1	1.3	0.71	0.26	1.8	0.66	1.7	1.4	1.1	1.4	1.1	1.5	0.98	0.52	1.1	1.2	0.26	1.8	0.005	Lu	0.27
417	428	451	103	360	383	298	414	425	268	414	299	427	323	126	312	384	103	478	<LOD	∑REE	446
0.61	0.59	0.66	0.19	3.0	0.76	0.64	1.7	1.2	1.3	1.1	1.0	1.2	0.91	0.60	0.99	0.81	0.19	3.0	0.006	Th	2.6
<LOD	<LOD	<LOD	0.04	<LOD	0.07	1.3	0.03	<LOD	0.08	<LOD	0.08	<LOD	0.01	0.58	<LOD	0.08	0.002	1.3	0.005	U	<LOD
0.03	<LOD	0.05	0.95	<LOD	0.19	1.4	0.29	2.0	5.6	3.8	9.6	<LOD	5.0	2.5	1.4	2.8	0.03	55.4	<LOD	Pb	0.26
68.7	71.4	57.5	61.1	73.1	126	77.7	66.1	78.3	81.8	92.5	76.1	82.4	78.5	125	68.1	87.5	57.5	126	7.9	Fe	73.0
35.5	37.8	39.2	155	23.6	49.9	34.9	49.3	129	46.8	57.0	129	49.1	49.6	23.2	35.6	45.9	23.2	155	0.01	Sr	13.6
0.18	<LOD	0.17	4.8	0.08	1.7	2.4	5.3	30.6	1.8	3.6	20.2	<LOD	10.1	1.1	0.36	2.9	0.06	30.6	0.05	Ba	0.07
20.5	17.8	36.6	161	5.0	54.8	186	37.3	3130	251	470	1920	30.6	600	360	66.0	212	5.0	3800	5.0	Na	7.4
<LOD	<LOD	<LOD	<LOD	<LOD	<LOD	<LOD	<LOD	<LOD	<LOD	<LOD	<LOD	<LOD	<LOD	<LOD	<LOD	1.3	1.1	1.5	0.81	Al	<LOD
370	236	260	331	307	216	355	419	282	378	257	347	303	317	322	298	295	204	419	132	Si	331
11.8	22.9	<LOD	11.7	13.0	19.4	12.8	28.9	15.0	12.8	19.2	20.7	<LOD	18.8	17.1	17.9	17.4	10.2	29.9	11.2	P	26.4
<LOD	<LOD	<LOD	16.0	<LOD	<LOD	13.6	<LOD	207	54.0	95.0	149	<LOD	67.0	26.6	7.8	63.2	6.2	280	7.2	K	<LOD
<LOD	<LOD	<LOD	<LOD	<LOD	0.10	<LOD	0.12	<LOD	<LOD	<LOD	<LOD	<LOD	<LOD	<LOD	<LOD	0.11	0.10	0.12	0.10	Sc	<LOD
<LOD	<LOD	<LOD	<LOD	<LOD	<LOD	<LOD	<LOD	<LOD	<LOD	<LOD	<LOD	<LOD	<LOD	<LOD	<LOD	0.31	0.38	0.31	0.44	Ti	<LOD
<LOD	<LOD	<LOD	<LOD	<LOD	<LOD	<LOD	<LOD	<LOD	<LOD	<LOD	<LOD	<LOD	<LOD	<LOD	<LOD	0.09	0.05	0.13	0.06	V	<LOD
<LOD	<LOD	<LOD	0.65	<LOD	<LOD	<LOD	<LOD	<LOD	<LOD	<LOD	<LOD	<LOD	<LOD	0.64	<LOD	0.78	0.64	1.1	0.78	Cr	<LOD
<LOD	<LOD	<LOD	<LOD	<LOD	58.0	1.4	<LOD	1.2	9.9	9.6	1.5	<LOD	6.6	3.2	0.71	5.1	0.34	58.0	0.28	Mn	<LOD
<LOD	<LOD	0.20	0.21	<LOD	<LOD	0.12	0.19	0.17	<LOD	<LOD	<LOD	0.15	0.18	0.18	<LOD	0.17	0.11	0.25	0.14	Ni	<LOD
<LOD	<LOD	<LOD	<LOD	<LOD	0.24	8.9	0.41	1.4	1.8	0.57	1.3	<LOD	1.1	1.0	1.1	2.1	0.24	21.5	0.25	Cu	0.30
<LOD	<LOD	<LOD	1.3	<LOD	<LOD	1.1	<LOD	3.1	8.6	2.5	3.4	<LOD	6.4	1.8	1.2	3.4	0.92	27.5	0.69	Zn	<LOD
<LOD	<LOD	<LOD	0.10	<LOD	<LOD	<LOD	<LOD	0.90	0.21	0.40	0.63	<LOD	0.25	0.11	<LOD	0.33	0.10	1.1	0.10	Rb	<LOD
<LOD	<LOD	<LOD	<LOD	<LOD	0.02	0.67	0.01	<LOD	<LOD	<LOD	0.03	<LOD	<LOD	0.06	<LOD	0.03	0.009	0.67	0.02	Zr	<LOD
<LOD	<LOD	<LOD	<LOD	<LOD	<LOD	<LOD	<LOD	<LOD	<LOD	<LOD	<LOD	<LOD	<LOD	<LOD	<LOD	0.005	0.005	0.005	0.01	Nb	<LOD
<LOD	<LOD	<LOD	<LOD	<LOD	<LOD	<LOD	<LOD	<LOD	<LOD	<LOD	<LOD	<LOD	<LOD	<LOD	<LOD	0.07	0.07	0.07	0.07	Ag	<LOD
0.02	<LOD	<LOD	<LOD	<LOD	<LOD	<LOD	<LOD	<LOD	<LOD	<LOD	<LOD	<LOD	<LOD	<LOD	<LOD	0.58	0.02	2.4	0.04	Bi	<LOD

; green

2	3	4	5	6	7	8	9	10	11	12	13	14	15	16	17	18	19	20	21	22	23	24
323	312	298	965	380	308	1226	1110	1075	64.0	1030	63.9	972	1021	64.7	253	63.5	1138	1090	1149	1183	1264
22.5	25.4	19.0	23.1	27.3	10.0	7.2	27.1	27.1	27.9	51.7	25.0	55.4	25.0	25.5	55.6	45.6	51.3	24.5	23.0	27.2	24.6	23.5
111	117	92.0	114	132	43.6	35.6	144	127	129	107	122	109	117	124	108	102	103	115	108	130	121	112
20.8	23.7	17.8	21.1	26.4	7.9	6.6	24.5	25.0	25.3	9.3	24.2	9.4	22.4	24.4	9.6	10.8	8.7	22.0	21.1	25.0	23.3	21.1
107	118	87.1	109	133	47.5	33.9	125	122	131	21.9	123	24.1	117	118	23.6	35.1	22.3	112	105	127	116	110
17.8	20.6	14.3	17.2	26.6	8.6	6.2	26.4	25.2	25.8	2.8	25.1	2.6	23.7	24.8	2.5	5.6	2.6	22.1	21.2	25.8	23.1	22.5
8.0	8.9	5.9	7.5	12.6	4.1	3.3	12.5	12.3	12.7	1.3	11.8	1.2	10.9	11.6	1.3	3.0	1.2	11.2	10.3	13.2	11.6	11.2
19.5	22.4	16.0	18.5	35.0	11.1	8.5	33.7	34.1	35.7	2.8	33.4	2.8	31.8	32.3	2.8	7.2	2.6	32.6	29.7	35.3	34.1	32.3
2.9	3.7	2.2	2.6	6.4	2.1	1.7	6.7	6.7	7.0	0.75	6.0	0.75	5.9	6.0	0.84	1.8	0.74	6.1	5.5	6.6	6.5	6.6
15.7	20.1	12.1	14.1	40.9	14.2	11.0	47.0	43.2	43.7	6.3	40.3	6.3	38.7	41.5	6.2	11.3	6.1	43.0	39.5	44.5	46.0	47.4
3.1	4.1	2.5	2.7	9.1	3.2	2.4	10.6	9.6	9.4	1.4	9.0	1.3	8.7	8.9	1.3	2.4	1.4	10.2	9.1	9.9	10.1	10.9
6.8	9.1	6.4	6.2	21.9	8.3	6.3	25.2	23.9	25.8	3.3	21.7	3.5	19.8	21.5	3.4	6.6	3.7	24.4	23.4	23.0	24.9	27.1
0.73	1.0	0.68	0.66	2.2	0.81	0.76	3.0	2.5	2.6	0.45	2.5	0.45	2.2	2.3	0.49	0.80	0.49	2.7	2.6	2.6	2.8	3.1
4.2	5.5	3.8	3.8	13.0	5.1	4.2	16.8	15.5	14.9	2.5	14.4	2.9	13.1	13.5	2.7	4.8	2.8	16.2	15.3	15.4	16.5	18.9
0.42	0.55	0.39	0.43	1.4	0.55	0.46	1.7	1.6	1.5	0.26	1.5	0.29	1.4	1.4	0.30	0.51	0.26	1.7	1.7	1.6	1.8	1.9
340	380	280	341	488	167	128	504	475	493	211	460	220	438	455	218	238	207	443	416	487	461	449
0.97	0.97	1.4	1.5	1.2	0.72	0.66	1.6	1.5	1.5	0.01	1.4	0.01	1.1	1.1	0.02	0.27	0.02	1.4	1.1	1.5	1.7	1.6
0.008	0.03	0.05	0.07	<LOD	0.009	<LOD	0.12	<LOD	<LOD	<LOD	<LOD	<LOD	<LOD	<LOD	<LOD	<LOD	<LOD	<LOD	<LOD	0.008	<LOD	<LOD
0.67	1.4	0.90	0.21	<LOD	4.5	37.1	0.14	6.4	<LOD	<LOD	<LOD	<LOD	<LOD	0.09	0.04	4.1	<LOD	0.08	<LOD	11.4	0.47	5.6
68.4	72.3	71.1	63.1	58.2	80.0	97.0	68.1	95.0	68.0	72.0	69.3	61.2	59.7	69.5	63.5	84.3	60.6	61.2	61.2	110	65.9	121
17.1	29.2	15.1	16.8	42.3	122	1040	57.7	59.0	57.3	14.0	46.6	15.2	43.4	45.6	14.5	34.2	13.9	51.2	47.7	99.0	57.0	82.2
0.22	3.5	1.1	0.61	<LOD	27.0	220	<LOD	3.3	4.5	<LOD	<LOD	<LOD	<LOD	0.05	<LOD	2.7	<LOD	<LOD	<LOD	11.2	1.2	7.5
10.7	138	47.0	38.8	26.8	2150	33000	39.9	126	500	<LOD	60.0	6.9	27.6	44.0	35.0	166	8.3	48.0	39.5	373	172	223
<LOD	<LOD	0.98	<LOD	<LOD	<LOD	<LOD	<LOD	<LOD	0.93	<LOD	1.1	<LOD	<LOD	<LOD	0.99	0.77	<LOD	<LOD	<LOD	<LOD	0.96	<LOD
261	208	262	328	283	359	175	222	142	183	187	299	291	270	278	244	204	310	277	293	284	288	225
11.5	23.4	15.2	16.5	12.1	20.4	<LOD	12.6	29.3	13.2	12.8	12.3	17.2	18.2	12.0	12.5	12.0	<LOD	<LOD	<LOD	19.9	10.9	17.4
<LOD	<LOD	<LOD	<LOD	<LOD	218	1700	<LOD	111	34.0	<LOD	<LOD	<LOD	<LOD	<LOD	<LOD	73.0	<LOD	<LOD	<LOD	370	18.7	133
<LOD	<LOD	0.06	<LOD	<LOD	<LOD	<LOD	<LOD	<LOD	<LOD	<LOD	<LOD	<LOD	<LOD	<LOD	<LOD	<LOD	<LOD	<LOD	0.09	<LOD	<LOD	0.29
<LOD	<LOD	<LOD	<LOD	0.34	<LOD	<LOD	<LOD	<LOD	<LOD	0.41	<LOD	<LOD	<LOD	<LOD	<LOD	0.42	<LOD	<LOD	<LOD	<LOD	<LOD	<LOD
0.45	<LOD	<LOD	<LOD	<LOD	<LOD	<LOD	<LOD	<LOD	<LOD	<LOD	<LOD	<LOD	<LOD	<LOD	<LOD	<LOD	<LOD	<LOD	<LOD	0.48	<LOD	<LOD
0.68	1.5	<LOD	<LOD	7.4	<LOD	7.5	15.7	2.3	<LOD	<LOD	0.12	<LOD	<LOD	<LOD	0.41	15.3	0.26	<LOD	<LOD	52.0	0.43	26.2
0.09	<LOD	0.13	<LOD	<LOD	<LOD	<LOD	0.19	0.18	<LOD	<LOD	0.44	0.33	<LOD	0.32	0.29	0.39	<LOD	0.32	<LOD	2.8	0.21	0.12
0.45	1.3	2.1	<LOD	0.77	163	<LOD	4.3	<LOD	4.6	<LOD	0.14	<LOD	<LOD	<LOD	<LOD	3.1	<LOD	<LOD	<LOD	12.0	1.2	1.6
<LOD	0.76	<LOD	<LOD	4.5	29.0	<LOD	0.51	0.26	<LOD	<LOD	0.14	<LOD	<LOD	<LOD	<LOD	0.29	<LOD	<LOD	<LOD	1.7	<LOD	7.1
<LOD	<LOD	<LOD	<LOD	0.98	6.5	<LOD	<LOD	<LOD	<LOD	<LOD	<LOD	<LOD	<LOD	0.02	0.04	<LOD	0.005	<LOD	<LOD	<LOD	0.02	0.49
<LOD	<LOD	0.02	0.01	<LOD	<LOD	0.05	<LOD	<LOD	<LOD	<LOD	<LOD	<LOD	<LOD	<LOD	<LOD	<LOD	<LOD	<LOD	<LOD	<LOD	<LOD	0.01
<LOD	<LOD	<LOD	<LOD	<LOD	<LOD	<LOD	<LOD	<LOD	<LOD	<LOD	<LOD	<LOD	<LOD	<LOD	<LOD	<LOD	<LOD	<LOD	<LOD	<LOD	<LOD	<LOD
<LOD	<LOD	0.04	<LOD	<LOD	<LOD	<LOD	<LOD	0.06	<LOD	0.04	<LOD	<LOD	<LOD	<LOD	<LOD	<LOD	<LOD	<LOD	<LOD	<LOD	<LOD	<LOD
<LOD	<LOD	0.04	<LOD	<LOD	<LOD	0.08	<LOD	<LOD	<LOD	<LOD	<LOD	<LOD	<LOD	<LOD	<LOD	<LOD	<LOD	<LOD	<LOD	<LOD	<LOD	<LOD

25	26	27	28	29	30	31	32	33	34	35	36	37	38	39	40	41	42	43	44	45	46	47
358	1014	1048	1084	1076	1120	1210	1128	995	1180	1021	980	427	715	1109	1122	1175	509	934	283	233	595	754
8.2	23.9	24.9	24.6	23.1	27.9	24.2	24.4	25.4	22.3	25.1	20.7	13.2	15.4	24.0	22.0	20.0	10.1	18.7	6.0	3.9	13.0	16.1
36.6	115	116	118	111	130	117	119	125	108	119	98.1	50.8	70.4	116	104	94.9	45.4	92.7	25.9	18.4	60.6	74.8
7.1	22.0	21.9	22.1	21.3	24.2	21.8	22.8	24.0	20.4	23.0	19.0	9.1	14.2	21.3	19.5	18.1	8.4	17.1	5.0	3.4	11.7	14.2
35.5	109	116	115	115	126	114	118	124	107	119	95.1	46.0	68.5	116	105	93.1	47.0	89.5	24.9	18.4	60.9	72.8
6.4	21.3	22.5	22.7	22.8	25.8	24.4	22.7	24.7	22.2	23.8	18.4	8.3	14.2	22.9	21.4	19.8	9.3	18.5	5.0	3.3	11.5	14.8
3.1	10.7	11.0	11.4	10.9	13.0	11.7	11.8	11.6	10.9	11.7	9.3	3.9	6.5	11.1	10.4	9.5	5.0	8.6	2.3	1.6	5.7	7.3
9.5	30.5	30.9	32.7	30.7	36.0	34.0	32.2	31.5	31.8	32.2	26.0	12.1	19.5	32.8	28.9	28.7	12.2	25.6	6.2	4.6	16.4	20.1
1.6	5.7	6.0	6.0	6.0	6.6	6.5	6.4	5.9	6.0	5.9	5.0	2.3	3.5	6.0	5.7	5.7	2.4	4.5	1.3	0.94	3.0	3.9
12.1	38.1	40.5	40.7	40.8	45.2	44.2	44.4	38.5	43.7	40.6	33.9	15.4	25.4	43.2	41.2	42.8	17.4	35.8	9.6	7.8	22.5	27.1
2.7	8.7	8.8	9.3	9.5	10.0	10.0	9.9	8.6	9.9	9.4	7.8	3.5	5.9	9.7	9.7	10.0	4.5	8.0	2.3	1.8	4.9	6.2
6.6	21.6	22.6	23.5	25.2	24.9	25.8	25.2	21.0	25.8	22.7	19.7	9.1	14.8	24.7	23.0	25.2	10.5	19.8	5.6	4.5	12.6	15.7
0.73	2.4	2.5	2.6	2.7	2.7	2.8	2.7	2.2	2.9	2.4	2.2	1.1	1.6	2.7	2.6	2.9	1.1	2.2	0.69	0.54	1.5	1.8
4.4	13.8	14.1	16.3	17.4	15.7	17.0	16.5	13.1	18.0	14.3	13.6	6.5	9.4	16.4	15.5	18.1	7.3	13.5	3.8	3.2	8.4	10.8
0.46	1.5	1.5	1.6	1.7	1.7	1.7	1.7	1.4	1.9	1.5	1.4	0.64	1.0	1.8	1.6	1.9	0.76	1.4	0.43	0.36	0.92	1.1
135	424	439	447	437	489	455	457	457	431	451	370	182	270	448	411	391	181	356	98.9	72.6	234	287
1.2	1.2	1.5	1.3	1.4	1.5	1.6	1.5	1.3	3.1	1.4	1.4	1.2	1.4	1.4	1.4	1.5	1.2	1.8	0.92	0.82	1.2	1.4
0.01	<LOD	<LOD	<LOD	<LOD	<LOD	0.46	<LOD	<LOD	<LOD	<LOD	0.38	<LOD	0.03	<LOD	<LOD	<LOD	0.42	<LOD	0.23	<LOD	<LOD	<LOD
3.7	<LOD	<LOD	0.31	0.95	0.22	8.0	0.23	12.4	<LOD	<LOD	1.6	4.5	6.8	<LOD	10.8	82.3	38.4	3.9	4.6	12.1	46.8	7.6
61.4	59.0	61.0	68.7	69.5	69.8	65.3	60.8	106	102	61.9	74.2	69.0	67.4	56.2	98.0	125	141	72.5	67.0	108	75.0	67.7
34.0	44.7	46.6	50.4	55.0	56.1	114	48.2	67.7	137	47.3	61.1	31.4	46.8	48.9	128	960	104	457	30.0	38.7	104	41.5
10.0	<LOD	<LOD	1.2	3.6	1.3	33.0	0.10	8.8	24.0	<LOD	7.6	1.1	1.3	0.05	15.7	246	17.5	216	2.9	5.3	13.6	1.5
650	31.1	31.2	97.0	208	195	2700	39.0	630	2090	30.5	399	157	830	35.9	1730	20300	900	11700	475	500	700	110
<LOD	<LOD	<LOD	<LOD	<LOD	<LOD	<LOD	<LOD	<LOD	<LOD	<LOD	<LOD	<LOD	<LOD	<LOD	<LOD	<LOD	<LOD	<LOD	<LOD	<LOD	<LOD	<LOD
305	327	358	273	293	301	280	223	339	323	268	355	289	253	312	338	261	333	210	211	227	234	345
16.9	10.9	<LOD	14.4	<LOD	15.0	12.5	10.3	17.4	<LOD	18.7	14.6	19.6	13.1	16.1	<LOD	17.6	<LOD	19.1	16.9	13.2	13.0	13.0
92.0	<LOD	<LOD	<LOD	0.09	0.12	<LOD	<LOD	<LOD	290	<LOD	55.0	50.0	145	<LOD	397	2260	440	650	89.0	179	460	62.5
<LOD	<LOD	<LOD	<LOD	0.37	<LOD	<LOD	<LOD	<LOD	<LOD	<LOD	<LOD	<LOD	<LOD	<LOD	<LOD	<LOD	<LOD	<LOD	<LOD	<LOD	<LOD	<LOD
<LOD	<LOD	<LOD	<LOD	0.06	<LOD	<LOD	<LOD	<LOD	0.28	<LOD	<LOD	<LOD	<LOD	<LOD	<LOD	<LOD	<LOD	<LOD	<LOD	0.33	<LOD	<LOD
<LOD	<LOD	<LOD	<LOD	<LOD	<LOD	<LOD	<LOD	<LOD	<LOD	<LOD	<LOD	<LOD	<LOD	<LOD	<LOD	<LOD	<LOD	<LOD	<LOD	<LOD	<LOD	<LOD
3.6	<LOD	<LOD	0.31	3.1	0.33	1.4	0.69	35.5	31.0	<LOD	5.6	6.6	9.6	<LOD	35.8	160	40.0	2.6	6.6	24.0	26.8	7.6
<LOD	0.16	0.14	<LOD	<LOD	0.13	0.19	<LOD	<LOD	0.21	<LOD	0.22	<LOD	<LOD	0.10	<LOD	<LOD	<LOD	0.16	<LOD	<LOD	<LOD	<LOD
0.68	<LOD	<LOD	0.33	0.29	<LOD	0.42	<LOD	2.8	<LOD	<LOD	0.64	2.0	5.5	<LOD	0.48	<LOD	3.9	2.2	8.2	3.3	6.8	1.5
1.7	<LOD	<LOD	<LOD	<LOD	<LOD	1.9	0.44	8.8	19.7	<LOD	3.1	3.8	7.0	<LOD	9.8	130	63.0	8.1	3.9	8.0	64.0	8.5
0.26	<LOD	<LOD	<LOD	<LOD	<LOD	0.29	<LOD	1.2	1.2	<LOD	0.15	0.19	0.37	<LOD	1.3	9.4	1.6	2.0	0.25	0.82	1.8	0.25
<LOD	<LOD	0.02	<LOD	<LOD	<LOD	<LOD	<LOD	<LOD	<LOD	<LOD	<LOD	<LOD	<LOD	<LOD	<LOD	<LOD	0.19	<LOD	<LOD	<LOD	<LOD	<LOD
<LOD	<LOD	<LOD	<LOD	<LOD	<LOD	<LOD	<LOD	<LOD	<LOD	<LOD	<LOD	<LOD	<LOD	<LOD	<LOD	<LOD	<LOD	<LOD	<LOD	<LOD	<LOD	<LOD
<LOD	<LOD	<LOD	<LOD	<LOD	<LOD	0.06	<LOD	<LOD	<LOD	<LOD	<LOD	<LOD	<LOD	<LOD	<LOD	<LOD	<LOD	<LOD	<LOD	<LOD	<LOD	<LOD
<LOD	<LOD	<LOD	0.03	<LOD	<LOD	<LOD	<LOD	<LOD	<LOD	<LOD	<LOD	<LOD	0.02	<LOD	<LOD	<LOD	<LOD	<LOD	<LOD	<LOD	<LOD	<LOD

48	49	50	51	52	53	54	55	56	57	58	59	60	61	62	63	64	65	66	67	68	69	70
594	361	425	897	271	1168	1162	1181	1231	1198	931	1097	1035	983	1007	846	1033	1029	907	1010	985	459	803
13.0	9.8	8.3	17.4	6.0	24.6	24.7	23.4	23.7	24.4	24.3	24.8	23.3	25.6	23.6	24.3	24.2	23.4	25.5	23.8	22.8	10.8	17.7
58.4	44.1	38.4	82.2	27.9	123	121	110	114	114	117	124	114	121	117	120	119	118	119	118	110	46.7	83.4
10.6	7.7	7.4	15.8	5.1	23.4	23.0	21.4	21.2	22.7	22.9	23.2	20.9	23.9	22.2	22.4	22.7	22.0	22.3	22.2	21.3	9.7	15.7
54.2	39.4	36.7	80.5	27.0	122	120	109	110	111	118	116	111	118	113	118	117	113	113	115	109	46.5	82.4
10.2	7.3	7.3	16.3	5.2	23.7	23.2	21.6	23.4	24.0	23.5	22.4	22.7	23.2	23.4	23.3	22.4	22.9	23.0	23.4	20.9	8.7	14.7
5.3	3.6	3.6	7.8	2.3	12.1	12.2	11.4	11.4	11.4	10.9	11.9	11.1	11.6	11.2	10.7	11.5	11.2	10.5	10.6	10.7	4.1	7.5
14.5	9.7	10.3	23.9	6.7	35.0	33.2	33.6	33.1	33.9	30.8	31.2	29.4	32.6	31.3	31.0	33.1	32.1	29.8	30.8	29.8	11.6	21.5
2.9	1.9	2.0	4.5	1.2	6.6	6.7	6.3	6.8	6.5	5.6	6.3	5.9	6.0	5.9	5.6	6.0	5.8	5.4	5.9	5.6	2.2	4.1
21.0	12.8	14.8	31.6	9.3	44.4	46.1	46.2	47.2	45.0	37.2	42.6	38.1	38.8	38.2	35.5	39.9	39.7	35.9	39.9	38.0	15.6	28.2
4.9	3.0	3.4	7.4	2.1	10.2	10.0	10.0	10.7	10.4	8.2	9.5	8.7	8.5	8.6	8.0	8.8	8.6	7.8	8.7	8.6	3.8	6.4
11.9	7.7	9.1	19.1	5.6	25.0	25.2	26.3	27.3	26.5	20.0	24.0	21.9	20.8	21.5	19.6	22.5	22.4	19.4	21.6	21.1	9.3	16.4
1.4	0.81	1.0	2.1	0.59	2.7	2.8	3.0	3.2	2.9	2.2	2.7	2.4	2.1	2.3	2.1	2.5	2.4	2.0	2.4	2.3	1.1	1.8
8.6	4.9	6.2	12.6	4.3	17.0	16.4	18.9	18.9	18.1	13.0	16.5	13.8	13.3	13.1	12.7	15.0	14.7	13.4	14.1	13.8	6.4	11.1
0.99	0.50	0.66	1.3	0.42	1.7	1.9	1.9	2.0	1.8	1.3	1.8	1.6	1.4	1.4	1.3	1.5	1.5	1.3	1.5	1.4	0.67	1.2
218	153	149	322	104	471	466	443	452	452	435	457	425	447	433	434	445	438	429	438	415	177	312
1.3	1.0	0.86	1.6	0.88	1.5	1.7	1.5	1.7	1.6	1.1	1.2	1.1	1.0	1.0	0.96	1.2	1.2	1.0	1.1	0.99	1.0	1.5
<LOD	<LOD	<LOD	<LOD	<LOD	<LOD	<LOD	<LOD	<LOD	<LOD	0.05	0.01	0.04	0.04	<LOD	<LOD	<LOD	<LOD	<LOD	<LOD	<LOD	<LOD	<LOD
42.2	33.1	89.3	9.5	48.6	<LOD	<LOD	<LOD	<LOD	<LOD	0.18	0.28	0.83	0.12	<LOD	<LOD	<LOD	0.13	0.35	<LOD	0.09	29.1	18.0
88.0	105	73.0	67.3	151	59.9	53.3	62.8	61.0	54.3	62.4	50.0	59.4	59.8	56.9	58.1	58.2	65.6	60.0	61.4	56.4	77.5	69.3
79.0	64.0	186	47.8	183	50.6	53.2	55.0	57.9	55.7	81.0	48.0	47.8	52.4	46.7	41.8	47.8	60.2	42.9	44.2	64.7	133	50.7
15.7	9.9	31.0	1.3	42.0	0.24	<LOD	<LOD	<LOD	0.43	36.0	0.17	0.39	9.8	<LOD	0.10	<LOD	6.6	0.23	<LOD	7.8	42.0	5.2
700	410	1460	113	2060	38.7	55.0	<LOD	47.6	48.6	830	<LOD	52.6	537	35.2	25.1	46.0	369	33.0	45.0	590	2800	268
<LOD	<LOD	<LOD	<LOD	1.5	<LOD	<LOD	0.60	2.1	<LOD	2.2	<LOD	<LOD	<LOD	<LOD	<LOD	<LOD	<LOD	<LOD	<LOD	<LOD	<LOD	<LOD
400	256	212	307	284	296	350	277	291	236	251	327	<LOD	247	228	304	257	237	288	233	272	272	330
<LOD	10.9	13.0	11.1	16.7	14.7	14.5	16.2	24.5	13.3	16.1	12.9	21.6	11.8	13.8	9.2	17.5	12.0	12.5	14.2	<LOD	11.5	15.7
520	229	890	61.0	1200	<LOD	<LOD	<LOD	9.1	<LOD	71.0	47.0	11.8	26.9	<LOD	<LOD	<LOD	46.0	8.0	<LOD	22.2	352	84.0
<LOD	<LOD	<LOD	<LOD	<LOD	<LOD	0.11	<LOD	<LOD	<LOD	<LOD	0.10	<LOD	<LOD	<LOD	<LOD	<LOD	<LOD	<LOD	<LOD	<LOD	<LOD	0.27
<LOD	<LOD	<LOD	<LOD	<LOD	<LOD	<LOD	<LOD	<LOD	<LOD	<LOD	<LOD	<LOD	<LOD	<LOD	<LOD	<LOD	0.04	<LOD	<LOD	<LOD	<LOD	<LOD
<LOD	<LOD	<LOD	<LOD	0.49	<LOD	<LOD	<LOD	<LOD	<LOD	<LOD	<LOD	<LOD	<LOD	<LOD	<LOD	<LOD	<LOD	<LOD	<LOD	<LOD	<LOD	<LOD
49.0	33.6	54.0	9.8	43.0	<LOD	0.11	0.21	<LOD	<LOD	<LOD	0.26	0.18	2.4	<LOD	<LOD	<LOD	0.31	0.51	<LOD	0.09	18.3	8.5
<LOD	<LOD	<LOD	<LOD	<LOD	<LOD	<LOD	<LOD	<LOD	<LOD	0.75	1.3	0.35	<LOD	<LOD	<LOD	<LOD	0.52	0.36	<LOD	<LOD	0.18	<LOD
11.4	5.7	8.1	4.4	<LOD	<LOD	<LOD	<LOD	0.31	<LOD	<LOD	<LOD	<LOD	<LOD	<LOD	<LOD	<LOD	1.4	<LOD	<LOD	0.56	8.4	4.4
32.2	27.2	140	7.2	89.0	<LOD	<LOD	<LOD	<LOD	<LOD	<LOD	<LOD	<LOD	<LOD	<LOD	<LOD	<LOD	0.10	<LOD	<LOD	0.12	29.0	14.4
2.6	1.1	3.0	0.25	4.9	<LOD	0.11	<LOD	0.10	<LOD	0.32	0.27	0.12	0.11	<LOD	<LOD	0.09	<LOD	<LOD	0.10	<LOD	1.2	0.25
<LOD	<LOD	<LOD	0.04	<LOD	<LOD	0.02	<LOD	0.01	<LOD	0.04	0.03	<LOD	0.03	<LOD	<LOD	<LOD	<LOD	<LOD	<LOD	<LOD	<LOD	<LOD
<LOD	<LOD	<LOD	<LOD	<LOD	<LOD	<LOD	<LOD	<LOD	<LOD	<LOD	0.007	<LOD	<LOD	<LOD	<LOD	<LOD	<LOD	<LOD	<LOD	<LOD	<LOD	<LOD
0.02	<LOD	0.03	<LOD	<LOD	<LOD	<LOD	<LOD	<LOD	<LOD	<LOD	0.02	<LOD	<LOD	<LOD	<LOD	<LOD	<LOD	<LOD	<LOD	<LOD	<LOD	<LOD

71	72	73	74	75	76	77	78	79	80	81	82	83	84	85	86	87	88	89	90	91	92	93
346	908	805	1224	1339	1273	624	1302	959	1162	166	1094	456	1354	1307	1275	1316	1279	349	1308	673	1249	1113
8.6	20.7	19.9	25.0	24.5	27.0	13.0	25.7	19.9	25.0	3.9	22.0	7.5	26.4	25.1	21.9	23.7	23.7	8.8	23.8	13.9	26.9	22.1
40.1	99.1	90.0	115	115	123	56.4	125	89.6	117	15.2	104	36.8	129	115	105	114	111	38.5	110	63.1	124	104
7.7	18.6	17.4	22.2	21.9	23.4	11.5	23.7	16.6	22.7	2.9	19.9	6.8	24.3	22.3	19.9	22.5	21.7	6.7	21.6	12.4	24.4	19.6
39.0	92.8	91.2	117	112	123	58.7	124	82.8	114	13.2	107	33.5	112	118	98.7	113	109	34.6	116	62.5	125	99.5
7.0	19.6	18.0	23.2	23.5	25.9	12.2	24.1	16.5	23.8	2.2	21.9	7.4	25.7	23.4	21.6	24.2	22.3	6.5	22.9	12.0	25.4	21.8
3.5	9.0	8.9	11.9	11.6	12.4	5.6	12.5	7.9	11.3	1.2	10.9	3.1	12.7	11.7	11.5	11.6	11.3	2.9	11.1	6.0	11.9	10.5
9.6	26.2	23.2	32.7	32.9	34.4	15.3	35.5	23.3	31.7	3.8	31.1	10.1	34.3	34.5	31.0	34.1	31.1	7.6	32.9	17.3	36.4	30.5
1.9	5.0	4.4	6.7	6.5	6.7	3.1	6.8	4.5	6.2	0.64	5.8	1.9	6.9	6.4	6.4	6.6	6.5	1.6	6.3	3.3	7.0	5.6
12.6	32.5	30.8	45.8	47.0	48.7	22.5	46.8	33.2	42.5	4.8	41.8	13.7	48.3	48.5	44.2	47.7	45.3	10.8	47.3	23.0	47.1	40.8
2.7	7.4	7.0	10.8	10.8	10.5	5.2	11.0	7.5	9.6	1.1	8.8	3.3	11.7	11.5	10.7	10.8	10.8	2.6	10.7	5.4	10.8	9.3
7.5	18.9	17.2	26.6	27.0	27.3	13.3	26.7	19.2	24.1	3.2	21.9	9.1	29.6	28.6	27.6	28.9	28.2	6.5	27.7	14.1	27.0	23.0
0.80	2.1	1.9	3.0	3.1	2.9	1.5	3.0	2.2	2.6	0.33	2.3	1.0	3.1	3.2	3.2	3.1	3.1	0.75	3.2	1.5	2.9	2.6
4.9	12.7	11.8	18.1	18.4	17.3	9.9	18.0	13.1	15.3	2.4	14.8	6.4	19.8	19.7	20.0	18.2	18.7	5.0	19.2	9.3	17.9	15.4
0.50	1.4	1.2	1.9	1.9	1.8	1.1	1.9	1.4	1.7	0.23	1.6	0.67	2.1	2.1	2.1	2.0	1.9	0.47	2.0	1.0	1.9	1.6
146	366	343	460	456	484	229	484	338	448	55.2	414	141	486	469	424	460	444	133	455	245	489	406
0.71	1.1	0.99	2.1	1.9	2.0	1.2	2.0	1.8	2.0	0.81	1.9	1.1	2.2	2.0	1.9	1.9	1.9	1.3	1.9	1.6	1.8	1.6
<LOD	<LOD	0.009	<LOD	<LOD	0.003	<LOD	<LOD	<LOD	<LOD	0.01	<LOD	0.01	0.007	<LOD	<LOD	<LOD	0.004	0.12	<LOD	0.02	<LOD	0.04
9.9	9.0	53.6	0.67	2.3	2.3	6.1	<LOD	3.8	3.3	5.5	0.58	5.2	0.92	<LOD	0.11	<LOD	4.5	0.93	<LOD	13.9	2.3	2.2
63.3	66.2	62.2	58.6	62.2	65.0	60.7	58.4	66.6	131	57.9	56.4	53.9	57.0	56.9	52.9	61.2	71.9	62.7	50.3	62.7	69.5	71.0
36.1	65.7	48.3	52.8	60.4	80.4	41.6	53.3	45.7	57.6	16.9	47.6	34.1	61.3	53.8	52.0	54.9	54.4	20.3	51.8	70.0	59.3	55.0
3.1	13.0	3.3	0.62	0.80	3.2	2.1	0.58	0.53	3.9	1.8	0.59	1.7	0.71	<LOD	<LOD	<LOD	0.75	0.34	<LOD	8.0	2.6	0.59
196	910	109	52.4	103	1980	143	91.0	63.7	77.0	117	43.1	236	73.0	45.6	134	43.8	67.6	82.9	49.3	460	123	66.4
<LOD	<LOD	2.4	<LOD	<LOD	0.71	<LOD	<LOD	<LOD	<LOD	<LOD	<LOD	<LOD	<LOD	<LOD	<LOD	<LOD	<LOD	<LOD	<LOD	<LOD	<LOD	0.96
311	258	273	287	270	279	300	301	300	309	305	315	292	256	<LOD	312	322	221	274	246	306	264	335
12.6	11.9	14.2	<LOD	13.7	12.9	10.1	12.6	11.1	14.5	16.3	12.4	16.8	12.9	10.5	11.6	13.5	14.7	<LOD	10.8	15.7	<LOD	12.4
126	100	59.0	<LOD	39.0	168	84.0	<LOD	15.2	30.0	26.4	<LOD	66.0	17.4	<LOD	<LOD	<LOD	20.3	<LOD	<LOD	218	29.5	31.3
0.08	<LOD	<LOD	<LOD	<LOD	<LOD	<LOD	<LOD	<LOD	0.08	<LOD	<LOD	<LOD	<LOD	<LOD	<LOD	<LOD	<LOD	<LOD	<LOD	<LOD	<LOD	<LOD
<LOD	<LOD	42.0	<LOD	<LOD	<LOD	<LOD	<LOD	<LOD	<LOD	0.28	<LOD	<LOD	<LOD	<LOD	<LOD	<LOD	<LOD	<LOD	0.41	<LOD	<LOD	<LOD
<LOD	0.04	<LOD	<LOD	<LOD	<LOD	<LOD	<LOD	<LOD	<LOD	<LOD	<LOD	<LOD	<LOD	<LOD	<LOD	<LOD	<LOD	<LOD	0.03	<LOD	<LOD	<LOD
<LOD	<LOD	<LOD	<LOD	<LOD	<LOD	<LOD	<LOD	<LOD	<LOD	<LOD	<LOD	<LOD	<LOD	<LOD	<LOD	<LOD	<LOD	<LOD	<LOD	<LOD	<LOD	<LOD
8.3	13.4	2.0	1.7	3.1	14.3	3.5	<LOD	3.6	131	4.3	1.0	7.8	2.3	<LOD	<LOD	<LOD	11.9	0.91	<LOD	12.8	6.8	8.2
<LOD	0.13	<LOD	<LOD	0.22	<LOD	<LOD	<LOD	<LOD	0.14	0.14	<LOD	0.20	<LOD	0.12	0.13	<LOD	<LOD	0.17	<LOD	<LOD	<LOD	0.09
1.1	4.2	12.3	0.34	<LOD	<LOD	4.0	<LOD	1.4	2.0	7.3	0.39	3.0	0.59	<LOD	0.54	<LOD	3.7	2.5	<LOD	1.9	0.36	1.6
9.0	13.4	19.7	0.76	1.7	3.0	14.4	<LOD	3.7	3.7	3.7	0.40	4.6	0.69	<LOD	<LOD	<LOD	4.3	<LOD	<LOD	25.0	1.2	2.1
0.45	0.48	0.25	<LOD	0.17	0.36	0.40	<LOD	<LOD	0.11	<LOD	<LOD	0.26	<LOD	0.12	<LOD	<LOD	<LOD	<LOD	0.10	0.93	0.16	0.16
<LOD	<LOD	0.03	<LOD	<LOD	<LOD	<LOD	<LOD	<LOD	<LOD	<LOD	<LOD	<LOD	0.02	<LOD	<LOD	<LOD	0.03	<LOD	<LOD	<LOD	<LOD	<LOD
<LOD	<LOD	0.01	<LOD	<LOD	<LOD	<LOD	<LOD	<LOD	<LOD	<LOD	<LOD	<LOD	<LOD	<LOD	<LOD	<LOD	<LOD	<LOD	<LOD	<LOD	<LOD	<LOD
<LOD	<LOD	<LOD	<LOD	<LOD	0.04	0.08	<LOD	0.06	<LOD	<LOD	<LOD	<LOD	<LOD	<LOD	<LOD	<LOD	<LOD	<LOD	<LOD	<LOD	<LOD	<LOD
<LOD	<LOD	<LOD	<LOD	<LOD	<LOD	<LOD	<LOD	<LOD	<LOD	<LOD	<LOD	0.03	<LOD	<LOD	<LOD	<LOD	0.04	<LOD	<LOD	<LOD	<LOD	<LOD

94	95	96	97	98	99	100	101	102	103	104	105	106	107	108	109	110	111	112	113	114	115	116
1217	962	866	186	1208	1169	997	1257	1127	1113	1146	986	445	1059	1198	649	936	70.4	269	898	139	987	<LOD
23.5	26.7	28.3	27.2	28.2	25.5	31.4	25.5	24.1	26.6	22.9	25.3	30.7	26.3	25.8	37.2	23.7	52.2	15.6	29.4	27.0	24.3	<LOD
113	123	132	138	134	126	113	125	116	128	113	126	140	128	124	109	123	106	65.8	119	136	110	<LOD
21.7	24.1	24.4	27.0	26.3	23.4	19.0	23.5	22.1	25.2	23.0	23.3	26.9	24.6	24.9	14.9	22.7	9.2	12.5	21.2	27.5	21.4	<LOD
110	121	131	134	133	121	90.5	122	118	131	116	118	139	132	123	68.5	118	25.0	65.3	108	147	108	<LOD
22.1	24.6	25.1	22.1	26.1	26.1	17.7	24.6	24.0	27.0	23.5	23.8	24.7	26.7	25.9	13.3	23.5	2.8	10.9	20.1	23.6	21.7	<LOD
10.7	11.2	11.5	8.7	12.7	12.3	8.8	12.4	11.3	12.7	11.5	11.4	10.8	12.1	12.4	6.3	11.5	1.2	4.2	10.1	8.2	11.0	<LOD
32.2	31.5	32.6	19.6	37.3	34.0	26.3	35.1	31.8	35.1	31.4	32.8	26.3	32.8	36.0	19.0	29.9	2.8	9.9	28.0	19.1	30.5	<LOD
6.2	5.8	5.8	2.5	7.2	6.6	5.1	6.7	6.1	6.7	6.0	5.8	4.2	6.5	7.0	3.6	5.5	0.83	1.5	5.0	2.1	5.6	<LOD
44.1	38.4	36.6	10.0	46.6	45.1	36.6	47.3	42.8	44.4	40.2	39.1	22.9	43.7	46.8	26.2	36.5	6.3	8.3	36.0	8.3	37.5	<LOD
10.2	8.4	9.1	7.9	1.6	10.0	8.5	10.4	9.8	9.7	9.7	8.6	4.5	9.3	10.3	6.0	8.1	1.4	2.0	8.0	1.3	8.6	<LOD
25.7	20.0	21.8	18.9	3.4	24.4	21.5	25.7	24.1	23.3	23.8	21.0	10.6	22.9	25.7	15.1	20.9	3.5	5.6	19.6	2.7	21.6	<LOD
2.8	2.2	2.5	1.9	0.34	2.6	2.3	2.9	2.6	2.5	2.4	2.1	1.0	2.4	2.8	1.7	2.2	0.45	0.66	2.2	0.28	2.4	<LOD
18.0	13.3	14.9	11.5	2.0	15.7	14.0	17.4	16.1	15.1	15.6	12.8	6.0	13.8	16.6	10.8	12.9	2.7	4.4	13.4	1.5	14.4	<LOD
1.9	1.4	1.6	1.3	0.20	1.7	1.5	1.8	1.7	1.6	1.7	1.5	0.67	1.5	1.7	1.2	1.4	0.32	0.47	1.3	0.15	1.5	<LOD
442	452	405	469	396	474	396	480	450	489	441	451	448	482	483	333	439	214	207	421	404	419	<LOD
1.5	1.0	1.9	1.2	3.2	1.8	1.6	1.2	1.7	1.4	1.7	1.5	1.2	1.1	1.6	1.7	0.84	1.2	0.03	1.6	1.2	4.2	1.1
<LOD	0.008	0.007	0.01	<LOD	<LOD	<LOD	<LOD	<LOD	<LOD	<LOD	0.14	<LOD	<LOD	<LOD	<LOD	<LOD	0.002	0.12	<LOD	<LOD	<LOD	<LOD
0.32	0.65	8.2	0.43	0.83	<LOD	0.20	6.1	<LOD	2.5	<LOD	1.9	0.09	3.1	<LOD	<LOD	0.08	<LOD	2.4	1.3	<LOD	0.13	
58.1	61.8	68.6	66.0	64.1	53.9	61.5	88.5	54.0	62.3	51.8	64.6	54.4	54.0	61.5	65.5	48.1	56.5	51.5	55.6	54.0	61.0	46.0
54.9	76.0	101	45.2	12.2	48.1	50.6	59.6	51.8	56.5	47.3	54.0	48.0	27.8	46.3	54.1	36.8	42.6	13.2	13.1	45.2	8.9	49.0
0.29	17.2	10.8	<LOD	0.44	<LOD	<LOD	2.6	<LOD	2.9	<LOD	0.12	0.07	0.55	<LOD	<LOD	<LOD	<LOD	<LOD	4.6	0.16	<LOD	0.12
122	1330	780	27.4	30.5	33.0	43.0	96.0	39.3	193	23.1	68.0	19.4	50.5	27.8	35.9	22.4	27.6	14.0	21.7	33.7	<LOD	52.8
<LOD	<LOD	<LOD	<LOD	<LOD	<LOD	<LOD	<LOD	<LOD	<LOD	<LOD	<LOD	<LOD	<LOD	<LOD	<LOD	<LOD	0.97	<LOD	<LOD	<LOD	<LOD	<LOD
289	293	223	280	282	214	291	263	246	234	208	230	251	276	315	296	277	204	223	256	214	205	285
12.6	11.8	19.2	15.8	8.7	10.5	15.3	<LOD	<LOD	13.3	11.0	13.2	14.6	14.0	13.1	15.8	<LOD	12.8	<LOD	22.4	10.5	<LOD	15.0
<LOD	51.0	132	<LOD	12.0	<LOD	<LOD	174	<LOD	16.5	<LOD	59.0	<LOD	29.5	<LOD	<LOD	<LOD	<LOD	<LOD	<LOD	<LOD	<LOD	<LOD
<LOD	<LOD	<LOD	<LOD	<LOD	<LOD	<LOD	<LOD	<LOD	<LOD	<LOD	0.11	<LOD	<LOD	<LOD	<LOD	<LOD	<LOD	<LOD	<LOD	<LOD	<LOD	<LOD
<LOD	<LOD	<LOD	<LOD	<LOD	<LOD	0.37	<LOD	<LOD	<LOD	<LOD	<LOD	<LOD	<LOD	<LOD	<LOD	<LOD	<LOD	<LOD	<LOD	<LOD	<LOD	<LOD
<LOD	<LOD	<LOD	<LOD	<LOD	<LOD	<LOD	<LOD	<LOD	<LOD	<LOD	<LOD	<LOD	<LOD	<LOD	<LOD	<LOD	<LOD	<LOD	<LOD	<LOD	<LOD	<LOD
<LOD	<LOD	<LOD	<LOD	<LOD	<LOD	<LOD	<LOD	<LOD	<LOD	<LOD	<LOD	<LOD	<LOD	<LOD	<LOD	<LOD	<LOD	<LOD	<LOD	<LOD	<LOD	<LOD
0.94	<LOD	20.2	<LOD	2.1	<LOD	0.25	24.6	<LOD	3.5	<LOD	6.7	<LOD	8.1	<LOD	<LOD	<LOD	<LOD	0.51	1.3	0.21	<LOD	<LOD
<LOD	<LOD	<LOD	<LOD	0.15	<LOD	0.17	0.15	<LOD	0.39	<LOD	0.65	<LOD	0.14	<LOD	<LOD	<LOD	<LOD	0.21	10.5	0.55	<LOD	<LOD
0.32	1.5	1.9	2.5	0.69	0.59	0.31	0.72	<LOD	2.1	<LOD	2.2	6.0	<LOD	<LOD	<LOD	<LOD	<LOD	0.57	<LOD	<LOD	<LOD	<LOD
<LOD	<LOD	10.6	<LOD	<LOD	<LOD	0.59	4.9	<LOD	0.09	<LOD	0.25	0.20	<LOD	<LOD	<LOD	<LOD	<LOD	<LOD	<LOD	<LOD	<LOD	<LOD
<LOD	0.19	0.39	<LOD	0.09	<LOD	<LOD	0.68	<LOD	0.09	<LOD	0.25	<LOD	<LOD	<LOD	<LOD	<LOD	<LOD	<LOD	<LOD	<LOD	<LOD	<LOD
<LOD	<LOD	<LOD	<LOD	<LOD	<LOD	<LOD	<LOD	<LOD	<LOD	<LOD	<LOD	<LOD	<LOD	<LOD	<LOD	<LOD	<LOD	<LOD	<LOD	<LOD	<LOD	<LOD
<LOD	<LOD	<LOD	<LOD	<LOD	<LOD	<LOD	<LOD	<LOD	<LOD	<LOD	<LOD	<LOD	<LOD	<LOD	<LOD	<LOD	<LOD	<LOD	<LOD	<LOD	<LOD	<LOD
<LOD	<LOD	<LOD	<LOD	<LOD	<LOD	<LOD	<LOD	<LOD	<LOD	<LOD	<LOD	<LOD	<LOD	<LOD	<LOD	<LOD	<LOD	<LOD	<LOD	<LOD	<LOD	<LOD
<LOD	<LOD	0.02	<LOD	<LOD	<LOD	0.02	<LOD	0.02	<LOD	<LOD	<LOD	<LOD	<LOD	<LOD	<LOD	<LOD	0.02	0.12	<LOD	<LOD	<LOD	<LOD

117	118	119	120	121	122	*AVG*	*MIN*	*MAX*	AVG LOD
152	952	75.1	1064	1043	1139	886	63.5	1354	0.009
47.9	25.0	51.5	24.1	24.2	24.5	23.2	3.9	55.6	0.007
104	124	99.0	119	120	118	108	15.2	154	0.007
9.6	24.5	8.6	23.1	22.8	22.4	19.6	2.9	29.4	0.005
32.8	124	23.1	119	121	117	99.6	13.2	152	0.03
4.2	23.8	2.9	23.5	23.8	23.0	19.8	2.2	27.0	0.04
2.3	12.0	1.2	11.1	11.5	11.5	9.5	1.2	13.2	0.01
5.0	30.4	2.8	30.9	31.6	32.7	26.6	2.6	37.3	0.04
1.4	5.8	0.83	6.0	5.9	6.0	5.0	0.64	7.2	0.005
9.8	37.8	6.9	41.4	40.1	41.5	33.9	4.8	48.7	0.02
2.3	8.2	1.5	9.0	9.0	9.5	7.6	1.1	11.7	0.005
5.7	20.0	3.7	23.8	21.1	24.5	18.9	2.7	29.6	0.01
0.67	2.0	0.43	2.5	2.4	2.6	2.1	0.28	3.2	0.005
4.1	12.2	3.0	14.9	14.3	16.2	12.5	1.5	20.0	0.02
0.45	1.3	0.32	1.6	1.6	1.7	1.3	0.15	2.1	0.005
230	450	206	450	449	451	389	55.2	506	<LOD
0.10	1.1	0.03	1.3	1.4	1.4	1.4	0.01	4.2	0.006
<LOD	0.002	<LOD	<LOD	<LOD	<LOD	0.05	0.002	0.46	0.005
0.04	0.14	<LOD	<LOD	2.2	<LOD	4.5	0.04	89.3	<LOD
58.0	53.7	53.9	63.0	64.0	58.1	64.6	46.0	151	8.2
16.4	45.3	11.8	48.9	53.9	50.4	50.9	8.9	1040	0.01
<LOD	<LOD	<LOD	<LOD	1.4	<LOD	4.9	0.05	246	0.06
7.0	25.7	<LOD	26.3	78.3	35.2	198	6.9	33000	5.3
<LOD	<LOD	<LOD	<LOD	<LOD	<LOD	1.2	0.60	2.4	0.76
278	324	384	252	313	207	275	142	400	115
10.0	<LOD	13.5	13.2	15.4	14.5	14.0	8.7	29.3	9.3
<LOD	<LOD	<LOD	<LOD	41.4	<LOD	118	8.0	2260	6.4
<LOD	<LOD	<LOD	<LOD	<LOD	<LOD	0.09	0.06	0.12	0.09
<LOD	<LOD	0.37	<LOD	<LOD	<LOD	0.36	0.27	42.0	0.40
<LOD	<LOD	<LOD	<LOD	<LOD	<LOD	0.04	0.03	0.06	0.05
<LOD	<LOD	<LOD	<LOD	<LOD	<LOD	0.47	0.45	0.49	0.60
<LOD	<LOD	<LOD	<LOD	9.0	<LOD	10.2	0.25	160	0.26
<LOD	0.21	<LOD	<LOD	0.10	0.11	0.16	0.09	0.41	0.15
0.37	0.59	<LOD	<LOD	<LOD	<LOD	1.9	0.29	163	0.29
0.52	<LOD	<LOD	0.51	1.8	<LOD	7.3	0.40	140	0.53
<LOD	<LOD	<LOD	<LOD	0.24	<LOD	0.47	0.09	9.4	0.09
<LOD	<LOD	<LOD	<LOD	0.01	<LOD	0.02	0.005	0.19	0.02
<LOD	<LOD	<LOD	<LOD	<LOD	<LOD	0.01	0.007	0.01	0.01
0.03	<LOD	<LOD	<LOD	<LOD	<LOD	0.05	0.03	0.08	0.06
<LOD	<LOD	<LOD	<LOD	<LOD	<LOD	0.03	0.02	0.12	0.02

Ore feed

n=28	1	2	3	4	5	6	7	8	9	10	11
Y	128	99.0	82.0	75.0	38.0	1380	577	249	488	383	658
La	8.3	15.9	3.4	2.3	1.0	14.1	180	0.80	1340	4.1	30.4
Ce	32.2	30.4	11.5	7.8	4.8	69.0	324	3.0	1800	8.9	67.8
Pr	6.2	3.1	1.9	1.4	0.70	5.7	27.7	0.50	163	1.5	9.2
Nd	33.4	13.6	10.5	5.1	4.9	45.0	95.0	3.5	514	6.2	42.8
Sm	9.0	4.5	2.5	2.1	0.20	24.0	9.2	4.2	59.0	3.3	7.8
Eu	2.4	2.5	1.2	1.2	0.20	3.3	5.3	<LOD	9.4	2.3	7.1
Gd	7.0	3.4	4.5	1.0	2.2	11.3	11.7	5.6	31.8	14.9	18.5
Tb	0.80	<LOD	<LOD	0.20	<LOD	13.0	2.6	1.1	4.8	3.4	6.3
Dy	3.7	5.4	4.5	2.7	1.4	35.3	17.1	7.2	24.4	31.9	47.9
Ho	0.80	1.0	0.90	0.40	0.30	12.6	5.1	1.7	6.2	8.2	12.9
Er	1.2	3.2	3.3	2.1	1.1	37.0	18.9	6.5	14.9	30.5	31.4
Tm	0.20	0.50	0.50	0.20	<LOD	16.0	3.3	0.50	3.7	3.3	5.0
Yb	0.10	3.3	4.5	1.0	0.50	68.0	19.3	2.4	19.0	23.1	31.7
Lu	0.10	0.50	0.40	0.20	<LOD	14.8	2.9	<LOD	3.9	3.2	4.6
∑REE	105	87.3	49.6	27.7	17.3	369	722	37.0	3994	145	323
Th	0.27	19.1	18.1	8.4	1.0	0.30	1.9	1.1	<LOD	<LOD	0.20
U	4.4	4.5	8.0	2.4	3.9	14.1	38.0	1.2	0.50	1.8	2.1
Pb	2.6	0.70	1.6	0.70	1.0	4.8	11.3	0.10	0.10	0.90	4.9
Fe	4480	560	1320	360	<LOD	1600	<LOD	6500	<LOD	<LOD	1540
Sr	186	43.5	29.1	29.9	21.1	1400	80.4	53.2	144	26.5	304
Ba	13.9	<LOD	21.1	<LOD	2.6	20.0	3.2	1110	<LOD	<LOD	7.4
Na	138	<LOD	<LOD	<LOD	<LOD	<LOD	390	500	<LOD	<LOD	570
Al	6060	109	375	98.0	167	1800	3900	1050	99.0	245	2740
Si	9500	<LOD	<LOD	<LOD	<LOD	5300	3800	5600	<LOD	<LOD	<LOD
P	<LOD	<LOD	<LOD	<LOD	<LOD	<LOD	<LOD	<LOD	<LOD	1110	<LOD
Cu	18.1	13.9	22.8	27.0	60.0	24.0	77.0	<LOD	<LOD	23.1	31.0
Rb	16.7	<LOD	<LOD	<LOD	<LOD	28.0	<LOD	6.7	<LOD	<LOD	<LOD
Bi	<LOD	<LOD	<LOD	<LOD	<LOD	<LOD	<LOD	<LOD	<LOD	<LOD	<LOD

12	13	14	15	16	17	18	19	20	21	22	23	24	25	26	27	28	*AVG*	*MIN*	*MAX*	AVG LOD
656	248	501	651	451	222	507	3910	2055	361	178	108	433	590	360	1195	1003	*480*	*38.0*	*3910*	0.08
29.2	362	79.0	89.2	66.3	14.0	4.9	296	221	0.70	4.6	17.0	8.0	11.6	2020	440	353	*94.0*	*0.70*	*2020*	0.004
69.5	763	140	159	155	21.9	11.8	592	401	3.2	26.5	20.6	30.4	30.4	2710	670	710	*182*	*3.0*	*2710*	0.03
7.6	88.3	11.5	16.2	10.3	3.3	2.2	70.6	48.2	0.30	5.3	5.0	4.1	3.6	216	66.0	65.0	*19.4*	*0.30*	*216*	0.02
35.9	317	45.6	55.3	53.0	11.6	8.7	274	185	0.50	41.9	25.9	18.8	17.9	600	184	208	*72.5*	*0.50*	*600*	0.13
7.8	52.1	7.2	9.0	1.3	0.50	2.2	61.8	39.4	1.4	11.8	7.8	0.40	1.6	61.0	23.2	25.0	*13.2*	*0.20*	*61.8*	0.25
6.7	10.9	4.0	5.7	1.0	0.60	0.80	45.1	21.1	<LOD	3.0	1.5	2.2	1.2	8.9	9.2	4.9	*4.3*	*<LOD*	*45.1*	0.09
25.5	26.7	16.9	17.7	9.6	3.0	2.8	114	49.6	0.60	11.5	5.4	5.1	0.30	29.0	14.6	21.0	*12.5*	*0.30*	*114*	0.55
7.1	3.9	2.3	2.6	1.0	<LOD	0.80	26.2	12.9	<LOD	1.7	1.6	<LOD	0.80	4.4	1.8	2.3	*3.4*	*<LOD*	*26.2*	0.02
44.6	20.1	29.5	28.7	12.3	4.6	9.1	272	121	3.2	11.9	7.5	9.7	9.6	13.0	25.3	19.9	*17.8*	*1.4*	*272*	0.11
11.8	4.4	7.7	8.2	3.6	1.8	2.7	77.8	30.1	1.2	1.8	0.30	2.4	3.0	4.0	8.8	10.3	*5.1*	*0.30*	*77.8*	<LOD
34.7	12.4	22.7	30.3	15.5	6.8	15.2	271	95.8	3.3	4.8	0.40	7.7	13.5	7.0	41.0	33.4	*16.6*	*0.40*	*271*	0.21
4.3	1.3	4.6	4.7	2.6	1.0	3.0	39.4	15.4	1.1	0.30	<LOD	0.80	1.7	1.7	6.2	6.7	*3.3*	*<LOD*	*39.4*	0.02
29.1	8.1	22.1	25.8	17.8	8.3	22.8	299	112	5.2	1.7	0.90	6.3	14.1	12.2	37.2	41.9	*17.7*	*0.10*	*299*	0.16
6.0	1.7	3.0	3.8	3.7	1.5	5.8	39.3	12.6	0.40	<LOD	<LOD	0.60	1.6	1.4	7.6	5.5	*3.4*	*<LOD*	*39.3*	0.01
320	1672	396	456	353	78.9	92.8	2478	1365	21.1	127	93.9	96.5	111	5689	1535	1507	*523*	*17.3*	*5689*	<LOD
0.50	5.9	<LOD	<LOD	<LOD	0.20	0.40	1.7	87.0	0.40	0.80	1.8	<LOD	<LOD	<LOD	0.50	0.60	*2.7*	*<LOD*	*87.0*	0.03
4.0	163	0.90	1.9	151	1.7	73.0	1.6	6.8	98.0	2.6	6.5	0.90	1.5	1.1	9.7	23.5	*13.1*	*0.50*	*163*	0.04
5.1	56.2	0.40	0.30	33.9	0.60	15.2	0.50	10.3	27.6	0.50	2.6	0.50	0.50	0.10	3.3	9.3	*4.4*	*0.10*	*56.2*	<LOD
1980	1320	<LOD	460	3990	<LOD	980	660	630	630	610	1550	250	<LOD	<LOD	1940	810	*1286*	*<LOD*	*6500*	241
264	1590	156	263	88.7	31.7	46.5	469	523	83.0	138	112	61.3	70.5	173	179	248	*157*	*21.1*	*1590*	0.23
2.8	38.2	<LOD	5.5	<LOD	<LOD	113	3.0	8.7	7.7	2.1	10.2	<LOD	<LOD	<LOD	16.1	13.0	*17.9*	*<LOD*	*1110*	0.20
380	<LOD	<LOD	600	<LOD	<LOD	<LOD	<LOD	640	<LOD	<LOD	<LOD	<LOD	<LOD	<LOD	<LOD	<LOD	*460*	*<LOD*	*640*	230
288	6880	673	1038	<LOD	147	240	1200	1730	395	2410	3410	74.0	600	26.0	4420	370	*1196*	*26.0*	*6880*	18.6
<LOD	<LOD	<LOD	<LOD	<LOD	<LOD	<LOD	<LOD	6400	<LOD	<LOD	<LOD	<LOD	<LOD	<LOD	<LOD	<LOD	*6120*	*<LOD*	*9500*	4714
<LOD	3880	<LOD	<LOD	<LOD	<LOD	<LOD	<LOD	<LOD	<LOD	<LOD	<LOD	<LOD	<LOD	<LOD	<LOD	<LOD	*2495*	*<LOD*	*3880*	607
47.0	22.7	26.0	<LOD	17.0	50.0	88.0	23.0	598	89.0	40.0	55.0	<LOD	<LOD	17.0	71.0	<LOD	*40.2*	*<LOD*	*598*	15.0
<LOD	4.9	<LOD	<LOD	<LOD	<LOD	<LOD	<LOD	6.4	<LOD	7.7	13.7	<LOD	<LOD	<LOD	10.5	<LOD	*11.8*	*<LOD*	*28.0*	3.60
<LOD	<LOD	<LOD	<LOD	<LOD	<LOD	0.60	<LOD	<LOD	<LOD	<LOD	<LOD	<LOD	<LOD	<LOD	0.50	3.2	*1.4*	*<LOD*	*3.2*	0.33

Appendix C: EPMA methodology and set-up details (Tables C1 & C2).

Operating conditions and Processing

Combined operating conditions were utilized in which for each individual spot, major and mobile elements were analyzed first at 17 kV/20 nA, then the beam subsequently changed to 17 kV/100 nA for the remaining analysis of low-level elements. All analyses were done with a 5 μm-diameter defocused beam.

The full list of elements analyzed along with primary and interference standards are presented in Tables C1 & C2. Matrix corrections of Armstrong-Love/Scott φ(ρz) (Armstrong 1988) and Henke MACs were used for data reduction.

All elements were acquired using a traditional 2-point linear, excluding F Ka which was acquired using a multi-point fit. Following traditional 2-point background analysis, the "shared" background fit option in Probe for EPMA was used across the list of elements. In simple background regions, a traditional 2-point linear fit was still used. For more complex regions of the spectrum such as in the case some of the REE, multipoint or "shared" fits were used to accurately model the background continuum and/or avoid off peak interferences (Goemann et al. 2016, Geomann et al. 2017, Geoeman and Donovan 2017).

Due to beam damage and alkali element migration (e.g. F, Na) in fluorite, analyses were monitored and minimized via analysis of these elements first on the detector, plus application of the Time Dependent Intensity (TDI) correction feature of Probe for EPMA (e.g. Donovan and Rowe (2005)). Using this method, the decay of x-ray counts over time is measured and modelled to return a t=0 intercept, and from this a concentration is calculated.

References

Armstrong, J.T. Quantitative analysis of silicate and oxide minerals: Comparison of Monte Carlo, ZAF, and φ(ρz) procedures. Microbeam Analysis, D.E. Newbury, ed., San Francisco Press. **1988**, 239-246.

Donovan, J.J.; Tingle, T.N. An Improved Mean Atomic Number Background Correction for Quantitative Microanalysis. Microscopy and Microanalysis **1996,** 1, 1-7.

Goemann, K.; Donovan, J.J. Electron probe microanalysis of complex natural sulphides using shared background measurements. In: AMAS 2017, 14th Biennial Australian Microbeam Analysis Symposium, 6-10 February 2017,

Brisbane, Australia. *The Australian Microscopy & Microanalysis Society* **2017,** 61-62, ISBN 978-0-9580408-6-0.

Goemann, K.; Donovan, J.J.; Feig, S.T.; Thompson, J. "Sharing" Background Measurements in Wavelength Dispersive Electron Probe Microanalysis. In: Microanalysis Society - Topical Conference on Electron-Probe Microanalysis, Program Guide with Abstracts, 16-19 May 2016, Madison, WI, USA. *The Microanalysis Society* **2016**, 28-29. ISBN 978-1-5323-0217-6.

Goemann, K.; Donovan, J.J.; Feig, S.T.; Thompson, J. Shared backgrounds in wavelength-dispersive electron probe microanalysis. In: Book of Tutorials and Abstracts, 15th European Workshop on Modern Developments and Applications in Microbeam Analysis, 7th Meeting of the International Union of Microbeam Analysis Societies, 7-11 May 2017, Konstanz, Germany. *European Microbeam Analysis Society eV* **2017,** 378-379. ISBN 978-90-8827-693-0.

Table C1. EPMA setup for spot analysis of fluorite

Element and Line	Diffracting Crystal (Sp#)	Background type/fit	kV/nA	Peak Count Time	Bkgd Count Times		# bkgd points acquired (Lo/Hi)	Standards*		Overlapping element and order/interference correction standard			
					Lo	Hi		Primary Standard	Interference Standards	Interfering line	Int. std	Interfering line	Int. std
Zr La	LPET (1)	2-pt	17/20	15	10	10	1/1	723					
Ca Ka	LPET (1)	2-pt	17/20	20	20	20	1/1	523					
K Ka	LPET (1)	2-pt	17/100	40	20	20	1/1	541					
P Ka	LPET (1)	2-pt	17/100	40	20	20	1/1	504					
Y La	LPET (1)	2-pt	17/100	120	60	60	1/1	1214					
U Mb	LPET (1)	2-pt	17/100	200	100	100	1/1	631					
Ce La	LPET (1)	2-pt	17/100	100	50	50	1/1	1201					
Ti Ka	LPET (1)	2-pt	17/100	100	50	50	1/1	540					
F Ka	PC0 (2)	Multipoint	17/20	20	10	10	2/2	523	502,723	Fe La (I)	502	Zr La1 (III)	723
Fe Ka	LLIF (3)	2-pt	17/20	40	20	20	1/1	502					
Hf La	LLIF (3)	2-pt	17/20	20	10	10	1/1	723					
Sc Ka	LLIF (3)	2-pt	17/100	40	20	20	1/1	619					
Mn Ka	LLIF (3)	2-pt	15/20	40	20	20	1/1	539					
Lu La	LLIF (3)	2-pt	17/100	40	20	20	1/1	1213					
Yb La	LLIF (3)	2-pt	17/100	40	20	20	1/1	1212					
Er La	LLIF (3)	Shared	17/100	40	20	20	3/2	1210					
Gd Lb	LLIF (3)	2-pt	17/100	40	20	20	1/1	1206					
Dy La	LLIF (3)	Shared	17/100	40	20	20	1/2	1208					
Tb La	LLIF (3)	2-pt	17/100	40	20	20	1/1	1207					
Sm Lb	LLIF (3)	2-pt	17/100	40	20	20	1/1	1204					
Eu La	LLIF (3)	2-pt	17/100	40	20	20	1/1	1205					
Nd Lb	LLIF (3)	2-pt	17/100	40	20	20	1/1	1203					
Pr Lb	LLIF (3)	2-pt	17/100	40	20	20	1/1	1202					
Tm La	LLIF (3)	Shared	17/100	40	20	20	1/2	1211					
Ho Lb	LLIF (3)	2-pt	17/100	40	20	20	1/1	1209					
Na Ka	TAP (4)	Shared	17/20	20	20	20	7/5	501					
Si Ka	TAP (4)	2-pt	17/20	15	10	10	1/1	723					
Al Ka	TAP (4)	2-pt	15/20	20	20	20	1/1	501					
Mg Ka	TAP (4)	2-pt	15/20	30	20	20	1/1	502					
Cl Ka	LPET (5)	2-pt	17/20	60	30	30	1/1	545					
La La	LPET (5)	2-pt	17/100	100	50	50	1/1	1200					
Th Ma	LPET (5)	2-pt	17/100	150	75	75	1/1	629					
Pb Mb	LPET (5)	Shared	17/100	200	100	100	3/1	627					
Nb La	LPET (5)	2-pt	17/100	100	50	50	1/1	616	723	Zr Lb4 (I)	723		

* Standard # refers to internal database. Full list of standards in Table C2

Table C2. Standard information

Reference #	Mineral composition	Natural/Synthetic	Manufacturer
501	Albite	Natural	Astimex
502	Almandine garnet	Natural	Astimex
504	Apatite	Natural	Astimex
523	Fluorite	Natural	Astimex
535	Plagioclase	Natural	Astimex
539	Rhodonite	Natural	Astimex
540	Rutile	Natural	Astimex
541	Sanidine	Natural	Astimex
545	Tugtupite	Natural	Astimex
616	Niobium	Synthetic	Astimex
619	Scandium	Natural	P&H and Associates
627	K227 (Pb silicate)	Synthetic	NIST
629	Huttonite	Natural	DAS
631	UO2	Synthetic	DAS
723	Zircon	Synthetic	GJ Zircon standard
1200	LaPO4	Synthetic	Cherniak phosphate
1201	CePO4	Synthetic	Cherniak phosphate
1202	PrPO4	Synthetic	Cherniak phosphate
1203	NdPO4	Synthetic	Cherniak phosphate
1204	SmPO4	Synthetic	Cherniak phosphate
1205	EuPO4	Synthetic	Cherniak phosphate
1206	GdPO4	Synthetic	Cherniak phosphate
1207	TbPO4	Synthetic	Cherniak phosphate
1208	DyPO4	Synthetic	Cherniak phosphate
1209	HoPO4	Synthetic	Cherniak phosphate
1210	ErPO4	Synthetic	Cherniak phosphate
1211	TmPO4	Synthetic	Cherniak phosphate
1212	YbPO4	Synthetic	Cherniak phosphate
1213	LuPO4	Synthetic	Cherniak phosphate
1214	YPO4	Synthetic	Cherniak phosphate

Appendix D: Complete dataset for EPMA analysis of RX11077 and RX11078 with measured wt. %, calculated apfu, and average dection limit.

Sample	wt. %	Ca	F	Ce	Y	Sr	Si	P	Sc	U	Pb	Gd	Nd	Na	Mg	Tb	Sm	Ho	Tm	Er	Dy	Yb	Eu	Pr	Al	Fe
	1	55.7	46.0	0.01	0.09	0.03	0.00	0.02	0.02	<LOD	-	-	<LOD	-	<LOD	-	-	-	-	-	-	<LOD	<LOD	-	<LOD	-
	2	51.1	48.6	0.01	0.10	0.03	0.00	0.02	0.03	<LOD	-	0.04	0.03	0.03	0.01	-	<LOD	-	-	<LOD	<LOD	-	<LOD	-	<LOD	<LOD
	3	51.5	48.1	0.01	0.08	0.03	0.01	0.02	0.01	<LOD	0.01	-	-	0.02	-	<LOD	-	-	-	<LOD	<LOD	<LOD	-	<LOD	<LOD	-
	4	51.9	47.1	0.01	0.06	0.03	0.01	0.02	0.01	<LOD	-	<LOD	-	<LOD	<LOD	-	-	-	-	-	-	-	<LOD	<LOD	<LOD	-
	5	51.6	47.3	0.02	0.09	0.03	0.01	0.03	0.01	0.01	<LOD	-	0.04	-	0.01	-	-	-	-	-	-	<LOD	<LOD	<LOD	<LOD	<LOD
	6	51.4	47.6	0.01	0.10	0.03	0.01	0.02	0.01	0.01	0.02	<LOD	<LOD	-	0.00	-	-	<LOD	<LOD	-	<LOD	<LOD	-	<LOD	<LOD	<LOD
	7	52.0	47.6	0.01	0.08	0.03	0.01	0.02	0.02	0.01	0.01	-	-	<LOD	<LOD	<LOD	-	-	<LOD	-	<LOD	-	-	<LOD	<LOD	<LOD
	8	51.9	47.7	0.02	0.09	0.03	0.01	0.02	0.02	0.01	<LOD	-	<LOD	<LOD	-	-	<LOD	-	-	-	-	<LOD	-	<LOD	<LOD	-
	9	51.4	48.1	0.01	0.10	0.03	0.01	0.02	0.01	-	<LOD	<LOD	<LOD	-	<LOD	0.020	-	-	-	-	-	-	-	<LOD	<LOD	-
	10	51.7	48.0	0.01	0.11	0.03	0.01	0.02	0.02	<LOD	-	0.06	<LOD	<LOD	0.00	-	-	0.054	<LOD	-	-	-	-	<LOD	<LOD	<LOD

RX11077	*apfu*	Ca	F	Ce	Y	Sr	Si	P	Sc	U	Pb	Gd	Nd	Na	Mg	Tb	Sm	Ho	Tm	Er	Dy	Yb	Eu	Pr	Al	Fe
	1	0.998	1.89	0.000	0.001	0.000	0.000	0.000	0.000																	
	2	0.996	2.00	0.000	0.001	0.000	0.000	0.000	0.001			0.000	0.000	0.001	0.000											
	3	0.997	1.98	0.000	0.001	0.000	0.000	0.001	0.000		0.000			0.001												
	4	0.998	1.94	0.000	0.001	0.000	0.000	0.000	0.000																	
	5	0.997	1.95	0.000	0.001	0.000	0.000	0.001	0.000	0.000			0.000		0.000											
	6	0.997	1.96	0.000	0.001	0.000	0.000	0.001	0.000	0.000	0.000				0.000											
	7	0.998	1.96	0.000	0.001	0.000	0.000	0.001	0.000	0.000	0.000															
	8	0.998	1.96	0.000	0.001	0.000	0.000	0.000	0.000	0.000																
	9	0.998	1.98	0.000	0.001	0.000	0.000	0.001	0.000							0.000										
	10	0.997	1.97	0.000	0.001	0.000	0.000	0.001	0.000			0.000			0.000			0.000								

Sample	wt. %	Ca	F	Ce	Y	Sr	Si	P	Sc	U	Pb	Gd	Nd	Na	Mg	Tb	Sm	Ho	Tm	Er	Dy	Yb	Eu	Pr	Al	Fe
	1	52.3	48.1	0.01	0.14	0.03	<LOD	0.02	<LOD	<LOD	<LOD	-	<LOD	-	<LOD	-	-	<LOD	-	<LOD	-	<LOD	-	<LOD	<LOD	-
	2	51.5	49.2	0.01	0.17	0.03	0.01	0.02	0.02	-	0.02	0.04	-	-	<LOD	-	<LOD	-	<LOD	<LOD	<LOD	<LOD	<LOD	-	<LOD	-
	3	52.7	47.0	0.01	0.13	0.03	0.01	0.02	0.01	-	-	-	<LOD	-	-	-	-	<LOD	<LOD	0.021	-	<LOD	<LOD	-	<LOD	-
	4	52.5	46.8	0.01	<LOD	0.03	-	0.02	0.02	0.01	<LOD	<LOD	<LOD	<LOD	<LOD	-	<LOD	-	-	<LOD	-	<LOD	-	-	<LOD	<LOD
	5	52.6	47.2	<LOD	0.03	0.03	0.01	0.02	0.02	-	<LOD	-	<LOD	<LOD	<LOD	<LOD	-	-	-	<LOD	-	<LOD	-	-	<LOD	<LOD
	6	51.5	48.2	0.01	0.13	0.03	0.00	0.02	0.02	-	0.01	-	0.04	<LOD	<LOD	-	-	-	-	-	<LOD	-	<LOD	<LOD	<LOD	-
	7	51.3	48.0	0.01	0.13	0.03	<LOD	0.02	0.02	0.01	<LOD	-	-	-	-	-	0.035	<LOD	-	-	<LOD	<LOD	<LOD	-	<LOD	<LOD
	8	51.6	48.3	0.01	0.14	0.03	0.00	0.02	0.01	-	<LOD	<LOD	<LOD	<LOD	-	<LOD	-	-	-	<LOD	<LOD	-	<LOD	<LOD	<LOD	-
	9	51.2	47.7	0.01	0.15	0.03	0.00	0.02	0.01	-	-	<LOD	-	<LOD	<LOD	-	-	-	-	-	-	<LOD	<LOD	-	<LOD	<LOD
	10	51.6	47.8	0.01	0.14	0.03	0.00	0.02	0.02	-	<LOD	<LOD	-	-	-	<LOD	-	-	0.02	<LOD	-	-	-	<LOD	<LOD	<LOD

RX11078	*apfu*	Ca	F	Ce	Y	Sr	Si	P	Sc	U	Pb	Gd	Nd	Na	Mg	Tb	Sm	Ho	Tm	Er	Dy	Yb	Eu	Pr	Al	Fe
	1	0.998	1.98	0.000	0.001	0.000		0.000																		
	2	0.997	2.02	0.000	0.001	0.000	0.000	0.001	0.000		0.000	0.000														
	3	0.998	1.93	0.000	0.001	0.000	0.000	0.001	0.000											0.000						
	4	0.999	1.92	0.000		0.000		0.000	0.000	0.000																
	5	0.999	1.94		0.000	0.000	0.000	0.001	0.000																	
	6	0.997	1.98	0.000	0.001	0.000	0.000	0.001	0.000		0.000		0.000													
	7	0.998	1.97	0.000	0.001	0.000		0.000	0.000	0.000							0.000									
	8	0.998	1.99	0.000	0.001	0.000	0.000	0.001	0.000																	
	9	0.997	1.96	0.000	0.001	0.000	0.000	0.001	0.000																	
	10	0.997	1.97	0.000	0.001	0.000	0.000	0.001	0.000										0.000							

Average Detection Limits	Ca	F	Ce	Y	Sr	Si	P	Sc	U	Pb	Gd	Nd	Na	Mg	Tb	Sm	Ho	Tm	Er	Dy	Yb	Eu	Pr	Al	Fe
	0.006	0.031	0.007	0.007	0.006	0.003	0.003	0.006	0.008	0.010	0.036	0.032	0.017	0.005	0.019	0.034	0.040	0.021	0.021	0.020	0.022	0.018	0.034	0.003	0.015

<LOD = less than limit of detection; - = unreliable value from exaggerated error; apfu = atoms per formula unit

Cl	Th	Nb	Hf	Mn	K	La	Lu	Total
<LOD	<LOD	<LOD	<LOD	<LOD	<LOD	<LOD	<LOD	101.9
<LOD	<LOD	<LOD	<LOD	-	<LOD	<LOD	<LOD	100.0
-	<LOD	<LOD	<LOD	-	<LOD	<LOD	<LOD	99.8
	<LOD	<LOD	<LOD	<LOD	<LOD	<LOD	<LOD	99.1
-	<LOD	<LOD	<LOD	-	<LOD	<LOD	-	99.2
<LOD	<LOD	<LOD	<LOD	<LOD	<LOD	<LOD	<LOD	99.2
<LOD	<LOD	-	-	-	<LOD	<LOD	-	99.8
<LOD	<LOD	<LOD	<LOD	<LOD	<LOD	<LOD	-	99.7
<LOD	<LOD	<LOD	<LOD	-	<LOD	<LOD	<LOD	100.0

Cl	Th	Nb	Hf	Mn	K	La	Lu	Total	cat-ion sum
								2.89	1.00
								3.00	1.00
								2.98	1.00
								2.94	1.00
								2.95	1.00
								2.96	1.00
								2.96	1.00
								2.98	1.00
								2.97	1.00

Cl	Th	Nb	Hf	Mn	K	La	Lu	Total	cat-ion sum
-	<LOD	-	<LOD	<LOD	<LOD	<LOD	-	100.6	1.00
-	<LOD	-	<LOD	<LOD	<LOD	<LOD	<LOD	100.9	1.00
-	<LOD	<LOD	<LOD	-	<LOD	<LOD	-	99.9	1.00
<LOD	<LOD	<LOD	<LOD	-	<LOD	<LOD	<LOD	99.4	1.00
-	<LOD	<LOD	<LOD	-	<LOD	<LOD	<LOD	99.9	1.00
-	<LOD	-	<LOD	<LOD	<LOD	<LOD	<LOD	99.9	1.00
-	<LOD	<LOD	<LOD	<LOD	<LOD	<LOD	-	99.5	1.00
<LOD	<LOD	<LOD	-	<LOD	<LOD	<LOD	<LOD	100.2	1.00
<LOD	<LOD	<LOD	<LOD	<LOD	<LOD	<LOD	<LOD	99.1	1.00
<LOD	<LOD	<LOD	<LOD	<LOD	<LOD	<LOD	-	99.6	1.00

Cl	Th	Nb	Hf	Mn	K	La	Lu
0.005	0.008	0.009	0.059	0.008	0.003	0.007	0.023

SUPPLEMENTARY MATERIAL E

APPENDIX FOR CHAPTER 6

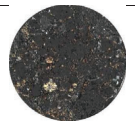
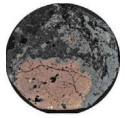
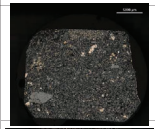
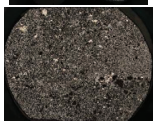
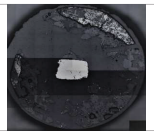
Lead chalcogenides and Pb-isotope signature in ores and concentrates from Olympic Dam deposit, South Australia

INCLUDES:

APPENDIX A: SUMMARY SAMPLE DESCRIPTIONS WITH PB-RATIO SUMMARIES.

APPENDIX B: FULL LA-ICP-MS DATASET OF PB-RATIOS.

Appendix A: Sample descriptions, sample image, and summary (mean, minimum, maximum) of Pb ratios.

Drill hole/ Location	Sample	Pb minerals	Associations	Sample Picture	summary Pb ratios															No. of data points
					$^{208}Pb/^{204}Pb$			$^{207}Pb/^{204}Pb$			$^{206}Pb/^{204}Pb$			$^{208}Pb/^{206}Pb$			$^{207}Pb/^{206}Pb$			
					mean	min	max	mean	min	max	mean	min	max	mean	min	max	mean	min	max	
RD3554; SE edge	RX7316	galena, altaite	Pb minerals mostly hosted in Cu-(Fe)-sulfides: chalcocite, bornite, chalcopyrite (Cu sulfides mostly disseminated and in small aggregates within breccia matrix); gangue of mostly sericite, qtz, and barite; Pb minerals generally <20 µm		35.4	33.2	38.8	16.5	15.3	17.4	44.1	40.4	49.3	0.80	0.74	0.89	0.38	0.35	0.41	37
	RX7319	galena, altaite	Pb mineral mostly hosted completly in the sphalerite, also within qtz and Cu minerals (Cu minerals disseminated or in clumps in breccia; massive bn zone, one Pb mineral within but too small for analysis) Common REE minerals and tourmaline; Pb minerals generally <20 µm		36.3	34.7	37.3	15.5	14.7	16.0	18.7	16.6	42.6	2.03	0.88	2.20	0.87	0.39	0.94	15
RU27-7550; NW arm	7550A	galena	Hematite breccia with copper and base metal sulfides disseminated and as clustered aggregates; galena is intergrown with sulfides in distinct domains with net-like textures, mosly pyrite, and then sphalerite, chalcopyrite, and barite, minor carrollite and cobaltite; main gangue of hematite, sericite, quartz, rimmed by and rimming uraninite; larger massive of galena up to 100 µm but with inclusions and mostly <30 µm		36.4	34.6	38.1	15.7	14.8	16.7	18.6	17.5	20.0	1.99	1.87	2.11	0.85	0.82	0.88	46
	7550B																			
Grab sample; center	1036	galena	~4 mm3 euhedral galena grain exhibiting open space growth; galena also as small (~5 µm-sized) inclusions in carbonate and hematite; carbonates display zonation expressed by varying Ca vs. (Mg+Mn) content and Pb concentrations		62.3	54.3	66.7	20.3	17.3	22.1	77.6	66.8	83.8	0.81	0.78	0.93	0.26	0.24	0.27	36
Flotation concentrate	>53 µm & 26-53 µm size fractions	galena, altaite, clausthalite	All Pb minerals with Cu sulfides due to being in upgraded concentrate, Cu sulfides mostly bornite and chalcocite, gangue mostly sericite or pyrite; also some liberated galena.	NA	50.0	32.6	65.9	42.8	14.0	122	450	21.1	1510	0.28	0.04	1.66	0.15	0.07	0.71	37

Samples are all one inch blocks; Images are reflected light mosaics

Pb-isotope ratios in minerals from LA-ICP-MS analysis; Full Pb-isotope ratio dataset can be found in Appendix A.

Appendix B: Full Pb-isotope ratio dataset for Pb minerals in rock samples and ore concentrate material

RD3554: samples RX7316 and RX7319	Drill Hole	RD3554	RD3554	RD3554	RD3554	RD3554	RD3554	RD3554	RD3554	RD3554	RD3554	RD3554	RD3554	RD3554	RD3554	RD3554	RD3554	RD3554	RD3554	RD3554	RD3554
	Sample	RX7319	RX7319	RX7319	RX7319	RX7319	RX7319	RX7319	RX7319	RX7319	RX7319	RX7319	RX7319	RX7319	RX7319	RX7319	RX7319	RX7319	RX7319	RX7319	RX7319
	Number	1	2	3	4	5	6	7	8	9	10	11	12	13	14	15	16	17	18	19	
	Mineral	galena	galena	galena	galena	galena	galena	galena	galena	galena	galena	galena	galena	galena	galena	galena	galena	galena	galena	galena	galena	
	$^{208}Pb/^{204}Pb$	35.69	35.9	36.7	36.2	36.15	34.7	36.53	36.7	36.19	36.33	35.94	35.78	37.17	36.22	36.3	35.98	36.3	36.85	37.28	
	$^{207}Pb/^{204}Pb$	15.29	15.52	15.58	15.45	15.25	15.18	15.38	15.84	15.2	15.65	15.25	15.41	15.76	15.46	16.04	15.5	15.24	15.5	15.7	
	$^{206}Pb/^{204}Pb$	16.59	16.74	16.77	16.81	16.84	16.87	16.87	16.93	16.94	16.96	16.99	16.99	17	17.04	17.09	17.1	17.15	17.18	17.2	
	$^{208}Pb/^{206}Pb$	2.18	2.14	2.18	2.15	2.13	2.01	2.16	2.19	2.14	2.15	2.12	2.09	2.2	2.14	2.12	2.12	2.07	2.14	2.16	
	$^{207}Pb/^{206}Pb$	0.93	0.93	0.93	0.92	0.91	0.88	0.91	0.94	0.91	0.92	0.91	0.91	0.92	0.91	0.93	0.92	0.89	0.91	0.92	
	$^{204}Pb/^{206}Pb$	0.060	0.060	0.060	0.059	0.059	0.059	0.059	0.059	0.059	0.059	0.059	0.059	0.059	0.059	0.059	0.058	0.058	0.058	0.058	
RD7550: Samples A and B	Drill Hole	RD7550	RD7550	RD7550	RD7550	RD7550	RD7550	RD7550	RD7550	RD7550	RD7550	RD7550	RD7550	RD7550	RD7550	RD7550	RD7550	RD7550	RD7550	RD7550	RD7550
	Sample	A	A	A	A	A	A	A	A	A	A	A	A	A	A	A	A	A	A	A	
	Number	1	2	3	4	5	6	7	8	9	10	11	12	13	14	15	16	17	18	19	
	Mineral	galena	galena	galena	galena	galena	galena	galena	galena	galena	galena	galena	galena	galena	galena	galena	galena	galena	galena	galena	galena	
	$^{208}Pb/^{204}Pb$	36.2	36.25	37.36	37.64	35.19	35.1	37.8	36.28	34.63	36.12	36.36	37.54	36.13	36.4	37.14	36.81	36.25	36.43	36.13	
	$^{207}Pb/^{204}Pb$	16.18	15.86	16.1	16.7	15.02	15.42	15.98	15.53	14.93	15.85	15.92	14.92	15.66	15.53	15.86	16.12	15.85	15.72	15.48	
	$^{206}Pb/^{204}Pb$	19.9	18.88	19.27	19.97	18.1	18.25	19.55	18.88	18.06	18.91	18.79	18.52	17.97	17.93	18.09	19.05	18.93	18.26	17.93	
	$^{208}Pb/^{206}Pb$	1.89	1.94	1.96	1.87	2.03	1.91	1.95	1.95	1.94	1.95	1.97	2.08	2.06	2.07	2.11	1.98	1.94	2.03	2.04	
	$^{207}Pb/^{206}Pb$	0.82	0.84	0.85	0.82	0.84	0.83	0.83	0.83	0.84	0.84	0.86	0.83	0.88	0.87	0.87	0.86	0.85	0.87	0.87	
	$^{204}Pb/^{206}Pb$	0.050	0.053	0.052	0.050	0.055	0.055	0.051	0.053	0.055	0.053	0.053	0.054	0.056	0.056	0.055	0.052	0.053	0.055	0.056	
Sample 1036	Sample	1036	1036	1036	1036	1036	1036	1036	1036	1036	1036	1036	1036	1036	1036	1036	1036	1036	1036	1036	
	Type	cube	cube	cube	cube	cube	cube	cube	cube	cube	cube	cube	cube	cube	cube	cube	cube	cube	cube	cube	
	Number	1	2	3	4	5	6	7	8	9	10	11	12	13	14	15	16	17	18	19	
	Mineral	galena	galena	galena	galena	galena	galena	galena	galena	galena	galena	galena	galena	galena	galena	galena	galena	galena	galena	galena	galena	
	$^{208}Pb/^{204}Pb$	59.8	59.2	59.8	60.4	60	59.8	60.8	61.4	59.5	59.7	63.1	62	61.2	62.4	63.2	61.9	61.1	63.8	63.7	
	$^{207}Pb/^{204}Pb$	19.35	19.4	19.69	19.48	19.42	19.73	19.98	19.44	19.5	19.73	20.25	20.16	20.04	20.3	20.2	20.52	20.3	21.11	20.8	
	$^{206}Pb/^{204}Pb$	73.6	73.7	74.2	74.4	74.8	75	75.1	75.1	75.4	76	76.5	76.7	76.9	77.2	77.2	77.4	77.7	78.8	79.3	
	$^{208}Pb/^{206}Pb$	0.82	0.81	0.82	0.81	0.82	0.81	0.81	0.82	0.8	0.79	0.83	0.81	0.81	0.82	0.84	0.81	0.8	0.82	0.81	
	$^{207}Pb/^{206}Pb$	0.27	0.26	0.27	0.26	0.26	0.26	0.26	0.26	0.26	0.26	0.27	0.26	0.27	0.26	0.26	0.27	0.26	0.27	0.26	
	$^{204}Pb/^{206}Pb$	0.014	0.014	0.013	0.013	0.013	0.013	0.013	0.013	0.013	0.013	0.013	0.013	0.013	0.013	0.013	0.013	0.013	0.013	0.013	
Ore Concentrate: size fractions >53um and 26-53 um	Sample	OreCon	OreCon	OreCon	OreCon	OreCon	OreCon	OreCon	OreCon	OreCon	OreCon	OreCon	OreCon	OreCon	OreCon	OreCon	OreCon	OreCon	OreCon	OreCon	OreCon
	Size fraction	>53 um	>53 um	>53 um	>53 um	>53 um	>53 um	>53 um	>53 um	>53 um	>53 um	>53 um	>53 um	>53 um	26-53 um	26-53 um	26-53 um	26-53 um	26-53 um	26-53 um	
	Number	1	2	3	4	5	6	7	8	9	10	11	12	13	1	2	3	4	5	6	
	Mineral	galena	galena	galena	galena	galena	galena	galena	galena	galena	galena	galena	galena	galena	galena	galena	galena	galena	galena	galena	galena	
	$^{208}Pb/^{204}Pb$	34.1	57.5	52.1	58.6	58.9	58.8	52.4	62.4	65.9	61.8	55.2	55.8	53.5	32.6	47.7	47.4	49.2	44	49.1	
	$^{207}Pb/^{204}Pb$	15.7	88.4	31.8	121.8	54.7	52.2	35.3	95.7	37.4	39.5	57.3	55.7	55.4	13.97	37.9	102	18.4	34.1	43.9	
	$^{206}Pb/^{204}Pb$	22.1	1079	332	1510	589	601	324	1109	351	350	587	582	571	21.1	385	1420	117.5	418	543	
	$^{208}Pb/^{206}Pb$	1.66	0.053	0.156	0.04	0.102	0.099	0.16	0.056	0.187	0.18	0.094	0.096	0.093	1.535	0.124	0.035	0.42	0.105	0.093	
	$^{207}Pb/^{206}Pb$	0.705	0.083	0.094	0.08	0.091	0.087	0.107	0.085	0.105	0.112	0.095	0.094	0.094	0.669	0.097	0.074	0.153	0.084	0.08	
	$^{204}Pb/^{206}Pb$	0.045	0.001	0.003	0.001	0.002	0.002	0.003	0.001	0.003	0.003	0.002	0.002	0.002	0.047	0.003	0.001	0.009	0.002	0.002	

RD3554	RD3554	RD3554	RD3554	RD3554	RD3554	RD3554	RD3554	RD3554	RD3554	RD3554	RD3554		RD3554		RD3554	RD3554	RD3554	RD3554	RD3554
RX7319	RX7319	RX7319	RX7319	RX7319	RX7319	RX7319	RX7319	RX7319	RX7319	RX7319	RX7319		RX7319		RX7316	RX7316	RX7316	RX7316	RX7316
20	21	22	23	24	25	26	27	28	29	30	37		37		1	2	3	4	5
galena	galena	galena	galena	galena	galena	galena	galena	altaite	altaite	galena	galena	Mean	Min	Max	galena	galena	altaite	altaite	galena
35.43	35.78	37.33	35.89	37	36.32	36.98	35.91	35.57	35.7	37.23	36.92	36.29	34.70	37.33	35.57	35.9	33.88	34.2	37.3
15.15	15.45	15.84	15.5	15.52	15.4	15.49	15.69	15.14	14.67	15.65	16.01	15.47	14.67	16.04	16.8	16.12	15.31	16.06	17.08
17.23	17.23	17.24	17.27	17.31	17.39	17.49	17.52	18.26	19.2	38.6	42.6	18.69	16.59	42.60	40.36	40.9	41.26	41.27	41.8
2.07	2.07	2.16	2.07	2.15	2.07	2.1	2.06	1.95	1.83	0.96	0.88	2.03	0.88	2.20	0.87	0.89	0.8	0.82	0.89
0.89	0.9	0.92	0.9	0.9	0.89	0.88	0.9	0.83	0.76	0.4	0.39	0.87	0.39	0.94	0.41	0.4	0.37	0.38	0.41
0.058	0.058	0.058	0.058	0.058	0.058	0.057	0.057	0.055	0.052	0.026	0.023	0.06	0.02	0.06	0.025	0.024	0.024	0.024	0.024

RD7550	RD7550	RD7550	RD7550	RD7550	RD7550	RD7550	RD7550	RD7550	RD7550	RD7550	RD7550	RD7550	RD7550	RD7550	RD7550	RD7550	RD7550	RD7550	RD7550	RD7550
A	A	A	A	A	A	A	A	A	A	B	B	B	B	B	B	B	B	B	B	B
20	21	22	23	24	25	26	27	28	29	1	2	3	4	5	6	7	8	9	10	11
galena	galena	galena	galena	galena	galena	galena	galena	galena	galena	galena	galena	galena	galena	galena	galena	galena	galena	galena	galena	galena
35.98	36.08	36.48	35.96	36.1	35.02	36.28	35.99	34.69	35.56	36.51	35.92	36.3	35.99	37.06	36.5	35.95	37	36.96	35.9	37.6
15.41	15.4	15.37	15.36	15.59	14.85	15.62	15.58	14.75	15.06	15.38	15.07	15.6	15.55	16	15.6	15.48	15.26	16.08	15.95	16.28
18.23	17.79	17.68	17.63	18.2	17.9	18.28	18.22	17.54	17.96	17.74	18.02	18.11	18.2	18.4	18.6	18.61	18.7	18.98	19.04	19.14
2.02	2.01	2.07	2.02	2.02	1.98	2.04	1.99	2	1.99	2.07	1.99	2.02	1.96	2.01	1.95	1.93	1.96	1.97	1.93	1.97
0.86	0.86	0.87	0.86	0.86	0.83	0.87	0.86	0.85	0.84	0.87	0.84	0.87	0.86	0.87	0.84	0.83	0.83	0.86	0.86	0.84
0.055	0.056	0.057	0.057	0.055	0.056	0.055	0.055	0.057	0.056	0.056	0.055	0.055	0.055	0.054	0.054	0.054	0.053	0.053	0.053	0.052

1036	1036	1036	1036	1036	1036	1036	1036	1036	1036	1036	1036	1036	1036	1036	1036	1036		1036		
cube	cube	cube	cube	cube	cube	cube	cube	cube	cube	cube	cube	cube	cube	in carbonate	in carbonate	in carbonate		cube and in carbonate		
20	21	22	23	24	25	26	27	28	29	30	31	32	33	1	2	3		36		
galena	galena	galena	galena	galena	galena	galena	galena	galena	galena	galena	galena	galena	galena	galena	galena	galena	Mean	Min	Max	
64.5	64.67	62.3	64.3	64	64.1	65.2	63.6	64.8	64.2	65.3	65.6	66.3	66.7	61.2	58	54.3	62.27	54.30	66.70	
20.9	20.6	20.6	21.2	21	20.98	21.47	21.35	21.3	21.3	21.3	21.8	21.9	22.06	17.26	18.1	17.26	20.27	17.26	22.06	
79.3	79.4	79.5	80.4	80.9	81.1	81.4	81.9	81.9	82	82.1	82.6	83.3	83.8	66.8	74.8	67.5	77.60	66.80	83.80	
0.81	0.82	0.8	0.79	0.81	0.8	0.81	0.79	0.79	0.81	0.81	0.81	0.81	0.8	0.925	0.781	0.797	0.81	0.78	0.93	
0.26	0.26	0.26	0.26	0.26	0.26	0.27	0.26	0.26	0.26	0.26	0.27	0.27	0.27	0.264	0.2435	0.2577	0.26	0.24	0.27	
0.013	0.013	0.013	0.012	0.012	0.012	0.012	0.012	0.012	0.012	0.012	0.012	0.012	0.012	0.015	0.013	0.015	0.013	0.012	0.015	

OreCon	OreCon	OreCon	OreCon	OreCon	OreCon	OreCon	OreCon	OreCon	OreCon	OreCon	OreCon	OreCon	OreCon	OreCon	OreCon	OreCon	OreCon	Ore Concentrate		
26-53 um	26-53 um	26-53 um	26-53 um	26-53 um	26-53 um	26-53 um	26-53 um	26-53 um	26-53 um	>53 um	>53 um	>53 um	>53 um	26-53 um	26-53 um	26-53 um	26-53 um	>53 um and 26-53 um		
7	8	9	10	11	12	13	14	15	16	1	2	3	4	1	2	3	1	37		
galena	galena	galena	galena	galena	galena	galena	galena	galena	galena	clausthalite	clausthalite	clausthalite	clausthalite	clausthalite	clausthalite	clausthalite	altaite	Mean	Min	Max
39.7	42.3	47.2	53.3	44.6	53.3	49.1	46.5	45.7	48.3	53.3	52.2	50.2	47	45.9	45.7	45.1	43.7	50.0	32.6	65.9
28.9	28.5	41.8	47.2	19.5	42.2	22.8	57.1	55.6	66.7	35.3	27.1	19.4	19.1	20.1	16.5	18	26.8	42.8	14.0	122
266	279	544	665	109	542	153.3	677	671	697	298	209	78.3	73.8	85.7	69	77	229	450	21.10	1510
0.151	0.156	0.09	0.083	0.419	0.104	0.33	0.07	0.07	0.072	0.172	0.25	0.632	0.623	0.53	0.682	0.578	0.192	0.28	0.04	1.66
0.112	0.104	0.077	0.072	0.184	0.078	0.148	0.084	0.084	0.093	0.111	0.128	0.238	0.251	0.239	0.255	0.224	0.119	0.15	0.07	0.71
0.004	0.004	0.002	0.002	0.009	0.002	0.007	0.001	0.001	0.001	0.003	0.005	0.013	0.014	0.012	0.014	0.013	0.004	0.007	0.001	0.05

RD3554 RX7316	RD3554 RX7316	RD3554 RX7316	RD3554 RX7316	RD3554 RX7316	RD3554 RX7316	RD3554 RX7316	RD3554 RX7316	RD3554 RX7316	RD3554 RX7316			
6	7	8	9	10	11	12	13	14	15	Mean	Min	Max
altaite	altaite	altaite	galena	galena	altaite	altaite	galena	galena	galena			
34.72	34.3	33.23	34.5	38.8	34.46	35.5	35	35.3	38.8	35.43	33.23	38.80
15.76	16.65	15.66	16.28	17.43	16.72	16.95	16.54	16.6	17.42	16.49	15.31	17.43
41.8	44.4	44.7	45.11	45.5	45.6	46.1	46.2	46.8	49.29	44.07	40.36	49.29
0.83	0.77	0.74	0.76	0.86	0.76	0.76	0.76	0.75	0.77	0.80	0.74	0.89
0.38	0.38	0.36	0.36	0.4	0.36	0.36	0.36	0.36	0.35	0.38	0.35	0.41
0.024	0.023	0.022	0.022	0.022	0.022	0.022	0.022	0.021	0.020	0.023	0.020	0.025

RD7550 B	RD7550 B	RD7550 B	RD7550 B	RD7550 B	RD7550		RD7550 A & B				
12	13	14	15	16	17	Mean	46	Min	Max		
galena	galena	galena	galena	galena	galena						
36.71	36.57	36.9	37.02	38.1	37.16	36.39	34.63	38.10			
15.69	15.97	16.3	16.12	16.55	16.21	15.67	14.75	16.70			
19.24	19.3	19.4	19.4	19.4	19.6	18.58	17.54	19.97			
1.97	1.95	1.95	1.97	2	1.9	1.99	1.87	2.11			
0.85	0.84	0.85	0.85	0.86	0.82	0.85	0.82	0.88			
0.052	0.052	0.052	0.052	0.052	0.051	0.054	0.050	0.057			

ADDITIONAL MATERIAL F

^{210}Pb and ^{210}Po in geological and related anthropogenic materials: implications for their mineralogical distribution in base metal ores

Nigel J. Cook[1], Kathy J. Ehrig[2], Mark Rollog[1], Cristiana L. Ciobanu[1], Daniel J. Lane[1], **Danielle S. Schmandt** [1], Nicholas D. Owen[1], Toby Hamilton[3] and Stephen R. Grano[4]

[1] School of Chemical Engineering, The University of Adelaide, Adelaide, SA 5005, Australia;

[2] BHP Olympic Dam, Adelaide, SA 5000, Australia;

[3] School of Chemical Engineering, The University of Queensland, Brisbane, QLD 4072, Australia;

[4] Institute for Mineral and Energy Resources, The University of Adelaide, Adelaide, SA 5005, Australia;

Article published in 2018, Minerals, 8, 211

doi. 10.3390/min8050211

minerals

MDPI

Review

^{210}Pb and ^{210}Po in Geological and Related Anthropogenic Materials: Implications for Their Mineralogical Distribution in Base Metal Ores

Nigel J. Cook [1,*], Kathy J. Ehrig [2], Mark Rollog [1], Cristiana L. Ciobanu [1], Daniel J. Lane [1], Danielle S. Schmandt [1], Nicholas D. Owen [1], Toby Hamilton [3] and Stephen R. Grano [4]

1 School of Chemical Engineering, The University of Adelaide, Adelaide, SA 5005, Australia; mark.rollog@adelaide.edu.au (M.R.); cristiana.ciobanu@adelaide.edu.au (C.L.C.); daniel.lane@adelaide.edu.au (D.J.L.), danielle.schmandt@adelaide.edu.au (D.S.S); nicholas.owen@adelaide.edu.au (N.D.O.)
2 BHP Olympic Dam, Adelaide, SA 5000, Australia; Kathy.J.Ehrig@bhpbilliton.com
3 School of Chemical Engineering, The University of Queensland, Brisbane, QLD 4072, Australia; t.hamilton1@uq.edu.au
4 Institute for Mineral and Energy Resources, The University of Adelaide, Adelaide, SA 5005, Australia; stephen.grano@adelaide.edu.au
* Correspondence: nigel.cook@adelaide.edu.au; Tel.: +61-8-8313-1096

Received: 19 April 2018; Accepted: 10 May 2018; Published: 13 May 2018



Abstract: The distributions of ^{210}Pb and ^{210}Po, short half-life products of ^{238}U decay, in geological and related anthropogenic materials are reviewed, with emphasis on their geochemical behaviours and likely mineral hosts. Concentrations of natural ^{210}Pb and ^{210}Po in igneous and related hydrothermal environments are governed by release from crustal reservoirs. ^{210}Po may undergo volatilisation, inducing disequilibrium in magmatic systems. In sedimentary environments (marine, lacustrine, deltaic and fluvial), as in soils, concentrations of ^{210}Pb and ^{210}Po are commonly derived from a combination of natural and anthropogenic sources. Enhanced concentrations of both radionuclides are reported in media from a variety of industrial operations, including uranium mill tailings, waste from phosphoric acid production, oil and gas exploitation and energy production from coals, as well as in residues from the mining and smelting of uranium-bearing copper ores. Although the mineral hosts of the two radionuclides in most solid media are readily defined as those containing parent ^{238}U and ^{226}Ra, their distributions in some hydrothermal U-bearing ores and the products of processing those ores are much less well constrained. Much of the present understanding of these radionuclides is based on indirect data rather than direct observation and potential hosts are likely to be diverse, with deportments depending on the local geochemical environment. Some predictions can nevertheless be made based on the geochemical properties of ^{210}Pb and ^{210}Po and those of the intermediate products of ^{238}U decay, including isotopes of Ra and Rn. Alongside all U-bearing minerals, the potential hosts of ^{210}Pb and ^{210}Po may include Pb-bearing chalcogenides such as galena, as well as a range of sulphates, carbonates, and Fe-oxides. ^{210}Pb and ^{210}Po are also likely to occur as nanoparticles adsorbed onto the surface of other minerals, such as clays, Fe-(hydr)oxides and possibly also carbonates. In rocks, unsupported ^{210}Pb- and/or ^{210}Po-bearing nanoparticles may also be present within micro-fractures in minerals and at the interfaces of mineral grains. Despite forming under very limited and special conditions, the local-scale isotopic disequilibrium they infer is highly relevant for understanding their distributions in mineralized rocks and processing products.

Keywords: ^{210}Pb; ^{210}Po; uranium decay chain; radionuclides; mineral deportment

Minerals **2018**, *8*, 211

1. Introduction

^{210}Pb and ^{210}Po are intermediate isotopes within the ^{238}U decay-series (Figure 1) and occur in minute amounts in nature [1]. Details of the uranium (^{238}U, ^{235}U) and thorium (^{232}Th) decay-series radionuclides are concisely provided in the review by Cowart and Burnett (1994) [2].

^{210}Pb has a half-life of 22.2 years and is generated via: (i) the decay of atmospheric ^{222}Rn gas ("unsupported" ^{210}Pb); and (ii) via the continuous production of ^{222}Rn from natural ^{226}Ra contained in crustal materials ("supported" ^{210}Pb). ^{210}Pb decays to ^{210}Bi by emission of a beta particle. ^{210}Pb is useful for determining the age of a recent sediment in that, provided that the atmospheric flux is constant, the decay profile relates directly to sedimentation rate. Hence, ^{210}Pb is useful for dating sediments up to a century or so old.

Polonium has no stable isotope [3,4]. ^{210}Po is by far the longest-lived of the 7 naturally-occurring Po isotopes in the U and Th decay-series (half-life = 138.376 days). ^{210}Po is generated via beta decay from ^{210}Bi (half-life 5.01 days) and decays to ^{206}Pb by emission of an alpha particle. It has a high specific activity (1.66×10^{14} Bq·g^{-1}) and is highly toxic [5] and one of the most radioactive natural radioisotopes; 1 mg of ^{210}Po emits as many alpha particles per second as 5 g ^{226}Ra. Its toxicity in nature is, however, limited by its vanishingly small mass concentration, even compared to ^{226}Ra. As an energy-generating alpha emitter, ^{210}Po has been used as a lightweight heat source to power thermoelectric cells, for example in the Russian Lunokhod lunar rovers to keep their internal components warm during the lunar nights. The principal source of both ^{210}Pb and ^{210}Po in the environment is natural ^{222}Rn gas which escapes to the atmosphere and undergoes radioactive decay. Airborne particles containing sorbed amounts of these highly particle-reactive decay products of ^{222}Rn fall to the land or water surface and either dissolve, are deposited onto soils, or become subject to sedimentation.

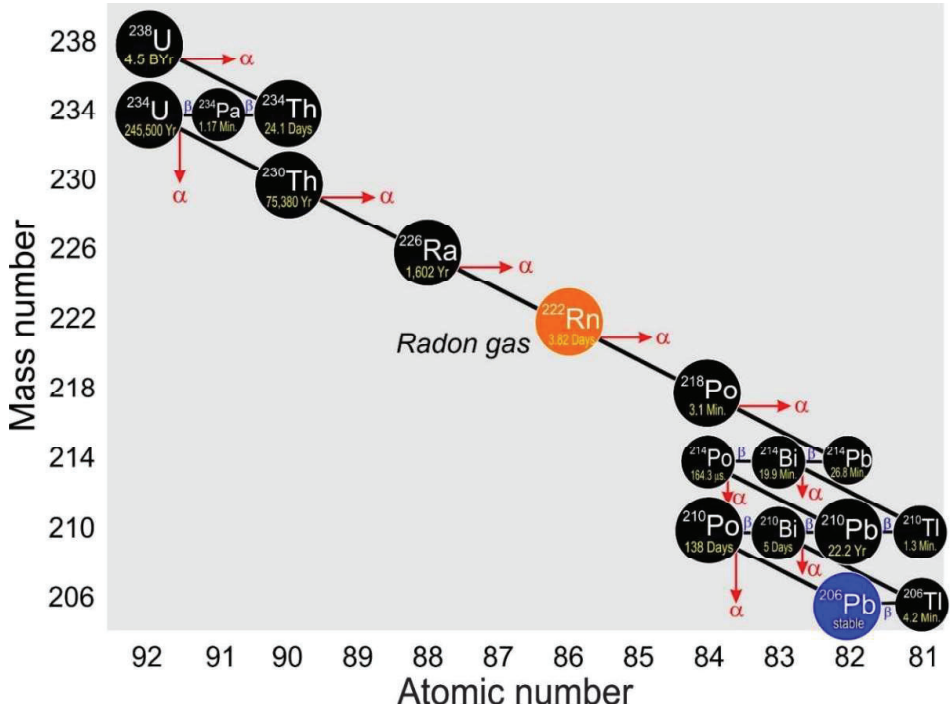


Figure 1. The uranium (radium series) decay chain, indicating half-lives, adapted from various publicly available sources.

Both radionuclides are, however, found in trace amounts in a range of solid media, both natural and anthropogenic in origin. ^{210}Pb and ^{210}Po are present in higher activity concentrations relative to crustal averages in uranium-bearing ores, and in the products of mining and processing from such deposits, including concentrates and wastes. While polonium concentrations are extremely low (< 0.1 mg/tonne even in high-grade uranium ores [6]), the presence of short half-life radionuclides (RN) can impact on the treatment, processing and transport of ore and resulting concentrates. In mining operations in which uranium is present, whether exploited or not, a knowledge of the geochemical behaviour of ^{210}Pb and ^{210}Po during mineral processing is critical to ensure that produced concentrates are as clean as possible. These radionuclides, whether occurring together with parent uranium in the mineralized rocks, or spatially decoupled from it as U-bearing minerals begin to break down, may represent a non-target element that could attract a financial penalty when sold on the open market. If present at high enough concentrations, saleability of that product may be prevented altogether (e.g., [7]). More extensive, and expensive, safety protocols and transport measures may also be required [8].

A comprehensive understanding of the geochemical behaviour and mineralogical distribution of ^{226}Ra, ^{210}Pb and ^{210}Po during ore processing is a pre-requisite for the development of methods to remove or reduce their concentration in products from minerals processing, and provides the motivation behind the present study. The following review of the distributions of ^{210}Pb and ^{210}Po (and of parent ^{226}Ra) in a broad range of geological materials builds on existing reviews of various length [9–12], many of which have emphasised the environmental and health risks that ^{210}Pb and ^{210}Po present. Our emphasis is on the concentrations and distributions of ^{210}Pb and ^{210}Po in solid media, with focus on mineralized rocks and ores, and in anthropogenic materials resulting from the exploitation of natural resources. An assessment of the likely mineral hosts for both ^{210}Pb and ^{210}Po in critical geological environments, including ores and in non-nuclear industrial sources (technologically enhanced naturally occurring radionuclide material (TENORM; [11]) follows.

2. Crustal Distribution of ^{210}Pb and ^{210}Po

^{210}Pb and ^{210}Po are widely dispersed in a large variety of natural media because they often mimic the distributions of parental ^{238}U, ^{226}Ra, or ^{222}Rn. Much of the literature on ^{210}Pb and ^{210}Po distributions in nature is focused on their concentrations in the atmosphere (e.g., [13]), in oceans (e.g., [14–17]), rivers (e.g., [18]), lakes (e.g., [19]), groundwaters (e.g., [20–23]), drinking waters (e.g., [24–26]), and soils [27–29]. Attention has also been given to mosses and lichens, which efficiently capture atmospheric ^{210}Pb and ^{210}Po, peat bogs (also anomalous with respect to ^{210}Pb and ^{210}Po), and in the animal and human food chains, e.g., milk or berries, and particularly seafood (e.g., [12,30–32]). A smaller body of data is available for some natural environments, notably hydrothermal ore deposits or active volcanic fumaroles, where there is evidence for the selective fractionation of ^{210}Pb and ^{210}Po from other ^{238}U decay products, and where ^{210}Pb and ^{210}Po are concentrated in "new" precipitates. These particle-sensitive decay product isotopes are always fractionated from gaseous parent ^{222}Rn that has extreme dispersion and mobility in the environment, particularly in the atmosphere.

There is a large body of data addressing the distribution and behaviour of ^{210}Pb and ^{210}Po in both magmatic and marine/lacustrine sedimentary environments, as well as in relation to the mining, processing and smelting of uranium-bearing ores, processing of phosphate ores for phosphoric acid production and other human activity. Somewhat less well documented are concentrations of ^{226}Ra, ^{210}Pb and ^{210}Po in other anthropogenic materials such as coal ash (e.g., [33,34]), and as scales and sludges associated with oil and gas production [35–37]. Not infrequently, observed distributions are the product of a complex interplay between natural and anthropogenic ^{226}Ra, ^{210}Pb and ^{210}Po from different mining and non-mining sources, the effects of which can only be elucidated by high-quality analysis and a good understanding of the physical and historical context of the samples in question (e.g., [38,39]). There is generally a strong link between the distributions of ^{210}Pb and ^{210}Po and that of parent ^{226}Ra in many industrial wastes (uranium mill tailings, phosphogypsum, coal fly ash, oilfield

scales and sludges) such that understanding the mode-of-occurrence of ^{226}Ra will enable prediction of ^{210}Pb and ^{210}Po behaviour. There are, however, some exceptions in which selective fractionation and concentration of ^{210}Pb and ^{210}Po takes place, as will be shown below.

A detailed treatment of analytical techniques for the determination of short-lived isotopes at concentrations of small fractions of parts-per-billion, and quantification of ^{210}Pb and ^{210}Po in rocks, minerals, concentrates and leachates, lie beyond the scope of this contribution. The reader is referred to References [1,40,41], in which comprehensive reviews of methodologies used for the determination of ^{210}Po in environmental materials are provided, building on earlier studies [42] and others. Clayton and Bradley (1995) [43] describe their methodology to measure ^{210}Pb and ^{210}Po in a range of environmental materials. In a series of papers, Jia and co-authors [44–46] have put forward procedures for analysis of ^{210}Pb and ^{210}Po in mineral, biological and soil samples. Particularly relevant to our focus on ^{210}Pb and ^{210}Po distributions in ores and ore processing residues are separation techniques outlined by Prud'homme et al. (1999) [47] for fine-grained multi-phase materials.

2.1. Magmatic Rocks and Related Hydrothermal Systems

Volcanoes represent the largest single contributor of atmospheric ^{210}Pb and ^{210}Po. For example, Allard et al. [48] document extremely high fluxes from the Ambrym basaltic volcano, Vanuatu Island Arc, in the South Pacific Ocean. Based on direct measurements, these authors maintain that this volcano is among the most powerful volcanic gas emitters on Earth, producing between 5% and 9% of current estimates for global subaerial volcanic emissions of ^{210}Pb and ^{210}Po. Data for both dissolved and emitted magmatic volatiles are used to estimate the depth, size and degassing rate of the basaltic magma reservoir that sustains the eruptive activity [48]. In the aforementioned paper, Allard et al. note radioactive disequilibrium of ^{210}Pb, ^{210}Bi and ^{210}Po in the volcanic gas phase and use this to constrain the renewal rate and dynamic time scales of the magma reservoir. Extensive radioactive disequilibrium between the three radionuclides reported in Ambrym volcanic gas is concordant with observations from other basaltic volcanoes [49,50]. The radioisotopic disequilibrium is attributed by Allard et al. [48] to the very different volatilisation rates of the three radionuclides during high-temperature basalt degassing (^{210}Po > ^{210}Bi > ^{210}Pb). All ^{210}Po is volatilised, whereas the emanation rate is two orders of magnitude lower. ^{210}Po–^{210}Pb geochronology is routinely used to date recent volcanic eruptions (e.g., [51]). Measurable activity of ^{210}Pb, ^{210}Bi and ^{210}Po is not restricted to basaltic volcanoes. The volatility of all three radionuclides have been studied in andesitic gases from Merapi Volcano, Indonesia [52], although the authors note that the emanation coefficients are significantly lower than observed at basaltic volcanoes, a feature attributed to lower magma temperatures. The same authors state that the radionuclides are mainly transported in the volcanic gases as Pb-chlorides, and as "Bi- and Po-metallic species".

The radionuclide systematics of igneous activity nevertheless differ considerably with respect to tectonic environments [53]. Enrichment of ^{210}Po and ^{226}Ra relative to ^{230}Th is noted to be more common and greater in island arcs than in continental margin subduction environments. Levels of enrichment tend to decrease with differentiation. Differences were attributed [53] to variations in the process of melt extraction, changes in bulk partition coefficients within the mantle wedge, or preferential addition of U from subducted lithosphere.

Interest in the activity of ^{210}Pb and relationships with parent radionuclides in young volcanic rocks centres on the useful geochronological information the radioisotope distributions can provide. The literature reveals substantial debate about the possible causes of observed isotopic disequilibria in many young volcanic rocks (e.g., [54]). The observed ^{210}Pb deficits relative to ^{226}Ra are attributed to magma degassing over decades rather than partial melting or interaction with cumulates [55].

Most igneous rocks contain both U and Th, with concentrations increasing as silica content increases. Granites are thus the rock type with the highest concentration of all daughter radionuclides, which remain in secular equilibrium until weathered. Uranium, Th and daughter radionuclides are important heat producers in granitic rocks [56].

Radionuclide concentrations have been examined in volcanic fumaroles from La Fossa cone, Vulcano Island, Italy [57,58]. Sulphur and sulphide incrustations show relative but variable enrichments in ^{210}Po (as high as 500 Bq·g^{-1}), and in ^{210}Pb relative to ^{226}Ra, which are related to degassing of the fumarolic fluids. The published data record mobility of sublimates within the fumaroles. ^{210}Po is almost fully volatilised due to the relatively high velocity of the gas, even though temperatures did not exceed 280–350 °C. Much ^{210}Po may therefore be present in gaseous form within the fumarole. Sublimates at La Fossa Crater, Aeolian Islands, Italy [59] contain an abundance of rare Pb–Bi-sulphosalt mineral species (e.g., wittite, cannizzarite, mozgovaite, etc. [60,61]). Several of sulphosalts, including Cl- and Br-bearing species (e.g., vurroite [62]) have been first described from the locality.

The unusually high sulphur-reducing environments offered by deep-sea hydrothermal vents display ^{210}Pb and ^{210}Po enrichment relative to ^{226}Ra. Boisson et al. (2001) [63], for example, describe the relative enrichment in naturally-occurring ^{210}Po and ^{210}Pb associated with the high particle fluxes brought about by hydrothermal venting off the island of Milos, Aegean Sea. ^{210}Po levels in organisms living on or near the microbial mat in the vent zone were higher than from non-vent areas. It was, however, stressed [63] that input of ^{210}Po and ^{210}Pb to oceans through venting activity is probably not significant compared to that of atmospheric origin. High levels of natural radioactivity, including ^{210}Po–^{210}Pb, in vent biota from both the East Pacific Rise and Mid-Atlantic Ridge have been confirmed [64].

2.2. Sedimentary Environments

Measurable concentrations of ^{210}Pb and ^{210}Po in sedimentary environments, whether marine, lacustrine, deltaic or fluvial have proven invaluable for understanding age relationships of sediments on the decade-scale and for calculation of rates of sedimentation. Many dozens of case studies, e.g., [65–68], document the spatial distributions of ^{210}Pb and ^{210}Po, and successfully separate natural from anthropogenic sources. Activities of ^{210}Pb and ^{210}Po have also proven valuable for studies of glaciation and the accumulation and melting rates of ice sheets [69]. Remarkably few of these studies have addressed the mineralogy of the sediments, and the likely host(s) of ^{210}Pb and ^{210}Po.

A key feature of many studies of sediments and water columns in marine or lake waters is the recognition of disequilibrium between ^{210}Pb and ^{210}Po that is linked to differential cycling patterns, rates of sequestration by sediments, as well as the contributions of atmospheric deposition, particularly for ^{210}Po.

Some sedimentary rocks contain anomalous radionuclide concentrations. Of particular note are restricted marine and estuary environments supplied by organic- and clay-rich sediment. Under reducing conditions, uranium is readily adsorbed onto the organics and/or clay particles.

Sedimentary rocks are also the host for many of the World's largest and richest uranium deposits, formed via migration of dissolved U^{6+} in oxidising waters along paleoaquifers and deposited in reduced rocks. The genesis of such deposits has been amply described elsewhere [70].

3. ^{210}Pb and ^{210}Po from Anthropogenic Sources

The mining of uranium, smelting of copper and polymetallic ores, phosphoric acid and oil/gas production and combustion of coal (and peat) are the main extractive activities leading to generation of materials with high contents of ^{210}Pb, ^{210}Po, and other RN. Surveys of the generation of Naturally Occurring Radioactive Materials (NORM) from industrial operations [71–75] also cover other industrial sectors, including manufacture of zirconia, titanium dioxide pigment production, cement production and alumina and iron and steel production.

3.1. ^{210}Pb and ^{210}Po in Uranium Mill Tailings

The radiological risks associated with management of uranium mill tailings have been discussed by [76–79], among many others. Several authors have suggested that ^{226}Ra occurs in radium-bearing sulphate minerals in uranium mill tailings [80–82]. Landa et al. [83] examined uranium mill tailings from Monticello, Utah. ^{226}Ra was found to be associated with particles and colloids of alkaline-earth sulphates, alkaline-earth carbonates, and surfaces of quartz, clay, and feldspar. Landa [77] inferred from the leaching behaviour of uranium mill tailings that ^{226}Ra occurs with hydrous oxides of iron and manganese. In one study specially aimed at understanding the mineralogy of ^{210}Po [84], material from three uranium mill sites in the USA were examined to establish where contaminants reside as a prerequisite for modelling contaminant mobilisation. Four mineral hosts were suggested using a combination of electron probe microanalysis, thin-section petrography, α-emission mapping, and selective chemical extractions (although none of these techniques can identify mineral hosts for specific radioactive decay products): uranium minerals, authigenic siliceous material, Ba–Sr-sulphates, and Fe–Ti–V-oxides. These themes are explored further by Landa and Bush [79], who recognised a redistribution of radium by particle size during milling but also of the components in the tailings onto which radionuclides are adsorbed. The following potential sorbents were identified: clay minerals, Fe- and Al-oxides, feldspars, fluorite, barite, jarosite, coal, and volcanic glass. Both ^{226}Ra and ^{210}Pb showed both higher degrees of adsorption than either ^{238}U or ^{230}Th, attributable to either selective adsorption or ingrowth of ^{210}Pb daughter isotopes in minerals containing substituted radium (e.g., Ra^{2+} for Ca^{2+}).

In a review of the mineralogical controls on radionuclide mobility in uranium mill tailings [78], the importance of amorphous silica, carbonates and phosphates, and microbial reduction processes is noted. The same publication also examines radionuclide behaviour (although not mentioning ^{210}Pb and ^{210}Po in this context) during in-situ leach (ISL) recovery operations. Jarosite [$KFe_3(SO_4)_2(OH)_6$], which may precipitate and severely restrict permeability along ISL aquifers, is said to be a significant host for radium. The presence of sulphides and Fe-(hydr)oxides will also impact on recovery dependent on the extracting agent used. These ideas are expanded in a more recent study of uranium mill tailings [85] that also stresses the potential role of sulphates and secondary galena as hosts for ^{210}Pb. It is reasonable to infer that these minerals scavenge ^{210}Pb dissolved within pore fluids.

Radionuclide distributions, including ^{210}Pb deposition rates and inventories, have been examined in and around the Ranger Uranium Mine, N.T., Australia [86]. Natural redistributions of ^{222}Rn and ^{210}Pb occur via atmospheric dispersion of ^{222}Rn, (seasonal) deposition of ^{210}Pb on surfaces, and eventual migration creating ^{210}Pb depth profiles prior to decay to ^{206}Pb. A net loss of ^{210}Pb from the region occurs during the dry season by attachment to aerosols.

3.2. ^{210}Pb and ^{210}Po in Copper and Polymetallic Ores and Products of Their Mining and Processing

Some copper ores contain anomalously high concentrations of RN, meaning that daughter radionuclides are present in products of mining and smelting, and within wastes resulting from those activities. Due to selective volatilization/condensation of ^{210}Pb and ^{210}Po, smelter dusts tend to be enriched in ^{210}Pb and ^{210}Po compared to ^{226}Ra, compared to their activity concentrations in the original ore feed, and compared to their activity concentrations in other solids produced during processing. Such a scenario is documented for the Olympic Dam copper mining and smelting operation, South Australia [87]. The behaviour of ^{210}Pb and ^{210}Po during concentration and smelting of copper ores, and their preferential partitioning into smelter flue dusts where they may accumulate, has been documented in several studies. One of the best studied examples is the contamination generated through centuries of exploitation of copper-bearing bituminous shales (Kupferschiefer) in the Mansfeld district of eastern Germany. A characterisation of scrubber dust slurries (*Theisenschlamm*) containing ^{210}Pb and ^{210}Po, which were produced as a by-product of the Mansfeld smelting operations, is given in [88]. Around 220,000 tonnes of these sludges are deposited at several sites and continue to represent a serious environmental risk [89–92]. The material contains: 18% Zn (as sphalerite and wurtzite);

14% Pb (as galena and secondary anglesite); a wide variety of hazardous (As, Tl, Cd) elements and rare metals (Ag, Ge, Re); polycyclic aromatic hydrocarbons and other organic compounds, as well as radionuclides. ^{210}Pb and ^{210}Po are concentrated in the finest size fractions, typically of sub-micron size and combined as aggregates with mean diameter of 1.25 μm [88]. Additional characterisation of the *Theisenschlamm* is provided by Morency et al. [93], with experimental evidence in support of oxidative processes designed to immobilize elements and isotopes of concern. Of relevance to the overarching aim of the present study is the observation that almost all ^{210}Pb and ^{210}Po can be concentrated into a lead sulphate phase. Ores of comparable age and origin, albeit with generally lower associated radioactivity, are currently mined in the Lubin region, Poland [94]. The highly selective enrichment of ^{210}Pb and ^{210}Po compared to ^{226}Ra in certain wastes from copper smelting highlights the importance of understanding the distribution of these isotopes when designing plant operations or planning waste clean-up or handling.

Hypogene tin ores are generally genetically related to granites and often contain anomalous concentrations of Cu, Pb, Bi, U and Te relative to crustal averages. They may contain measurable concentrations of ^{210}Pb, ^{210}Po and ^{210}Bi. The smelter process, for which feedstock may not only comprise tin ores/concentrates but also tin-rich residues from other processes, involves a molten metal stream and separation into tin, lead and lead-bismuth alloys. ^{210}Po will rapidly volatilise, and according to Martin et al. [71], can be highly enriched in smelter fumes (200,000 Bq·kg^{-1}). Slags will contain the non-volatile radionuclides but also some ^{210}Pb and ^{210}Po (10,000 Bq·kg^{-1}). Within the bismuth metal, short-lived ^{210}Bi rapidly decays to ^{210}Pb, which may have activity concentrations up to 100,000 Bq·kg^{-1}. Hipkin and Paynter (1991) [95] address activity concentrations of materials and the radiation exposures of workers in the tin industries of Bolivia and SE Asia, while background data on ^{210}Pb and ^{210}Po behaviour during the tin smelting and electro-refining process are given by Harvey et al. [96]. ^{210}Pb and ^{210}Po activities in and around a large, now-closed, tin smelter in northern England are discussed by Baxter et al. [97]. Here, over the course of ca. 55 years of tin production, about 30% of the ^{210}Po was isolated in tellurium dross, 48% decayed within the refinery, 19% went to waste slag, and 2% was released into the atmosphere.

3.3. ^{210}Pb and ^{210}Po in Mining and Processing of Phosphates

Many phosphate formations exploited for the fertiliser industry contain concentrations of naturally occurring radionuclides of the uranium and thorium decay series that exceed those in other rocks. The risks associated with mining, milling and manufacturing of phosphoric acid and phosphate fertilizers have been widely documented at different sites around the world. Solid waste products of the phosphate industry, notably gypsum ($CaSO_4 \cdot 2H_2O$), termed phosphogypsum, but also dusts generated during milling, can carry particularly high concentrations of ^{226}Rn, ^{210}Pb and ^{210}Po (e.g., [74,98–109]. Although waste from the phosphate industry has, in some cases, been disposed of in the marine environment (e.g., [101]), elsewhere, most spectacularly in Florida, where the World's largest phosphoric acid industry is centred, huge waste piles (gypstacks) have been generated, creating serious waste management issues.

In the manufacture of phosphoric acid, an important industrial chemical, phosphate rock (which typically contains U within apatite or other phosphates) is treated with sulphuric acid, resulting in by-product gypsum in volumes three times greater than the phosphoric acid (Figure 2). The reaction involved in phosphoric acid production can be simplified, after Burnett et al. [103], as:

$$Ca_{10}(PO_4)_6F_2 + 10H_2SO_4 + 20H_2O \rightarrow 10CaSO_4 \cdot 2H_2O + 6H_3PO_4 + 2HF$$

The above reaction creates disequilibrium between U, Th and Ra. The majority of U if found in the phosphoric acid, ca. 90% of the ^{226}Ra, and effectively all the ^{210}Pb and ^{210}Po, will be preferentially concentrated within the phosphogypsum (e.g., [110]), with ^{210}Pb and ^{210}Po in secular equilibrium [111]. The ^{210}Pb and ^{210}Po activities in phosphogypsum are typically a few hundreds of Bq·kg^{-1}. For example,

Brasilian phosphogypsum described by Mazzilli et al. [106] shows concentration ranges of 47–894 Bq·kg^{-1} and 53–677 Bq·kg^{-1} for ^{210}Pb and ^{210}Po, respectively. These activities depend on the uranium concentrations in the phosphate ore, which can vary over as much as an order of magnitude. For comparison, phosphate rocks in Florida, Morocco and Jordan, three important producing areas, contain 1300–1850 Bq·kg^{-1} U [112]. In the phosphate rocks, U (and Th) is present mostly within the mineral apatite. U^{4+} has a similar ionic radius to Ca^{2+} (0.97 and 0.99 Å, respectively) and readily substitutes into the apatite lattice, resulting in less abundant uraninite in some ores.

The physical distribution of ^{226}Ra and ^{210}Pb in phosphogypsum waste piles is addressed by Rutherford et al. [100], who note heterogeneity in which ^{210}Pb is concentrated in the finest fraction (no more than a few microns). In studies of Florida phosphogypsum, ^{210}Pb/^{210}Po disequilibrium in mature phosphogypsum samples has been demonstrated [104], suggesting that ^{210}Pb was more mobile than either ^{210}Po or ^{226}Ra. Although none of the phosphogypsum research has demonstrated that the mineral hosts for each radionuclide differ (phosphogypsum is, in any case essentially monomineralic with around 1% impurities), these observations are indirect evidence to the suggestion that ^{210}Pb may be less well bound within the crystal lattice of gypsum.

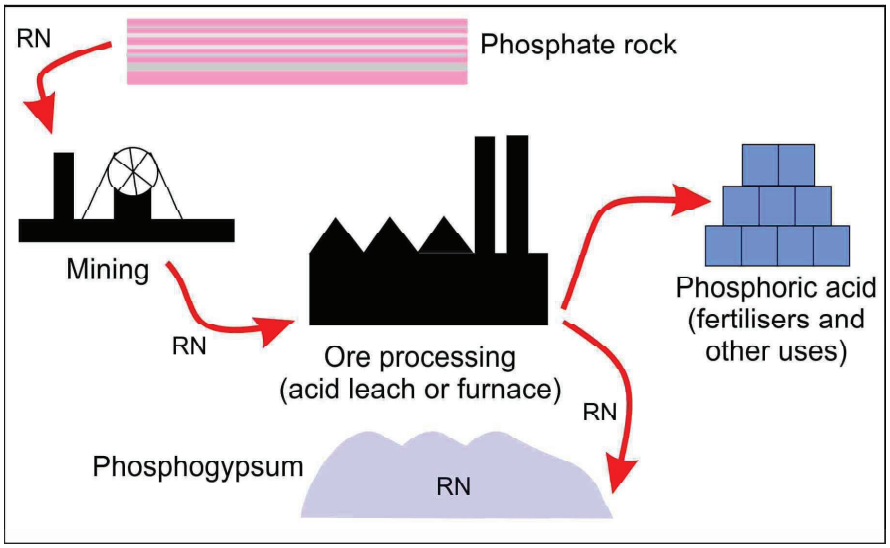


Figure 2. Schematic diagram showing RN behaviour during phosphate production.

3.4. ^{210}Pb and ^{210}Po Associated with Oil and Gas Production

Radioactive scales and sludges associated with offshore oil and gas production often contain anomalously high concentrations of ^{226}Ra, ^{210}Pb and ^{210}Po, and have been well documented [35–37,113,114]. After the mixture of oil, gas and water is brought to the surface, and the gas and formation waters are separated from the oil, hard scales will build up on the internal surfaces of the oil field extraction and production equipment. Well fluids (saline formation waters that are co-produced with oil and gas and require separate handling) are characteristically enriched in Ca, Sr, Ba and associated Ra. Pipes and tanks that come into contact with these waters are subject to scale and sludge build-up. The relative amounts of solid waste (sludges and sands) vary with the production area due to the different geological and fluid characteristics of the reservoirs. ^{226}Ra, ^{210}Pb and ^{210}Po-enriched scales precipitate as solids directly from the formation waters following changes in temperature, pressure and salinity.

The volumes of these materials are, however, generally rather small and typically comprise a mixture of carbonate and sulphate compounds of calcium, strontium and barium. Generation of ^{210}Pb and ^{210}Po is due to the presence of parent U and Th in the oil/gas source rocks, which decays to Ra that dissolves within the saline formation waters that also contain P, Sr, Ba and Ca. The radium isotopes, ^{226}Ra and ^{228}Ra, co-precipitate with the salts of these elements, enriching the sludges and, particularly, scales in radium and products of radium decay, including radon isotopes, ^{210}Pb and ^{210}Po. The relatively longer-lived decay products such as ^{210}Pb, will accumulate as very thin films and deposits in gas handling equipment and storage tanks.

3.5. ^{210}Pb and ^{210}Po from Combustion of Coal and Other Solid Fuels

The combustion of solid fuels such as coal for heat and power applications is an important source of atmospheric ^{210}Pb and ^{210}Po and has been studied in detail in various parts of the World. During the combustion of solid fuels, trace elements, including ^{210}Pb and ^{210}Po, partially volatilise along with organic constituents in the fuel matrix. The remaining trace elements remain in the fuel bed and are eventually collected as bottom ash. The volatilised fraction generally condenses on fly ash particles in the flue gases as the flue gases are cooled [115]. Fly ash samples collected from coal-fired power stations have been reported to contain elevated concentrations of ^{210}Pb and ^{210}Po, when compared with the original feedstocks [116], indicating that these two radionuclides volatilise to a large extent during the combustion of solid fuels. The United Nations Scientific Committee on the Effects of Atomic Radiation (UNSCEAR) provide further evidence for the enrichment of ^{210}Pb and ^{210}Po relative to precursor RN in fly ashes during solid fuel combustion in their survey on the activity concentrations of radionuclides in coal samples sourced from a wide range of geographical locations and in fly ashes sourced from various coal-fired power stations [117]. Country-averaged activity concentrations for coal were all within 50 Bq·kg^{-1} for both ^{210}Pb and ^{210}Po. Average concentrations of ^{210}Pb and ^{210}Po in the fly ash samples were much higher by comparison (930 Bq·kg^{-1} for ^{210}Pb and 1700 Bq·kg^{-1} for ^{210}Po). Studies on the size distribution of radionuclides in fly ash show ^{210}Pb and ^{210}Po to preferentially condense on fine particles below 10 microns in size [118,119]. This makes the capture of ^{210}Pb and ^{210}Po difficult, since conventional particulate control devices (e.g., electrostatic precipitators and bag filters) generally become less effective with diminishing particle size [119]. Consequently, a small but nevertheless not insignificant fraction of the ^{210}Pb and ^{210}Po in solid fuels is emitted from the stack into the atmosphere. According to Roeck et al. [120], in old coal-fired power plants, ca. 3% of the initial radioactivity will be discharged from the stack but this proportion is no more than 0.5% in modern plants. UNSCEAR [121] state that annual emissions from a "typical" 600 MW coal fired power station was 0.4 GBq for ^{210}Pb and 0.8 GBq for ^{210}Pb. ^{210}Pb and ^{210}Po may also accumulate in deposits on furnace walls and on the fireside of boiler tubes.

The amounts of ^{210}Pb and ^{210}Po released into the different product streams during solid fuel combustion not only depend on processing parameters (e.g., combustion temperature and gas atmosphere) but also on the properties of the feedstock, particularly the activity concentrations of ^{210}Pb and ^{210}Po. Most coals contain small amounts of parent U and Th but their concentrations can vary over several orders of magnitude from deposit to deposit. There is a substantial volume of literature on naturally occurring radionuclide distributions in coals and fly ash [116,122–125]. Coal is formed via reduction of organic material, in which uranium is trapped or adsorbed onto clay particles, carbonaceous matter, pyrite and organic matter. In contrast, Th occurs within minerals such as monazite or apatite. Since organic matter is an effective reductant, coal horizons may accumulate additional uranium over time by extracting dissolved uranium from circulating groundwaters [126]. Lower rank sub-bituminous coals, brown coals, and lignites may contain higher concentrations of parent U and Th ([125] and references therein). Unconsolidated analogues, including peats, may also contain anomalous RN concentrations.

Enhanced atmospheric ^{210}Po in urban areas may be attributed to coal-fired power stations [127,128]. In a comparison of emissions from power plants fuelled by different hydrocarbon fuels, Häsänen et al. [129] point out that the greatest emissions of ^{210}Po per burnt volume of fuel were from combustion of peat.

3.6. ^{210}Pb and ^{210}Po from Exploitation of Mineral Sands

Anomalous concentrations of ^{210}Pb and ^{210}Po are associated with exploitation of mineral sands for production of zircon and zirconia, titanium dioxide and rare earth elements. Radiological risks associated with such ores (and corresponding products and wastes) are generally low (around 10,000 Bq·kg^{-1} [71]). This could, however, be an area in which ^{210}Pb and ^{210}Po release is set to increase, since demand for these commodities, especially REE, is booming, and new mineral sands operations are being established around the globe.

Mineral sands are of particular interest because of the indirect information they provide on potential mineral hosts for ^{210}Pb and ^{210}Po. The minerals within such sands (zircon, baddeleyite, monazite, xenotime, ilmenite, rutile, etc.) all host trace to minor amounts of uranium and thorium (varying up to as much as 1 wt % depending on primary source) and are all highly refractory. Despite this, there are relatively few published studies detailing ^{210}Pb and ^{210}Po geochemistry in mineral sands enabling an understanding of whether daughter radionuclides are retained in the crystal structures. The manufacture of zirconia for glazes and ceramics involves production of small volumes (~1% of feed) of highly RN-enriched waste, as well as volatilisation of ^{210}Pb and ^{210}Po.

Titanium oxide pigment production, from rutile, a mineral that also commonly contains primary minor U and Th, also results in a RN-enriched solid waste residue.

3.7. ^{210}Pb and ^{210}Po in Other Anthropogenic Materials

Most iron ores contain only low concentrations of ^{210}Pb and ^{210}Po and thus accumulation of radioactivity in waste materials produced by iron and steel production are mostly attributable to other feed materials (coal/coke and limestone). ^{210}Pb and ^{210}Po tend to accumulate in the sinter plant in dust collected from the gas cleaning systems and are generally very low or absent in saleable products. According to Martin et al. [71], for every million tonnes of steel produced, 2000 tonnes of contaminated dust will be generated. In a study of sinter plant radioactivity in the Port Kembla foundry, NSW, Australia, Brown et al., in a report cited by Martin et al. [71], report activities of 18,900 and 15,600 Bq·kg^{-1} for ^{210}Pb and ^{210}Po, respectively, in ductwork dust.

Production of the elements niobium and tantalum is also associated with generation of RN-rich residues. Like tin ores, Nb–Ta ores are granite-related and commonly contain minor amounts of other elements including uranium (and thorium). Pyrochlore, a primary ore mineral of niobium and tantalum, will often contain actinides at measurable concentrations. ^{210}Pb activities as high as 16,700 Bq·kg^{-1} in slags from a Brasilian niobium processing facility are reported [11].

Martin et al. (1997) [71] compiled information on ^{210}Pb and ^{210}Po in cement, bricks and other building materials, and provide activity concentrations for ^{226}Ra and ^{232}Th. They note that activities are only of concern if substantial amounts of waste materials in which ^{210}Pb and ^{210}Po are concentrated are added into the materials. Examples include the common addition of copper slag in concrete (in the former East Germany), phosphogypsum waste in wallboard and road construction, and fly-ash in bricks and some cements. Lightweight building blocks may contain both slag and fly-ash. Several publications detail representative ^{210}Pb and ^{210}Po activity concentration data for building materials, focussing on eastern European countries where the practice of adding smelter slags and fly-ash was commonplace [130–132]. The environmental impact of radionuclide release during processing of granite rock for ornamental stone has also been explored [133]. In this paper, Guillén et al. suggest that even basic mechanical processing of granites can lead to increased levels of ^{210}Po and ^{210}Pb in the surrounding environment, as dusts, solid waste and slurries.

Numerous studies have sought to demonstrate the impact of historical human industrial activity by monitoring the levels of lead isotopes in peat bogs, salt marsh, lakes and estuarine sediments [38,134–140].

4. Mineral Repositories for ^{210}Pb and ^{210}Po

The literature contains extensive reference to the potential mineral repositories for ^{210}Pb and ^{210}Po, although much of this evidence has been obtained indirectly. Very few studies to date have been able to provide direct confirmation that a given phase contains these RN. This is largely due to those RN with relatively short half-lives being present at minute concentrations well below minimum detection limits of conventional microanalysis.

Polonium has no non-radioactive isotope and does not occur naturally as a metal or essential component of naturally occurring compounds, although the compound PbPo has been reported [141] and has been attributed to natural alpha decay of polonium to form lead. Polonium is readily vaporised, forming Po_2 molecules even well below the melting and boiling points (254 and 962 °C, respectively) via small clusters of polonium atoms spalled off by alpha decay. These particles are readily adsorbed. Chemically, polonium displays similar behaviour to that of tellurium and bismuth [141,142]. More than 50 polonium compounds have been synthesized including metal polonides, polonium hydride, the two oxides PoO_2 and PoO_3, halides and sulphates. Various oxidation states, including $^{2+}$, $^{4+}$ and $^{2-}$, are known.

Valuable insights into the behaviour of ^{210}Pb and ^{210}Po in polymetallic ores are provided by Golubev et al. [143]. By comparative analysis of different volumes of ore within a single vein-type uranium orebody, these authors provide critical evidence for migration of ^{238}U and, critically, of intermediate decay products within an effectively open system, creating disturbances of U–Pb systematics, expressed as local enrichments or depletions in ^{206}Pb, giving rise to discrepancies between ages based on ^{206}Pb/^{238}U and ^{207}Pb/^{235}U ratios. The authors note the presence of zones with low U contents but with excess ^{206}Pb. These contain pyrite/marcasite onto which migrating longer-lived radionuclides, including ^{210}Po and ^{210}Pb, are considered to accumulate, effectively playing the role of geochemical barriers within the system.

In a study attempting to identify the solid-phase partitioning of ^{210}Po and ^{210}Pb in anoxic marine sediments [144], the influence of early diagenetic processes on distribution patterns is documented. In sediment, ^{210}Po was found to be either bound to organic matter, sulphides such as pyrite, clay minerals or refractory oxides. ^{210}Po was found not to be significantly bound to acid volatile sulphides in sediment, even if the authors considered that ^{210}Po initially bound to acid volatile sulphides may have been redistributed by bioturbation.

Because of the extremely low concentrations and the difficulty of separating fine-grained minerals, there is a paucity of published concentration data for ^{210}Pb and ^{210}Po in individual minerals. Identification of the potential mineral repositories for either radionuclide, except for post-decay reincorporation of daughter RN into parent U-minerals is therefore reliant on indirect observation. Good indications as to potential hosts can nevertheless be made based on the literature we have summarised above (Table 1).

Table 1. Summary of potential mineral hosts for ^{210}Pb and ^{210}Po.

Mineral Group	Mineral	Formula (e)	Host for
Uranium minerals	Uraninite	UO_2 (ideally)	U, radiogenic Pb, minor Th
	Coffinite	$U(SiO_4)_{1-x}(OH)_{4x}$	ditto -
	Brannerite	$(U,Ca,REE)(Ti,Fe)_2O_6$	ditto -
	Uranothorite	$(Th,U)SiO_4$	Th, U, radiogenic Pb
	Carnotite	$K_2(UO_2)_2(VO_4)_2 \cdot 3H_2O$	U, (Th and Pb?)
REE-, Zr- and Nb–Ta-minerals	Monazite	$(REE)PO_4$	Minor U, Th radiogenic Pb?)
	Bastnäsite	$REE(CO_3)F$	ditto -
	Synchysite	$Ca(REE)(CO_3)_2F$	ditto -
	Xenotime	$(Y,REE)PO_4$	ditto -
	Alunite Supergroup Minerals (especially crandallite and beudantite groups)	(Various minerals)	ditto -
	Baddeleyite	ZrO_2	ditto -
	Zircon	$ZrSiO_4$	ditto -
	Tantalite-(Fe)–tantalite-(Mn) series	$(Fe,Mn,Mg)(Nb,Ta)_2O_6$	Trace U,Th,Pb (?)
	Euxinite	$(Y,Ca,Ce,U,Th)(Nb,Ta,Ti)_2O_6$	ditto -
Sulphides/selenides/tellurides	Galena	PbS	Radiogenic Pb
	Clausthalite	PbSe	ditto -
	Altaite	PbTe	ditto -
	Bi-chalcogenides	$Bi_x(Te,Se,S)_y$	?
	Pb-Bi-sulphosalts	(various)	?
	Pyrite	FeS_2	as a sorbent (?)
Carbonates	Calcite, dolomite, ankerite	$CaCO_3$, $CaMg(CO_3)_2$, $Ca(Fe,Mg)(CO_3)_2$	Ra, minor Pb
	Strontianite	$SrCO_3$	ditto -
	Rhodocrosite	$MnCO_3$	ditto -
	Magnesite	$MgCO_3$	ditto -
	Witherite	$PbCO_3$	Pb
Sulphates	Barite	$BaSO_4$	Ra, Pb
	Celestite	$SrSO_4$	ditto -
	Anglesite	$PbSO_4$	Pb
	Gypsum	$CaSO_4 \cdot 2H_2O$	Pb (?)
Fe-oxides, hydroxides	Hematite	α-Fe_2O_3	Minor/trace U, Pb, and as sorbent
	Goethite	FeO(OH)	As sorbent
Fe–Ti-oxides, Ti-oxides	Ilmenite	$FeTiO_3$	Minor U and Th
	Rutile	TiO_2	ditto -
Jarosite sub-group	Jarosite	$KFe(SO_4)_2(OH)_6$	Pb?
Other potential hosts	Apatite group	$Ca_5(PO_4)_3(F,Cl,OH)$	Minor U and Th
	Fluorite	CaF_2	?
	Feldspar group	-	Pb (replacing Ca?)

4.1. Re-Incorporation of Radionuclides into Parent Minerals

All minerals originally containing uranium will host daughter RN if those products do not migrate from the parent. Plausible ^{210}Pb and ^{210}Po carriers thus include the more common uranium minerals, such as uraninite, coffinite, uranothorite and brannerite, as well as the large number of minerals which carry trace to minor amounts of uranium. The latter include REE-fluorocarbonates and phosphates (monazite, bastnäsite, synchysite, florencite, xenotime, etc.), and common accessory minerals in rocks and ores such as apatite, allanite, zircon, titanite and rutile). The assumption that ^{210}Pb and ^{210}Po can be found in these minerals, however, infers that all decay chain products, including ^{234}Th, ^{226}Ra and ^{222}Rn, are retained within the parent mineral, either within the crystal lattice, or as inclusions.

In the case of the mineral uraninite, strong supporting evidence for this emerges from our own recent research on the Olympic Dam Cu–U–Au–Ag ore deposit, South Australia, where (re-)incorporation of radiogenic lead within the crystal lattice of uraninite is recognised [145–147]. Lead concentrations in Olympic Dam uraninite can, locally exceed 10 wt % in solid solution within the uraninite structure. This contradicts the findings of Janeczek and Ewing [148], where it is maintained that Pb^{2+} is incompatible within the fluorite-type uraninite structure at concentrations greater than a few wt %. Other U-minerals will also contain Pb, albeit at lower concentrations, e.g., coffinite and

brannerite from Olympic Dam [149]. Lower Pb concentrations relative to contained U suggest these structures accommodate daughter RN less well than uraninite.

The presence of radiogenic lead is also well known in minerals such as monazite and zircon where it directly substitutes into the crystal structure (e.g., [150,151]). The ratios between parent uranium, thorium and radiogenic lead underpin U–Pb geochronology. In the Olympic Dam deposit, both U and Pb (^{206}Pb) are also noted in a characteristic oscillatory-zoned textural type of hematite [152,153]. Hematite is the most abundant gangue mineral in the deposit. Within this hematite, uranium and lead isotopes, both in solid solution and as nanoparticle inclusions [154] are in apparent secular equilibrium, indicating a closed system and providing a basis for U–Pb geochronology using hematite [152,155,156].

4.2. Migration and Precipitation as New Minerals

During radioactive decay of U-bearing minerals, metamictisation will take place. This is a natural process occurring over geological time (millions to billions of years) in which the crystal structure of the parent mineral is gradually, and ultimately completely, destroyed, rendering that mineral amorphous [157]. During that process, any impurities may be expelled from the metamict phase. Even if a portion of the ^{210}Pb and ^{210}Po is retained within the U-bearing parent mineral, migration of daughter isotopes and other trace elements initially incorporated within the parent mineral (Th, REE, Nb, etc.) is widely observed to take place following metamictisation, alteration and recrystallization. The radionuclides are either precipitated as new minerals, or alternatively, are incorporated into other existing minerals at distances ranging from microns to metres from the parent phase. Such phenomena are particularly common in hydrothermal ores, in which transport is assisted by permeability and the presence of fluids. There thus exist several potential mineral hosts for daughter RN. Obvious products resulting from ^{210}Pb and ^{210}Po migration include the common lead mineral, galena, which is often observed within, or immediately adjacent to parent U-minerals ([158,159], and many others). For example, nanometre-scale galena is documented within uraninite in parts of grains in which Cu-sulphides and fluorite fill sub-micron-scale fractures [145]. Finch and Murakami [160] have outlined how galena will form in close association with uraninite if the sulphur activity is high enough. Direct evidence for the presence of ^{210}Pb within galena is limited but has been shown within recently formed galena from burning heaps associated with coal mining in the Lower Silesian basin, Czech Republic, [161]. Migrating radiogenic lead may also combine with Se or Te, either within existing minerals or from fluid, to form clausthalite (PbSe) or altaite (PbTe). Owen et al. [162] have recently documented the formation of ^{206}Pb-enriched nanoscale inclusions of clausthalite in Cu–(Fe)-sulphides, which formed via interaction between migrating Pb in fluids with Se initially hosted in solid solution within the sulphides. These may be as small as 1–2 nm in size but display coarsening.

Rollog et al. [163] have used nanoSIMS mapping to directly observe the sub-micron-scale distributions of ^{210}RN in copper ores and flotation concentrates from Olympic Dam; measurements are the sum of ^{210}Po + ^{210}Bi + ^{210}Pb but are overwhelmingly dominated by ^{210}Pb. Although concentrated within U-bearing minerals, migration of ^{210}RN away from the parent is observed on the scale of microns, with formation of nanoinclusions of "new" phases at sulphide grain boundaries, within microfractures, and within micropores in a range of host minerals. This phenomenon leads to daughter ^{210}RN becoming readily trapped within their host phases and accompanying those hosts through processing. Figure 3 shows an example of this innovative method to visualise RN distributions within individual mineral grains.

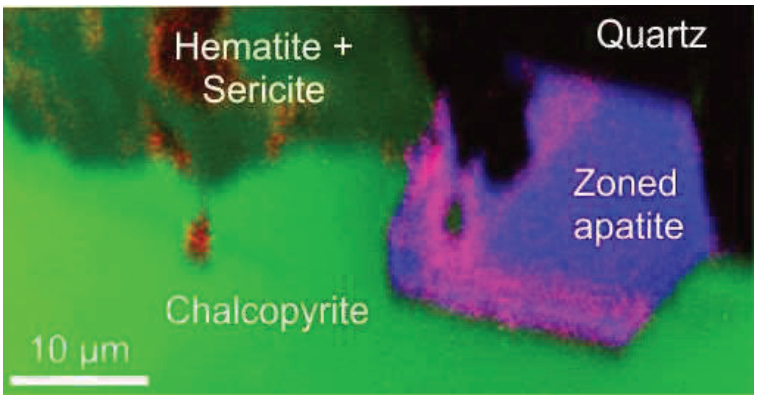


Figure 3. nanoSIMS map, modified from Rollog et al. [163] confirming the presence of ^{210}RN in apatite that is compositionally-zoned with respect to REE. Green = Fe, blue = Ca, pink = ^{210}RN.

4.3. Sulphates, Carbonates, and Other Potential Hosts

Sulphates, notably barite ($BaSO_4$), celestine ($SrSO_4$), anglesite ($PbSO_4$) and gypsum are commonly considered as hosts for radium and subsequent daughter radionuclides including ^{210}Pb and ^{210}Po. Prieto et al. [164] provide compelling experimental evidence for $(Ba,Pb)SO_4$ solid solution. We are nevertheless unaware of empirical proof for the presence of ^{210}Pb and ^{210}Po in these sulphates.

The similarity in chemical behaviour between Ra and Ba, and to some extent also Pb, makes sulphates a good host for ^{210}Pb and, potentially, for ^{210}Po. For example, Al Attar et al. [114] report barite-strontianite solid solution and *hokutolite* [$(Ba,Pb)SO_4$] as the main mineral components of radionuclide-containing scales associated with oil production. Extensive solid solution between isostructural Ba- and Ra-sulphates (so called *radiobarite*, $(Ba,Ra)SO_4$ [165–174] has been modelled, and a number of natural occurrences have been documented e.g., [175,176]. In a detailed mineralogical insight into radionuclide host phases, Landa and Bush [79] document intense alpha particle activity associated with the presence of ^{210}Pb within micron-scale inclusions of anglesite within laths of gypsum.

Other possible candidates as hosts for ^{210}Pb and ^{210}Po in natural samples include common carbonates, notably the Pb-carbonate cerussite ($PbCO_3$). Reactions of dissolved Ra and Ba onto the surfaces of different carbonate minerals were examined by Jones et al. [177]. Calcite, dolomite, strontianite, rhodochrosite, ankerite and witherite all showed evidence of a co-precipitation reaction (increased uptake with increasing Ra concentration), siderite, magnesite and ankerite demonstrated a behaviour suggesting simple sorption. Magnesite showed a particularly high sorption capacity. An extensive treatment of the principles and mechanisms of co-precipitation with application to radionuclide incorporation within, and onto carbonate substrates, is given by Curti [178].

The role played by tellurium-bearing minerals, notably altaite (PbTe) and bismuth tellurides, as hosts for ^{210}Pb and/or ^{210}Po is unknown at the present time. These phases, as well as the selenide analogue of galena, clausthalite (PbSe) are minor yet persistent components of many hydrothermal ores, could potentially be important carriers of either radionuclide, especially given the similar chemistry of Po and Te. The environmental geochemistry of tellurium itself is only recently beginning to become better understood [179]. There may be a number of less obvious candidate hosts for ^{210}Pb and ^{210}Po. We can reasonably speculate that these will include those minerals capable of trapping gaseous radon within pore spaces during, or subsequent to growth.

4.4. Clay Minerals, Iron-Manganese-Oxides and Organics

Clay minerals, Fe–Mn oxy-hydroxides, and organic matter are well known sorbants for dissolved uranium and radium. ^{210}Pb and ^{210}Po sorption may not be primary and abundances may relate to

in-situ decay of the sorbed U and Ra. As an alternative, sorption of ^{222}Rn daughter isotopes, including ^{210}Po and ^{210}Pb may follow their generation via decay of dissolved ^{222}Rn.

In a study of a range of sites on the River Danube, preferential accumulation of ^{210}Po in sediments that are rich in clay minerals has been shown [180]. These authors invoked the ion exchange and adsorption characteristics of different types of clay minerals, suggesting that they may represent both a sink or a source for ^{210}Pb and ^{210}Po and other contaminants, as element mobilities are influenced by evolving physical, chemical and biological conditions.

A strong association between ^{210}Po and ^{210}Pb and iron oxide minerals is demonstrated in beach sands [181], even if other, far more voluminous hosts contained the majority of these and other radionuclides. Yang et al. [182] report on the adsorption properties of ^{210}Po and ^{210}Pb onto micro-particles and reported that Fe- and Mn-oxides were stronger sorbents of ^{210}Po and ^{210}Pb than SiO_2 and $CaCO_3$. They did, however, note preferential adsorption of ^{210}Po over ^{210}Pb onto both SiO_2 and $CaCO_3$. In the presence of the protein BSA; acid polysaccharides appeared to produce the opposite effect, enhancing ^{210}Pb adsorption.

Interaction, by both adsorption and incorporation, between Pb and Fe(III) (oxyhydr) oxide minerals, has been demonstrated by Yang et al. [183], who considered that the presence or absence of these minerals plays a major influence on the partitioning and transport of lead. They have shown how Pb is both surface-adsorbed and incorporated within ferrihydrite during crystallisation to hematite and goethite, depending on pH conditions.

Further evidence for the importance of both organic compounds and nanoparticles is given by Yang et al. [184], who have documented adsorption and fractionation of ^{210}Po and ^{210}Pb onto chemically simple oxide and carbonate nanoparticles in the presence or absence of various macromolecular organic compounds (MOCs) in natural seawater. MOCs were found to enhance sorption of selected nuclides on most nanoparticles (partition coefficients for ^{210}Po and ^{210}Pb increasing 2.9- and 5-fold, respectively), even if adsorption was largely dependent on particle composition.

In soils, ^{210}Po is adsorbed onto clay particles and organic material [9,185]. Sequential leaching techniques enable insights into the speciation of ^{210}Pb and ^{210}Po in soils to be gained [46]. Of the five fractions into which ^{210}Pb and ^{210}Po were fractionated, they found the majority of both ^{210}Pb (67.2%) and ^{210}Po (77.4%) bound to the insoluble residue. Small, but still significant fractions of the total ^{210}Pb (14.3%) and ^{210}Po (21.0%) were extracted with $NH_2OH{\cdot}HCl$ in 25% v/v acetic acid, which may indicate partial association of the radionuclides with Fe–Mn-oxides [186]. The bio-reactivity of ^{210}Pb and ^{210}Po was demonstrated by Kim and Kim [187], who asserted that colloids play a major role in their cycling within oceans.

Further supporting evidence for the affinity of ^{210}Pb and ^{210}Po for Fe-oxides comes from the Talvivaara mine, Eastern Finland, where microbe-induced heap leaching is used to recover Ni and by-product Zn, Cu, Co from a black schist [188,189]. Non-target metals in the deposit include uranium (as uraninite) and its daughter isotopes. The behaviour of ^{226}Ra, ^{210}Pb and ^{210}Po were studied in the mining process. It was found that they mostly remain in the heaps during leaching, where they are associated with jarosite, goethite and gypsum.

5. Discussion

5.1. Geochemical Behaviour of Daughter Radionuclides

Considerations of the likely mineral hosts for ^{210}Pb and ^{210}Po needs to include not only the geochemistry of each specific radionuclide, but the geochemical behaviour of the entire ^{238}U decay chain in the context of half-lives that range from fractions of a seconds (^{214}Po) to billions of years (^{238}U 4.5×10^9 years). The geochemical behaviours of each daughter radionuclide differ fundamentally from those of parent uranium, and thus, if released from the parent mineral and able to migrate, even if only at the sub-micron-scale, they will be readily incorporated, by virtue of ionic size and/or charge, into quite different minerals. They may potentially even undergo several "metamorphoses" before

Minerals **2018**, *8*, 211

accumulation of stable radiogenic lead within minerals such as galena or clausthalite that which do not necessarily coexist with the parent phases. Geochemical differences are particularly pronounced between U and Th, between Th and Ra, between Ra and Rn, and between Rn and Pb [2]. Figure 4 is a schematic diagram that attempts to illustrate how RN behaviour in different minerals may be viewed, also indicating how decoupling of RN within the decay chain might be achieved.

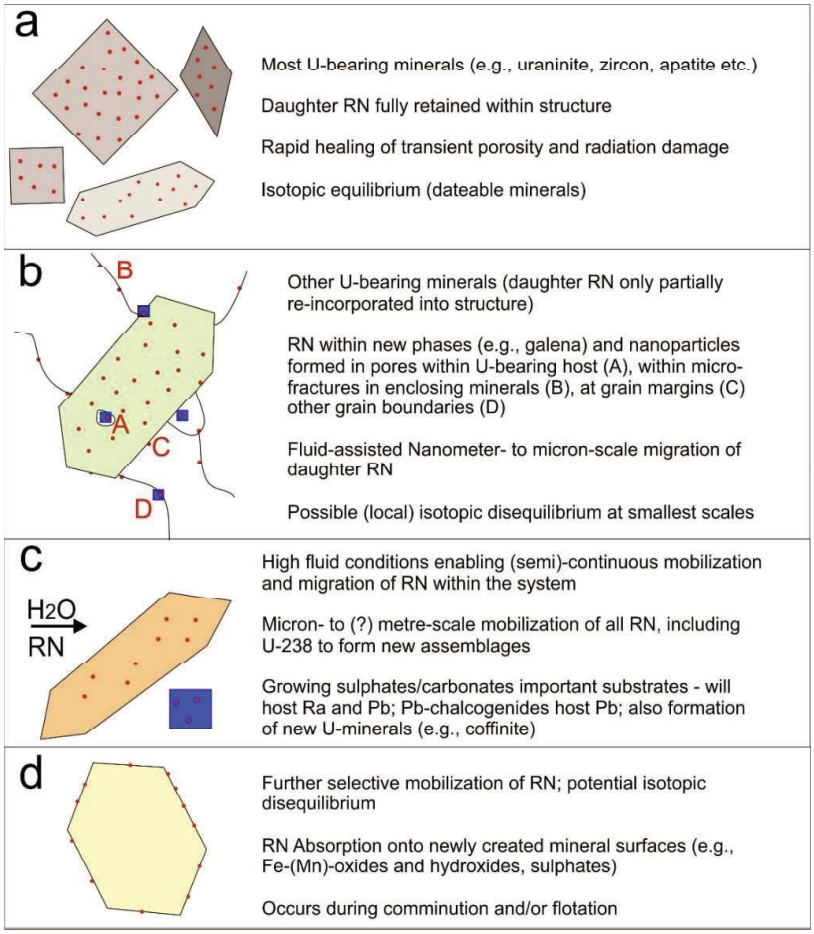


Figure 4. Schematic illustration of RN (red dots) behaviour in selected minerals within a mineralized rock, including reincorporation into parent mineral (**a**); grain-scale migration of daughter RN (**b**); fluid-assisted migration to be incorporated into new minerals (**c**) and potential adsorption of decoupled species (**d**).

Uranium can form a great variety of stable phases with different ligands. No less than 262 different uranium minerals are currently recognised, one of the largest numbers for any element in the periodic table [190]. Uranium thus belongs among a small group of elements whose mineralogical diversity is anomalous compared to its low crustal abundance. The unusual mineralogical behaviour of uranium is attributable to the unique combination of relatively large-size, high-valence and unusual coordination geometry displayed by the U^{6+} ion [191]. The hexavalent oxidation state is dominant in most U-minerals although U occurs in the tetravalent state in the most common minerals, including uraninite. Uranium mineral diversity has been amplified by Earth evolution over time with respect to oxidation state [192]. Although U^{4+} is not especially mobile, U^{6+} is highly mobile under oxidising conditions when it will readily dissolve, re-precipitating upon contact with reductants such as

sulphides or graphite. Certain minerals containing uranium undergo a process of structural breakdown (metamictisation), during which daughter radionuclides are not normally captured within the host lattice but rather migrate within or outside the mineral (e.g., [157]). In the case of uraninite, rapid annealing kinetics (e.g., [145,193]), do, however, allow for repair of radiation damage, allowing for sustained inclusion of decay product radionuclides in the mineral.

A good example of how daughter products differ geochemically from their parents is the ability for radium (^{226}Ra), unlike U or Th, to be readily enriched in the common Ba-sulphate mineral, barite. This, as examined above, takes place via direct ionic substitution (Ra^{2+} for Ba^{2+}) due to its comparable geochemical behaviour to barium with respect to charge, electronegativity and ionic size (0.143 and 0.134 nm for Ra and Ba, respectively). Although less well constrained, the potential incorporation of ^{210}Pb into galena and other Pb-bearing minerals, and of ^{210}Bi and ^{210}Po into bismuth minerals (including tellurides and other chalcogenides) may be viewed in the same way.

Decay of ^{226}Ra involves production of ^{222}Rn, a gas, which will seek to escape from the host mineral. Malczewski and Malczewski [194] have provided empirical data on ^{222}Rn and ^{220}Rn emanations from a range of metamict oxides, phosphates and silicates. These data demonstrate exponential differences in emanation rates among common minerals. Moreover, these rates vary as a function of many factors [195] closely linked to crystal structure and placing important controls on the decoupling of post-^{222}Rn decay products from parent ^{238}U. Significantly, minerals with the highest ^{238}U concentrations, notably uraninite and brannerite, showed some of the lowest ^{222}Rn and ^{220}Rn emanation coefficients. We believe that these rates—which are closely linked to crystal structure—place important controls on the decoupling of post-^{222}Rn daughter isotopes, including ^{210}Po and ^{210}Pb, from parent ^{238}U. This decoupling is expressed as secular disequilibrium on the small scale yet may not be noticed in bulk samples, or on the scale of a mineral deposit. The importance of the "radon stage" is illustrated in detailed mineralogical-isotopic study on a weathered aplite dyke [196], which showed significant (>40%) release of radon, leading to significant differences in the absolute concentrations of distributions of pre-Ra and post-Ra radionuclides.

Several studies cited in this review have given compelling evidence that particles of, or containing, ^{210}Pb and ^{210}Po are readily adsorbed onto the surfaces of clay minerals, Fe-oxides, and potentially also other minerals that can readily adsorb heavy atoms. This raises the possibility that the two radionuclides may not necessarily occur within the crystal structures of mineral phases. Evidence from disparate sources suggests that any study addressing the mineralogical deportment of ^{210}Po and ^{210}Pb must also consider that these radionuclides, or at least a significant part thereof, may not be hosted within minerals at all, but largely as nanoparticles of unknown speciation, which are adsorbed onto the surface of other minerals, such as clays, and probably, Fe-(hydr)oxides. In solid rocks, such nanoparticles may be present within micro-fractures in minerals and/or at the interfaces of mineral grains. We also believe that the affinity of ^{210}Po and ^{210}Pb for organic matter, and the potential role of organic complexes in the transport and sequestration of ^{210}Pb and ^{210}Po (e.g., biopolymers [197], should also be taken into consideration in any effort to derive a quantitative mineralogical balance for ^{210}Pb and ^{210}Po.

The physical process involved in radionuclide decay has profound consequences for understanding the mineralogical location of each daughter radionuclide. An alpha particle comprises two protons and two neutrons, the nucleus of a helium atom. When alpha decay takes place, the energy of the nucleus recoiling from alpha decay is sufficient to break chemical bonds [198], and the newly-formed nucleus (with new geochemical behaviour) will be deposited at a different site in the damaged crystal. This new position and matrix damage may make the nucleus more vulnerable to mobilisation or leaching [2]. A newly-formed radionuclide may thus migrate and be incorporated into another mineral, although this may be limited if the half-life is short, e.g., for ^{222}Rn (3.83 days) or ^{210}Bi (5 days). Cowart and Burnett [2], citing Reference [199], also make the valuable point that, if sited close to a grain boundary, the resulting nucleus may be recoiled across the grain boundary and end up in an entirely different matrix.

Roudil et al. [200] explored the creation of "bubbles" in uranium minerals from production of radiogenic helium as a product of alpha decay. This He may be concentrated in the mineral grains, or trapped at grain boundaries, also generating matrix damage. Their measurements of He outgassing from a uranium ore showed that less than 5% of the He produced was conserved, and that one-third of the residual He is occluded in the matrix and vacancy defects, and two-thirds occurred as bubbles observable by high-resolution transmission electron microscopy.

5.2. Research Trends and Future Directions

A large part of the existing literature on ^{210}Pb and ^{210}Po and their distributions in rocks and minerals concerns radioactive contamination resulting from nuclear weapons testing, uranium mining, energy generation and industrial production of fertilisers and other products from materials containing RN. These issues remain serious but have attracted markedly less research attention in the 21st century literature as industrial practices have improved. This has been compounded no doubt by the relatively short half-lives of ^{210}Pb and ^{210}Po such that their concentrations, in at least some materials produced by human activity in the past, have declined to safer levels. The contemporary literature also reflects the many ways in which radioactive waste can be efficiently treated and immobilised ([201] and references therein). Indeed, the "benefits" of man-made contamination have been highlighted in the more recent literature, notably the potential of short-lived anthropogenic radionuclides, including ^{210}Pb and ^{210}Po, as geochemical tracers for understanding processes and rates of sedimentation (e.g., [67]).

The toxicological risks from exposure to ^{210}Pb and ^{210}Po in materials from a wide range of terrestrial and marine environments are likely to remain a research focus. As older anthropogenic sources of air- and water-borne radionuclides (e.g., nuclear testing, energy generation) begin to diminish in significance, others emerge, e.g., ^{210}Po release from large-scale burning of forest biomass (e.g., [202]), or even ingestion of ^{210}Pb from calcium dietary supplements [203]. It should, however, be borne in mind that natural sources of ^{210}Pb and ^{210}Po are more significant in scale than man-made sources, e.g., from volcanic eruption. Indeed, a study of radionuclide hazards in seafood from the NW Pacific fishing area contaminated following the 2011 Fukushima nuclear accident [204] showed that despite elevated Fukushima-derived ^{90}Sr, ^{134}Cs and ^{137}Cs, these were exponentially subordinate in dose terms to natural ^{210}Pb and ^{210}Po in the same ocean area.

Despite the relative slowdown in the construction of nuclear power stations in the aftermath of the Fukushima nuclear accident, production of uranium for power generation continues to increase. Nuclear power is currently advanced as a possible low-carbon emission "green" energy alternative among the conservationist movement (e.g., [205]). In the absence of available technology to process thorium (a potential alternative fuel; [206]), increased demand necessitates a continued supply of uranium, and inevitably, as for other commodities, a need to exploit lower-grade resources, and to optimise extraction from deposits in which uranium occurs alongside other metals, notably copper, as in giant iron-oxide copper gold deposits such as Olympic Dam, South Australia.

6. Conclusions

This review has highlighted some of the many advances made in understanding the distribution of radionuclides in the environment during the past three decades. It also highlights that although the deportment and behaviour of ^{210}Pb and ^{210}Po at the scale of individual minerals is reasonably well understood, or at least predictable to some degree, there remains a paucity of direct observational data at the nano- to micron-scales to support these models. This is particularly true for metal ores and the products of their processing, for which there is an outstanding gap in knowledge. Bridging this gap is essential for generation of clean concentrates from a range of uranium-bearing ores.

Characterisation of short half-life radionuclides down to the atomic scale is now possible via use of a combination of nanoscale techniques: nanoSIMS isotope mapping [163]; scanning transmission electron microscopy with electron energy-loss spectroscopy (e.g., [207]); and high angle annular dark-field scanning transmission electron microscopy on foils prepared in-situ using focused ion

beam methods (e.g., [162,208,209]). Valuable additional constraints on RN deportment may also come from the application of nanoscale analysis techniques to radioisotope dating of minerals within hydrothermal mineral deposits forming on the present-day seafloor [210,211]. Despite these crucial advances, a fully quantitative understanding of the physical form of ^{210}Pb and ^{210}Po, and the quantitative mineral deportment of these RN in solid media, remains elusive. Researchers can, however, expect to respond to these outstanding challenges by capitalising on micro-/nanoanalytical technology, which is rapidly advancing in terms of both spatial resolution and analytical sensitivity. This will enable reliable, predictive information on the physical state of ^{210}Pb, ^{210}Po and other RN to be communicated to stakeholders, including mining companies and environmental authorities.

Author Contributions: N.J.C. conceived and coordinated this contribution. He wrote the paper in collaboration with K.J.E. and C.L.C. All other authors (M.R., D.J.L., D.S.S., N.D.O., T.H and S.R.G.) contributed otherwise unpublished data, literature and valuable discussion.

Acknowledgments: This research is a contribution to the ARC Research Hub on Australian Copper-Uranium (project number: IH130200033), funded by the Australian Research Council, BHP Olympic Dam, OZ Minerals and the South Australian Department of State Development. The authors appreciate valuable comments from three *Minerals* reviewers as well as two anonymous reviewers of a previous incarnation of this text. These have helped us improve the clarity of this manuscript.

Conflicts of Interest: The authors declare no conflict of interest. The project sponsors approve publication of the manuscript.

References

1. Lehto, J.; Hou, X. *Chemistry and Analysis of Radionuclides–Laboratory Techniques and Methodology*; Wiley-VCH: Weinheim, Germany, 2011.
2. Cowart, J.B.; Burnett, W.C. The distribution of uranium and thorium decay-series radionuclides in the environment–A review. *J. Environ. Q.* **1994**, *23*, 651–662. [CrossRef]
3. Strominger, D.; Hollander, J.M.; Seaborg, G.T. Table of isotopes. *Rev. Mod. Phys.* **1958**, *30*, 585. [CrossRef]
4. Fry, C.; Thoennessen, M. Discovery of the thallium, lead, bismuth, and polonium isotopes. *At. Data Nucl. Data Tables* **2013**, *99*, 365–389. [CrossRef]
5. Harrison, J.; Leggett, R.; Lloyd, D.; Phipps, A.; Scott, B. Polonium-210 as a poison. *J. Radiol. Prot.* **2007**, *27*, 17–40. [CrossRef] [PubMed]
6. Figgins, P.E. *The Radiochemistry of Polonium. National Academy of Sciences Nuclear Science Series*; U.S. Atomic Energy Commission: Washington, DC, USA, 1961.
7. Lane, D.J.; Cook, N.J.; Grano, S.R.; Ehrig, K. Selective leaching of penalty elements from copper concentrates: A review. *Miner. Eng.* **2016**, *98*, 110–121. [CrossRef]
8. International Atomic Energy Agency (IAEA). *Regulations for the Safe Transport of Radioactive Material*; IAEA: Vienna, Austria, 2012.
9. Parfenov, Y.D. Polonium 210 in the environment and in the human organism. *At. Energy Rev.* **1974**, *12*, 75–143. [PubMed]
10. Coppin, F.; Roussel-Debet, S. Comportement du ^{210}Po en milieu terrestre: Revue bibliographique. *Radioprotection* **2004**, *39*, 39–58. [CrossRef]
11. Landa, E.R. Naturally occurring radionuclides from industrial sources: Characteristics and fate in the environment. *Radioact. Environ.* **2007**, *10*, 211–237.
12. Persson, B.R.R.; Holm, E. Polonium-210 and lead-210 in the terrestrial environment: A historical review. *J. Environ. Radioact.* **2011**, *102*, 420–429. [CrossRef] [PubMed]
13. Baskaran, M. Po-210 and Pb-210 as atmospheric tracers and global atmospheric Pb-210 fallout: A Review. *J. Environ. Radioact.* **2011**, *102*, 500–513. [CrossRef] [PubMed]
14. Shannon, L.V.; Cherry, R.D.; Orren, M.J. Polonium-210 and lead-210 in the marine environment. *Geochim. Cosmochim. Acta* **1970**, *34*, 701–711. [CrossRef]
15. Nozaki, Y.; Thomson, J.; Turekian, K.K. The distribution of ^{210}Pb and ^{210}Po in the surface waters of the Pacific Ocean. *Earth Plan. Sci. Lett.* **1976**, *32*, 304–312. [CrossRef]
16. Bacon, M.P.; Brewer, P.G.; Spencer, D.W.; Murray, J.W.; Goddard, J. Lead-210, polonium-210, manganese and iron in the Cariaco Trench. *Deep Sea Res. Part A Oceanogr. Res. Pap.* **1980**, *27*, 119–135. [CrossRef]

17. Bacon, M.P.; Huh, C.-A.; Fleer, A.P.; Deuser, W.G. Seasonality in the flux of natural radionuclides and plutonium in the deep Sargasso Sea. *Deep Sea Res. Part A Oceanogr. Res. Pap.* **1985**, *32*, 273–286. [CrossRef]
18. González-Labajo, J.; Bolívar, J.P.; García-Tenorio, R. Natural radioactivity in waters and sediments from a Spanish mining river. *Radiat. Phys. Chem.* **2001**, *61*, 643–644. [CrossRef]
19. Balistrieri, L.S.; Murray, J.W.; Paul, B. The geochemical cycling of stable Pb, ^{210}Pb, and ^{210}Po in seasonally anoxic Lake Sammamish, Washington, USA. *Geochim. Cosmochim. Acta* **1995**, *59*, 4845–4861. [CrossRef]
20. Andrews, J.N.; Ford, D.J.; Hussain, N.; Trivedi, D.; Youngman, M.J. Natural radioelement solution by circulating groundwaters in the Stripa granite. *Geochim. Cosmochim. Acta* **1989**, *53*, 1791–1802. [CrossRef]
21. Harada, K.; Burnett, W.C.; LaRock, P.A.; Cowart, J.B. Polonium in Florida groundwater and its possible relationship to the sulfur cycle and bacteria. *Geochim. Cosmochim. Acta* **1989**, *53*, 143–150. [CrossRef]
22. Lehto, J.; Kelokaski, P.; Vaaramaa, K.; Jaakkola, T. Soluble and particle-bound ^{210}Po and ^{210}Pb in groundwaters. *Radiochim. Acta* **1999**, *85*, 149–155. [CrossRef]
23. Seiler, R.L.; Stillings, L.L.; Cutler, N.; Salonen, L.; Outola, I. Biogeochemical factors affecting the presence of ^{210}Po in groundwater. *Appl. Geochem.* **2011**, *26*, 526–539. [CrossRef]
24. Ortega, X.; Vallés, I.; Serrano, I. Natural radioactivity in drinking water in Catalonia (Spain). *Environ. Int.* **1997**, *22* (Suppl. 1), S347–S354. [CrossRef]
25. Katzlberger, C.; Wallner, G.; Irlweck, K. Determination of ^{210}Pb, ^{210}Bi and ^{210}Po in natural drinking water. *J. Radioanal. Nucl. Chem.* **2001**, *249*, 191–196.
26. Skwarzec, B.; Strumińska, D.I.; Boryło, A. Radionuclides of ^{210}Po, ^{234}U and ^{238}U in drinking bottled mineral water in Poland. *J. Radioanal. Nucl. Chem.* **2003**, *256*, 361–364. [CrossRef]
27. Simon, S.L.; Ibrahim, S.A. The plant/soil concentration ratio for calcium, radium, lead, and polonium: Evidence for non-linearity with reference to substrate concentration. *J. Environ. Radioact.* **1987**, *5*, 123–142. [CrossRef]
28. Martínez-Aguirre, A.; García-Orellana, I.; García-León, M. Transfer of natural radionuclides from soils to plants in a marsh enhanced by the operation of non-nuclear industries. *J. Environ. Radioact.* **1997**, *35*, 149–171. [CrossRef]
29. Malczewski, D.; Źaba, J. ^{222}Rn and ^{220}Rn concentrations in soil gas of Karkonosze-Izera Block (Sudetes, Poland). *J. Environ. Radioact.* **2007**, *92*, 144–164. [CrossRef] [PubMed]
30. Heyraud, M.; Cherry, R.D.; Oschadleus, H.-D.; Augustyn, C.J.; Cherry, M.I.; Sealy, J.C. Polonium-210 and Lead-210 in edible molluscs from near the Cape of Good Hope: Sources of variability in polonium-210 concentrations. *J. Environ. Radioact.* **1994**, *24*, 253–272. [CrossRef]
31. Thomas, P.A.; Gates, T.E. Radionuclides in the lichen-caribou-human food chain near uranium mining operations in northern Saskatchewan, Canada. *Environ. Health Perspect.* **1999**, *107*, 527–537. [CrossRef] [PubMed]
32. Carvalho, F.P. Polonium (^{210}Po) and lead (^{210}Pb) in marine organisms and their transfer in marine food chains. *J. Environ. Radioact.* **2011**, *102*, 462–472. [CrossRef] [PubMed]
33. Rosner, G.; Bunzl, K.; Hötzl, H.; Winkler, R. Low level measurements of natural radionuclides in soil samples around a coal-fired power plant. *Nucl. Instrum. Meth. Phys. Res.* **1984**, *223*, 585–589. [CrossRef]
34. Sahu, S.K.; Tiwari, M.; Bhangare, R.C.; Pandit, G.G. Enrichment and particle size dependence of polonium and other naturally occurring radionuclides in coal ash. *J. Environ. Radioact.* **2014**, *138*, 421–426. [CrossRef] [PubMed]
35. Schmidt, A.P. Lead precipitates from natural gas production installations. *J. Geochem. Explor.* **1998**, *62*, 193–200. [CrossRef]
36. Schmidt, A.P.; Hartog, F.A.; Van Os, B.J.H.; Schuiling, R.D. Production of ^{210}Pb from a Slochteren sandstone gas reservoir. *Appl. Geochem.* **2000**, *15*, 1317–1329. [CrossRef]
37. Al Attar, L.; Doubal, W.; Al Abdullah, J.; Khalily, H.; Abdul Ghani, B.; Safia, B. Characterization of NORM solid waste produced from the petroleum industry. *Environ. Tech.* **2015**, *36*, 1104–1113. [CrossRef] [PubMed]
38. Seen, A.; Townsend, A.; Atkinson, B.; Ellison, J.; Harrison, J.; Heijnis, H. Determining the history and sources of contaminants in sediments in the Tamar Estuary, Tasmania, using ^{210}Pb dating and stable Pb isotope analyses. *Environ. Chem.* **2004**, *1*, 49–54. [CrossRef]
39. Schindler, M.; Kamber, B.S. High-resolution lake sediment reconstruction of industrial impact in a world-class mining and smelting center, Sudbury, Ontario, Canada. *Appl. Geochem.* **2013**, *37*, 102–116. [CrossRef]

40. Matthews, K.M.; Kim, C.-K.; Martin, P. Determination of ^{210}Po in environmental materials: A review of analytical methodology. *Appl. Radiat. Isot.* **2007**, *65*, 267–279. [CrossRef] [PubMed]
41. Henricsson, F.; Ranebo, Y.; Holm, E.; Roos, P. Aspects on the analysis of ^{210}Po. *J. Environ. Radioact.* **2011**, *102*, 415–419. [CrossRef] [PubMed]
42. Flynn, W.W. The determination of low levels of polonium-210 in environmental materials. *Anal. Chim. Acta* **1968**, *43*, 221–227. [CrossRef]
43. Clayton, R.F.; Bradley, E.J. A cost effective method for the determination of ^{210}Po and ^{210}Pb in environmental materials. *Sci. Total Environ.* **1995**, *173–174*, 23–28. [CrossRef]
44. Jia, G.G.; Torri, G. Determination of ^{210}Pb and ^{210}Po in soil or rock samples containing refractory matrices. *Appl. Radiat. Isot.* **2007**, *65*, 1–8. [CrossRef] [PubMed]
45. Jia, G.G.; Belli, M.; Blasi, M.; Marchetti, A.; Rosamilia, S.; Sansone, U. Determination of ^{210}Pb and ^{210}Po in mineral and biological environmental samples. *J. Radioanal. Nucl. Chem.* **2001**, *247*, 491–499. [CrossRef]
46. Jia, G.G.; Belli, M.; Liu, S.; Sansone, U.; Xu, C.H.; Rosamilia, S.; Xiao, X.; Gaudino, S.; Chen, L.; Yang, H. The fractionation and determination procedures for the speciation of ^{210}Pb and ^{210}Po in soil samples. *Anal. Chim. Acta* **2006**, *562*, 51–58. [CrossRef]
47. Pud'homme, F.; Morency, M.; Freyer, K.; Weiss, H.; Bourne, J.; Daus, B.; Fontaine, D.; Mattusch, J.; Mineau, R.; Préda, M.; et al. Surfactant separation as a technique for physical and chemical characterization of ore processing residues. *Sci. Total Environ.* **1999**, *243/244*, 9–20.
48. Allard, P.; Aiuppa, A.; Bani, P.; Métrich, N.; Bertagnini, A.; Gauthier, P.-J.; Shinohara, H.; Sawyer, G.; Parello, F.; Bagnato, E.; et al. Prodigious emission rates and magma degassing budget of major, trace and radioactive volatile species from Ambrym basaltic volcano, Vanuatu island Arc. *J. Volc. Geotherm. Res.* **2016**, *322*, 119–143. [CrossRef]
49. Lambert, G.; Le Cloarec, M.-F.; Ardouin, B.; Le Roulley, J.-C. Volcanic emission of radionuclides and magma dynamics. *Earth Plan. Sci. Lett.* **1985**, *76*, 185–192. [CrossRef]
50. Gauthier, P.-J.; Le Cloarec, M.-F.; Condomines, M. Degassing processes at Stromboli volcano inferred from short-lived disequilibria (^{210}Pb–^{210}Bi–^{210}Po) in volcanic gases. *J. Volc. Geotherm. Res.* **2000**, *102*, 1–19. [CrossRef]
51. Rubin, K.H.; Macdougall, J.D.; Perfit, M.R. ^{210}Po–^{210}Pb dating of recent volcanic eruptions on the sea floor. *Nature* **1994**, *368*, 841–844. [CrossRef]
52. Le Cloarec, M.-F.; Gauthier, P.-J. Merapi Volcano, Central Java, Indonesia: A case study of radionuclide behavior in volcanic gases and its implications for magma dynamics at andesitic volcanoes. *J. Geophys. Res.* **2003**, *108*, 2243. [CrossRef]
53. Gill, J.B.; Williams, R.W. Th isotope and U-series studies of subduction-related volcanic rocks. *Geochim. Cosmochim. Acta* **1990**, *54*, 1427–1442. [CrossRef]
54. Berlo, K.; Turner, S. ^{210}Pb–^{226}Ra disequilibria in volcanic rocks. *Earth Plan. Sci. Lett.* **2010**, *296*, 155–164. [CrossRef]
55. Turner, S.; Reagan, M.; Vigier, N.; Bourdon, B. Origins of ^{210}Pb–^{226}Ra disequilibria in basalts: New insights from the 1978 Asal Rift eruption. *Geochem. Geophys. Geosyst.* **2012**, *13*, Q07002. [CrossRef]
56. Artemieva, I.M.; Thybo, H.; Jakobsen, K.; Sørensen, N.K.; Nielsen, L.S.K. Heat production in granitic rocks: Global analysis based on a new data compilation GRANITE2017. *Earth-Sci. Rev.* **2017**, *172*, 1–26. [CrossRef]
57. Le Cloarec, M.-F.; Pennisi, M.; Corazza, E.; Lambert, G. Origin of fumarolic fluids emitted from a nonerupting volcano: Radionuclide constraints at Vulcano (Aeolian Islands, Italy). *Geochim. Cosmochim. Acta* **1994**, *58*, 4401–4410. [CrossRef]
58. Voltaggio, M.; Tuccimei, P.; Branca, M.; Romoli, L. U-series disequilibrium radionuclides in sulphur incrustations from the fumarolic field of Vulcano Island. *Geochim. Cosmochim. Acta* **1998**, *62*, 2111–2127. [CrossRef]
59. Garavelli, A.; Laviano, R.; Vurro, F. Sublimate deposition from hydrothermal fluids at the Fossa crater (Vulcano, Italy). *Eur. J. Miner.* **1997**, *9*, 423–432. [CrossRef]
60. Vurro, F.; Garavelli, A.; Garbarino, C.; Moëlo, Y.; Borodaev, Y.S. Rare sulfosalts from Vulcano, Aeolian Islands, Italy. II. Mozgovaite, $PbBi_4(S,Se)_7$, a new mineral species. *Can. Miner.* **1999**, *37*, 1499–1506.
61. Borodaev, Y.S.; Garavelli, A.; Garbarino, C.; Grillo, S.M.; Mozgova, N.N.; Organova, N.I.; Trubkin, N.V.; Vurro, F. Rare sulfosalts from Vulcano, Aeolian Islands, Italy. III. Wittite and cannizzarite. *Can. Miner.* **2000**, *38*, 23–34. [CrossRef]

62. Garavelli, A.; Mozgova, N.N.; Orlandi, P.; Bonaccorsi, E.; Pinto, D.; Moëlo, Y.; Borodaev, Y.S. Rare sulfosalts from vulcano, Aeolian Islands, Italy. VI. Vurroite, $Pb_{20}Sn_2(Bi,As)_{22}S_{54}Cl_6$, a new mineral species. *Can. Miner.* **2005**, *43*, 703–711. [CrossRef]
63. Boisson, F.; Miquel, J.-C.; Cotret, O.; Fowler, S.W. ^{210}Po and ^{210}Pb cycling in a hydrothermal vent zone in the coastal Aegean Sea. *Sci. Total Environ.* **2001**, *281*, 111–119. [CrossRef]
64. Charmasson, S.; Sarradin, P.-M.; Le Faouder, A.; Agarande, M.; Loyen, J.; Desbruyères, D. High levels of natural radioactivity in biota from deep-sea hydrothermal vents: A preliminary communication. *J. Environ. Radioact.* **2009**, *100*, 522–526. [CrossRef] [PubMed]
65. Begy, R.C.; Dumitru, O.A.; Simon, H.; Steopoaie, I. An improved procedure for the determination of ^{210}Po by alpha spectrometry in sediments samples from Danube Delta. *J. Radioanal. Nucl. Chem.* **2015**, *303*, 2553–2557. [CrossRef]
66. Farmer, J.G.; MacKenzie, A.B.; Graham, M.C.; Macgregor, K.; Kirika, A. Development of recent chronologies and evaluation of temporal variations in Pb fluxes and sources in lake sediment and peat cores in a remote, highly radiogenic environment, Cairngorm Mountains, Scottish Highlands. *Geochim. Cosmochim. Acta* **2015**, *156*, 25–49. [CrossRef]
67. Franklin, R.L.; Fávaro, D.I.T.; Damatto, S.R. Trace metal and rare earth elements in a sediment profile from the Rio Grande Reservoir, São Paulo, Brazil: Determination of anthropogenic contamination, dating, and sedimentation rates. *J. Radioanal. Nucl. Chem.* **2015**, *307*, 99–110. [CrossRef]
68. Jones, P.; Maiti, K.; McManus, J. Lead-210 and Polonium-210 disequilibria in the northern Gulf of Mexico hypoxic zone. *Mar. Chem.* **2015**, *169*, 1–15. [CrossRef]
69. Swarzenski, P.W. ^{210}Pb Dating. In *Encyclopedia of Scientific Dating Methods*; Rink, W.J., Thompson, J.W., Eds.; Springer: Berlin, Germany, 2015; pp. 626–631.
70. Dahlkamp, F.J. *Uranium Ore Deposits*; Springer: Berlin, Germany, 1993; 460p.
71. Martin, A.; Mead, S.; Wade, B.O. *Nuclear Science and Technology: Materials Containing Natural Radionuclides in Enhanced Concentrations*; Final report for European Commission Directorate-General, Environment, Nuclear Safety and Civil Protection; Alan Martin Associates: Penetanguishene, ON, Canada, 1997; 104p.
72. Cooper, J.R.; Randle, K.; Sokhi, R.S. *Radioactive Releases in the Environment: Impact and Assessment*; John Wiley and Sons: Hoboken, NJ, USA, 2003; 773p.
73. Cooper, M.B. *Naturally Occurring Radioactive Materials (NORM) in Australian Industries–Review of Current Inventories and Future Generation: A Report Prepared for the Radiation Health and Safety Advisory Council*; EnviroRad Services Pty. Ltd.: Beaumaris, Austrilia, 2005; 40p.
74. García-Tenorio, R. ^{210}Po and ^{210}Pb in NORM mineral processing industries. In Proceedings of the EU-NORM 1st International Symposium, Tallinn, Estonia, 5–8 June 2012; pp. 202–209.
75. Xhixha, G.; Bezzon, G.P.; Broggini, C.; Buso, G.P.; Caciolli, A.; Callegari, I.; De Bianchi, S.; Fiorentini, G.; Guastaldi, E.; Kaçeli Xhixha, M.; et al. The worldwide NORM production and a fully automated gamma-ray spectrometer for their characterization. *J. Radioanal. Nucl. Chem.* **2013**, *295*, 445–457. [CrossRef]
76. Fernandes, H.M.; Franklin, M.R.; Veiga, L.H.S.; Freitas, P.; Gomiero, L.A. Management of uranium mill tailing: Geochemical processes and radiological risk assessment. *J. Environ. Radioact.* **1996**, *30*, 69–95. [CrossRef]
77. Landa, E.R. Leaching of radionuclides from uranium ore and mill tailings. *Uranium* **1982**, *1*, 53–64.
78. Landa, E.R. Uranium mill tailings: Nuclear waste and natural laboratory for geochemical and radioecological investigations. *J. Environ. Radioact.* **2004**, *77*, 1–27. [CrossRef] [PubMed]
79. Landa, E.R.; Bush, C.A. Geochemical hosts of solubilized radionuclides in uranium mill tailings. *Hydrometallurgy* **1990**, *24*, 361–372. [CrossRef]
80. Shearer, S.D., Jr.; Lee, G.F. Leachability of radium-226 from uranium mill solids and river sediments. *Health Phys.* **1964**, *10*, 217–227. [CrossRef] [PubMed]
81. Seeley, F.G. Problems in the separation of radium from uranium mill tailings. *Hydrometallurgy* **1977**, *2*, 249–263. [CrossRef]
82. Somot, S.; Pagel, M.; Thiry, J. Speciation of radium in uranium mill tailings from Ecarpière (Vendée, France). *Comptes Rendues Acad. Sci.* **1997**, *325*, 111–118.
83. Landa, E.R.; Stieff, L.R.; Germani, M.S.; Tanner, A.B.; Evans, J.R. Intense alpha particle emitting crystallites in uranium mill wastes. *Nucl. Geophys.* **1994**, *8*, 443–454.

84. Morrison, S.J.; Cahn, L.S. Mineralogical residence of alpha-emitting contamination and implications for mobilization from uranium mill tailings. *J. Contam. Hydrol.* **1991**, *8*, 1–21. [CrossRef]
85. Campbell, K.M.; Gallegos, T.J.; Landa, E.R. Biogeochemical aspects of uranium mineralization, mining, milling, and remediation. *Appl. Geochem.* **2015**, *57*, 206–235. [CrossRef]
86. Lawrence, C.E. Measurement of ^{222}Rn Exhalation Rates and ^{210}Pb Deposition Rates in a Tropical Environment. Unpublished Ph.D. Thesis, Queensland University of Technology, Brisbane City, Australia, 2006.
87. BHP Billiton Olympic Dam Expansion. Draft Environmental Impact Statement 2009. Appendix S. Uranium and Radiation. Available online: www.bhp.com (accessed on 10 April 2018).
88. Weiss, H.; Morency, M.; Freyer, K.; Bourne, J.; Fontaine, D.; Ghaleb, B.; Mineau, R.; Möder, M.; Morgenstern, P.; Popp, P.; et al. Physical and chemical characterization of a complexly contaminated scrubber dust–A by-product of copper smelting in Sachsen-Anhalt, Germany. *Sci. Total Environ.* **1997**, *203*, 65–78. [CrossRef]
89. Schreck, P. Flue dust from copper shale smelting in Central Germany: Environmental pollution and its prevention. In Proceedings of the International Mine Water Association Congress, Sevilla, Spain, 13–17 September 1999; pp. 163–167.
90. Freyer, K.; Morency, M.; Weiss, H.; Treutler, H.C.; Bourne, J. High-Alpha-Active Particles in Industrial and Mining Residues. In Proceedings of the 10th International Congress of the International Radiation Protection Association on Harmonization of Radiation, Human Life and the Ecosystem, Japan Health Physics Society, Tokyo, Japan, 14–19 May 2000.
91. Schubert, M.; Morgenstern, P.; Wennrich, R.; Freyer, K.; Paschke, A.; Weiss, H. The weathering behavior of complexly contaminated ore processing residues in the region of Mansfeld/Germany. *Mine Water Environ.* **2003**, *22*, 2–6. [CrossRef]
92. Schubert, M.; Osenbrück, K.; Knöller, K. Using stable and radioactive isotopes for the investigation of contaminant metal mobilization in a metal mining district. *Appl. Geochem.* **2008**, *23*, 2945–2954. [CrossRef]
93. Morency, M.; Weiss, H.; Freyer, K.; Bourne, J.; Fontaine, D.; Mineau, R.; Möder, M.; Morgenstern, P.; Popp, P.; Preda, M.; et al. Oxidation treatment of a sulphide-bearing scrubber dust from the Mansfeld Region, Germany: Organic and inorganic phase changes and multi-element partition coefficients between liquid and solid phases. *Sci. Total Environ.* **1998**, *223*, 87–97. [CrossRef]
94. Chau, N.D.; Jodłowski, P.; Kalia, S.J.; Olko, P.; Chruściel, E.; Maksymowicz, A.; Waligórski, M.; Bilski, P.; Budzanowski, M. Natural radiation and its hazard in copper ore mines in Poland. *Acta Geophys.* **2008**, *56*, 505–517. [CrossRef]
95. Hipkin, J.; Paynter, R.A. Radiation Exposures to the Workforce from Naturally Occurring Radioactivity in Industrial Processes. *Radiat. Prot. Dosim.* **1991**, *36*, 97–100. [CrossRef]
96. Harvey, M.P.; Hipkin, J.; Simmonds, J.R.; Mayall, A.; Cabianca, T.; Fayers, C.; Haslam, I. *Radiological Consequences of Waste Arising with Enhanced Natural Radioactivity Content from Special Metal and Ceramic Processes*; European Commission: Environment, Nuclear Safety and Civil Protection; European Commission: Brussels, Belgium, 1994.
97. Baxter, M.S.; MacKenzie, A.B.; East, B.W.; Scott, E.M. Natural decay series radionuclides in and around a large metal refinery. *J. Environ. Radioact.* **1996**, *32*, 115–133. [CrossRef]
98. Rutherford, P.M.; Dudas, M.J.; Samek, R.A. Environmental impacts of phosphogypsum: A review. *Sci. Total Environ.* **1994**, *149*, 1–38. [CrossRef]
99. Rutherford, P.M.; Dudas, M.J.; Arocena, J.M. Radium in phosphogypsum leachates. *J. Environ. Q.* **1995**, *24*, 307–314. [CrossRef]
100. Rutherford, P.M.; Dudas, M.J.; Arocena, J.M. Heterogeneous distribution of radionuclides, barium and strontium in phosphogypsum by-product. *Sci. Total Environ.* **1996**, *180*, 201–209. [CrossRef]
101. Poole, A.J.; Allington, D.J.; Baxter, A.J.; Young, A.K. The natural radioactivity of phosphate ore and associated waste products discharged into the eastern Irish Sea from a phosphoric acid production plant. *Sci. Total Environ.* **1995**, *173–174*, 137–149. [CrossRef]
102. Sam, A.K.; Holm, E. The natural radioactivity in phosphate deposits from Sudan. *Sci. Total Environ.* **1995**, *162*, 173–178. [CrossRef]
103. Burnett, W.C.; Schultz, M.H.; Hull, C.D. Radionuclide flow during the conversion of phosphogypsum to ammonium sulfate. *J. Environ. Radioact.* **1996**, *32*, 33–51. [CrossRef]

104. Hull, C.D.; Burnett, W.C. Radiochemistry of Florida phosphogypsum. *J. Environ. Radioact.* **1996**, *32*, 213–238. [CrossRef]
105. Travesí, A.; Gascó, C.; Pozuelo, M.; Palomares, J.; García, M.R.; Pérez del Villar, L. Distribution of natural radioactivity within an estuary affected by releases from the phosphate industry. *Stud. Environ. Sci.* **1997**, *68*, 267–279.
106. Mazzilli, B.; Palmiro, V.; Saueia, C.; Nisti, M.B. Radiochemical characterization of Brazilian phosphogypsum. *J. Environ. Radioact.* **2000**, *49*, 113–122. [CrossRef]
107. Silva, N.C.; Fernandes, E.A.N.; Ciprianai, M.; Taddei, M.H.T. The natural radioactivity of Brazilian phosphogypsum. *J. Radioanal. Nucl. Chem.* **2001**, *249*, 251–255.
108. Beddow, H.; Black, S.; Read, D. Naturally occurring radioactive material (NORM) from a former phosphoric acid processing plant. *J. Environ. Radioact.* **2006**, *86*, 289–312. [CrossRef] [PubMed]
109. Aoun, M.; El Samrani, A.G.; Lartiges, B.S.; Kazpard, V.; Saad, Z. Releases of phosphate fertilizer industry in the surrounding environment: Investigation on heavy metals and polonium-210 in soil. *J. Environ. Sci.* **2010**, *22*, 1387–1397. [CrossRef]
110. Hurst, F.J.; Arnold, W.D. A discussion of uranium control in phosphogypsum. *Hydrometallurgy* **1982**, *9*, 69–82. [CrossRef]
111. Pennders, R.M.J.; Köster, H.W.; Lembrechts, J.F. Characteristics of ^{210}Po and ^{210}Pb in effluents from phosphate-processing industries: A first orientation. *Radiat. Prot. Dosim.* **1992**, *45*, 737–740. [CrossRef]
112. International Atomic Energy Agency (IAEA). *The Extent of Environmental Contamination by Naturally Occurring Radioactive Material (NORM) and Technological Options for Mitigation*; IAEA Draft Technical Report; IAEA: Vienna, Austria, 2002.
113. Zielinski, R.A.; Budahn, J.R. Mode of occurrence and environmental mobility of oil-field radioactive material at US Geological Survey research site B, Osage-Skiatook Project, northeastern Oklahoma. *Appl. Geochem.* **2007**, *22*, 2125–2137. [CrossRef]
114. Al Attar, L.; Safia, B.; Abdul Ghani, B.; Al Abdullah, J. Recovery of NORM from scales generated by oil extraction. *J. Environ. Radioact.* **2016**, *153*, 149–155. [CrossRef] [PubMed]
115. Clarke, L.B.; Sloss, L.L. *Trace Elements–Emissions from Coal Combustion and Gasification*; IEA Coal Research: London, UK, 1992.
116. Tadmore, J. Radioactivity from coal-fired power plants: A review. *J. Environ. Radioact.* **1986**, *4*, 177–204. [CrossRef]
117. United Nations Scientific Committee on the Effects of Atomic Radiation (UNSCEAR). *Ionizing Radiation: Sources and Biological Effects*; United Nations: New York, NY, USA, 1982.
118. Coles, D.G.; Ragaini, R.C.; Ondov, J.M. Behaviour of natural radionuclides in western coal-fired power plants. *Environ. Sci. Tech.* **1978**, *12*, 442–446. [CrossRef]
119. Senior, C.L.; Helble, J.J.; Sarofim, A.F. Emissions of mercury, trace elements, and fine particles from stationary combustion sources. *Fuel Proc. Technol.* **2000**, *65–66*, 263–288. [CrossRef]
120. Roeck, D.R.; Reavey, T.C.; Hardin, J.M. Partitioning of natural radionuclides in the waste streams of coal-fired utilities. *Health Phys.* **1987**, *52*, 311–323. [CrossRef] [PubMed]
121. UNSCEAR. *Sources and Effects of Ionizing Radiation. Report to the General Assembly with Scientific Annexes*; United Nations: New York, NY, USA, 2010; Volume 1, 245p.
122. Barber, D.E.; Giorgio, H.R. Gamma-ray Activity in Bituminous, Subbituminous and Lignite Coals. *Health Phys.* **1977**, *32*, 83–88. [CrossRef] [PubMed]
123. Fardy, J.; McOrist, G.; Farrar, Y. Neutron activation analysis and radioactivity measurements of Australian coals and fly ashes. *J. Radioanal. Nucl. Chem.* **1989**, *133*, 217–226. [CrossRef]
124. Bhangare, R.; Tiwari, M.; Ajmal, P.; Sahu, S.; Pandit, G. Distribution of natural radioactivity in coal and combustion residues of thermal power plants. *J. Radioanal. Nucl. Chem.* **2014**, *300*, 17–22. [CrossRef]
125. Lauer, N.E.; Hower, J.C.; Hsu-Kim, H.; Taggart, R.K.; Vengosh, A. Naturally occurring radioactive materials in coals and coal combustion residuals in the United States. *Environ. Sci. Tech.* **2015**, *49*, 11227–11233. [CrossRef] [PubMed]
126. Zielinski, R.A.; Finkelman, R.B. Radioactive Elements in Coal and Fly Ash: Abundance, Forms and Environmental Significance. U.S. Geological Survey Fact Sheet FS-163-97; 1997; 4p. Available online: http://greenwood.cr.usgs.gov/energy/factshts/163-97/FS-163-97.html (accessed on 11 May 2018).

127. Długosz-Lisiecka, M. Excess of ^{210}polonium activity in the surface urban atmosphere. Part (1) fluctuation of the ^{210}Po excess in the air. *Environ. Sci. Process. Impacts* **2015**, *17*, 458–464.
128. Długosz-Lisiecka, M. Excess of polonium-210 activity in the surface urban atmosphere. Part 2: Origin of ^{210}Po excess. *Environ. Sci. Process. Impacts* **2015**, *17*, 465–470.
129. Häsänen, E.; Pohjola, V.; Hahkala, M.; Zilliacus, R.; Wickström, K. Emissions from power plants fuelled by peat, coal, natural gas and oil. *Sci. Total Environ.* **1986**, *54*, 29–51. [CrossRef]
130. Gallyas, M.; Török, I. Natural Radioactivity of Raw Materials and Products in the Cement Industry. *Radiat. Prot. Dosim.* **1986**, *7*, 69–71. [CrossRef]
131. Stojanovska, Z.; Nedelkovskia, D.; Ristovab, M. Natural radioactivity and human exposure by raw materials and end product from cement industry used as building materials. *Radiat. Meas.* **2010**, *45*, 969–972. [CrossRef]
132. Eštoková, A.; Palaščáková, L. Assessment of Natural Radioactivity Levels of Cements and Cement Composites in the Slovak Republic. *Int. J. Environ. Res. Public Health* **2013**, *10*, 7165–7179. [CrossRef] [PubMed]
133. Guillén, J.; Tejado, J.J.; Baeza, A.; Salas, A.; Muñoz-Muñoz, J.G. Environmental impact of a granite processing factory as source of naturally occurring radionuclides. *Appl. Geochem.* **2014**, *47*, 122–129. [CrossRef]
134. Harrison, J.; Heijnis, H.; Caprarelli, G. Historical pollution variability from abandoned mine sites, Greater Blue Mountains World Heritage Area, New South Wales, Australia. *Environ. Geol.* **2003**, *43*, 680–687.
135. Plater, A.J.; Appleby, P.G. Tidal sedimentation in the Tees estuary during the 20th century: Radionuclide and magnetic evidence of pollution and sedimentary response. *Estuar. Coast. Shelf Sci.* **2004**, *60*, 179–192. [CrossRef]
136. Le Roux, G.; Weiss, D.; Grattan, J.; Givelet, N.; Krachler, M.; Cheburkin, A.; Rausch, N.; Kober, B.; Shotyk, W. Identifying the sources and timing of ancient and medieval atmospheric lead pollution in England using a peat profile from Lindow bog, Manchester. *J. Environ. Monit.* **2004**, *6*, 502–510. [CrossRef] [PubMed]
137. Cloy, J.M.; Farmer, J.G.; Graham, M.C.; MacKenzie, A.B.; Cook, G.T. A comparison of antimony and lead profiles over the past 2500 years in Flanders Moss ombrotrophic peat bog, Scotland. *J. Environ. Monit.* **2005**, *7*, 1137–1147. [CrossRef] [PubMed]
138. Mayer, B.; Alpay, S.; Gould, W.D.; Lortie, L.; Rosa, F. The onset of anthropogenic activity recorded in lake sediments in the vicinity of the Horne smelter in Quebec, Canada: Sulfur isotope evidence. *Appl. Geochem.* **2007**, *22*, 397–414. [CrossRef]
139. Hansen, A.M. Lake sediment cores as indicators of historical metal(loid) accumulation–A case study in Mexico. *Appl. Geochem.* **2012**, *27*, 1745–1752. [CrossRef]
140. Gray, J.E.; Pribil, M.J.; Van Metre, P.C.; Borrok, D.M.; Thapalia, A. Identification of contamination in a lake sediment core using Hg and Pb isotopic compositions, Lake Ballinger, Washington, USA. *Appl. Geochem.* **2013**, *29*, 1–12. [CrossRef]
141. Weigel, F. Chemie des Poloniums. *Angew. Chem.* **1959**, *71*, 289–316. [CrossRef]
142. Bagnall, K.W. The Chemistry of Polonium. In *Advances in Inorganic Chemistry and Radiochemistry*; Academic Press: New York, NY, USA, 1962; Volume 4, pp. 197–226.
143. Golubev, V.N.; Chernyshev, I.V. Differential behavior of components of the ^{238}U-^{206}Pb and ^{235}U-^{207}Pb isotopic systems in polymineralic U ores. *Geochem. Int.* **2009**, *47*, 321–328. [CrossRef]
144. Connan, O.; Boust, D.; Billon, G.; Solier, L.; Rozet, M.; Bouderbala, S. Solid partitioning and solid-liquid distribution of ^{210}Po and ^{210}Pb in marine anoxic sediments: Roads of Cherbourg at the northwestern France. *J. Environ. Radioact.* **2009**, *100*, 905–913. [CrossRef] [PubMed]
145. Macmillan, E.; Cook, N.J.; Ehrig, K.; Ciobanu, C.L.; Pring, A. Uraninite from the Olympic Dam IOCG-U-Ag deposit: Linking textural and compositional variation to temporal evolution. *Am. Miner.* **2016**, *101*, 1295–1320. [CrossRef]
146. Macmillan, E.; Ciobanu, C.L.; Ehrig, K.; Cook, N.J.; Pring, A. Chemical zoning and lattice distortion: Uraninite from Olympic Dam, South Australia. *Am. Miner.* **2016**, *101*, 2351–2354. [CrossRef]
147. Macmillan, E.; Ciobanu, C.L.; Ehrig, K.; Cook, N.J.; Pring, A. Replacement of uraninite by bornite via coupled dissolution-reprecipitation: Evidence from texture and microstructure. *Can. Miner.* **2016**, *54*, 1369–1383. [CrossRef]
148. Janeczek, J.; Ewing, R.C. Mechanisms of lead release from uraninite in the natural fission reactors in Gabon. *Geochim. Cosmochim. Acta* **1995**, *59*, 1917–1931. [CrossRef]

149. Macmillan, E.; Cook, N.J.; Ehrig, K.; Pring, A. Chemical and textural interpretation of late-stage coffinite and brannerite from the Olympic Dam IOCG-Ag-U deposit. *Miner. Mag.* **2017**, *81*, 1323–1366. [CrossRef]
150. Utsunomiya, S.; Palenik, C.S.; Valley, J.W.; Cavosie, A.J.; Wilde, S.A.; Ewing, R.C. Nanoscale occurrence of Pb in an Archean zircon. *Geochim. Cosmochim. Acta* **2004**, *68*, 4679–4686. [CrossRef]
151. Kramers, J.; Frei, R.; Newville, M.; Kober, B.; Villa, I. On the valency state of radiogenic lead in zircon and its consequences. *Chem. Geol.* **2009**, *261*, 4–11. [CrossRef]
152. Ciobanu, C.L.; Wade, B.P.; Cook, N.J.; Schmidt Mumm, A.; Giles, D. Uranium-bearing hematite from the Olympic Dam Cu–U–Au deposit, South Australia: A geochemical tracer and reconnaissance Pb–Pb geochronometer. *Precambrian Res.* **2013**, *238*, 129–147. [CrossRef]
153. Verdugo-Ihl, M.R.; Ciobanu, C.L.; Cook, N.J.; Ehrig, K.; Courtney-Davies, L.; Gilbert, S. Textures and U–W–Sn–Mo signatures in hematite from the Cu–U–Au–Ag orebody at Olympic Dam, South Australia: Defining the archetype for IOCG deposits. *Ore Geology Reviews Ore Geol. Rev.* **2017**, *91*, 173–195. [CrossRef]
154. Cook, N.J.; Ciobanu, C.L.; Ehrig, K.; Slattery, A.; Verdugo-Ihl, M.R.; Courtney-Davies, L.; Gao, W. Advances and opportunities in ore mineralogy. *Minerals* **2017**, *7*, 233. [CrossRef]
155. Courtney-Davies, L.; Zhu, Z.Y.; Ciobanu, C.L.; Wade, B.P.; Cook, N.J.; Ehrig, K.; Cabral, A.R.; Kennedy, A. Matrix-matched iron-oxide laser ablation ICP-MS U–Pb geochronology using mixed solution standards. *Minerals* **2016**, *6*, 85. [CrossRef]
156. Apukhtina, O.B.; Kamenetsky, V.S.; Ehrig, K.; Kamenetsky, M.B.; Maas, R.; Thompson, J.; McPhie, J.; Ciobanu, C.L.; Cook, N.J. Early, deep magnetite-fluorapatite mineralization at the Olympic Dam Cu–U–Au–Ag deposit, South Australia. *Econ. Geol.* **2017**, *112*, 1531–1542. [CrossRef]
157. Ewing, R.C.; Meldrum, A.; Wang, L.M.; Wang, S.X. Radiation-Induced Amorphization. *Rev. Miner. Geochem.* **2000**, *39*, 319–361. [CrossRef]
158. Kerr, P.F. U-galena and uraninite in Bedford, New York cyrtolite. *Am. Miner.* **1935**, *20*, 443–450.
159. Trocki, L.K.; Curtis, D.B.; Gancarz, A.J.; Banar, J.C. Ages of Major Uranium Mineralization and Lead Loss in the Key Lake Uranium Deposit, Northern Saskatchewan, Canada. *Econ. Geol.* **1984**, *79*, 1378–1386. [CrossRef]
160. Finch, R.J.; Murakami, T. Systematics and paragenesis of uranium minerals. *Rev. Miner. Geochem.* **1999**, *38*, 91–179.
161. Čurda, M.; Goliáš, V.; Klementová, M.; Strnad, L.; Matěj, Z.; Škoda, R. Radiation damage in sulfides: Radioactive galena from burning heaps, after coal mining in the Lower Silesian basin (Czech Republic). *Am. Miner.* **2017**, *102*, 1788–1795. [CrossRef]
162. Owen, N.D.; Ciobanu, C.L.; Cook, N.J.; Slattery, A.; Basak, A. Nanoscale study of clausthalite-bearing symplectites in Cu-Au-(U) ores: Implications for ore genesis. *Minerals* **2018**, *8*, 67. [CrossRef]
163. Rollog, M.; Cook, N.J.; Guagliardo, P.; Kilburn, M.; Ehrig, K.; Ciobanu, C.L. NanoSIMS Mapping of ^{210}RN and ^{226}Ra in South Australian Copper Concentrates. Abstract, Goldschmidt Conference, Paris. 2017. Available online: https://goldschmidtabstracts.info/2017/3392.pdf (accessed on 9 May 2018).
164. Prieto, M.; Heberling, F.; Rodríguez-Galán, R.M.; Brandt, F. Crystallization behavior of solid solutions from aqueous solutions: An environmental perspective. *Progress Cryst. Growth Charact. Mater.* **2016**, *62*, 29–68. [CrossRef]
165. Takano, B.; Watanuki, K. Geochemical implications of the lead content of barite from various origins. *Geochem. J.* **1974**, *8*, 87–95. [CrossRef]
166. Rosenberg, Y.O.; Metz, V.; Ganor, J. Radium removal in a large scale evaporitic system. *Geochim. Cosmochim. Acta* **2013**, *103*, 121–137. [CrossRef]
167. Vinograd, V.L.; Brandt, F.; Rozov, K.; Klinkenberg, M.; Refson, K.; Winkler, B.; Bosbach, D. Solid-aqueous equilibrium in the $BaSO_4$-$RaSO_4$-H_2O system: First-principles calculations and a thermodynamic assessment. *Geochim. Cosmochim. Acta* **2013**, *122*, 398–417. [CrossRef]
168. Klinkenberg, M.; Brandt, F.; Breuer, U.; Bosbach, D. Uptake of Ra during the recrystallization of barite: A microscopic and time of flight-secondary ion mass spectrometry study. *Environ. Sci. Tech.* **2014**, *48*, 6620–6627. [CrossRef] [PubMed]
169. Brandt, F.; Curti, E.; Klinkenberg, M.; Rozov, K.; Bosbach, D. Replacement of barite by a (Ba,Ra)SO_4 solid solution at close-to-equilibrium conditions: A combined experimental and theoretical study. *Geochim. Cosmochim. Acta* **2015**, *155*, 1–15. [CrossRef]
170. Weber, J.; Barthel, J.; Klinkenberg, M.; Bosbach, D.; Kruth, M.; Brandt, F. Retention of ^{226}Ra by barite: The role of internal porosity. *Chem. Geol.* **2017**, *466*, 722–732. [CrossRef]

171. Heberling, F.; Metz, V.; Böttle, M.; Curti, E.; Geckeis, H. Barite recrystallization in the presence of 226 Ra and 133 Ba. *Geochim. Cosmochim. Acta* **2018**. [CrossRef]
172. Rosenberg, Y.O.; Sade, Z.; Ganor, J. The precipitation of gypsum, celestine, and barite and coprecipitation of radium during seawater evaporation. *Geochim. Cosmochim. Acta* **2018**, in press. [CrossRef]
173. Vinograd, V.L.; Kulik, D.A.; Brandt, F.; Klinkenberg, M.; Weber, J.; Winkler, B.; Bosbach, D. Thermodynamics of the solid solution-Aqueous solution system (Ba,Sr,Ra)SO_4 + H_2O: I. The effect of strontium content on radium uptake by barite. *Appl. Geochem.* **2018**, *89*, 59–74. [CrossRef]
174. Vinograd, V.L.; Kulik, D.A.; Brandt, F.; Klinkenberg, M.; Weber, J.; Winkler, B.; Bosbach, D. Thermodynamics of the solid solution-Aqueous solution system (Ba,Sr,Ra)SO_4 + H_2O: II. Radium retention in barite-type minerals at elevated temperatures. *Appl. Geochem.* **2017**. [CrossRef]
175. Ulrych, J.; Adamovič, J.; Žák, K.; Frána, J.; Řanda, Z.; Langrová, A.; Chvátal, M. Cenozoic "radiobarite" occurrences in the Ohře (Eger) Rift, Bohemian Massif: Mineralogical and geochemical revision. *Chemie der Erde–Geochem.* **2007**, *67*, 301–312. [CrossRef]
176. Zielinski, R.; Al-Hwaiti, M.; Budahn, J.; Ranville, J. Radionuclides, trace elements, and radium residence in phosphogypsum of Jordan. *Environ. Geochem. Health* **2011**, *33*, 149–165. [CrossRef] [PubMed]
177. Jones, M.J.; Butchins, L.J.; Charnock, J.M.; Pattrick, R.A.D.; Small, J.S.; Vaughan, D.J.; Wincott, P.L; Livens, F.R. Reactions of radium and barium with the surfaces of carbonate minerals. *Appl. Geochem.* **2011**, *26*, 1231–1238. [CrossRef]
178. Curti, E. *Coprecipitation of Radionuclides: Basic Concepts, Literature Review and First Applications*; Report 97-10; Paul Scherrer Institut: Villigen, Switzerland, 1997; 116p.
179. Belzile, N.; Chen, Y.W. Tellurium in the environment: A critical review focused on natural waters, soils, sediments and airborne particles. *Appl. Geochem.* **2015**, *63*, 83–92. [CrossRef]
180. Mihai, S.A.; Mather, J.D. Role of mineralogical structure of sediments in accumulation of radionuclides and trace elements. *J. Radioanal. Nucl. Chem.* **2003**, *256*, 425–430. [CrossRef]
181. McCubbin, D.; Leonard, K.S.; Maher, B.A.; Hamilton, E.I. Association of ^{210}Po(^{210}Pb), $^{239+240}$Pu and ^{241}Am with different mineral fractions of a beach sand at Seascale, Cumbria, UK. *Sci. Total Environ.* **2000**, *254*, 1–15. [CrossRef]
182. Yang, W.F.; Guo, L.D.; Chuang, C.Y.; Schumann, D.; Ayranov, M.; Santschi, P.H. Adsorption characteristics of ^{210}Pb, ^{210}Po and ^{7}Be onto micro-particle surfaces and the effects of macromolecular organic compounds. *Geochim. Cosmochim. Acta* **2013**, *107*, 47–64. [CrossRef]
183. Vu, H.P.; Shaw, S.; Brinza, L.; Benning, L.G. Partitioning of Pb(II) during goethite and hematite crystallization: Implications for Pb transport in natural systems. *Appl. Geochem.* **2013**, *39*, 119–128. [CrossRef]
184. Yang, W.F.; Guo, L.D.; Chuang, C.Y.; Santschi, P.H.; Schumann, D.; Ayranov, M. Influence of organic matter on the adsorption of ^{210}Pb, ^{210}Po and ^{7}Be and their fractionation on nanoparticles in seawater. *Earth Plan. Sci. Lett.* **2015**, *423*, 193–201. [CrossRef]
185. Häsänen, E. Dating of sediments based on 210 Po measurements. *Radiochem. Radioanal. Lett.* **1977**, *31*, 207–214.
186. Tessier, A.; Campbell, P.G.C.; Bisson, M. Sequential extraction procedure for the speciation of particulate trace metals. *Anal. Chem.* **1979**, *51*, 844–851. [CrossRef]
187. Kim, T.H.; Kim, G. Important role of colloids in the cycling of ^{210}Po and ^{210}Pb in the ocean: Results from the East/Japan Sea. *Geochim. Cosmochim. Acta* **2012**, *95*, 134–142. [CrossRef]
188. Tuovinen, H. Mobilization of Natural Uranium Series Radionuclides at Three Mining Sites in Finland. Doctoral Dissertation, University of Helsinki, Helsinki, Finland, 2015.
189. Tuovinen, H.; Pohjolainen, E.; Lempinen, J.; Vesterbacka, D.; Read, D.; Solatie, D.; Lehto, J. Behaviour of radionuclides during microbially-induced mining of nickel at Talvivaara, Eastern Finland. *J. Environ. Radioact.* **2016**, *151*, 105–113. [CrossRef] [PubMed]
190. Christy, A.G. Causes of anomalous mineralogical diversity in the Periodic Table. *Miner. Mag.* **2015**, *79*, 33–49. [CrossRef]
191. Burns, P.C. The crystal chemistry of uranium. In: Burns, P.C.; Finch, R., eds., Uranium: Mineralogy, Geochemistry and the Environment. *Rev. Miner.* **1999**, *38*, 23–90.
192. Hazen, R.M.; Ewing, R.C.; Sverjensky, D.A. Evolution of uranium and thorium minerals. *Am. Miner.* **2009**, *94*, 1293–1311. [CrossRef]

193. Janeczek, J.; Ewing, R.C. X-ray powder diffraction study of annealed uraninite. *J. Nucl. Mater.* **1991**, *185*, 66–77. [CrossRef]
194. Malczewski, D.; Malczewski, M. ^{222}Rn and ^{220}Rn emanations as a function of the absorbed α-doses from select metamict minerals. *Am. Miner.* **2015**, *100*, 1378–1385. [CrossRef]
195. Krupp, K.; Baskaran, M.; Brownlee, S.J. Radon emanation coefficients of several minerals: How they vary with physical and mineralogical properties. *Am. Miner.* **2017**, *102*, 1375–1383. [CrossRef]
196. Trindade, M.J.; Prudêncio, M.I.; Burbidge, C.I.; Dias, M.I.; Cardoso, G.; Marques, R.; Rocha, F. Study of an aplite dyke from the Beira uraniferous province in Fornos de Algodres area (Central Portugal): Trace elements distribution and evaluation of natural radionuclides. *Appl. Geochem.* **2014**, *44*, 111–120. [CrossRef]
197. Chuang, C.Y.; Santschi, P.H.; Ho, Y.F.; Conte, M.H.; Guo, L.D.; Schumann, D.; Ayranov, M.; Li, Y.H. Role of biopolymers as major carrier phases of Th, Pa, Pb, Po, and Be radionuclides in settling particles from the Atlantic Ocean. *Mar. Chem.* **2013**, *157*, 131–143. [CrossRef]
198. Osmond, J.K.; Cowart, J.B. The theory and uses of natural uranium isotopic variations in hydrology. *At. Energy Rev.* **1976**, *14*, 621–679.
199. Kigoshi, K. Alpha recoil thorium-234: Dissolution into water and the uranium-234/uranium-238 disequilibrium in nature. *Science* **1971**, *173*, 47–48. [CrossRef] [PubMed]
200. Roudil, D.; Bonhoure, J.; Pik, R.; Cuney, M.; Jégou, C.; Gauthier-Lafaye, F. Diffusion of radiogenic helium in natural uranium oxides. *J. Nucl. Mater.* **2008**, *378*, 70–78. [CrossRef]
201. Ewing, R.C.; Whittleston, R.A.; Yardley, B.W.D. Geological Disposal of Nuclear Waste: A Primer. *Elements* **2016**, *12*, 233–237. [CrossRef]
202. Carvalho, F.P.; Oliveira, J.M.; Malta, M. Exposure to radionuclides in smoke from vegetation fires. *Sci. Total Environ.* **2014**, *472*, 421–424. [CrossRef] [PubMed]
203. Strumińska-Parulska, D. Radiolead ^{210}Pb and ^{210}Po/^{210}Pb activity ratios in calcium supplements and the assessment of their possible dose to consumers. *J. Environ. Sci. Health Part A Toxic/Hazard. Subst. Environ. Eng.* **2016**, *51*, 851–854.
204. Povinec, P.P.; Hirose, K. Fukushima radionuclides in the NW Pacific, and assessment of doses for Japanese and world population from ingestion of seafood. *Sci. Rep.* **2015**, *5*, 9016. [CrossRef] [PubMed]
205. Brook, B.W.; Bradshaw, C.J.A. Key role for nuclear energy in global biodiversity conservation. *Conserv. Biol.* **2014**, *29*, 702–712. [CrossRef] [PubMed]
206. World Nuclear Association. Thorium. 2015. Available online: http://www.world-nuclear.org/information-library/current-and-future-generation/thorium.aspx (accessed on 24 July 2016).
207. Utsunomiya, S.; Kogawa, M.; Kamiishi, E.; Ewing, R.C. Scanning Transmission Electron Microscopy and Related Techniques for Research on Actinide and Radionuclide Nanomaterials. In *Actinide Nanoparticle Research*; Kalmykov, S.N., Denecke, M.A., Eds.; Springer: Berlin/Heidenberg, Germany, 2011; pp. 33–62.
208. Ciobanu, C.L.; Cook, N.J.; Maunders, C.; Wade, B.P.; Ehrig, K. Focused Ion Beam and Advanced Electron Microscopy for Minerals: Insights and Outlook from Bismuth Sulphosalts. *Minerals* **2016**, *6*, 112. [CrossRef]
209. Ciobanu, C.L.; Kontonikas-Charos, A.; Slattery, A.; Cook, N.J.; Ehrig, K.; Wade, B.P. Short-Range Stacking Disorder in Mixed-Layer Compounds: A HAADF STEM Study of Bastnäsite-Parisite Intergrowths. *Minerals* **2017**, *7*, 227. [CrossRef]
210. Uchida, A.; Toyoda, S.; Ishibashi, J.; Nakai, S. ^{226}Ra-^{210}Pb and ^{228}Ra-^{228}Th Dating of Barite in Submarine Hydrothermal Sulfide Deposits Collected at the Okinawa Trough and the Southern Mariana Trough. In *Subseafloor Biosphere Linked to Hydrothermal Systems*; Ishibashi, J., Okino, K., Sunamura, M., Eds.; Springer: Tokyo, Japan, 2015; pp. 607–615.
211. Ditchburn, R.G.; de Ronde, C.E.J. Evidence for Remobilization of Barite Affecting Radiometric Dating Using ^{228}Ra, ^{228}Th, and ^{226}Ra/Ba Values: Implications for the Evolution of Sea-Floor Volcanogenic Massive Sulfides. *Econ. Geol.* **2017**, *112*, 1231–1245. [CrossRef]



© 2018 by the authors. Licensee MDPI, Basel, Switzerland. This article is an open access article distributed under the terms and conditions of the Creative Commons Attribution (CC BY) license (http://creativecommons.org/licenses/by/4.0/).

ADDITIONAL MATERIAL G

Why detailed mineralogy is important: Understanding evolution of the giant Olympic Dam iron-oxide copper-gold system, South Australia

Cook, N.J.[1], Ehrig, K.J[2]., Ciobanu, C.L.[1], Courtney-Davies, L.[1], Verdugo-Ihl, M.R.[1], Rollog, M.[1], **Schmandt, D.S.[1]**, Owen, N.D.[1], Macmillan, E.[2], Kontonikas-Charos, A.[1], Krneta, S.[1], and Dmitrijeva, M.[1]

[1]*School of Chemical Engineering, The University of Adelaide, SA 5005, Australia*

[2]*BHP Olympic Dam, Adelaide, SA 5000, Australia*

Conference abstract in 15th Quadrennial IAGOD Symposium, Salta, Argentina, 28-31 August 2018. Symposium Proceedings Volume, SegemAR, 371-372.

15th Quadrennial IAGOD International Association on the Genesis of Ore Deposits Symposium, Salta, Argentina.



WHY DETAILED MINERALOGY IS IMPORTANT: UNDERSTANDING EVOLUTION OF THE OLYMPIC DAM IRON-OXIDE COPPER-GOLD SYSTEM, SOUTH AUSTRALIA

Nigel Cook[1], Kathy Ehrig, Cristiana Ciobanu, Liam Courtney-Davies, Max Verdugo-Ihl, Mark Rollog, Danielle Schmandt, Nicholas Owen, Edeltraud Macmillan, Alkiviadis Kontonikas-Charos, Sasha Krneta, Marija Dmitrijeva

[1]*School of Chemical Engineering, University of Adelaide, Australia - nigel.cook@adelaide.edu.au*

Olympic Dam is one of the largest deposits on Earth and a significant producer of copper, uranium, gold and silver (Ehrig, *et al.*, 2013). Uranium-Pb geochronology using undisturbed magmatic and hydrothermal minerals allows interpretation of the initial and major hydrothermal ore- forming event at ~1593 Ma, associated with emplacement of the Gawler Silicic Large Igneous Province. The >10 billion-tonne resource is heterogeneous and contained within a breccia complex, itself confined to the ~1593 Ma Roxby Downs Granite. Ore textures suggest multiple episodes of replacement, remobilization and recrystallization and are supported by (radio) isotope data yielding a range of younger ages. Conceptual models for ore formation, necessary for exploration in the region, and optimised processing of complex fine-grained ores characterised by enrichment in an extraordinarily wide variety of elements are dependent on an exceptionally thorough understanding of mineralogy and geochemistry underpinned by high-quality, high-resolution assay data, extensive MLA datasets, and deportment models for multiple elements.

Micron - to nanoscale studies of feldspars and accessory phases within the alteration envelope, and of Fe-oxides, Cu-(Fe)-sulphides, sulphates, U- and REE-bearing minerals within the deposit all point to common mechanisms involved in formation of the mineral assemblages as observed today, the prevailing Mm-scale mineral textures, and measured variations in mineral compositions. Detailed mineralogical investigation has proven pivotal in establishing a framework for ore evolution.

Each of the 100 minerals in the Olympic Dam deposit has a story to tell. The complex fine- grained, intergrown, heterogeneous assemblages necessitate ultra-careful investigation on multiple representative samples and with compositional data requiring verification by examination at the nanoscale. We therefore use a combination of whole rock assay, optical and scanning electron microscopy, electron probe microanalysis (EPMA), laser-ablation inductively-coupled plasma mass spectrometry, complemented by imaging and nanoscale compositional analysis by transmission electron microscopy (TEM) on foils extracted *in-situ* by focussed ion beam SEM methods.

Investigation of feldspars from within and outside the deposit allows an understanding of the magmatic to hydrothermal transition and early Fe-metasomatism (Kontonikas-Charos, *et al.*, 2017). Nanoscale characterization of feldspars undergoing transformation from early post-magmatic (deuteric) to hydrothermal stages in granites hosting the deposit reveals complex perthitic textures, anomalously Ba, Fe, or REE-rich compositions, and REE-fluorocarbonate+molybdenite assemblages that pseudomorph feldspars (Kontonikas-Charos, *et al.*, 2018). Epitaxial orientations between (igneous) cryptoperthite, (deuteric) patch and albite replacive within vein perthite support interface-mediated reactions between pre-existing alkali-feldspars and pervading fluid, irrespective of micron-scale crystal morphology. Such observations are consistent with coupled dissolution-replacement reactions (CDRR), indicating that albitization enhances rock permeability via the generation of transient pores which facilitate grain-scale element remobilization and trap elements as nanoscale inclusions. These inclusions represent the earliest stage of REE remobilization at the grain-scale, and reflect the significant role feldspar replacement reactions play in concentrating REE during hydrothermal alteration.

Hematite is by far the most abundant hydrothermal mineral and preserves oscillatory and sectorial zoning and incorporation of U, W, Mo, Sn and other trace elements, including REE (Verdugo-Ihl, *et al.*, 2017). The presence of U and Pb allows application of hematite U-Pb geochronology [e.g., Courtney-Davies, *et al.*, 2018]. These primary textures give way to repeated processes of brecciation, fluid-assisted reworking, element redistribution, recrystallization and overprinting. CDRR permits release of trace elements from the lattice to be trapped as nm- to Mm-scale inclusions (e.g., uraninite), or to form discrete minerals (e.g., scheelite molybdenite) in the near vicinity.

EPMA-scale compositional data combined with TEM investigation of chalcocite-group minerals, bornite and chalcopyrite has shown that Cu-Fe-sulphides from different ore zones feature nanoscale intergrowths, lattice defects, superstructure domains and antiphase boundary domains (Ciobanu, *et al.*, 2017). Such features can be interpreted as having originated via a combination of exsolution, coarsening, and phase transformation during cooling from high-T solid solutions (e"400°C) in the system Cu-Fe-S and sub-systems. A scenario of 'exsolution from primary solid-solution, corroborated by the consistency in phase relations within each zone across different scales of observation from deposit- to nanoscale, supports a model of primary hypogene ore precipitation rather than replacement, and



accounts for the observed zoning patterns at OD. Nonetheless, evidence for CDRR, replacement, phase transformation and local (Mm- to tens m-wide) remobilization is evident.

Uraninite, coffinite, brannerite and hematite are the dominant U hosts [Courtney-Davies, *et al.*, 2018, Macmillan, *et al.*, 2016, Macmillan, *et al.,* 2017). Although some uraninite and hematite retain U and daughter isotopes, breakdown and replacement can lead to release, remobilization and redistribution of radionuclides (RN) at scales from nm upwards. New minerals may be formed (late uraninite, coffinite) and U and Pb can also be incorporated into existing minerals (barite, svanbergite-woodhouseite). RN are, however, also concentrated as sub-microscopic particles within pores, microfractures and at grain boundaries in the near vicinity of altered or replaced U-bearing mineral grains (Rollog, *et al.*, 2018) attesting to fluid-mediated processes. Such redistribution carries implications for ore processing and, potentially also for the interpretation of geochronological data.

Three groups of REE-minerals are observed: REE-fluorocarbonates (bastnosite and subordinate synchysite (Schmandt, *et al.*, 2017), which appear paragenetically early; REE-phosphates (dominantly florencite of variable age and association but also minor xenotime, the main carrier of HREE); and Ca-, Sr-, REE-bearing phosphate-sulphates (svanbergite- woodhouseite], which are generally late and replace earlier-formed minerals (Owen, *et al.,* 2018). Minor REE are also contained in apatite, which displays evolving chondrite-normalized REE fractionation trends that can be explained in terms of changes in fluid parameters and speciation of REY in ore-forming fluids (Krneta, *et al.,* 2017). Under hydrothermal conditions typical of iron- oxide copper gold mineralization, a decrease in salinity, pH and temperature is associated with hematite-sericite alteration sufficient to produce a characteristic MREE-enriched apatite. However, anomalous high-pH (~7) fluids at 300 °C may account for high-grade Cu ores as modelled from apatite with strong positive Eu anomalies (Krneta, *et al.,* 2017).

Although primary assemblages are identified, a persistent narrative is offered by multiple episodes of fluid-assisted replacement, phase transition, remobilization, migration, and re- precipitation of all ore components. These processes played a major role in the modification of textural and geochemical patterns in many minerals. However, more refractory minerals, notably hematite, apatite, pyrite, some REE-minerals, and some sub-types of U-minerals, can preserve primary geochemical signatures and can also record and retain evidence of evolving and overprinting fluid signatures. Fluid regimes were likel heterogeneous given observations of texturally and geochemically distinct generations of the same mineral within single samples.

REFERENCES

Ehrig, K., McPhie, J., Kamenetsky, V., 2013. Geology and mineralogical zonation of the Olympic Dam iron oxide Cu-U-Au-Ag deposit, South Australia. In: Hedenquist, J.W., Harris, M., Camus, F. (Eds), Geology and Genesis of Major Copper Deposits and Districts of the World, a Tribute to Richard Sillitoe. SEG Special Publication 16, pp. 237-268.

Kontonikas-Charos, A., Ciobanu, C.L., Cook, N.J., Ehrig, K., Krneta, S., Kamenetsky, V.S., 2017. Feldspar evolution in the Roxby Downs Granite, host to Fe-oxide Cu-Au-(U) mineralization at Olympic Dam, South Australia. Ore Geology Reviews, 80, 838-859.

Kontonikas-Charos, A., Ciobanu, C.L., Cook, N.J., Ehrig, K., Ismail, R., Krneta, S., Basak, A., 2018. Feldspar mineralogy and rare earth element (re)mobilization in iron-oxide copper gold systems from South Australia: a nanoscale study. Mineralogical Magazine 82 (S1), S173–S197.

Verdugo-Ihl, M.R., Ciobanu, C.L., Cook, N.J., Ehrig, K., Courtney-Davies, L., Gilbert, S., 2017. Textures and U-W-Sn-Mo signatures in hematite from the Cu-U-Au-Ag orebody at Olympic Dam, South Australia: defining the archetype for IOCG deposits. Ore Geology Reviews 91, 173–195.

Courtney-Davies, L., Ciobanu, C.L., Tapster, S.R., Cook, N.J., Ehrig, K.J., Kennedy, A.K., Condon, D.J., Verdugo-Ihl, M.R., Wade, B.S., Gilbert, S.E., 2018. The U-Pb systematics of hydrothermal hematite; insights from the IOCG system at Olympic Dam, South Australia. IAGOD Symposium, Salta (this volume).

Ciobanu, C.L., Cook, N.J., Ehrig, K., 2017. Ore minerals down to the nanoscale: Cu-(Fe)- sulphides from the iron oxide copper gold deposit at Olympic Dam, South Australia. Ore Geology Reviews 81, 1218-1235.

Macmillan, E., Cook, N.J., Ciobanu, C.L., Ehrig, E., Pring, A., 2016. Uraninite from the Olympic Dam IOCG-U-Ag deposit: linking textural and compositional variation to temporal evolution. American Mineralogist 101, 1295–1320.

Macmillan, E., Cook, N.J., Ehrig, K., Pring, A., 2017. Chemical and textural interpretation of late-stage coffinite and brannerite from the Olympic Dam IOCG-Ag-U deposit. Mineralogical Magazine 81, 1323-1366.

Rollog, M., Cook, N.J., Gugliardo, P., Ehrig. K., Kilburn, M., 2018. In situ spatial distribution mapping of radionuclides in minerals by nanoSIMS. Geochemistry – Exploration, Environment, Analysis (in press).

Schmandt, D.S., Cook, N.J., Ciobanu, C.L., Ehrig, K., Wade, B.P., Gilbert, S., Kamenetsky, V.S., 2017. Rare earth element fluorocarbonate minerals from the Olympic Dam Cu-U-Au-Ag deposit, South Australia. Minerals 7(10), 202; doi: 10.3390/min7100202.

Owen, N.D., Ciobanu, C.L., Cook, N.J., Slattery, A., Basak, A., 2018. Nanoscale study of clausthalite-bearing symplectites in Cu-Au-(U) ores: Implications for ore genesis. Minerals, 8(2), 67; doi:10.3390/min8020067.

Krneta, S., Ciobanu, C.L., Cook, N.J., Ehrig, K., Kontonikas-Charos, A., 2017. Rare earth element behaviour in apatite from the Olympic Dam Cu-U-Au-Ag deposit, South Australia. Minerals 7(8), 135; doi:10.3390/min7080135.

ADDITIONAL MATERIAL H

CONFERENCE ABSTRACT:

Mineral hosts and deportment of radionuclides in uranium-bearing copper ores and concentrates

D.S. Schmandt[1*], N.J. Cook[1], M. Rollog[1], K. Ehrig[2], B. Triffett[3], C.L. Ciobanu[1]

*[1]School of Chemical Engineering, Univ. of Adelaide, Adelaide, SA 5005, Australia (*Correspondence: Danielle.Schmandt@adelaide.edu.au)*

[2]BHP Billiton Olympic Dam, Adelaide, SA 5000, Australia

[3]OZ Minerals, 162 Greenhill Rd., Parkside SA 5063, Australia

Conference presentation at The AusIMM International Uranium Conference 2016, June 7-8, Adelaide, South Australia. ISBN 9781925100471.

Mineral Hosts and Deportment of Radionuclides in Uranium-bearing Copper Ores and Concentrates

D S Schmandt[1], N J Cook[2], M Rollog[2], K Ehrig[3], B Triffett[4] and C L Ciobanu[2]

ABSTRACT

Uranium-bearing minerals are common within Mesoproterozoic copper ores of South Australia. Natural decay of ^{238}U creates radionuclides that can be mobilised independently from the original ^{238}U-bearing mineral. Parent-daughter decoupling can happen during geologic events and potentially, also during ore processing. The mobility and ultimate associations of the radionuclides in minerals have not previously been explored in detail or quantified, neither on the geologic scale nor as a function of ore processing.

The deportment and separation of different radionuclides is of interest because some, specifically the short half-life α-emitters ^{210}Po and ^{210}Pb, can be preferentially enriched in copper concentrates from selected South Australian copper deposits. The lack of published information on the likely mineralogical hosts of ^{210}Po and ^{210}Pb makes prediction of its location in complex fine-grained ores and concentrates a significant challenge. This information is, however, essential to guide attempts to reduce or eliminate target radionuclides in copper concentrates and other processing products.

Adding to the challenge is the extremely low concentrations of ^{210}Po- and ^{210}Pb. At concentrations of only fractions of one part-per-trillion, they are unidentifiable using conventional microanalytical methods. We thus rely on indirect deductions drawn from assays and RN measurements on bulk material, comprehensive mineralogical characterisation at the micron- to nano-scales, and determination of proxy elements within the crystal lattice of specific minerals. Using scanning electron microscopy (SEM) at the maximum magnification we can identify potential ^{210}Po- and ^{210}Pb-bearing

1. School of Chemical Engineering, University of Adelaide, Adelaide SA 5005. Email: danielle.schmandt@adelaide.edu.au
2. School of Chemical Engineering, University of Adelaide, Adelaide SA 5005.
3. BHP Billiton Olympic Dam, Adelaide SA 5000.
4. MAusIMM, OZ Minerals, Parkside SA 5063.

mineral grains and their textures within mill feed, concentrate and leached concentrates, including nanoparticles within sulfides, or at mineral-mineral boundaries. These data and future FIB-SEM and TEM investigations will assist in building a robust qualitative model for radionuclide deportment within ore and gangue minerals and contribute towards achieving an understanding of the mechanisms responsible for changes in response to geological events and ore processing.

ADDITIONAL MATERIAL I

CONFERENCE ABSTRACT:

Identifying hosts for non-target uranium and associated radionuclides in copper ores and concentrates

D.S. Schmandt[1]*, N.J. Cook[1], M. Rollog[1], K. Ehrig[2], B. Triffett[3], C.L. Ciobanu[1]

[1]School of Chemical Engineering, Univ. of Adelaide, Adelaide, SA 5005, Australia

[2]BHP Billiton Olympic Dam, Adelaide, SA 5000, Australia

[3]OZ Minerals, 162 Greenhill Rd., Parkside SA 5063, Australia

Conference presentation at Goldschmidt 2016, June 26- July 1, Yokahama, Japan.

Goldschmidt Conference Abstracts, 2771.

Identifying hosts for non-target uranium and associated radionuclides in copper ores and concentrates

D.S. SCHMANDT[1*], N.J. COOK[1], M. ROLLOG[1], K. EHRIG[2], B. TRUFFETT[3], C.L. CIOBANU[1]

[1]School of Chemical Engineering, Univ. of Adelaide, Adelaide, SA 5005, Australia (*Correspondence: Danielle.Schmandt@adelaide.edu.au)

[2]BHP Billiton Olympic Dam, Adelaide, SA 5000, Australia

[3]OZ Minerals, 162 Greenhill Rd., Parkside SA 5063, Australia

Mesoproterozoic copper ores in South Australia contain low to moderate concentrations of uranium. Dependent on concentration, the uranium may be an economic by-product, a contaminant or both. Daughter products of ^{238}U and ^{232}Th decay are also present in the ores. However, due to the distinct physical and chemical properties of each daughter radionuclide, including the short half-life α-emitters, ^{210}Po and ^{210}Pb (hereafter ^{210}RN), these may decouple from the parent uranium to form, or be incorporated into, different minerals. This process may be exacerbated by geological events causing different re-obilization pathways for different elements. Similarly, parent-daughter separation is also possible during ore processing, and has the potential to create smelter dusts or other processing products enriched in ^{210}RN relative to ^{238}U. There is currently limited available data about mineralogical hosts for ^{210}RN, making prediction of its location in complex, fine-grained ores or concentrates a significant challenge. Information on potential mineral hosts for ^{210}RN is, however, essential to guide attempts to eliminate or reduce unwanted ^{210}RN in copper concentrates and processing wastes.

Concentrations of ^{210}RN are so low (fractions of one part-per-billion) that their presence in individual minerals cannot be measured directly by conventional microanalytical methods. In order to understand their distribution in millfeed and concentrates, we thus rely on indirect information drawn from assays and RN measurements on bulk material, comprehensive mineralogical characterization at micron scales, and determination of concentrations of proxy elements and isotopes within the crystal lattice of specific minerals. SEM analysis at maximum magnification provides identification of potential sub-μm-sized ^{210}RN-bearing mineral grains, including nanoparticles within sulfides and gangue minerals, and at mineral-mineral boundaries. These data and future FIB-SEM and TEM investigations will assist in building a robust qualitative model for ^{210}RN deportment within ore and an understanding of the different pathways responsible for changes in that deportment as a response to geological events and ore processing.

ADDITIONAL MATERIAL J

CONFERENCE ABSTRACT:

Rare earth element minerals in the Olympic Dam deposit, South Australia: petrography and compositional variation

Danielle S. Schmandt[1,2], Nigel J. Cook[1,2], Kathy J. Ehrig[3], Benjamin P. Wade[4], Cristiana L. Ciobanu[1]

[1] *School of Chemical Engineering, The University of Adelaide, Adelaide, SA, 5005, Australia*

[2] *ARC Transformation Research Hub for Australian Copper-Uranium*

[3] *BHP Billiton Olympic Dam, Adelaide, SA, 5000, Australia*

[4] *Adelaide Microscopy, The University of Adelaide, Adelaide, SA, 5005, Australia*

Conference presentation at SEG 2017: Ore Deposits of Asia: China and Beyond, September 17-20, Beijing, China.

©2017 Society of Economic Geologists, Inc.
SEG 2017 Conference

Rare earth element minerals in the Olympic Dam deposit, South Australia: Petrography and compositional variation

Danielle S Schmandt*, Nigel J Cook, Kathy J Ehrig, Benjamin P Wade, Cristiana L Ciobanu

*The University of Adelaide, Adelaide, Australia, South Australia, Email: danielle.schmandt@adelaide.edu.au

Olympic Dam is a world-class iron-oxide copper-gold-uranium ore system located in the Gawler Craton of South Australia. It contains elevated concentrations of rare earth elements (REE), almost exclusively LREE (0.18 wt% La_2O_3, 0.27 wt% Ce_2O_3, 0.06 wt.% Nd_2O_3), although not sufficiently high enough to be economically exploited at present. Discrete REE-minerals at Olympic Dam are typically fine-grained (<50 µm), and occur as disseminations in sulphide and gangue minerals throughout all ore zones in the deposit, although they can be locally concentrated to macroscopic REE-mineral rich pockets. REE abundance broadly correlates with whole-rock Fe concentration and the presence of sulphide mineralization; REEs are, however, depleted in the barren, Fe-dominant core of the deposit. Aside from REE-minerals, trace to minor REE occur in uraninite and apatite, among other minerals. While REE-minerals are documented in previous studies of Olympic Dam, there has been no prior, focused investigation on their mineralogy, or variation, either compositionally or spatially. Documenting the speciation, occurrence, and compositional variation of REE-minerals has potential value for constraining variation in fluid parameters by thermodynamic studies.

The most widespread REE-mineral within the sample suite is the REE-fluorocarbonate bastnäsite [$REE(CO_3)F$], followed in abundance by the REE-phosphate florencite [$(REE)Al_3(PO_4)_2(OH)_6$] and crandallite group minerals [$(REE, Ca, Sr)(Al, Fe)_3(SO_4, PO_4)(PO_3OH)(OH)_6$]. Also present are subordinate synchysite [$CaREE(CO_3)_2F$] and monazite [$(REE, Th)PO_4$], only observed in some samples, and most commonly around the deposit margins. Xenotime [$(Y, REE)PO_4$], frequently as overgrowths on zircon, and phases of intermediate xenotime-coffinite-thorite solid solution are also present. Bastnäsite is observed to replace, and as twinned grains with, synchysite. Florencite appears paragenetically late, occasionally replacing apatite and overprinting bastnäsite, synchysite, and Cu-(Fe)- sulphides. Bastnäsite can also be replaced by copper-(iron)-sulphides.

Electron probe microanalysis of REE-minerals within drillcore samples and flotation tailings reveals significant compositional variation among all REE-mineral groups. Ce-dominant species are most prevalent; synchysite is always Ce-dominant, (~1:2 La to Ce), whereas the La/Ce ratio in bastnäsite can range significantly from 0.3 to >1, with the majority around 0.6. Florencite and crandallite group minerals display the highest overall La/Ce ratios, with many analyzed grains being La-dominant. ∑REE+Y (hereafter REY) does, however, vary significantly (from 4.9 to 30.1 wt.%) in the alumino-phosphates. The same minerals also display significant variation with respect to SrO (0.6-12.9 wt.%) and SO_3 (0.5-12.1 wt.%), suggestive of significant solid solution. The HREE (Tb-Lu) +Y are generally slightly more enriched in synchysite (up to 6% of the ∑REY) while more depleted in the florencite (typically <1% of ∑REY but can be up to 2%); bastnasite shows a range from 0.3 to 4% HREE+Y of ∑REY. Xenotime is the most significant host for Y and HREE in the deposit.

ADDITIONAL MATERIAL K

CONFERENCE ABSTRACT:

Rare earth element minerals and their compositional variation in the Olympic Dam deposit, South Australia

Danielle S. Schmandt[1,2], Nigel J. Cook[1,2], Kathy J. Ehrig[3], Benjamin P. Wade[4], Cristiana L. Ciobanu[1]

[1]School of Chemical Engineering, The University of Adelaide, Adelaide, SA, 5005, Australia

[2] ARC Transformation Research Hub for Australian Copper-Uranium

[3] BHP Billiton Olympic Dam, Adelaide, SA, 5000, Australia

[4] Adelaide Microscopy, The University of Adelaide, Adelaide, SA, 5005, Australia

Conference presentation at SEG 2018: Minerals, Metals, and Society, September 22-25, Keystone, CO, USA.

Theme: *	Technology and Energy Metals and Minerals: Co, Li, U, REE
Presentation Type: *	Speed Talk
Title of Abstract: *	Rare earth element minerals and their compositional variation in the Olympic Dam deposit, South Australia
Authors and Affiliations:	Danielle S. Schmandt[1], Nigel J. Cook[1], Cristiana L. Ciobanu[1], Kathy Ehrig[2], Benjamin P. Wade[3], Sarah Gilbert[3] 1. University of Adelaide, Adelaide, SA, Australia, 2. BHP Olympic Dam, Adelaide, SA, Australia, 3. Adelaide Microscopy, The University of Adelaide, Adelaide, SA, Australia

Olympic Dam is a World-class iron-oxide copper-gold-uranium ore system hosted in Mesoproterozoic rocks of the Gawler Craton, South Australia. The deposit contains elevated concentrations of rare earth elements (REE), almost exclusively light REE (LREE) with a mean LREE concentration of 3,050 ppm. Average heavy REE+Y concentrations are 110 ppm. Because of their typically disseminated, fine-grained character, individual REE-minerals are generally not identifiable in hand specimen, necessitating microscopic study to understand their occurrence and paragenesis. Documenting the speciation and compositional variation among REE-minerals allows new constraints to be placed on the formation of the deposit.

The most widespread REE-mineral within the sample suite from across the deposit is the REE-fluorcarbonate bastnäsite, followed in abundance by the REE-Al-phosphate florencite and a compositionally varied REE-, Sr- and Ca-bearing group of minerals belonging to the crandallite group. Also present are subordinate synchysite, monazite, and xenotime. LREE-minerals are typically fine-grained and disseminated within the breccia matrix and as inclusions in sulphide and gangue minerals. They can nevertheless be locally concentrated within REE-rich pockets. Bastnäsite may be twinned with, and in some cases, may replace synchysite. Florencite often appears paragenetically late, replacing apatite, bastnäsite and synchysite. Xenotime commonly forms on zircon; monazite is rare.

Chondrite-normalized REE fractionation trends for the above minerals are compared with published data for other mineral groups from Olympic Dam which contain minor REE. U-minerals and apatite both show a trend of progressive relative depletion in LREE from paragenetically early to late, suggesting changes in LREE availability, physicochemical conditions, and/or the speciation of complexes transporting REE in hydrothermal fluid as the system evolved. The REE-minerals display progressive relative enrichment in LREE from paragenetically early to late. Florencite is most enriched in LREE, representing either the end of a continuous fluid evolution, or a discrete REE-Al-phosphate mineralization event post-dating the main REE-fluorcarbonate mineralization.

ADDITIONAL MATERIAL L

CONFERENCE ABSTRACT & POSTER:

Rare Earth Element mineralogy at Olympic Dam, South Australia

Danielle S. Schmandt[1], Nigel J. Cook[1], Cristiana L. Ciobanu[1], Kathy J. Ehrig[2], Nicholas D. Owen[1], Benjamin P. Wade[3], Sarah E. Gilbert[3]

[1]School of Chemical Engineering, The University of Adelaide, Adelaide, SA, 5005, Australia

[2]BHP Billiton Olympic Dam, Adelaide, SA, 5000, Australia

[3]Adelaide Microscopy, The University of Adelaide, Adelaide, SA, 5005, Australia

Poster presentation at Gordon Research Seminar and Conference, Geochemistry of Mineral Deposits: Mineralizing Processes Across All Scales, August (4)5-10, 2018, Waterville Valley, NH, USA.

Abstract

The World-class Olympic Dam breccia-hosted iron-oxide copper-gold-uranium ore deposit is enriched in light rare earth elements (LREE). By far the most abundant LREE-mineral is the fluorocarbonate bastnäsite [$REECO_3F$] which represents the dominant LREE mineralization stage and likely deposited during the main sulfide mineralization event at 1595 Ma. Minor Ca-bearing REE-fluorocarbonate minerals present include synchysite [$CaREE(CO_3)_2F$] and parisite [$CaREE_2(CO_3)_3F_2$], which may have commenced precipitation immediately prior to bastnäsite. Although these Ca-REE-fluorocarbonates are limited in occurrence, they show a greater enrichment in middle-REE than later bastnäsite, although also with comparatively high LREE. The REE-Al-phosphate, florencite [$REEAl_2(PO_4)_2(OH)_6$] is the second most abundant REE-mineral. Based on textural relationships, this is later than the REE-fluorocarbonates in the same samples, Cu-(Fe)-sulfides, and primary hematite. Florencite is more LREE-enriched and middle- and heavy-REE-depleted than the REE-fluorocarbonates.

Whereas the REE-fluorocarbonates and florencite display progressive LREE enrichment correlating with paragenetic sequence, other REE-bearing minerals in the deposit (uraninite, brannerite, coffinite, and apatite) all show patterns of progressive LREE depletion across successive generations. This supports multiple fluid-assisted dissolution, remobilization, and re-precipitation processes that have impacted on LREE distributions. Late-stage florencite is the most La-rich of all REE-bearing phases. Such florencite forms extensive solid solutions with REE-depleted Sr-Ca-bearing phosphate-sulfates that are pervasive across the deposit, and likely formed at lower temperature and lower-pH conditions under which other phosphates (*e.g.* monazite, apatite) are unstable.

Rare Earth Element Mineralogy at Olympic Dam, South Australia

Danielle S. Schmandt[1], Nigel J. Cook[1], Cristiana L. Ciobanu[1], Kathy J. Ehrig[2], Nicholas D. Owen[1], Benjamin P. Wade[3], Sarah E. Gilbert[3]

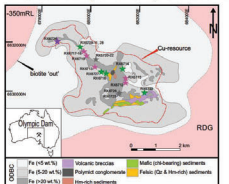
[1] School of Chemical Engineering, The University of Adelaide; [2] BHP Olympic Dam; [3] Adelaide Microscopy, The University of Adelaide

Abstract

The World-class Olympic Dam breccia-hosted iron-oxide copper-gold-uranium ore deposit is enriched in light rare earth elements (LREE). By far the most abundant LREE-mineral is the fluorocarbonate bastnäsite [REECO$_3$F] which represents the dominant LREE mineralization stage and likely deposited during the main sulfide mineralization event at 1595 Ma. Minor Ca-bearing REE-fluorocarbonate minerals present include synchysite [CaREE(CO$_3$)$_2$F] and parisite [CaREE$_2$(CO$_3$)$_3$F$_2$], which may have commenced precipitation immediately prior to bastnäsite. Although these Ca-REE-fluorocarbonates are limited in occurrence, they show a greater enrichment in middle-REE than later bastnäsite, although also with comparatively high LREE. The REE-Al-phosphate, florencite [REEAl$_3$(PO$_4$)$_2$(OH)$_6$] is the second most abundant REE-mineral. Based on textural relationships, this is later than the REE-fluorocarbonates in the same samples, Cu-(Fe)-sulfides, and primary hematite. Florencite is more LREE-enriched and middle- and heavy-REE-depleted than the REE-fluorocarbonates.

The REE-fluorocarbonates and florencite display progressive LREE enrichment correlating with paragenetic sequence, whereas other REE-bearing minerals in the deposit (uraninite, brannerite, coffinite, and apatite) all show patterns of progressive LREE depletion across successive generations. This supports multiple fluid-assisted dissolution, remobilization, and re-precipitation processes that have impacted on LREE distributions. Late-stage florencite is the most La-rich of all REE-bearing phases. Such florencite forms extensive solid solutions with REE-depleted Sr-Ca-bearing phosphate-sulfates that are pervasive across the deposit, and likely formed at lower temperature and lower-pH conditions under which other phosphates (e.g. monazite, apatite) are unstable.

1. Resource map and sample locations



Simplified Olympic Dam deposit map at -350m RL, after Ehrig et al. [2]. Stars indicate locations of samples and are color-coded with logged lithology. RDG: Roxby Downs Granite.

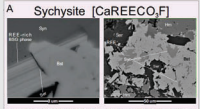
- Average LREE grade of approximately 3,050 ppm. Heavy rare earth elements + Y grade of ~110 ppm.
- Olympic Dam is a large and complex deposit with a prolonged geological history (e.g., [1], [2], [3]) located entirely within the RDG.

2. Petrography

All images are backscatter electron (BSE) images.

All REE-minerals occur throughout the Olympic Dam deposit, however they are generally sparse, disseminated, fine-grained, and almost always intergrown with other minerals making quantitative microanalysis challenging. The petrographic and chemical analysis presented here are from a suite of 20 samples selected based on routine BHP Olympic Dam core assays indicating anomalously high La and Ce values and where the REE-minerals locally concentrated to macroscopic REE-mineral rich pockets and are coarse and abundant.

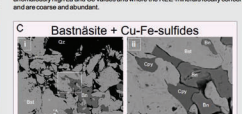
A Sychysite [CaREECO$_3$F]



Synchysite with intergrowths of a very fine REE-rich phase along long axis. Bastnäsite intergrown with synchysite and REE intergrowths.

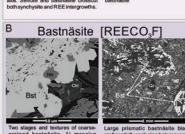
Synchysite as patchy, interstitial filling between aggregates of bladed bastnäsite

C Bastnäsite + Cu-Fe-sulfides



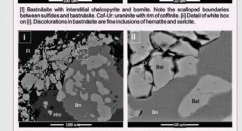
[I] Bastnäsite with interstitial chalcopyrite and bornite. Note the scalloped boundaries between sulfides and bastnäsite. Cof-Ur: uraninite with rim of coffinite. [i] Detail of white box on [I]. Discolorations in bastnäsite are fine inclusions of hematite and sericite.

B Bastnäsite [REECO$_3$F]



Two stages and textures of coarse-grained bastnäsite, 1) massive aggregates of bastnäsite with 2) overgrowing, open-space euhedral bastnäsite.

Large prismatic bastnäsite blades preferentially replacing heterogeneous clasts in hematite breccia. Bastnäsite also in the matrix.



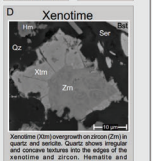
[I] Patchy, irregular bastnäsite in matrix and within bornite. [i] Detail of white box on [I]. Bornite displays lamellar exsolution of chalcopyrite. Uraninite is included in and interstitial to bastnäsite, black is sericite.

Mineral abbreviations

Bst:	bastnäsite
Syn:	synchysite
Flo:	florencite
Hm:	hematite
Qz:	quartz
Ser:	sericite
Chl:	chlorite
Fl:	fluorite
Bn:	bornite
Cpy:	chalcopyrite

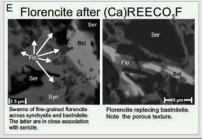
All microanalytical work was undertaken at Adelaide Microscopy, The University of Adelaide.

D Xenotime



Xenotime (Xtm) overgrowth on zircon (Zrn) in quartz and sericite. Quartz shows irregular and concave textures into the edges of the xenotime and zircon. Hematite and bastnäsite are also in the assemblage.

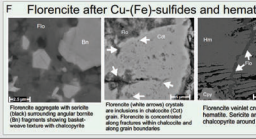
E Florencite after (Ca)REECO$_3$F



Swarms of fine-grained florencite across synchysite and bastnäsite. The latter are in close association with sericite.

Florencite replacing bastnäsite. Note the porous texture.

F Florencite after Cu-(Fe)-sulfides and hematite

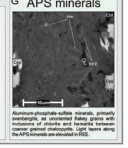


Florencite aggregate with sericite and Cu-(Fe)-sulfides. Florencite (Bn) fragments showing lapilli-weave-texture with chalcocyte

Florencite (white arrows) crystals are inclusions in chalcocite (Cct) grain. Florencite is concentrated along fractures within chalcocite and along grain boundaries

Florencite veinlet crosscutting hematite, Sericite and chalcopyrite around hematite

G APS minerals



Aluminum-phosphate-sulfate minerals, primarily woodhouseite-svanbergite, with minor to trace inclusions of chlorite and hematite between coarser grained chalcocyte. Light layers along the APS minerals are elevated in REE.

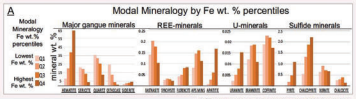
3. Bulk Mineral Analysis (Mineral Liberation Analyzer)

The MLA dataset used for this analysis consists of 607 15-meter-long composites drill core samples from the southeastern lobe of the deposit.

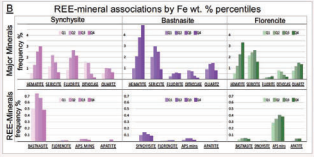
Most commonly, the REE-minerals at Olympic Dam are fine-grained and disseminated within breccia, in both matrix and clasts, making MLA analysis extremely helpful for understanding deposit-scale trends.

To organize the large numerical MLA dataset into a 'geological' context, the data was divided into percentiles based on the assayed wt. % Fe. Fe content has been shown to be an indication of alteration intensity [2]. All samples in this dataset are from within the Cu-resource, so all samples are altered to some extent. The lowest Fe wt. % (Q1) represents the 'least altered' and Q4 represents the 'most altered' with the highest-Fe wt. %, up to 60 wt. % Fe.

A Modal Mineralogy by Fe wt. % percentiles



B REE-mineral associations by Fe wt. % percentiles



A The most altered zones (up to ~65% hematite) display a positive correlation between the relative abundances of siderite, florencite, apatite, uraninite, pyrite, and chalcopyrite.

A The REE-fluorocarbonates abundance do not positively correlate with hematite abundance.

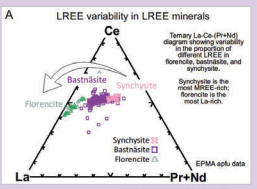
B Synchysite is almost exclusive with bastnasite, reconfirming their petrographic relationship. Synchysite has the weakest association with hematite of the three REE-minerals.

B Bastnasite, being the dominant REE-mineral, is less dependent on the other REE-minerals and has the strongest occurrence with hematite.

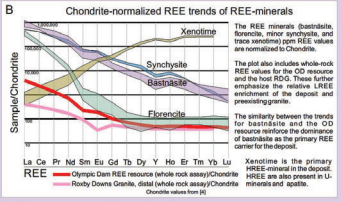
B Florencite shows a predictable strong relationship with it's REE-depleted mineral group minerals of the aluminum-phosphate-sulfate (APS) group.

4. REE Trends

A LREE variability in LREE minerals



B Chondrite-normalized REE trends of REE-minerals



The REE minerals (bastnäsite, florencite, minor synchysite, and trace xenotime) ppm REE values are normalized to Chondrite.

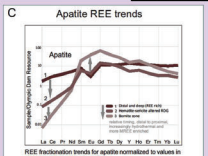
The plot also includes whole-rock REE values for the OD resource and the host RDG. These further emphasize the relative LREE enrichment of the deposit and preexisting granite.

The similarity between the trends for bastnäsite and the OD resource reinforce the dominance of bastnäsite as the primary REE carrier for the deposit.

Xenotime is the primary HREE-mineral in the deposit. HREE are also present in U-minerals and apatite.

Evolution of REE trends in different minerals from Olympic Dam

C Apatite REE trends



REE fractionation trends for apatite normalized to values in the total Olympic Dam resource.

The REE trends of apatite show hydrothermal progression, preserved spatially from distal, magmatic to proximal, hydrothermal: distal apatite (dark) to the hematite-sericite alteration zone (middle) to the bornite zone (light). This mineralization progression shows a decrease in LREE concentration and an increase in MREE concentration with increased hydrothermal alteration suggesting enhanced LREE mobilization (and LREE leaching), forcing MREE enrichment of hydrothermal apatite.

Data from Kmeta et al. [5].

D U-minerals REE trends

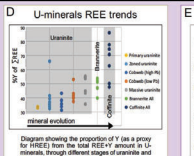
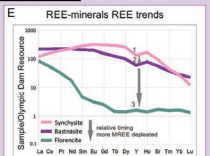


Diagram showing the proportion of Y (as a proxy for HREE) from the total REE-Y amount in U-minerals, through different stages of uraninite and then subsequent brannerite and coffinite.

These REE trends show that HREE becomes enriched relative to LREE with progression of U mineralization. This is possibly caused by REY fractionation due to transport, crystallographic control, and LREE preferentially forming with basinasite.

Data from Macmillan et al. [6] and [7].

E REE-minerals REE trends



Average value for major REE minerals at Olympic Dam normalized to the total Olympic Dam resource.

The REE minerals show a pattern of relative LREE enrichment with sequence of mineralization. Synchysite is more MREE enriched than bastnäsite, nearly flat in the LREE segment, and then the final REE mineralization stage (florencite) is relatively enriched in LREE.

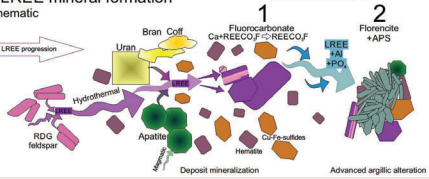
Data from Schmandt et al. [8] and [9].

REE-fluorocarbonates, primary uraninite, and hydrothermal apatite all display intimate associations with hematite and Cu-(Fe)-sulfides and likely formed together at relatively high temperatures (up to 425 °C; [10]). Florencite and paragenetically-late U-minerals are evidence for an evolution towards latter, lower-temperature conditions. Uranium minerals and apatite both show similar patterns of M/HREE enrichment and LREE depletion as mineralization progresses.

The discrete REE minerals, on the other hand, show progressive LREE enrichment and MREE depletion. These REY trends of apatite, U-minerals, and REE-minerals are evidence of LREE leaching from apatite [5] as well as a dominance of LREE across the entire deposit, which suggests enhanced LREE transport during deposit evolution.

5. LREE mineral formation

Schematic



Schematic diagram depicting the leaching of and subsequent formation of LREE minerals at Olympic Dam.

The cartoon follows the "path" of the LREE from left to right, starting with leaching from the host Roxby Downs Granite (RDG) feldspars, then mobility, further leaching during deposit formation via hydrothermal fluids (purple arrows), and massive LREE mineralization (pink = parisite/synchysite, purple = bastnäsite). A later LREE mobilization event, that included Al, PO_4, and SO_4 (blue arrows) redistributed the LREE as florencite.

REE mineralization summary

The formation of LREE minerals at OD can be considered in terms of a sequence of events.

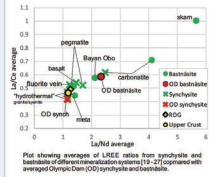
Minerals that formed early include Ca-REE- fluoro-carbonates, including parisite (K-feldspar stable [10, 12]) and synchysite [8].

These were followed by the major stage of REE mineralization consisting of bastnäsite, associated with hematite and Cu-(Fe)-sulfide formation.

Florencite is paragenically late, representing a different stage or evolved formation conditions, which overprints the REE fluorocarbonates, hematite, and Cu-(Fe)-sulfides and replaces apatite [5]. REE-depleted APS minerals of primarily the woodhousite-svanbergite series are also an expression of the florencite event in areas without as abundant REE availability or as a progression of the event after REE-mobility.

6. OD REE mineral compositions compared to other occurrences

OD Bastnäsite vs others: REE ratios



Plot showing averages of LREE ratios from synchysite and bastnäsite of different mineralization systems [19 - 27] copmared with averaged Olympic Dam (OD) synchysite and bastnäsite.

Also plotted are the ratios for the host Roxby Downs Granite (RDG) and average value for the upper crust, which both plot rather close together.

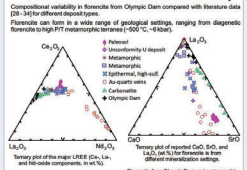
The Olympic Dam bastnäsite and Bayan Obo bastnäsite also plot similarly.

The Olympic Dam synchysite is the most La-poor of the plotted minerals.

OD Florencite vs others: Geochemistry

Compositional variability in florencite from Olympic Dam compared with literature data [28 - 34] for different deposit types.

Florencite can form in a wide range of geological settings, ranging from diagenetic florencite to high-P/T metamorphic terranes (~500 °C, ~6 kbar).



The relative distributions of these LREE show a distinct difference between florencite from the different deposits. OD florencite is the richest in La, followed by florencite from a carbonatite setting, through metamorphic, unconformity, paleosol, and epithermal florencite (which overlap significantly), and then the Au-quartz veins are the most varied and Nd-rich.

Florencite from Olympic Dam and metamorphic environments have the least Ca and Sr; the metamorphic florencite has greater Ca than Sr, different to the rest of the florencite data that plots Sr > Ca. Florencite from the RDG, florencite from Olympic Dam and carbonatite settings have less Ca, compared to other low temperature and even florencite.

7. Discussion and Conclusions

Leaching of LREE from pre-existing minerals, including but not restricted to early U-minerals, magmatic apatite, monazite, and feldspars ([12 - 14]) likely contributed to the LREE-dominant mineralogy of the deposit.

The earliest REE phase was likely Ca-REE-fluorocarbonates, including parisite and synchysite and possibly intermediate phases. These are intimately associated with bastnäsite.

The dominant REE-mineralization phase is pervasive bastnäsite, present across the deposit as fine-grained minerals in the breccia matrix and clasts..

Geological data and modeling of REE bearing systems ([15, 16]), suggest that LREE preferentially formed REE-fluorocarbonates, and effectively removed LREE from solution. This then left the M/HREE to become concentrated in minerals such as late U-minerals and hydrothermal apatite that can more readily incorporate HREE, and that these HREE-rich minerals and minor xenotime probably formed during or after the REE-fluorocarbonates.

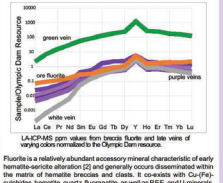
Mixing of hydrothermal and carbonate-rich fluids, or REE-carbonate complexes precipitating from magma degassing are both viable options for the promotion of fluorocarbonate-dominant minerals.

Florencite appears late and likely represents the result of a LREE-dominant remobilization event that took place after REE-fluorocarbonate and sulfide formation. This correlates with the REE-depleted APS-minerals as part of a late advanced argillic alteration stage or evolution of the deposit.

The REE-mineral compositions are broadly similar across the expensive deposit although with localized variation. Compositional heterogeneity at the grain- and sample-scale has been observed in many other mineral species from Olympic Dam (e.g., [6],[7], [17], [18]). Such variation is intrinsically linked to evolving fluid compositions, long-lived fluid regimes, highly heterogeneous protoliths and breccias, and to differential fluid-rock ratios driven by differences in permeability.

F Fluorite REE Trends

ore fluorite and late-stage fluorite veins



LA-ICP-MS ppm values from breccia fluorite and late veins of varying colors normalized to the Olympic Dam resource.

Fluorite is a relatively abundant accessory mineral characteristic of early hematite-sericite alteration [2] and generally occurs disseminated within the matrix of hematite breccias and clasts. It co-exists with Cu-(Fe)-sulphides, hematite, quartz, fluorapatite, as well as REE- and U-minerals.

The deposit also has late fluorite-bearing veins that crossout hematite breccias and dated as ~500 Ma [11]. These veins are minor but they are conspicuous and can be distinct white, purple, and green varieties of fluorite.

Ore-associated fluorite is likely depleted in LREE because of the precipitation of LREE-minerals, which also would result in the slight HREE enrichment compared to the OD resource.

Vein fluorite is more sharply LREE depleted, with flat HREE trends, and all have strong positive Y anomalies. Green fluorite has the most REE.

This research is a contribution to the ARC research Hub for Australian Copper-Uranium.

References

[1] ORESKES, N. & EINAUDI, M.T. (1990) Origin of Rare Earth Element-Enriched Hematite Breccias at the Olympic Dam Cu-U-Au-Ag Deposit, Roxby Downs, South Australia. Economic Geology, 85, 1-28.

[2] EHRIG, K., MCPHIE, J., KAMENETSKY, V.S. (2012) Geology and Mineralogical Zonation of the Olympic Dam Iron Oxide Cu-U-Au-Ag Deposit, South Australia. In Geology and Genesis of Major Copper Deposits and Districts of the World, a Tribute to Richard Sillitoe (J.W. Hedenquist, M. Harris, & F. Camus, eds.). Society of Economic Geologists, Inc. Special Publication 16, Littleton, USA 237-267).

[3] EHRIG, K., MCPHIE, J., KAMENETSKY, V.S., & GOEMANN, C.L. (2011) Olympic Dam-iron oxide Cu-U-Au-Ag deposit. In Australian Ore Deposits (K. Phillips, ed.). AusIMM, Australia 201-410.

[4] MCDONOUGH, W.F. & SUN, S.S. (1995) Composition of the Earth. Chemical Geology, 120, 223–253.

[5] KRNETA, S., CIOBANU, C.L., COOK, N.J., EHRIG, K., & KONTONIKAS-CHAROS, A. (2017a) Rare earth element behaviour in apatite from the Olympic Dam IOCG deposit. Ore Geology Reviews, 82, 84-102.

[6] MACMILLAN, E., COOK, N.J., EHRIG, K., CIOBANU, C.L., & PRING, A. (2016a) Uraninite from the Olympic Dam IOCG-U-Ag deposit: Linking textural and compositional variation to mineral evolution. American Mineralogist, 101, 1280–1300. doi: 10.2138/am-2016-5411

[7] MACMILLAN, E., COOK, N.J., EHRIG, K. & PRING, A. (2017) Chemical and textural interpretation of late-stage coffinite and brannerite from the Olympic Dam deposit. Mineralogy and Petrology, 111, 165-183.

[8] SCHMANDT, D.S., COOK, N.J., CIOBANU, C.L., EHRIG, K., WADE, B.P., GILBERT, S., & KAMENETSKY, V.S. (2017) Rare Earth Element Fluorocarbonate Minerals from the Olympic Dam Cu-U-Au-Ag Deposit, South Australia. Minerals, 7, 202.

[9] SCHMANDT, D.S., COOK, N.J., CIOBANU, C.L., EHRIG, K., WADE, B.P., GILBERT, S., & KAMENETSKY, V.S. (2017) Textures and U-rich-clay alteration of rare earth element fluorocarbonates from Olympic Dam Cu-U-Au-Ag deposit, South Australia: Recognizing temporal-spatial controls on REE mineralogy in an evolved IOCG systems. In review.

[10] CIOBANU, C.L., KONTONIKAS-CHAROS, A., SLATTERY, A., COOK, N.J., EHRIG, K., & WADE, B.P. (2017b) Short-Range Blocking Disorder in Feldspars from the Olympic Dam Iron Oxide Cu-U-Au-Ag Deposit, South Australia. Minerals, 7, 53.

[11] Maas, R., Kamenetsky, V.S., Ehrig, K., Neffke, S., McPhie, J., Danner, S., 2011. Olympic Dam Cu-U-Au Deposit, Australia: New Age Constraints, Gawler Craft Conference abstract

[12] KRNETA, S., CIOBANU, C.L., COOK, N.J., EHRIG, K., KRNETA, S., & KAMENETSKY, V.S. (2016b) Rare earth element behaviour in hematite from the Olympic Dam Cu-U-Au-Ag deposit, South Australia. Mineralogy and Petrology, 110, 149-172.

[13] KONTONIKAS-CHAROS, A., CIOBANU, C.L., COOK, N.J., EHRIG, K., KRNETA, S., & KAMENETSKY, V.S. (2017) Feldspar evolution in the Roxby Downs Granite, host to Olympic Dam Cu-(U-Au) deposit, South Australia. Ore Geology Reviews, 86, 838-856.

[14] KONTONIKAS-CHAROS, A., CIOBANU, C.L., COOK, N.J., EHRIG, K., ISMAIL, R., KRNETA, S., & BAKAKA, A. (2016a) Feldspar mineralogy and trace element characteristics of unaltered and altered host rocks to iron oxide copper-gold systems: Olympic Dam South Australia, a nanoscale study. Mineralogical Magazine, 80(01), 5173-5197.

[15] MEDEIROS, D.A., WILLIAMS-JONES, A.E., SRIDEVI, J., & DAPOIGNOSO, FA. (2016) Hydrothermal transport, deposition, and fractionation of the REE: Experimental data and thermodynamic calculations. Geochimica et Cosmochimica Acta, 192, 255-273.

[16] SITU, A.P.A. WILLIAMS-JONES, A.E. (2017) The thermodynamics of florencite (Ce) and parisite (Ce). Chem. Geol. 360, 87–101.

[17] CIOBANU, C.L., COOK, N.J., UTSUNOMIYA, S., KONTONIKAS-CHAROS, A. (2012) Haematite-hosted gold deposits: Nanoscale imaging of gold and associated ore and gangue minerals from the Mt Woods Inlier, South Australia. Ore Geology Reviews, 46, 1-26.

[18] CIOBANU, C.L., COOK, N.J., UTSUNOMIYA, S., KONTONIKAS-CHAROS, A. (2011) Gold telluride nanoparticles in haematite and the origin of the Au-Bi association in iron oxide copper-gold deposits. Mineralium Deposita, 46, 341-363.

[19] CIOBANU, C.L., COOK, N.J., ALDERTON, D.H.M., PRING, A., ONEILL, B., GILBERT, S.E. (2009) In situ trace element analysis, textural and genetic investigations of arsenopyrite from Amphitheatre Zone, Curnamona Province, South Australia. Neues Jahrbuch für Mineralogie, Abhandlungen, 186, 173-202.

[20] CIOBANU, C.L., COOK, N.J., PRING, A., MCPHAIL, D., DANYUSHEVSKY, L., ONEILL, B., GILBERT, S.E. (2010) Silver-bismuth microparticles in pyrite and chalcopyrite: Evidence for the extent of invisible gold deposition. Ore Geology Reviews, 38, 322-350.

[21] CIOBANU, C.L., COOK, N.J., UTSUNOMIYA, S., PRING, A. (2011) Intergrowth-controlled trace-element variability in natural pyrite from the Curnamona Province, South Australia. Mineralogical Magazine, 75, 211-241.

[22] CIOBANU, C.L., COOK, N.J., UTSUNOMIYA, S., KONTONIKAS-CHAROS, A., STANLEY, C., GRGURIC, B. (2012) Multi-generation formation of iron oxide-copper-gold mineralization demonstrated by complex gold and tellurobismuthide associations. Mineralogy and Petrology, 105, 37-54.

[23] CIOBANU, C.L., COOK, N.J., KONTONIKAS-CHAROS, A. (2016) Adularia-type gold deposits: Evidence for the significance of colloidal and replacement processes in bonanza environments. Ore Geology Reviews, 76, 211-235.

[24] CRAW, D., KERROD, E., HUNTER, K. (2006) Lanthanide geochemistry, fluid source and gold mineralization in the Macraes mesothermal gold deposit, East Otago, New Zealand. Lithos, 88, 17-42.

[25] FINDLAY, D., BRADLEY, K., WALL, F., GUNN, G., DAWES, W. REE Minerals at the Songwe Hill Carbonatite, Malawi: HREE-Enrichment in Late-Stage Apatite. Elements, 11, 55-60.

[26] GUALDA, G.A.R., GUALDA, M.P.R., GIBB, F.G.F., SCOTT, S.R., CUSTODIO, M.A., BOLLERO, R. (2010) Quantitative morphology of sanidine crystals from pumice and pyroclastic deposits as a tool to evaluate the evolution of silicic magmas. Journal of Volcanology and Geothermal Research, 198, 314-334.

[27] HANGE, T., BALLY, A., BIDAUX, Y. (2010) Rift-related Cretaceous Occurrence of Syntaxitic-(Ce) in Amygdules from the Eastern Volcanic Rocks, France: Implications for Rare Earth Element Mobility. Can. Mineral, 48, 1-19.

[28] LEVICAN, I., SOMELAR, P., LAANSALU, S., KIRS, J., & KIRSIMÄE, K. (2010) Origin and paleoenvironmental interpretation of aluminum phosphate–sulfate minerals in Ediacaran sandstones, Estonia. Sedimentary Geology, 230, 1-12.

[29] DAGENAIS, A., CHAPDELAINE, C., GUARI, G., BEAUFORT, D., PATRIER, P., & MATHIEU, R. (2007) Significance of aluminum phosphate-sulfate minerals associated with Unconformity-type deposits: The Athabasca basin, Canada. American Mineralogist, 92, 297–280.

[30] MACHEYEKI, A.S., SINHA, A.K., SINHA, R., & FERNANDEZ, A.N. (2008) Hydrothermal REE mineralization in the Amba Dongar carbonatite complex, Gujarat, India. Canadian Mineralogist, 47, 1103-1116.

[31] GEORGIEVA, S. & VELINOVA, N. (2004) Florencite-(Ce, La, Nd) and crandallite from the advanced argillic alteration in the Chalupech high-sulfidation epithermal Cu-Au deposit, Bulgaria: Complex redox or fluctuating fugacities and activities. Geochemistry, 64, 1-12.

[32] REPPAS, S.A., KHILLER, V.V., & MAGADOVV, E.F. (2014) Monoheterogeneity of Crystal Growth Zones as a Result of REE Fractionation. Geochemistry International, 52, 1067–1071.

[33] NADY, D., DRAGANITS, E., DEMENY, A., PANTO, G., & ARKAI, P. (2002) Genesis and transformations of monazite, florencite and rhabdophane during Neogene lateritic weathering in the Darnó Hill area, NE Hungary. Chem. Geol, 191, 109-142.

[34] CHAKRABORTY, M., BISWAS, A., SENGUPTA, S. & DENGUPTA, P. (2014) First Report of Florencite from the Singhbhum Shear Zone of the East Indian Craton. International Journal of Mineralogy, 2014, 1-8.

CHAPTER 9

REFERENCES

Airey, P., Hinton, T. & Twining, J. (2012) The Scientific Basis: In J. R. Twining (ed.) Radioactivity in the Environment Vol 18, Chapter 1. Elsevier Ltd. doi: 10.1016/B978-0-08-045016-2.00001-1.

Allen, R.D. (1952) Variations in Chemical and Physical Properties of Fluorite. American Mineralogist, 37, 910–930.

Allen, S.R., McPhie, J., Ferris, G. & Simpson, C. (2008) Evolution and architecture of a large felsic Igneous Province in Western Laurentia: The 1.6 Ga Gawler Range Volcanics, South Australia. Journal of Volcanology and Geothermal Research, 172, 132–147. doi: 10.1016/j.jvolgeores.2005.09.027.

Aoki, M., Comsti, E.C., Lazo, F.B. & Matsuhisa, Y. (1993) Advanced Argillic Alteration and Geochemistry of Alunite in an Evolving Hydrothermal system at Baguio, Norther Luzon, Philippines. Resource Geology, 43, 155–164.

Apukhtina, O.B. (2016) Distribution, petrology, geochemistry and geochronology of carbonate assemblages at the Olympic Dam deposit. Unpublished Ph.D. thesis, University of Tasmania, Hobart. https://eprints.utas.edu.au/23013/.

Apukhtina, O.B., Ehrig, K., Kamenetsky, V.S., Kamenetsky, M.B., Geomann, K., Maas, R., McPhie, J., Ciobanu, C.L. & Cook, N.J. (in preparation) Carbonates in the Olympic Dam Cu-U-Au-Ag deposit. Part I: Distribution, textures, associations and stable isotope (C, O) signatures. Ore Geology Reviews.

Apukhtina, O.B., Kamenetsky, V.S., Ehrig, K., Kamenetsky, M.B., McPhie, J., Maas, R., Meffre, S., Goemann, K., Rodemann, T., Cook, N.J. & Ciobanu, C.L. (2016) Postmagmatic magnetite–apatite assemblage in mafic intrusions: a case study of dolerite at Olympic Dam, South Australia. Contributions to Mineralogy and Petrology, 171, 1–15. doi: 10.1007/s00410-015-1215-7.

Apukhtina, O.B., Kamenetsky, V.S., Ehrig, K., Kamenetsky, M.B., Maas, R., Thompson, J., McPhie, J., Ciobanu, C.L. & Cook, N.J. (2017) Early, deep magnetite-fluorapatite mineralization at the Olympic Dam Cu-U-Au-Ag deposit, South Australia. Economic Geology, 112, 1531–1542. doi: 10.5382/econgeo.2017.4520.

Armstrong, J.T. (1988) Quantitative analysis of silicate and oxide minerals: Comparison of Monte Carlo, ZAF, and φ(ρz) procedures. Microbeam Analysis, D.E. Newbury (ed.) San Francisco Press. 239–246.

Arribas, A., Cunningham, C.G., Rytuba, J.J., Rye, R.O., Kelly, W.C., Podwysocki, M.H. & Tosdal, R.M. (1995) Geology, geochemistry, fluid inclusion and isotope geochemistry of the Rodalquilar gold-alunite deposit, Spain. Economic Geology, 90, 795–822.

Augé, T., Bailly, L. & Wille, G. (2014) An Unusual Occurrence of Synchysite-(Ce) in Amygdules from the Esterel Volcanic Rocks, France: Implications for Rare-Earth Element Mobility. The Canadian Mineralogist, 52, 1–19.

Bajnoczi, B., Seres-Hartai, E. & Nagy, G. (2004) Phosphate-bearing minerals in the advanced argillic alteration zones of high-sulphidation type ore deposits in the Carpatho-Pannonian region. Acta Mineralogica-Petrographica, Szeged, 45, 81–92.

Barton, M.D. (2014) Iron Oxide (-Cu-Au-REE-P-Ag-U-Co) Systems. In Turekian, K. & Holland, H. (eds.) Treatise on Geochemistry: 2nd Edition, Vol. 13, 515–541. Elsevier Ltd. doi: 10.1016/B978-0-08-095975-7.01123-2.

Bau, M. & Dulski, P. (1995) Comparative-Study of Yttrium and Rare-Earth Element Behaviors in Fluorine-Rich Hydrothermal Fluids. Contributions to Mineralogy and Petrology, 119, 213–223. doi: 10.1007/bf00307282.

Bau, M. (1996) Controls on the Fractionation of Isovalent Trace Elements in Magmatic and Aqueous Systems: Evidence from Y/Ho, Zr/Hf, and lanthanide tetrad effect. Contributions to Mineralogy and Petrology, 123, 323–333.

Bayliss, P., Kolitsch, U., Nickel, E.H. & Pring, A. (2010) Alunite supergroup: recommended nomenclature. Mineralogical Magazine, 74, 919–927. doi: 10.1180 /minmag.2010.074.5.919.

Berman, R. (1956) Some Physical Properties of Naturally Irradiated Fluorite. USGS Trace Elements Investigations, Report 372, 191–203. doi: 10.3133/tei569.

Bevan, D.J.M., Strähle, J. & Greis, O. (1982) The crystal structure of tveitite, an ordered yttrofluorite mineral. Journal of Solid State Chemistry, 44, 75–81. doi: 10.1016/0022-4596(82)90402-9.

Beyer, S.R., Kyser, T.K., Hiatt, E.E., Polito, P.A., Alexandre, P. & Hoksbergen, K. (2012) Basin evolution and unconformity-related uranium mineralization: The Camie River U prospect, Paleoproterozoic Otish Basin, Quebec. Economic Geology, 107, 401–425.

BHP Annual Report (2017) Copper Mineral Resources, 256–257. www.bhp.com.

BHP Annual Report (2018) https://www.bhp.com/-/media/documents/investors/annual-reports/2018/ bhpannualreport2018.pdf.

BHP Billiton (2009) Olympic Dam Expansion. Draft Environmental Impact Statement. Appendix S, 30. www.bhp.com. ISBN 978-0-9806218-4-6.

BHP Billiton (2011) Olympic Dam Expansion Supplementary Environmental Impact Statement, Chapter 26, 689–758. www.bhp.com. ISBN 978-0-9806218-5-3, 978-0-9806218-6-0.

BHP Billiton (2016) http://www.bhpbilliton.com/home/investors/annualreporting2016.pdf.

Bierlein, F.P., Foster, D.A. & Plimer, I.R. (1996) Tectonotermal implications of laser $^{40}Ar/^{39}Ar$ ages of sulphide-bearing veins and their host rocks in in the Willyama Supergroup, South Australia. Mineralogy and Petrology, 58, 1–22. doi: 10.1007/BF01165760.

Bill, H. & Calas, G. (1978) Color centers, associated rare-earth ions and the origin of coloration in natural fluorites. Physics and Chemistry of Minerals, 3, 117–131. doi: 10.1007/BF00308116.

Bosbach, D., Böttle, M. & Metz, V. (2010) Experimental study on Ra^{2+} uptake by barite ($BaSO_4$). Svensk Kärnbranslehantering AB. Technical report TR-10–43, 111.

Bourdon, B., Henderson, G.M., Lundstrom, C.C. & Turner, S.P. (eds.) (2003) Uranium-Series Geochemistry, Volume 52, Reviews in Mineralogy & Geochemistry. Washington: Mineralogical Society of America, Geochemical Society. ISSN 1529-6466.

Bowden, B., Fraser, G., Davidson, G.J., Meffre, S., Skirrow, R., Bull, S. & Thompson, J. (2017) Age constraints on the hydrothermal history of the Prominent Hill iron oxide copper-gold deposit, South Australia. Mineralium Deposita, 52, 863–881.

Bowell, R.J., Grogan, J., Hutton-Ashkenny, M., Brough, C., Penman, K. & Sapsford, D.J. (2011) Geometallurgy of uranium deposits. Minerals Engineering, 24, 1305–1313. doi: 10.1016/j.mineng.2011.05.005.

Brandt, F., Curti, E., Klinkenberg, M., Rozov, K. & Bosbach, D. (2015) Replacement of barite by a $(Ba,Ra)SO_4$ solid solution at close-to-equilibrium conditions: A combined experimental and theoretical study. Geochimica et Cosmochimica Acta, 155, 1–15.

Britt, A., Summerfield, D., Senior, A., Roberts, D., Kay, P., Hitchman, A., Champion, D., Huston, D., Simpson, R., Smith, M., Sexton, M. & Schofield, A. (2016) Australia's Identified Mineral Resources 2016. Canberra: Geoscience Australia. doi: 10.11636/1327-1466.2016.

Broom-Fendley, S., Brady, A.E., Wall, F., Gunn, G. & Dawes, W. (2017) REE minerals at the Songwe Hill carbonatite, Malawi: HREE-enrichment in late-stage apatite. Ore Geology Reviews, 81, 23–41. doi: 10.1016/j.oregeorev.2016.10.019.

Brugger, J., Liu, W., Etschmann, B., Mei, Y., Sherman, D.M. & Testemale, D. (2016) A Review of the Coordination Chemistry of Hydrothermal Systems, or Do Coordination Changes Make Ore Deposits? Chemical Geology, 447, 219–253.

Brugger, J., Ogierman, J., Pring, A., Waldron, H. & Kolitsch, U. (2006) Origin of the secondary REE-minerals at the Paratoo copper deposit near Yunta, South Australia. Mineralogy Magazine, 70, 609–627. doi: 10.1180/0026461067060361.

Calas, G., Allard, T., Balan, E. & Morin, G. (2003) Radiation-induced Defects in Nonradioactive Natural Minerals: Mineralogical and Environmental Significance. Symposium R - Radiation Effects Ion Beam Processing of Materials, 792, R2.6. doi: 10.1557/PROC-792-R2.6.

Chakraborty, M., Biswas, S., Sengupta, N. & Sengupta, P. (2014) First Report of Florencite from the Singhbhum Shear Zone of the East Indian Craton. International Journal of Mineralogy, 2014, 1–9. doi: 10.1155/2014/978793.

Champion, D.C. & Huston, D.L. (2016) Radiogenic isotopes, ore deposits and metallogenic terranes: Novel approaches based on regional isotopic maps and the mineral systems concept. Ore Geology Reviews, 76, 229–256.

Chapman, N.D., Meffre, S., Kamenetsky, V., Kathy, E. & Kontonikas-Charos, A. (2016) The Pb-isotopes of Olympic Dam and beyond – the uranium story of the Gawler Craton. Australian Earth Sciences Convention 2016, June 26-30, Adelaide, SA, Geological Society of Australia Abstract No 118. Abstracts book, 72–73. ISSN: 0729 011 X.

Cherry, A.R., Ehrig, K., Kamenetsky, V.S., Ehrig, K., McPhie, J., Croley, J.L. & Kamenetsky, M.B. (2018) Precise geochronological constraints on the origin, setting and incorporation of ca. 1.59 Ga surficial facies into the Olympic Dam Breccia Complex, South Australia. Precambrian Research 315, 162–178. doi: 10.1016/j.precamres.2018.07.012.

Cherry, A.R., Kamenetsky, V.S., McPhie, J., Thompson, J.M., Ehrig, K., Meffre, S., Kamenetsky, M.B. & Krneta, S. (2018) Tectonothermal events in the Olympic IOCG Province constrained by apatite and REE-phosphate geochronology. Australian Journal of Earth Sciences. 65:5, 643–659. doi: 10.1080/08120099.2018.1465473.

Cherry, A.R., McPhie, J., Kamenetsky, V.S., Ehrig, K., Keeling, J.L., Kamenetsky, M.B, Meffre, S., and Apukhtina, O.B. (2017) Linking Olympic Dam and the Cariewerloo Basin: Was a sedimentary basin involved in formation of the world's largest uranium deposit?. Precambrian Research, 300, 168–180. doi: 10.1016/j.precamres.2017.08.002.

Ciobanu, C.L., Cook, N.J. & Ehrig, K. (2017) Ore minerals down to the nanoscale: Cu-(Fe)-sulphides from the iron oxide copper gold deposit at Olympic Dam, South Australia. Ore Geology Reviews, 81, 1218–1235.

Ciobanu, C.L., Cook, N.J., Ehrig, K., Wade, B.P. & Kamenetsky, V.S. (2015) Trace element signatures in iron oxides from the Olympic Dam IOCG deposit, South Australia. 13th SGA Biennial Meeting 2015. Mineral Resources for a Sustainable World 3, 1071–1074.

Ciobanu, C.L., Kontonikas-Charos, A., Slattery, A., Cook, N.J., Ehrig, K. & Wade, B.P. (2017) Short-Range Stacking Disorder in Mixed-Layer Compounds: A HAADF STEM Study of Bastnäsite-Parisite Intergrowths. Minerals, 7, 227. doi: 10.3390/min7110227.

Ciobanu, C.L., Wade, B.P., Cook, N.J., Schmidt Mumm, A. & Giles, D. (2013) Uranium-bearing hematite from the Olympic Dam Cu-U-Au deposit, South Australia: A geochemical tracer and reconnaissance Pb-Pb geochronometer. Precambrian Research, 238, 129–147. doi: 10.1016/j.precamres.2013.10.007.

Clark, J.M., Poznik, N., Ehrig, K., Cherry, A., McPhie, J. & Kamenetsky, V.S. (2018) Syn- to Postmineralization Structural Dismemberment of the Olympic Dam Fe-Cu-U-Au-Ag Deposit, Gawler Craton in SEG 2018 Conference Proceeding, Keystone 22-15, Enders, M.S. & Broughton, D.W. (eds.).

Conor, C., Raymond, O.L., Baker, T., Teale, G., Say, P. & Lowe, G. (2010) Alteration and mineralisation in the Moonta-Wallaroo Copper-Gold Mining Field Region, Olympic Domain, South Australia: In Porter, T.M. (ed.) Hydrothermal Iron Oxide Copper-Gold & Related Deposits: A Global Perspective vol. 3-4, 1–24. Adelaide: PGC Publishing.

Cook, N.J., Ciobanu, C.L., Ehrig, K., Slattery, A., Verdugo-Ihl, M.R., Courtney-Davies, L. & Gao, W. (2017) Advances and opportunities in ore mineralogy. Minerals 7, 233. doi: 10.3390/min7120233.

Cook, N.J., Ciobanu, C.L., George, L. & Ehrig, K. (2016) Trace Element Analysis of Minerals in Magmatic-Hydrothermal Ores by Laser Ablation Inductively-Coupled Plasma Mass Spectrometry: Approaches and Opportunities. Minerals, 6, 111. doi: 10.3390/min6040111.

Cook, N.J., Ehrig, K., Ciobanu, C.L., Courtney-Davies, L., Verdugo-Ihl, M.R., Rollog, M., Schmandt, D.S., Owen, N.D., Macmillan, E., Kontonikas-Charos, A., Krneta, S. & Dmitrijeva, M. (2018) Why detailed mineralogy is important: Understanding evolution of the giant Olympic Dam iron-oxide copper-gold system, South Australia. 15th Quadrennial IAGOD Symposium, Salta, Argentina, 28-31 August 2018. Symposium Proceedings Volume, SegemAR, 371–372.

Cook, N.J., Ehrig, K., Rollog, M., Ciobanu, C.L., Lane, D.J., Schmandt, D.S., Owen, N.D., Hamilton, T. & Grano, S.R. (2018) ^{210}Pb and ^{210}Po in geological and related anthropogenic materials: Implications for their mineralogical distribution in base metal ores. Minerals, 8. doi: 10.3390/min8050211.

Corriveau, L. (2007) Iron Oxide Copper-Gold (±Ag ±Nb ±P ±Ree ±U) Deposits: a Canadian Perspective: In W. D. Goodfellow (ed.) Mineral Deposits of Canada: A Synthesis of Major Deposit-Types, District Metallogeny, the Evolution of Geological Provinces, and Exploration Methods. Special Publication, 307–328. Geological Association of Canada, Mineral Deposits Division.

Courtin-Nomade, A., Soubrand-Colin, M., Marcus, M.A. & Fakra, S.C. (2008) Evidence for the incorporation of lead into barite from waste rock pile materials. Environmental Science & Technology, 42, 2867–2872.

Courtney-Davies, L., Ciobanu, C.L., Verdugo-Ihl, M.R., Slattery, A., Cook, N.J., Dmitrijeva, M., Keyser, W., Wade, B.P., Domnick, U.I., Ehrig, K., Xu, J. & Kontonikas-Charos, A. (in review) Zircon down to the nanoscale: A record of metasomatic processes leading to large magmatic-hydrothermal ore systems. Earth and Planetary Science Letters.

Courtney-Davies, L., Tapster, S.R., Ciobanu, C.L., Cook, N.J., Verdugo-Ihl, M.R., Ehrig, K., Kennedy, A., Gilbert, S., Condon, D.J. & Wade, B.P. (2019) A multi-technique evaluation of hydrothermal hematite U-Pb isotope systematics: Implications for ore deposit geochronology. Chemical Geology, 513, 54–72. doi: 10.1016/j.chemgeo.2019.03.005.

Courtney-Davies, L., Zhu, Z., Ciobanu, C.L., Wade, B.P., Cook, N.J., Ehrig, K., Cabral, A.R. & Kennedy, A. (2016) Matrix-Matched Iron-Oxide Laser Ablation ICP-MS U–Pb Geochronology Using Mixed Solution Standards. Minerals, 6, 85. doi:10.3390/min6030085.

Creaser, R.A. & Cooper, J.A. (1993) U-Pb Geochronology of Middle Proterozoic felsic magmatism surrounding the Olympic Dam Cu-U-Au-Ag and Moonta Cu-Au-Ag deposits, South Australia. Economic Geology, 88, 186–197.

Creaser, R.A. (1989) The geology and petrology of Middle Proterozoic felsic magmatism of the Stuart Shelf, South Australia. Unpublished Ph.D. Thesis, La Trobe University, Melbourne.

Cumming, G.L. & Richards, J.R. (1975) Ore lead isotope ratios in a continously changing Earth. Earth and Planetary Science Letters, 28, 155–171.

Curti, E. (1997) Coprecipitation of radionuclides: basic concepts, literature review and first applications. Report 97-10, Paul Scherrer Institut, Villigen, Switzerland, 116.

Curti, E., Fujiwara, K., Iijima, K., Tits, J., Cuesta, C., Kitamura, A., Glaus, M.A. & Muller, W. (2010) Radium uptake during barite recrystallization at 23 ± 2 °C as a function of solution composition: An experimental ^{133}Ba and ^{226}Ra tracer study. Geochimica et Cosmochimica Acta, 74, 3553–3570.

Curti, E., Xto, J., Borca, C.N., Henzler, K., Huthwelker, T., Prasianakis, N.I. (2018) Modelling Ra-bearing baryte nucleation/precipitation kinetics at the pore scale: application to radioactive waste disposal. European Journal of Mineralogy, 1–16. doi: 10.1127/ejm/2019/0031-2818.

Daly, S.J., Fanning, C.M. & Fairclough, M.C. (1998) Tectonic evolution and exploration potential for the Gawler Craton, South Australia. AGSO Journal of Australian Geology and Geophysics, 17, 145–168.

Darling, J.R., Storey, C.D., Hawkesworth, C.J. & Lightfoot, P.C. (2012) In-Situ Pb isotope analysis of Fe-Ni-Cu sulphides by Laser Ablation Multi-Collector ICPMS: New insights into ore formation in the Sudbury Impact Melt Sheet. Geochimica et Cosmochimica Acta, 99, 1–17.

Davidson, G.J., Paterson, H., Meffre, S. & Berry, R.F. (2007) Characteristics and Origin of the Oak Dam East Breccia-Hosted, Iron Oxide Cu-U-(Au) Deposit: Olympic Dam Region, Gawler Craton, South Australia. Economic Geology, 102, 1471–1498.

Deconinck, I., Latkoczy, C., Cunther, D., Govaert, F. & Vanhaecke, F. (2006) Capabilities of laser ablation — inductively coupled plasma mass spectrometry for (trace) element analysis of car paints for forensic purposes. Journal Of Analytical Atomic Spectrometry, 21, 279–287. doi: 10.1039/b514007b.

Deer, W.A., Howie, R.A. & Zussman, J. (eds.) (1992) An Introduction to the Rock-Forming Minerals, 2nd ed., Harlow, Essex, England: New York, NY: Longman Scientific & Technical.

DePaolo, D.J. (2011) Surface kinetic model for isotopic and trace element fractionation during precipitation of calcite from aqueous solutions. Geochimica et Cosmochimica Acta, 75, 1039–1056. doi: 10.1016/j.gca.2010.11.020.

Didier, A., Bosse, V., Boulvais, P., Bouloton, J., Paquette, J.L., Montel, J.M. & Devidal, J.L. (2013) Disturbance versus preservation of U-Th-Pb ages in monazite during fluid-rock

interaction: Textural, chemical and isotopic in situ study in microgranites (Velay Dome, France). Contributions to Mineralogy and Petrology, 165, 1051–1072.

Diemar, G.A. (2014) The Petrology of Hydrothermal Rare Earth Element Bearing Minerals in the Olympic Dam IOCG Deposit Support a 1.3 Ga formation. Unpublished M.Sc. thesis, University of Tasmania, Hobart.

Dill, H.G. & Weber, B. (2010) Variation of color , structure and morphology of fluorite and the origin of the hydrothermal F-Ba deposits at Nabburg- Wölsendorf, SE Germany. Neues Jahrbuch für Mineralogie-Abhandlungen, 187, 113–132. doi: 10.1127/0077-7757/2010/0169.

Dill, H.G. (2001) The geology of aluminium phosphates and sulphates of the alunite group minerals: a review. Earth-Science Reviews, 53, 35–93.

Direen, N.G. & Lyons, P. (2007) Regional Crustal Setting of Iron Oxide Cu-Au Mineral Systems of the Olympic Dam Region, South Australia: Insights from Potential-Field Modeling. Economic Geology, 102, 1397–1414.

Ditchburn, R.G. & de Ronde, C.E.J. (2017) Evidence for remobilization of barite affecting radiometric dating using ^{228}Ra, ^{228}Th, and ^{226}Ra/Ba values: Implications for the evolution of sea-floor volcanogenic massive sulfides. Economic Geology, 112, 1231–1245.

Dmitrijeva, M., Ehrig, K., Ciobanu, C.L., Cook, N.J., Verdugo-Ihl, M.R. & Metcalfe, AV. (2019) Defining IOCG signatures through compositional data analysis: a case study of lithogeochemical zoning at Olympic Dam, South Australia. Ore Geology Reviews, 105, 86–101. doi: 10.1016/j.oregeorev.2018.12.013.

Domnick, U., Cook, N.J., Bluck, R., Brown, C. & Ciobanu, C.L. (2018) Petrography and geochemistry of granitoids from the Samphire Pluton, South Australia: Implications for uranium mineralisation in overlying sediments. Lithos, 300-301, 1–19.

Donnay, G. & Donnay. J.D.H. (1953) The crystallography of bastnaesite, parisite, roentgenite and synchysite. American Mineralogist, 38, 932–963.

Donovan, J.J. & Tingle, T.N. (1996) An Improved Mean Atomic Number Background Correction for Quantitative Microanalysis. Microscopy and Microanalysis, 1, 1–7.

Doroshkevich, A.G., Viladkar, S.G., Ripp, G.S. & Burtseva, M.V. (2009) Hydrothermal REE mineralization in the Amba Dongar carbonatite complex, Gujarat, India. The Canadian Mineralogist, 47, 1105–1116. doi: 10.3749/canmin.47.5.1105.

Ehrig, K. (2013) Geometallurgy-What do you really need to know from exploration through to production?: In Proceedings MetPlant 2013, 28–33. The Australasian Institute of Mining and Metallurgy: Melbourne.

Ehrig, K., Kamenetsky, V.S., McPhie, J., Cook, N.J. & Ciobanu, C.L. (2017) Olympic Dam iron oxide Cu-U-Au-Ag deposit; in Phillips, G.N. (ed.), Australian Ore Deposits, 601–610. Melbourne: The Australasian Institute of Mining and Metallurgy.

Ehrig, K., Liebezeit, V., Macmillan, E., Lower, C., Kamenetsky, V.S., Cook, N.J. & Ciobanu, C.L. (2015) Uranium mineralogy versus the recovery of uranium at Olympic Dam. The AusIMM International Uranium Conference 2015, Adelaide.

Ehrig, K., McPhie, J. & Kamenetsky, V.S. (2012) Geology and Mineralogical Zonation of the Olympic Dam Iron Oxide Cu-U-Au-Ag Deposit, South Australia. In Hedenquist, J.W., Harris, M. & Camus, F. (eds.) Geology and Genesis of Major Copper Deposits and Districts of the World, a Tribute to Richard Sillitoe, Society of Economic Geology Special Publication, Vol. 16, 237–267. Littleton, CO, USA: SEG.

Eisenbud, M. & Gesell, T. (1997) Environmental Radioactivity from Natural, Industrial & Military Sources. Oxford, UK: Academic Press.

Eppinger, R.G. & Closs, L.G. (1990) Variation of Trace Elements and Rare Earth Elements in Fluorite: A Possible Tool for Exploration. Economic Geology, 85, 1896–1907.

Eppinger, R.G. (1988) Trace element and rare earth element variation in fluorites collected from skarn and epithermal mineral deposits in the Sierra Cuchillo area, south-central New Mexico. USGS, Open-File Report 88-566, 108.

Ferris, G.M., Schwarz, M.P. & Heithersay, P. (2002) The geologic framework, distribution, and controls of Fe-oxide Cu-Au mineralisation in the Gawler Craton, South Australia: Part I: Geological and tectonic framework. In Porter, T.M. (ed.) Hydrothermal Iron Oxide Copper-Gold and Related Deposits: A Global Perspective, vol. 2, 9–31. Adelaide: PGC Publishing.

Fleischer, M. (1978) Relative proportions of the lanthanides in minerals of the bastnaesite group. The Canadian Mineralogist, 16, 361–363.

Foden, J., Elburg, M.A., Dougherty-Page, J. & Burtt, A. (2006) The Timing and Duration of the Delamerian Orogeny: Correlation with the Ross Orogen and Implications for Gondwana Assembly. The Journal of Geology, 114, 189–210. doi: 10.1086/499570.

Förster, H.J. (2000) Cerite-(Ce) and thorian synchysite-(Ce) from the Niederbobritzsch Granite, Erzgebirge, Germany: Implications for the differential mobility of the LREE and Th during alteration. The Canadian Mineralogist, 38, 67–79.

Förster, H.J. (2006) Composition and origin of intermediate solid solutions in the system thorite-xenotime-zircon-coffinite. Lithos, 88, 35–55.

Freeman, H. & Tomkinson, M. (2010) Geological setting of iron oxide related mineralisation in the Southern Mount Woods Domain, South Australia: In Porter, T.M. (ed.) Hydrothermal Iron Oxide Copper-Gold & Related Deposits: A Global Perspective, v.3-Advances in the Understanding of IOCG Deposits, 1–20. Adelaide: PGC Publishing.

Fulignati, P., Gioncada, A. & Sbrana, A. (1999) Rare-earth element (REE) behaviour in the alteration facies of the active magmatic-hydrothermal system of Vulcano (Aeolian Islands, Italy). Journal of Volcanology and Geothermal Research, 88, 325–342. doi: 10.1016/S0377-0273(98)00117-6.

Gaboreau, S., Cuney, M., Quirt, D., Beaufort, D., Patrier, P. & Mathieu, R. (2007) Significance of aluminum phosphate-sulfate minerals associated with U unconformity-type deposits: The Athabasca basin, Canada. American Mineralogist, 92, 267–280. doi: 10.2138/am.2007.2277.

Gagnon, J.E., Samson, I.M., Fryer, B.J. & Williams-Jones, A.E. (2003) Compositional heterogeneity in fluorite and the genesis of fluorite deposits: Insights from LA-ICP-MS analysis. The Canadian Mineralogist, 41, 365–382.

Georgieva, S. & Velinova, N. (2014) Florencite-(Ce, La, Nd) and crandallite from the advanced argillic alteration in the Chelopech high-sulphidation epithermal Cu-Au deposit, Bulgaria. Comptes rendus de l'Académie bulgare des sciences: sciences mathématiques et naturelles, 67, 1669–1678.

Goemann, K. & Donovan, J.J. (2017) Electron probe microanalysis of complex natural sulphides using shared background measurements: In The Australian Microscopy & Micronalysis Society AMAS 2017, 14th Biennial Australian Microbeam Analysis Symposium, Brisbane, Australia, 6-10 February 2017, 61–62. ISBN: 978-0-9580408-6-0.

Goemann, K., Donovan, J.J., Feig, S.T. & Thompson, J. (2016) "Sharing" Background Measurements in Wavelength Dispersive Electron Probe Microanalysis. In: Microanalysis Society-Topical Conference on Electron-Probe Microanalysis, Program Guide with Abstracts, 16-19 May 2016, Madison, WI, USA. The Microanalysis Society, 28–29. ISBN: 978-1-5323-0217-6.

Goemann, K., Donovan, J.J., Feig, S.T. & Thompson, J. (2017) Shared backgrounds in wavelength-dispersive electron probe microanalysis. In: Book of Tutorials and Abstracts, 15th European Workshop on Modern Developments and Applications in Microbeam Analysis, 7th Meeting of the International Union of Microbeam Analysis Societies, 7-11 May 2017, Konstanz, Germany. European Microbeam Analysis Society eV 2017, 378–379. ISBN: 978-90-8827-693-0.

Government of South Australia Department for Energy and Mining (2016, Feb) South Australia's Copper Strategy. http://www.energymining.sa.gov.au/minerals.

Grammatikopoulos, T., Mercer, W., Gunning, C. & Prout, S. (2011) Quantitative characterization of the REE minerals by QEMSCAN from the Nechalacho Heavy Rare Earth Deposit, Thor Lake Project, NWT, Canada. SGS Mineral Services Technical Paper, 7, 1–11.

Grandell, L., Lehtilä, A., Kivinen, M., Koljonen, T., Kihlman, S. & Lauri, L.S. (2016) Role of critical metals in the future markets of clean energy technologies. Renewable Energy, 95, 53–62. doi: 10.1016/j.renene.2016.03.102.

Grandia, F., Merino, J. & Bruno, J. (2008) Assessment of the radium-barium co-precipitation and its potential influence on the solubility of Ra in the near-field. Svensk Kärnbranslehantering AB. Technical Report TR-08-07, 52.

Groves, D.I. & Vielreicher, N.M. (2001) The Phalabowra (Palabora) carbonatite-hosted magnetite-copper sulfide deposit, South Africa: An end-member of the iron-oxide copper-gold-rare earth element deposit group? Mineralium Deposita, 36, 189–194.

Groves, D.I., Bierlein, F.P., Meinert, L.D. & Hitzman, M.W. (2010) Iron Oxide Copper-Gold (IOCG) Deposits through Earth History: Implications for Origin, Lithospheric Setting, and Distinction from Other Epigenetic Iron Oxide Deposits. Economic Geology, 105, 641–654.

Gu, Y. (2003) Automated scanning electron microscope based mineral liberation analysis: an introduction to JKMRC/FEI Mineral Liberation Analyzer. Journal of Minerals and Materials Characterization and Engineering, 2, 33–41.

Guastoni, A., Nestola, F. & Giaretta, A. (2009) Mineral Chemistry and Alteration of Rare Earth Element (REE) Carbonates from Alkaline Pegmatites of Mount Malosa, Malawi. American. Mineralogist, 94, 1216–1222. doi: 10.2138/am.2009.3185.

Gupta, C. K. (2003) Chemical Metallurgy: Principles and Practice. Weinheim, Germany: Wiley-VCH. doi: 10.1016/B978-0-408-00567-8.50011-0.

Gysi, A.P. & Williams-Jones, A.E. (2015) The thermodynamic properties of bastnasite-(Ce) and parisite-(Ce). Chemical Geology, 392, 87–101.

Haas, J.R., Shock, E.L. & Sassani, D.C. (1995) Rare Earth Elements in Hydrothermal Systems: Estimates of Standard Partial Molal Thermodynamic Properties of Aqueous Complexes of the Rare Earth Elements at High Pressures and Temperatures. Geochemistry: Exploration, Environment, Analysis, 59, 4329–4350.

Hand, M., Reid, A. & Jagodzinski, L. (2007) Tectonic Framework and Evolution of the Gawler Craton, Southern Australia. Economic Geology, 102, 1377–1395.

Hatert, F., Lefevre, P., Pasero, M. & Fransolet, A. (2003) Graulichite-(Ce), a new arsenate mineral from the Stavelot Massif, Belgium. European Journal of Mineralogy, 15, 733–739.

Haynes, D.W., Cross, K.C., Bills, R.T. & Reed, M.H. (1995) Olympic Dam Ore Genesis: A Fluid-Mixing Model. Economic Geology, 90, 281–307. doi: 10.2113/gsecongeo.90.2.281.

Hayward, N. & Skirrow (2010) Geodynamic Setting and Controls on Iron Oxide Cu-Au-(+-U) Ore in the Gawler Craton, South Australia: In Porter, T.M. (ed.) Hydrothermal Iron Oxide Copper-Gold & Related Deposits: A Global Perspective, v. 3 - Advances in Understanding of IOCG deposits, 1–28. Adelaide: PGC Publishing.

Hazen, R.M., Ewing, R. C. & Sverjensky, D. A. (2009) Evolution of uranium and thorium minerals. American Mineralogist, 94, 1293–1311. doi: 10.2138/am.2009.3208.

Heberling, F., Metz, V., Böttle, M., Curti, E. & Geckeis, H. (2018) Barite recrystallization in the presence of 226 Ra and 133 Ba. Geochimica et Cosmochimica Acta, 232, 124–139. doi: 10.1016/j.gca.2018.04.007.

Hetherington, C.J., Jercinovic, M.J., Williams, M.L. & Mahan, K. (2008) Understanding geologic processes with xenotime: Composition, chronology, and a protocol for electron probe microanalysis. Chemical Geology, 254, 133–147. doi: 10.1016/j.chemgeo.2008.05.020.

Hikov, A., Lerouge, C. & Velinova, N. (2010) Geochemistry of alunite group minerals in advanced argillic altered rocks from the Asarel porphyry copper deposit, Central Srednogorie. Review of the Bulgarian Geology Society, 71, 133–148.

Hikov, A., Velinova, N., Lerouge, C. & Kunov, A. (2017) Geochemistry of advanced argillic altered rocks in the area of Breznik, Western Srednogorie Unit (Bulgaria). Geological Balcanica, 1, 93–108.

Hitzman, M.W. & Valenta, R.K. (2005) Uranium in iron oxide-copper-gold (IOCG) systems. Economic Geology, 100, 1657–1661. doi: 10.2113/gsecongeo.100.8.1657.

Hitzman, M.W., Oreskes, N. & Einaudi, M.T. (1992) Geological characteristics and tectonic setting of Proterozoic iron oxide (Cu-U-Au-REE) deposits. Precambrian Research, 58, 241–287.

Holk, G.J., Kyser, T.K., Chipley, D., Hiatt, E.E. & Marlatt, J. (2003) Mobile Pb-isotopes in Proterozoic sedimentary basins as guides for exploration of uranium deposits. Journal of Geochemical Exploration, 80, 297–320.

Holtstam, D. & Andersson, U.B. (2007) The REE minerals of the Bastnäs-type deposits, South-Central Sweden. The Canadian Mineralogist, 45, 1073–1114.

Holtstam, D., Grins, J. & Nysten, P. (2004) Haleniusite-(La) from the Bastnäs deposit, Västmanland, Sweden: A new REE Oxyfluoride mineral species. The Canadian Mineralogist, 42, 1097–1103.

Hsu, L.C. (1992) Synthesis and Stability of Bastnaesites in a Part of the System (Ce,La)-F-H-C-O. Mineralogy and Petrology, 47, 87–101.

Huang, Q., Kamenetsky, V.S., Ehrig, K., Mcphie, J., Kamenetsky, M., Apukhtina, O. & Chambefort, I. (2017) Effects of hydrothermal alteration on mafic lithologies at the Olympic Dam Cu-U-Au-Ag deposit. Precambrian Research, 292, 305–322. doi: 10.1016/j.precamres.2017.02.013.

Huang, Q., Kamenetsky, V.S., McPhie, J., Ehrig, K., Meffre, S., Maas, R., Thompson, J., Kamenetsky, M., Chambefort, I., Apukhtina, O. & Hu, Y. (2015) Neoproterozoic (ca. 820-830Ma) mafic dykes at Olympic Dam, South Australia: Links with the Gairdner Large Igneous Province. Precambrian Research, 271, 160–172. doi: 10.1016/j.precamres.2015.10.001.

Institute of Nuclear Physics and Particle Physics & EDP-Sciences (2018, Dec) Radioactive Series, http://www.radioactivity.eu.com.

Ismail, R., Ciobanu, C.L., Cook, N.J., Teale, G.S., Giles, D., Schmidt Mumm, A. & Wade, B.P. (2014) Rare Earths and other trace elements in minerals from skarn assemblages, Hillside iron oxide-copper-gold deposit, Yorke Peninsula, South Australia. Lithos, 184–187,456–477. doi: 10.1016/j.lithos.2013.07.023.

Ivanovich, M. & Harmon, R.S. (eds.) (1992) Uranium-series Disequilibrium: Applications to Earth, marine, and Environmental Sciences. 2nd ed, 910. Oxford, UK: Clarendon Press. ISBN: 0 19 854278 X.

Jackson, S.E., Ablation, O.F.L., Fryer, B.J., Longerich, H.P., Dunning, G.R. & Jackson, S.E. (1992) The application of laser-ablation microprobe-inductively coupled plasma- mass spectrometry (LAM-ICP-MS) to in situ trace-element determinations in minerals. The Canadian Mineralogist, 30, 1049–1064.

Jagodzinski, E. (2005) Compilation of SHRIMP U-Pb geochronological data, Olympic Domain, Gawler Craton. South Australia, 2001-2003. Geoscience Australia Record 2005/020.

Jagodzinski, E. (2014) The age of magmatic and hydrothermal zircon at Olympic Dam. Proceedings, Australian Earth Sciences Convention, Sustainable Australia, Newcastle, NSW: July 7-10, Abstract 110, 260.

Janeczek, J. & Ewing, R.C. (1996) Florencite-(La) with fissiogenic REEs from a natural fission reactor at Bangombe, Gabon. American Mineralogist, 81, 1263–1269.

Johnson, C.A., Piatak, N.M. & Miller, M.M. (2017) Chapter D, Barite (Barium): In Schulz, K.J., DeYoung, J.H., Jr., Seal, R.R., II & Bradley, D.C. (eds.) Critical mineral resources of the United States—Economic and environmental geology and prospects for future supply: U.S. Geological Survey Professional Paper 1802. D1–D18. doi: 10.3133/ pp1802D.

Johnson, J.P. & Cross, K.C. (1995) U-Pb Geochronological Constraints on the Genesis of the Olympic Dam Cu-U-Au-Ag Deposit, South Australia. Economic Geology, 90, 1046–1063.

Johnson, J.P. (1993) The geochronology and radiogenic isotope systematics of the Olympic Dam copper-uranium-gold-silver deposit, South Australia. Unpublished Ph.D. thesis, The Australian National University, Canberra. https://openresearch-repository.anu.edu.au/ handle/1885/10918.

Jones, M.J., Butchins, L.J., Charnock, J.M., Pattrick, R.A.D., Small, J.S., Vaughan, D.J., Wincott, P.L. & Livens, F.R. (2011) Reactions of radium and barium with the surfaces of carbonate minerals. Applied Geochemistry, 26, 1231–1238.

Kamenetsky, V.S., Ehrig, K., Maas, R., Meffre, A., Kamenetsky, M., McPhie, J., Apukhtina, O., Huang, Q., Thompson, J., Ciobanu, C.L. & Cook, N.J. (2015) The Supergiant Olympic Dam Cu-U-Au-Ag Ore Deposit: Toward a New Genetic Model. SEG 2015: World Class Ore Deposits: Discovery to Recovery. Hobart: Society of Economic Geologists.

Kamona, A.F., Lévêque, J., Friedrich, G. & Haack, U. (1999) Lead Isotopes of the carbonate-Hosted Kabwe, Tsumeb, and Kipushi Pb-Zn-Cu sulphide deposits in relation to Pan African

orogenesis in the Damaran-Lufilian Fold Belt of Central Africa. Mineralium Deposita, 34, 273–283.

Keyser, W.M., Ciobanu, C.L., Cook, N.J., Dmitrijeva, M., Courtney-Davies, L., Feltus, H., Gilbert, S., Johnson, G. & Ehrig, K. (2019) Iron-oxides constrain BIF evolution in terranes with protracted geological histories: the Iron Count prospect, Middleback Ranges, South Australia. Lithos, 324–325, 20–38.

Khashgerel, B., Kavalieris, I. & Hayashi, K. (2008) Mineralogy, textures, and whole-rock geochemistry of advanced argillic alteration: Hugo Dummett porphyry Cu – Au deposit, Oyu Tolgoi mineral district, Mongolia. Mineralium Deposita, 43, 913–932. doi: 10.1007/s00126-008-0205-3.

Kirchenbaur, M., Maas, R., Ehrig, K., Kamenetsky, V.S., Strub, E., Ballhaus, C. & Münker, C. (2016) Uranium and Sm isotope studies of the supergiant Olympic Dam Cu–Au–U–Ag deposit, South Australia. Geochimica et Cosmochimica Acta, 180, 15–32. doi: 10.1016/j.gca.2016.01.035.

Klinkenberg, M., Brandt, F., Breuer, U. & Bosbach, D. (2014) Uptake of Ra during the recrystallization of barite: a microscopic and time of flight-secondary ion mass spectrometry study. Environmental Science & Technology, 48, 6620–6627. doi: 10.1021/es405502e.

Kontonikas-Charos, A., Ciobanu, C.L. & Cook, N.J. (2014) Albitization and redistribution of REE and Y in IOCG systems: Insights from Moonta-Wallaroo, Yorke Peninsula, South Australia. Lithos 208, 178–201.

Kontonikas-Charos, A., Ciobanu, C.L., Cook, N.J., Ehrig, K., Ismail, R., Krneta, S. & Basak, A. (2018) Feldspar mineralogy and rare earth element (re)mobilization in iron-oxide copper gold systems from South Australia: a nanoscale study. Mineralogical Magazine, 82(S1), S173-S197. doi: 10.1180/minmag.2017.081.040.

Kontonikas-Charos, A., Ciobanu, C.L., Cook, N.J., Ehrig, K., Krneta, S. & Kamenetsky, V.S. (2017) Feldspar evolution in the Roxby Downs Granite, host to Fe-oxide Cu-Au-(U) mineralisation at Olympic Dam, South Australia. Ore Geology Reviews, 80, 838–859. doi: 10.1016/j.oregeorev.2016.08.019.

Kontonikas-Charos, A., Ciobanu, C.L., Cook, N.J., Ehrig, K., Krneta, S. & Kamenetsky, V.S. (2018) Rare earth element geochemistry of feldspars: examples from Fe-oxide Cu-Au systems in the Olympic Cu-Au Province, South Australia. Mineralogy and Petrology, 112, 145–172. doi: 10.1007/s00710-017-0533-z.

Krivovichev, S.V., Krivovichev, V.G. & Hazen, R.M. (2018) Structural and chemical complexity of minerals: correlations and time evolution. European Journal of Mineralogy, 30, 231-236.

Krneta, S., Ciobanu, C.L., Cook, N.J. & Ehrig, K. (2018) Numerical Modeling of REE Fractionation Patterns in Fluorapatite from the Olympic Dam Deposit (South Australia). Minerals, 8, 342. doi: 10.3390/min8080342.

Krneta, S., Ciobanu, C.L., Cook, N.J., Ehrig, K. & Kontonikas-Charos, A. (2016) Apatite at Olympic Dam, South Australia: A petrogenetic tool. Lithos, 262, 470–485. doi: 10.1016/j.lithos.2016.07.033.

Krneta, S., Ciobanu, C.L., Cook, N.J., Ehrig, K. & Kontonikas-Charos, A. (2017) Rare earth element behaviour in apatite from the Olympic Dam Cu-U-Au-Ag deposit, South Australia. Minerals, 7, 1–26. doi: 10.3390/min7080135.

Krneta, S., Cook, N.J., Ciobanu, C.L., Ehrig, K. & Kontonikas-Charos, A. (2017) The Wirrda Well and Acropolis prospects, Gawler Craton, South Australia: Insights into evolving fluid conditions through apatite chemistry. Journal of Geochemical Exploration, 181, 276–291.

Lane, D.J., Cook, N.J., Grano, S.R. & Ehrig, K. (2016) Selective leaching of penalty elements from copper concentrates: A review. Minerals Engineering, 98, 110–121.

Lefebvre, J. & Gasparrini, C. (1987) Florencite, an occurrence in the Zairian Copperbelt. The Canadian Mineralogist, 18, 301–311.

Lehto, J. & Hou, X. (2011) Chemistry and Analysis of Radionuclides, Laboratory Techniques and Methodology, 426. Weinheim, Germany: Wiley-VCH. ISBN 978-3-527-63302-9.

Lottering, M.J., Lorenzen, L., Phala, N.S., Smit, J.T. & Schalkwyk, G.A.C. (2008) Mineralogy and uranium leaching response of low grade South African ores. Minerals Engineering, 21, 16–22. doi: 10.1016/j.mineng.2007.06.006.

Lottermoser, B.G. (1992) Rare earth elements and hydrothermal ore formation processes. Ore Geology Reviews, 7, 25–41. doi: 10.1016/0169-1368(92)90017-F.

Lottermoser, B.G. (1995) Rare earth element mineralogy of the Olympic Dam Cu-U-Au-Ag deposit, Roxby Downs, South Australia: Implications for ore genesis. Neues Jahrbuch für Mineralogie Monatshefte, 8, 371–384.

Lucas, J., Lucas, P., Le Mercier, T., Rollat, A. & Davenport, W. (2015) Rare Earths. Science, Technology, Production and Use. Amsterdam, Netherlands: Elsevier. doi.10.1016/B978-0-444-62735-3.09992-7.

Maas, R., Apukhtina, O.B., Kamenetsky, V.S., Ehrig, K. & Sprung, P. (in preparation) Carbonates at the supergiant Olympic Dam deposit, South Australia. Part II: Radiogenic isotopes (Sr, Nd, Pb, Hf).

Maas, R., Kamenetsky, V.S., Ehrig, K., Meffre, S., McPhie, J. & Diemar, G. (2011) Olympic Dam U-Cu-Au deposit, Australia: New age constraints. Mineralogical Magazine, 75, 1375.

Macmillan, E., Ciobanu, C.L., Ehrig, K., Cook, N.J. & Pring, A. (2016) Chemical zoning and lattice distortion in uraninite from Olympic Dam, South Australia. American Mineralogist, 101, 2351–2354.

Macmillan, E., Ciobanu, C.L., Ehrig, K., Cook, N.J. & Pring, A. (2016) Replacement of uraninite by bornite via coupled dissolution-reprecipitation: Evidence from texture and microstructure. The Canadian Mineralogist, 54, 1369–1383.

Macmillan, E., Cook, N.J., Ehrig, K. & Pring, A. (2017) Chemical and textural interpretation of late-stage coffinite and brannerite from the Olympic Dam IOCG-Ag-U deposit. Mineralogical Magazine, 81, 1323–1366. doi: 10.1180/minmag.2017.081.006.

Macmillan, E., Cook, N.J., Ehrig, K., Ciobanu, C.L. & Pring, A. (2016) Uraninite from the Olympic Dam IOCG-U-Ag deposit: Linking textural and compositional variation to temporal evolution. American Mineralogist, 101, 1295–1320. doi: 10.2138/am-2016-5411.

Mao, M., Simandl, G.J., Spence, J., Neetz, M. & Marshall, D. (2015) Trace element composition of fluorite and its potential use as an indicator in mineral exploration. In Geological Fieldwork, British Columbia Ministry of Energy and Mines, 181–206.

Mattinson, J.M. (2013) Revolution and evolution: 100 years of U-Pb geochronology. Elements, 9, 53–57.

Mauger, A.J., Ehrig, K., Kontonikas-Charos, A., Ciobanu, C.L., Cook, N.J. & Kamenetsky, V.S. (2016) Alteration at the Olympic Dam IOCG–U deposit: insights into distal to proximal feldspar and phyllosilicate chemistry from infrared reflectance spectroscopy. Australian Journal of Earth Sciences, 63, 959–972.

McDonough, W.F. & Sun, S.S. (1995) Composition of the Earth. Chemical Geology, 120, 223–253.

McFarlane, C., Lentz, D. & Dehnavi, A. (2016) Pb-Isotopic study of galena by LA-Q-ICP-MS: Testing a new methodology with applications to base-metal sulphide deposits. Minerals, 6, 1–17. doi: 10.3390/min6030096.

McInnes, B.I.A., Keays, R.R., Lambert, D.D., Hellstrom, J. & Allwood, J.S. (2008) Re-Os geochronology and isotope systematics of the Tanami, Tennant Creek and Olympic Dam Cu-Au deposits. Australian Journal of Earth Sciences, 55, 967–981.

McPhie, J., Kamenetsky, V., Allen, S., Ehrig, K., Agangi, A. & Bath, A. (2011) The fluorine link between a supergiant ore deposit and a silicic large igneous province. Geology, 39, 1003–1006, doi: 10.1130/G32205.1.

McPhie, J., Orth, K., Kamenetsky, V., Kamenetsky, M. & Ehrig, K. (2016) Characteristics, origin and significance of Mesoproterozoic bedded clastic facies at the Olympic Dam Cu–U–Au–Ag deposit, South Australia. Precambrian Research, 276, 85–100. doi: 10.1016/j.precamres.2016.01.029.

Meffre, S., Kamenetsky, V., McPhie, J., Maas, R., Ehrig, K. & Chambefort, I. (2010) Pb isotopes at Olympic Dam: constraining sulphide growth. 13th Quadrennial IAGOD Symposium, Giant Ore Deposits Down-Under, Adelaide. Abstract volume, 78–79.

Meng, D., Wu, X., Han, Y. & Meng, X. (2002) Polytypism and microstructures of the mixed-layer member B_2S, $CaCe_3(CO_3)_4F_3$ in the bastnaesite-(Ce)-synchysite-(Ce) series. Earth and Planetary Science Letters, 203, 817–828.

Migdisov, A., Williams-Jones, A.E., Brugger, J. & Caporuscio, F.A. (2016) Hydrothermal transport, deposition, and fractionation of the REE: Experimental data and thermodynamic calculations. Chemical Geology, 439, 13–42. doi: 10.1016/j.chemgeo.2016.06.005.

Mills, S.J., Kartashov, P.M., Kampf, A.R. & Raudsepp (2010) Arsenoflorencite-(La), a new mineral from the Kommi Republic, Russian Rederation: description and crstal sturcutre. European Journal of Mineralogy, 22, 613–621.

Mondillo, N., Boni, M., Balassone, G., Spoleto, S., Stellato, F., Marino, A., Santoro, L. & Spratt, J. (2016) Rare Earth Elements (REE)—Minerals in the Silius Fluorite Vein System (Sardinia, Italy). Ore Geology Reviews, 74, 211–224.

Montel, J.M., Kato, T., Enami, M., Cocherie, A., Finger, F., Williams, M. & Jercinovic, M. (2018) Electron-microprobe dating of monazite: The story. Chemical Geology, 484, 4–15. doi: 10.1016/j.chemgeo.2017.11.001.

Morrell, J.S. & Jackson, M.J. (eds.) (2013) Uranium Processing and Properties. New York: Springer.

Nagy, G., Draganits, E., Demeny, A., Panto, G. & Arkai, P. (2002) Genesis and transformations of monazite, florencite and rhabdophane during medium grade metamorphism: examples from the Sopron Hills, Eastern Alps. Chemical Geology, 191, 25–46.

Ni, Y., Hughes, J.M. & Mariano, A.N. (1995) Crystal chemistry of the monazite and xenotime structures. American Mineralogist, 80, 21–26. doi: 0003-004X/95/0102-0021.

Ni, Y., Hughes, J.M. & Mariano. A.N. (1993) The Atomic Arrangement of Bastnäsite-(Ce), $Ce(CO_3)F$, and Structural Elements of Synchysite-(Ce), Rontgenite-(Ce), and Parisite-(Ce). American Mineralogist, 78, 415–418.

Ni, Y., Post, J.E. & Hughes, J.M. (2000) The Crystal Structure of Parisite-(Ce), $Ce_2CaF_2(CO_3)_3$. American Mineralogist, 85, 251–258.

Nickel, E.H. & Temperly, J.E. (1987) Aresenoflorencite-(Ce): a new arsenate mineral from Australia. Mineralogical Magazine, 51, 605–609.

Oostingh, K. (2011) Analysis of Rare Earth Element concentrations in barite ($BaSO_4$). Determination of the environment of formation of Archean barites by Rare Earth Element fractionation measurements. Unpublished M.Sc. thesis, Utrecht University, Netherlands.

Oreskes, N. & Einaudi, M.T. (1990) Origin of Rare Earth Element-Enriched Hematite Breccias at the Olympic Dam Cu-U-Au-Ag Deposit, Roxby Downs, South Australia. Economic Geology, 85, 1–28.

Oreskes, N. & Einaudi, M.T. (1992) Origin of hydrothermal fluids at Olympic Dam: preliminary results from fluid inclusions and stable isotopes. Economic Geology, 87, 64–90. doi: 10.2113/gsecongeo.87.1.64.

Oreskes, N. (1990) Uranium content of Olympic Dam hematite: Implications for fluid chemistry and ore depositional mechanisms. Abstracts, A137, Eighth International Association on the Genesis of Ore Deposits, Ottawa.

Owen, N.D., Ciobanu, C., Cook, N., Slattery, A. & Basak, A. (2018) Nanoscale Study of Clausthalite-Bearing Symplectites in Cu-Au-(U) Ores: Implications for Ore Genesis. Minerals, 8, 1-28. doi:10.3390/min8020067.

Owen, N.D., Cook, N.J., Rollog, M., Ehrig, K., Schmandt, D.S. & Ciobanu, C.L. (2018) REE-, Sr- Ca-arsenate-phosphate-sulphate minerals of the woodhouseite series and their role as hosts for radionuclides. Extended abstract, 15th Quadrennial IAGOD Symposium, 187-188, Salta, Argentina.

Owen, N.D., Cook, N.J., Rollog, M., Ehrig, K., Schmandt, D.S., Ram, R., Brugger, J., Ciobanu, C.L., Wade, B.P. & Guagliardo, P. (in review) REE-, Sr-Ca-aluminum phosphate-sulphate minerals of the woodhouseite series and role as hosts for radionuclides. American Mineralogist.

Papoutsa, A. & Pe-Piper, G. (2014) Variation of REE-Hydrothermal Circulation in Complex Shear Zones: The Cobequid Highlands, Nova Scotia. The Canadian Mineralogist, 52, 943–968.

Paton, C., Hellstrom, J., Paul, B., Woodhead, J. & Hergt, J. (2011) Iolite: Freeware for the visualisation and processing of mass spectrometric data. Journal Analytical Atomic Spectrometry, 26, 2508–2518. doi: 10.1039/c1ja10172b.

Paul, B., Woodhead, J., Hergt, J., Danyushevsky, L., Kunihiro, T. & Nakamura, E. (2011) Melt inclusion Pb-isotope analysis by LA-MC-ICPMS: Assessment of analytical performance and application to OIB genesis. Chemical Geology, 289, 210–223.

Pe-Piper, G. & Dolansky, L.M. (2015) Early diagenetic origin of Al phosphate-sulfate minerals (woodhouseite and crandallite series) in terrestrial sandstones, Nova Scotia, Canada. American Mineralogist, 90, 1434–1441. doi: 10.2138/am.2005.1790.

Porter, T.M. (ed.) (2000) Hydrothermal Iron Oxide Copper–Gold and Related Deposits: A Global Perspective, vol. 1, 349. Adelaide: PGC Publishing.

Porter, T.M. (ed.) (2002) Hydrothermal Iron Oxide Copper–Gold and Related Deposits: A Global Perspective, vol. 2, 378. Adelaide: PGC Publishing.

Porter, T.M. (ed.) (2010) Hydrothermal Iron Oxide Copper–Gold and Related Deposits: A Global Perspective – Advances in the Understanding of IOCG Deposits, vols 3 and 4, 600. Adelaide: PGC Publishing.

Pownceby, M.I. & Johnson, C. (2014) Geometallurgy of Australian uranium deposits. Ore Geology Reviews, 56, 25–44. doi: 10.1016/j.oregeorev.2013.07.001.

Preiss, W.V. (1987) The Adelaide Geosyncline: Late Proterozoic stratigraphy, sedimentation, palaeontology and tectonics. Geological Survey of South Australia Bulletin 53, Dep. Mines Energy.

Prieto, M., Astilleros, J.M. & Fernández-Díaz, L. (2013) Environmental remediation by crystallization of solid solutions. Elements. 9, 195–201. doi: 10.2113/gselements.9.3.195.

Putnis, C.V. & Ruiz-Agudo, E. (2013) The mineral–water interface. Where Minerals React with the Environment. Elements, 9, 177–182. doi: 10.2113/gselements.9.3.177.

Putnis, C.V., Tsukamoto, K. & Nishimura, Y. (2005) Direct observations of pseudomorphism: compositional and textural evolution at a fluid–solid interface. American Mineralogist. 90, 1909–1912. doi: 10.2138/am.2005.1990.

Rashed, M.N. (2001) Lead removal from contaminated water using mineral adsorbents. The Environmentalist, 21, 187–195.

Rasmussen, B. & Muhling, J.R. (2009) Reactions destroying detrital monazite in greenschist-facies sandstones from the Witwatersrand basin, South Africa. Chemical Geology, 264, 311–327. doi: 10.1016/j.chemgeo.2009.03.017.

Rasmussen, B. (1996) Early diagenetic REE-phosphate minerals (florencite, gorceixite, crandallite, and xenotime) in marine sandstones:A major sink for oceanic phosphorus. American Journal of Science, 296, 601–632.

Reed, S.J.B., Trueman, N.A. & Long, J.V.P. (1987) Ion microprobe U-Pb dating of pitchblende: In Benninghaven, A., Huber, A.W. & Werner, H.W. (eds) Secondary Ion Microscopy (SIMS VI). Wiley, 945–948.

Reeve, J.S., Cross, K. C., Smith, R.N. & Oreskes, N. (1990) Olympic Dam Cu-U-Au-Ag deposit: In Hughes, F.E. (ed.) Geology of the Mineral Deposits of Australia and Papua New Guinea. Victoria, Australia, 1828. Australasian Institute of Mining and Metallurgy. ISBN: 0949106534, 9780949106537.

Reid, A.J. & Hand, M. (2012) Mesoarchean to Mesoproterozoic evolution of the southern Gawler Craton, South Australia. Episodes, 35, 216–225.

Reid, A.J., Hand, M., Jagodzinski, E., Kelsey, D. & Pearson, N. (2008) Paleoproterozoic orogenesis in the southeastern Gawler Craton, South Australia Paleoproterozoic orogenesis in the southeastern Gawler. Australian Earth Sciences Convention, 55, 449–471. doi: 10.1080/08120090801888594.

Repina, S.A., Khiller, V.V. & Makagonov, E.P. (2014) Microheterogeneity of Crystal Growth Zones as a Result of REE Fractionation. Geochemistry International, 52, 1057–1071.

Roberts, D.E. & Hudson, G.R.T. (1983) The Olympic Dam Copper-Uranium-Gold Deposit, Roxby Downs, South Australia. Economic Geology, 78, 799–822.

Rollog, M., Cook, N.J., Guagliardo, P., Ciobanu, C.L., Ehrig. K. & Kilburn, M. (2018) Mobility of radionuclides in the Olympic Dam Cu-U-Au-Ag deposit, South Australia. Extended abstract, International Association on the Genesis of Ore Deposits Quadrennial Symposium, Salta Argentina, August 2018.

Rollog, M., Cook, N.J., Guagliardo, P., Ehrig. K. & Kilburn, M. (2019) In situ spatial distribution mapping of radionuclides in minerals by nanoSIMS. Geochemistry: Exploration. Environment, Analysis. doi: 10.1144/geochem2018-038.

Rosenberg, Y.O., Metz, V. & Ganor, J. (2011) Co-precipitation of radium in high ionic strength systems: 1. Thermodynamic properties of the Na-Ra-Cl-SO_4-H_2O system – Estimating Pitzer parameters for $RaCl_2$. Geochimica et Cosmochimica Acta, 75, 5489–5402.

Rosenberg, Y.O., Metz, V. & Ganor, J. (2013) Radium removal in a large scale evaporitic system. Geochimica et Cosmochimica Acta, 103, 121–137.

Rosenberg, Y.O., Metz, V., Oren, Y., Volkman, Y. & Ganor, J. (2011) Co-precipitation of radium in high ionic strength systems: 2. Kinetic and ionic strength effects. Geochimica et Cosmochimica Acta, 75, 5403–5422.

Rosenberg, Y.O., Sade, Z. & Ganor, J. (2018) The precipitation of gypsum, celestine, and barite and coprecipitation of radium during seawater evaporation. Geochimica et Cosmochimica Acta, 233, 50–65. doi: 10.1016/j.gca.2018.04.019.

Rosenberg, Y.O., Sadeh, Y., Metz, V., Pina, C.M. & Ganor, J. (2014) Nucleation and growth kinetics of $Ra_xBa_{1-x}SO_4$ solid solution in NaCl aqueous solutions. Geochimica et Cosmochimica Acta, 125, 290–307.

Rosholt, J.N., Zartman, R.E. & Nkomo, I.T. (1973) Lead isotope systematics and uranium depletion in the Granite Mountains, Wyoming. Bulletin of the Geological Society of America, 84, 989–1002.

Ruiz-Agudo, C., Putnis, C.V., Ruiz-Agudo, E. & Putnis, A. (2015) The influence of pH on barite nucleation and growth. Chemical Geology, 391, 7–18. doi: 10.1016/j.chemgeo.2014.10.023.

Ruiz-Agudo, E., Putnis, C.V. & Putnis, A. (2014) Coupled dissolution and precipitation at mineral–fluid interfaces. Chemical Geology, 282, 132–146. doi: 10.1016/j.chemgeo.2014.06.007.

Savko, K.A. & Bazikov, N.S. (2011) Phase Equilibria of Bastnaesite, Allanite, and Monazite: Bastnaesite-out Isograde in Metapelites of the Vorontsovskaya Group, Voronezh Crystalline Massif. Petrology, 19, 445–469.

Schmandt, D.S., Cook, N.J., Ciobanu, C.L., Ehrig, K., Wade, B.P., Gilbert, S. & Kamenetsky, V.S. (2017) Rare earth element fluorocarbonate minerals from the Olympic Dam Cu-U-Au-Ag deposit, South Australia. Minerals, 7. doi: 10.3390/min7100202.

Schmandt, D.S., Cook, N.J., Ciobanu, C.L., Ehrig, K., Wade, B.P., Gilbert, S. & Kametetsky, V.S. (2019) Rare earth element phosphates from the Olympic Dam Cu-U-Au-Ag deposit, South Australia: Recognizing temporal-spatial controls on REE mineralogy in an evolved IOCG system. The Canadian Mineralogist, 57, 1–22. doi: 10.3749/canmin.1800043.

Schmandt, D.S., Cook, N.J., Ehrig, K., Gilbert, S., Wade, B.P., Rollog, M., Ciobanu, C.L. & Kamenetsky, V.S. (2019) Uptake of trace elements during copper ore processing: a case study from Olympic Dam, South Australia. Minerals Engineering, 135, 83–94. doi: 10.1016/j.mineng.2019.02.034.

Schönenberger, J., Köhler, J. & Markl, G. (2008) REE systematics of fluorides, calcite and siderite in peralkaline plutonic rocks from the Gardar Province, South Greenland. Chemical Geology, 247, 16–35. doi: 10.1016/j.chemgeo.2007.10.002.

Shivaramaiah, R., Anderko, A., Riman, R.E. & Navrotsky, A. (2016) Thermodynamics of Bastnaesite: A Major Rare Earth Ore Mineral. American Mineralogist, 101, 1129–1134.

Sizaret, S., Marcoux, E., Jébrak, M. & Touray, J.C. (2004) The Rossignol Fluorite Vein, Chaillac, France: Multiphase hydrothermal activity and intravein sedimentation. Economic Geology, 1107–1122. doi: 10.2113/gsecongeo.99.6.1107.

Skirrow, R.G., Bastrakov, E., Davidson, G., Raymond, O.L. & Heithersay, P. (2002) The Geological Framework, Distribution and Controls of Fe-Oxide Cu-Au Mineralization in the Gawler Craton, South Australia. Part II - Alteration and Mineralisation: In Porter, T.M. (ed.) Hydrothermal Iron Oxide Copper–Gold and Related Deposits: A Global Perspective, vol. 2. Adelaide: PGC Publishing.

Skirrow, R.G., Bastrakov, E.N. & Barovich, K. (2006) Metals and fluids in IOCG systems of the Gawler Craton: Constraints from Nd, O, H and S isotopes. Goldschmidt Conference Abstracts, A595. doi: 10.1016/j.gca.2006.06.1105.

Skirrow, R.G., Bastrakov, E.N., Barovich, K., Fraser, G.L., Creaser, R.A., Fanning, C.M., Raymond, O.L. & Davidson, G.J. (2007) Timing of Iron Oxide Copper-Gold Hydrothermal Activity and Nd Isotope Constraints on Metal Sources in the Gawler Craton, South Australia. Economic Geology, 102, 1441–1470. doi: 10.2113/gsecongeo.102.8.1441.

Skirrow, R.G., van der Wielen, S.E., Champion, D.C., Czamota, K. & Thiel, S. (2018) Lithospheric Architecture and Mantle Metasomatism Linked to Iron Oxide Cu-Au Ore Formation: Multidisciplinary Evidence from the Olympic Dam Region, South Australia. Geochemistry, Geophysics, Geosystems, 19, 2673–2705. doi: 10.1029/2018GC007561.

Smith, M.P., Henderson, P. & Campbell, L.S. (2000) Fractionation of the REE during Hydrothermal Processes: Constraints from the Bayan Obo Fe-REE-Nb Deposit, Inner Mongolia, China. Geochimica et Cosmochimica Acta, 64, 3141–3160.

Stoffregen, R.E. & Alpers, C.N. (1987) Woodhouseite and svanbergite in hydrothermal ore deposits: products of apatite destruction during advanced argillic alteration. The Canadian Mineralogist, 25, 201–211.

Sugden, T.J. & Cross, K.C. (1991) Significance of overprinting fault systems in the Olympic Dam Breccia Complex: In Structural Geology in Mining and Exploration, Geology Department (Key Centre) & University Extension, The University of Western Australia, 93–98.

Švedkauskaitė-LeGore, J., Mayer, K., Millet, S., Nicholl, A., Rasmussen, G. & Baltrūnas, D. (2007) Investigation of the isotopic composition of lead and of trace elements concentrations in natural uranium materials as a signature in nuclear forensics. Radiochimica Acta, 95, 601–605.

Sverdrup, T.L. (1968) Yttrofluorite-yttrocerite-cerfluorite in Norwegian Pegmatites. Contribution to the Mineralogy of Norway No. 37, Norsk Geologisk Tidsskrift, 48, 245–252.

Sylvester, P. (2008) Laser Ablation–ICP–MS in the Earth Sciences Current Practices and Outstanding Issues. Mineralogical Association of Canada Short Course, 40.

Takano, B. & Watanuki, K. (1974) Geochemical implications of the lead content of barite from various origins. Geochemical Journal, 8, 87–95.

Tanaka, K., Takahashi, Y. & Shimizu, H. (2008) Local structure of Y and Ho in calcite and its relevance to Y fractionation from Ho in partitioning between calcite and aqueous solution. Chemical Geology, 248, 104–113.

Torapava, N., Ramebäck, H., Curti, E., Lagerkvist, P. & Ekberg, C. (2014) Recrystallization of 223Ra with barium sulfate. Journal of Radioanalytical and Nuclear Chemistry, 301, 545–553. doi: 10.1007/s10967-014-3170-6.

Tungpalan, K., Manlapig, E., Andrusiewicz, M., Keeney, L., Wightman, E. & Edraki, M. (2015) An integrated approach of predicting metallurgical performance relating to variability in deposit characteristics. Minerals Engineering, 71, 49–54. doi: 10.1016/j.mineng.2014.10.004.

Tungpalan, K., Wightman, E. & Manlapig, E. (2015) Relating mineralogical and textural characteristics to flotation behaviour. Minerals Engineering, 82, 136–140. doi: 10.1016/j.mineng.2015.02.005.

Uchida, A., Toyoda, S., Ishibashi, J. & Nakai S. (2015) ^{226}Ra-^{210}Pb and ^{228}Ra-^{228}Th Dating of Barite in Submarine Hydrothermal Sulfide Deposits Collected at the Okinawa Trough and the Southern Mariana Trough: In Ishibashi J., Okino K. & Sunamura M. (eds.) Subseafloor Biosphere Linked to Hydrothermal Systems, 607–615. Tokyo: Springer.

University of Adelaide Institute for Mineral and Envery Resources (Aug, 2018) https://www.adelaide.edu.au/copper-uranium-research/.

Van Landuyt, J. & Amelinckx, S. (1975) Multiple Beam Direct Lattice Imaging of New Mixed-Layer Compounds of the Bastnaesite-Synchisite Series. American Mineralogist, 60, 351–358.

Varga, Z., Wallenius, M., Mayer, K., Keegan, E. & Millet, S. (2009) Application of lead and strontium isotope ratio measurements for the origin assessment of uranium ore concentrates. Analytical Chemistry, 81, 8327–8334.

Vasyukova, O. & Williams-Jones, A.E. (2016) The Evolution of Immiscible Silicate and Fluoride Melts: Implications for REE Ore-Genesis. Geochimica et Cosmochimica Acta, 172, 205–224.

Veksler, I.V., Dorfman, A.M., Kamenetsky, M., Dulski, P. & Dingwell, D.B. (2005) Partitioning of lanthanides and Y between immiscible silicate and fluoride melts, fluorite and cryolite and the origin of the lanthanide tetrad effect in igneous rocks. Geochimica et Cosmochimica Acta, 69, 2847–2860. doi: 10.1016/j.gca.2004.08.007.

Verdugo-Ihl, M.R., Ciobanu, C.L., Cook, N.J., Ehrig, K., Courtney-Davies, L. & Gilbert, S. (2017) Textures and U-W-Sn-Mo signatures in hematite from the Olympic Dam Cu-U-Au-Ag deposit, South Australia: Defining the archetype for IOCG deposits. Ore Geology Reviews, 91, 173–195. doi: 10.1016/j.oregeorev.2017.10.007.

Vinograd, V.L., Brandt, F., Rozov, K., Klinkenberg, M., Refson, K., Winkler, B. & Bosbach, D. (2013) Solid-aqueous equilibrium in the $BaSO_4$-$RaSO_4$-H_2O system: First-principles calculations and a thermodynamic assessment. Geochimica et Cosmochimica Acta, 122, 398–417.

Vinograd, V.L., Kulik, D.A., Brandt, F., Klinkenberg, M., Weber, J., Winkler, B. & Bosbach, D. (2018) Thermodynamics of the solid solution-Aqueous solution system $(Ba,Sr,Ra)SO_4$ + H_2O: I. The effect of strontium content on radium uptake by barite. Applied Geochemistry, 89, 59–74. doi: 10.1016/j.apgeochem.2017.11.009.

Vinograd, V.L., Kulik, D.A., Brandt, F., Klinkenberg, M., Weber, J., Winkler, B. & Bosbach, D. (2018) Thermodynamics of the solid solution-Aqueous solution system $(Ba,Sr,Ra)SO_4$ + H_2O: II. Radium retention in barite-type minerals at elevated temperatures. Applied Geochemistry, 93, 190–208. doi: 10.1016/j.apgeochem.2017.10.019.

Vircava, I., Somelar, P., Liivamägi, S., Kirs, J. & Kirsimäe, K. (2015) Origin and paleoenvironmental interpretation of aluminum phosphate–sulfate minerals in a Neoproterozoic Baltic paleosol. Sedimentary Geology, 319, 114–123. doi: 10.1016/j.sedgeo.2015.02.003.

Wade, C.E., Reid, A.J., Wingate, M.T.D., Jagodzinski, E.A. & Barovich, K. (2012) Geochemistry and geochronology of the c. 1585Ma Benagerie Volcanic Suite, southern Australia: Relationship to the Gawler Range Volcanics and implications for the petrogenesis of a Mesoproterozoic silicic large igneous province. Precambrian Research, 206–207, 17–35. doi: 10.1016/j.precamres.2012.02.020.

Wang, L., Ni, Y., Hughes, J.M., Bayliss, P. & Drexler, J.W. (1994) The atomic arrangement of synchysite-(Ce), $CeCaF(CO_3)_2$. The Canadian Mineralogist, 32, 865–871.

Wang, R.S., Chau, A.S.Y., Liu, F., Cheng, H., Nar, P., Chen, X.M. & Wu, Q.Y. (1993) Studies on the adsorption and migration of radium in the natural minerals. Journal of Radioanalytical and Nuclear Chemistry, 171, 347–364.

Watson, E.B. (2004) A conceptual model for near-surface kinetic controls on the trace- element and stable isotope composition of abiogenic calcite crystals. Geochimica et Cosmochimica Acta, 68, 1473–1488. doi: 10.1016/j.gca.2003.10.003.

Weber, J., Barthel, J., Brandt, F., Klinkenberg, M., Breuer, U., Kruth, M. & Bosbach, D. (2016) Nano-structural features of barite crystals observed by electron microscopy and atom probe tomography. Chemical Geology, 424, 51–59.

Weber, J., Barthel, J., Klinkenberg, M., Bosbach, D., Kruth, M. & Brandt, F. (2017) Retention of ^{226}Ra by barite: The role of internal porosity. Chemical Geology, 466, 722–732.

Webster, A.E. (2004) The Structural Evolution of the Broken Hill Pb-Zn-Ag Deposit, New South Wales. Unpublished Ph.D. thesis, University of Tasmania, Hobart.

Weng, Z., Jowitt, S.M., Mudd, G.M. & Haque, N. (2015) A Detailed Assessment of Global Rare Earth Element Resources: Opportunities and Challenges. Economic Geology, 110, 1925–1952.

Williams, P.J., Barton, M.D., Johnson, D.A., Fontbote, L., de Haller, A., Mark, G., Oliver, N.H.S. & Marschik, R. (2005) Iron Oxide Copper-Gold Deposits: Geology, Space-Time Distribution, and Possible Modes of Origin. Economic Geology 100th Anniversary Volume, 371–405.

Williams-Jones, A.E. & Wood, S.A. (1992) A preliminary petrogenetic grid for REE fluorocarbonates and associated minerals. Geochimica et Cosmochimica Acta, 56, 725–738.

Williams-Jones, A.E., Migdisov, A.A. & Samson, I.M. (2012) Hydrothermal Mobilisation of the Rare Earth Elements–a Tale of "Ceria" and "Yttria". Elements, 8, 355–360. doi: 10.2113/gselements.8.5.355.

Woodhead, J.A., Hergt, J., Meffre, S., Large, R.R., Danyushevsky, L. & Gilbert, S. (2009) In situ Pb-isotope analysis of pyrite by Laser Ablation (Multi-Collector and Quadrupole) ICPMS. Chemical Geology, 262, 380–390.

Wu, X., Dawei, M., Zhaolu, P. & Guangming, Y. (1998) Transmission Electron Microscopic Study of New, Regular, Mixed-Layer Structures in Calcium-Rare-Earth Fluorocarbonate Minerals. Mineralogical Magazine, 62, 55–64.

Yang, H., Dembowski, R.F., Conrad, P.G. & Downs, R.T. (2008) Crystal Structure and Raman Spectrum of Hydroxyl-Bästnasite-(Ce), $CeCO_3(OH)$. American Mineralogist, 93, 698–701.

Zainurin, A.H.M., Cook, N.J., Ciobanu, C.L., Slattery, A., Schmandt, D.S. & Liu, W. (2018) Compositional and Textural Characterization of Rare Earth Element Fluorocarbonate Minerals. University of Adelaide, B. Eng. (Hons.) poster, Ingenuity 2018.

Zaitsev, A.N., Wall, F. & Le Bas, M.J. (1998) REE-Sr-Ba minerals from the Khibina Carbonatites, Kola Peninsula, Russia: Their mineralogy, paragenesis and evolution. Mineralogical Magazine, 62, 225–250.